DANMARKS OG GRØNLANDS GEOLOGISKE UNDERSØGELSE RAPPORT 2012/106

Nanok-1 Core Well, GGU 517004, Hold with Hope, Northeast Greenland – Final Well Report

Contribution to Petroleum Geological Studies, Services, and Data in East and Northeast Greenland

Volume 1(2)

Jussi Hovikoski, Jørgen A. Bojesen-Koefoed,
John Boserup, Kirsten Fries, Paul Green,
Rikke Weibel, Morten Leth Hjuler, Peter Japsen,
Claus Kjøller, Lotte Melchior Larsen,
Holger Lindgren, Caterina Morigi, Peter Nytoft,
Henrik Nøhr-Hansen, Mette Olivarius,
Henrik Ingermann Petersen,
Anders Pilgaard, Emma Sheldon,
Niels Springer & Jens Therkelsen

GEOLOGICAL SURVEY OF DENMARK AND GREENLAND
MINISTRY OF ENVIRONMENT AND ENERGY

G E U S

DANMARKS OG GRØNLANDS GEOLOGISKE UNDERSØGELSE RAPPORT 2012/106

Nanok-1 Core Well, GGU 517004, Hold with Hope, Northeast Greenland – Final Well Report

Contribution to Petroleum Geological Studies, Services, and Data in East and Northeast Greenland

Volume 1(2)

Jussi Hovikoski, Jørgen A. Bojesen-Koefoed, John Boserup, Kirsten Fries, Paul Green, Rikke Weibel, Morten Leth Hjuler, Peter Japsen, Claus Kjøller, Lotte Melchior Larsen, Holger Lindgren, Caterina Morigi, Peter Nytoft, Henrik Nøhr-Hansen, Mette Olivarius, Henrik Ingermann Petersen, Anders Pilgaard, Emma Sheldon, Niels Springer & Jens Therkelsen

Confidential report

Copy No.

Released 01-07-2025

GEOLOGICAL SURVEY OF DENMARK AND GREENLAND
DANISH MINISTRY OF CLIMATE, ENERGY AND BUILDING

G E U S

1. Executive summary

This report presents the core data package of the Nanok-1 core drilled in eastern Hold with Hope, NE Greenland in 2011. The report is delivered to the participating sponsoring companies of the specific analytical programme of the Nanok-1 core as described in appendix B4 in the collaboration agreement between GEUS and sponsoring oil companies regarding petroleum geological studies, services and data in East and Northeast Greenland.

The Nanok-1 drill site is situated at Knudshoved, east coast of Hold-with Hope. The main target of the drilling was the Campanian – Upper Cenomanian interval of the Fosdalen Formation (note the redefined usage after Bjerager *et al.*, 2012). The primary objectives were to investigate reservoir quality, source rock potential and preliminary cap-rock properties of the drilled interval. The core reached a total depth of 168 m with > 96 % core recovery.

The coring was followed by an extensive analytical programme that included total GR- and density logging, detailed sedimentological description of the core, erection of biostratigraphic and lithostratigraphic divisions, determination of mineralogy, diagenesis, inorganic geochemistry and preliminary cap-rock properties, sonic velocity measurements, analyses of petroleum potential, thermal maturity, biomarkers and stable carbon isotopes, characterization of an igneous intrusion and an uplift (AFTA) study.

The Nanok-1 core penetrates the Upper Cenomanian – Lower Campanian interval of the Fosdalen Formation. This interval is subdivided into 1) the Upper Cenomanian – Coniacian undifferentiated Fosdalen Formation (~160–~84.2m); 2) the Middle Coniacian – Lower Santonian Nanok Member (~84.2–83m); 3) the Upper Santonian – Lower Campanian Østersletten Member (~83–42.5m); and 4) the Lower Campanian Knudshoved Member (~42.5–0m). The base of the core (TD–~160m) consists of an igneous intrusion. The Nanok Member is inferred to be present at a thin interval of non-recovery of core and limited rubble below the Østersletten Member.

The sedimentary facies show that the Upper Cenomanian Fosdalen Formation was deposited in a basinal and/or incipient slope setting. The data suggest that the zone of maximum flooding of the drilled succession situates within this interval. This interpretation is in line with source rock screening data, which shows incipient source rock development in this zone (see below).

The basinal/incipient slope sedimentation was replaced by tidally-influenced mudstones and sandstones during the latter part of the Upper Cenomanian and Coniacian. This interval is also characterized by recurring, minor hiatal surfaces. Although relatively little is known about the relationship between deep sea tides and sea level change, some data suggest that tidal-currents are amplified in deep sea environments during forced regressions.

The overall Upper Cenomanian – Coniacian regressive and/or forced regressive development was apparently punctuated by two flooding events during the Turonian (~107–100 m) and in particular during the Middle Coniacian (at ~93–85 m), which led to reestablishment of transitional basinal conditions.

A major relative sea level drop allegedly took place during the Middle Coniacian – Early Santonian (the Nanok Mb). This was followed by deposition of structureless high density turbidites mainly during the Upper Santonian. These Østersletten Mb sandstones are interpreted to be part of a small-scale sand-dominated fan near base of slope. In addition to the sedimentary facies, pervasive coal particles and locally decreasing dinoflagellate diversity are in line with a low stand phase during this time.

The Early Campanian records an abrupt drowning of the lowstand fan system and reappearance of bottom current influenced basinal mudstone sedimentation (the Knudshoved Mb). The Campanian succession is somewhat aggradational and lacks clear relative sea level trends.

The Østersletten Mb comprises approximately 40 m of sandstones considered to be of reasonably good reservoir quality. The net/gross ratio is estimated to be 81–88% based on a 15% porosity cut-off value. The average porosity of the reservoir quality sandstone is 21–22%, and the average permeability ranges between 50–150 mD.

The mudstones analyzed in general show no petroleum source potential, but downwards from a depth of app. 100 m, a steady increase in petroleum potential is observed.

Most of the drilled mudstones are thermally immature (VR= ~0.60%R_o.), but as a result of local heating from an intrusion at the base, about 20 m of mudstones pass through the oil window.

There are two oil shows in core, which according to the biomarker data are not older than Cretaceous. Moreover, the biomarker analyses indicate that the oil shows have a composition related to that of the mudstones from the core, but originate from a more marine-dominated interval than is present/preserved in the drilled interval. The relatively more marine character of the oil shows is confirmed by stable carbon isotopic data. The source of the oil shows is thought to be the interval around the intrusion at the base and below the core. However, due to high levels of thermal maturity, mudstones deeper than approximately 150 m do not lend themselves to analysis, and the assumption thus cannot be tested analytically.

Although the original petroleum potential of the presumed source mudstones cannot be evaluated, circumstantial evidence allows a rough estimate to be made leading to two scenarios, a conservative and an optimistic. The conservative scenario suggests a source thickness of 50 m with a petroleum potential of 4–6 kg HC/ton, i.e. app. 625,000 ton HC/km^2 or app. 4,000,000 bbl/km^2. The optimistic scenario suggest a source thickness of 50 m with a petroleum potential of 4–9 kg HC/ton, i.e. app. 750,000 ton HC/km^2 or app. 5,000,000 bbl/km^2

Finally, the preliminary cap rock data suggests that the Fosdalen Formation mudstones are excellent caprocks having extremely small pore throats and very high capillary entry pressures.

1.1 Main conclusions

Stratigraphy

- The Nanok-1 core penetrates the Upper Cenomanian – Lower Campanian interval of the Fosdalen Formation (note redefined use). This interval is subdivided into 1) the Upper Cenomanian – Middle Coniacian undifferentiated Fosdalen Formation (~160–~84.2m); 2) the ?Middle Coniacian – ?Middle Santonian Nanok Member (~84.2–83m); 3) the Upper Santonian – Lower Campanian Østersletten Member (~83–42.5m); and 4) the Lower Campanian Knudshoved Member (~42.5–0m). The base of the core (TD–

~160m) consists of an igneous intrusion. The Nanok Member is inferred to be present at a thin interval of non-recovery of core and limited rubble below the Østersletten Member.

Sedimentology

- The deposits are interpreted to comprise basinal or incipient slope mudstones (FA1), tidally-influenced mudstones and sandstones (FA2), lowstand fan related gravity flow sandstones (FA3) and bottom current influenced fossiliferous mudstones (FA4). The condensed Nanok MB is represented by missing core and a few core pieces of rubble.

Mineralogy, diagenesis and inorganic geochemistry

- The diagenetic sequence for the sandstones in Østersletten Member comprises early pyrite, often associated with organic matter, which is very common in the sandstones. Pyrite is followed by siderite and kaolinite, which are common authigenic minerals in the sandstones and both seem to be related to and/or formed from mica. Dissolution of feldspars and shell fragments may have promoted ankerite precipitation. Ankerite is post-dating siderite but is believed to be forming later or contemporaneous with kaolinite. Dissolution of K-feldspar is probably later than ankerite precipitation. Quartz overgrowths occur only as minor amounts in the sandstones and quartz was the last cement to develop.
- The reservoir quality of the Østersletten Mb sandstones is mainly influenced by porosity and permeability reduction caused by abundant detrital mica, which again has caused precipitation of kaolinite and siderite. Further, facies, which contain abundant mica, coal fragments and are finer-grained often show lower porosity and especially low permeability (see below).
- The hiatal surfaces common for FA2 contain mainly ankerite and siderite cements. The cements are an early diagenetic phase, which is seen by the detrital grains “floating” in the cement.
- Hematite and goethite are present in the outcrop sample from the Nanok Mb.
- The two mudstone intervals, the undifferentiated part of the Fosdalen Formation and the Knudshoved Member, are geochemically almost identical. The sandstones of the Østersletten Member are geochemically somewhat different from the mudstones of the Fosdalen Formation. The muddy sandstones of the Østersletten member have geochemical ratios similar to the mudstones, but distinctly different ratios compared to the sandstones. The heavy mineral content seems to be different between the sandstones and the mudstones, as the Østersletten Member has more mature composition.

- Ankerite-dolomite cement is typical in the Østersletten Member, whereas siderite cement besides other carbonate cement occurs in the Fosdalen Formation.

CCAL and Reservoir quality

- The Østersletten Mb comprises approximately 40 m of sandstones considered to be of reasonably good reservoir quality. The net/gross ratio is estimated to be 81–88% based on a 15% porosity cut-off value. The average porosity of the reservoir quality sandstone is 21–22%, and the average permeability ranges between 50–150 mD.

Petroleum Geochemistry

- The mudstones in general show no petroleum source potential, but downwards from a depth of app. 100 m, a steady increase in petroleum potential is observed.
- From a depth of app. 140 m, the trend is reversed due to thermal maturation caused by the intrusion encountered at app. 160 m.
- The succession down to a depth of approximately 140 m is thermally immature with VR values around 0.60%R_o.
- A rapid increase in thermal maturity is recognised below 140 m towards the intrusion encountered at 160 m. Within these about 20 m the mudstones are locally matured by the intrusion-induced increase in heat flow, and they pass through the oil window as demonstrated by several independent maturity parameters.
- Hence, the over a thickness of less than 15 m the deposits realize their total petroleum potential and thermal destruction takes over closer to the intrusion.
- Oil presumably generated from the sediments are preserved as marked oil staining in a sandstone/heterolith interval from app. 95–100 m and as less pronounced staining near the top of the Østersletten Mb. sandstones at approximately 46 m.
- Stable Carbon isotopic data indicate an overall terrestrially influenced marine or "deltaic" depositional environment for all samples. All stain samples show very similar composition. The mudstone samples yield slightly more terrestrial signals compared to the stain samples, which is in keeping with the assumption that the oil was primarily generated by more marine mudstones closer to the intrusion encountered at the base of the corehole.
- Biomarkers indicate source age not older than Cretaceous for the oil stains. Moreover, the stains contain e.g., moderate concentration of bicadinanes (angiosperm input), which has not been previously found in North East Greenland.
- The original petroleum potential of the presumed source mudstones cannot be evaluated but circumstantial evidence allows a rough estimate to be made leading to two sce-

narios, a conservative and an optimistic. The conservative scenario suggests a source thickness of 50 m with a petroleum potential of 4–6 kg HC/ton, i.e. app. 625,000 ton HC/km^2 or app. 4,000,000 bbl/km^2. The optimistic scenario suggest a source thickness of 50 m with a petroleum potential of 4–9 kg HC/ton, i.e. app. 750,000 ton HC/km^2 or app. 5,000,000 bbl/km^2

Caprock

- Caprock analyses show that the Fosdalen Formation mudstones are excellent caprocks having extremely small pore throats and very high capillary entry pressures.

Interpreted thermal history

- VR values define maximum palaeotemperatures between 93 and 100°C which are highly consistent with AFTA data. The VR data confirm that this episode represents post-depositional heating and that these VR values represent a palaeo-thermal maximum from which cooling began sometime after deposition of the sedimentary sequence (Lower Campanian) and 40 Ma.
- Deeper VR data show the effects of contact heating due to an intrusion intersected at depth in the borehole. The likely age of the intrusion is thought to be 51–53 Ma (see Igneous intrusion below) and the timing of the earlier event identified from AFTA is consistent with this timing. It therefore seems likely that the whole section above the intrusion cooled from maximum post-depositional palaeotemperatures following emplacement of the intrusion in the Early Eocene. While contact heating effects are likely to be restricted to the vicinity of the intrusion, more widespread effects may be caused by hydrothermal effects as a result of the intrusive activity.
- AFTA and VR data in numerous samples from the region around Hold with Hope and to the north and south define a major period of cooling at ~35 Ma, which is interpreted as representing the initial post-rift uplift of the continental margin. AFTA data in sample GC1104-24 show no direct evidence of such an event, but given the consistent regional evidence for cooling at this time, it seems highly likely that this event affected the region in the vicinity of the Nanok-1 borehole. Therefore the palaeo-thermal maximum identified from AFTA in sample GC1104-24 probably represents the unresolved effects of the two Palaeogene palaeo-thermal episodes identified in this region (related to Early Eocene intrusive activity and to regional, Late Eocene exhumation, respectively).

Sonic Velocity

- Sonic velocity measurements show that the Fosdalen Formation mudstones (the Knudshoved Mb and undifferentiated Fosdalen Fm) commonly show similar velocities (Vp) 2750–3100m/s (n=6). The Østersletten Mb shows a wide range of sonic velocity values ranging from 1750–3250 m/s (n=6). The structureless sandstones (Facies 4A) that form the bulk of unit record less variable values 1750–2750 m/s. The sample recording the highest velocity value (3250 m/s) and anomalously low porosity (6%) represents a mudstone-rich interbed (Facies 4B/C).
- Two samples from the igneous intrusion from the base of the core show extreme velocity values 4350 and 5250 m/s. Likewise, these samples record also the lowest porosity values and highest grain density.

Igneous intrusion

- The intrusion consists of slightly enriched tholeiitic basalt. It is similar to other intrusions (dykes) in NE Greenland, and in particular to dykes from Hold with Hope and Wollaston Forland. In terms of trace elements it clearly groups with the other dykes in the region. These dykes are dissimilar to the sills and dykes in the Jameson Land region.
- The Nanok intrusion is unsuited for dating by the $^{39}Ar/^{40}Ar$ method. However, two dated dykes from Wollaston Forland and Bontekoe Ø, which are not too different from the Nanok intrusion, have $^{39}Ar/^{40}Ar$ ages of 51–53 Ma, and this is considered the likely age of the Nanok intrusion.

1.2 Implications for exploration

The Nanok-1 core provides an exceptional insight into the mid – Upper Cretaceous depositional systems of NE Greenland. The succession that was previously mainly considered as dominantly monotonous shale succession (cf., “the Mid Cretaceous sandy shale”) is now revealing a highly complex and dynamic depositional history characterized by periods of bottom current influenced sedimentation, tidal-modulation, stratigraphic condensation, recurring hiatal surfaces as well as low and high density turbidite sedimentation.

The results are promising from the exploration perspective in that the studied interval points to the development of extensive cap-rock and a good-quality reservoir unit. Moreover, a number of lines of evidence point to Cretaceous source rock development.

The two oil shows in the core almost certainly have a Cretaceous source. The head space gas analyses indicate that the oil shows have a very similar composition to the mudstones from the core, but originate from a more marine-dominated interval than is present/preserved in the drilled interval. Biomarkers contain a moderate concentration of bicadinanes (angiosperm input), a feature that has not been previously recorded in North East Greenland, and generally indicates a source not older than Cretaceous.

The best candidate for the source rock interval is the Cenomanian succession at the base and below the drilled interval. This is suggested e.g., by the screening data that shows a steady increase in petroleum potential from 100 m downwards until thermal destruction caused by the intrusion at the base of the core.

The interpretation is also supported by the inferred sequence stratigraphic trends suggesting that the zone of maximum flooding of the drilled interval is situated in the Cenomanian section. Moreover, the sea level curves of Miller *et al.* (2011), suggest that a zone of maximum flooding within the mid–Late Cretaceous situates somewhere in the mid Cenomanian. Considering that the lower part of the core is Upper Cenomanian, it is reasonable to assume that the best source rock interval is situated at the base and below the core, and that the intrusion may have truncated parts of it.

Based on the available data, the source thickness has been tentatively estimated to be 50 m with a petroleum potential of 4–9 kg HC/ton, i.e. app. 625,000–750,000 ton HC/km^2 or app. 4,000,000–5,000,000 bbl/km^2.

Delineating the petroleum generation potential of the Cretaceous source rock requires further work in the future. In particular, a core well targeting the entire Cenomanian, placed as distally as possible to the paleocoastline, would reveal the potential of the mid Cretaceous source rock.

The Nanok-1 core well also confirms that the Cretaceous has potential for reservoir development. The analyzed Østersletten Mb comprises approximately 40 m of sandstones considered to be of reasonably good reservoir quality. The net/gross ratio is estimated to 81–88% based on a 15% porosity cut-off value. The average porosity of the reservoir quality sandstone is 21–22%, and the average permeability ranges between 50–150 mD.

The Østersletten sandstones are interpreted to be part of a small-scale sand-dominated fan near base of slope. Paucity of clay even in beds that show preserved tops, and the inferred proximal locus of sand accumulation suggest a low sediment transport efficiency system. This would further point to decreasing net/gross ratio towards the basin and a possibly relatively abrupt mid fan – basin floor gradation.

The tectonostratigraphic position of the Østersletten Mb suggests filled rift-topography and mainly east directed flow, which may have promoted development of east-oriented radial fan development rather than e.g., elongate axial deposition. The sandstones allegedly pinch out towards the slope (west) and are sharply (without gradation) overlain by the Knudshoved Mb mudstones pointing to abrupt abandonment of the fan system. Thus, the trap could be stratigraphic in analogous deposits.

The results of the preliminary cap-rock study are very promising. The samples analysed suggest that the studied mudstone successions possess excellent cap-rock properties. Further considering their late post-rift setting, these units are likely laterally widespread. Uncertainties include the effects of post-depositional faulting, in particular the possible later Campanian renewed rifting.

Finally, the drilled interval contains potential sediment by pass interval to offshore basins. The uppermost Cenomanian – Turonian section shows evidence of the development of several minor hiatal surfaces. The sedimentological data point to tidal modulation in this interval, which is in line with forced regressive conditions. Probably the most dramatic sea level drop and stratigraphic condensation/hiatus is associated with the ?Middle Coniacian – ?Middle Santonian Nanok Mb, which is thought to reflect prolonged exposure to non-depositional, oxygen-rich bottom currents. These stratigraphic levels potentially correspond to a major increase in depositional rate e.g., in the Northern Vøring Basin, which was situated ~100 km offshore from the drill site during the Cretaceous (Lien, 2005).

The Nanok-1 data package forms the second and last phase of the Cretaceous project of GEUS, and thus completes the study. Selected results of the reports are combined and their implications will be addressed in a coming report supplement available to the sponsors of both data packages.

1.3 References

Bjerager, M. *et al.* 2012: The Cretaceous of NE Greenland: Lithostratigraphic subdivision (Subproject 3). Contribution to Petroleum Geological Studies Services and Data in East and Northeast Greenland. Danmarks og Grønlands Geologiske Undersøgelse Rapport 2012/50, 56 pp.

Miller, K.G., Mountain, G.S., Wright, J.D. & Browning, J.V. 2011: A 180-million-year record of sea level and ice volume variations from continental margin and deep-sea isotopic records. Oceanography, **24**(2), 40–53.

Lien, T., 2005: From rifting to drifting: effects on the development of deep-water hydrocarbon reservoirs in a passive margin setting, Norwegian Sea. Norwegian Journal of Geology, **85**, 319–332.

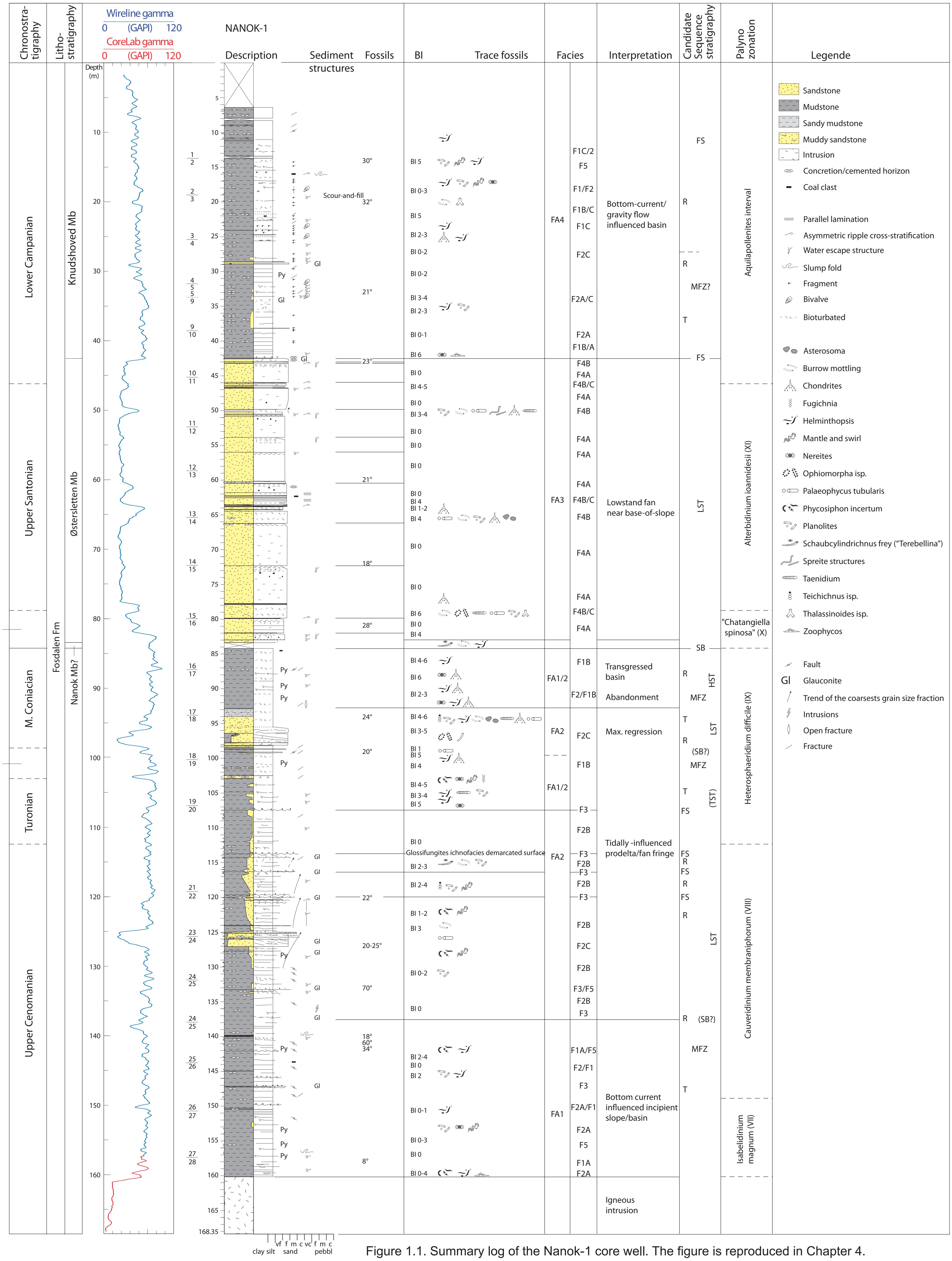

Figure 1.1. Summary log of the Nanok-1 core well. The figure is reproduced in Chapter 4.

2. Introduction

This report presents the core data package of the Nanok-1 core drilled in eastern Hold with Hope, NE Greenland in 2011. The report is delivered to the participating sponsoring companies of the specific analytical programme of the Nanok-1 core as described in Appendix B4 in the collaboration agreement between GEUS and sponsoring oil companies regarding petroleum geological studies, services and data in East and Northeast Greenland.

The core-well, which was named Nanok-1 after a nearby trapper's hut of the same name, is the fifth core-well in the drilling programme of the project Petroleum geological studies, services and data in East and North-east Greenland. Three of the four previous ones – Blokelv (Appendix B1), Rødryggen-1 (Appendix B2), Brorson Halvø-1 (Appendix B3) – targeted the Upper Jurassic source rock interval in the E-NE Greenland whereas the fourth, Store Koldewey-1 (Appendix K1), targeted both the Cretaceous and the Jurassic. Nanok-1 is the first core in the program that focuses entirely on the Cretaceous.

The Nanok-1 drill site is situated at Knudshoved, east coast of Hold-with Hope. The main target of the drilling was the ?Campanian – Upper Cenomanian interval of the Fosdalen Formation (note the redefined usage after Bjerager *et al.*, 2012). The primary objectives were to investigate reservoir quality, source rock potential and preliminary cap-rock properties of the drilled interval. The core reached a total depth of 168 m with > 96 % core recovery.

The Nanok-1 core penetrates the Upper Cenomanian – Lower Campanian interval of the Fosdalen Formation. This interval is subdivided into 1) the Upper Cenomanian – Coniacian undifferentiated Fosdalen Formation (~160–~84.2m); 2) the ?Middle Coniacian – ?Middle Santonian Nanok Member (~84.2–83m); 3) the Upper Santonian – Lower Campanian Østersletten Member (~83–42.5m); and 4) the Lower Campanian Knudshoved Member (~42.5–0m). The base of the core (TD–~160m) consists of an igneous intrusion. The Nanok Member is inferred to be present at a thin interval of non-recovery of core and limited rubble below the Østersletten Member.

2.1 Objectives

The primary objectives of the Nanok-1 core are to investigate reservoir quality, source rock potential and preliminary cap-rock properties of the drilled interval. In addition, the project aims to describe sedimentary facies, interpret depositional environments, erect biostratigraphic and lithostratigraphic divisions, determine mineralogy, diagenesis, chemostratigraphic and sonic velocity properties, characterise igneous intrusion, and to assess uplift history (using AFTA).

2.2 Well data, general information

General information

Country	Greenland / Denmark
Borehole number	GGU 517004
Borehole name	Nanok 1
Area	North-East Greenland, Hold with Hope
Operator	GEUS
Drilling operator	GEUS

Borehole Location	
Altitude:	63 m above mean sea level.
Coordinates WGS 84:	Latitude: 73°42.387´ N, Longitude: 20°32.732´ W
UTM Zone:	27 0514232 N - 8179343 E

Drill rig	Sandvik DE 130
Drilling contractor	GEUS
Casing diameter	74/67 mm, 64/57 mm,
Casing depth	Casing 74/67 mm to 6.31 m. Casing 64/57 mm to 31.5 m
Borehole diameter	56 mm
Core diameter	42 mm
Total depth	168.15 m
Core recovery	96%
Status	Plugged and abandoned

Logistic history:	
Transportation of rig and crew to drill site at Hold with Hope	August 1st–2nd 2011
Establishment of field camp and drilling rig	August 2nd–3rd 2011
Spud	August 3rd 2011
Drilling completed	August 10th 2011
Drill rig transported to Nyhavn (Mestersvig)	August 14th 2011
Effective drilling	8 days
Total days on drill location	14 days

2.3 Sampling and logging program at the drill site

A total of 14 whole core samples for gas analyses were collected immediately from the recovered core for every 5 m in average. Samples have lengths up to about 10 cm and they were stored in sealed metal cans. 117 samples from the core were collected for Rock-Eval/TOC screening and biostratigraphic age identification based on dinoflagellate cysts at GEUS.

A total gamma ray log was run in the drill string after drilling completed to 157 m, which was the safety distance for the probe to TD. Gamma ray logging was completed at GEUS laboratory together with density logging covering the Østersletten Mb.

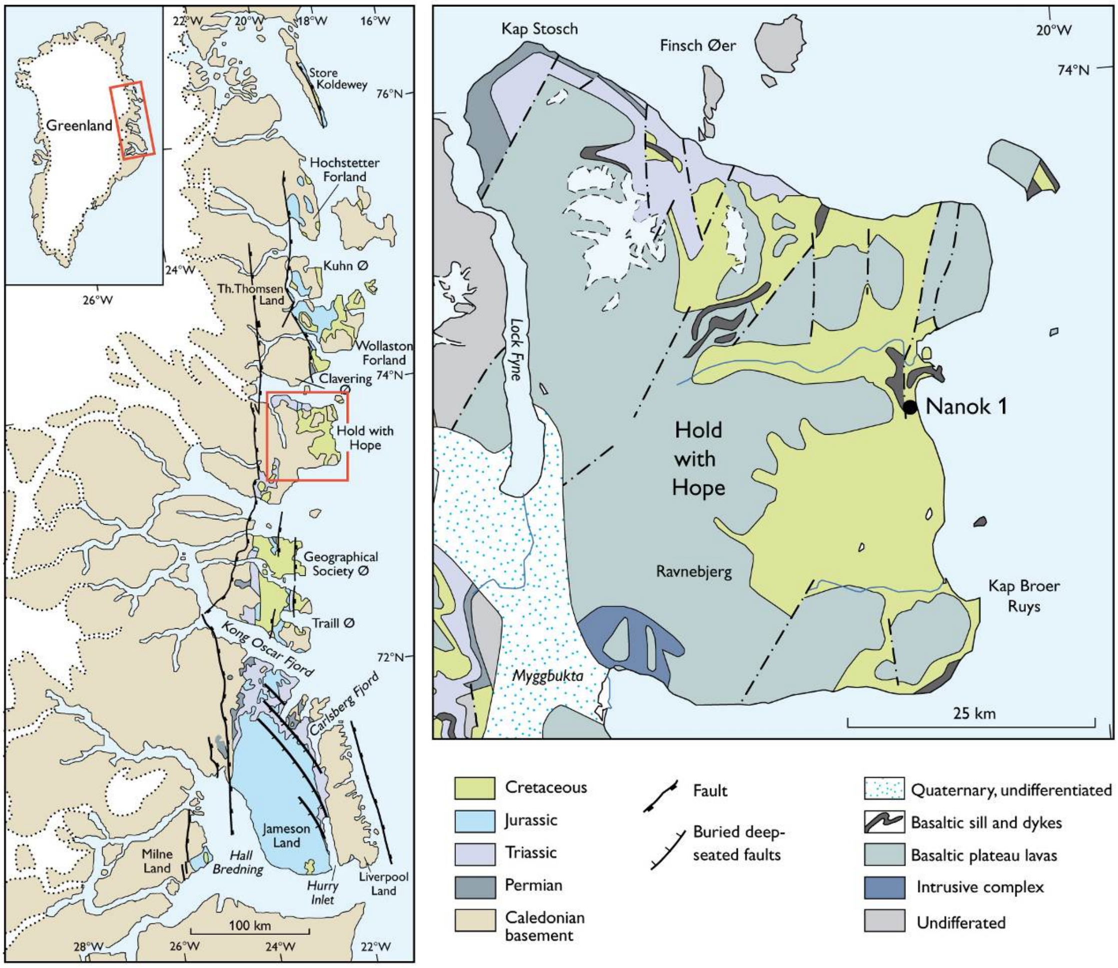

Figure 2.1. Geological map of northeast Greenland showing the Nanok 1 drill site. Map of northeast Greenland based on Surlyk (2003).

3. Stratigraphy

3.1 Lithostratigraphy

The Nanok-1 core penetrates the Upper Cenomanian – Lower Campanian interval of the Fosdalen Formation. Earlier works in the area include that of Kelly *et al.* (1998), in which formal lithostratigraphic division was erected for these deposits. According to this scheme, the drilled interval belonged to Home Forland Formation, which was further divided into four members; Fosdalen-, Nanok-, Østersletten- and Knudshoved Members. This lithostratigraphic scheme was redefined in the recently completed lithostratigraphy sub-project of the Cretaceous project (Bjerager *et al.*, 2012). In the new stratigraphic scheme, the Fosdalen Member was redefined and elevated to the rank of a formation (part of the Home Forland Group), whereas the other units retain their status as members within the Fosdalen Formation (Fig. 3.1.1). Consequently, according to the revised scheme, the drilled interval comprises the following units: 1) the Upper Cenomanian – Middle Coniacian undifferentiated Fosdalen Formation (~160–~84.2 m); 2) the ?Middle Coniacian – ?Middle Santonian Nanok Member (~84.2–83 m); 3) the Upper Coniacian – Lower Campanian Østersletten Member (~83–42.5 m); and 4) the Lower Campanian Knudshoved Member (~42.5–0 m). The base of the core (TD–~160 m) consists of an intrusion (Fig. 3.1.2). The Nanok Member is inferred to be present in the section at a thin interval of non-recovery of core (or limited rubble).

3.1.1 Fosdalen Formation

The unit was originally defined by Kelly *et al.* (1998) as the Fosdalen Member outcropping in Hold with Hope. In the recent lithostratigraphic report (Bjerager *et al.*, 2012), the unit was elevated into Formation and redefined to include all Middle Albian–Campanian marine mudstones from Traill Ø in south to Wollaston Forland in North. For complete redefined description, see Bjerager et al (2012).

The type area and section are situated in the North coast of Hold with Hope where it has been estimated to be ~1200 m-thick (Kelly *et al.*, 1998). The main lithology is mudstone, but the formation contains sand-dominated units (e.g., the Østersletten Member).

The lower boundary of the formation is an unconformity in Hold with Hope. There, the deposits onlap a westward rising surface that has a topographic relief up to ~600 m. The surface is interpreted as a degraded footwall (Kelly *et al.*, 1998). The Fosdalen Formation onlaps the surface diachronically from east to west. The top boundary is an unconformity to Palaeocene sediments and lavas. The drilled interval covers the top of the Fosdalen Fm in the area.

Finally, upper part of the undifferentiated Fosdalen Formation (~137–~93 m; Facies association 2) should be assigned to its own member in the future.

3.1.2 Nanok Mb

The ?Middle Coniacian – ?Middle Santonian Nanok Member was described by Kelly *et al.* (1998). The type section situates at Knudshoved, ~1 km south from the drill site. The member is only exposed in this area. The lower boundary is sharp and interpreted to be erosional, and marked by an abrupt change from grey mudstones to reddish poorly-sorted sandstone. The lower part of the unit consists dominantly of reddish brown, pebbly muddy sandstone. These rocks are characterized by mainly reworked clasts of phosphatized burrow fills (Kelly *et al.*, 1998). The red color is due to diagenetic hematite, which has been largely limonitized (Kelly *et al.*, 1998). Upward, the unit turns grey and comprises pebbly sandstone and argillaceous sediments. The Nanok Member is estimated to be up to ~6 m-thick (Kelly *et al.*, 1998).

In the core, the Nanok Member is inferred to be present in the section at a thin interval of non-recovery of core and limited rubble (~84.2–~83 m).

3.1.3 Østersletten Mb

The Upper Santonian – Lower Campanian Østersletten Mb was originally described by Kelly *et al.* (1998), who dated the unit as Santonian. The type section situates at the drill site and the unit is only exposed at East Coast of Hold with Hope. The lower boundary is sharp, possibly erosional, and marked by abrupt change in lithology. In the core, the Østersletten Member overlies a rubble interval. The unit consists dominantly of m-scale beds of fine to medium grained structureless sandstones. The top of the beds are commonly rich in mica and coal fragments. The Member is ~46 m-thick (Kelly *et al.*, 1998).

3.1.4 Knudshoved Member

The Lower Campanian Knudshoved Member was erected by Kelly *et al.*, (1998), who based the description partly on the Knudshoved beds of Maync (1949). The type section situates at the Nanok-1 drill site. Originally, the unit was only described from Hold with Hope, but the according the refined stratigraphic scheme, its occurrence is extended to Jackson Ø and Wollaston Forland (Bjerager *et al.*, 2012).

The lower boundary is sharp and marked by abrupt fining of the grain size from sandstone to mudstone. The surface is interpreted as a flooding surface. The upper boundary is erosional to Palaeocene rocks.

The Knudshoved Member comprises dominantly dark grey fossiliferous mudstones and heteroliths. In outcrop, only its lower part is exposed. Its thickness is estimated to be at least 25 m, but may reach 80 m (Kelly *et al.*, 1998).

3.1.5 References

Bjerager, M. *et al.*, 2012: The Cretaceous of NE Greenland: Lithostratigraphic subdivision (Subproject 3). Contribution to Petroleum Geological Studies Services and Data in East and Northeast Greenland. Danmarks og Grønlands Geologiske Undersøgelse Rapport 2012/50, 56 pp

Kelly, S.R.A., Whitham, A.G., Koraini, A.M., & Price, S.P., 1998: Lithostratigraphy of the Cretaceous (Barremian-Santonian) Hold with Hope Group, NE Greenland. Journal of the Geological Society, London **155**, 993–1008.

Maync, W., 1949: The Cretaceous Beds between Kuhn Island and Cape Franklin (Gauss Peninsula), Northern East Greenland. Meddelelser om Grønland **133**(3), 291 pp.

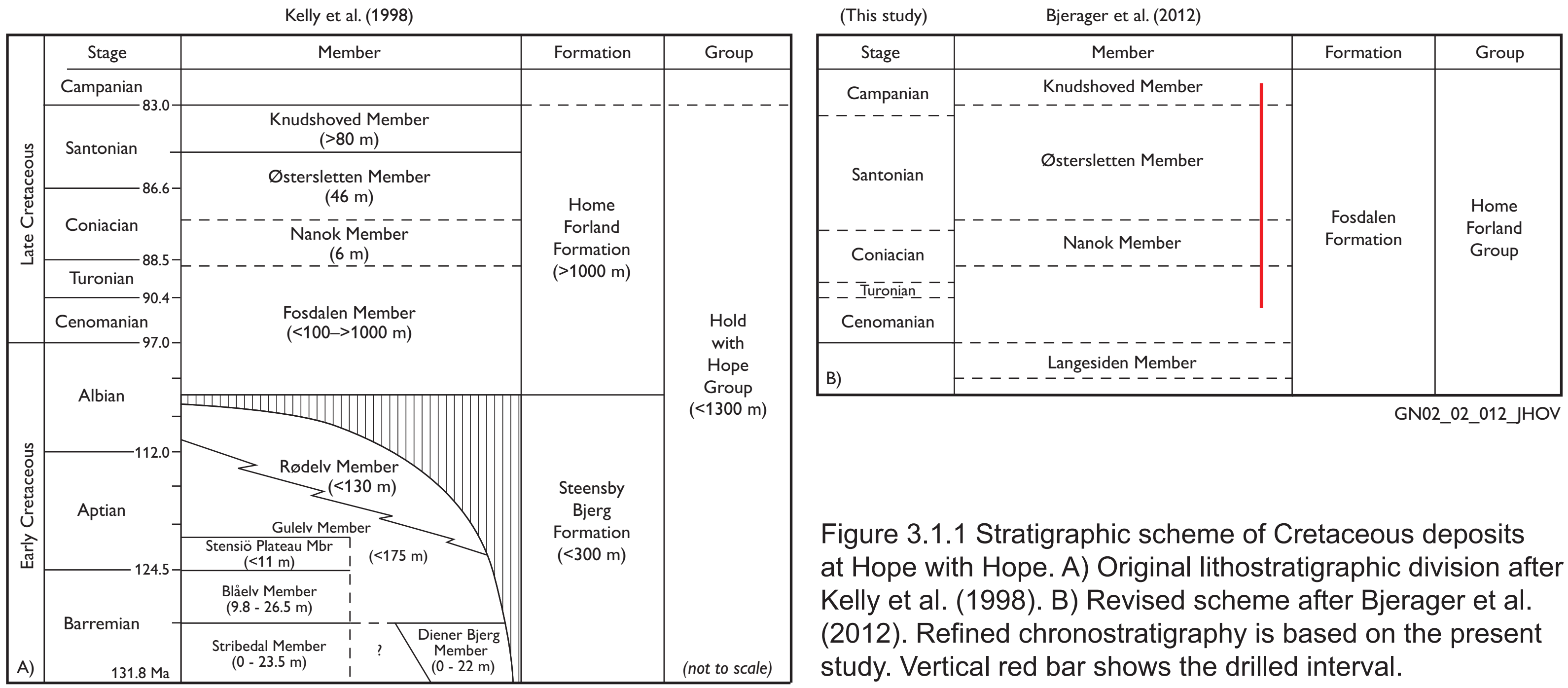

Figure 3.1.1 Stratigraphic scheme of Cretaceous deposits at Hope with Hope. A) Original lithostratigraphic division after Kelly et al. (1998). B) Revised scheme after Bjerager et al. (2012). Refined chronostratigraphy is based on the present study. Vertical red bar shows the drilled interval.

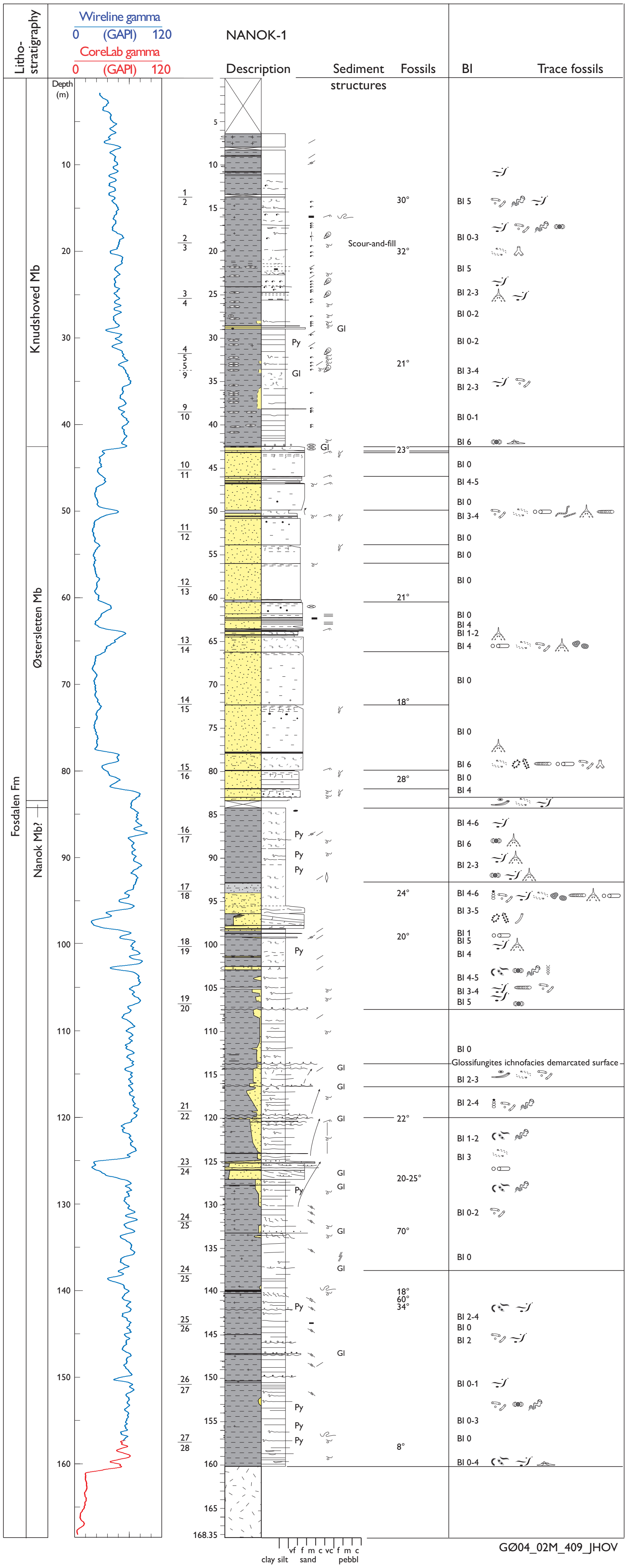

Figure 3.1.2 Lithostratigraphic division of the Nanok-1 core. See Figure 4.1 for legend and facies division.

3.2 Biostratigraphy

3.2.1 Palynostratigraphy

3.2.1.1 Material and methods

Samples were collected from the Nanok-1 core by splitting the core in two and crushing 4 to 6 cm of the half-core for analysis. The core has GGU nr. 517004 and the samples are characterized by a sub-number and a depth below surface (in the range-chart). The depth is the medium point of the length of the sample.

A total of 52 samples from the Nanok-1 core were processed by palynological preparation methods, including treatment with HCl, HF, oxidation with HNO_3 and heavy liquid separation. Each preparation step is represented by a slide to follow the process. Finally, the organic residue was sieved using 21 µm and also often 30 µm filters, was sometimes swirled and was finally mounted on glass slides using a glycerine jelly medium. The palynological content was analyzed using a normal light microscope.

The dinoflagellates (dinoflagellate cysts), acritarchs and selected stratigraphically important spores and pollen (miospores) species were recorded from the slides with sieved, oxidized or gravity-separated residue. Approximately 100 specimens were counted whenever possible (except for the samples at 42.51 m and at 102.97 m, which have only been screened). In addition, one or two slides were scanned for rare taxa.

The organic content is briefly described and the thermal maturity is estimated on the basis of sporomorph colors (Thermal Alteration Index; TAI). The taxonomy used herein follows that found in the Lentin and Williams Index of Fossil Dinoflagellates 2004 Edition, unless otherwise indicated by author references (Fensome & Williams 2004).

The results of the palynological study and the few records of nannofossil and foraminifera are presented in a range-chart (Fig. 3.2.1). The dinoflagellate species are sorted after their lowest occurrence and presented with their relative proportion of the dinoflagellate assemblage. No recorded occurrences of dinoflagellate taxa are interpreted as being a result of caving, as all analyzed material is from cores. Reworked dinoflagellate taxa are shown in a separate panel. The spore and pollen flora is not recorded systematically. Occurrences marked with a "?" indicate uncertainty of the identification.

Stratigraphic methods

Based on first- and last occurrence of stratigraphically important species (events) the studied Cretaceous marine sedimentary successions in East and North-East Greenland are now well dated primarily with dinoflagellates but supplemented with data from ammonites, foraminifers and nannofossils in certain intervals (Nøhr-Hansen *et al.* 2012). The dinoflagellate stratigraphy has been correlated with Upper Cretaceous North-West European and North American stratigraphies (Braman & Sweet (2012) Costa & Davey 1992, Dodsworth (2000), Fensome *et al.* (2008), Nichols & Sweet (1993), Nøhr-Hansen (1996, 2012), Pearce 2010, Pearce *et al.* (2003, 2009), Prince *et al.* (1999, 2008), Schiøler (1992) Williams *et al.* (2004)).

The terminology first occurrence (FO) and last occurrence (LO) is used here to facilitate reading and understanding of the text. The "first" occurrence is the stratigraphically lowest occurrence and "last" occurrence is the stratigraphically highest occurrence.

In this chapter dinoflagellate biozones and events are identified by the full name in italics (e.g. top of abundant *Isabelidinium magnum*).

In an attempt to identify the Cenomanian–Turonian boundary the $\delta^{13}C_{org}$ values were measured for 25 samples representing the interval from 90.87 m to 123.17 m. The data are illustrated on Figure 3.2.1.

3.2.1.2 Dinoflagellate stratigraphy

Igneous intrusion 168.00 m (TD) – 160.18 m

This part of the succession from the terminal core depth to 160.18 m is represented by an igneous intrusion and is barren of palynomorphs.

Barren interval 160.18 m – 155.33 m

The succession from the top of the volcanic intrusion to the first appearance of *Isabelidinium magnum* (155.33m). The palynological content from this part of the core is thermally over mature due to heating from the underlying volcanic intrusion. No palynomorphs have been recognized within this interval.

***Isabelidinium magnum* (VII) Zone: 155.33 m – 148.90 m**
The succession is from the first occurrence (FO) of *Isabelidinium magnum* (155.33m) to the FO of *Cauveridinium membraniphorum* (148.90 m).

Dinoflagellate assemblage

A single thermally affected specimen of *Isabelidinium magnum* and *Palaeoperidinium pyrophorum* has been recorded (155.33 m). The assemblage is low diverse and poor.

Biostratigraphy

The presence of *Isabelidinium magnum* suggests a Late Cenomanian to Late Turonian age (Costa & Davey 1992). But the strata above confine a Cenomanian age.

Age

Late Cenomanian, Late Cretaceous

Organic matter and maturity

Amorphous organic material dominates, terrestrial organic material especially black and brown woody material is common, finely dispersed amorphous material is present together with rare dinoflagellates and miospores.
The TAI Index is 3 to 3+, brown to dark brown i.e. in the upper part of the oil window or in the beginning of the gas generation window.

***Cauveridinium membraniphorum* (VIII) Zone: 148.90 m – 112.31 m**
The succession from the first occurrence (FO) of *Cauveridinium membraniphorum* (148.90 m) to the FO of *Heterosphaeridium difficile* (112.31 m).

Dinoflagellate assemblage

The dinoflagellate assemblage is dominated of *Isabelidinium* spp., *Spiniferites* spp., *Surculosphaeridium longifurcatum, Chlamydophorella nyei* and *Palaeohystrichopohora infusorioides* in the uppermost part of the interval, whereas *Oligosphaeridium complex* and *Palaeoperidinium pyrophorum* are common locally. The assemblage is diverse and abundant.

Biostratigraphy

The first common occurrence of *Cauveridinium membraniphorum* is reported in the Upper Cenomanian of onshore UK, according to Dodsworth (2000) and Pearce *et al.* (2009). Recently *Cauveridinium membraniphorum* was recorded in the Upper Cenomanian of Kangerlussuaq, southern East Greenland (Nøhr-Hansen 2012). The FO of *Trithyrodinium suspectum* suggests a Late Cenomanian age (Costa & Davey 1992, Williams *et al.* 2004).

Age

Latest Cenomanian.

Organic matter and maturity

The lower interval 148.90 m – 142.63 m is dominated by black and brown woody material together with common finely dispersed, amorphous material and dinoflagellates and rare miospores.

The TAI Index is 3-, light brown i.e. in the middle part of the oil window.

The upper interval 138.80 m – 112.31 m is dominated by amorphous organic material together with common black and brown woody material and dinoflagellates and rare miospores, occasional with common cuticles (e.g. at 129.05 m).

The TAI Index is 2+ to 3-, dark orange to light brown i.e. in the lower part of the oil window.

Heterosphaeridium difficile (IX) Zone: 112.31 m – 84.10 m

The succession is from the FO of *Heterosphaeridium difficile* (112.31 m) to the FO of the undescribed species informally named "*Chatangiella spinosa"* in industrial reports (84.10 m).

Dinoflagellate assemblage

Isabelidinium magnum is common in the lowermost part of the interval (109.70 m – 111.48 m), above this four subzones: *Chatangiella granulifera* (1)*, Senoniasphaera rotundata* (2), *Odontochitina* cf. *rhakodes* (3) and *Xenascus gochtii* (4) have been distinguished.

Biostratigraphy

Heterosphaeridium difficile has its FO at the base of the Turonian according to Costa & Davey (1992). Pearce *et al.* (2003) and Williams *et al.* (2004) suggest the FO of *Heterosphaeridium difficile* to be within the lowermost Turonian, whereas Bell & Selnes (1997) suggest an Early to Middle Cenomanian age for the FO of *Heterosphaeridium difficile* offshore Norway.

Age

Early Turonian – ?Middle Coniacian.

Organic matter and maturity

The Interval 84.51 m – 112.31 m is dominated by charcoal particles and black to brown woody material, common dinoflagellates and rare miospores. Amorphous organic material constitutes a moderate amount of the organic content but decreases to a minor amount above 107.00 m.

The TAI Index is 2- to 2+ dark yellow to dark orange, immature to early mature with respect to oil generation.

Chatangiella granulifera (1) Subzone: 106.73 m – 105.73 m

The succession is from the FO of *Chatangiella granulifera* (106.73 m) to the FO of *Senoniasphaera rotundata* (105.73 m).

Dinoflagellate assemblage

The dinoflagellate assemblage is dominated of *Chatangiella* spp. and *Spiniferites* spp. The assemblage is diverse and abundant.

Biostratigraphy

The FO of *Chatangiella granulifera* indicates an age not older than Early Turonian according to Costa & Davey (1992).

Age

Early Turonian.

Senoniasphaera rotundata (2) Subzone: 105.73 m – 102.97 m

The succession is from the FO of *Senoniasphaera rotundata* (105.73 m) to the FO of *Odontochitina* cf. *rhakodes* (102.97 m).

Dinoflagellate assemblage

The dinoflagellate assemblage is dominated of *Chlamydophorella nyei*, whereas *Spiniferites* spp. and *Trithyrodinium suspectum* are common. *Raphidodinium furcatum* has its FO at the base of the interval (105.73 m). The assemblage is diverse and abundant.

Biostratigraphy

The FO of *Raphidodinium furcatum* indicates an age not older than Middle Turonian according to Costa & Davey (1992), whereas they suggest Late ?Turonian/Early Coniacian FO of *Senoniasphaera rotundata.* Later, Pearce *et al.* (2003) recorded the FO of *Senoni-*

asphaera rotundata in the Middle Turonian and the first common occurrence in the uppermost Turonian.

Age

Middle to Late Turonian

Odontochitina cf. _rhakodes_ (3) Subzone: 102.97 m – 98.50 m

The succession is from the FO of *Odontochitina* cf. *rhakodes* (102.97 m) to the FO of *Xenascus gochtii* (98.50 m).

Dinoflagellate assemblage

The dinoflagellate assemblage is dominated of *Chatangiella* spp. whereas *Palaeohystrichophora infusorioides, Spiniferites* spp. and *Surculosphaeridium longifurcatum* are common. *Laciniadinium arcticum* has FO at the base of the interval (102.97 m). The assemblage is diverse and abundant.

Biostratigraphy

Fensome *et al.* (2008) reported an Early Turonian LO for *Odontochitina rhakodes* from offshore eastern Canada. An Early Coniacian FO of the genus *Laciniadinium* is generally accepted (e. g. Costa & Davey 1992) and a FO of *Laciniadinium arcticum* was reported as most likely in the Early Coniacian in West Greenland by Nøhr-Hansen (1996), however an Upper Turonian occurrence has previously been described from Alberta, Canada (Sweet & McIntyre 1988). Based on the presence of *Laciniadinium arcticum* and the age of the underlying succession the present interval is dated as ?Late Turonian to Early Coniacian.

Age

A ?Late Turonian to Early Coniacian age are suggested.

Xenascus gochtii (4) Subzone: 98.50 m – 84.10 m

The succession is from the FO of *Xenascus gochtii* (98.50 m) to the FO of the undescribed species informally named "*Chatangiella spinosa"* in industrial reports (84.10 m).

Dinoflagellate assemblage

The dinoflagellate assemblage is dominated of *Chatangiella* spp., *Palaeohystrichophora infusorioides, Palaeoperidinium pyrophorum* and *Spiniferites* spp. *Heslertonia cylindrata* and *Stephodinium coronatum* have their LOs at the top of the interval (84.51 m). The assemblage is diverse and abundant.

Biostratigraphy

The FO of *Xenascus gochtii* indicates an age not older than Middle Coniacian (Prince *et al.* 2008) and the LO of *Stephodinium coronatum* in the uppermost part indicates an age not younger than Middle Coniacian (Williams *et al.* 2004). *Heslertonia cylindrata* was described from the Lower Santonian in Germany (Yun 1981) and was later recorded from Middle Coniacian deposits on Bornholm, Denmark (Schiøler, 1992). The absence of Upper Coniacian marker species mentioned below also indicates a Middle Coniacian age.

Correlation with foraminifera

A badly preserved, low diversity foraminiferal assemblage from the transition of the undifferentiated Fosdalen Formation to the Nanok Member (sample 84.29 – 84.35 m) indicates a mid-Cenomanian – Middle Campanian age.

Age

Middle Coniacian.

***"Chatangiella spinosa"* (X) Zone: 84.10 m – 78.86 m**

The succession is from the FO of the undescribed species informally named "*Chatangiella spinosa"* in industrial reports (84.10 m) to the FO of *Alterbidinium ioannidesii* (78.86 m).

Dinoflagellate assemblage

The dinoflagellate assemblage is dominated by *Catangiella* spp., whereas *Circulodinium distinctum* and *Spiniferites* spp. are common. *Spinidinium echinoideum*, *Trithyrodinium vermiculatum* and *Xenascus* sp. A Kirsch 1991 have their FOs at the base of the interval (84.10 m). The assemblage is moderately diverse to poor.

Biostratigraphy

The FO *Spinidinium echinoideum* indicates a Late Coniacian age or younger (Williams *et al.* 2004).

The FO of abundant "*Chatangiella spinosa"* is supposedly to be in the Late Coniacian and apparently has a Late Coniacian to top Early Santonian range in the Norwegian Sea (Martin A. Pearce, personal communication, 2010). *Trithyrodinium vermiculatum* has been recorded from mid-Coniacian deposits on Bornholm, Denmark (Schiøler 1992) and from Santonian deposits in the Antarctic (Keating 1992).

Age

A Late Coniacian maximum age to a Middle Santonian minimum age is suggested for this interval.

Organic matter and maturity

The interval is dominated by charcoal particles and black to brown woody material. Dinoflagellates and miospores are present to rare. The amorphous organic material constitutes a minor amount.

The TAI Index is 2- dark yellow, immature with respect to oil generation.

Alterbidinium ioannidesii (XI) Zone: 78.86 – 46.36 m

The succession is from the FO *Alterbidinium ioannidesii* (78.86 m) to the FO of *Aquilapollenites* spp.

Dinoflagellate assemblage

Catangiella spp. is common within the dinoflagellate assemblage, which is relatively diverse and poor.

Biostratigraphy

Alterbidinium ioannidesii has a stratigraphic range from the ?Upper Santonian to the mid Lower Campanian in the Norwegian Sea (Pearce 2010). Pearce noted that the species ranges from the lower part of the *Offaster pilula* belemnite Zone (lowermost Campanian) to the lower part of the *Gonioteutus quadrata* belemnite Zone (middle Lower Campanian) in Norfolk, United Kingdom.

Age

Late Santonian.

Organic matter and maturity

The interval is dominated by charcoal particles and black to brown woody material. Dinoflagellates and miospores are present to rare. The amorphous organic material constitutes a minor amount. The TAI Index is 2- dark yellow, immature in respect to oil generation.

***Aquilapollenites* interval Nøhr-Hansen 1996: 46.36m – 9.11 m**

Definition: From the FO of the pollen genus *Aquilapollenites* to the top of the core (9.11 m).

Dinoflagellate assemblage

The dinoflagellate assemblage is dominated of *Palaeoperidinium pyrophorum* whereas *Alterbidinium ioannidesii*, *Chatangiella* spp., *Chlamydophorella nyei* and *Spiniferites* spp. are common. *Xenascus* sp. A Kirsch 1991 has an acme in the lower part (42.36 m). *Aquilapollenites* cf. *clarireticulatus* has its FO at the base of the interval (46.36 m). The assemblage is diverse and abundant.

Biostratigraphy

The pollen genus *Aquilapollenites* has its first common occurrence in the Lower Campanian (Costa & Davey, 1992; Nøhr-Hansen 1996). Nichols & Sweet (1993) recorded *Aquilapollenites* cf. *clarireticulatus* from the Lower Campanian and recently Braman & Sweet (2012) recorded the FO of *Integricorpus calrireticulatus* (formerly *Aquilapollenites clarireticulatus*) from the Lower Campanian in Canada. The presence of *Alterbidinium ioannidesii* indicates an age not younger than middle Early Campanian.

Correlation with nannoplankton and foraminifera

One sample (22.05 m) yielded a high diversity nannofossil assemblage which indicated a late Early to Late (not latest) Campanian age, nannofossil Zone UC15$^{BP.}$ One sample (25.29-25.33 m) yielded a low abundance foraminiferal assemblage suggesting a Coniancian to early Late Campanian age (zone 17-21b of the FCS scheme).

Age

Early Campanian.

Organic matter and maturity

The interval is dominated by charcoal particles and black to brown woody material. Dinoflagellates and miospores are present to rare. The amorphous organic material constitutes a minor amount in the lower part representing the Østersletten Member, whereas it increases to a moderate amount in the Knudshoved Member. The TAI Index is 2- dark yellow, immature with respect to oil generation.

3.2.1.3 Discussion

Dinoflagellates are recovered in fairly good preservation although the specimens from the lower part of the core are often thermally affected and or shrouded in amorphous organic matter. This stratigraphy is based on palynology alone (mainly dinoflagellates and minor pollen). No ammonites and only very few nannofossil and foraminifera have been recovered from the core.

The present dinoflagellate stratigraphy of the Upper Cretaceous Nanok-1 core, East Greenland has so far only been tested on a few local outcrop sections and need further studies to realise its full potential.

The present study of the dinoflagellates of the Nanok-1 core demonstrates the presence of assemblages similar to those found in the clastic deposits of the Shetland Group whereas many species recorded from the Chalk Group of the southern North Sea (Costa & Davey 1992) are absent or present in low numbers in North-East Greenland.

The presence of *Cauveridinium membraniphorum*, *Isabelidinium magnum* and *Trithyrodinium suspectum* in the lower part of the core indicate a Late Cenomanian age. The Cenomanian–Turonian boundary is placed by the first stratigraphic occurrence of *Heterosphaeridium difficile* (112.31 m) in the present study.

The common occurrence of *Cauveridinium membraniphorum* is known from the Upper Cenomanian organic rich Plenus marl onshore UK and the organic rich Blodoeks Formation offshore Norway according to Dodsworth (2000, pers. com 2010) and Pearce *et al.* (2009). These organic rich sediments represent the Oceanic Anoxic Event 2 (OAE2) characterised by a major positive excursion in carbon-13 isotopes (Pearce *et al.* 2009, Jarvis *et al.* 2011). In order to correlate the Cenomanian–Turonian boundary in the present study with the OAE2 recorded elsewhere; $\delta^{13}C_{org}$ values were measured for 25 samples across the boundary transition (90.87 m – 123.17 m, Fig. 3.2.1).The result clearly illustrates a positive excursion which starts decreasing at 112.31 m (FO of *Heterosphaeridium difficile*) and ends the decrease at 106.76 m (FO of *Chatangiella granulifera*). The relatively high $\delta^{13}C_{org}$ values measured below 106.76 m from the Nanok-1 core show good correlation with data from well-dated Cenomanian–Turonian boundary successions (Jarvis *et al.* 2011).

The sedimentary succession of the Fosdalen Formation that represents the Turonian to Middle Coniacian appears to be very condensed (112.31 m– 84.10 m).

The succession from the undifferentiated Fosdalen Formation through the Nanok Member to the lower part of the Østersletten Member also seems to be very condensed (84.10 m - 78.86 m) and may include one or more hiati. This transitional part of the core is dated as ?Late Coniacian to ?Middle Santonian. It has not been possible to prove, based on palynostratigraphy, if the Nanok member represents a continuous Middle to Upper Coniacian succession or if it represents an Upper Coniacian to Middle Santonian succession including a hiatus. The reason for the uncertainty is that the LO of *Stephodinium coronatum* in the uppermost part of the undifferentiated Fosdalen Formation in the Nanok -1 core and in the lowermost part of the Nanok Member in outcrop section at its type locality (Nøhr-Hansen *et al.* 2012) indicates an age not younger than Middle Coniacian (Williams *et al.* 2004) and that the FO *Spinidinium echinoideum* in the dark shales of the upper Nanok Member indicates a Late Coniacian age or younger (Williams *et al.* 2004).

The FO of the Upper Santonian indicator *Alterbidinium ioannidesii* was recorded from the lower part of the Østersletten Member (78.86 m). Therefore it cannot be excluded that the lowermost part of the Østersletten Member also is of Late Santonian age, however the sample from that part of the succession (82.07 m) only contains a poor and low diverse assemblage without age diagnostic marker species.

3.2.1.4 Conclusions

- The succession in the Nanok-1 core is dated as Late Cenomanian – Early Campanian on the basis of dinoflagellate and pollen stratigraphy.
- The undifferentiated Fosdalen Formation is dated as Upper Cenomanian – Middle Coniacian.
- The Nanok Member is dated as ?Upper Coniacian – ?Middle Santonian.
- The Østersletten Member is dated as Upper Santonian – Lower Campanian.
- The Knudshoved Member is Lower Campanian.
- A positive $\delta^{13}C_{org}$ excursion has been measured across the palynologically identified Cenomanian–Turonian boundary transition.
- The organic material from the lower part of the undifferentiated Fosdalen Formation (155.33 m – 107.00 m) is mainly dominated by amorphous organic material together with common black and brown woody material, dinoflagellates and rare miospores.
- The organic material of the upper part of the undifferentiated Fosdalen Formation, the Nanok Member and the Østersletten Member (107.00 m – 43.50 m) is mainly

dominated by charcoal particles and black to brown woody material, dinoflagellates and miospores are present to rare. The amorphous organic material constitutes a minor amount.

- The organic material from the Knudshoved Member (43.50 m – 9.11 m) is dominated by charcoal particles and black to brown woody material. Dinoflagellates and miospores are present to rare. The amorphous organic material constitutes a moderate amount.
- The dinoflagellate stratigraphy is, when possible, correlated with the micropaleaeontology studies, however the majority of the samples studied for micropaleaeontology where barren with respect to nannofossil and foraminifera (see below).
- The organic material is immature in the upper core, TAI 2. Downwards in the core, there is a shift to slightly darker sporomorph colours and consequently to higher thermal maturity. The interval between 140 m and 155 m is characterised by TAI 3- to 3+, brown to dark brown, suggesting the late part of the oil window or the beginning of the gas generation window. Below in the interval between 155 m and 160 m all organic material is black suggesting that the organic material is thermally over mature with respect to oil generation due to the contact with the local volcanic intrusive.

3.2.2 Nannofossils

22 samples from the Nanok-1 Core (from the Fosdalen Formation, including the Nanok Member and the Knudshoved Member) were examined for nannofossil content. Most samples were barren with respect to calcareous nannofossils. Only one sample, from the Knudshoved Member yielded a high diversity nannofossil assemblage which was useful for biostratigraphic dating.

3.2.2.1 Materials and methods

Fifteen samples were taken from the ‘undifferentiated’ Fosdalen Formation, 2 from the ?Nanok Member of the Fosdalen Formation and 5 from the Knudshoved Member of the Fosdalen Formation. Where possible, samples were taken from light sediment, inferring possible high carbonate content, or, from close proximity to shell fragments in the Knudshoved Member. The ‘undifferentiated’ Fosdalen Formation and the ?Nanok Member were barren with respect to nannofossil content. The Knudshoved Member yielded one useful nannofossil sample at 22.05 m.

Nannofossil slides were prepared using the simple smear slide technique of Bown & Young (1998). Where samples appeared to be barren with respect to calcareous nannofossils, at least 3 length traverses of the smear slide were examined. Biostratigraphic ranges of nannofossils and the Upper Cretaceous Nannofossil zonation scheme used (UC Zonation) are from Burnett (1998).

3.2.2.2 Results

Fosdalen Formation (undifferentiated)

160.60 – 160.65 m:
Assemblage: Barren with respect to calcareous nannofossils.

Age: Not assigned.

153.20 – 153.24 m:
Assemblage: Barren with respect to calcareous nannofossils.

Age: Not assigned.

153.16 – 153.20 m:
Assemblage: Barren with respect to calcareous nannofossils.

Age: Not assigned.

139.60 – 139.70 m:
Assemblage: Barren with respect to calcareous nannofossils.

Age: Not assigned.

138.60 m:
Assemblage: Barren with respect to calcareous nannofossils.

Age: Not assigned.

137.08 m:

Assemblage: Barren with respect to calcareous nannofossils.

Age: Not assigned.

133.72 – 133.76 m:

Assemblage: Barren with respect to calcareous nannofossils.

Age: Not assigned.

111.35 – 111.40 m:

Assemblage: Barren with respect to calcareous nannofossils.

Age: Not assigned.

110.30 – 110.34 m:

Assemblage: Barren with respect to calcareous nannofossils.

Age: Not assigned.

109.70 – 109.73 m:

Assemblage: Barren with respect to calcareous nannofossils.

Age: Not assigned.

108.73 – 108.76 m:

Assemblage: Barren with respect to calcareous nannofossils.

Age: Not assigned.

107.70 – 107.72 m:

Assemblage: Barren with respect to calcareous nannofossils.

Age: Not assigned.

105.65 – 105.67 m:

Assemblage: Barren with respect to calcareous nannofossils.

Age: Not assigned.

104.92 – 104.97 m:

Assemblage: Barren with respect to calcareous nannofossils.

Age: Not assigned.

86.67 – 86.73 m:

Assemblage: Barren with respect to calcareous nannofossils.

Age: Not assigned.

Fosdalen Formation (?Nanok Member)

84.00 – 84.03 m:

Assemblage: Barren with respect to calcareous nannofossils.

Age: Not assigned.

84.29 – 84.35 m:

Assemblage: Barren with respect to calcareous nannofossils.

Age: Not assigned.

Fosdalen Formation (Knudshoved Member)

25.29 – 25.33 m:

Assemblage: *Eiffellithus turriseiffelii* (broken piece)

Age: Albian–Maastrichtian

24.44 m:

Assemblage: Barren with respect to calcareous nannofossils.

Age: Not assigned.

22.05 m:

Assemblage: A badly preserved, but fairly high diversity nannofossil assemblage comprising *Biscutum magnum, Biscutum ellipticum, Watznaueria barnesiae, Bukrylithus ambiguus, Eiffellithus turriseiffelii, Ahmuellerella octoradiata, Zeugrhabdotus trivectis, Placozygus* cf *P.fibuliformis, Zeugrhabdotus diplogrammus, Kamptnerius magnificus, Zeugrhabdotus spiralis, Retecapsa surirella, Prediscosphaera cretacea, Micula decussata,* ?*Tortolithus pagei,Neocrepidolithus cohenii, Seribiscutum primitivum, Cribrosphaerella ehrenbergii, Chiastozygus amphipons, Tranolithus orionatus* and *Eiffellithus eximius.*

Remarks: The ranges of the useful marker species in this sample are as follows: *Biscutum magnum*: Lower Campanian to the upper Lower Maastrichtian in Europe, *Bukrylithus ambiguus*: Berriasian–?Campanian, *Zeugrhabdotus diplogrammus*: Valanginian–Campanian, *Tortolithus pagei*: Campanian–Maastrichtian and *Neocrepidolithus coheni*: Campanian–Maastrichtian. The last occurrence of *Eiffellithus eximius* is found at the top of nannofossil Zone UC15 (lower Upper Campanian), and the first occurrence of *Tortolithus* spp. is found within UC15a^{BP}, Burnett (1998) and references therein and Bown *et al.* (1998).

Age: Late Early Campanian –Late (not latest) Campanian, nannofossil Zone UC15^{BP}.

18.00 – 18.06 m:

Assemblage: Barren with respect to calcareous nannofossils.

Age: Not assigned.

17.50 – 17.55 m:

Assemblage: Barren with respect to calcareous nannofossils.

Age: Not assigned.

The results are displayed in a biostratigraphic distribution chart (Fig. 3.2.1) using ‘presence/absence’ data.

3.2.2.3 Discussion and Conclusions

Only 1 sample, at 22.05 m, from the Knudshoved Member of the Fosdalen Formation yielded a fairly high diversity, low abundance nannofossil assemblage. This sample also contained organic material which left the nannofossils in a fairly bad state of preservation (partly dissolved). Sample 22.05 m was taken from close to pieces of shell fragment seen in the core and was dated as from nannofossil Zones $UC15^{BP}$. The sample at 25.29 – 25.33 m contained one broken piece of *E. turriseiffelii*. When examined under the microscope, most of the samples were dominated by organic material but several revealed probable calcite: unfortunately they did not contain nannofossils.

Palaeoenvironment

Paleocological interpretation of the single sample yielding nannofossils is not possible due to the low abundance of fossils.

3.2.3 Foraminifera

19 samples from the Nanok-1 Core (from the Fosdalen Formation, including the Nanok Member and the Knudshoved Member) were examined for microfossil content. Most samples were barren with respect to foraminifera. Only 1 sample, from 25.29–33 m from the Knudshoved Member yielded relatively good foraminifera recovery.

3.2.3.1 Materials and methods

From 25 to 80 g of sediment was prepared for microfossil analysis, washed over a 63 µm sieve and dried at 45°C. The samples were quantitatively and qualitatively analysed and the foraminifera found in the fraction > 63 µm were picked and mounted in a micropaleontological slide. Biostratigraphic ranges of foraminifera are from Hart *et al.* (1989), King *et al.* (1989) and Gradstein *et al.* (1999).

3.2.3.2 Results

Fosdalen Formation (undifferentiated)

160.60 – 160.65 m:

Assemblage: Barren with respect to microfossils.

Age: Not assigned.

153.20 – 153.24 m:
Assemblage: Barren with respect to microfossils.

Remarks: Pyrite present in the residue.

Age: Not assigned.

153.16 – 153.20 m:
Assemblage: Barren with respect to microfossils.

Remarks: Pyrite more abundant than in sample 153.20 –153.24 m.

Age: Not assigned.

139.60 – 139.70 m
Assemblage: Barren with respect to microfossils.

Age: Not assigned.

133.72 – 133.76 m
Assemblage: One deformed agglutinated benthic foraminifera. Identification was not possible.

Remarks: Sandy residue.

Age: Not assigned.

111.35 – 111.40 m
Assemblage: Barren with respect to microfossils.

Age: Not assigned.

110.30 – 110.34 m

Assemblage: Barren with respect to microfossils.

Age: Not assigned.

109.70 – 109.73 m
Assemblage: Barren with respect to microfossils.

Age: Not assigned.

108.73 – 108.76 m
Assemblage: Barren with respect to microfossils.

Remarks: Pyrite present in the residue.

Age: Not assigned.

107.70 – 107.72 m
Assemblage: barren with respect to foraminifera. Presence of pyritised Diatoms and Radiolaria: *Pseudodictyomitra* cf. *pseudomacrocephala* (San Filippo & Riedel, 1985).

Remarks: Pyrite present in the residue.

Age: Albian–Cenomanian

105.65 – 105.67 m
Assemblage: Barren with respect to microfossils.

Age: Not assigned.

104.92 – 104.97 m
Assemblage: Broken pieces of *Bathysiphon* spp.

Age: Not assigned.

86.67 – 86.73 m
Assemblage: Barren with respect to microfossils.

Age: Not assigned.

Fosdalen Formation (?Nanok Member)

84.29 – 84.35 m
Assemblage: badly preserved, low diversity assemblage: *Glomospira* spp., cf. *Dorothia filiformis* (Hart *et al.,* 1989) and a few other coarse agglutinated benthic foraminifera.

Age: mid-Cenomanian – Middle Campanian

84.00 – 84.03 m
Assemblage: Barren with respect to microfossils.

Age: Not assigned.

Fosdalen Formation (Knudshoved Member)

25.29 – 25.33 m
Assemblage: badly preserved assemblage: *Praebulimina* cf. *laevis*, *Gavellinella usakensis* (cf. King *et al*., 1989), *Gyroidina* sp., *Bathysiphon* spp., and other undetermined species.

Age: Coniancian to early Late Campanian

18.00 – 18.06 m
Assemblage: pyritised Diatoms, and one benthic foraminifera, *Trochammina globigeri-noides*

Assemblage: Cretaceous–Recent.

17.50 – 17.55 m
Assemblage: pyritised Diatoms, and one benthic foraminifera, *Ammodiscus* sp.

Assemblage: Cretaceous–Recent.

Palaeoenvironment

The low number of foraminifera and the bad preservation of the specimens do not allow any paleocological interpretation.

3.2.3.3 Discussion and Conclusions

Only 1 sample, at 25.29 – 33 m, from the Knudshoved Member of the Fosdalen Formation yielded a low abundance foraminiferal assemblage. *G. usakensis* present in sample 25.29 – 33 m and was dated by King *et al.* (1989) as Coniancian to early Late Campanian (zone 17-21b of the FCS scheme) and by Hart et al., (1989) as Middle Campanian to Early–Late Campanian in the northern part of the north Norfolk Coast,UK.

3.2.4 References

Bell, D.G. & Selnes, H. 1997: The First Appearance Datum (FAD) of *Heterosphaeridium difficile* (Manum & Cookson), dinoflagellata in clastic deposits offshore Norway. Journal of Micropalaeontology, **16**, 30.

Braman, D.R. & Sweet, A.R. 2012: Biostratigraphically useful Late Cretaceous–Paleocene terrestrial palynomorphs from the Canadian Western Interior Sedimentary Basin. Palynology, **36,** (1), 8–35.

Bown, P. & Young, J. 1998: Techniques. In: Bown, P.R. (ed.), Calcareous Nannofossil Biostratigraphy. British Micropalaeontological Society Series. Chapman & Hall/Kluwer Academic, 16–28.

Bown, P.R. 1998: Lower Cretaceous. In: Bown, P.R. (ed.), Calcareous Nannofossil Biostratigraphy. British Micropalaeontological Society Series. Chapman & Hall/Kluwer Academic, 86–131.

Burnett, J.A., 1998: Upper Cretaceous. In: Bown, P.R. (ed.): Calcareous Nannofossil Biostratigraphy. British Micropalaeontological Society Series. Chapman & Hall/Kluwer Academic, 132–199.

Costa, L.I. & Davey, R.J. 1992: Dinoflagellate cysts of the Cretaceous System. In: Powell, A.J. (ed.), A stratigraphic index of dinoflagellate cysts. British Micropalaeontological Society Publication Series, London, 99–131.

Dodsworth, P. 2000: Trans-Atlantic dinoflagellate cyst stratigraphy across the Cenomanian–Turonian (Cretaceous) Stage boundary. Journal of Micropalaeontology, **19**, 69–84.

Fensome, R.A. & Williams, G.L. 2004: Lentin and Williams Index of Fossil Dinoflagellates 2004 Edition. AASP Contribution Series Number, **42**, 909 pp.

Fensome, R.A., Crux, J.A., Gard, I.G., MacRae, A., Williams, G.L., Thomas, F.C., Fiorini, F. & Wach, G. 2008: The last 100 million years on the Scotian Margin, offshore eastern Canada: an event-stratigraphic scheme emphasizing biostratigraphic data. Atlantic Geology, **44**, 93–126.

Gradstein, F.M., Kaminski, M.A. & Agterberg, F.P.,1999: Biostratigraphy and paleoceanography of the Cretaceous seaway between Norway and Greenland. Earth-Science Reviews, **46**, 27–98.

Hart, C., Bailey, H.W., Crittenden, S., Fletcher, B.N., Price, R.J. & Swiecicki, A. 1989: Cretaceous. In: Jenkins, D.G. and Murray, J.W. (eds.), Stratigraphical Atlas of fossil Foraminifera, 2nd ed., 273–365.

Keating, J.M. 1992: Palynology of the Lachman Crags Member, Santa Marta Formation (Upper Cretaceous) from north-west James Ross Island. Antarctic Science, **4**, 293–304.

King, C., Bailey, H.W., Burton, C.A. & King, A.D. 1989: Cretaceous of the North Sea. In: Jenkins, D.G. and Murray, J.W., (eds.), Stratigraphical Atlas of fossil Foraminifera, 2nd ed., 372–417.

Jarvis, I., Lignum, J.S., Gröcke, D.R., Jenkyns, H.C. & Pearce M.A. 2011: Black shale deposition, atmospheric CO_2 drawdown, and cooling during the Cenomanian–Turonian Oceanic Anoxic Event. Paleoceanography, **26,** PA3201, doi:10.1029/2010pa002081.

Nichols, D.J. & Sweet, A.R. 1993: Biostratigraphy of the Upper Cretaceous non-marine palynofloras in a north–south transect of the Western Interior Basin. In: Caldwell, W.G.E., Kauuffman, E.G. (eds.), Evolution of the Western Interior Basin: Geological Association of Canada Special Paper, **39**, 539–584.

Nøhr-Hansen, H. 1996: Upper Cretaceous dinoflagellate cyst stratigraphy, onshore West Greenland. Bulletin Grønlands Geologiske Undersøgelse, **170**, 104 pp.

Nøhr-Hansen, H. 2012: Palynostratigraphy of the Cretaceous–lower Palaeogene sedimentary succession in the Kangerlussuaq Basin, southern East Greenland. Review of Palaeobotany and Palynology, **178**, 59–90.

Nøhr-Hansen, H., Alsen, P., Piasecki, S., Sheldon, E. & Morigi, C. 2012: The Cretaceous of NE Greenland: Integrated biostratigraphy (Subproject 2) Contribution to Petroleum Geological Studies, Services and Data in East and Northeast Greenland. Danmarks og Grønlands Geologiske Undersøgelse Rapport 2012/49, **50** pp. Confidential to be released 01-06-2017.

Pearce, M.A., Jarvis, I., Swan, A.R.H., Murphy, A.M., Tocher, B.A. & Edmunds, W.M. 2003: Integrating palynological and geochemical data in a new approach to palaeoecological studies: Upper Cretaceous of the Banterwick Barn Chalk borehole, Berkshire, UK. Marine Micropaleontology, **47** (3–4), 271–306.

Pearce, M.A., Jarvis, I. & Tocher, B.A. 2009: The Cenomanian–Turonian boundary event, OAE2 and palaeoenvironmental change in epicontinental seas: new insights from the dinocyst and geochemical records. Palaeogeography, Palaeoclimatology, Palaeoecology, **280** (1–2), 207–234.

Pearce, M.A. 2010: New organic-walled dinoflagellate cysts from the Cenomanian to Maastrichtian of the Trunch borehole, UK. Journal of Micropalaeontology, **29,** 51–72.

Prince, I.M., Jarvis, I., & Tocher, B.A. 1999: High-resolution dinoflagellate cyst biostratigraphy of the Santonian–basal Campanian (Upper Cretaceous): new data from Whitecliff, Isle of Wight, England. Review of Palaeobotany and Palynology. **105**, 143–169.

Prince, I.A., Jarvis, I., Pearce, M.A. & Tocher, B.A. 2008: Dinoflagellate cyst biostratigraphy of the Coniacian–Santonian (Upper Cretaceous): new data from the English Chalk. Review of Palaeobotany and Palynology, **150** (1–4), 59–96.

San Filippo A. & Riedel, W.R. 1985: Cretaceous Radiolaria. In: Bolli, H.M., Saunders, J.B. & Perch-Nielsen, K. (eds.), Plankton Stratigraphy, 573–630.

Schiøler, P. 1992: Dinoflagellate cysts from the Arnager limestone formation (Coniacian, Late Cretaceous), Bornholm, Denmark. Review of Palaeobotany and Palynology, **72** (1–2), 1–25.

Sweet, A.R. & McIntyre, D.J. 1988: Late Turonian marine and nonmarine palynomorphs from the Cardium Formation, north-central Alberta Foothills, Canada. In: James, D.P., and Leckie, D.A. (eds.), Sequences, Stratigraphy, Sedimentology: Surface and Subsurface. Canadian Society of Petroleum Geologists Memoir, **15**, 499–516.

Williams, G.L., Brinkhuis, H., Pearce, M.A., Fensome, R.A., Weegink, J.W., *et al.*, 2004: Southern ocean and global dinoflagellate cyst events compared: index events for the Late Cretaceous– Neogene. In: Exon, N.F. (ed.), Proc. ODP, Sci. Results **189,** 1–98. Ocean Drilling Program, College Station. TX.

Yun, H.-S., 1981: Dinoflagellaten aus der Oberkreide (Santon) von Westfalen. Palaeontographica B, **177,** 1–89.

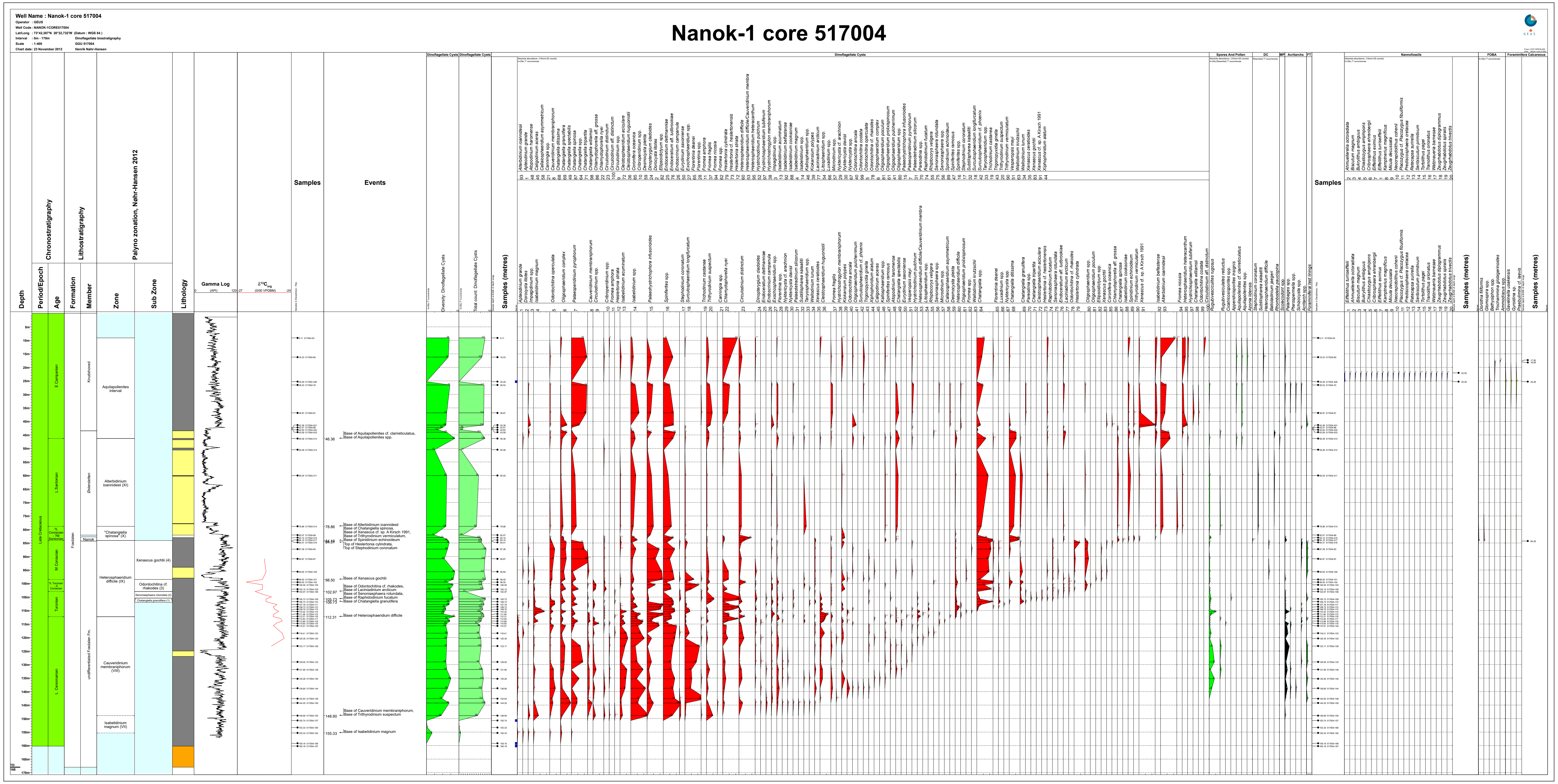

Figure 3.2.1 Biostratigraphic summary chart.

3.3 Chemostratigraphy and inorganic geochemistry

3.3.1 Objective

The geochemical investigations are performed in order to compare the different lithostratigraphic members encountered in the Nanok-1 well. Furthermore, data forms part of a database for future correlation between wells and with outcrop localities.

3.3.2 Samples

The geochemical investigations are based on core samples taken from the depth-interval 6.9 − 156 m in the Naonk-1 well. The Knudshoved and Østersletten members and the undifferentiated part of the Fosdalen Formation are sampled systematically, approximately in intervals of 3 m.

3.3.3 Methods

Geochemical analysis of the core samples were performed at Acme Labs. Total abundances of the major oxides and several minor elements are analysed by ICP-ES (inductively coupled plasma-emission spectrometry). Rare earth and refractory elements are determined by ICP-MS (inductively coupled plasma-mass spectrometry). Both methods apply 0.2 g sample fused by Lithium metaborate/ tetraborate and digested in dilute nitric acid. In addition a separate 0.5 g split is digested in Aqua Regia (mixture of nitric acid and hydrochloric acid) and analysed by ICP-MS to report the precious and base metals (Au, Ag, As, Bi, Cd, Cu, Hg, Mo, Ni, Pb, Sb, Se, Tl, Zn). Generally, ICP-MS can determine concentrations that are 1 to 2 orders of magnitude lower compared to ICP-ES. Detection limits are 0.01 % for all major elements; with exception of 0.04% for Fe (ACME labs 2009). Detection limits are less 1 ppm for trace elements including most REE (rare earth elements). The exception are Ba (5 ppm), Co (20 ppm), Nb (5 ppm), Ni (20 ppm), Sr (3 ppm), V (8 ppm), Y (2 ppm), Zn (5 ppm), Zr (5 ppm) and Ce (30 ppm). Total S and C is analysed by LECO with detection limits of 0.01 % and 0.02 %, respectively. Loss on ignition (LOI) is given as weight difference after ignition at 1000°C.

3.3.4 Geochemical variations with burial depth

The overall geochemical trends with burial for both the sandstones and the mudstones are compared. The upward gradual changes within the sandstone and mudstone intervals may potentially be applied for correlation between wells.

The Østersletten Mb, characterised by sandstones, is distinctly different from the two mudstone intervals, undifferentiated part of Fosdalen Formation and Knudshoved Member (Fig. 3.3.1). The sandstones of the Østersletten Mb have a generally high SiO_2 content, whereas the mudstones have high contents of Al_2O_3, K_2O, TiO_2 and Th. The high SiO_2 content probably origin form quartz in the sandstones. Clay minerals and mica is assumed to correspond to the high contents of Al_2O_3, K_2O, TiO_2 and Th.

The undifferentiated parts of Fosdalen Formation and Knudshoved Member have almost similar contents of the major elements. There are some fluctuations in the actual values in the lowermost undifferentiated parts of Fosdalen Formation, but the ratios are generally similar (Fig. 3.3.1). The Na/K ratio is generally upward decreasing in the undifferentiated parts of Fosdalen Formation, with the minimum level in the Østersletten Member, and upward increasing in the Knudshoved Member. Other ratios, like Si/Al, K/Al, Zr/Nb, P/Y and Ti/K, are relatively stable for the mudstones of Fosdalen Formation. The sandstones of the Østersletten Member have generally different ratios compared to the mudstones and commonly show more fluctuating ratios.

Heavy minerals

The Østersletten Member has some intervals of increased Zr, Hf, Y, Ce and other REE contents and high Zr/Nb, P/Y and U/V ratios (Fig. 3.3.1). Zircon grains are the most common Zr-bearing mineral, and the most likely origin of Zr and Hf. REE are common constituent of heavy minerals, but may also be associated with mica or clay minerals. P_2O_5 may be situated in apatite or other phosphate bearing heavy minerals, like monazite.

The Cr_2O_3 and W contents and the Cr/Zr ratio are fluctuating in the Østersletten Member, but relatively stable in the undifferentiated parts of Fosdalen Formation and the Knudshoved Member. These fluctuations are probably due to subdivision of gravity flow deposits into several series of flow units each with upward gradually varying heavy mineral content (cf. Kjær et al. 2007).

Locally low Si/Al, K/Al and K/Rb ratios and high Ti/K ratio in the Østersletten Mb is probably due to a relatively increased content of mica or clay in the sandstones, rather than heavy mineral laminae.

Diagenesis

Simultaneously occurrence of increased LOI, TOT/C, Fe_2O_3, MgO, CaO, and MnO contents and relatively low amounts of SiO_2 and Al_2O_3 are interpreted as carbonate cemented intervals. The lowermost undifferentiated parts of Fosdalen Formation and one sample in the Knudshoved Member are characterised by high Fe_2O_3 contents and increased but varying amounts of MgO, CaO, and MnO (Fig. 3.3.1). This is interpreted as siderite cemented intervals. The Østersletten Member has also intervals with relatively high amounts of Fe_2O_3, but additionally intervals characterised by increased MgO and CaO (and to a smaller extend Fe_2O_3). Consequently, the Østersletten Member seems to appear with cemented intervals of both siderite and ankerite or dolomite.

Peak amounts of Ba accompanied by Sr occur in one sample of the Østersletten Member. Barite was not used as an additive in the drilling mud. Barite cement, therefore, seems the most likely explanation, though this type of cement has not been described from the petrographical investigations.

3.3.5 Geochemical comparison of members

The element-mineral association is important, when applying chemostratigraphy or comparing the inorganic geochemistry. Elements associated with relatively stable minerals, for example Zr, Hf, Ti, P, Cr, Ce and Th are preferred when comparing sediments, as these elements most likely reflect mineralogical variations in the source area. Zr and Hf are most likely associated with zircon grains. Cr commonly occurs in chrome spinel, whereas P may be present as apatite or other heavy minerals, like monazite. Th, Ce and other rare earth elements (REE) are usually present in heavy mineral assemblage. Ti is usually present in ilmenite, titanomagentie or their alteration products (leucoxene), but Ti may also be incorporated in mica and clay minerals. Some elements are related to less stable minerals, for example K_2O and Na_2O which origin from K-feldspar and plagioclase and clay minerals. Other elements as Fe, Mg, Mn, Ca and base metals are more likely to have been mobilised and should be applied with care as they are reflecting the diagenetic changes.

Sandstone

The sandstone samples are geochemically similar; only the muddy sandstone samples are commonly detached from the group and plot in the diagrams more towards the mudstone samples (Figs. 3.3.2–5, 3.3.8–11 and 3.3.13). The Østersletten Member can be distinguished from the mudstones by a higher Zr/TiO_2 ratio, lower Ce/Zr ratio and generally lower TiO_2 content (Figs. 3.3.2–5). The higher Zr / TiO_2 ratio of the sandstone samples compared to the mudstones (Fig. 3.3.4) may reflect a higher maturity or simply the higher abundance of Ti in the fine fraction. The high P_2O_5 content in the Østersletten Member is accompanied by high amounts of Zr and may origin from heavy mineral concentrations (Fig. 3.3.6).On the other hand there seem to be no correlation between Zr and Cr_2O_3 (Fig. 3.3.7), so chromium may not simply be associated with chrome spinel but also a trace element in other minerals, possibly mica.

The very low Na_2O/Al_2O_3 ratio of the Østersletten Member indicates that plagioclase must be very rare (Fig. 3.3.9). The undifferentiated parts of Fosdalen Formation and Knudshoved Member have equally low or a little higher Na_2O/Al_2O_3 ratio and probably reflect the composition of the clays. The K_2O/Al_2O_3 ratio for the Østersletten Member is higher than for the mudstones, suggesting that mica and K-feldspar may be a more common constituent in the Østersletten Member than in the mudstones of the undifferentiated parts of Fosdalen Formation and Knudshoved Member (Fig. 3.3.10). The different Rb/K_2O ratios for Østersletten Member and the mudstones also suggest that different K_2O phases are present (Fig. 3.3.11).

The relatively high contents of Fe_2O_3, MnO and MgO in the undifferentiated parts of Fosdalen Formation and Knudshoved Member (Figs. 3.3.14 and 3.3.15) suggest the presence of siderite cement. The Østersletten Member show an almost perfect correlation between MgO and CaO (Fig. 3.3.15), which plot between the lines reflecting the dolomite and the chosen ankerite composition. Dolomite and ankerite form a solid solution series and the carbonate cement in Østersletten Member may be a Fe-rich dolomite or an ankerite.

Mudstones

The two mudstones seem to geochemical very similar and typically group together in most plots (Figs. 3.3.2–13). The only marked differences seem to be generally higher TiO_2 and Al_2O_3 contents and higher Cu/V ratio in the undifferentiated parts of Fosdalen Formation compared to the Knudshoved Member (Figs. 3.3.2–4, 3.3.8–10 and 3.3.13). The actual TiO_2 and Al_2O_3 values reflect the clay content and small variation in the abundance of other minerals for example quartz, which reflect minute variation in depositional environment rather than differences in sediment sources. Only differences in ratios are associated with base metal components (for example Cu) which are likely to be mobilised during diagenesis and therefore less reliable elements. The two mudstones, the undifferentiated parts of Fosdalen Formation and Knudshoved Member, consequently seem to be geochemically similar and probably have similar sediment sources.

The positive correlation of the low amounts of Fe_2O_3 with total sulphur (TOT/S) forming the similar trend as pyrite suggests that pyrite is one of the most important Fe-bearing phases, beside siderite, in the undifferentiated parts of Fosdalen Formation and Knudshoved Member (Fig. 3.3.16).

Trace elements

Chondrite normalised (according to McDonough & Sun 1995) REE distributions show a clear separation of sandstone intervals from the mudstones in the Nanok-1 well (Fig. 3.3.17). The sandstone intervals have local minima at Ce and commonly also minima at Dy and maxima at Er. Measurements close to or below the detection limit of Ce may be the reason for the Ce minima, which is therefore not a reliable difference. The mudstone intervals have maxima at Ce and commonly minima at Er. The Knudshoved Member and the undifferentiated parts of Fosdalen Formation seem to be similar, only the uppermost undifferentiated parts of Fosdalen Formation (depth interval: 84.54 – 106.73 m) seem to have relatively higher HREE (heavy rare earth elements) than both the lowermost undifferentiated parts of Fosdalen Formation and the Knudshoved Member (Fig. 3.3.18). One sample (at 90.10 m) has an atypical REE distribution, which cannot be explained.

3.3.6 Conclusions

The sandstones of the Østersletten Member are geochemically somewhat different from the mudstones of the Fosdalen Formation. The muddy sandstones of the Østersletten member have ratios similar to the mudstones, but distinctly different ratios compared to the sandstones. The heavy mineral content seems to be different between the sandstones and the mudstones, as the Østersletten Member has more mature composition. Ankerite-dolomite cement is typical in the Østersletten Member, whereas siderite cement besides other carbonate cement occurs in the Fosdalen Formation.

The two mudstone intervals, the undifferentiated part of the Fosdalen Formation and the Knudshoved Member, are geochemically almost identical. Only subtle geochemical differences are recognized, which mainly origin from small variations in base metals, which are potentially highly mobile.

3.3.7 References

ACME Labs, 2009: Schedules of services and fees, 33p.

Kjær, M. L., Friis, H., Svendsen, J. B., Jensen, C. B. & Bruhn, R. 2007: The application of bulk geochemistry to reveal heavy mineral sorting and flow units in thick massive gravity flow deposits, Siri Canyon Palaeocene sandstones, Danish North Sea. In: Mange, M. A. and Wright, D. T. (eds.), Heavy minerals in use. Developments in Sedimentology, Elsevier 58, 1099–1121.

McDonough, W. F. & Sun, S.-s. 1995: The composition of the Earth. Chemical Geology **120**, 223–253.

Weibel, R., Johannessen, P.N., Dybkjær, K., Rosenberg, P. & Knudsen, C. 2010: Chemostratigraphy of Upper Jurassic reservoir sandstones, Danish Central Graben, North Sea. Marine and Petroleum Geology, **27**, 1572–1594.

Table 3.3.1. Core samples taken from the Nanok-1 well during the present study.

Sample	Depth (m)	Rock type	Member	Formation
517004-51	6.93	Mudstone	Knudshoved	Fosdalen
517004-54	9.96	Mudstone	Knudshoved	Fosdalen
517004-58	14.27	Mudstone	Knudshoved	Fosdalen
517004-61	17.16	Mudstone	Knudshoved	Fosdalen
517004-64	20.06	Mudstone	Knudshoved	Fosdalen
517004-67	23.14	Mudstone	Knudshoved	Fosdalen
517004-70	26.53	Mudstone	Knudshoved	Fosdalen
517004-73	29.11	Mudstone	Knudshoved	Fosdalen
517004-76	32.27	Mudstone	Knudshoved	Fosdalen
517004-79	34.86	Mudstone	Knudshoved	Fosdalen
517004-82	37.53	Mudstone	Knudshoved	Fosdalen
517004-86	40.98	Mudstone	Knudshoved	Fosdalen
517004-267	44.22	Sandstone	Østersletten	Fosdalen
517004-268	46.26	Sandstone	Østersletten	Fosdalen
517004-269	47.25	Sandstone	Østersletten	Fosdalen
517004-270	51.00	Sandstone	Østersletten	Fosdalen
517004-271	53.29	Sandstone	Østersletten	Fosdalen
517004-272	55.03	Sandstone	Østersletten	Fosdalen
517004-273	56.93	Sandstone	Østersletten	Fosdalen
517004-274	58.66	Sandstone	Østersletten	Fosdalen
517004-275	62.14	Sandstone	Østersletten	Fosdalen
517004-276	63.55	Sandstone	Østersletten	Fosdalen
517004-277	65.47	Sandstone (muddy)	Østersletten	Fosdalen
517004-278	66.63	Sandstone	Østersletten	Fosdalen
517004-279	68.32	Sandstone	Østersletten	Fosdalen
517004-280	70.19	Sandstone	Østersletten	Fosdalen
517004-281	72.93	Sandstone	Østersletten	Fosdalen
517004-282	74.25	Sandstone	Østersletten	Fosdalen
517004-283	76.08	Sandstone	Østersletten	Fosdalen
517004-284	78.03	Sandstone (muddy)	Østersletten	Fosdalen
517004-285	79.97	Sandstone	Østersletten	Fosdalen
517004-286	82.89	Sandstone	Østersletten	Fosdalen
517004-90	84.54	Mudstone	(undifferentiated)	Fosdalen
517004-92	86.43	Mudstone	(undifferentiated)	Fosdalen
517004-96	90.10	Mudstone	(undifferentiated)	Fosdalen
517004-100	95.65	Sandstone	(undifferentiated)	Fosdalen
517004-103	100.50	Mudstone	(undifferentiated)	Fosdalen
517004-106	102.97	Mudstone	(undifferentiated)	Fosdalen
517004-110	106.73	Mudstone	(undifferentiated)	Fosdalen
517004-112	108.73	Mudstone	(undifferentiated)	Fosdalen

517004-117	112.93	Mudstone	(undifferentiated)	Fosdalen
517004-120	115.57	Mudstone	(undifferentiated)	Fosdalen
517004-123	118.41	Mudstone	(undifferentiated)	Fosdalen
517004-126	121.33	Mudstone	(undifferentiated)	Fosdalen
517004-130	125.16	Sandstone?	(undifferentiated)	Fosdalen
517004-134	130.04	Mudstone	(undifferentiated)	Fosdalen
517004-137	132.82	Mudstone	(undifferentiated)	Fosdalen
517004-141	136.09	Mudstone	(undifferentiated)	Fosdalen
517004-145	139.99	Mudstone	(undifferentiated)	Fosdalen
517004-147	141.99	Mudstone	(undifferentiated)	Fosdalen
517004-151	145.27	Mudstone	(undifferentiated)	Fosdalen
517004-154	147.76	Mudstone	(undifferentiated)	Fosdalen
517004-157	150.74	Mudstone	(undifferentiated)	Fosdalen
517004-161	154.33	Mudstone	(undifferentiated)	Fosdalen
517004-163	156.35	Mudstone	(undifferentiated)	Fosdalen

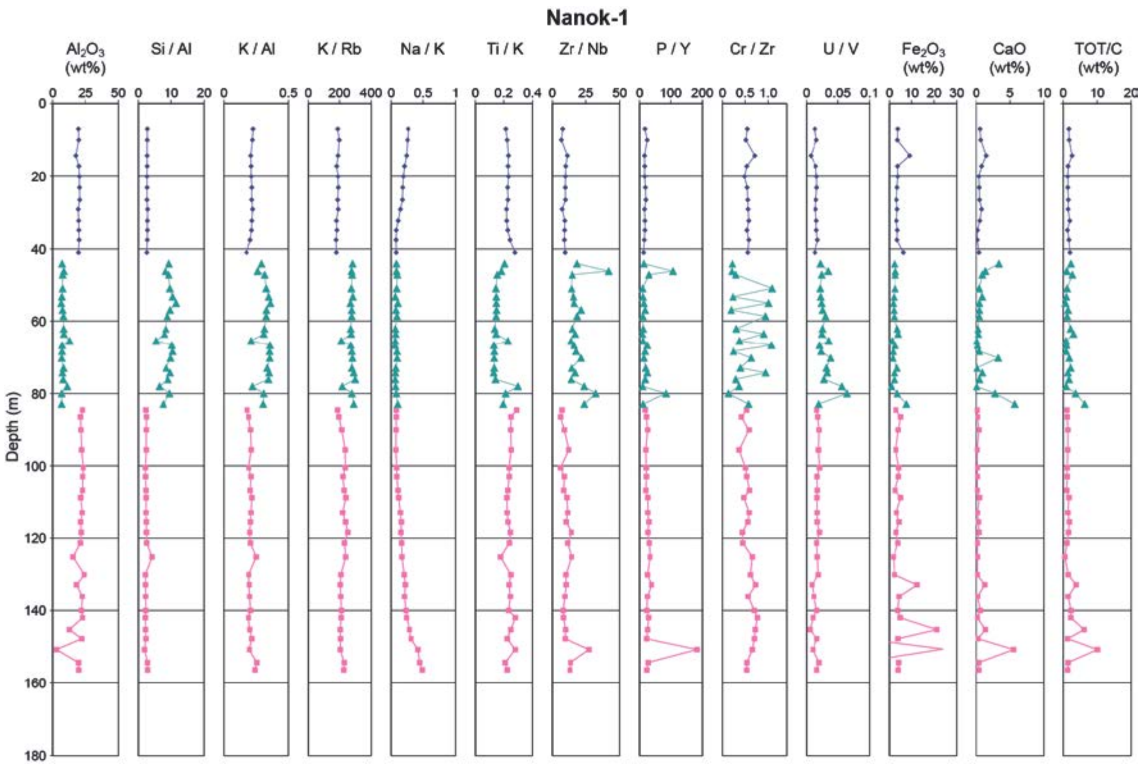

Figure 3.3.1. Graph showing variation with depth of the undifferentiated part of Fosdalen Formation (pink), Østersletten Member (green) and Knudshoved Member (blue) in the Nanok-1 well.

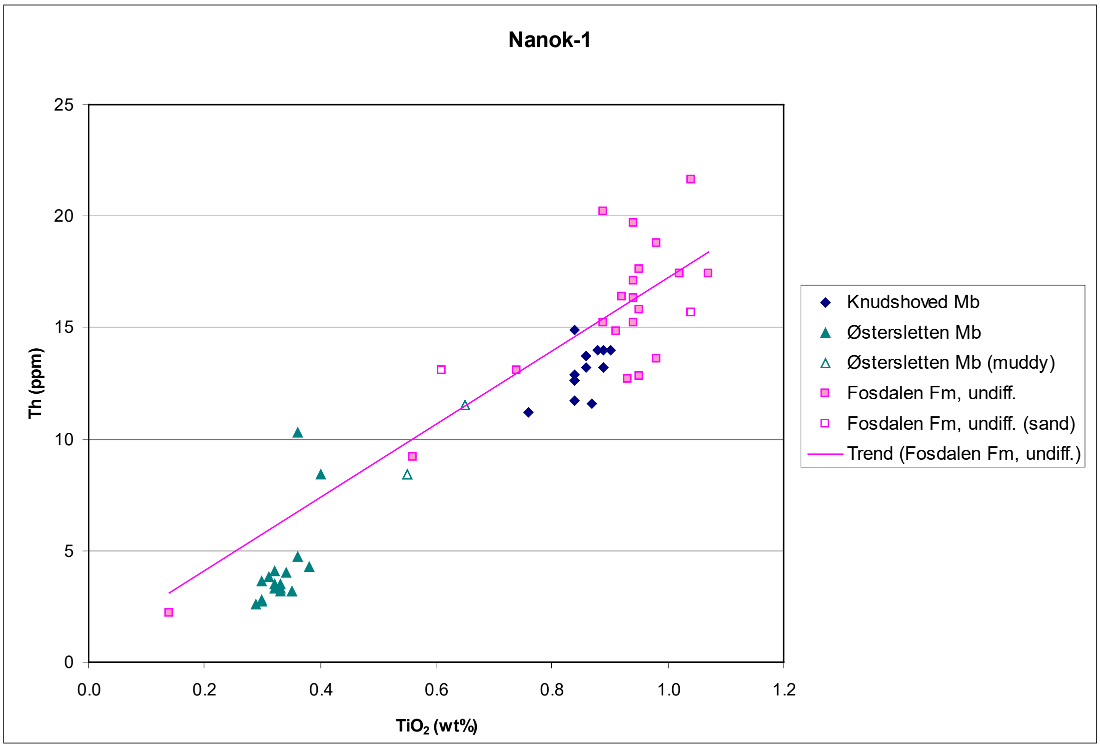

Figure 3.3.2. Graph showing positive correlation between Th (ppm) and TiO_2 (wt%) for both the Østersletten Mb, the undifferentiated parts of Fosdalen Formation and Knudshoved Member.

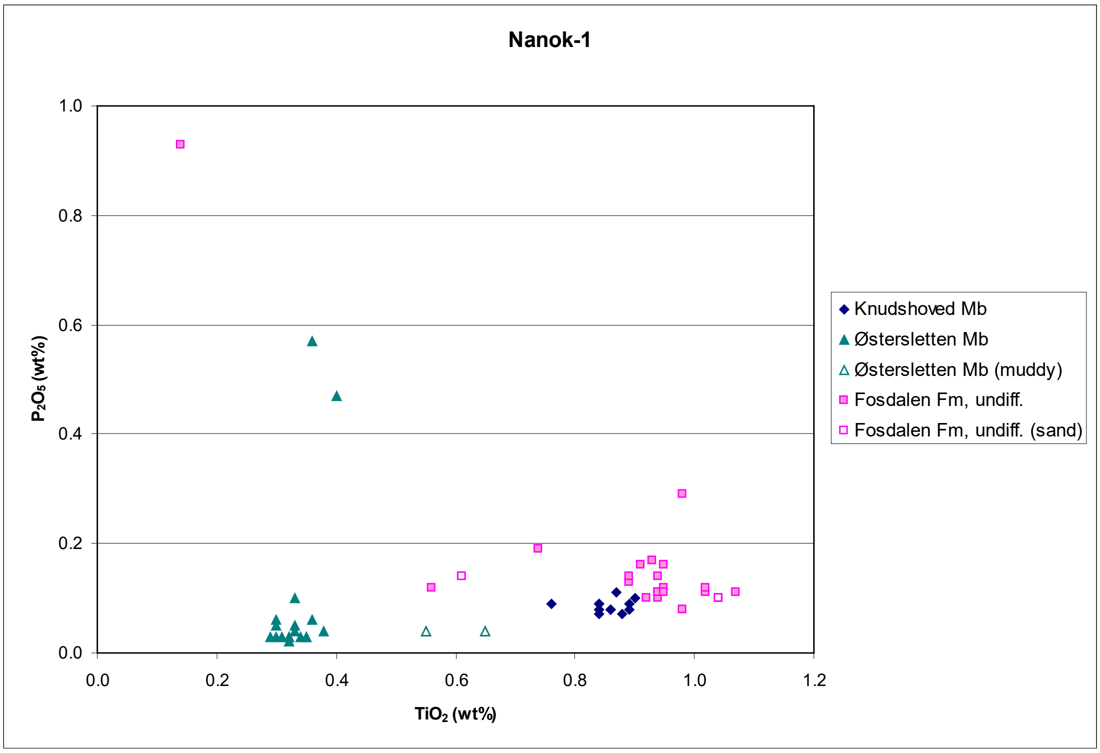

Figure 3.3.3 (previous page). Graph showing positive correlation between P_2O_5 (wt%) and TiO_2 (wt%) for both the undifferentiated parts of Fosdalen Formation, Østersletten and Knudshoved members, though with the exception of few samples enriched in P_2O_5.

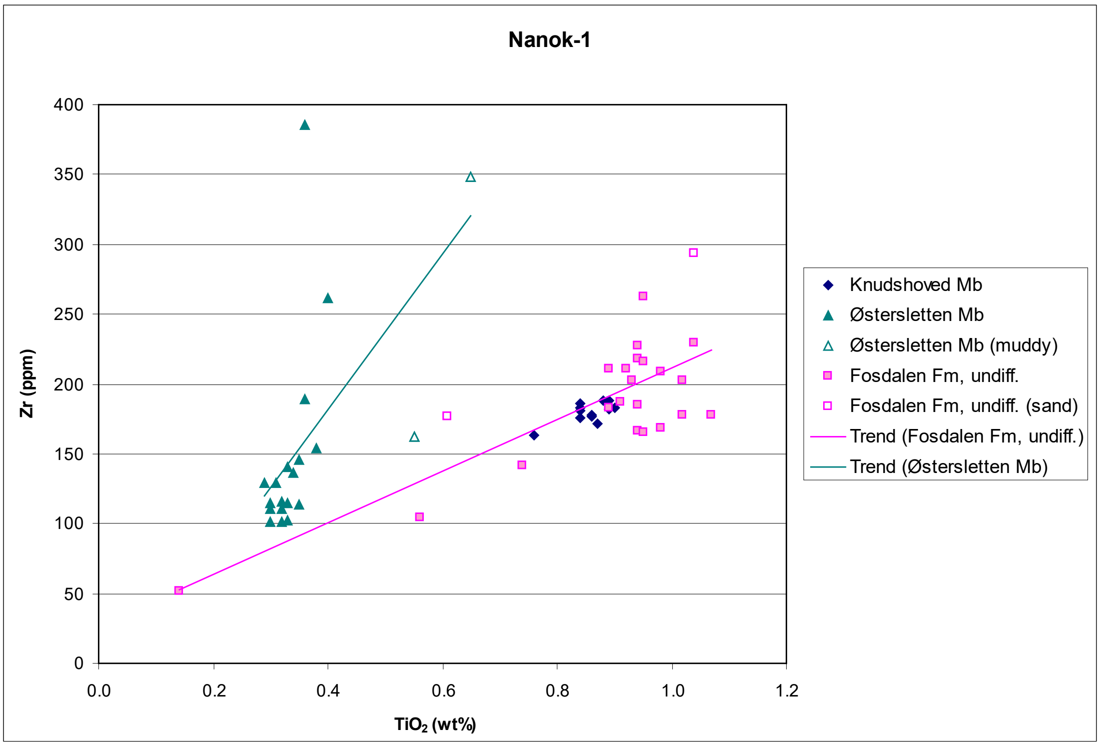

Figure 3.3.4. Graph showing positive correlation between Zr (ppm) and TiO_2 (wt%) with different ratios for the sandstones of the Østersletten Member and the mudstones of the Fosdalen Formation.

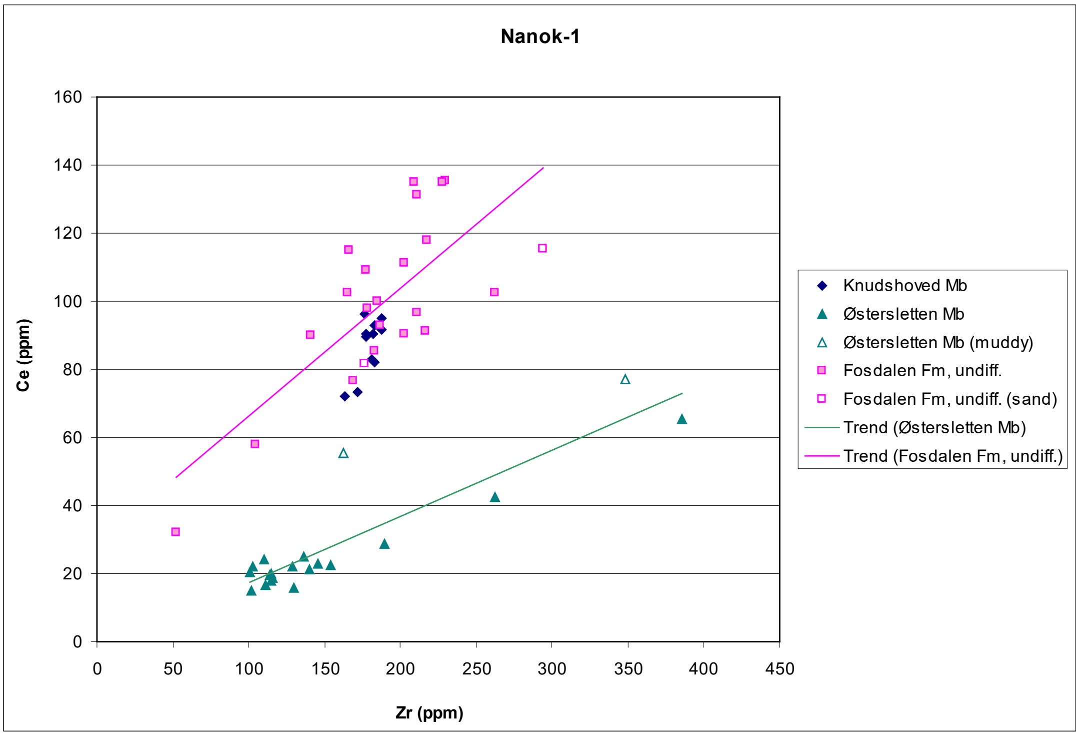

Figure 3.3.5. Graph showing positive correlation between Zr (ppm) and Ce (ppm) with different ratios for the sandstones of the Østersletten Member and the mudstones of the Fosdalen Formation.

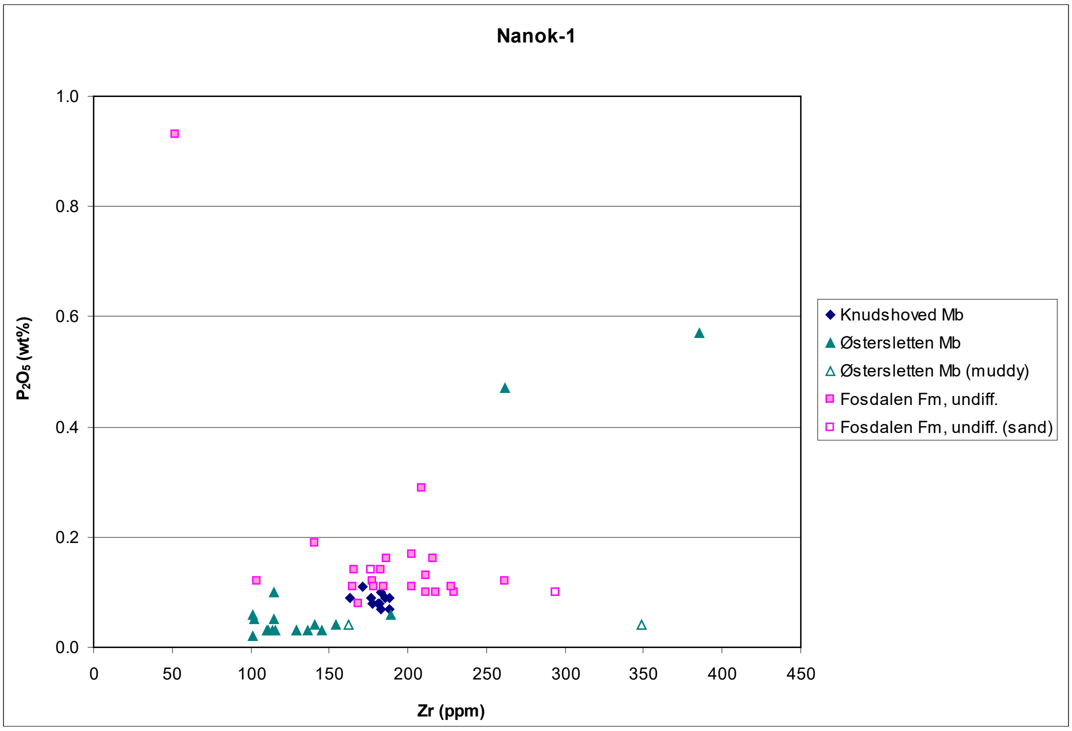

Figure 3.3.6. Graph showing possible positive relation between P_2O_5 (wt%) and Zr (ppm). High P_2O_5 values are associated with high Zr values for the sandstones, but not for the mudstone samples.

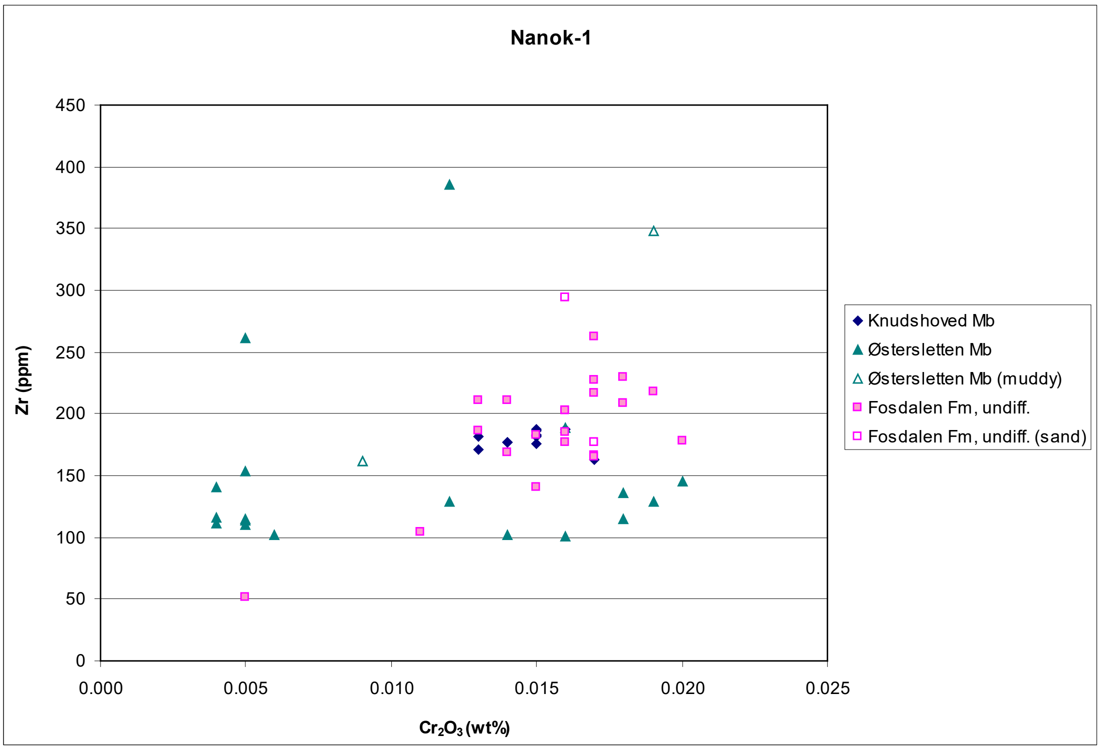

Figure 3.3.7. Graph showing lack of correlation between Zr (ppm) and Cr_2O_3 (wt%).

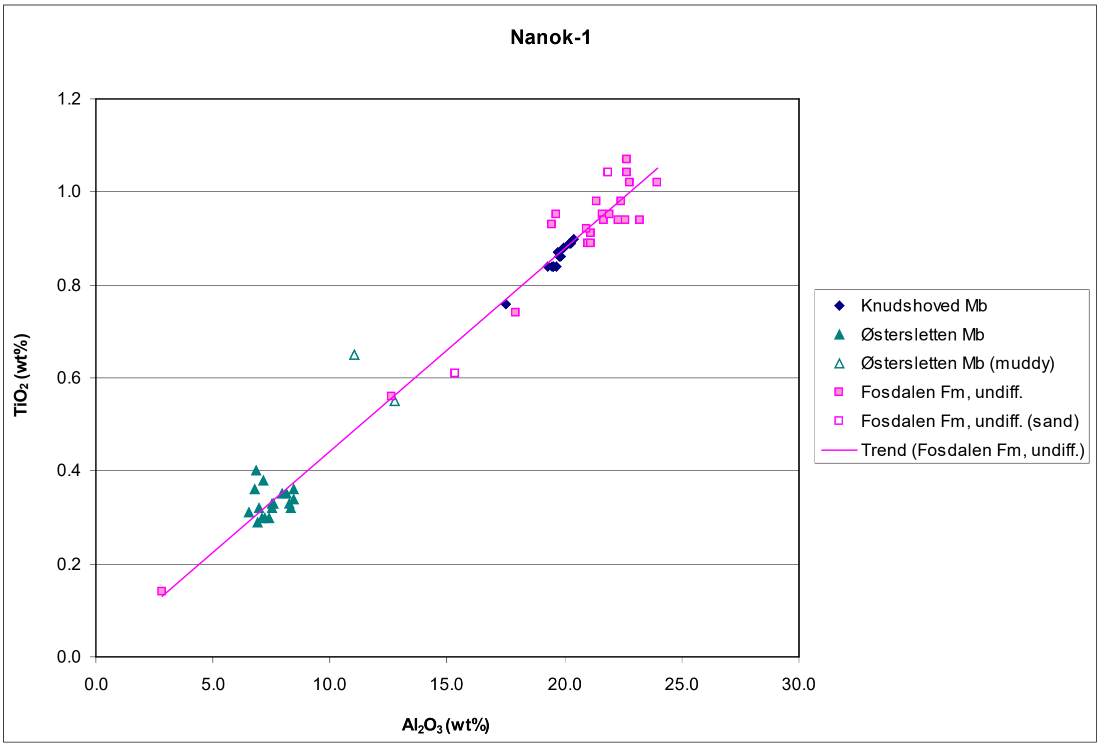

Figure 3.3.8. Graph showing positive correlation between TiO_2 (wt%) and Al_2O_3 (wt%) for both the Østersletten Mb and the mudstones of the undifferentiated parts of Fosdalen Formation and the Knudshoved Member.

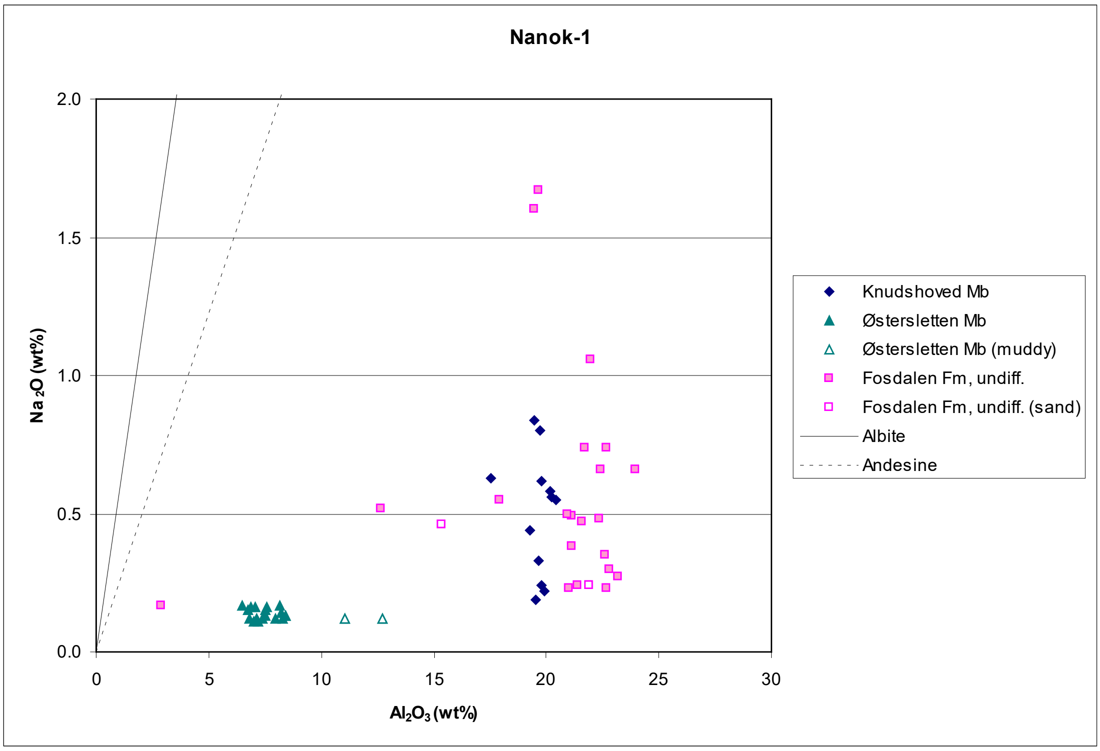

Figure 3.3.9. Graph showing overall positive correlation between Na_2O (wt%) and Al_2O_3 (wt%). Note the Na_2O / Al_2O_3 ratios for both sandstone and mudstone samples are very low compared to the ratios of plagioclase (albite and andesine).

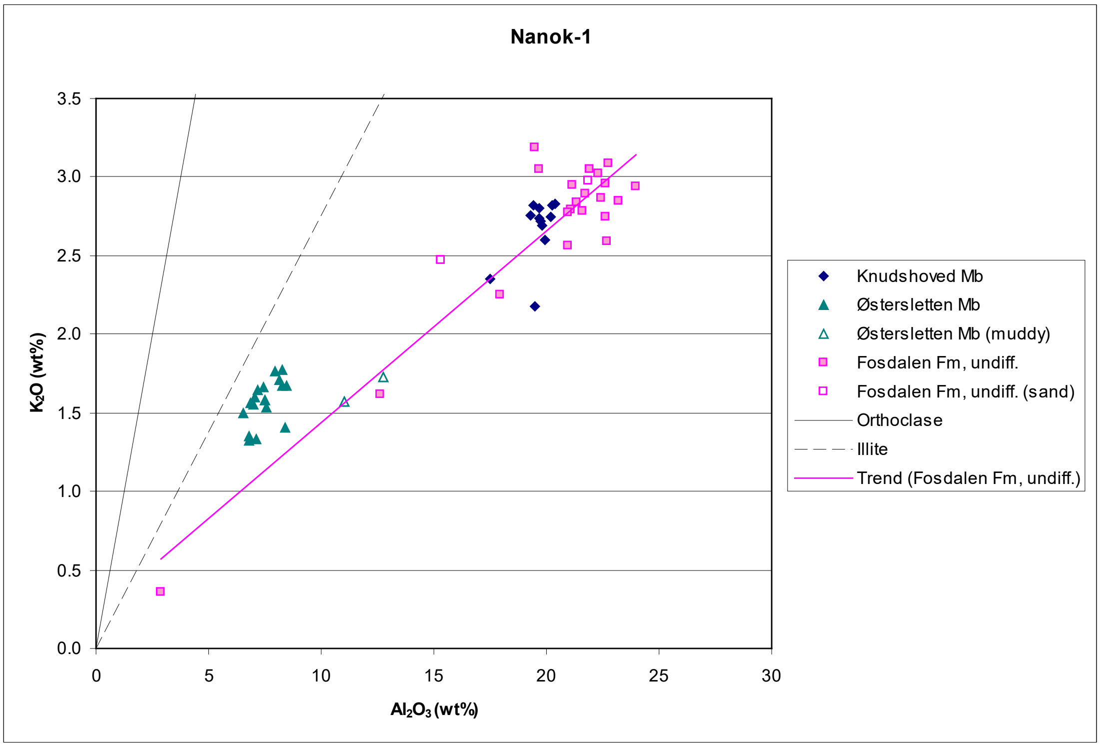

Figure 3.3.10. Graph showing overall positive correlation between K_2O (wt%) and Al_2O_3 (wt%). Note the K_2O / Al_2O_3 ratio is higher for the sandstone than for the mudstones indicating that the sandstones probably contain relatively more mica and K-feldspar.

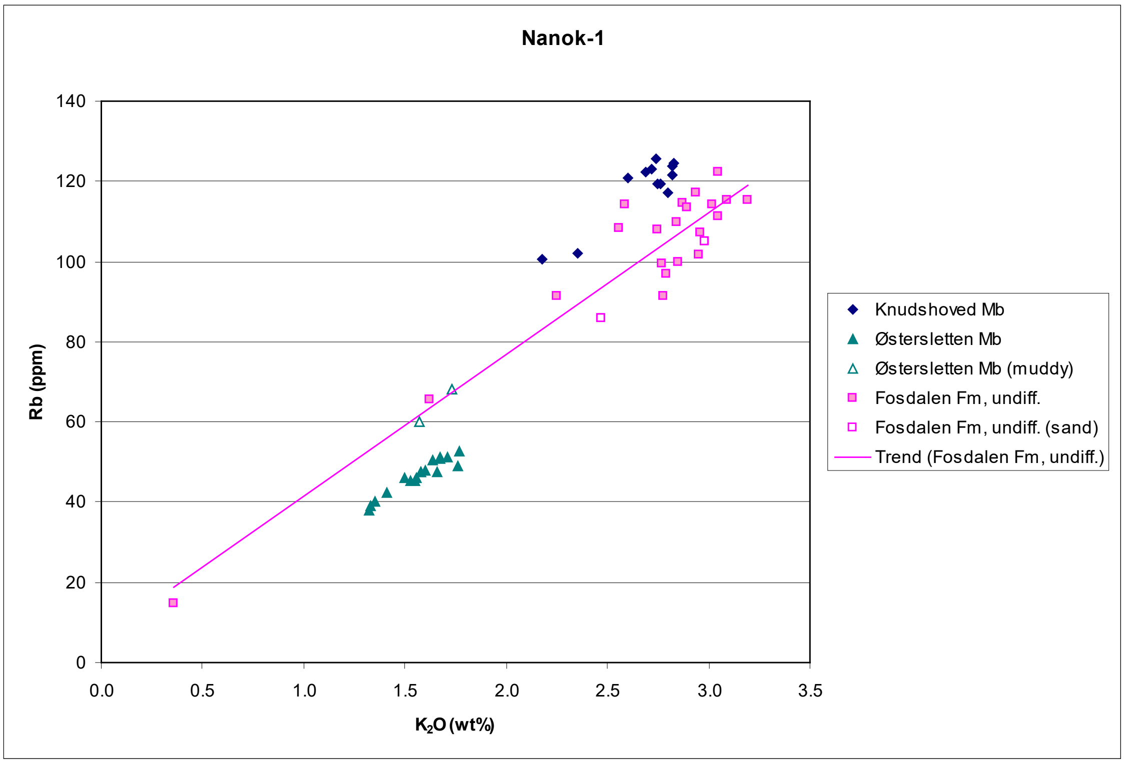

Figure 3.3.11. Graph showing positive correlation between Rb (ppm) and K_2O (wt%). Note the different ratios for the sandstone and mudstone samples.

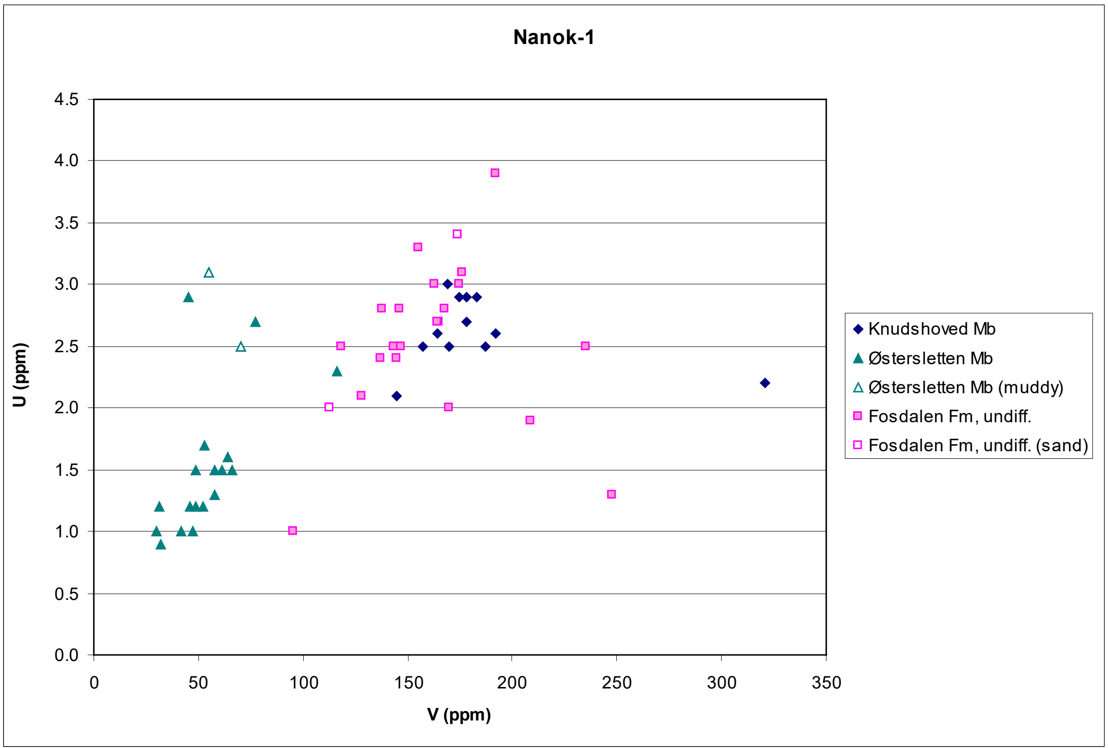

Figure 3.3.12. Graph showing positive correlation between U (ppm) and V (ppm). Note a slightly different ratio for the sandstone samples compared to the mudstone samples.

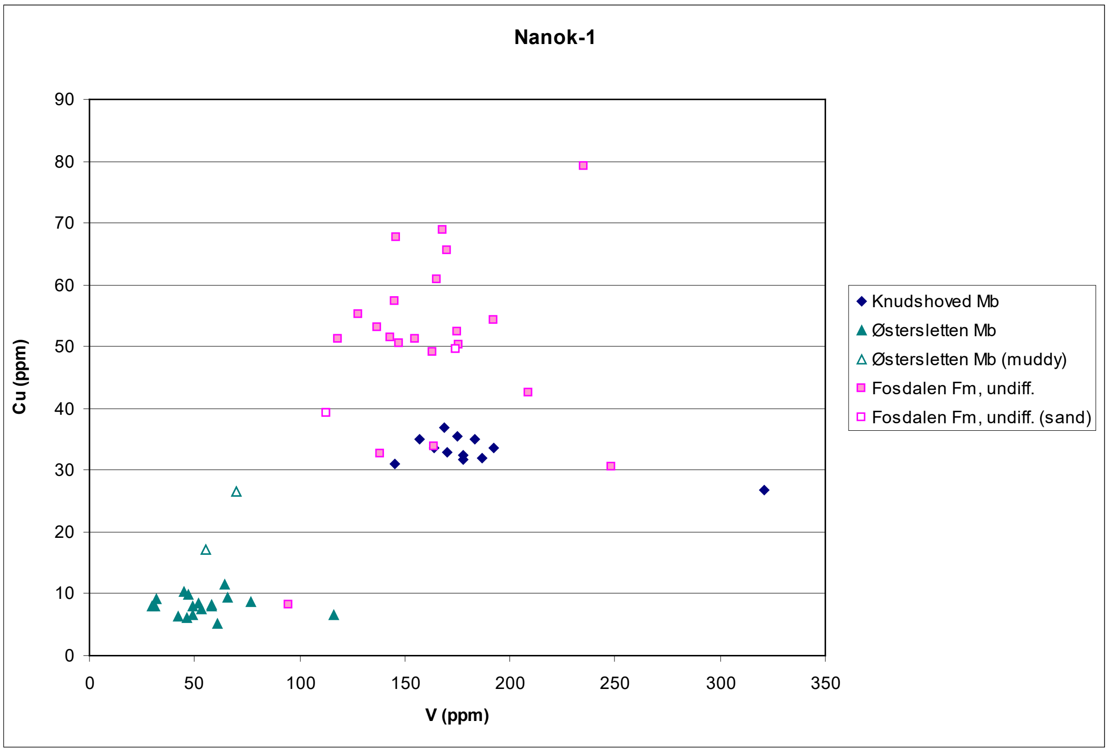

Figure 3.3.13. Graph showing positive correlation between Cu (ppm) and V (ppm). Note the highest content of Cu is in the undifferentiated part of Fosdalen Formation and the lowest content is in the Østersletten Member.

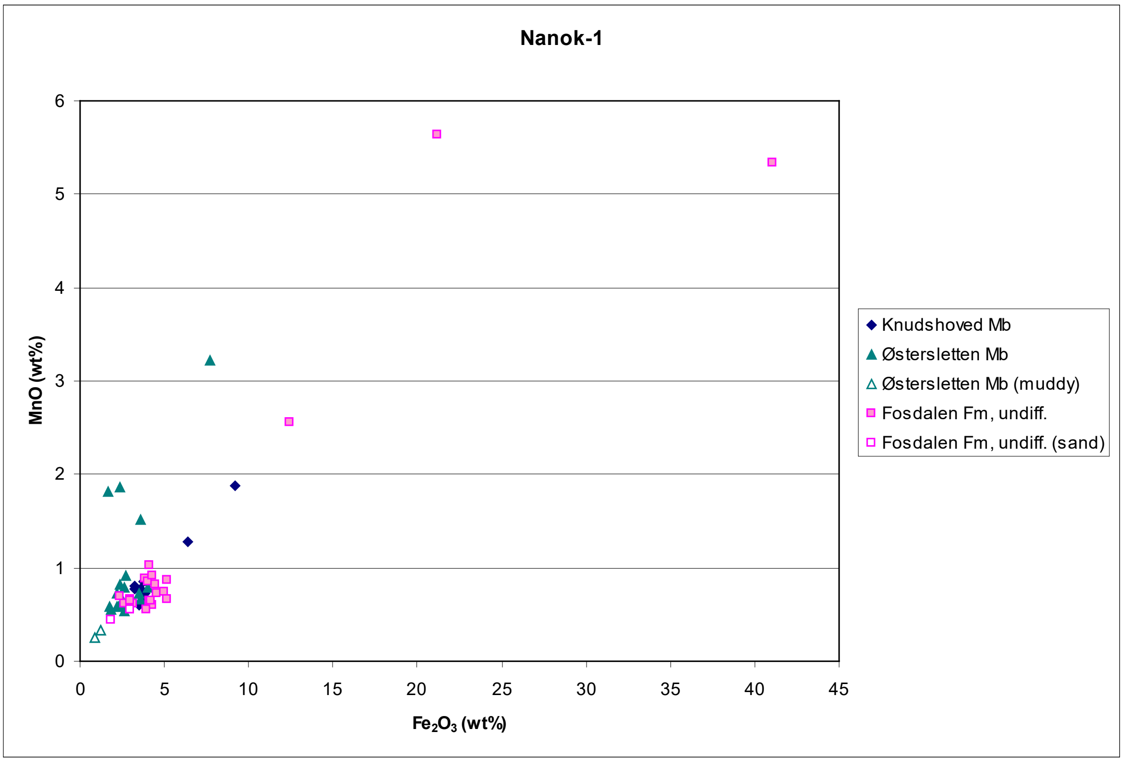

Figure 3.3.14 (previous page). Graph showing positive correlation between MnO (wt%) and Fe_2O_3 (wt%). Note few samples with a remarkable high content of MnO and Fe_2O_3 due to siderite cement.

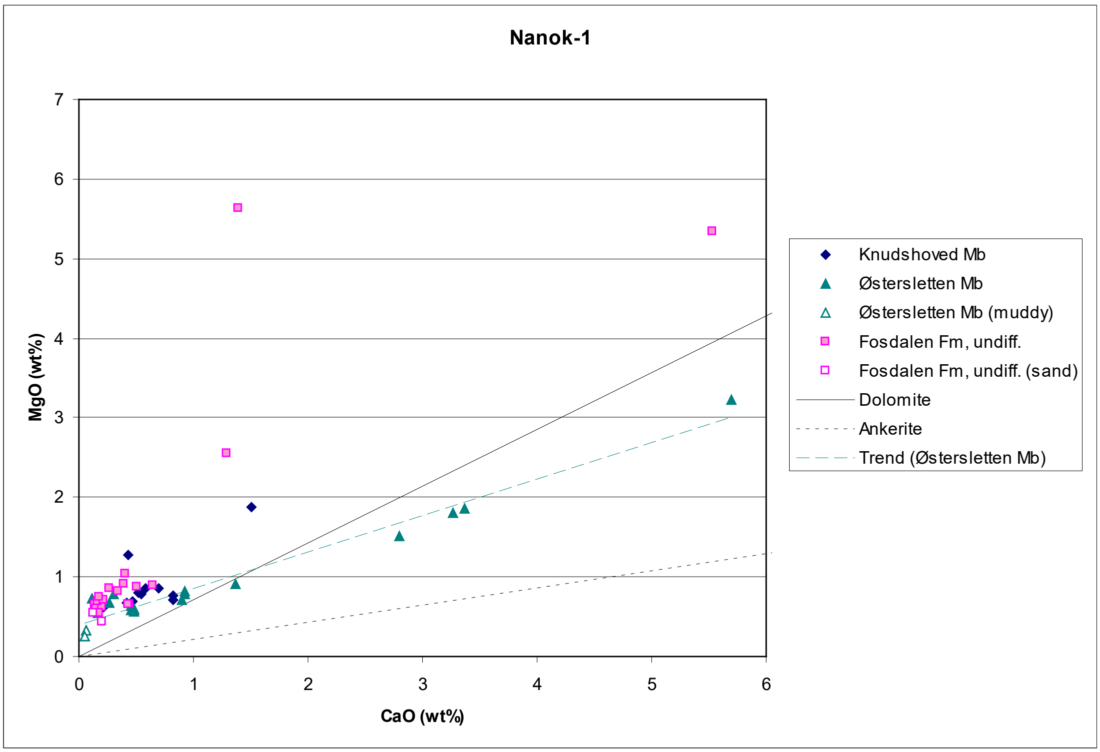

Figure 3.3.15. Graph showing positive correlation between MgO (wt%) and CaO (wt%) for Østersletten Mb with a ratio between the ratios of ankerite and dolomite. Note the more varying MgO and CaO contents of the undifferentiated part of Fosdalen Formation indicating the presence of different types of carbonate cement.

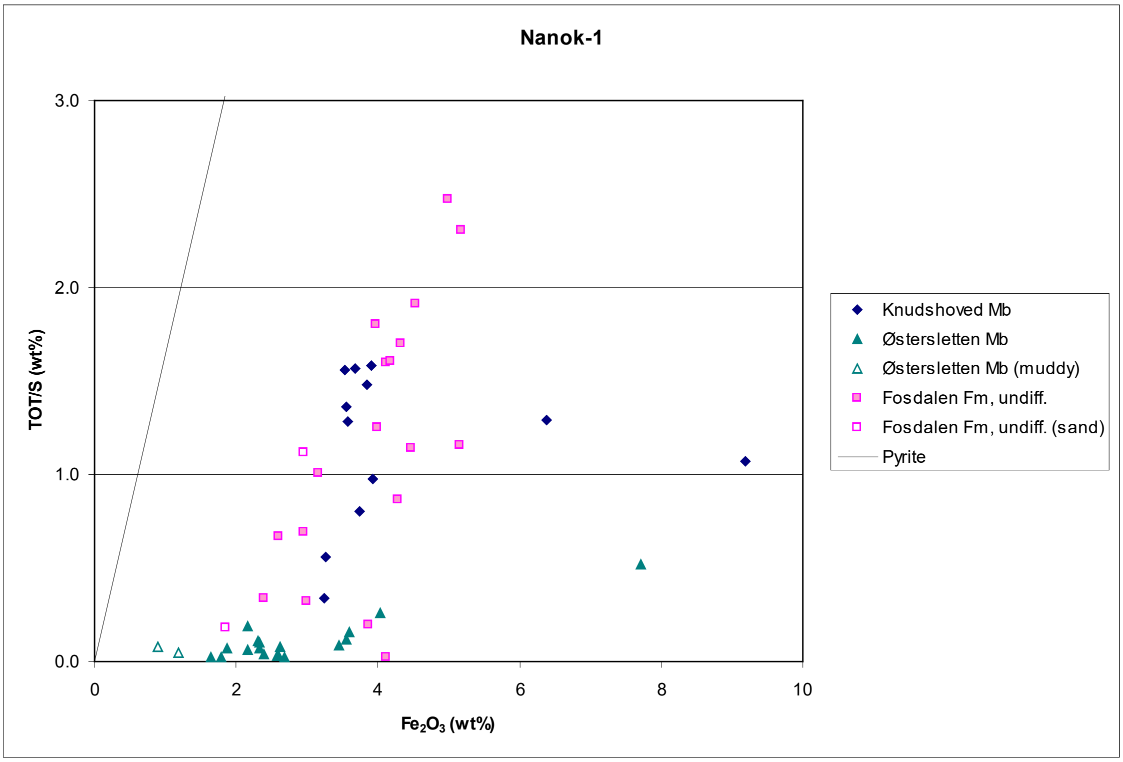

Figure 3.3.16. Graph showing positive correlation between TOT/S (wt%) and Fe_2O_3 (wt%) for the mudstones of the undifferentiated part of Fosdalen Formation and Knudshoved Member with a ratio identical to the ratio of pyrite, thereby indicating the presence of pyrite. Note that the total length of the x-axis is not shown.

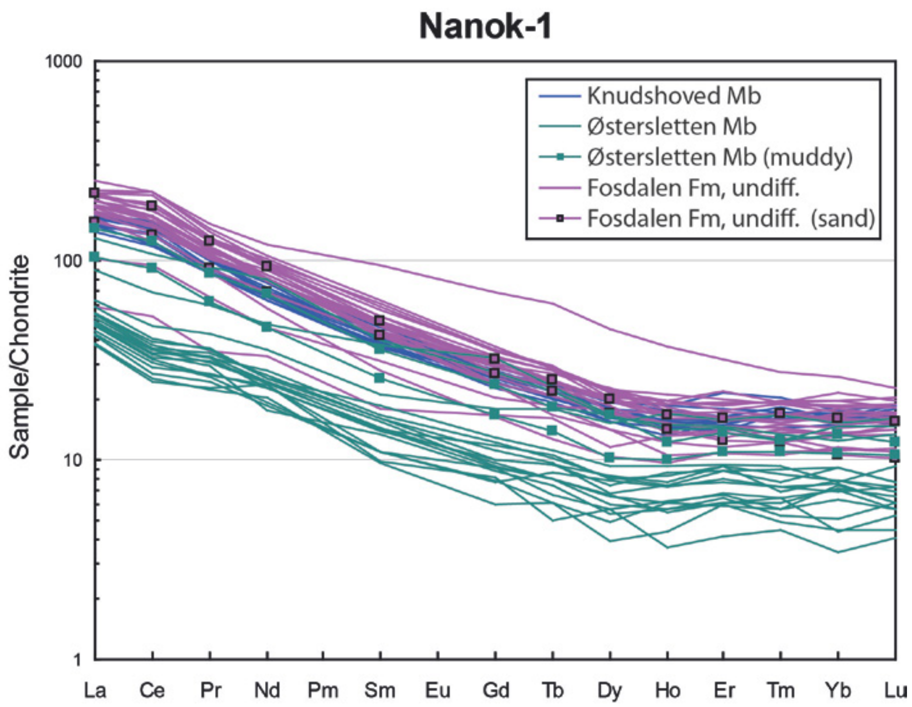

Figure 3.3.17. REE distribution, chondrite normalised (according to McDonough & Sun 1995), of the all samples from the Nanok-1 well.

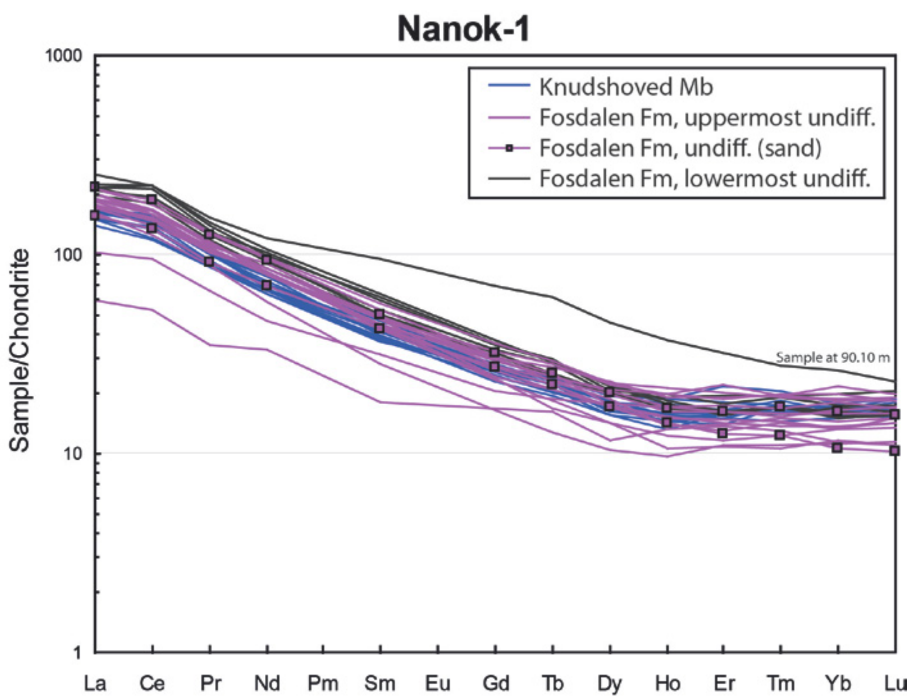

Figure 3.3.18. REE distribution, chondrite normalised (according to McDonough & Sun 1995) of the mudstones Fosdalen Formation.

3.4 Petrophysical core log stratigraphy

Petrophysical logs recorded in the Nanok-1 core well include a total gamma ray log (GR-log) from interval 0–157 m, which was logged in the open drill hole. Later, total GR logging was carried out in the core-lab at GEUS on the lower part of the core in order to obtain a complete GR-log representative for the entire drilled succession. The merged GR-log and the log measured in the field are shown in Figure 3.4.1 together with the GR-log measured in the core-lab. The total GR-log measured in the lab is considered as a separate data set due to different measuring conditions and procedures and illustrated with red colour.

Finally, the Østersletten Mb was scanned with the purpose of establishing a spectral gamma log and pseudo-porosity log for reservoir characterization purposes (Fig. 3.4.2; Chapter 7).

3.4.1 Laboratory scanning of selected core pieces

Results of spectral gamma and bulk density scanning of core sections from the well Nanok-1/1A, are reported below. The work was conducted at GEUS Core Laboratory in spring 2012.

Two intervals of the Nanok-1/1A core were scanned; the interval between 145.89 m and 168.13 m was scanned with the main purpose of completing the wireline gamma-log of the well while the interval between 38.54 m and 84.81 m was scanned with the purpose of establishing a spectral gamma log and pseudo-porosity log of the Østersletten Mb.

Analytical procedure

The Nanok-1/1A core was received as 1 meter sections wrapped in alumina foil. With intervals of approximately 2 meters in the depth direction, the core contained a depth indicator, indicating the depth at that point in meters. The core diameter was 4.2 cm.

A total of approximately 46 meters of core were scanned. The cores were in reasonable condition, with recovery close to 100%. A large majority of the core length presented a full diameter, cylindrical core to the scanner. The fundamental requirement of the scanning procedure, that the scanned material is cylindrical, was therefore fulfilled for a large majority of the cores. However, in mudstone and siltstone intervals, the core showed various degrees of disintegration and in some cases only rubble was present. The bulk density log trace gives a good indication of the quality of the core: core sections where significant parts of the core are missing have bulk density traces with large amplitude variations and minimum bulk density readings below 1.8 g/mL.

The core sections were scanned with the spectral gamma and bulk density scanner of GEUS Core Laboratory. The core sections were scanned sequentially with the core sections being fitted together to present the scanner to a continuous core slowly passing the detectors of the scanner. The core sections were scanned without removing the alumina foil because the alumina foil prevented the cores from falling apart. However, the alumina foil wrapping was opened along the upper side of the core so that the gamma rays of the density scanner only penetrated the alumina foil layer along the lower part of the core. It is estimated that the thin foil had a negligible effect on both the gamma activity and the measured bulk densities.

Scanning was performed in two separate runs (i.e. one run for the extension of the wireline log and one run for the Østersletten Mb.) with a speed of 1 cm/min with read-out of the collected gamma and density data every 60 seconds. Each of the runs was initiated with a calibration of the scanner. The spectral gamma data have intrinsically a low signal-to-noise ratio. To improve the readability of the gamma log, the spectral gamma data were smoothed with a boxcar filter with a bandwidth of 10 cm. This procedure removes little spatial information from the data as the gamma scanner has a depth resolution of approximately 17 cm. Smoothing of the bulk density data was not necessary, because these data intrinsically have a high signal-to-noise ratio and a depth resolution of approximately 1 cm.

Filtering of the density data was done in order to remove the large amplitude variations caused by missing or crushed core. The filtering was preformed in a way that the original high signal-to-noise ratio and depth resolution of approximately 1 cm is preserved.

The calculation of the K, U and Th concentrations assumes a bulk density of 2.4 g/ml.

Measurement of the water content of selected core pieces in the laboratory showed water content below 0.05 % (w/w). Thus, it is assumed that the results pertain to an unsaturated core.

The merged gamma-log consisting of the wireline gamma-log and the recalculated (to GAPI units) gamma-log from the laboratory is presented in Figure 3.4.1.

In addition, the spectral gamma log, the bulk density log, and the pseudo-porosity log of the Østersletten Mb. are presented in Figure 3.4.2.

Analytical methods

Spectral core gamma scanning

The natural gamma radiation of a core is recorded within an energy window of 0.5 - 3.0 MeV, using Tl activated NaI scintillation detectors, connected to a multichannel analyzer.

The core passes through a lead shielded tunnel at constant speed while the gamma activity is continuously recorded. For the Nanok-1/1A scanning, a speed of 1 cm/min was used throughout the scanning, with data read-out every 1 minute, resulting in data points with 1 cm spacing. Nominally, each data point represents the mean gamma activity over a 1 cm depth interval, the assigned depth being the middle of the interval. Actually, the scintillation detectors record the gamma activity in a broader section of the core. The sensitivity profile in the depth direction of the core has approximately the shape of a gauss-function with a Full Width at Half Maximum (FWHM) of approximately 17 cm. The measured gamma activity is corrected for background gamma activity.

To improve the readability of the logs, the raw data were filtered with a box-car filter with a bandwidth of 10 cm. The smoothing causes a slight deterioration of the sensitivity profile in the depth direction to approximately 19 cm FWHM, still with an approximate gauss-shape.

Total gamma activity is reported in counts per second (cps). Bore-hole wireline logs are usually reported with gamma activity in GAPI units traceable to the calibration facility known as the API pit at the University of Houston in Texas. The following empirical relationship has been established between GAPI units and the cps (counts per second) unit reported for total gamma activity on the GEUS core gamma scanner. The relationship is not certified and should be used only as a rough guideline:

$$GAPI = cps * (10/d)^2 * 3.3$$

Eq. 1

where d is the nominal core diameter in cm.

For the Nanok-1/1A core scanning Equation 1 becomes:

*GAPI = cps * 18.7*
Eq. 2

Radiation from decay of potassium and the uranium and thorium decay series are recorded in separate energy windows. Concentrations are calculated using synthetic standards of concrete doped with known amounts of radioactive minerals in decay equilibrium. Concentrations of K, U and Th are reported as % K, ppm U and ppm Th, respectively. Relevant ratios are given. Concentrations are calculated on the assumption that decay equilibrium is established for both the thorium and uranium decay series. This is generally assumed to be true for geological samples (Schlumberger: Log interpretation principles/applications, Schlumberger Educational Services, 1991).

Because a concentration is the mass ratio between the mass of the element of concern and the total mass being analyzed, the calculation of a concentration requires knowledge of the mass being analyzed. For the spectral core gamma log this knowledge is provided by assuming a constant bulk density for the core. In principle, the bulk density measured for each data point along the log could be used for calculating concentrations. However, a significant part of the measured bulk density values are biased by missing core material, fractures, and the presence of alumina foil or metal cans. Therefore, a fixed bulk density value of 1.5 g/mL was chosen as basis for the concentration calculation, rather than a measured but potentially erroneous value.

The processing of the spectral core gamma data assumes that the core has a constant diameter. Core sections where this assumption does not hold have concentrations that are systematically biased. If core material is missing, the calculated concentration values are too low.

Bulk density scanning
The measurement of the core bulk density is based on the attenuation of gamma rays passing through the core. The gamma rays come from a 30 mCi ^{137}Cs radioactive source emitting photons of energy 662 keV. A collimated beam of gamma rays with a diameter of 0.8 cm passes through the core and is recorded by a NaI scintillation detector.

At the scanning, the core passes the gamma ray source and detector assembly at a constant speed while the gamma ray attenuation is continuously recorded. The density scanning was conducted contemporaneously with the gamma scanning and therefore the scanning speed of 1 cm/min that applies for this operation also applies for the density scanning.

Similarly, a read-out interval of 1 cm was used for the density scanning. However, the density data were not box-car filtered because the reproducibility of the density data was so good that smoothing was not necessary.

The processing of the bulk density data assumes that the core has a constant diameter. Core sections where this assumption does not hold have densities that are systematically biased. If core material is missing, the resulting density values are too low.

Filtering of the density data was done in order to remove the large amplitude variations caused by missing core, crushed core or from gaps between the termination of one core section and the beginning of the next. The filtering was performed in a way that the original high signal-to-noise ratio and the depth resolution of approximately 1 cm are preserved.

The density log includes data measurements with a spacing of approximately 1 cm. Minimum bulk density readings below 1.8 g/ml was prior to the filtering removed from the data since these low values clearly reflects measurements of gaps.

The principle in the filtering process is a comparison of a running average measure of the data and the data itself. Step 1 in the filtering was to establish a running average measurement calculated in a 5 sample point window according to

$$Ravgi = \frac{\sum di + di \pm 1 + di \pm 2}{n}$$

Eq. 3

where *di* is the data value in depth *i* and *n* is the number of data measurement in the 5 point data window. The number of real data in the 5 sample point window may vary from 5 to 0, depending on the number of missing values.

Step 2 was the actual filtering part and was done according to

$$Ravgi - di \leq 0.1 g / ml$$

Eq. 4

The data, *di*, with a difference above 0.1 g/mL was removed from the data set by replacing it with the symbol '-999999', which is the missing value identifier in the present work. It should be noted that since the filtering according to Eq. 4 is only one sided then density measurements heavier than 0.1 g/mL compared to the average value is not filtered away.

Step 1 and 2 was repeated 5 times giving a total of 4 filtering runs. Only a very small number of data measurements were removed in the last filtering run.

Calculation of pseudo-porosity log

The measurement of the core bulk density provides a basis for the calculation of a pseudo-porosity log using the filtered bulk density data set. The calculation requires knowledge about the grain density and the water content of the sample. In the present case, the core was assumed to be dry and a constant grain density of 2.68 g/mL was assumed based on the average measured grain density of CCAL sandstone plugs with grain densities above 2.60 g/mL. The application of a constant grain density provides a slight overestimation of the porosity for intervals containing large amounts of coal or organic matter while for intervals of the core where average grain densities are higher than 2.68 g/mL, the pseudo-porosity slightly underestimates porosity. However, for the majority of the core, the CCAL data suggests the grain density to vary between 2.60 g/mL and 2.70 g/mL. The corresponding maximum error in the calculated pseudo-porosity is up to 3 p.u.

The pseudo-porosity log (in %) is calculated from the following relationship:

$$\Phi = 100*(\rho_g - \rho_b)/\rho_g$$
Eq. 5

where Φ is the porosity calculated in % of bulk volume; ρ_g is the grain density (in g/mL); ρ_g is the bulk density (in g/mL).

Depth assignment

The Nanok-1/1A core was scanned with a constant speed of 1 cm/min. The actual length of every core section in its scanning position was recorded, as well as the position of the section top and section bottom relative to the detectors of the scanner. Using this information every data point were assigned a laboratory depth relative to the top of the core. Because the lengths of core sections during scanning were not necessarily equal to the nominal lengths of the sections, the laboratory depth relative to the top of the core could not be converted to true core depth by simple translation. For every core section a rubber-band depth conversion was applied according to:

$$CoreDepth(I,J) = Top(J) + (I - 0.5) * Increment * \frac{Bottom(J) - Top(J)}{Length(J)}$$

Eq. 6

where *CoreDepth(I,J)* is the depth assigned to data point no. *I* in core section no. *J*, *Top(J)* and *Bottom(J)* are the nominal depth of top and bottom of the core section, *Increment* is the depth interval between data points, and *Length(J)* is the length of section *J* during scanning. Additional minor corrections were applied to data points where the data collection had occurred across sections borders.

The depths assigned by the depth assignment procedure have an uncertainty relative to section borders of approximately 1 cm.

3.4.2 GR-log signature of lithostratigraphic units

The igneous intrusion (TD–~160 m), the undifferentiated Fosdalen Formation (~160–~84.2 m), the Østersletten Member (~83–~42.5 m) and the Knudshoved Member (~42.5–0 m) are expressed on the GR-log in the following way:

The mudstone units, the lower part of the undifferentiated Fosdalen Formation (~160–~138 m; Facies Association 1) and the Knudshoved Member (~42.5–0 m; Facies Association 4), show similar, generally trendless and locally serrated GR patterns. The serrated response is caused by locally occurring thin sandstone interbeds as well as cm-to dm-scale, ankerite and siderite cemented intervals. In general, the GR baseline situates around 70–80 GAPI.

The upper part of the undifferentiated Fosdalen Formation (~138–94 m; Facies Association 2) shows distinct sedimentary facies, including common cemented intervals as well as m-scale sandstone occurrences. As a result, the GR-log shows more prominent low-reading peaks (~30–45 GAPI) in this part of the core. Subtle, funnel-shaped (upward coarsening) units a few m-thick occur locally.

The sandstones of the Østersletten Member (~83–~42.5 m; Facies Association 3) show a blocky GR-log response that clearly stands-out from the otherwise mud-dominated sedimentary series. This reflects the aggradational nature of the unit and general lack of clay in the sediments. The m-scale structureless sandstones beds that form bulk of the unit show

GR values around ~30 GAPI. The subordinate interbeds are more heterolithic and show values up to 60 GAPI.

Finally, the GR expression to the igneous intrusion at the base of the core is blocky with values around ~15 GAPI.

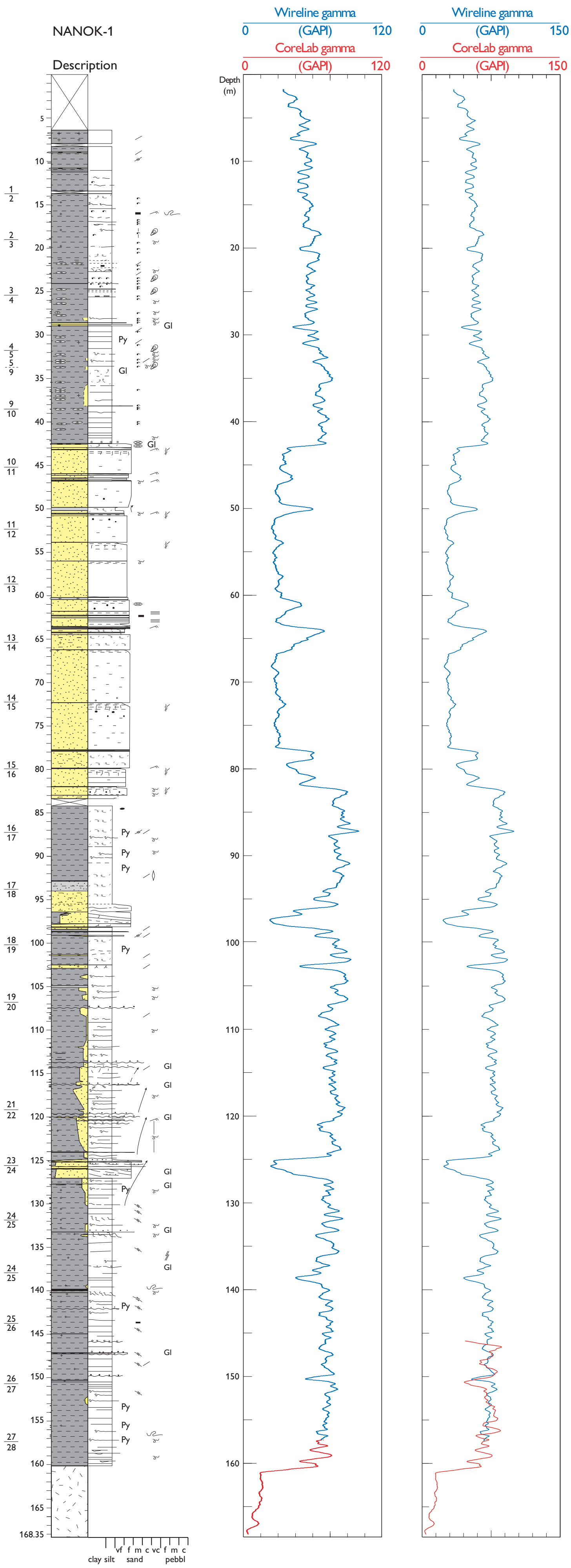

Figure 3.4.1 Gamma Ray logs (composite, measured in the field (blue) and in the laboratory(red)) and the lithological column of the Nanok-1 well

GØ04_02M_410_JHOV

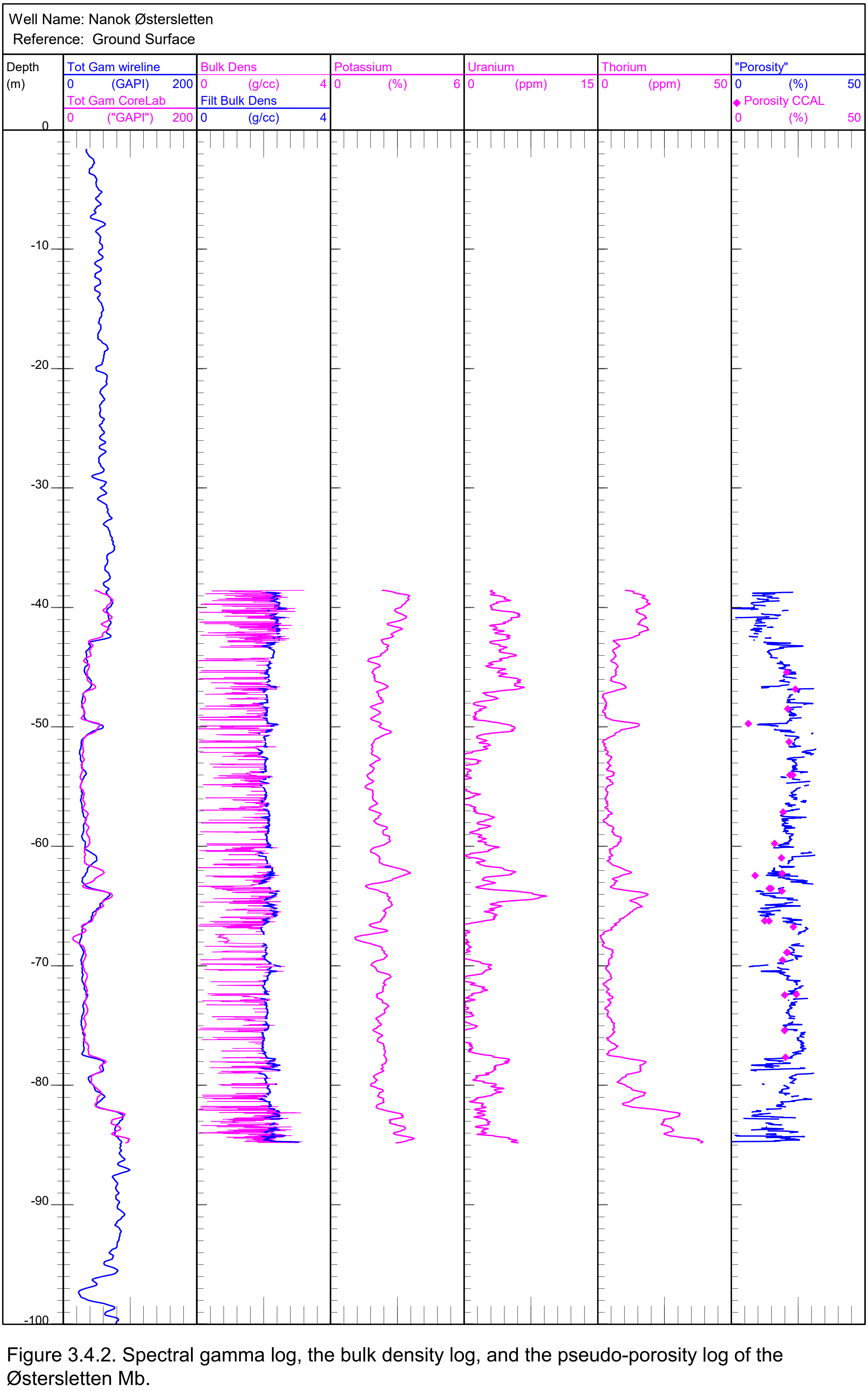

Figure 3.4.2. Spectral gamma log, the bulk density log, and the pseudo-porosity log of the Østersletten Mb.

3.5 Stratigraphic conclusions

The Nanok-1 core interval is subdivided into 1) the undifferentiated Fosdalen Formation (~160–~84.2 m); 2) the Nanok Member (~84.2–83 m); 3) the Østersletten Member (~83–42.5 m); and 4) the Knudshoved Member (~42.5–0 m). The base of the core (TD–~160 m) consists of an igneous intrusion. The Nanok Member is inferred to be present in a thin interval of non-recovery of core and limited rubble below the Østersletten Member. The lithostratigraphic division follows the recently redefined lithostratigraphic scheme of Bjerager *et al.* (2012).

The core is dated to be Late Cenomanian – Early Campanian on the basis of dinoflagellate stratigraphy. The mudstone-dominated undifferentiated part of the Fosdalen Formation (~160–~84.2 m) is dated as Upper Cenomanian – Middle Coniacian. The Cenomanian–Turonian boundary is placed at the first stratigraphic occurrence of *Heterosphaeridium difficile* (112.31 m). This is supported by high $\delta^{13}C_{org}$ values near this interval, which appear to correlate with data from well constrained Cenomanian–Turonian boundaries (Jarvis *et al.* 2011).

The Turonian–Coniacian interval shows evidence of stratigraphic condensation.

The Nanok Member (~84.2–83 m) is poorly represented in the core. Field data shows that the unit is sharp-based (Kelly *et al.*, 1998) and possibly truncates the top of the undifferentiated Fosdalen Formation. The change from the undifferentiated Fosdalen Formation to the Nanok Member is clearly expressed as a distinct lithofacies change from dark grey mudstones to red, hematite and goethite rich, muddy and pebbly sandstone. The top of the unit is finer grained. The Nanok Member is also very condensed and/or includes a significant hiatus. It was deposited between the Late Coniacian and Middle Santonian.

The Nanok Mb is overlain by the Østersletten Mb (~83–42.5 m). Its lower boundary is sharp (erosional) and readily recognizable in sedimentary facies as an abrupt appearance of structureless sandstones. Moreover, the member change is recognizable in GR-log and chemostratigraphic data. Most of the Østersletten Member is dated as Upper Santonian. The very top of the member contains the *Aquialapollenites* pollen zone suggesting an Early Campanian age for this interval.

The Østersletten Member is sharply overlain by the Lower Campanian Knudshoved Member (~42.5–0 m). The boundary is readily recognizable by an abrupt increase in the GR log values, which reflect lithofacies change from sandstone to mud-dominated lithology. Chemostratigraphically, the Knudshoved Member and the undifferentiated Fosdalen Formation are very similar.

Finally, the igneous intrusion present at the base of the core was not suitable for dating by the $^{39}Ar/^{40}Ar$ method. However, two dated dykes from Wollaston Forland and Bontekoe Ø, which are not too different from the Nanok intrusion, have $^{39}Ar/^{40}Ar$ ages of 51–53 Ma, and this is considered the likely age of the Nanok intrusion (Chapter 11).

3.5.1 References

Bjerager, M. *et al.*, 2012: The Cretaceous of NE Greenland: Lithostratigraphic subdivision (Subproject 3). Contribution to Petroleum Geological Studies Services and Data in East and Northeast Greenland. Danmarks og Grønlands Geologiske Undersøgelse Rapport 2012/50, 56 pp

Jarvis, I., Lignum, J.S., Gröcke, D.R., Jenkyns, H.C., & Pearce M.A., 2011: Black shale deposition, atmospheric CO_2 drawdown, and cooling during the Cenomanian–Turonian Oceanic Anoxic Event. Paleoceanography, **26,** PA3201, doi:10.1029/2010pa002081.

4. Sedimentology

The Nanok-1 core was described sedimentologically and ichnologically at a scale of 1:20. The sedimentological description included descriptions of lithology, grain size (visual estimation) and grain-size trends, primary and secondary sedimentary structures, bedding contacts, mineralogical accessories and the identification of important stratigraphic surfaces. Ichnological data comprises description of ichnogenera, trace fossil assemblage, cross-cutting relationship and bioturbation index (BI of Taylor and Goldring, 1993). BI provides a description of the degree to which original sedimentary fabric has been destroyed as a result of biogenic processes. This classification scheme allocates a numerical value ranging from 0 to 6 – the values corresponding to a percentage of bioturbation (cf. Taylor and Goldring, 1993). Undisturbed or non-bioturbated sedimentary fabrics are classified as BI 0 (0 percent reworked), while pervasively bioturbated media (100 per-cent reworked) are classified as BI 6. Intermediate levels of bioturbation are characterized using BI 1–5 and are defined as follows: BI 1, 1–4 percent reworked; BI 2, 5–30 percent reworked; BI 3, 31–60 percent reworked; BI 4, 61–90 percent reworked; and, BI 5, 91–99 percent reworked (Taylor and Goldring, 1993).

Lithostratigraphically, the cored section is referred to the Fosdalen Formation (Fig. 4.1), as redefined in the recently completed lithostratigraphy sub-project of the Cretaceous project (see below); the lower half of the core (Upper Cenomanian – Middle Coniacian) is referred to the undifferentiated Fosdalen Formation, the upper half to the Upper Santonian – Lower Campanian Østersletten Member and the Lower Campanian Knudshoved Member. The Nanok Member (?Middle Coniacian – ?Middle Santonian) is inferred to be present in the section at a thin interval of non-recovery of core and limited rubble. Note that these lithostratigraphic units were formerly included in the Home Forland Formation as members (Kelly *et al.*, 1998). In the refined stratigraphic scheme presented recently, the Fosdalen Member was elevated to the rank of a formation (part of the Home Forland Group), whereas the other units retain their status as members within the Fosdalen Formation.

4.1 Description and Interpretation

4.1.1 Sedimentary facies

The deposits are divided into 5 facies (F1–5).

F1: Mudstone

F1A: Laminated to massive mud

F1B: Bioturbated mud

F1C: Fossiliferous mud

F2: Heterolithic bedding/lamination

F2A: Interlaminated mud and sand

F2B: Biodeformational structures bearing Interlaminated mud and sand

F2C: Sand-dominated heterolithic bedding

F3: "Hiatal lags"

F4: Sandstone

F4A: Massive – stratified sandstone

F4B: Bioturbated muddy sandstone to sandstone

F4C: Parallel laminated to ripple cross-stratified sandstone

F5: Slumps

Facies F4A is a broad facies type that is sub-divided into 3 sub-facies, in particular for reservoir characterization purposes: these are structureless fine-grained sandstone ($F4A_1$), carbonaceous dewatered sandstone ($F4A_2$) and allochthonous sandy coal ($F4A_3$).

4.1.2 Facies Associations

The deposits are further divided into four facies associations (FA1–4). These are described and interpreted below under the relevant lithostratigraphic unit. GR-log signatures of each facies association are briefly discussed in Chapter 3.4.

Fosdalen Formation, undifferentiated

FA1: Basinal/incipient slope mudstones

Description: FA1 is present in the Upper Cenomanian interval (160–~138 m; Fig. 4.1.), where it is truncated by an igneous intrusion. It consists dominantly of laminated mudstone

(F1A), bioturbated mudstone (F1B), interlaminated mud and sand (F2), and slump units (F5). Locally present are glauconite-rich sandstone layers/surfaces (F2/F3). No clear facies trends were recognized in the sediments.

The laminated mudstone (F1A) forms cm- to dm-scale units and locally show color-banding that consists of interlaminated dark grey mud, and pyritized lamina (Fig. 4.2). This facies is commonly unbioturbated and is closely associated with slump units (folded lamination). Siderite and ankerite cemented mudstone intervals occur locally (Chapter 3.3).

These deposits are interbedded with interlaminated mud and sand and cm-scale intervals of bioturbated mudstone. The heterolithic interlamination consists of irregular interlamination that contains poorly-sorted sandstone lamina showing glauconite, coal-fragments and small-scale mud-clasts (Fig. 4.3A). In places, these strata show soft sedimentary deformation and can grade into sandy mud. Finally, small-scale erosional scours and lenses are present locally.

Bioturbation intensity is variable, ranging from common unbioturbated to moderately bioturbated (BI 0–3). The deposits are characteristically bioturbated with low-diversity trace fossil assemblages that consists of diminutive and large grazing structures (*Phycosiphon, Helminthopsis* and ?*Nereites*) and local *Chondrites*. Gradational occurrences with F2B show *Planolites* and burrow mottling.

Interpretation: The present facies and trace fossil assemblage point to a sub-storm wave base marine setting. The irregular, erosionally-based poorly-sorted laminae may point to bottom current influence (e.g., Stow *et al.*, 2002; see Discussion). The occasional minor slump units may suggest a marginal slope setting. The F1A color-banded mudstone intervals show some similarities with the Bernbjerg Formation and Lindemans Bugt Formation source rock facies (see e.g., Hovikoski *et al.*, 2012), and show slightly elevated S1, S2 and HI values (~140 m). However, these occurrences are thin and intimately interbedded with bioturbated deposits (F1B and F2).

FA2: Tidally-influenced "prodelta/fan fringe"

Description: FA2 is present in the uppermost Cenomanian – Middle Coniacian interval. It overlies FA1 conformably. The boundary is placed at ~137 m and marked by gradational facies change (see below).

FA2 comprises a ~50 m-thick irregular sedimentary succession that consists of various types of heterolithic bedding (F2; Figs. 4.3 and 4.4). Moreover, characteristically present are erosional surfaces that bear lag deposits (F3; Fig. 4.5). These strata are organized into a few m-thick upward coarsening (UC) successions that are commonly capped by the hiatal lag surfaces. Also present are upward fining (UF) and trendless successions.

The base of the UC successions consists of heterolithic interlamination that is characterized by abundant soft-sedimentary deformation, common biodeformational structures, and unbioturbated inversely to normally graded lamina sets (F2B; Fig. 4.3). Upwards, the graded lamina sets start showing more commonly erosionally-based sand-lamina so that the inversely graded part becomes partly or completely missing.

These deposits are variably bioturbated (BI 0–4) with a limited trace fossil assemblage consisting of biodeformational structures, *Planolites*, *Teichichnus* and escape structures. This fabric is locally interbedded with a *Phycosiphon, Helminthopsis* and *Chondrites* dominated assemblage (F2A).

The capping erosional surfaces show common glauconite fragments, concretion and mud clasts, and overlie sideritic and ankeritic intervals (Chapter 5). In some cases, a subtle, firmground trace fossil assemblage (*Glossifungites* Ichnofacies) descends from the erosional surface (Fig. 4.5A).

In two occurrences, the deposits show sand-dominated heterolithic bedding (F2C), which shows pervasive double mud-drapes (Figs. 4.4AB). Locally, the sand-clay couplets show cyclic thickening and thinning. At 97 m, sigmoidal cross-stratification is possibly present. F2C is burrowed with elements of the *Skolithos* Ichnofacies including *Ophiomorpha, Skolithos* and *Palaeophycus tubularis.* Moreover, the top of the bed can be intensively bioturbated by *Asterosoma* (Fig. 4.4D), *Teichichnus, Planolites*, burrow mottling and *Taenidium*. *Chondrites* reburrows *Asterosoma*.

Interpretation: Recurring double mud-drapes and locally occurring cyclic thickening and thinning of sand-clay couplets point to strong tidal-influence in these deposits. This interpretation is supported by the distribution of bioturbation in these strata as the burrows locally descend from the mud-drapes (semi-diurnal slack interval) and are concentrated in the intervals where sand-clay couplets are thinnest (neap tides). Moreover, FA2 is characterized by abundant fluid mud sedimentation as evidenced by widespread soft sedimentary deformation and biodeformational structures (or mantle-and-swirl trace fossils; Lobza and Schieber, 1999; Schieber, 2003), which indicate very low initial substrate consistency. This is characteristic of tidally-influenced "estuarine" environments where elevated water turbidity enhances mud-flocculation and formation of dense fluid mud layers. In this way, FA2 bears some similarities even with estuarine bay-head-deltas (e.g., Middle Jurassic deposits of the Bryne Fm.), which show characteristically stacked, fluid mud prone heteroliths that are locally interbedded with sandy mouth bar deposits. The differences include lack of wave-generated structures and the occasional *Nereites*-bearing trace fossil fabrics in these deposits, which reflect ambiental shelf – basinal conditions following the shut-off of the tidal currents.

The CU successions are interpreted as parasequences. Their top is commonly truncated by erosional surfaces that show lag deposits, firmground burrows and development of sideritic/ankeritic cements. These are interpreted to record erosional bottom current peaks.

In concert, considering the above mentioned sedimentological and ichnological characteristics of FA2, as well as its stratigraphic position, FA2 is interpreted as tidally-influenced prodeltaic/fan fringe deposits.

Nanok Mb

Description: The Nanok Mb is poorly represented in the core. The alleged location of the member is represented by a 1 m interval of missing core (~84.2–83 m). This is overlain by a rubble interval that contains a 5 cm-thick core piece of black and greenish clast-bearing siltstone. These fragments probably represent a fraction of the upper part of the Nanok Member as described by Kelly *et al.* (1998). Also present are core pieces showing bioturbated (BI 6), muddy fine-grained sandstone that are burrowed e.g., with *Terebellina (Schaubcylindrichnus freyi*).

Biostratigraphic data confirm that these sporadic core pieces are time equivalent to the Nanok Mb (?Middle Coniacian – ?Middle Santonian).

In the field, the unit is sharp-based and up to 6 m-thick. Its base comprises red, muddy and pebbly sandstone that is characterized by diagenetic hematite as well as common reworked, phosphatized burrows (Kelly *et al.*, 1998). A thin section and samples for SEM and XRD were produced from field samples collected from this interval and results are presented in Chapter 5. No thin section was eventually produced from the core material due to lack of comparable facies in the core.

The upper part of the member is more argillaceous and has not been described in detail. The core fragments present in the core probably come from that interval.

Interpretation: The reddish, hematite- and goethite-rich lower part of the Nanok Member is interpreted to reflect prolonged exposure to oxygenated bottom currents. This condensed interval is at least partially redeposited (Kelly *et al.*, 1998). The base of the unit is not exposed in the core, but is likely erosional (Kelly *et al.*, 1998). Biostratigraphic data suggest that the base may involve a stratigraphic break ranging from the Middle Coniacian (top undifferentiated Fosdalen Fm) to Late Coniacian/Middle Santonian (lowermost Nanok sample).

In concert, considering the available sedimentological, geochemical and biostratigraphic data as well as the stratigraphic position below gravity-flow sandstones of the Østersletten Mb (see below), the unit is interpreted to demarcate a major SB and base of a lowstand unit (see discussion).

Østersletten Mb

FA3: Lowstand fan

Description: FA3 comprises a ~40 m-thick aggradational sandstone succession. It sharply overlies a rubble interval showing bioturbated muddy sand (top of the Nanok Mb). FA3 consists dominantly of up to 5 m-thick structureless sandstone beds ($F4A_1$) that grade into carbonaceous and mica-rich sandstone at the top ($F4A_2$; Fig. 4.6). The upper levels of the also show common water-escape pipes. The boundary between the structureless sandstone and the carbonaceous sandstone locally shows mud-clasts. In places, the carbonaceous sandstone grades further into a few cm-thick intervals of sandy coal ($F4A_3$). No clay is observed in the matrix.

Intensively bioturbated (BI 4–6) sandstone-muddy sandstone intervals (F4B) are present locally; they show common indistinct burrow mottling, *Planolites, Palaeophycus, Taenidium and Chondrites*. *Asterosoma* are locally common (Fig. 4.6). F4B is commonly erosionally overlain by cm- to dm-scale intervals of parallel-laminated sandstone that may gradationally alternate with ripple cross-laminated sandstone (F4C).

Finally, paleocurrent measurements from outcrops suggest bipolar east and west directed flow (*n*=6, unpublished sedimentary logs measured by M. Larsen).

Interpretation: The several m-thick massive sandstone beds are interpreted as sustained, high density gravity-flow deposits (e.g., Stow and Johansson, 2000; Mulder and Alexander, 2001). The gradational alternation between parallel-laminated and ripple cross-laminated sandstones between the structureless sandstone beds suggests that the flow was, at least periodically, waxing and waning. These occurrences are typically sharply-based, may contain mud-lamina, and are interpreted to be unrelated to the structureless sandstone deposition. Finally, the fully bioturbated intervals may point to bottom current reworked intervals, characterized by lowered sediment concentration.

Massive sandstones are widespread in the rock record and described from a variety of deep sea depositional systems (Stow and Johansson, 2000). Such concentrated flows can be generated, for instance, near canyon or channel mouths where the change from confined to unconfined flow leads to a reduction in current velocity. Similar conditions can be achieved at the base of the slope where the decrease in slope gradient leads to deceleration of the flow. The initiation of the flow is commonly triggered by a mass failure, which would explain the thickness (up to 5 m) and the repeated motif in these beds. The sandstones of the Østersletten Mb are generally devoid of clay pointing to turbulent rather than cohesive flow at least in the latter phase of the flow. Furthermore, linked debrites are missing, which may be due to a proximal position in the fan system.

Although the Østersletten Mb outcrops are too localized and laterally limited to distinguish lateral patterns (e.g., canyon/gully fill vs. basin-floor sheet), deposition is interpreted to have taken place probably in a channelized environment(s) near the base of slope. This is interpretation is based on the following observations: 1) The Østersletten Mb is probably erosionally based and immediately overlies the similarly erosionally based Nanok Mb. The Nanok Mb shows lateral thickness variability suggesting some degree of erosional topography.; 2) Overlying sediments (the Knudshoved Mb; see below) do not contain common slump deposits, which points to a basinal rather than a slope setting.; and 3) the limited palaeocurrent data suggest bipolar east- and west-directed flow, which is suggestive of proximity to a canyon/slope gully, where internal waves commonly flow up and down the channel topography.

Considering the pervasive terrestrial organic matter and the local absence of dinoflagellates, it is believed that these deposits were intimately sourced from a nearby lowstand delta. Moreover, Whitham *et al.* (1999) noted the higher content of bisaccate pollen in these deposits than in the bounding mudstone units.

In summary, the unit is interpreted as a proximal part of a lowstand fan near the base of slope setting (see also Whitham *et al.*, 1999). The sediments were probably sourced by a shelf-edge delta mainly indirectly via repeated mass failures generated by delta front instability. The mass flow related events were sometimes followed by waxing and waning (hyperpycnal?) flow and low-sediment concentration flows (bottom currents). Bipolar palaeocurrents may point to influence of internal waves.

Knudshoved Mb

FA4: Bottom current influenced basinal mudstones

Description: FA4 comprises a ~40 m-thick mudstone-dominated succession, which sharply overlies the Østersletten Mb. The contact is marked by a hiatal lag (F3) that is overlain by an intensively bioturbated interval a few cm-thick. Upwards, the deposits consist dominantly of laminated mudstone (F1A), bioturbated mudstone (F1B), fossiliferous mudstone (F1C; Fig. 4.2D) and heterolithic interlamination (F2A). The heterolithic interlamination often comprises erosionally based, irregular and poorly-sorted sandstone and clast laminae, which are interlaminated with massive mudstone laminae. Locally, these lithosomes deform (even laterally) into sandy mudstone. Some of the glauconized clasts have a regular elongate shape. Slumps (F5) are very rare.

In the lower part of the Knudshoved Mb, the deposits form an upward coarsening succession 10 m-thick comprising Facies 1B and 2. This interval is succeeded by *Chondrites*-bearing mudstone. The upper part is characterized by shell hash-rich mudstone showing common inoceramid fragments. Commonly, this facies shows poorly-sorted, irregular shell hash rich laminae, which are interlaminated with mudstone laminae. Also present are erosionally-based sandstone lenses that show locally small scale mud-draped ripples.

Interpretation: The base of the unit is demarcated by a major flooding surface. The poorly-sorted, irregular, extraformational clasts, and shell hash-rich laminae are interpreted to have been influenced by bottom current reworking (see discussion below). The regular elongate form and size of some glauconized clasts suggests that they are faecal pellets. Although most occurrences of sandy mud can be assigned to post-depositional deformation of heterolithic interlamination, debris flow origin cannot be fully ruled out in few cases.

FA4 is similar to FA1 and is interpreted to reflect a somewhat similar depositional environment. In addition, chemostratigraphically these units are very similar (Chapter 3.3). The most obvious differences are that FA4 contains very common bioclasts, is more commonly intensively bioturbated, show more common erosionally-based scours and poorly sorted irregular sand lamina. These features are interpreted to reflect generally more energetic deposition and more intense bottom current influence than in FA1. This is possibly due to a shallower setting than during the deposition of FA1. Finally, considering that slumps are very rare in FA4, it is believed that it represents a basinal setting.

4.2 Discussion and Conclusions

The Nanok-1 core penetrated the Upper Cenomanian – Lower Campanian interval of the Fosdalen Formation. The deposits are interpreted to comprise basinal or incipient slope mudstones (FA1), tidally-influenced mudstones and sandstones (FA2), lowstand fan-related gravity-flow sandstones (FA3) and bottom current influenced fossiliferous mudstones (FA4). The condensed Nanok Mb is represented by missing core and a few core pieces of rubble. In the discussion below, characteristic depositional processes, depositional evolution and sequence stratigraphic trends of the drilled interval are summarized.

4.2.1 Characteristics of the Depositional System

In comparison to “archetypal” turbidite systems assumed to be characterized by surge-flow gravity flow currents, the drilled succession shows a rather surprising set of properties including common signs of bottom current reworking, tidal-modulation and recurring hiatal layers. The high density turbidites that form the bulk of the Østersletten Mb, however, are more commonly reported from the rock record.

The evidence for bottom current influence includes: 1) Common lag-deposits and poorly-sorted sand lamina enriched in glauconite grains, faecal pellets, coal and shell fragments as well as concretion and mud clasts. Such characteristics are common for quasi-maintained, low-sediment concentration flows (i.e. bottom currents) typified by winnowing, and saltation and rolling processes (e.g., Stow & Faugères, 2008).; 2) Locally, such layers show inverse grading and syndepositional “base-to-top” trace fossils. In particular, inversely graded bases do not develop in surge-flow low density turbidites characterized by waning flow (e.g., Stow & Faugères, 2008; Shanmugam, 2008). Moreover, syn-depositional trace fossils, especially those burrowing from base to top, are rare in surge-flow turbidites, which are characterized by post-depositional and pre-depositional suites (Wetzel *et al.*, 2008); 3) In those cases where the irregular poorly sorted laminae show erosional bases, subtle firmground burrow systems (i.e. *Glossifungites* Ichnofacies) may develop. This, coupled with the associated siderite and ankerite cements, indicates recurrent erosive bottom currents that generated intervals of non-deposition. The hematite- and goethite-rich base of the Nanok Mb is interpreted to represent an extreme example of a such condensed surface, formed as a result of prolonged exposure to oxygen-rich bottom currents.; and 4) Fully bioturbated intervals common in FA2, FA3 and FA4 are a common feature for bottom current influenced settings due to improved oxygenation and nutrient content coupled with lowered depositional rate in such settings (Wetzel *et al.*, 2008).

As described earlier (see FA2 description), the uppermost Upper Cenomanian – Middle Coniacian interval shows abundant evidence of periods of tidally-modulated sedimentation. Although it cannot be excluded that the undifferentiated bottom currents discussed above were, in fact, related to tidal currents, they are here kept separate in order to differentiate between quasi-sustained, low sediment concentration flows (i.e. undifferentiated bottom currents) and depositional currents characterized by traction and suspension processes that lead to deposition of tidal bedforms (tidal currents).

Tides are common in deep-sea environments especially near areas of topography on the sea floor such as the slope (Dykstra, 2012). In particular, tides are important processes in many modern submarine canyons (Shanmugam, 2008 and references therein). They can be generated by internal waves and/or surface tides, and currently there are no definite criteria to differentiate between these two from the rock record (Shanmugam, 2008; Dykstra, 2012). However, considering the abundant terrestrially derived organic matter, the local disappearance of dinoflagellates as well trace fossils more common of shallow marine environments, the depositional environment is interpreted to have been intimately sourced by tidally-influenced deltas.

Many of the facies associations suggest, directly or indirectly, slope or near base-of-slope deposition: Locally occurring small-scale slumps in the Cenomanian interval suggest a low-relief slope/basin setting (FA1). This interpretation is in line with field data from the vicinity of the drill site (Lygnelv mouth), which shows that during the Late Albian deposition took place in a well-defined slope setting (Hovikoski *et al.*, 2012b). This slope topography was probably inherited from mid-Albian tectonism, and was progressively filled during the Late Albian and Cenomanian (see also Whitham *et al.*, 1999). Post-Cenomanian strata nearly lack slump deposits, and considering the common presence of initially fluid-rich fine-grained sediments (e.g., fluid mud layers), this point to lack of depositional gradient. However, the Upper Cenomanian–Coniacian tidal facies (FA2) as well the Upper Santonian structureless sands interbedded with bipolar ripple facies (FA3, Østersletten Mb), suggest proximity to a canyon/gully mouth and a near base-of-slope setting during these time intervals.

Overall, the Østersletten Mb is interpreted as the proximal part of a small-scale sand-rich fan (see also Whitham *et al.*, 1999), which accumulated down-dip from the main canyon/slope channels near the base of the slope, where flow capacity decreased rapidly and deposited high-density turbidites. The sediments were probably sourced from a shelf-edge delta via repeated mass failure generated by delta front instability. The mass-flow related events were commonly followed by sustained low-sediment concentration flows that generated fully bioturbated intervals showing a wider range of grain size caliber (cf. bottom currents; F4B), and low density turbidites characterized by waxing and waning flow, which may have been directly delta-fed intervals (cf. hyperpycnal flow; F4C). The architecture of the unit is further speculated in Section 7.3.

4.2.2 Sequence stratigraphic trends

The data suggest that a zone of maximum flooding is situated near the base of core and/or around 140 m in the Upper Cenomanian interval (FA1). This is in line with source rock screening data, which shows a slight increase in source rock characteristics (e.g., HI) in this zone.

The Upper Cenomanian maximum flooding is followed by a generally regressive trend as indicated by tidally-influenced sedimentation, increasing trace fossil diversity and appearance of trace fossils that are less typical for deep sea environments (e.g., *Teichichnus, Asterosoma* and *Skolithos;* FA2). Although relatively little is known about the relationship between deep sea tides and sea level change, preliminary field data and modeling suggest that tidal-currents are amplified in deep sea environments during forced regressions

(Shanmugam, 2008; Carvajal & Steel, 2009; Dykstra, 2012). Carvajal & Steel (2009) speculated that incision in proximal parts of the depositional system can provide confined topography, which can amplify tidal currents and funnel them further offshore. The recurring hiatal surfaces and associated sideritic/ankeritic layers that are particularly common in this interval may relate to autocyclic factors or repeated, small-scale sea-level falls (see also the Nanok Mb).

A highly conjectural conformable SB may occur around 137 m, above which tidal facies and reworked glauconite become more common. Similarly, another candidate conformable SB occurs around ~99 m, above which abrupt progradation takes place.

The Upper Cenomanian – Coniacian regressive development was punctuated by two flooding events during the Turonian (~107–100 m) and Coniacian (at ~93–85 m), which led to re-establishment of transitional basinal conditions. These deposits show generally high bioturbation intensities and were also probably bottom current influenced. In particular, the Turonian – Lower Coniacian flooding event shows stratigraphic condensation (Chapter 3.2.)

A major relative sea level drop took place sometimes during the Late Coniacian – Middle Santonian (the Nanok Mb), which likely truncated the top of the Lower Coniacian interval. In addition to geochemical evidence, the development of sequence boundary at this level is also supported by the stratigraphic position below a significant gravity-flow sandstone unit.

The mainly Upper Santonian Østersletten Mb interval comprises a nearly aggradational succession of gravity-flow sandstones. In addition to the sedimentary facies, pervasive coal particles and locally decreasing dinoflagellate diversity are in line with a lowstand phase during this time.

The early Campanian records abrupt drowning of the lowstand fan system (~42.5 m). The overlying Lower Campanian succession is somewhat aggradational and lacks clear relative sea level trends. Evidence of temporally decreasing depositional energy at ~32 m and ~24 m may suggest that minor zones of maximum flooding may be situated around these intervals. However, these features could also be explained by variation in bottom current flow intensity, which can be controlled by other factors. Finally, a probable flooding event occurs around 10 m.

The uppermost Cenomanian – Turonian (FA2) and ?Middle Coniacian – ?Middle Santonian (the Nanok Mb) alleged forced regressive episodes that developed erosional hiatal surfaces may correspond to a major increase in depositional rate in the Northern Vøring Basin, which situated ~100 km offshore from the drill site during the Cretaceous (Færseth & Lien, 2002; Lien, 2005, his Figure 3).

4.3 References

Carvajal, C. & Steel, R. 2009: Shelf-Edge Architecture and Bypass of Sand to Deep Water: Influence of Shelf-Edge Processes, Sea Level and Sediment Supply. Journal of Sedimentary Research, **79**, 652–672.

Dykstra, M. 2012: Deep-water tidal sedimentology. In: Davis, R., & Dalrymple, R. (eds.), Principles of Tidal Sedimentology. Springer, Berlin, 371–395.

Færseth, R. & Lien, T. 2002: Cretaceous evolution in the Norwegian Sea—a period characterized by tectonic quiescence**.** Marine and Petroleum Geology**, 19,** 1005–1027**.**

Hovikoski, J., Bjerager, M., Bojesen-Koefoed, J. & Piasecki, S. 2012: Source Rock Development in an Evolving Half Graben: Upper Jurassic–Lower Cretaceous of Wollaston Forland, Northeast Greenland. Report Supplement to Rødryggen-1 and Brorson Halvø-1 Data Packages. Danmarks og grønlands geologiske undersøgelse rapport 2012/23, Confidential, 31 pp, 1 Appendix.

Kelly, S.R.A., Whitham, A.G., Koraini, A.M. & Price, S.P. 1998: Lithostratigraphy of the Cretaceous (Barremian-Santonian) Hold with Hope Group, NE Greenland. Journal of the Geological Society, London, **155**, 993–1008.

Lien, T. 2005: From rifting to drifting: effects on the development of deep-water hydrocarbon reservoirs in a passive margin setting, Norwegian Sea. Norwegian Journal of Geology, **85**, 319–332.

Lobza, V. & Schieber, J. 1999: Biogenic sedimentary structures produced by worms in soupy, soft muds: observations from the Chattanooga Shale (Upper Devonian) and experiments. Journal of Sedimentary Research, **69**, 1041–1049.

Mulder, T. & Alexander, J. 2001: The physical character of subaqueous sedimentary density currents and their deposits. Sedimentology, **48**, 269–299.

Schieber, J. 2003: Simple gifts and buried treasures—implications of finding bioturbation and erosion surfaces in black shales. The Sedimentary Record, 1, 4–9.

Shanmugam, G. 2008: Deep-water bottom currents and their deposits. In: Rebesco M, & Camerlenghi A., (eds.), Developments in sedimentology, 60. Elsevier, Amsterdam, 59–81

Stow, D. & Faugeres, J.-C. 2008: Contourite Facies and Facies Model. In: Rebesco, M., & Camerlenghi, A. (eds.), Contourites. Developments in Sedimentology, 60, Elsevier, Amsterdam, 224–255.

Stow, D., Faugeres, J., Howe, J., Pudsey, C. & Viana, A. 2002: Bottom currents, contourites and deep-sea sediment drifts: current state-of-the-art. In: Stow *et al.* (eds.), Deep-Water Contourite Systems: Modern Drifts and Ancient Series, Seismic and Sedimentary Characteristics. Geological Society, London, Memoirs, 22, 7–20.

Stow, D.A.V. & Johansson, M. 2000: Deep-water massive sands: nature, origin and hydrocarbon implications. Marine and Petroleum Geology, **17**, 145–174.

Taylor, A.M. & Goldring, R. 1993: Description and analysis of bioturbation and ichnofabric. Journal of the Geological Survey, London, **150**, 141–148.

Wetzel, A., Werner, F. & Stow, D. 2008: Bioturbation and biogenic sedimentary structures in contourites. In: Rebesco, M., & Camerlenghi, A. (eds.), Contourites. Developments in Sedimentology, 60, Elsevier, Amsterdam, 183–202.

Whitham, A.G., Price, S.P., Koraini, A.M. & Kelly, S.R.A. 1999: Cretaceous (post-Valanginian) sedimentation and rift events in NE Greenland (71°-77°N). In: Fleet, A.J. & Boldy, S.A.R. (eds.), Petroleum geology of Northwest Europe. Proceedings of the 5th Conference, Geological Society of London, 325–336.

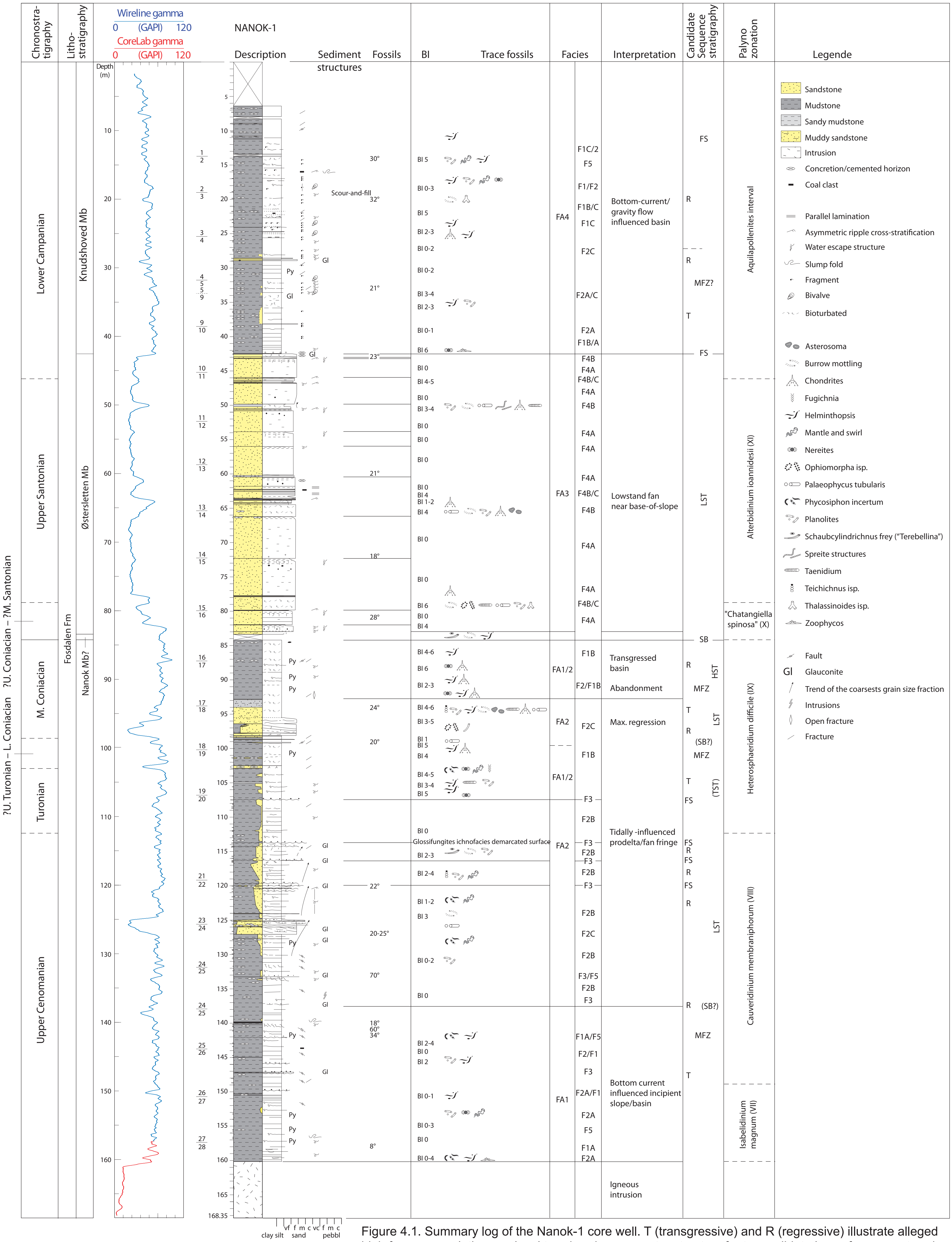

Figure 4.1. Summary log of the Nanok-1 core well. T (transgressive) and R (regressive) illustrate alleged high frequency relative sea level trends, whereas system tracts refer to candidate lower frequency trends.

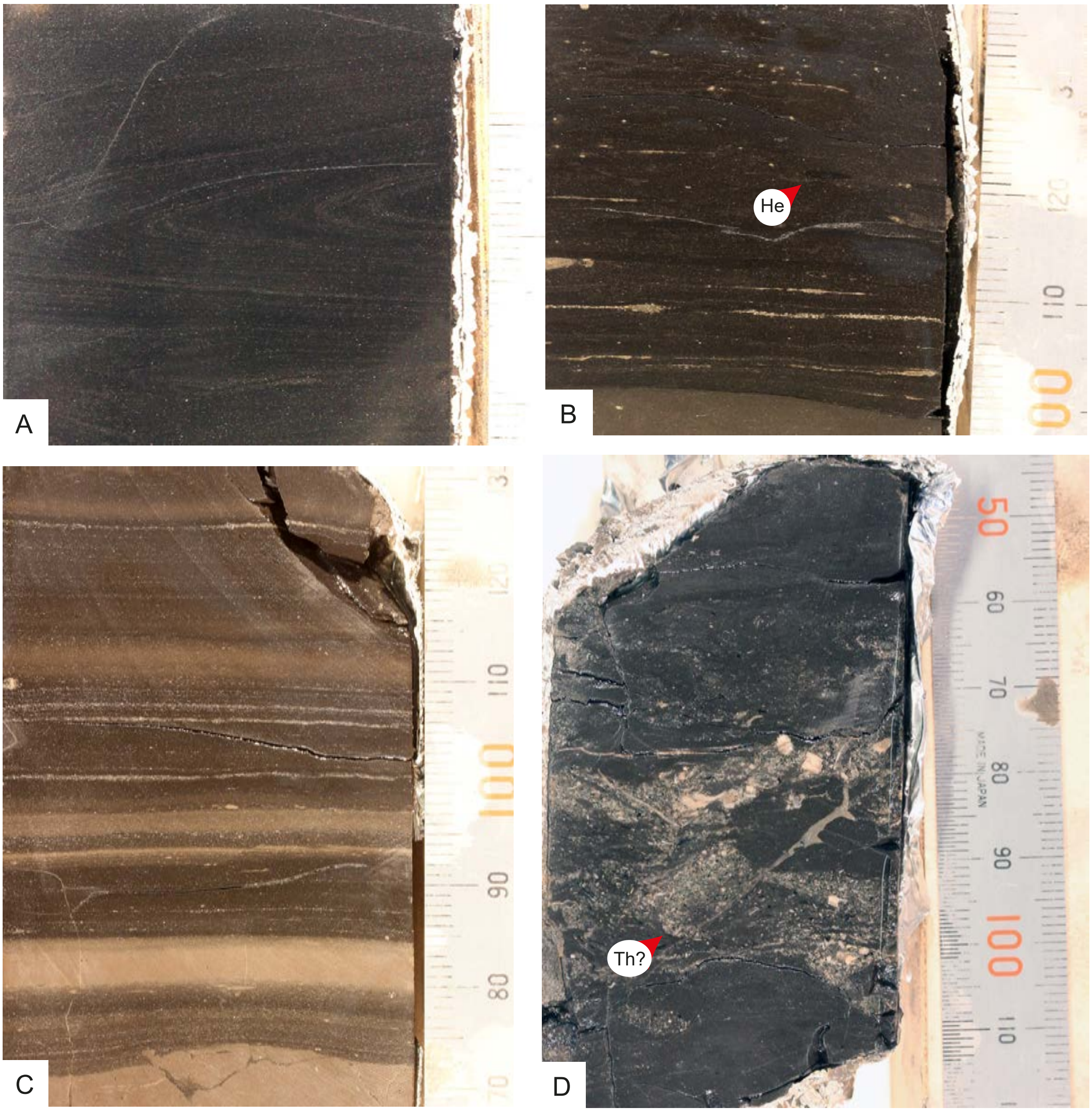

Figure 4.2. Examples of Facies 1. A) Laminated mudstone showing folded lamination (F1A/F5). B) Laminated to bioturbated mudstone (F1A and F1B, respectively). Some lamina are rich in pyrite. He-*Helminthopsis*. C) Laminated mudstone showing color-banding (F1A). D) Shell hash-rich mudstone (F1C). Possible *Thalassinoides* (Th) is indicated.

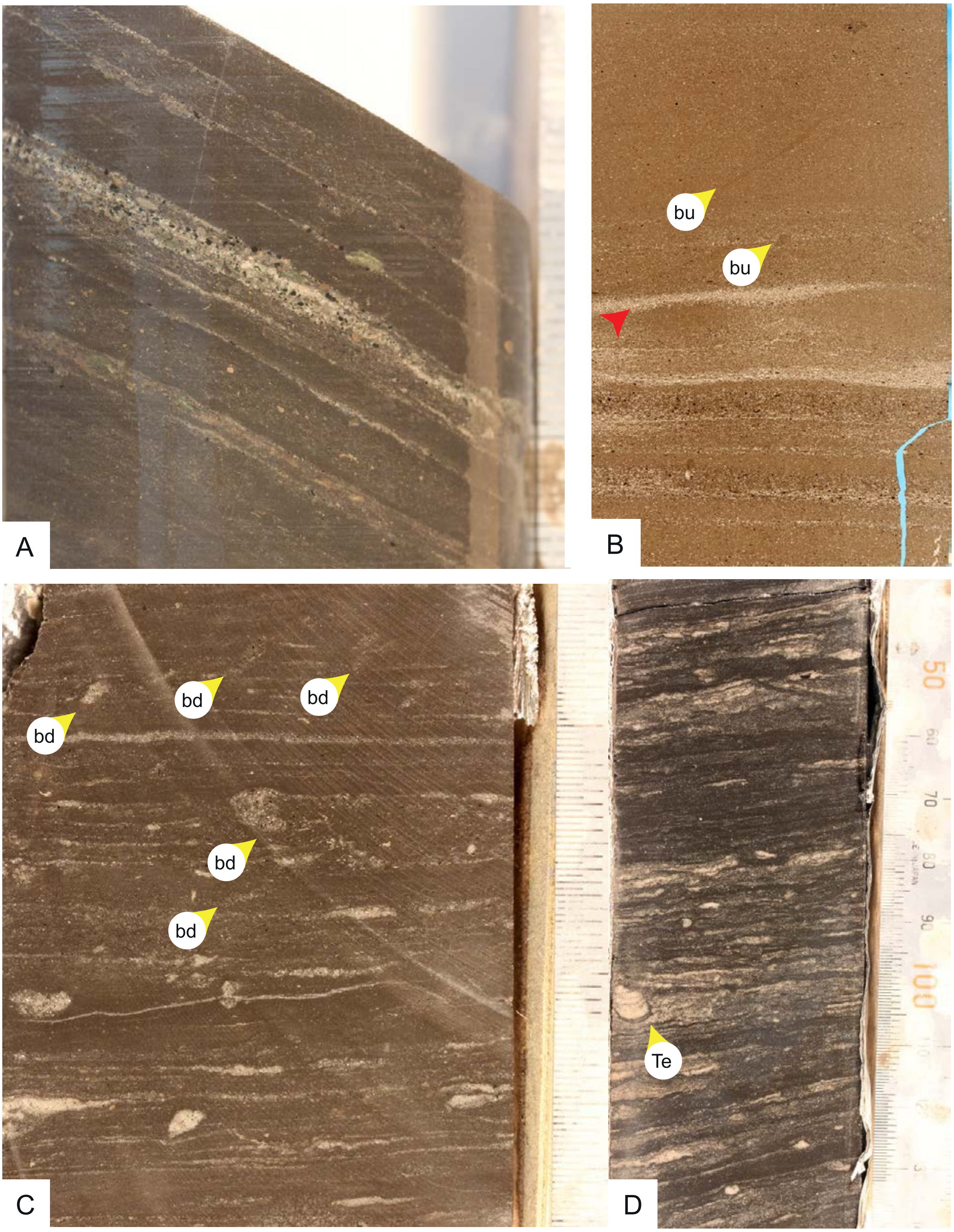

Figure 4.3. Examples of Facies 2A and B. A) Poorly-sorted, locally erosionally based, sand lamina that are enriched in mud-clast, glauconite and coal fragments. B) Interlaminated mud and sand showing inversely (red arrow) to normally graded lamina (F2A). Mud-filled burrows in the top of the figure are possibly *Chondrites.* Field of view ~2.5 cm. CD) Heterolithic interlamination showing common biodeformational structures (bd) and *Planolites* (F2B). In Figure D) a small *Teichichnus* (Te) is also present.

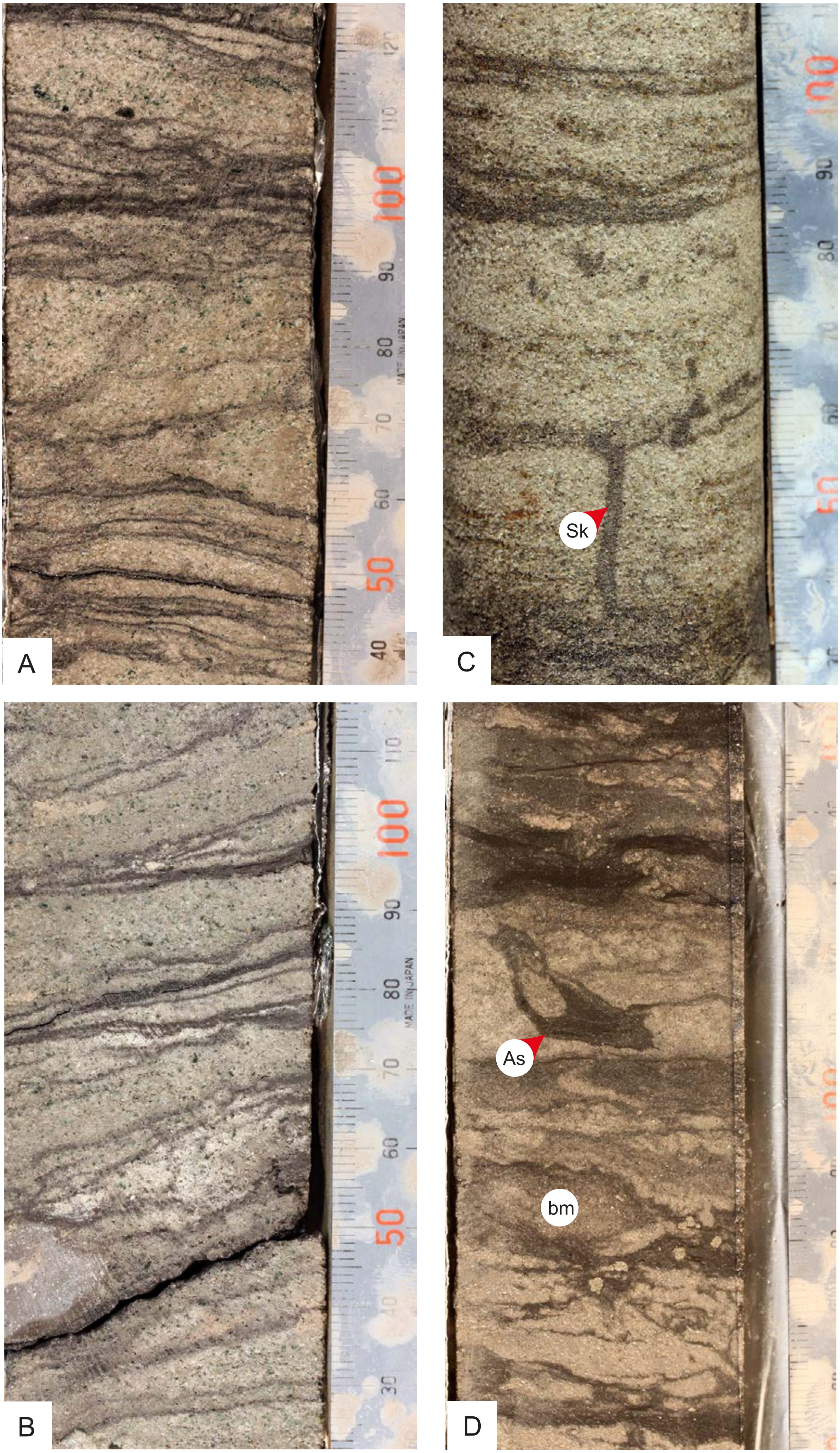

Figure 4.4. Examples of F2C. AB) Heterolithic stratification showing double mud-drapes. C) A burrow descending from a mud-drape. Sk-*Skolithos*. D) Mud-rich top of a F2C occurence. The deposits are burrowed with *Asterosoma* (As) and indistinct burrow mottling (bm).

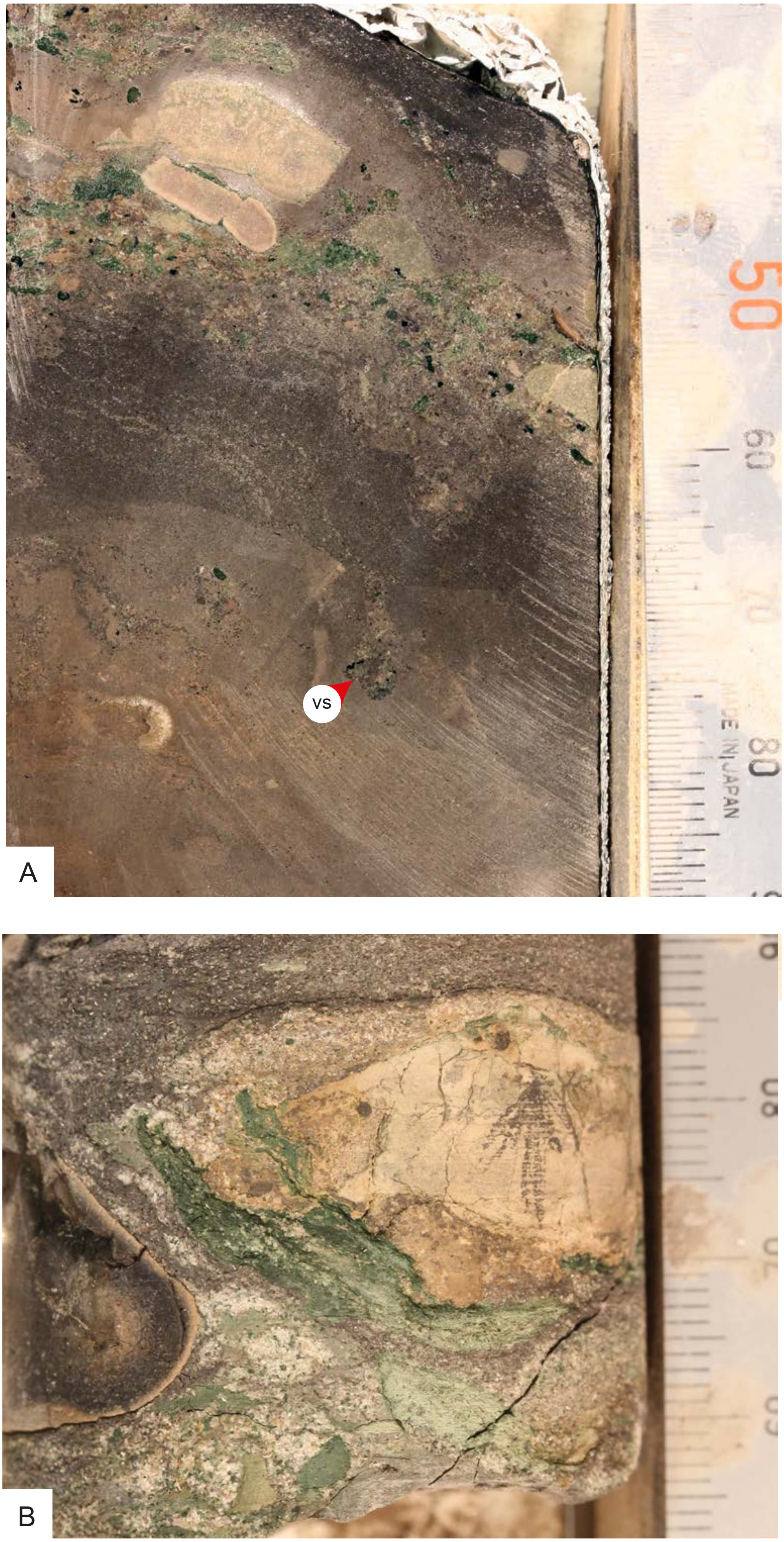

Figure 4.5. Examples of concretion-, glauconite?- and mud-clasts-bearing surfaces, which overlie cemented intervals (F3). Example A shows subtle, passively filled burrows descending from the surface. vs-vertical shaft.

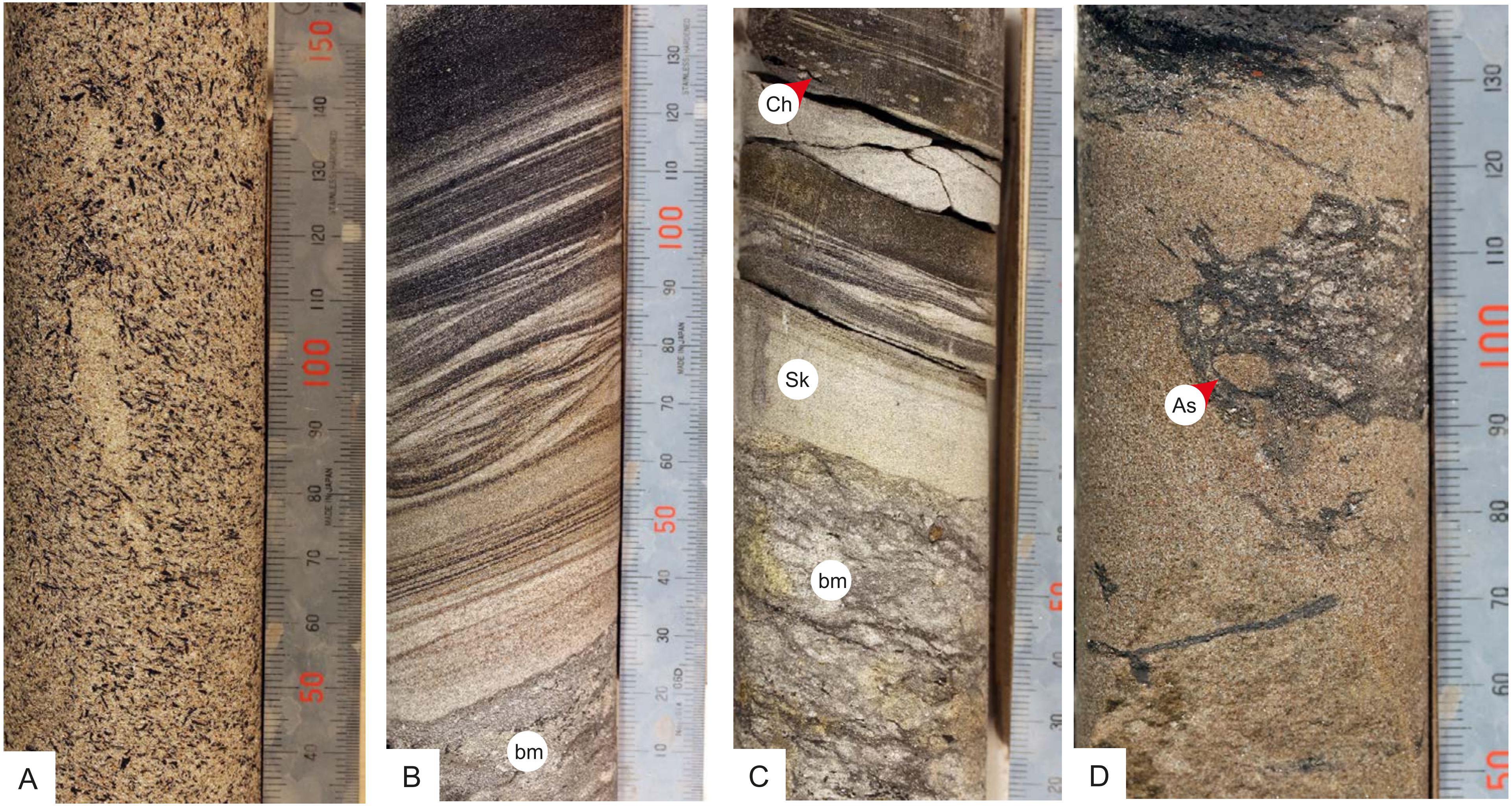

Figure 4.6. Facies examples of FA3. A) Carbonaceous top of a massive sandstone bed. Note common water escape stuctures (F4A). BC) Parallel laminated and ripple cross-stratified carbonaceous sandstone, which erosionally overlies burrow mottled (bm) muddy sandstone. Ch-*Chondrites*. D) Massive sandstone burrowed with probable *Asterosoma* probing.

5. Petrography and diagenesis

The Østersletten Mb sandstones from the Nanok core have been investigated mineralogically and diagenetically to evaluate the degree of diagenetic evolution. This knowledge is valuable as these alteration processes affect the porosity and permeability and therefore the reservoir quality of the rocks. The sandstones were examined by use of transmitted light and reflected light microscopy on polished thin sections, as well as SEM (Scanning Electron Microscopy) analyses and EDX (Energy Dispersive X-ray spectrometry) detector on thin sections and rock chips. From the results a diagenetic sequence has been established and a maximum burial temperature for the sandstones assessed. Further, diagenetic factors that have influenced the reservoir porosity and permeability are presented.

Finally samples from hiatal surfaces from the undifferentiated Fosdalen Fm, glauconitic and fossiliferous sand layers from the Knudshoved Mb and an outcrop sample from the Nanok Mb, has been examined to evaluate if there is any resemblance in mineralogy between these surfaces.

5.1 Laboratory methods

5.1.1 Petrography

The petrographic evaluation was done with transmitted light and reflected light microscopy on polished thin sections. The thin sections were impregnated by blue epoxy to help the identification of free pore space (Appendix 12.2).

SEM (Scanning Electron Microscopy) analyses were made at GEUS, Copenhagen, on a Philips XL40SEM equipped with a ThermoNoran EDX (Energy Dispersive X-ray spectrometry) detector. EDX was used for making elemental analyses of the grains to give a qualitative identification of the minerals. The SEM analyses were performed on carbon-coated thin sections of sandstone and gold-coated sandstone chips placed on stubs.

The bulk mineralogy was measured by XRD (X-Ray Diffraction) at the University of Copenhagen. Crushing to <63 μm preceded the analyses. The Bragg-Bretano method was used with powder diffraction run as reflection in a Bruker Advance D8 diffractometer with a Lynx-Eye detector. Only samples from the undifferentiated Fosdalen Formation, Knudshoved Member and outcrop samples from the Nanok Member have been analyzed. The mineralogical content has been evaluated, but not quantified

5.2 Laboratory analyses

5.2.1 Petrography of gravity flow sandstones (Østersletten Mb)

Twenty samples from the Østersletten Member have been examined. The depth interval for the samples is 45.40 m – 77.65 m. Numbers in brackets e.g. (Na-1 45.40) in the following text refers to thin section descriptions in Appendix 12.3, where Na-1 refers to well name and the following number to sample depth in core.

Detrital composition

The sandstones from the Østersletten Mb are mainly fine-grained, moderate to well sorted, with the grains being subangular to rounded. The sandstones have not been point counted but are assessed to be subarkoses (Folk, 1968). The framework grains consist of quartz and varying amounts of feldspar (mainly K-feldspar), varying but mostly high amounts of mica, minor rock fragments and traces of heavy minerals. Coal fragments are common but occur in varying amount, and one sample could be classified as sandy allochthonous coal (sample Na-1 72.38). Detrital clay matrix is rare except in bioturbated and laminated samples.

The majority of the detrital quartz grains are monocrystalline, whereas polycrystalline grains occur in a lesser amount. The grains show both uniform and undulose extinction, may contain mica-inclusions and probably have a metamorphic source. Contact dissolution/pressure solution (irregular grain line contacts) between adjacent quartz grains are rare and microstylolites have not been encountered. Contacts between quartz and mica have not necessarily resulted in bending or breaking of the mica and conformable and straight contacts are often seen (cf. Na-1 54.00). This is interpreted as a result of quartz dissolution (cf. Bjørkum, 1996).

Feldspars in the sandstones consist mainly of K-feldspar. Very few plagioclase grains have been observed and have possibly been subject to severe dissolution and therefore a contributor of secondary porosity. Most observed K-feldspar grains show evidence of some degree of leaching.

Mica is common in the sandstones and consists exclusively of muscovite. The muscovite may appear bent and fractured between quartz grains due to mechanical compaction, but as mentioned above, dissolution between quartz and mica grains may have prevented bending of the latter. Mica is often partially or totally altered to kaolinite.

The sandstones contain sporadic sedimentary rock fragments, such as mudstone and carbonate clasts, which may be deformed due to compaction.

Clasts of biogenic origin such as glauconite pellets and shell fragments occur sporadically, whereas coal fragments are common and in some samples abundant. The coal fragments appear as particles in size from 50 µm to 2000 µm and consist of well-preserved cellular tissue or accumulations of tissue splinters.

Heavy minerals such as rutile, tourmaline and zircon are only present in traces.

Authigenic phases

The dominating authigenic phases in the sandstones from Østersletten Member are kaolinite, Mg-rich siderite and ankerite. Authigenic quartz occurs only as a minor cement. Pyrite is common but mostly in association with coal fragments and not as a pore occluding phase. Apatite and Ti-oxides are only seen very rarely.

Kaolinite

Kaolinite is the most common authigenic phase in the examined sandstones. Generally kaolinite occurs as booklets, large vermiforms and densely packed large vermiform booklets in primary pore spaces (Na-1 45.40; Na-1 46.82) and more rarely in secondary porosity. The booklets and vermiforms are made up of individual thin pseudohexagonal, euhedral plates, c. 10–50 µm across. The kaolinite is very commonly observed to replace muscovite, resulting in the densely packed large vermiform and fan-shaped booklets that occlude pore spaces. Another occurrence is densely paralleled packed long flakes giving a striated appearance, which probably is a reminiscence from the transformation from mica (Na-1 75.40).

Clusters of small booklets are rarely seen in secondary pores resulting from dissolved K-feldspar or plagioclase. It is believed that the majority of occurring kaolinite in the sandstones originates from transformation of muscovite though a minor part may derive from feldspar dissolution/alteration.

Kaolinite occurring in primary pore spaces may appear overgrown by quartz and dolomite (Na-1 48.47). No illitization of the kaolinite in the sandstones has occurred.

Mg-rich siderite

When examined in light microscope and BSEM the siderite are mainly associated with ankerite cement, mica and kaolinite, and probably as a total replacement of former biotite flakes. In light microscope siderite occur brownish and blackish (and in BSEM they appear whitish). The siderite cement is patchy and is composed of vuggy amalgamated smaller rhombic and irregularly shaped crystals where only the edges remain. Siderite also appears as small single rhombic crystals scattered in pore spaces (Na-1 48.47). When occurring as patchy cement it appears pore-occluding and is sometimes seen expanded between quartz grains (Na-1 62.25). This may be the due to compaction and replacement of a former biotite clast.

The siderite is often associated with pore-filling kaolinite, where they occur as single rhombs scattered in the kaolinite, which is a transformation product from mica (cf. Na-1 46.82). Siderite also occurs with displacive growth within mica. Further, they occur overgrown and enclosed in ankerite cement (Na-1 48.47).

Ankerite

The ankerite cement occurs as patchy pore-space filling cement consisting of large rhombic crystals or smaller patchy crystals scattered in pore-spaces. The ankerite cement fills secondary porosity and partly replaces feldspars. The ankerite shows zonation indicating varying amounts of Fe-content. Ankerite cement is overgrowing and enclosing siderite crystals and kaolinite booklets, evidencing that they are postdating these but is overgrown by quartz (Na-1 48.47), which is then a later cement.

Quartz

Authigenic quartz occur more or less in all samples though in limited amount and as incipient overgrowths. Dust rims delimiting the detrital and authigenic quartz are absent and overgrowths can therefore be difficult to recognize, so overgrowths are distinguished from the detrital grains either by their inclusion-free appearance or the discrete euhedral crystal habit. In some cases quartz overgrowths partially enclose kaolinite and ankerite crystals, indicating that the formation was synchronous with, or subsequent to formation of these mineral phases (Na-1 48.47).

Pyrite

Pyrite is present especially in association with organic detritus/coal fragments. Both cubic pyrite and framboids are common and are often observed in-filling tissue cells in coal fragments (Na-1 72.38). Pyrite is believed to be very early cement, as it is overgrown by later cement phases.

Apatite and Ti-oxides

Apatite and Ti-oxides occurs in the sandstones as very rare and small crystals scattered in pore spaces.

Feldspar dissolution

Plagioclase grains are very rare in the sandstones, whereas K-feldspars are common though often partially dissolved. It is believed that plagioclase grains have been present but probably have experienced early severe dissolution and replacement by the present ankerite cements and kaolinite. K-feldspar dissolution is assessed to be postdating or relatively synchronous with precipitation of kaolinite and ankerite (Na-1 75.40). Generally K-feldspar dissolution seems to contribute in enhanced porosity.

Compaction

Generally the sandstones show only a moderate degree of compaction. The sandstones contain a relatively high amount of mica and in some samples also abundant coal fragments, which primarily occur unbroken or only slightly bended. Contact dissolution/pressure solution textures (irregular grain line contacts), between adjacent quartz grains are seen but is not common, and no severe dissolution seems to have occurred. Contacts between quartz grains and mica have not necessarily resulted in bending or breaking of the mica and conformable and straight contacts are often seen (Na-1 77.65). This is interpreted as a result of quartz dissolution and indicates that some chemical compaction has occurred. No micro-stylolites are encountered, but a few examples of grain-crushing and fracturing occur, especially in sandstones, with a lesser content of mica and coal fragments (Na-1 66.72). The almost absence of pressure solution textures and stylolites is probably a result of the high content of ductile grains, primarily mica-flakes.

Diagenetic changes

An evaluation of the diagenetic sequence for the sandstone in Østersletten Member is presented in Figure 5.1.

Pyrite is believed to be the first authigenic mineral, which has precipitated in the sandstones and is present in all samples. It is most often seen in association to organic matter, which in the sandstones are very common as recognizable woody coal fragments. The pyrite also occurs as framboids scattered in pore spaces (Na-1 66.22) and commonly as infilling in tissue cells in coal fragments (Na-1 60.90¸ Na-1 72.38). Pyrite is generally accepted as an early diagenetic mineral, related to marine or brackish environments (Berner, 1981; Berner & Raiswell, 1984). The presence of organic matter plays an important role in the eogenesis, as it serves as an energy source for microbes and creates reducing conditions, under which iron is highly soluble. Iron-oxides and -hydroxides are unstable under reducing conditions and are considered possible sources for early pyrite (Canfield *et al.* 1992), though no reminiscence of these has been seen in the sandstones.

Siderite is a common mineral in the sandstones and has probably followed shortly after the precipitation of pyrite. Siderite often precipitates when pore fluids are reducing and non-sulphidic, evolved in the sub-oxic and methanogenetic depositional environments (Morad, 1994). These conditions often occur in organic-rich sediments with sulphate-poor fluids and appreciable amounts of reactive iron minerals (Postma, 1982). After formation of pyrite the content of sulphate in the formation-water is expected to be relatively low, allowing siderite to precipitate. The siderite is often seen as pore-occluding amalgamated rhombs, which could have initiated between cleavage planes of biotite (Na-1 62.25), and biotite may be a contributor to supply iron as well as the magnesium contained in the siderite.

Alongside with or shortly after siderite precipitation, kaolinite formed. The kaolinite is often associated with the siderite (Na-146.82) and is interpreted to be formed from the transformation of mica and to some extent early feldspar alteration. The Østersletten Member sandstone is expected not to have experienced any meteoric water flushing after deposition, as the sandstone is a succession of gravity flows, without any contact to a landward meteoric hydraulic head. Meteoric flushing is by some authors believed to the primary reason for kaolinite to precipitate (e.g., Bjørlykke, 1982; Khanna *et al.*, 1997), but cannot be applied in this case. Acidic pore fluids due to thermal maturation of organic matter may in a late phase have contributed to kaolinitisation of feldspar (cf. Lanson *et al.*, 2002).

The Ca-ions of the feldspars liberated by plagioclase alteration and released from dissolution of shell fragments may have promoted the ankerite nucleation. Only very few bioclasts has been found, which probably could be due to early dissolution. Ankerite is post-dating siderite but is believed to be forming later or contemporaneous with kaolinite, as ankerite is seen within dense kaolinite (Na-1 57.10), interpreted as a relatively early cement and over-growing kaolinite booklets (Na-1 48.87). The ankerite may be displacive indicating a relative early precipitation before severe compaction (Na-1 57.10 and Na-1 69.50). Further it occurs with multiple zones, which indicates that the crystal growth have experienced varying content of iron in the pore fluids.

Plagioclase dissolution has probably been an early feature as described above, and no plagioclase grains have been preserved. K-feldspar is commonly partially dissolved. The dissolution of K-feldspar is probably later than ankerite precipitation, as the latter is seen growing around but not into partially dissolved K-feldspar (Na-1 75.40). The secondary pores after K-feldspar dissolution is normally not filled by authigenic cements, which shows that K-feldspar dissolution occurred late.

Quartz occurs only as minor amounts in the sandstones and was the last cement to develop. The overgrowths are incipient and are only seen to overgrow kaolinite (Na-1 51.22) and ankerite (Na-1 48.47). Source for the quartz could be dissolution of feldspar, kaolinitisation as well as dissolution in the contact between quartz and mica. No stylolites have been seen and only sporadic pressure dissolution between quartz grains occur, which also shows that the sandstones not have experienced severe compaction.

There is seen no signs of oxidation due to exhumation of the sandstones. The magmatic intrusion event seems not to have affected the diagenetic evolution in the sandstones.

Burial temperature estimates

The incipient and minor quartz overgrowths suggest that temperatures were at least 60°C (e.g., McBride, 1989; Weibel *et al.*, 2010) but maximum 80°C – 100°C, which is the onset temperature for macroquartz precipitation (Bjørløkke *et al.*, 2009). Kaolinite shows no signs of illitization, which occur at ~120°C – 140°C (Ehrenberg & Nadeau, 1989; Bjørlykke & Aagaard, 1992) as well as no diagenetic transformation of kaolinite into dickite, which occurs at temperatures between ~ 80°C and ~120°C (Ehrenberg *et al.*, 1993; McAulay *et al.*, 1994; Morad *et al.*, 1994) have been observed. Extensive K-feldspar dissolution occurs at temperatures >80°C (Wilkinson *et al.*, 2001). In all this suggests that the sandstones in Østerssletten Member may have experienced burial temperatures at approximately 80°C – 90°C (See Chapter 9).

Reservoir porosity and permeability

The porosity in the Østersletten Member sandstones ranges from 12–24 % (average 18 %) and permeability is in the range 4–535 mD (average 102 mD). The major porosity and permeability reducing factors in the sandstones are kaolinite, siderite and ankerite cement. Factors that influence the porosity and permeability are facies and detrital mineralogy. Those facies that contain abundant mica, coal fragments and are finer grained often show lower porosity and especially low permeability. Concerning detrital mineralogy, the relatively high content of mica has had an important impact on reservoir properties as it is believed to have been the main contributor for precipitation of siderite and kaolinite.

5.2.2 Mineralogy of inferred hiatal surfaces

Samples from surfaces interpreted as hiatal levels (Facies 3, Chapter 4) are examined to asses their mineralogy. In addition, data derived from the inferred hiatal surfaces from the Nanok-1 well are compared with data from an outcrop sample of the Nanok Mb. This is done to find out whether these surfaces show mineralogical similarities.

Selected samples

In the mudstone interpreted as tidally-influenced “prodelta/fan fringe” facies in the undifferentiated Fosdalen Formation characteristically erosional surfaces that bear lag deposits interpreted as hiatal lag surfaces are present. Three samples (114.30 m; 120.95 m; 133.10 m) from these inferred hiatal surfaces have been examined.

In the field, the Nanok Mb is an up to 6 m thick unit and is characterized as a red, muddy, poorly sorted pebbly sandstone, with reworked glauconitized and phosphatized clasts (Kelly *et al.*, 1998). The red coloring is due to hematite and goethite. The Nanok Member is interpreted to represent a condensed unit developed during a period of increased bottom current velocity. In the Nanok 1 well, the Nanok Member is not present as described in the outcrop samples above but is inferred to be present in the section at a thin interval of non-recovery of core. As a substitute for the absent Nanok Mb in the well core, an outcrop sample from the type section has been examined. The outcrop sample comprises one polished thin section whereas the sample for XRD has been divided into 3 sub-samples. Sub-sample A is reddish mudstone, sub-sample B is a light greyish concretion in the reddish mudstone and sub-sample C is greenish mudstone in the reddish mudstone.

The contact between Østersletten Mb and Knudshoved Mb is marked by a (hiatal?) flooding surface represented by the sample at 42.47 m. Further up in the Knudshoved Mb glauconitic and fossiliferous sand layers are locally present. These layers are represented by samples from the depth levels 32.65 m and 28.96 m and are chosen as they show some lithological resemblance with the hiatal surfaces.

All samples has been examined by XRD and by transmitted light and reflected light microscopy on polished thin sections as well as SEM-EDX.

Results

The results of the XRD analyses for bulk mineralogy in the examined samples are for each Formation/Member shown in Figures 5.2–4. In Table 5.1 an overview of the qualitative mineralogy found by the combination of XRD, light microscopy and SEM-EDX is given. This is done in order to better visualize the mineralogical contents of the hiatal levels in the core and the outcrop sample from the Nanok Mb. It should be noted that XRD analysis not necessarily has revealed all minerals in the sample but has been supplemented by the light microscopy and SEM-EDX analysis and vice versa.

All samples contain detrital quartz, feldspar as well as reworked greenish and brownish clay clasts and brownish carbonate clasts, which can be up to 15 mm. Microphotographs of the samples are shown in Figures 5.5–18 and overview photographs of whole thin sections are shown in Appendix 12.2. Glauconite pellets occurs in all samples except in the sample from 42.47 m. Apatitic clasts are seen in most samples though it is absent in the sample from 32.65 m. The clasts are floating in a brownish ankeritic-sideritic matrix and to a lesser degree greenish matrix (probably chloritic-kaolinitic). Minor apatite cement is also present.

Two samples from Knudshoved Mb (28.96 m and 32.65 m) differ from the rest in being finer-grained, with very well-rounded mud clasts and carbonate clasts in the grain size 500 µm–2 mm. These samples also commonly contain shell fragments. In appearance the outcrop sample from the Nanok Mb differs distinctively by the dark reddish-brown color.

5.3 Conclusion

The diagenetic sequence for the sandstone in Østersletten Member comprises early pyrite, often associated with organic matter, which is very common in the sandstones. Pyrite is followed by siderite and kaolinite, which are common authigenic minerals in the sandstones and both seem to be related to and/or formed from mica. Dissolution feldspars and shell fragments may have promoted ankerite precipitation. Ankerite is post-dating siderite but is believed to be forming later or contemporaneous with kaolinite. Dissolution of K-feldspar is probably later than ankerite precipitation, as ankerite is seen growing around but not into secondary pores from partially dissolved K-feldspar. Quartz overgrowths occur only as minor amounts in the sandstones and quartz was the last cement to develop.

The porosity in the Østersletten Member sandstones ranges from 12–24 % and permeability is in the range 4–535 mD. The reservoir quality of the Østersletten Mb sandstones is mainly influenced by porosity and permeability reduction caused by abundant detrital mica, which again has caused precipitation of kaolinite and siderite. Further, facies, which occur with abundant mica, coal fragments and, which is finer grained due to lower energy environment, often show lower porosity and especially low permeability.

The magmatic intrusion seems not to have affected the diagenetic evolution in the sandstones and maximum burial temperatures are on the basis of the diagenetic signatures estimated to be 80°C – 90°C.

The hiatal surfaces have developed lag deposits, with firm-grounds cemented mainly by ankerite and siderite and to a lesser degree dolomite. The cements are in an early diagenetic phase, which is seen by the detrital grains “floating” in the cement. Hematite and goethite are only present in the outcrop sample from the Nanok Mb. Goethite may have formed as a weathering product of e.g. siderite during and after uplift and exposure to the atmosphere. However hematite requires higher temperature and typically forms as transformation of goethite into hematite during burial (Weibel 1999).

From the comparison of the mineralogy of the examined samples, it is seen that some compositional similarity prevail between the hiatal surfaces, and that they therefore probably have experienced the same depositional and diagenetic conditions. One distinct difference is the presence of hematite and goethite in the outcrop sample from the Nanok Mb, which has not been found in the samples from the well core.

Mainly the mineralogy in the hiatal surfaces is similar and probably typical for these surfaces. However, it must be pointed out that generally the diagenetic evolution in these hiatal surfaces is very complex and need to be examined more thoroughly, to achieve a better understanding of the processes involved. Correlation of the individual hiatal surfaces from one locality to another is not anticipated to be possible.

5.4 References

Bjørkum, P.A. 1996: How important is pressure in causing dissolution of quartz in sandstones? Journal of Sedimentary Research, **66**, 147–154.

Bjørlykke, K. 1984: Formation of secondary porosity. How important is it?, In: D. A. McDonald, and R. C. Surdam, (eds.), Clastic Diagenesis. American Association of Petroleum Geologists, 285–292.

Bjørlykke, K. & Aagaard, P. 1992: Clay minerals in North Sea sandstones. In: D. W. Houseknecht and E. D. Pittman, (eds.), Origin, diagenesis, and petrophysics of clay minerals in sandstones. SEPM, Special Publication, **47**, 65–80.

Bjørløkke, K., Jahren, J., Mondol, N. H., Marcussen, Ø., Croize, D., Peltonen, C. & Thyberg, B. 2009: Sediment compaction and rock properties. Search and Discovery Article 50192.

Canfield, D. E., Raiswell, R. & Bottrell, S. 1992: The reactivity of sedimentary iron minerals toward sulphide. American Journal of Science, **292**, 659–683.

Ehrenberg, S. N. & Nadeau, P. H. 1989: Formation of diagenetic illite in sandstones of the Garn Formation, Haltenbanken area, Mid-Norwegian continental shelf. Clay Minerals, **24**, 233–253.

Ehrenberg, S. N., Aagaard, P., Wilson, M. J., Fraser, A. R. & Duthie, D. M. L. 1993: Depth-dependent transformation of kaolinite to dickite in sandstones of the Norwegian Continental shelf. Clay Minerals, **28**, 325–352.

Folk, R.L.1968: Petrology of Sedimentary Rocks: Austin, Hemphill Book Store, 170 p.

Kelly, S.R.A., Whitham, A.G., Koraini, A.M. & Price, S.P. 1998: Lithostratigraphy of the Cretaceous (Barremian-Santonian) Hold with Hope Group, NE Greenland. Journal of the Geological Society, London, **155**, 993–1008.

Khanna, M., Saigal, G. C. & Bjørlykke, K. 1997: Kaolinitization of Upper Triassic-Lower Jurassic sandstones of the Tampen Spur area, North Sea; implications for early diagenesis and fluid flow, in I. P. Montaneez, J. M. Gregg, and K. L. Shelton, eds., Basin-wide diagenetic patterns; integrated petrologic, geochemical, and hydrologic considerations, SEPM Special Publication No. **57**, 253–268.

Lanson, B., Beaufort, D., Berger, G., Bauer, A., Cassagnabere, A. & Meunier A. 2002: Authigenic kaolin and illitic minerals during burial diagenesis of sandstones: a review. Clay Minerals, **37**, 1–22.

McAulay, G. E., Burley, S. D., Fallick, A. E. & Kusznir, N. J. 1994: Palaeohydrodynamic fluid flow regimes during diagenesis of the Brent Group in the Hutton-NW Hutton reservoirs: constraints from oxygen isotope studies of authigenic kaolin and reverse flexural modeling. Clay Minerals, **29**, 609–626.

McBride, E. F. 1989: Quartz cement in sandstones: a review: Earth-Science Reviews, **26**, 69–112.

Morad, S. 1994: Carbonate cementation in sandstones: distribution patterns and geochemical evolution: Spec. Publs Int. Ass. Sediment., **26**, 1–26.

Morad, S., Ben Ismail, H., De ros, L. F., Al-Aasm, I. S. & Serrhini, N.-E. 1994: Diagenesis and formation water chemistry of Triassic reservoir sandstones from southern Tunisia: Sedimentology, **41**, 1253–1272.

Postma, D. 1982: Pyrite and siderite formation in brackish and freshwater swamp sediments. Am. J. Sci., **282**, 1151–1185.

Weibel , R., Friis, H., Kazerouni, A. M., Svendsen, J. B & Poulsen, M. L. 2010: Development of early diagenetic silica and quartz morphologies – Examples from the Siri Canyon, Danish North Sea. Sedimentary Geology, **228**, 151–170.

Member/Formation	Knudshoved Mb			Nanok Mb	Fosdalen Fm (lower part)		
Depth	28.96 m	32.65 m	42.47 m	Outcrop	114.30 m	120.95 m	133.10 m
Quartz	P	P	P	P	P	P	P
Feldspar	P	P	P	P	P	P	P
Muscovite	P	P	P	P	P	P	P
Kaolinite	P	P	P	P	P	P	P
Chlorite	P	P	P	P	P	P	P
Calcite	P	A	A	A	A	A	A
Dolomite	P	P	A	P	A	P	A
Ankerite	P	P	P	P	P	P	P
Siderite	P	A	P	P	P	P	P
Hematite	A	A	A	P	A	A	A
Goethite	A	A	A	P	A	A	A
Apatite	P	A	P	P	P	P	P
Pyrite	P	P	A	A	P	P	A

Tabel 5.1. Qualitative mineralogy of the samples. P: present in sample; A: absent in sample

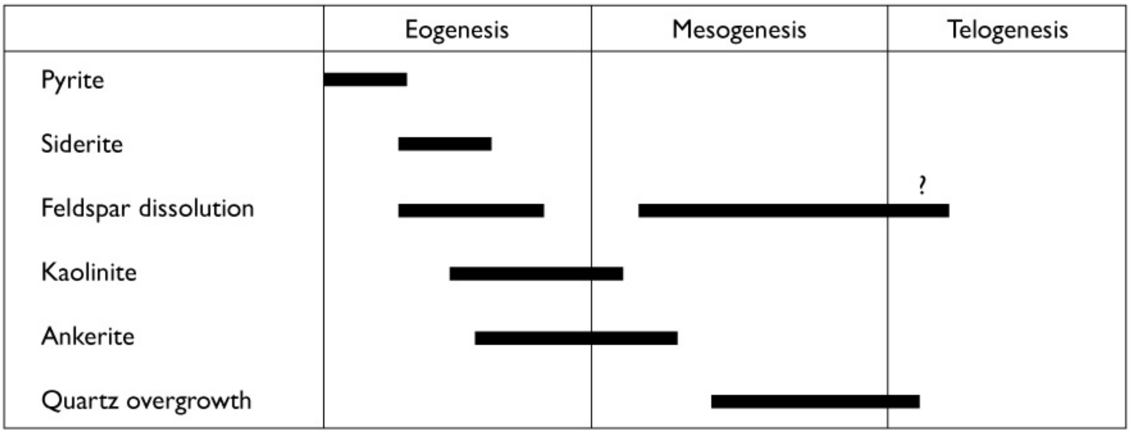

Figure 5.1. Diagenetic sequence of the Østersletten Mb.

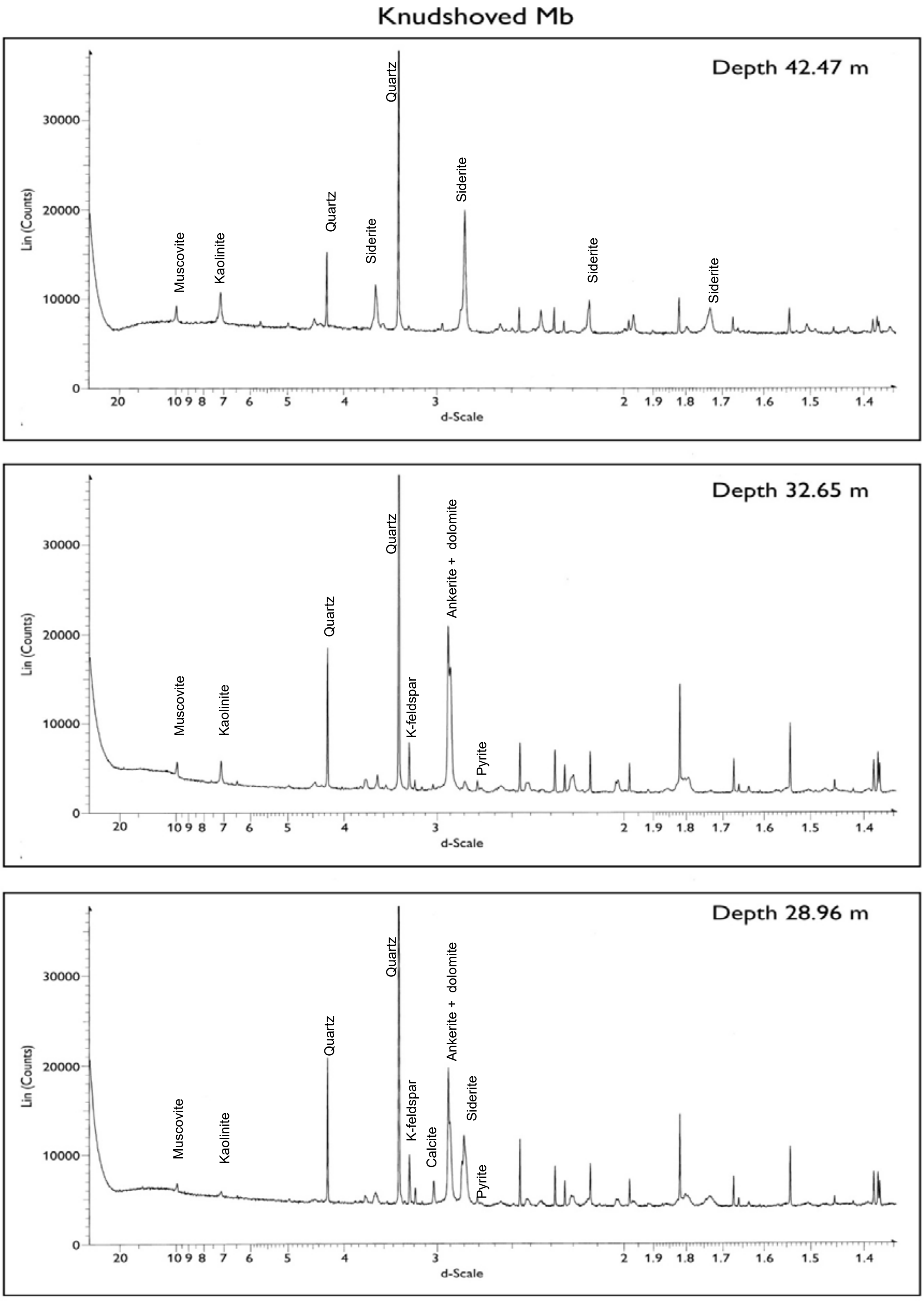

Figure 5.2. XRD diffractograms from 3 selected samples from Knudshoved Mb with indication of the minerals present in largest amounts and identified by their crystal lattice constants.

Nanok Mb

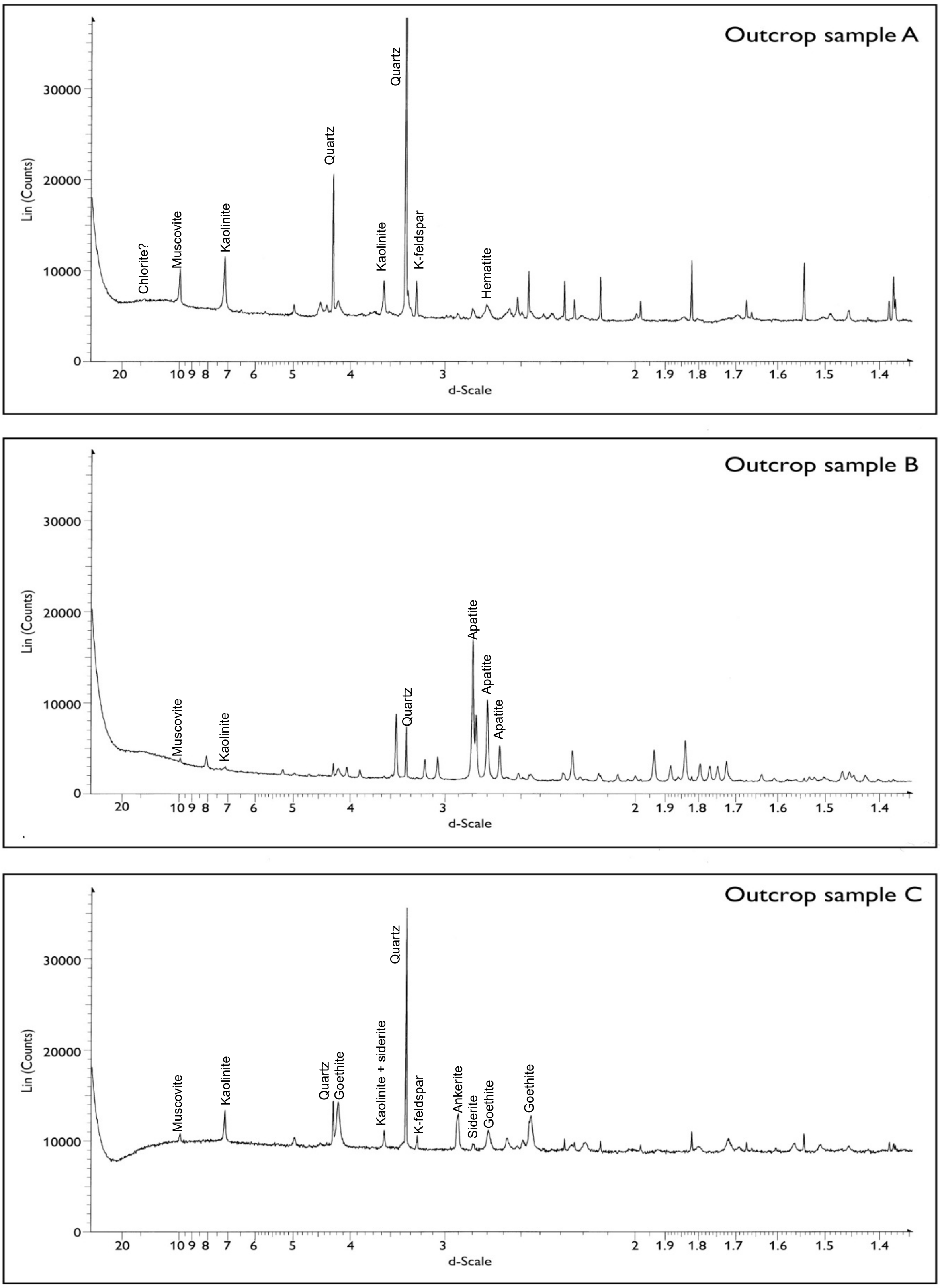

Outcrop sample A
Lin (Counts)
30000
20000
10000
0
Chlorite?
Muscovite
Kaolinite
Quartz
Kaolinite
Quartz
K-feldspar
Hematite
20
10 9 8 7 6 5 4 3 2 1.9 1.8 1.7 1.6 1.5 1.4
d-Scale
Outcrop sample B
Lin (Counts)
30000
20000
10000
0
Muscovite
Kaolinite
Quartz
Apatite
Apatite
Apatite
20
10 9 8 7 6 5 4 3 2 1.9 1.8 1.7 1.6 1.5 1.4
d-Scale
Outcrop sample C
Lin (Counts)
30000
20000
10000
0
Muscovite
Kaolinite
Quartz
Goethite
Kaolinite + siderite
Quartz
K-feldspar
Ankerite
Siderite
Goethite
Goethite
20
10 9 8 7 6 5 4 3 2 1.9 1.8 1.7 1.6 1.5 1.4
d-Scale

Figure 5.3 (previous page). XRD diffractograms from one outcrop sample from Nanok Mb divided into 3 sub-samples with indication of the minerals present in largest amounts and identified by their crystal lattice constants. See text for details.

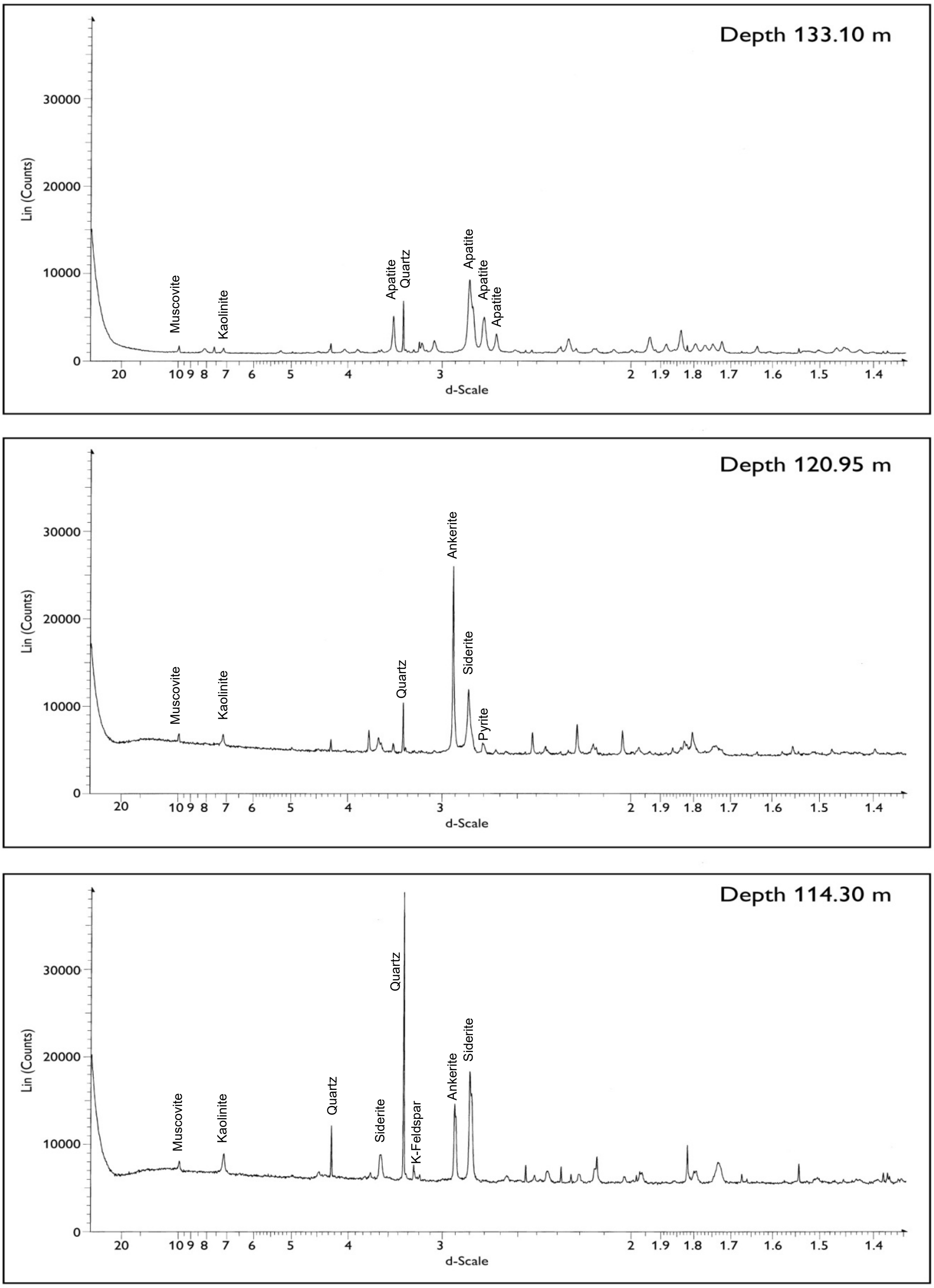

Figure 5.4. XRD diffractograms from 3 selected samples from Fosdalen Mb with indication of the minerals present in largest amounts and identified by their crystal lattice constants.

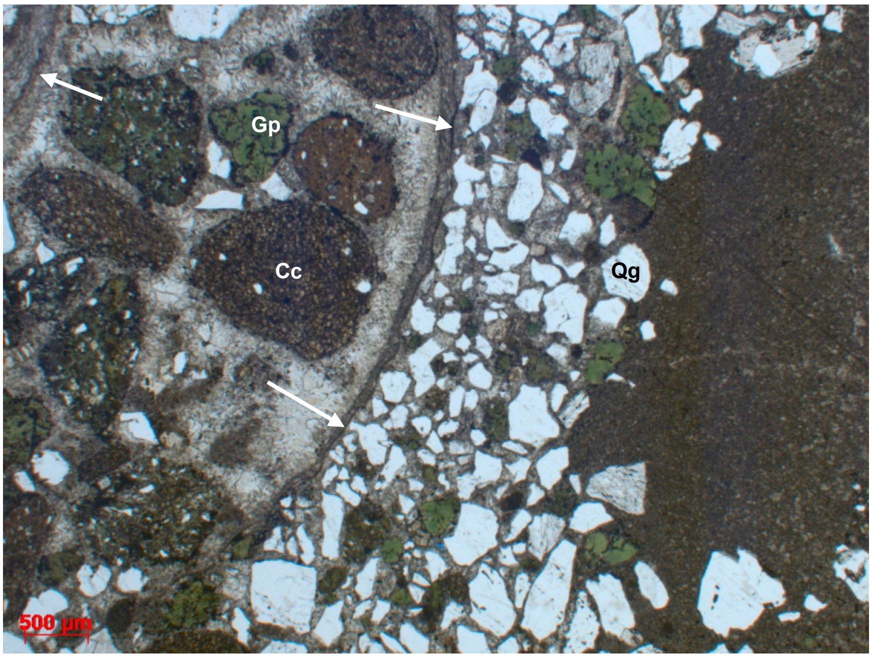

Figure 5.5. 28.96 m. Greenish Glauconitic pellets (Gp), brownish carbonate clasts (Cc) and quartz grains (Qg) in a ferroan dolomite cement. Note shell fragments (arrows).

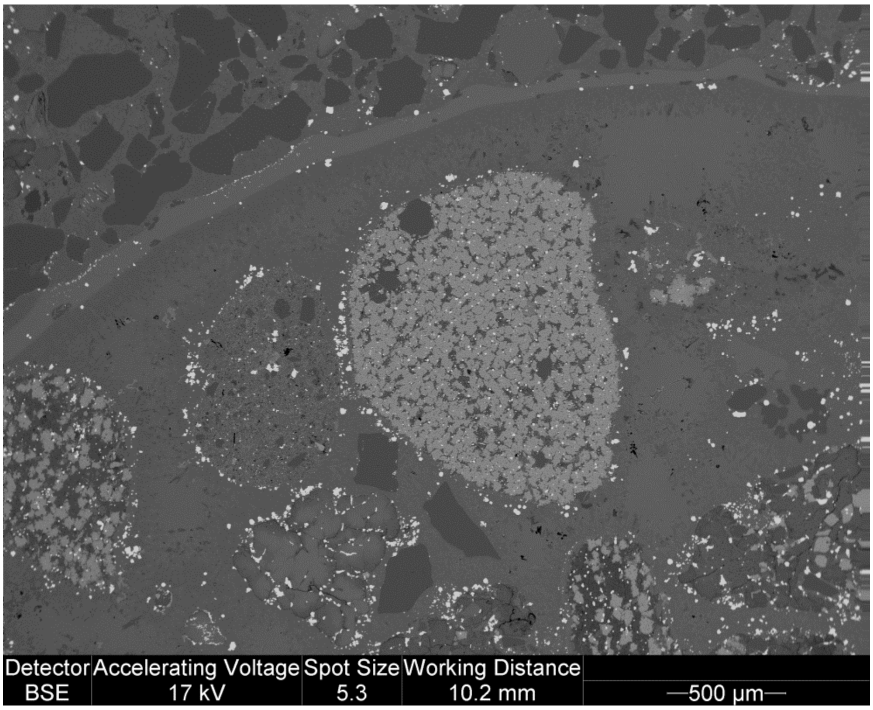

Figure 5.6. 28.96 m. Approximately same area as in Figure 5.5 (turned ~90°). Note rim of tiny crystals around glauconitic pellets and carbonate clasts (BSE image).

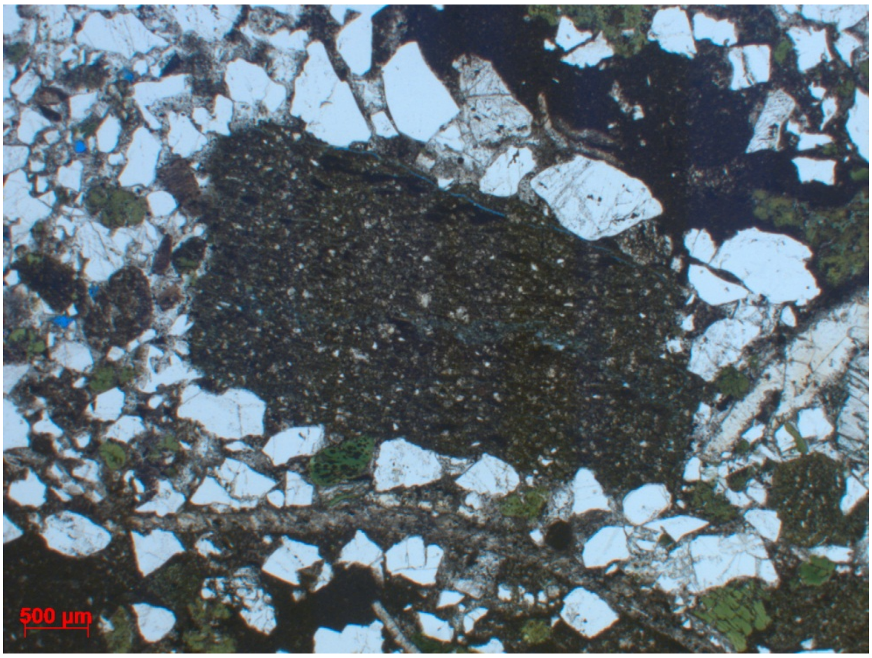

Figure 5.7. 32.65 m. Large chloritic/illitic mud clast, together with detrital quartz and glauconitic pellets in ankeritic cement.

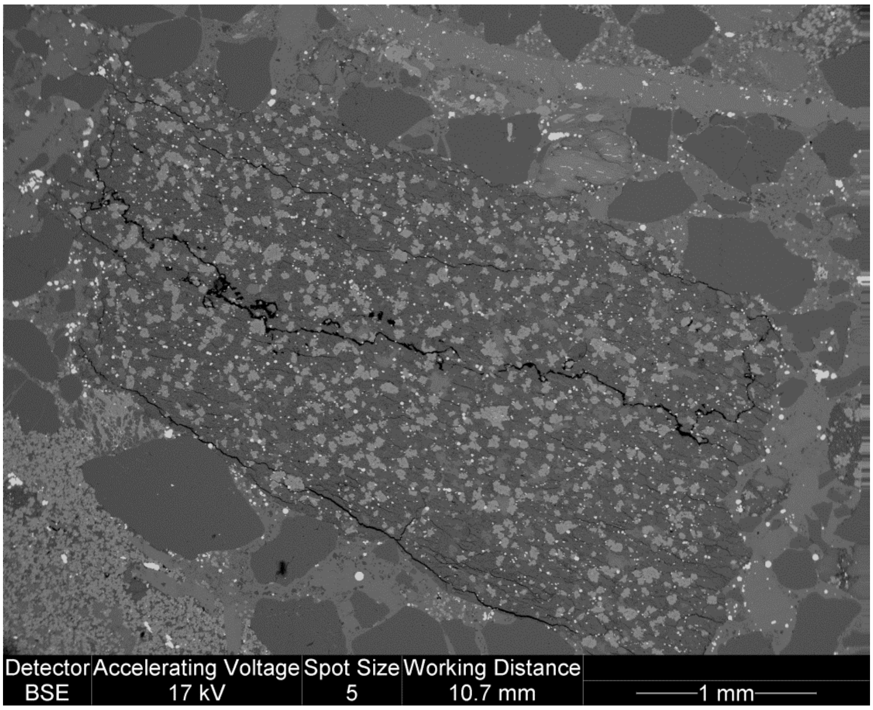

Figure 5.8. 32.65 m. Same area as in Figure 5.7 (turned ~180°). Light grey siderite crystals are recognized in chloritic/illitic mud clast (BSE image).

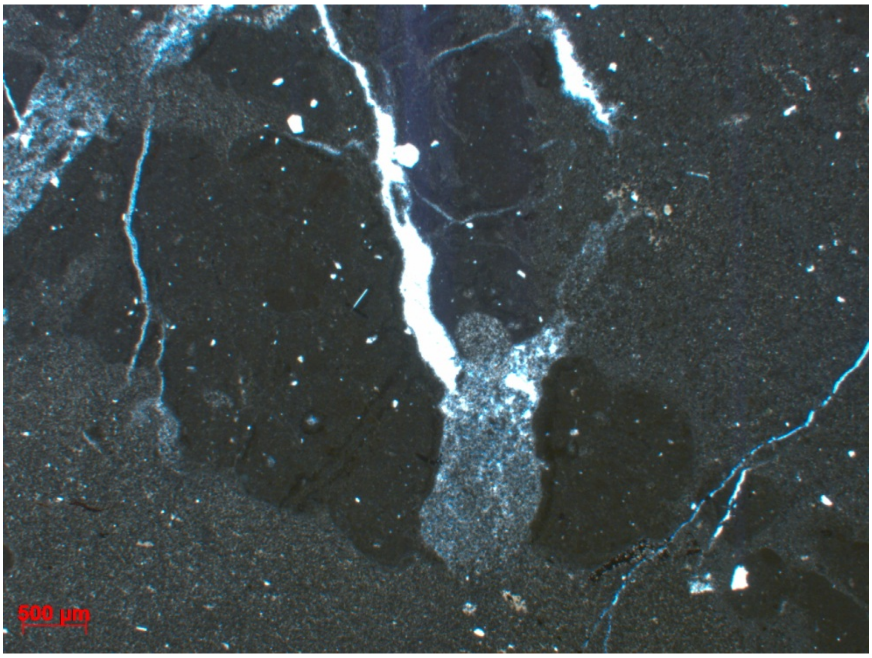

Figure 5.9. 42.47 m. Dark sideritic clasts in an ankeritic matrix. Cracks are filled by authigenic kaolinite.

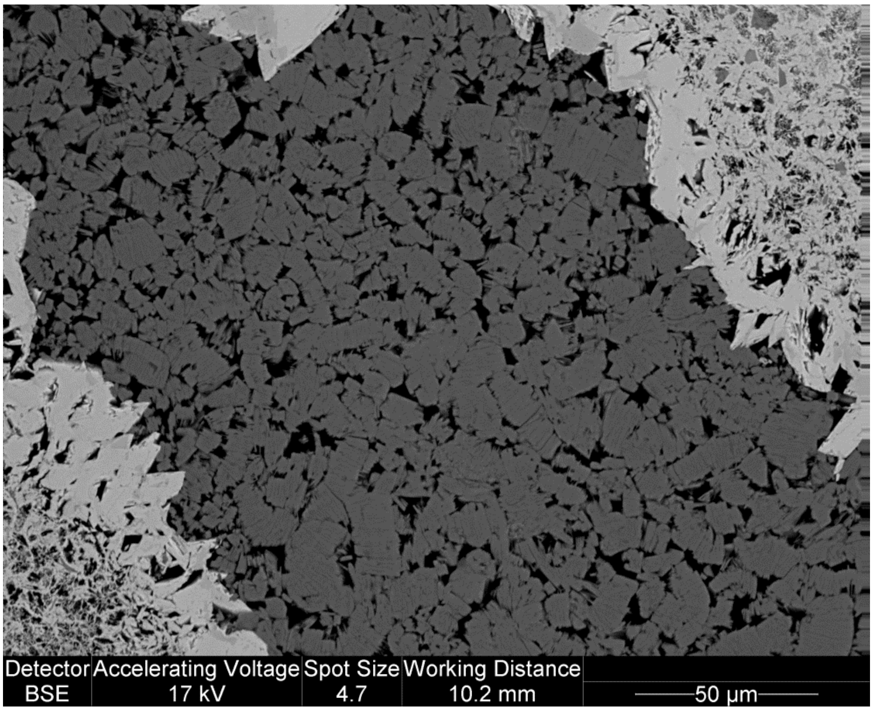

Figure 5.10. 42.47 m. Close up of authigenic kaolinite within cracks. Note whitish siderite crystals along the edges of the fissure and a more fine-crystalline siderite further away from the edges (BSE image).

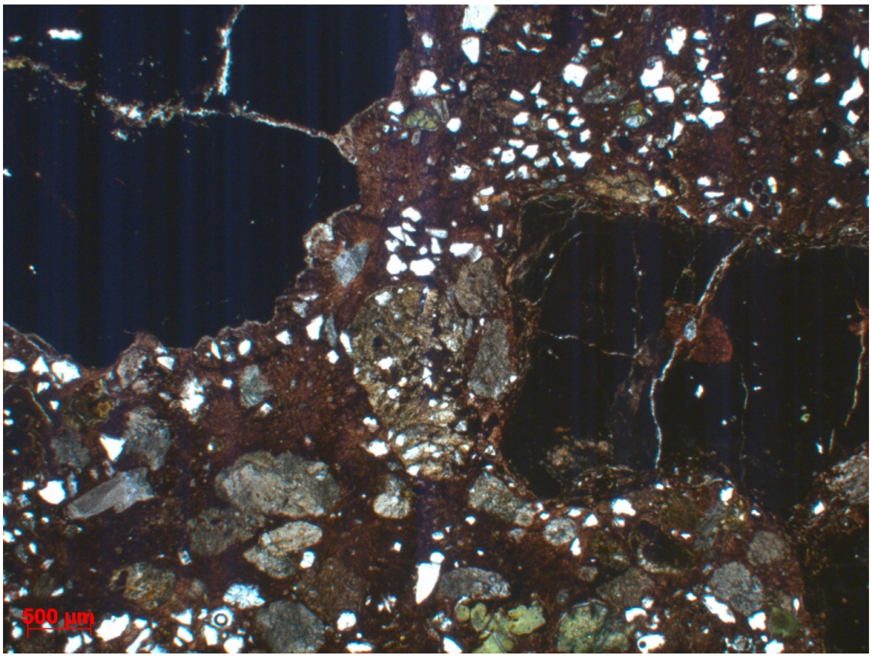

Figure 5.11. Nanok Mb, outcrop sample. Black apatitc clasts in an ankeritic/hematitic matrix. Also seen are greenish glauconitic pellets and quartz and carbonate clasts.

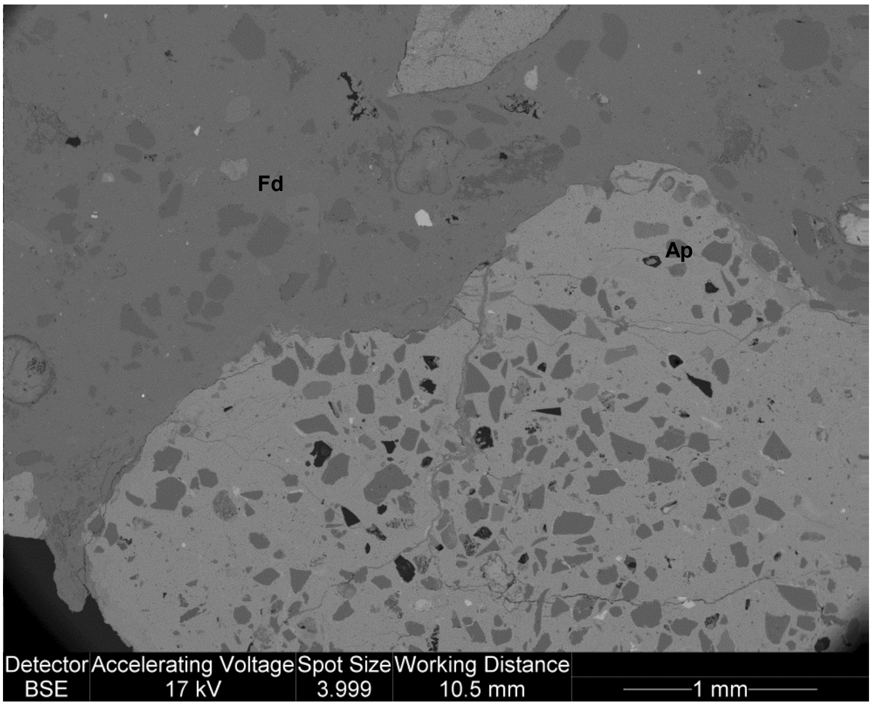

Figure 5.12. Nanok Mb, outcrop sample. Large whitish-grey clast is an apatitic concretion (Ap). The cement surrounding and infilling fractures in the concretion is ferrroan dolomite (Fd). Note floating detrital grains in both cements (BSE image).

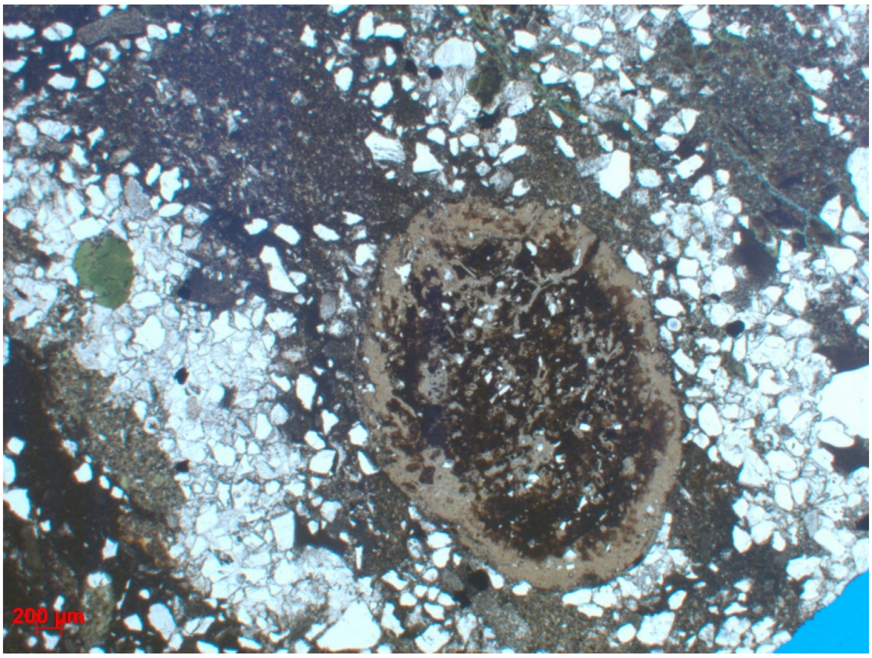

Figure 5.13. 114.30 m. Large rounded apatitic clast in a probably sideritic matrix. Note large greenish glauconitic pellet on the left.

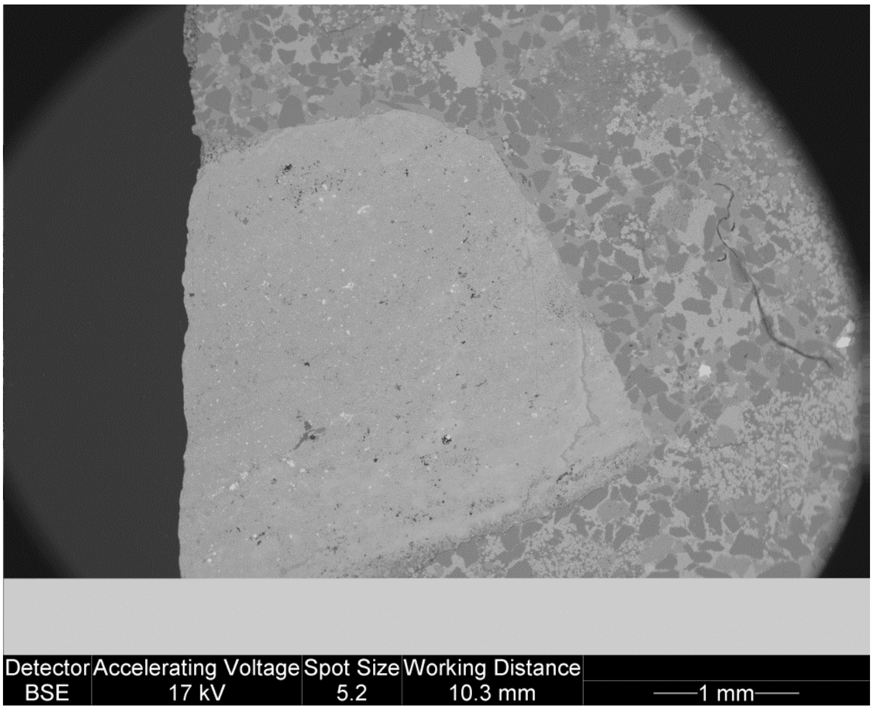

Figure 5.14. 114.30 m. Large apatitic clast in a sideritic/ankeritic matrix. Note that detrital grains are floating in the sideritic/ankeritic cement.

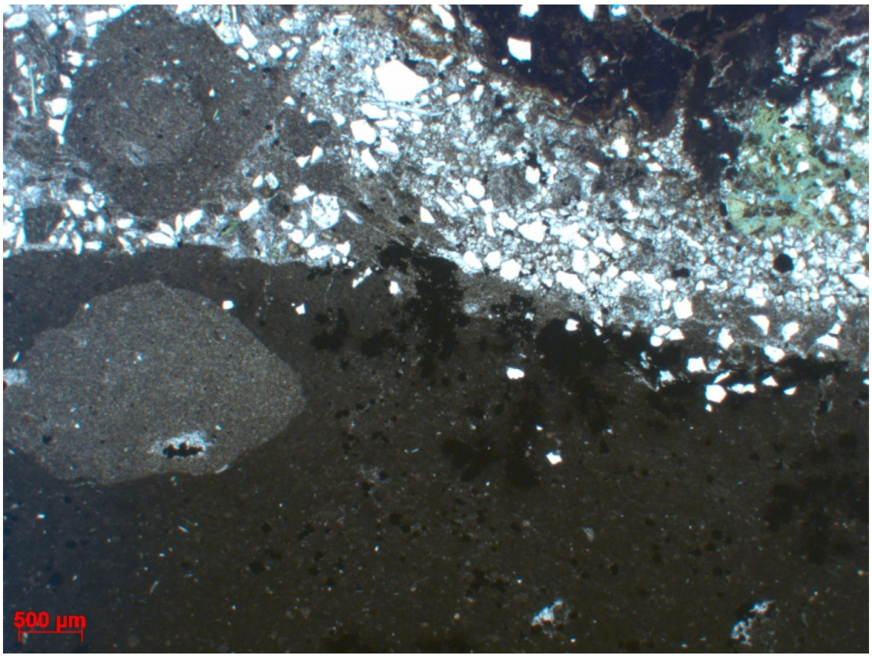

Figure 5.15. 120.95 m. In-filled burrow? in firm ground? (lower half of picture. In upper half greenish glauconitic matrix together with dark brown rounded carbonate clast (left) and apatitic clast at upper right.

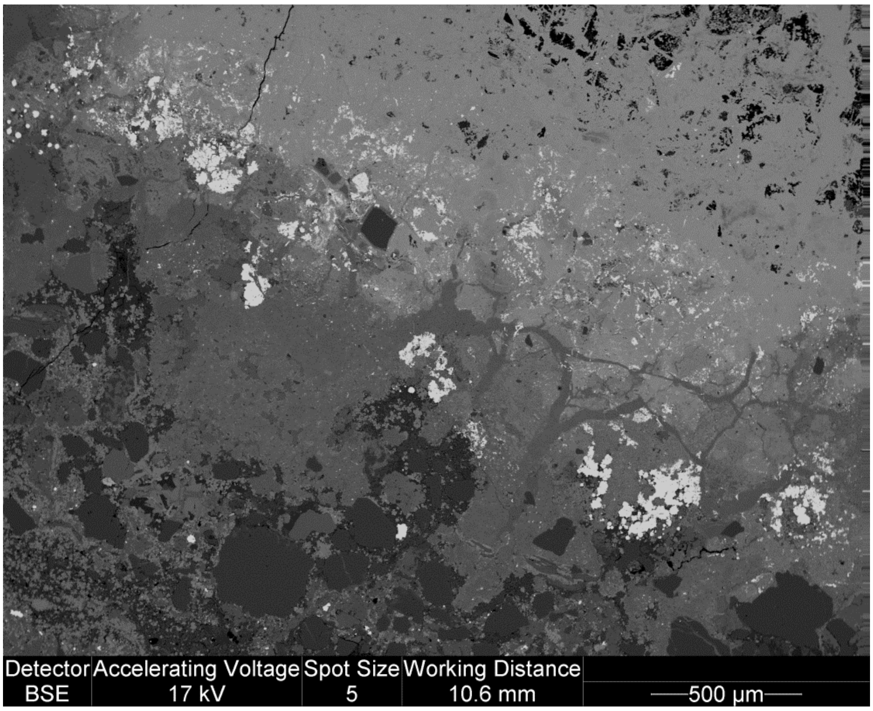

Figure 5.16. 120.95 m. Light grey concretion in upper part of photograph is probably rhodocrositic (Mn-carbonate). Darker cement in lower part is Mn-rich ankerite. Whitish minerals are pyrite (BSE image).

Figure 5.17. 133.30 m. Detrital grains, dark brown carbonate clasts and greenish glauconitic pellets in sideritic and ankeritic cement.

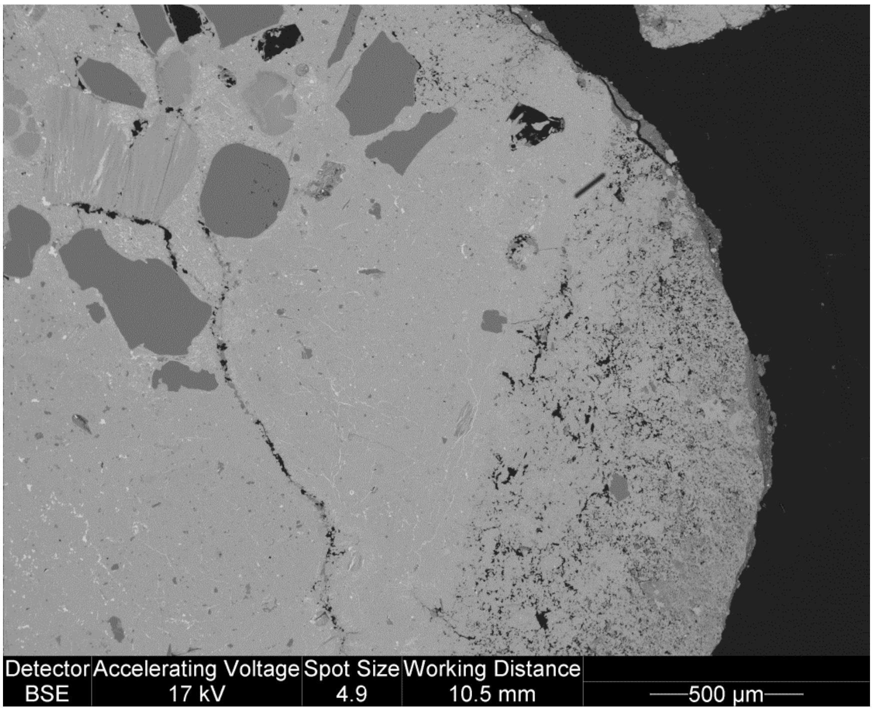

Figure 5.18. 133.30 m. Large apatitic concretion containing detrital quartz and mica. Note microporosity at edge of concretion.

6. Preliminary caprock properties

A minor number of shale samples have been taken from the core with the intention of carrying out a preliminary study of the caprock potential. The results are reported below.

6.1 Methods

Core analysis was carried out on small core pieces and left to dry at 60 ºC in an oven until constant weight. No cleaning was attempted because the core derives from the vadose / ground-water zone. The samples were analyzed in a dried condition according to “API recommended practice for core analysis procedure” (API, 1998). Porosity and grain density was measured by the He-expansion technique, no gas permeability was possible.

Porosity, capillary pressure and pore sizes were also measured on the same samples using a Micromeritics Autopore-IV porosimeter. Hg-drainage capillary pressure is measured in an injection sweep from vacuum to 60.000 psia [400 MPa]. Pore throat sizes can be measured from 200 µm down to ~ 3 nm, covering pore size distributions in the micro-, meso- and macropore range.

Mineralogical characterization required approx. 150 g of core material hand-ground to pass a 0.25 mm sieve. Samples used for grain size analysis were further dispersed by ultrasonic treatment. Chemical pretreatment involved removal of organic matter with NaAc at pH 5.5 (Anderson, 1963). The grain size distribution was then obtained from a particle size centrifuge (Slater and Cohen, 1962).

Quartz was identified by X-ray diffraction (XRD) of powdered randomly oriented specimens using a Philips 1050 instrument with pulse-height selection and β-filtered Co- K_α radiation. The amount of quartz was determined by using pure quartz of particle size 4.5 - 45 µm as a standard. The result is given as a weight percent.

Specific surface area and pore volume was determined from adsorption isotherms measured on a Coulter SA 3100 gas adsorptometer using liquid N2. The samples were outgassed at room temperature until stable vacuum. The specific surface area was calculated according to the BET model (Brunauer *et al.*, 1938). Gurvitsch pore volume in cm^3/g dry sample was calculated from the adsorption isotherm by the amount of liquid gas adsorbed at a relative pressure of P/P0=0.9.

The shales were analyzed for their content of total organic carbon (TOC, wt.%) by combustion in a LECO CS-200 induction furnace. Before TOC determination carbonate carbon had been removed by HCl treatment.

6.2 Core analysis

The porosity is below 10% for all samples, and data for Helium (He-) porosity and Mercury (Hg-) porosity are listed in Table 6.1 below. The significant difference between the two measures is due to the different techniques and the character of the sample material. In He-porosity measurement, the bulk volume of a sample is determined by submersion of the sample in a mercury bath. Narrow fractures and micro cracks, e.g. due to drying or handling of the core, may not always be penetrated by mercury during this room-condition submersion, thereby leading to an over-estimation of the porosity. This does not happen during a mercury injection test that starts from vacuum, but Hg-porosity tend to underestimate the effective porosity due to the inability of Hg to penetrate the very small pore throats < 3 nm at the maximum injection pressure of 60,000 psi (400 MPa).

The grain density is within the normal range for clastic rocks, except for the low figure of sample 241 that is due to a high content of organic material (coal fragments).

Mercury injection data listed in Table 6.2 are extracted from the diagrams in Appendix 12.4 part 1. Most samples have very high capillary entry pressures and narrow, well defined unimodal pore throat size distributions, except for sample 241. This sample is an organic shale with a significant fraction of fine sand grains as well (cf. Fig. 6.1).

6.3 Mineralogy

The grain size distribution and mineralogy are listed in Table 6.3 and Figure 6.1. It appears that most samples should be classified as laminated and non-laminated (massive) siltstones because they contain more than ⅔ silt size grains (Lundegaard & Samuels, 1980). Bulk XRD spectra detected quartz, feldspar, pyrite and clay in all samples. A nearly constant quartz content of approximately 25 wt-% for all samples should be noticed. The clay size fraction is generally 15-30 wt-% of the samples, but sample 248 and 250 have very little clay. Clay mineralogy identified illite, kaolinite and disordered mixed-layer illite-smectite; XRD spectra for 3 selected samples are attached in Appendix 12.4 part 2. The clay mineralogy is also visible from the SEM imaging that further shows minor amounts of pyrite present in most of the samples (cf. Appendix 12.4 part 3). Calcite was not detected, and TOC is generally low with exception of sample 241. Specific surface areas are moderate with figures in the interval 14-20 m^2/g, except for a few samples (241 and 250) that have lower BET surface areas (Table 6.3).

6.4 Seal capacity

The fundamental sealing capacity of a caprock is mainly defined by the grain size distribution and mineralogy, as well as the physical properties of the fluid to be contained below the seal. Based on data from Table 6.2 it has been attempted to evaluate the maximum height of an oil column the sedimentary succession at Nanok-1 core will hold assuming generalized figures for oil and brine density, and interfacial tension for an oil-brine fluid system. The failure strength as well as an evaluation of faults and fractures in the region from seismic mapping and/or core description is outside the scope of this preliminary study on the Nanok-1/1A core.

Table 6.4 lists the results for a hypothetical oil reservoir at a depth of 2000-3000 m overlain by the caprock succession at the Nanok locality with capillary properties as given in Table 2. Pore throat size has been set at the r50 level, and at the r10 level to test a very conservative estimate. The generalized data for oil and brine are held constant with depth. Although this is not strictly true, minor variation in these properties with depth cannot compromise the general conclusion that the caprock succession will hold an oil column of at least 3000 m.

6.5 Discussion and conclusion

From the data presented in this limited study of caprock properties it can be concluded that the fine-grained lithologies analyzed from the Nanok-1 core are siltstones with moderate quartz content and a low content of organic matter (< 2% TOC) for most samples. One sample (241) is classified as an organic siltstone and has, as expected, clearly inferior caprock properties relative to the other samples (Krushin, 1997). The sample is from a narrow mudstone layer occurring in the Østersletten sandstone unit.

The Nanok siltstones are excellent caprocks having extremely small pore throats and very high capillary entry pressures, even exceeding the figures measured previously for the siltstones at Brorson Halvø (Hovikoski *et al.*, 2011). Very few pore radii exceed 10 nm (cf. Appendix 12.4 part 1) which is quite unusual. This is believed to be due to a somewhat higher clay content in the Nanok siltstones compared to other siltstones of NE Greenland origin that have previously been analyzed .

However, the sealing properties of a potential caprock are not only a matter of having an effective capillary seal, but also depend on faults and fractures and the thickness of the caprock section. Faults and fractures may be evaluated from core description and or seismic interpretation, the thickness from regional mapping and other qualifiers indicating the burial of the geological section.

To conclude, the low porosity siltstones from the Nanok-1 core have demonstrated excellent capillary sealing properties that will hold an oil column of at least 3000 m.

6.6 References

Anderson, J.U., 1963: An improved pretreatment for mineralogical analyses of samples containing organic matter. Clays Clay Mineral, **10**, 380–388.

API RP 40, Recommended Practice for Core Analysis, second edition, 1998: Washington DC: American Petroleum Institute.

Brunauer, S., Emmett, P.H. & Teller, E., 1938: Adsorption of gases in multimolecular layers. J. Am. Chem. Soc., **60**, 309.

Hovikoski, J., Alsen, P., Bojesen-Koefoed, J.A., Boserup, J., Fries, K., Green, P., Japsen, P., Johannessen, P., Kazerouni, A.M., Kjøller, C., Lindgreen, H., Morigi, C., Nytoft, H.P., Nøhr-Hansen, H., Pauly, S., Petersen, H.I., Piasecki, S. and Springer, N. 2011: Borson Halvø-1 Core Well, GGU 517103, Wollaston Forland, Northeast Greenland – Final Well Report, Danmarks og Grønlands Geologiske Undersøgelse Rapport 2011/128, Confidential, 248 pp, 10 Appendices, 1 CD.

Krushin, J.T., 1997: Seal capacity of non-smectite shale. In: R.C. Surdam (ed.), Seals, traps and the petroleum system. AAPG Memoir, **67**, 31–47.

Lundegard, P.D. & Samuels, N.O., 1980: Field classification of fine-grained sedimentary rocks. J. Sedimentary Petrol., **50**, 781–786.

Slater, C. & Cohen, L., 1962: A centrifugal particle size analyzer. J. Sci. Instruments, **39**, 614–617.

Sample ID	Formation / unit	MD [m]	Porosity$_{(Hg)}$ [%]	Porosity$_{(He)}$ [%]	Grain density [g/cc]
241	Fosdalen Fm/Østersletten Mb	49.72	6.2	8.33	2.43
243	Fosdalen Fm	85.60	4.1	6.99	2.63
244	Fosdalen Fm/Knudshoved Mb	11.22	6.3	8.61	2.67
246	Fosdalen Fm/Knudshoved Mb	37.42	5.4	8.07	2.65
247	Fosdalen Fm/Knudshoved Mb	40.30	4.2	6.99	2.65
248	Fosdalen Fm	93.35	3.7	6.30	2.63
249	Fosdalen Fm	110.88	5.3	9.02	2.66
250	Fosdalen Fm	135.38	4.5	6.87	2.67

Table 6.1. Conventional core analysis data measured for massive and laminated shale-siltstone samples from the Nanok -1/1A wells. Two different measures of the sample porosity is given by Helium and Mercury injection respectively; for an explanation refer to the text above. Gas permeability was not measured.

Sample ID	MD [m]	Porosity$_{(Hg)}$ [%]	Entry P$_{(Air-Mercury)}$ [psi]	Pore radius r_{50} [nm]	r_{10}
241	49.72	6.2	650	11	88
243	85.60	4.1	~ 15,000	3.5	6.5
244	11.22	6.3	~ 13,000	4	7
246	37.42	5.4	~ 15,000	4	6.5
247	40.30	4.2	~ 19,000	3.5	5.5
248	93.35	3.7	~ 16,000	3.5	6
249	110.88	5.3	~ 13,000	4	7.5
250	135.38	4.5	~ 13,000	3.5	6.5

Table 6.2. Seal capacity data in an air-mercury fluid system read from high-pressure mercury injection measurements on 8 shale-siltstone samples from the Nanok-1/1A wells; r10 and r50 denotes the pore throat radius in nm (nano meter) where 10% and 50% respectively of the sample pore volume has been filled by injected mercury. A small difference between r10 and r50 identifies a narrow uni-modal pore throat size distribution and vice-versa. Entry pressure estimated by the tangent method.

Table 6.3. Grain size distribution and selected mineralogical and gas absorption data for 8 shale samples taken at different depths along the core from the Nanok-1/1A wells. Observe that summation of fractions making up less than 95 wt-% is due to organic material removed during the initial sample preparation.

Sample ID	Depth [m]	Porosity$_{(He)}$ [%]	>63 µm	63-20 µm	20-4 µm	4-2 µm	2 - 0.2 µm	< 0.2 µm	Σ [wt-%]	Σ clay [wt-%]	Carbonate [wt-%]	Quartz [wt-%]	N_{2BET} m^2/g	TOC [wt-%]
241	49.72	8.33	16	32	23	5	8	5	90	14	nd	25	3	8.37
243	85.6	6.99	4	43	20	7	14	11	98	24	nd	28	19	1.04
244	11.22	8.61	1	33	28	8	16	11	97	28	nd	25	14	1.03
246	37.42	8.07	1	51	22	5	11	8	99	19	nd	27	16	1.08
247	40.3	6.99	2	47	23	5	12	10	98	22	nd	25	14	1.21
248	93.35	6.30	9	41	34	1	2	1	89	3	nd	29	14	0.85
249	110.88	9.02	3	36	27	9	16	11	102	27	nd	22	18	1.71
250	135.38	6.87	1	66	28	1	0.4	0.2	97	1	nd	23	8	1.56

nd = not detected

Abbreviations and comments: organic material was removed from all samples

Depth [m]	ρ_w (brine) [kg/m^3]	ρ_{nw} (oil) [kg/m^3]	IFTxcosΘ [mN/m]	'r' (radius) [nm]	P_{ce} (entry P) [MPa]	H_{max} * [m]
2000 – 3000	1015	761	26	7	7.4	2981
				4	13.0	5217

Legend: ρ_w = density of wetting phase (brine); a brine density gradient of 0.44 psi/foot is assumed
ρ_{nw} = density of non-wetting phase (oil); an oil density gradient of 0.33 psi/foot is assumed
P_{ce} = capillary entry pressure,
r = pore radius from mercury injection test, Table 2
IFTxcosΘ = interfacial tension (IFT) x contact angle product

Table 6.4. Evaluation of the capillary seal capacity for a hypothetical oil reservoir capped by the shale succession at the Nanok-1 well. Pore radius data have been adopted from Table 2. Observe that a doubling of the pore throat radius 'r' will halve the height 'Hmax' of a potential oil colum that can be safely contained below the caprock. It is assumed that the fluid-rock system is waterwet *. Data in the table is given in SI units.

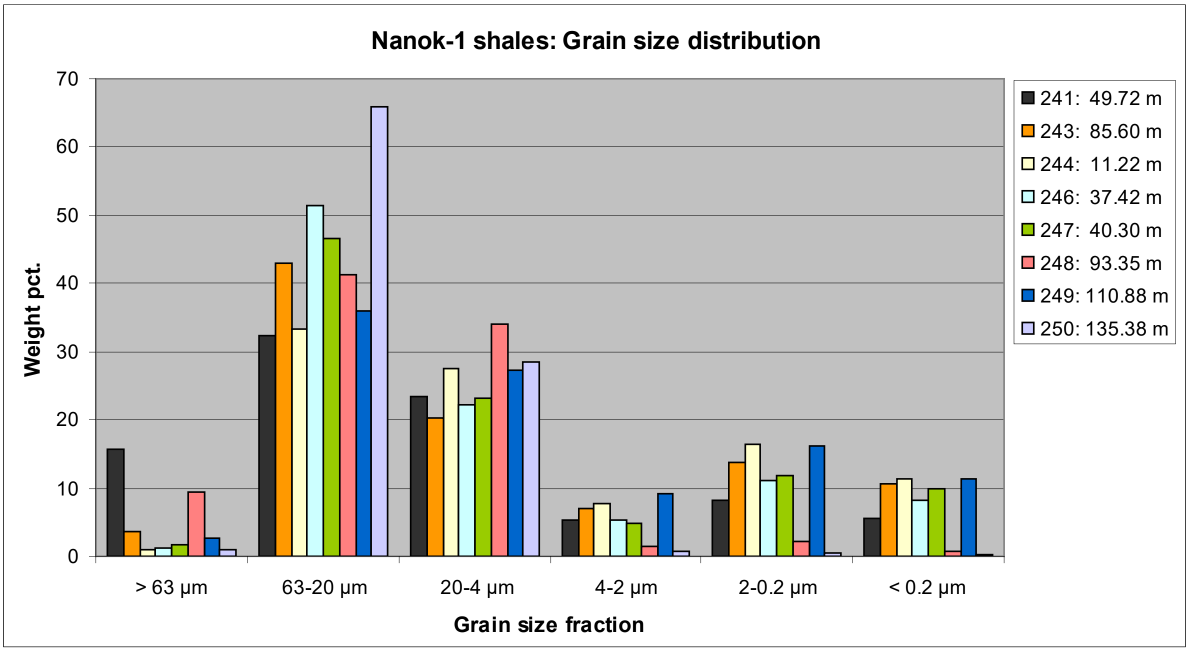

Figure 6.1. Grain size distribution data measured on 8 shale samples from the Nanok-1/1A wells. The silt and clay size fractions have been split into coarse and fine sub-fractions to help interpret other experimental data.

7. Conventional Core Analysis (CCAL) and Reservoir quality

This section first presents results of conventional core analysis from the sandstone intervals. Secondly, these data are combined with porosity log, sedimentary facies, inferred sedimentary architecture, as well as mineralogy and diagenesis patterns in order to delineate reservoir quality of the Østersletten Mb.

7.1 Methods

The following is a short description of the methods used by GEUS Core Laboratory for the conventional core analysis (CCAL) of the Nanok-1/1A well. For a more detailed description of methods, instrumentation and principles of calculation, the reader is referred to API recommended practice for core-analysis procedure /1/. Precision of the analysis is shown in Table 7.1.

Plugging

Plugging of the core was carried out from selected sandstone at irregular intervals. Plugs were taken as 1" plugs using tap water as coolant and both horizontal and vertical plugs were retrieved (cf. Table 7.2).

Cleaning and drying

Following plugging, the samples were placed in a Soxhlet extractor, which continuously soaks and washes the samples with methanol. This process removes water and dissolves salt precipitated in the pore space of the rock. Extraction was terminated when no chloride ions were present in the methanol. Subsequently, the samples were hot Soxhlet cleaned with toluene to remove any oil. Toluene extraction was terminated when the toluene was clear and showed no sign of oil contamination.

Following cleaning, the samples were left to evaporate the major part of the toluene at laboratory room temperature (20±2 °C) for 24 h and subsequently dried at 60 °C for 24 h.

Some of the plugs were broken as a consequence of the cleaning process due to the interbedded/heterolithic nature of the plugs. Thus, it was decided to resample plugs at these locations and carry out CCAL without cleaning. The plugs that were not cleaned are marked in Table 7.2.

Gas permeability, uncorrected (GEUS steady state instrument)

Each plug was mounted in a Hassler core holder, and a confining pressure of 400 psi was applied to the sleeve. The uncorrected permeability to gas was measured by flowing nitrogen gas through a plug of known dimensions at a mean pore pressure of 1.5 bara. No back pressure was applied. The readings of the digital gas permeameter are checked regularly by routine measurement of permeable steel reference plugs (Core Laboratories™ gas permeability reference plug set). Using the digital flowmeter-reading, the lower limit for permeability measurements is 0.05 mD.

He-porosity and grain density

The porosity of each plug was determined by subtraction of the measured grain volume from the measured bulk volume. The Helium technique, employing Boyle's Law, was used for grain volume determination, applying a double chambered Helium porosimeter with digital readout. The sample bulk volume was measured by submersion of the plug in a mercury bath using Archimedes principle. Grain density was calculated from the grain volume measurement and the weight of the cleaned and dried sample.

Before measurements, the Helium porosimeter was calibrated using a set of steel plugs (Core Laboratories™ volume reference plug set). The bulk volume apparatus is checked frequently as a laboratory routine using a steel plug with known volume.

Precision of analytical data

The table below gives the precision (= reproducibility) at the 68% level of confidence (+/- 1 standard deviation) for routine core analysis measurements performed at the GEUS Core Laboratory.

7.2 CCAL Results

The results of the CCAL are presented in Table 7.2 and Figures 7.1 and 7.2.

The majority of samples have grain densities between 2.60-2.70 g/cc, reflecting quartz rich sandstone with minor amounts of clay, organic matter or carbonates. However, a few samples have considerably lower grain densities, probably due to a high content of coal (e.g. plugs 232.1 and 233, Table 7.2).

A cross-plot of the gas permeability vs. porosity suggests an overall exponential relationship between permeability and porosity (Fig. 7.1), and the vertical permeability is roughly lower than the horizontal permeability by a factor of 10 (Fig. 7.1).

The low porosities and permeabilities are observed mainly in the interval between 60.0 m and 70.0 m depth, corresponding to the interval where the lithological description suggests that the Østersletten Mb. comprises interbedded sandstone and mudstone. Judging from a few low grain density measurements as well, the organic matter content may occasionally be relatively high as well in this interval (Fig. 7.2).

Low grain densities are also observed at a depth of 72.4 m, corresponding to the high coal content observed at this depth (Fig. 7.2C).

7.3 Reservoir properties of the Østersletten Mb

Figure 7.3 shows the porosity log and porosity CCAL measurements plotted against the GR and the lithological log of the Østersletten Mb. These data, together with mineralogy, diagenesis characteristics, bed thicknesses and sedimentological interpretation are summarized in Table 7.3. In the text below, porosity and permeability distribution in the Østersletten Mb is first summarized. This is followed by a brief speculation of larger-scale architecture and depositional context of the unit.

7.3.1 Sedimentary Facies and distribution of porosity and permeability

The Østersletten Mb reservoir comprises mainly m-scale, structureless fine-grained sandstone ($F4A_1$) that grade upward into carbonaceous dewatered sandstone ($F4A_2$). Locally, these beds may further grade into a few cm-thick intervals of allochthonous sandy coal in the top of the bed ($F4A_3$). These facies (F4A) are, in places, sharply inter-bedded with dm-scale intervals of bioturbated sandy mud/muddy sand (F4B) and parallel laminated to ripple cross-stratified very fine to fine-grained sandstone with rare mudstone interlamina (F4C).

The best quality reservoir intervals are associated with F4A, which forms ~84% of the total volume of the Østersletten Mb. In general, the porosity for F4A sub-facies ranges between 20–22%.

The interbedding subordinate facies F4B and F4C show average porosities in the order of 11% and 13%, respectively. In particular, the minimum values, 6% and 9% indicate that these facies host intervals of poor reservoir quality.

The porosity log data was compared with the corresponding GR log response (Fig. 7.3) in order to qualify a net/gross ratio estimate. Thus, net/gross ratio was estimated by using 15% porosity as a general cutoff value corresponding to a GR cut-off value of 50 API (Fig. 7.3). Based on these data, net/gross is estimated to be ~ 81–88%. As indicated by the CCAL data, the non-reservoir intervals correspond to Facies F4B and F4C occurrences (Table 7.3). The only exception to this is the base of the Østersletten Mb, where an F4A occurrence is slightly finer grained (lower fine-grained sandstone), enriched in detrital siderite fragments and shows limited porosity (Fig. 7.3).

The major difference between the porous reservoir rock facies F4A and the less porous facies F4B and F4C is the permeability: $F4A_1$ and $F4A_2$ show average permeabilities of 147 mD and 50 mD, respectively, whereas the interbedding facies are characterized by very low permeabilities, i.e. 1.8 mD (F4B) and 0.6 mD (F4C). In addition, sub-facies $F4A_3$ show reduced permeability (average K_v=~5mD).

Porosity and permeability reduction in these facies are mainly caused by abundant detrital mica, which caused precipitation of kaolinite and siderite cements (Chapter 5). In addition, low permeability is locally (e.g., $F4A_3$) related to the pervasive presence of coal fragments in this facies.

Sealing properties of a clay-rich F4B occurrence that showed the lowest porosity value of analyzed plugs (6%, 49.7 m; Chapter 6) were also analyzed. These data indicate 20–30 times lower entry pressure values and elevated pore throat diameters in comparison to the analyzed Fosdalen Fm shale units both over- and underlying the Østersletten Mb. However, from the present dataset it cannot be concluded whether or not the clay-rich occurrence comprises a pressure barrier between the upper and lower parts of the Østersletten Mb.

Finally, two plugs were analyzed from the generally non-reservoir interval of the undifferentiated Fosdalen Fm (not shown in Fig. 7.3). These tidal sandstone facies (F2) recorded good porosity and permeability (20–27%, K_h=311–1800 mD).

7.3.2 Architecture and depositional system

The architecture of the Østersletten gravity flow system is not well constrained due to sporadic and laterally limited outcrop exposures. Therefore, the following summary is largely based on characterization of similar depositional systems (e.g., Richards *et al.*, 1998) and should be considered as somewhat speculative.

1) The deposits are interpreted to be part of a small-scale sand-dominated fan near base of slope. Paucity of clay even in beds that show preserved tops, and the inferred proximal locus of sand accumulation suggest low sediment transport efficiency system. This would further point to decreasing net/gross ratio towards the basin and possibly relatively abrupt mid fan – basin floor gradation. The sharp base and top of the Østersletten Mb are in line with these interpretations.
2) The lack of clay may have hindered formation of stable channels and favored the formation of both sheet-like and lobate sand bodies.
3) The tectonostratigraphic position suggests late post-rift setting characterized by filled rift-topography and mainly east directed flow. This may have promoted development of east-oriented radial fan rather than e.g., elongate axial deposition.
4) The sandstones allegedly pinch out towards the slope (west).
5) The Østersletten Mb is sharply (without gradation) overlain by the Knudshoved Mb shale pointing to abrupt abandonment of the fan system. Thus, the deposits could form an analogue for a stratigraphic trap (see Chapter 6 for cap rock properties).
6) The minor sandstone intervals from the undifferentiated Fosdalen Formation are thought to be elongate features, similar to shallow water tidal mouth bars (cf. Shanmugam, 2008)

7.4 Conclusions

The Østersletten Mb comprises approximately 40 m of sandstones considered to be of reasonably good reservoir quality. The net/gross ratio is estimated to be 81–88% based on a 15% porosity cut-off value. The average porosity of the reservoir quality sandstones is 21–22%, and the average permeability ranges between 50–150 mD. The Østersletten sandstones are interpreted to be part of a small-scale sand-dominated fan near base of slope, possibly characterized by low-sediment transport efficiency.

7.5 References

/1/. American Petroleum Institute (API) 1998: Recommended Practices for Core Analysis. Exploration and Production Department, American Petroleum Institute, Second edition.

Richards, M., Bowman, B., & Reading, H., 1998: Submarine fan systems I: characterization and stratigraphic prediction. Marine and Petroleum Geology, **15**, p. 578–606.

Measurement	Range, mD	Precision
Grain density		0.003 g/cc
Porosity		0.1 porosity-%
Permeability: (Conventional)	0.05-0.1 > 0.1	15% 4%

Table 7.1. Precision of the CCAL data for Nanok-1/1A well

Plug	Lab ID	Depth [m]	Plug H/V	Porosity$_{(He)}$ [%]	Gas perm. [mD]	Grain density [g/cc]	Cleaned/ not cleaned
211	1	45.40	H	20.72	183.678	2.685	Cleaned
212	2	46.82	H	23.96	534.822	2.627	Cleaned
213	3	48.47	H	21.07	86.988	2.637	Cleaned
214.1	4.1	49.70	H	6.38	0.705	2.589	Not cleaned
215	5	51.22	H	21.63	132.705	2.674	Cleaned
216	6	54.00	H	21.9	90.509	2.654	Cleaned
217	7	54.00	V	22.98	86.241	2.655	Cleaned
218	8	57.10	H	19.37	43.409	2.654	Cleaned
219	9	59.75	H	16.18	6.459	2.657	Cleaned
220.1	10.1	60.95	H	18.76	4.753	2.099	Not cleaned
221	11	62.25	H	18.99	15.068	2.565	Cleaned
222.1	12.1	62.42	H	8.91	0.160	2.538	Not cleaned
223.1	13.1	63.50	H	14.22	1.314	2.250	Not cleaned
224.1	14.1	63.50	V	14.91	0.228	2.255	Not cleaned
225	15	63.72	H	18.93	26.279	2.654	Cleaned
226	16	66.22	H	12.47	3.765	2.627	Cleaned
227	17	66.22	V	14.14	0.930	2.629	Cleaned
228	18	66.72	H	23.23	264.765	2.678	Cleaned
229	19	68.85	H	20.73	148.235	2.665	Cleaned
230	20	68.85	V	20.92	94.153	2.662	Cleaned
231	21	69.50	H	19.13	154.853	2.680	Cleaned
232.1	22.1	72.43	V	19.93	1.687	1.781	Not cleaned
233	23	72.38	V	24.33	8.496	1.800	Cleaned
234	24	75.40	H	19.84	197.304	2.679	Cleaned
235	25	77.65	H	20.24	47.643	2.731	Cleaned
236	26	96.90	H	26.91	1803.848	2.679	Cleaned
237.1	27.1	98.15	H	1.75	#I/T	2.891	Not cleaned
238.1	28.1	126.75	H	20.30	311.430	2.653	Not cleaned
					#I/T = Permeability below 0.05 mD		

Table 7.2. CCAL data for Nanok-1/1A well – sandstone units. All plugs were 1" diameter plugs of various lengths. Cleaned/not cleaned refers to whether plugs were hot Soxhlet cleaned or not prior to analysis.

Facies	Sub-facies	Depositional Process	Environ.	Thickness	Porosity	Permeability	Mineralogy (framework grains)	Diagenesis
F4A	A1: Structureless fine-grained sandstone	Mainly high density turbidites formed by delta front collapse at shelf edge	Sand-rich fan near base-of-slope	Max. ~6 m Min.~15 cm Aver. ~2.16 m Vol% 76	Max. ~24% Min. ~19% Aver. ~20%	Max. ~535 mD Min. 7 mD Aver. ~147 mD	Quartz dominate; K-feldspars and mica are common; coal fragments are minor to common in amount; heavy minerals are rare	Minor pyrite; minor to common siderite, kaolinite and ankerite; sparse and incipient quartz cement; feldspars are wholly or partially dissolved
	A2: Carbonaceous sand with common dewatering structures			Max. ~80 cm Min. ~5 cm Aver.~24 cm Vol% ~7%	Max. ~23% Min.~19% Aver.~21%	Max. ~ 91 mD Min. ~ 5 mD Aver. ~ 50 mD	Quartz is abundant to dominating; K-feldspars are common and mica is abundant; coal fragments are common to abundant in amount; heavy minerals are rare	Minor pyrite; minor to common siderite and ankerite;common to abundant kaolinite; sparse and incipient quartz cement; feldspars are wholly or partially dissolved
	A3: Allocthonous sandy coal			Max. ~30 cm Min. ~3 cm Aver.~13 cm Vol% ~1%	Max. ~20% Min.~24% Aver.~22%	Max. ~9 mD Min.~1.7 mD Aver.~5 mD	Coal fragments dominate; common quartz, K-feldspar and mica	Common pyrite; minor kaolinite; feldspars are wholly or partially dissolved
F4B	Bioturbated sandy mud - muddy sand	Sustained low-sediment concentration flow (cf. bottom current)		Max. ~2.05 m Min. ~5 cm Aver.~54 cm Vol% ~12%	Max. ~14% Min.~6% Aver. ~11%	Max. ~3.8 mD Min. ~0.8 mD Aver. ~1.8 mD	Quartz dominate; K-feldspars, mica and coal fragmants are common; clayey matrix is abundant; heavy minerals are rare	Minor pyrite; siderite is absent or occur in minor amount; kaolonite is common; feldspars are wholly or partially dissolved
F4C	Paralell laminated - ripple cross-stratified sandstone and carbonaceous matter with subordinate mud-lamina/bed	Low density turbidites. Periodically waxing and waning flow (cf. hyperpycnal flow)		Max. ~55 cm Min. ~5 cm Aver.~19 cm Vol% ~3%	Max. ~15% Min.~9% Aver. ~13%	Max. ~1.3 mD Min.~0.2% mD Aver. ~0.6% mD	Quartz dominate; K-feldspars are common; abundant mica; coal fragments are common to abundant; heavy minerals are rare	Minor pyrite and siderite; abundant kaolinite; sparse and incipient quartz cement; feldspars are wholly or partially dissolved

Table 7.3. Summary of reservoir characteristics of the Østersletten Mb

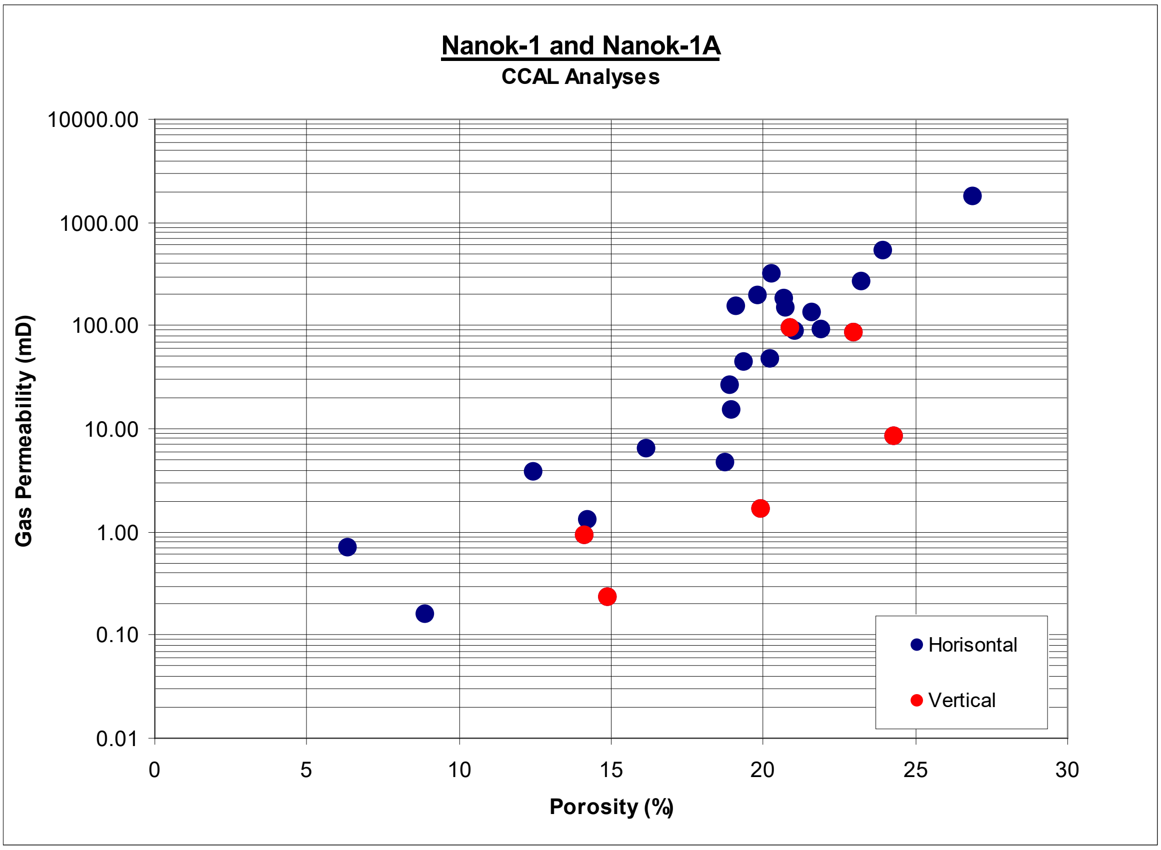

Figure 7.1. CCAL data for Nanok-1/1A well – sandstone units. Cross-plot of measured gas permeability vs. porosity.

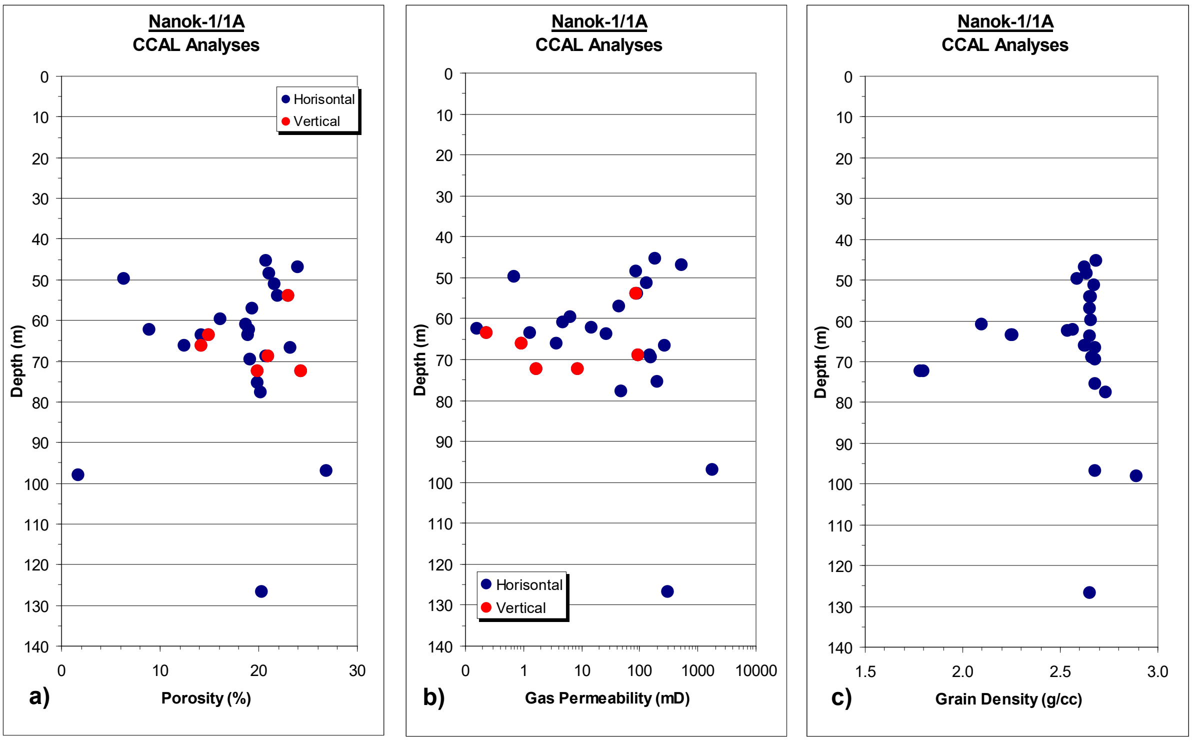

Figure 7.2. CCAL data for Nanok-1/1A well – sandstone units. Cross-plot of: a) measured porosity vs depth; b) measured gas permeability vs. depth; c) measured grain density vs. depth.

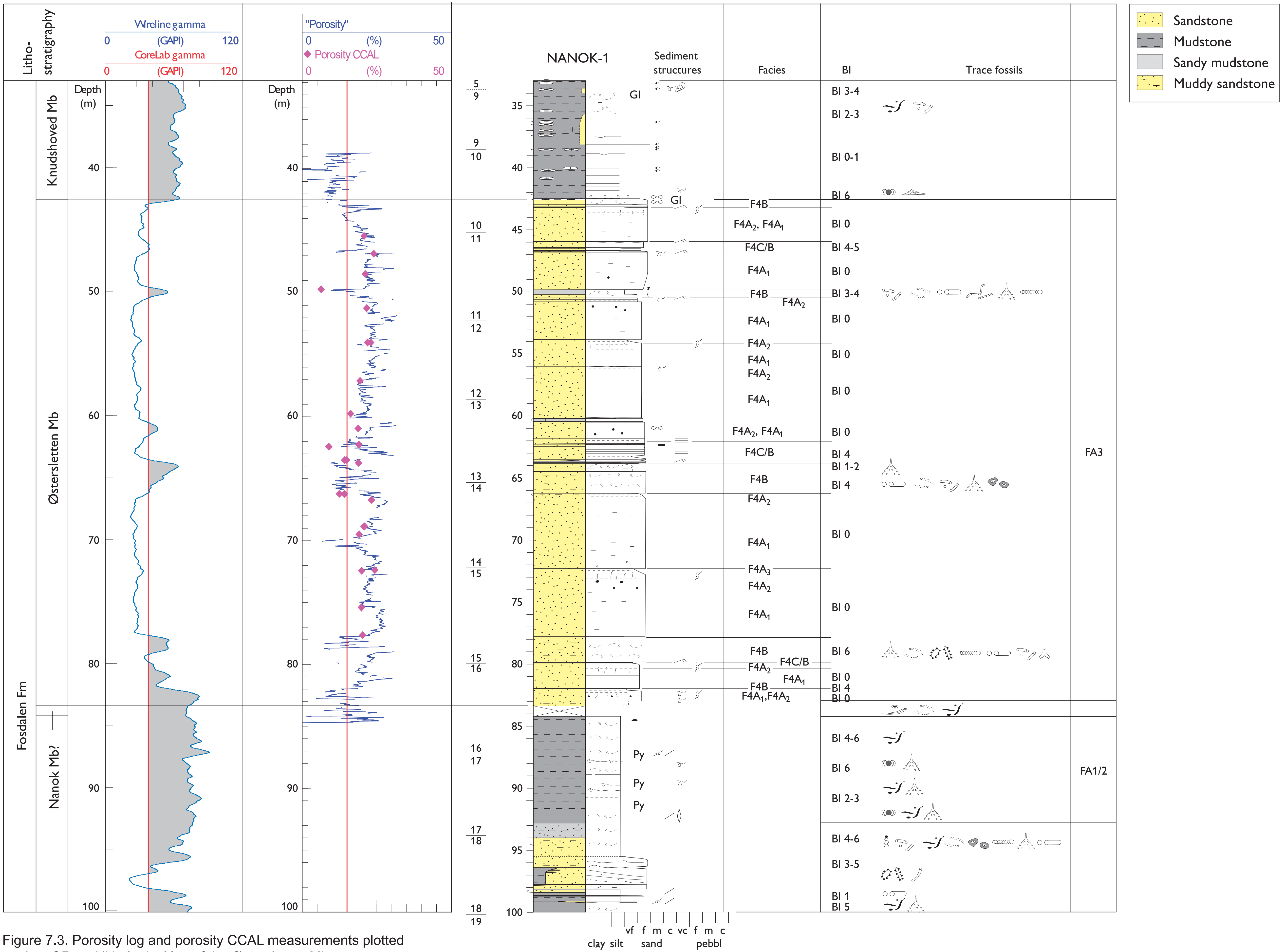

Figure 7.3. Porosity log and porosity CCAL measurements plotted against GR and lithological log of the Østersletten Mb.

8. Petroleum Geochemistry

8.1 Petroleum source potential and thermal maturity

This section reports on the results of TC/TOC/TS/Rock-Eval screening analysis and vitrinite reflectance analysis of samples from the Nanok-1 corehole.

8.1.1 Methods

A total of 117 samples covering the entire succession penetrated by the Nanok-1 corehole were analysed for total Carbon (TC), total Sulphur (TS), total organic Carbon (TOC), and subjected to Rock-Eval type screening pyrolysis.

Total Carbon (TC) and total Sulphur (TS) were determined by combustion of sample aliquots in a LECO CS-200 induction furnace.

Total organic carbon (TOC) was determined by combustion in a LECO CS-200 induction furnace after treatment of sample aliquots by hydrocloric acid in order to remove mineral-bound carbon, and recalculation based on loss of weight.

Rock-Eval-type screening pyrolysis was carried out using a Source Rock Analyser instrument (SRA) produced by Humble Instruments and Services (presently Weatherford Laboratories), calibrated using the IFP55000 pyrolysis standard in order to ensure full comparability with standard Rock-Eval data. An in-house standard (Marl Slate, Sunderland Quarry, UK) was used for stability control, with sets of one standard and one blank being run for every 10 samples.

Particulate blocks suited for reflected light microscopy were prepared from 8 samples covering the depth range 9.11 m to 158.26 m. The samples were lightly crushed and sieved between 63 µm and 1 mm. The analysis fraction from each sample was embedded in epoxy, and the epoxy blocks were ground and polished to obtain a smooth surface for microscopy. The preparation procedure follows international standards (Taylor *et al.*, 1998).

VR measurements (random, oil immersion) were conducted using a Leica DM4000M reflected light microscope equipped with a 50x objective and the Diskus Fossil system (Hilgers Technisches Buero). The VR readings were taken at 546 nm (monochromatic light). Before measurement the microscope was calibrated against a YAG 0.903%R_o standard with integrated optical zero standard. The average VR for each depth was calculated from a population selected from the total reflectance histogram (Appendix 12.5).

A number of samples were also qualitatively inspected for their kerogen content in reflected white light and fluorescing-inducing blue light using a Zeiss microscope.

8.1.2 Petroleum Potential

TC/TOC/TS/Rock-Eval type screening data are tabulated in Table 8.1.1. Analytical results are plotted versus depth in Figures 8.1.1 and 8.1.2. The entire drilled succession belongs to the Fosdalen Formation, and at least two members can be identified.

The uppermost ≈ 42.5 m of the drilled succession consist essentially of mudstones that are referred to the Knudshoved Member. The deposits are organically lean with TOC-yields in the range 0.6-1.6 wt-% with a mean value of 1.1 wt-% and variable sulphur contents, 0.1 – 3.2 wt-%. The petroleum potential is essentially non-existing, with S2-yields in the range 0.1–1.1 mg/g with a mean value of 0.6 mg/g, resulting in a mean Hydrogen Index of 50.

The Østersletten Member (≈ 42.5 m – ≈ 83.5 m) underlies the Knudshoved Member. Due to its generally sandy nature only one sample, collected at ≈ 82 m, of the Østersletten Member was analysed for petroleum potential. This sample shows high TOC (≈ 20 wt-%), but low Hydrogen Index (117) and elevated Production Index (0.16) suggesting oil staining. Microscopic examination (see below) shows high contents of transported terrestrial organic debris and bitumen. The Nanok Member that was supposed to underlie the Østersletten Member cannot be identified with certainty, partly due to missing section, but from a depth of ≈ 84.5 m to ≈ 160.5 m where an intrusion is encountered, the lithology reverts to mudstone albeit with a few sand intercalations. Two prominent sand-layers are found at ≈94–98 m and ≈125–127 m. At ≈160.5 m an intrusion is encountered. Over the interval ≈84.5 m to ≈160.5 m a number of general trends can be observed. From ≈84.5 m to ≈100 m TOC remains more or less constantly low, close to 1.0 wt-%. From ≈100 m to ≈140 m a slight but steady increase in TOC is observed until a value of ≈2.2 wt-% is reached. From ≈140 m to ≈160.5 m the trend is reversed, and TOC decreases rapidly with depth until a value of ≈0.5

wt-%. A similar, but somewhat more pronounced development is observed with respect to petroleum potential (as indicated by S2), which shows an increase from ≈0.3 mg/g to ≈3 mg/g, followed by rapid depletion. This results in a 4-5 fold increase in Hydrogen Index from ≈30 at ≈100 m to ≈150 at ≈140 m, followed by a rapid decrease over the interval ≈140 m to ≈155 m, from which depth the Hydrogen Index is essentially zero. This tripartite division of the petroleum potential observed through the core is illustrated in Figures 8.1.3 & 8.1.4.

The trend can be interpreted in light of the development in thermal maturity with depth, caused by the intrusion encountered at the base of the corehole. The oil window for Type II kerogen is defined as Tmax = 435–460°C (Espitalié *et al.* 1985, 1986; Bordenave et al, 1993; Peters & Cassa, 1994). Based on Tmax data the succession enters the oil window at approximately 140 m, peak oil is reached 4–5 metres deeper and the end of the oil window is found at approximately 155 m, with all petroleum generation potential being exhausted at greater depths. Hence, going deeper from a depth of approximately 100 m, the petroleum potential increases steadily until this development is curtailed by the onset of petroleum generation at approximately 140 m. This interpretation is supported by PI data (Production Index, PI=S1/(S1+S2)), that show a rapid increase from approximately 140 m, reaching a maximum of 0.9 close to 155 m, followed by an even faster decrease towards greater depth further to thermal destruction of the hydrocarbons generated (Fig. 8.1.5). It should be noted that the increase in PI is caused by a decrease in S2 further to generation, rather than to an increase in S1 further to accumulation of free hydrocarbons in the sediments. This may suggest a predominantly gas-prone nature of the kerogen in the mudstones, but can in part also be attributed to the high temperatures reached near the intrusion.

This view is supported by the fact that oil staining originating from migrated petroleum is encountered in sandstone units penetrated by the corehole. A sandstone interval at ≈94–98 m shows a prominent oil stain. The core gives off a distinct petroleum odour, and shows bright fluorescence when observed under fluorescence inducing blue light (Fig. 8.1. 6). Moreover, due to evaporation from the core during transportation, the lid of the corebox shows conspicuous brown precipitates of petroleum products (Fig 8.1.6). Solvent extract recovery from this part of the core amounts to more than 6000 ppm, which based on an assumption of 10% porosity and a density of 2.5 g/cm^3 for the sandstone, corresponds to a remaining oil saturation of around 20% (see Section 8.2 for details). This was, as testified by the precipitates on the corebox lid, even higher when the core was initially recovered.

The oil is strongly biodegraded, but a biomarker fingerprint can still be obtained, see Section 8.2 for details.

The uppermost part (≈45–46 m) of the thick sandstone unit representing the Østersletten Member also shows oil staining. The stains are not as prominent as those found in the sandstone interval mentioned above, and the saturation is lower.

Moreover, the organic-rich interval encountered at ≈82 m in the Nanok-1 corehole plus a number of more or less similar outcrop samples of the same unit, collected up to ≈1000 m from the drillsite contain bitumen/oil-stains compositionally more or less similar to the oil-stains encountered in the sandstones (Fig. 8.1.7 and Table 8.1.3). The presence of oil is manifest in Rock-Eval data, showing large S1-peaks and sometimes bimodal or irregular S2-peaks, partially merged with the S1-peak (Fig 8.1.8).

Microscopic examination of a few of these outcrop samples has been carried out, and the results are reported in Section 8.1.4 below.

Oil stains from both intervals in the Nanok-1 core and from outcrop samples are all severely biodegraded, but biomarkers are still useful. The composition of the oil stains is discussed in detail in Section 8.2 on biological marker analysis.

There can be little doubt that the oil stains in the corehole as well as in the outcrop samples were generated locally from the shale succession intruded by the sill encountered in the Nanok-1 corehole or by similar intrusions, and that the migration distance is small. Although the mudrocks presumably acting as source for the oil stains hardly can be described as source rocks in a traditional sense, the observation that they apparently have been able to generate and expel liquid hydrocarbons is positive for potential exploration in the shelf areas. The mudrocks drilled in the Nanok-1 corehole were deposited in an environment usually not conducive for the development of petroleum source rocks, so it may be reasonably assumed that better source rocks may have been deposited further offshore. Moreover, the increasing trend with depth in Hydrogen Index observed to be curtailed by maturation in the corehole may also suggest the presence of richer deposits deeper in the succession. In addition, a common field observation is that sills preferentially intrude the richer shales in a succession, presumably since rapid generation of hydrocarbons will lead to fracturing, which in turn will alleviate further intrusion, and additional hydrocarbon generation, thus initiating a “knock-on” effect to assist further intrusion and petroleum generation.

8.1.3 Kerogen composition

Four samples from the Nanok-1 corehole were qualitatively examined under the microscope: (1) sample 517004-089 [lab. no. 20823] from 82.07 m, (2) sample 517004-133 [lab. no. 20867] from 129.05 m, (3) sample 517004-146 [lab. no. 20880] from 140.99 m, and (4) sample 517004-156 [lab. no. 20890] from 149.78 m. In addition, three oil-stained outcrop samples of the Østersletten Mb. were examined (see discussion in Section 8.1.2, Fig. 8.1.7 and Table 8.1.3): samples 475091, 475114 and 475135.

The outcrop samples (475091, 475114 and 475135) are all dominated by inertinitic and huminitic organic matter, with few liptinitic components. However, oil bleeding from cracks and cavities in huminitic particles has been observed (Fig. 8.1.9), thus further confirming the presence of oil staining in these samples as discussed above in Section 8.1.2

Sample 517004-089 [20823] is characterised by having a high TOC content (20.14 wt.%). The HI of 117 mg HC/g TOC is relatively low. The kerogen is to a large extent composed of inertinite and both fusinite and semifusinite (fossil charcoal) is recognised (Fig. 8.1.10A, B, C1, D2). Vitrinite and associated framboidal pyrite is likewise present (Fig. 8.1.10B). Fluorescing organic matter appears largely to be absent (Fig. 8.1.10C2), but orange fluorescing bitumen has been observed (Fig. 8.1.10D1). This bitumen may tentatively be interpreted to be responsible for the in this context high S_1 and S_2 yields of sample 517004-089 (Table 8.1.1). However, assuming the elevated PI of the sample is caused by small amounts of migrated oil adsorbed to organic particles, fluorescence may be diffuse and the presence of oil not clearly manifest in fluorescing particles.

The other samples are characterised by low contents of organic matter (TOC ranging from 1.07 to 1.96 wt.%). The organic matter is composed of dispersed minor particles of vitrinite and inertinite, and liptodetrinite (Fig. 8.1.11A, B). In the mudstones close to the intrusion the virtinite is high-reflecting (Fig. 8.1.11C). The groundmass of mineral matter is non-fluorescing to weakly fluorescing suggesting the presence of only a minor amount of fluorescing amorphous kerogen (algal-derived). Sample 517004-156 contains yellowish fluorescing particles that tentatively are identified as alginite (Fig. 8.1.11D).

8.1.4 Vitrinite reflectance

Vitrinite reflectance histograms (Appendix 12.5 part 1) were measured for the eight samples. The samples contained sufficient dispersed vitrinitic material to take from 68 to 101 readings in the samples. The average VR values calculated for each depth from a selected VR population considered to represent the indigenous vitrinite are shown in Table 2. The average values are based on 39 to 95 measurements and are thus considered reliable. Because of the short section drilled by the Nanok-1 well the average VR values does not increase with depth from the top and down to approximately 130 m (Fig. 8.1.12). The average VR values vary from 0.56–0.61%R_o in this interval showing that the mudstones are thermally immature. The VR value at the surface is about 0.60%R_o, which is too high a value for peaty organic matter (VR <0.25%R_o; Cohen *et al.*, 1987). This shows that the succession at the well-site has been exhumed and parts of the strata have been removed by erosion.

Below approximately 130 m the VR values increase fast from 0.72%R_o at 140.99 m to 3.45%R_o at 158.26 m (Fig. 8.1.12). This indicates that the mudstones pass through the oil window (thermally mature to overmature) within only about 20 m.

All available maturity indicators are in perfect agreement both with respect to the overall level of thermal maturity relative to petroleum generation and with respect to the marked change in maturity in the lowermost part of the well. Hence, in addition to vitrinite reflectance (%R_o), Tmax, PI, and biological marker-based maturity indicators all point to the same results (see Section 8.2 on biological markers). The significant increase in thermal maturity below approximately 130–140 m is a local phenomenon caused by the igneous intrusion encountered at ≈160 m.

8.1.5 Source potential recalculation scenarios

In general, the deposits penetrated by the Nanok-1 corehole must be described as non-source rock quality. However, a steady downwards increase in source potential is observed from a depth of approximately 100 metres. This increase is curtailed by maturation and petroleum generation from a depth of approximately 140 metres, and below this depth measured data yield little information on the original petroleum potential. However a reasonable assessment can be obtained by making a few simple assumptions, and using one of several different published schemes for recalculation of original petroleum potential.

Here we use the simple spreadsheet approach described by Peters *et al.* (2005). The procedure will calculate original TOC (TOC^0), original potential ($S1^0+S2^0$), Expelled HC ($S1_{Ex}$), Expulsion efficiency (%), and fractional conversion (%) for a series of assumed original HI scenarios (for instance from HI^0=200 to HI^0=900 at increments of 100), based on measured data (Fig. 8.1.13). Based on knowledge of the sample maturity and kerogen composition, a "reasonable" HI scenario can be picked and the calculated values read off from the table. For details of the procedure, including equations used for the calculations, see Peters *et al.* (2005).

Four samples collected successively closer to the intrusion, thus showing increasing levels of thermal maturity were chosen. A common field observation is that intrusions preferentially follow organic rich strata, probably due to fracturing by petroleum components generated by heating from the intrusion itself. Accordingly, it can reasonably be assumed that the downwards increasing trend in petroleum potential observed originally extended at least until the contact with the intrusion, i.e. approximately 160 metres, and roughly similar thickness of potential source rock may be present beneath the intrusion. Thus for the sake of simplicity, we assume a source thickness of 50 metres, i.e. roughly 25 m above and below the intrusion.

Moreover, using the rule of thumb that the thermal impact of a sill extends for a distance approximately twice the thickness of the intrusion above it and one thickness below it, the sill is estimated at a thickness of 8–20 metres, which is in agreement with the size of intrusions exposed in the area.

Table 8.1.3 shows recalculation of original petroleum potential based on the the four selected samples, adopting a conservative approach. Based on this, the average Hydrogen Index was originally between 200 and 300, corresponding to values of TOC between 1.5 wt-% and 2.1 wt-%, and original petroleum potentials between 4 kg HC/ton and 6 kg HC/ton, corresponding to approximately 625,000 ton HC/km^2 (4,000,000 bbl/km^2) of source rock area, assuming a thickness of 50 metres. This corresponds to a "Source Potential Index" ("SPI", Demaison and Huizinga, 1991, 1994) of ≈0.6.

Table 8.1.4 shows recalculation of original petroleum potential based on the the four selected samples, adopting an optimistic approach. Based on this, the average Hydrogen Index was originally between 200 and 400, corresponding to values of TOC between 1.7 wt-% and 2.3 wt-%, and original petroleum potentials between 4 kg HC/ton and 9 kg

HC/ton, corresponding to approximately 750,000 ton HC/km^2 (5,000,000 bbl/km^2) of source rock area, assuming a thickness of 50 metres. This corresponds to a "Source Potential Index" ("SPI", Demaison and Huizinga, 1991, 1994) of ≈0.8. Plots of TOC versus S2 (= total potential S1+S2 for immature samples) for the two scenarios are shown in Figure 8.1.14.

The validity of the assumed Hydrogen Index scenarios and recalculated vales of TOC and petroleum potential may be supported by carrying out the assessment using a different method, for instance that of Dahl *et al.* (2004). The organic matter in the shales is a mixture of terrestrial and marine kerogen. The HI values are generally low, but the generative kerogen may be masked by the presence of non-generative kerogen, and the "reactive Hydrogen Index" is higher if non-reactive Carbon is excluded from the calculation. Thus, recalculation of the HI of the reactive kerogen in the interval ~130–142 m by excluding the 'dead carbon' using the method of Dahl *et al.* (2004) yields an $HI_{reactive}$ of 261. This figure agrees excellently with the assessment obtained using the method of Peters *et al.* (2005).

From the above it is evident that the shales drilled by the Nanok-1 corehole never were rich petroleum source rocks, irrespective of which of the two scenarios is favoured. However, bearing in mind that the deposits were formed in a sedimentary environment where such rich source rock are not very likely to form, the existence of petroleum potential, be it even marginal, is promising for the possible existence of Cretaceous petroleum source rocks in settings more conducive for the formation of such deposits further offshore.

8.1.6 Summary and conclusions

- The Nanok-1 corewell penetrated nearly 168 metres of Cretaceous sandstones, heteroliths and mudstones plus a few metres of dolerite intrusion at the very base of the drillhole.
- Apart from an inertinite-rich sample at 82.07 m the mudstones have a relatively low content of organic matter. Bitumen (early generated petroleum) has been recorded in the sample.
- Kerogen in the mudstones mainly consists of dispersed minor particles of vitrinite and inertinite, and liptodetrinite. The mineral-rich groundmass is non-fluorescing to weakly fluorescing. Alginite may be present in the sample collected at 149.78 m depth.

- The mudstones in general show no petroleum source potential, but downwards from a depth of app. 100 m, a steady increase in petroleum potential is observed.
- From a depth of app. 140 m, the trend is reversed due to thermal maturation caused by the intrusion encountered at app. 160 m.
- The succession down to a depth of approximately 140 m is thermally immature with VR values around 0.60%R_o.
- A rapid increase in thermal maturity is recognised below 140 m towards the intrusion encountered at 160 m. Within these about 20 m the mudstones are locally matured by the intrusion-induced increase in heat flow, and they pass through the oil window as demonstrated by several independent maturity parameters.
- Hence, the over a thickness of less than 15 m the deposits realize their total petroleum potential and thermal destruction takes over closer to the intrusion.
- Oil presumably generated from the sediments are preserved as marked oil staining in a sandstone/heterolith interval from app. 95–100 m and as less pronounced staining near the top of the Østersletten Mb. sandstones at approximately 46 m.
- The original petroleum potential of the presumed source mudstones cannot be evaluated but circumstantial evidence allows a rough estimate to be made leading to two scenarios, a conservative and an optimistic.
- The conservative scenario suggest a source thickness of 50 m with a petroleum potential of 4–6 kg HC/ton, i.e. app. 625,000 ton HC/km^2 or app. 4,000,000 bbl/km^2
- The optimistic scenario suggest a source thickness of 50 m with a petroleum potential of 4–9 kg HC/ton, i.e. app. 750,000 ton HC/km^2 or app. 5,000,000 bbl/km^2
- Based on the evolution in thermal maturity observed, the thickness of the intrusion is estimated to 8–20 m, which seems to be in accordance with field observations of nearby intrusions.

8.1.7 References

Bordenave, M. L., Espitalié, J., Leplat, P., Oudin, J. L. & Vandenbrouke, M. 1993: Chapter II-2: Screening techniques for source rock evaluation. In: Bordenave, M.L. (ed.), Applied petroleum geochemistry. Paris, Éditions Technip, 219–278.

Cohen, A. D., Raymond, R. Jr., Archuleta, L. M. & Mann, D. A. 1987: Preliminary study of the reflectance of huminite macerals in recent surface peat. Organic Geochemistry, **11**, 429–430.

Demaison, G. & Huizinga, B. J. 1991: Genetic classification of petroleum systems. AAPG Bulletin, **75**, 1626–1643.

Demaison, G. & Huizinga, B. J. 1994: Genetic classification of petroleum systems using three factors: charge, migration and entrapment. AAPG Memoir 60, 73–89.

Espitalié, J., Deroo, G. & Marquis, F. 1985 : La pyrolyse Rock-Eval et ses applications. Part II. Revue de l'Institut Francais du Pétrole, **40**, 755–784.

Espitalié, J., Deroo, G. & Marquis, F. 1986 : La pyrolyse Rock-Eval et ses applications. Part III. Revue de l'Institut Francais du Pétrole, **41**, 73–89.

Dahl, B., Bojesen-Koefoed, J.A., Holm, A., Justwan, H., Rasmussen, E. & Thomsen, E. 2004 : A new approach to interpreting Rock-Eval S_2 and TOC data for kerogen quality asessment. Organic Geochemistry, **35**, 1461–1477.

Peters, K. E. & Cassa, M. R. 1994: Applied source rock geochemisry. In: Magoon, L. B. & Dow, W. G. (eds.), The petroleum system – from source to trap. American Association of Petroleum Geologists Memoir 60, 93–120.

Peters, K. E., Walthers, C. C & Moldowan, J. M. 2005: The Biomarker Guide, 2nd edition, Cambridge University Press, 1155 pp.

Taylor, G. H., Teichmüller, M., Davis, A., Diessel, C. F. K., Littke, R. & Robert, P. 1998: Organic Petrology. Berlin, Stuttgart, Gebrüder Borntraeger, 704 pp.

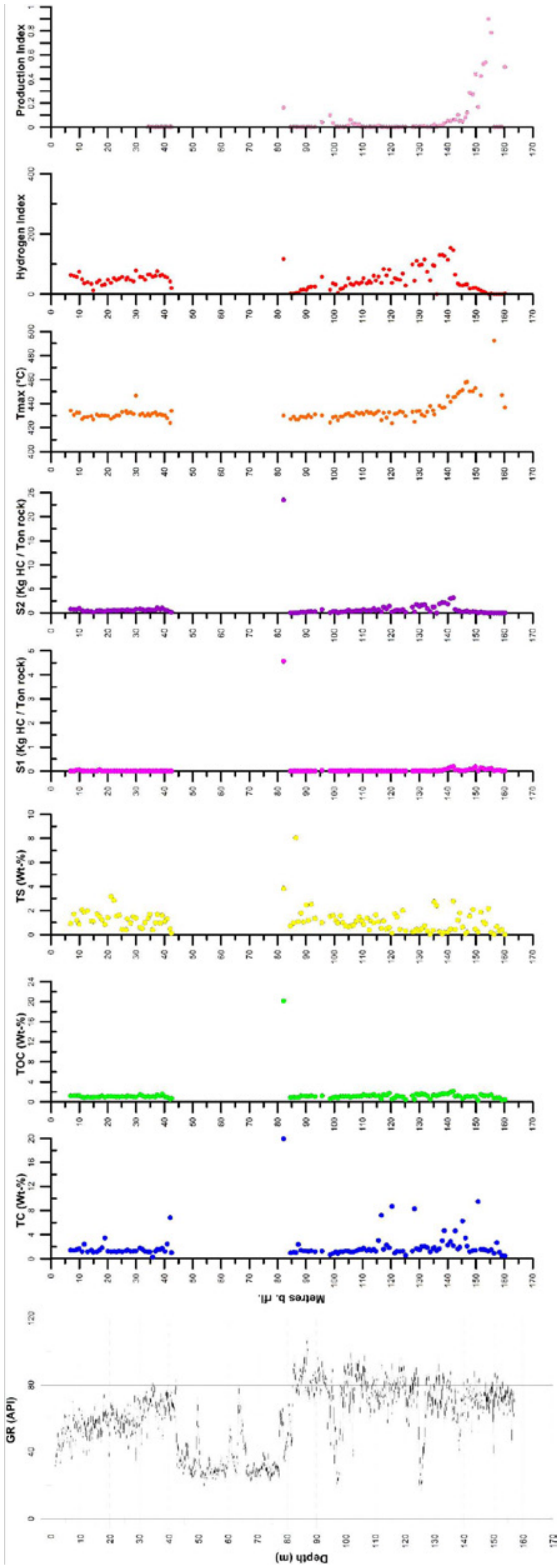

Figure 8.1.1 Organic geochemical screening data plottet versus depth. GR-log shown on the left.

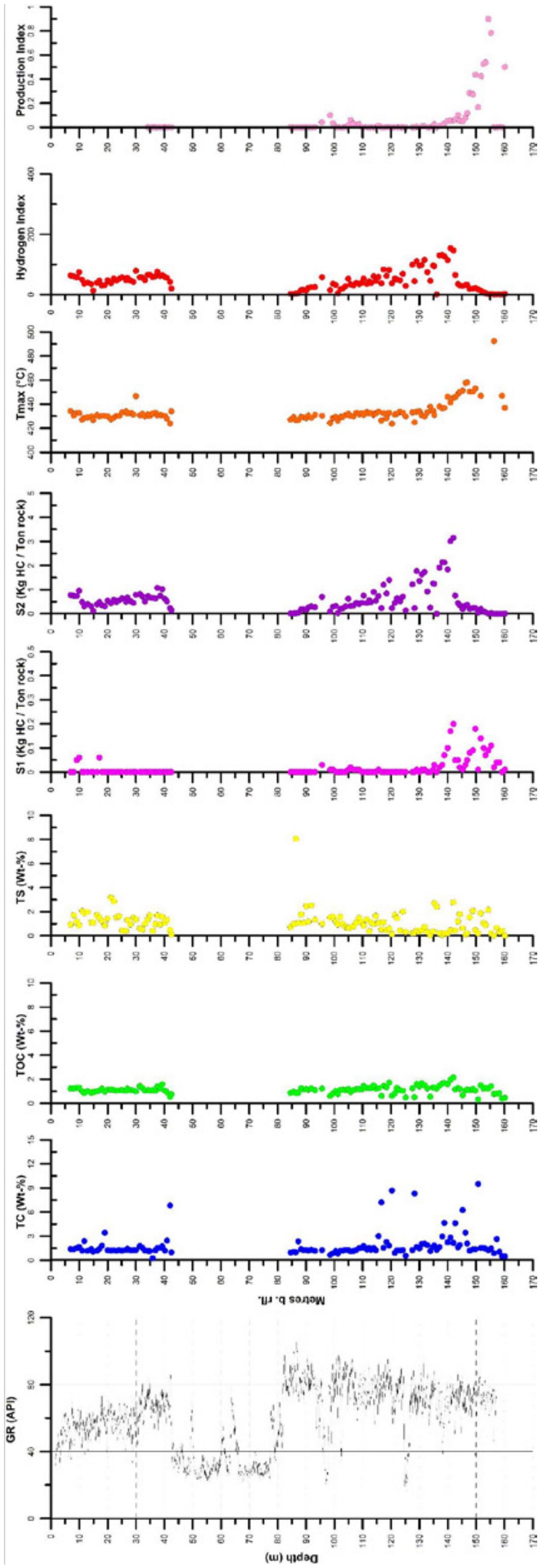

Figure 8.1.2. Organic geochemical screening data, similar to Fig. 1, but omitting high-TOC sample (82.07m) in order to enhance trends in measured data.

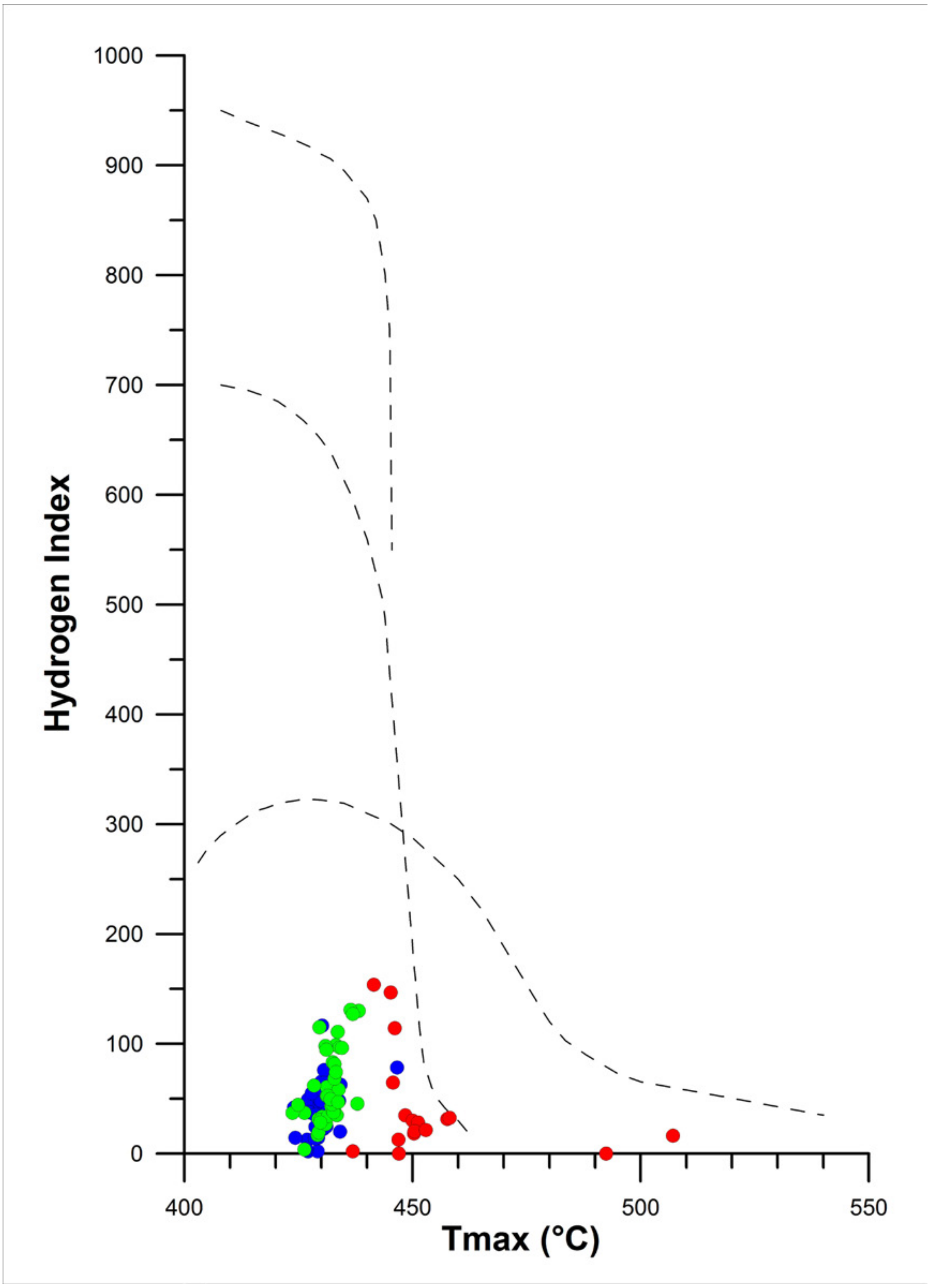

Figure 8.1.3. Tmax *versus* Hydrogen Index for samples from the Nanok-1 corehole. Blue symbols: 0-100 m, non-SR section; green symbols: 100-140 m, interval characterised by steady increase in Hydrogen Index with depth; red symbols: 140 m-TD, increase in Hydrogen index curtailed by increasing maturation with depth.

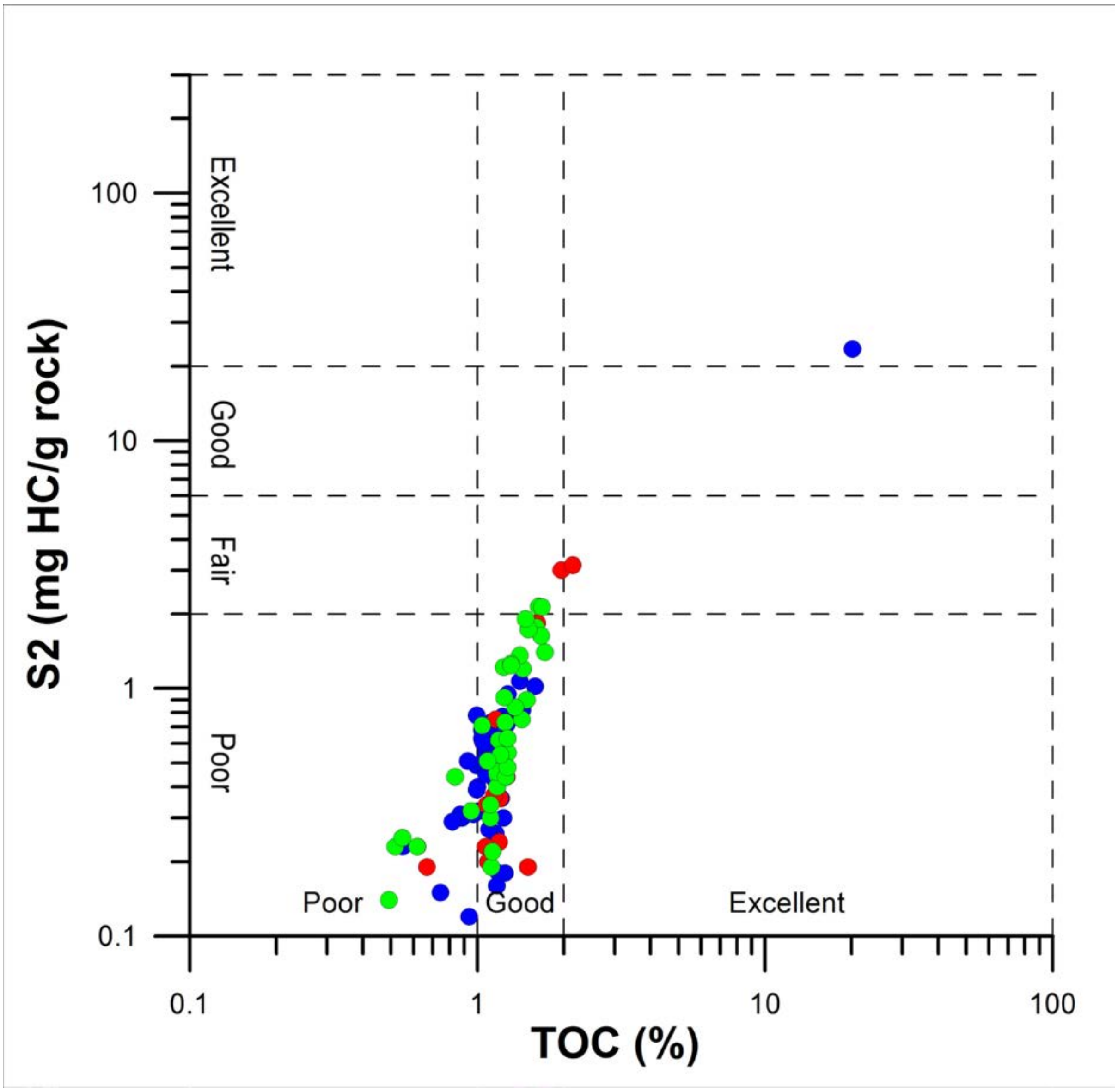

Figure 8.1.4. TOC versus S2 for samples from the Nanok-1 corehole. Blue symbols: 0-100 m, non-SR section; green symbols: 100-140 m, interval characterised by steady increase in Hydrogen Index with depth; red symbols: 140 m-TD, increase in Hydrogen index curtailed by increasing maturation with depth.

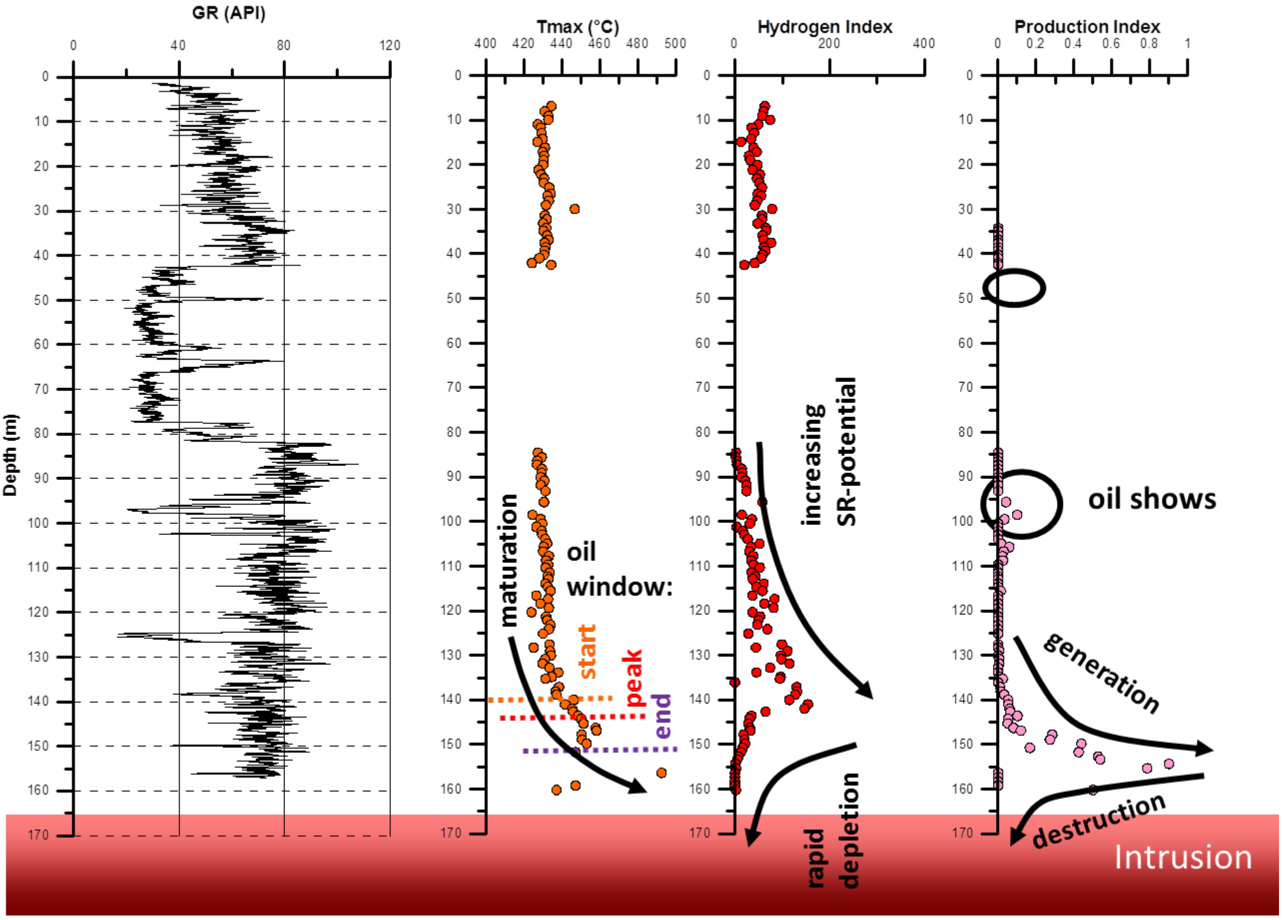

Figure 8.1.5. Interpretation of screening data in relation to maturation by the intrusion encountered at the base of the borehole.

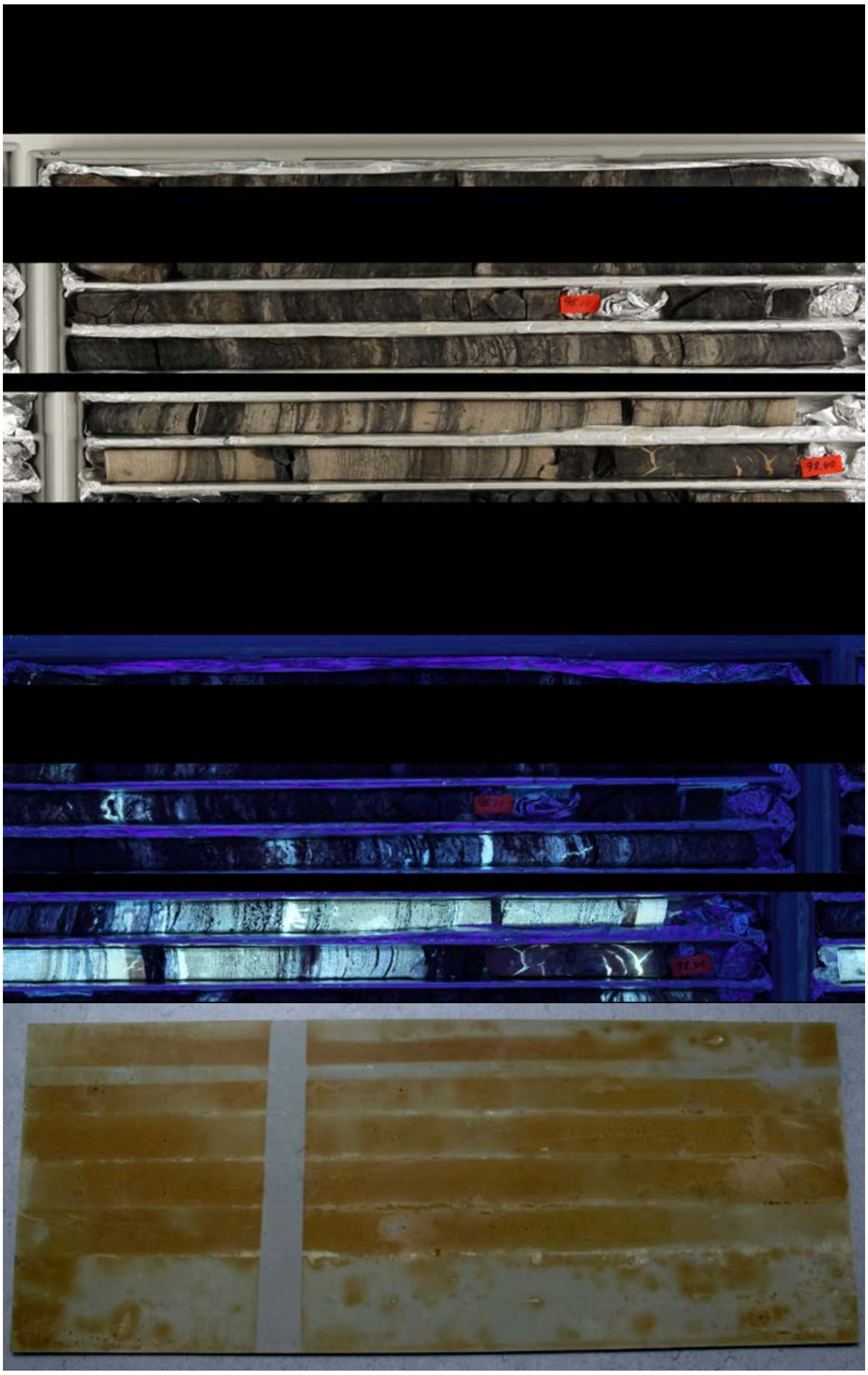

Figure 8.1.6. Corebox 18, comprising the oil-stained sandstone interval at ≈94-98 m. The uppermost photo shows the core in normal white light, the middle photo shows the same field in fluorescence inducing blue light. Note strong fluorescence in the sandstone. The lowermost photo shows the inner side of the corebox lid. Note brown petroleum-precipitates formed by material evaporated from the core during transportation from the drillsite.

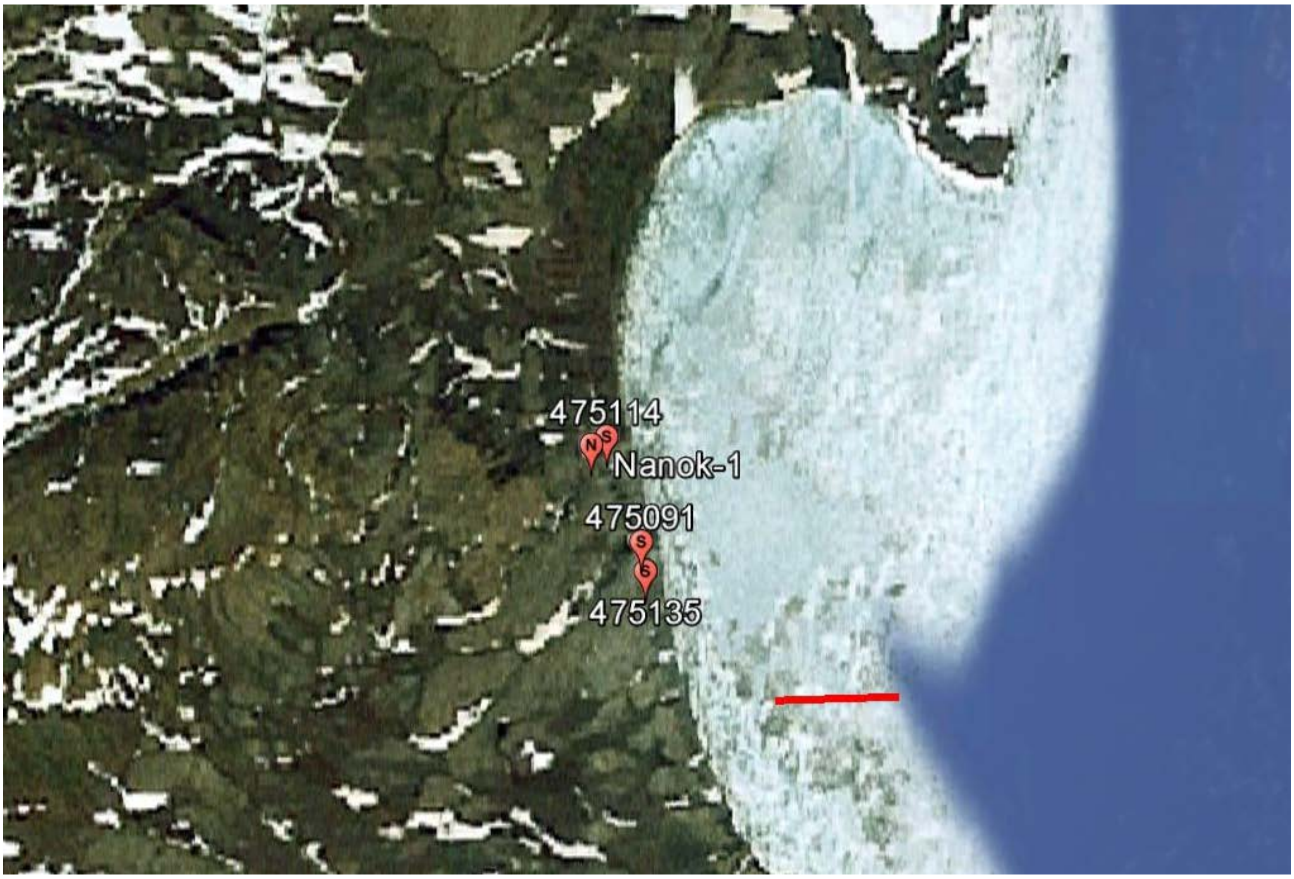

Figure 8.1.7 Satelite image (Google Earth) of eastern Hold with Hope with positions of the Nanok-1 corehole and oil-stained outcrop samples indicated. Red bar for scale: 1000 m.

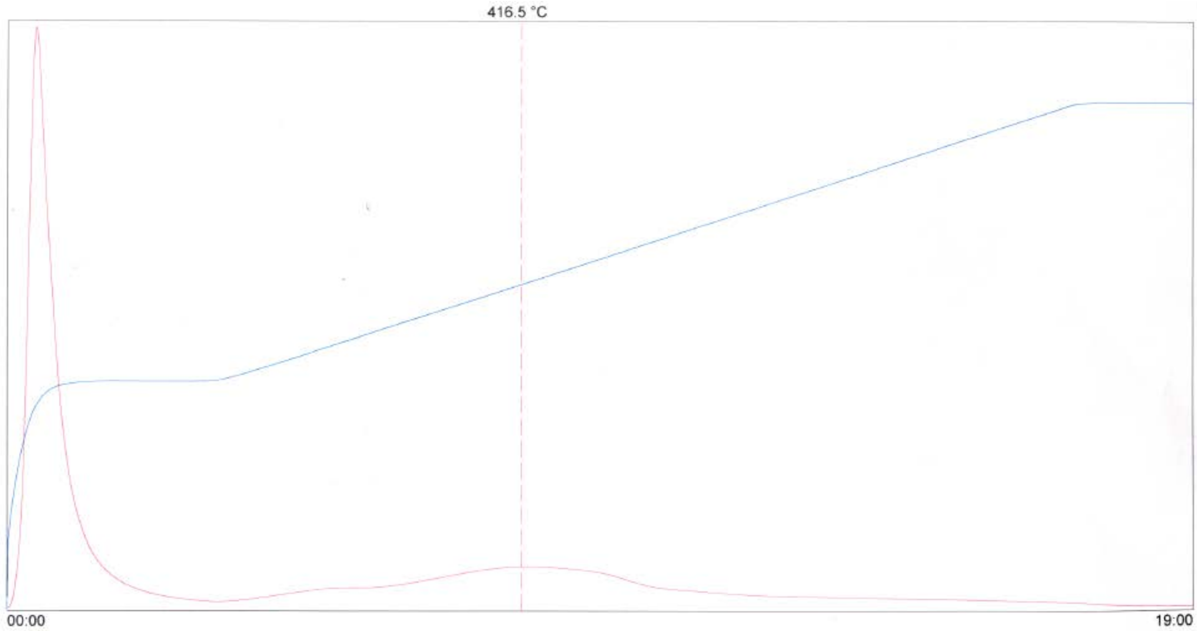

Figure 8.1.8. Pyrogram from Rock-Eval type pyrolysis of oil-stained outcrop sample collected approximately 1 kilometre from the Nanok-1 drillsite. Note large S1-peak and irregular S2-peak, partially merged with the S1-peak (red curve). Tmax temperature indicated is “true-Tmax”, whereas “standard Tmax” used for maturity assessment is significantly lower, 378 °C

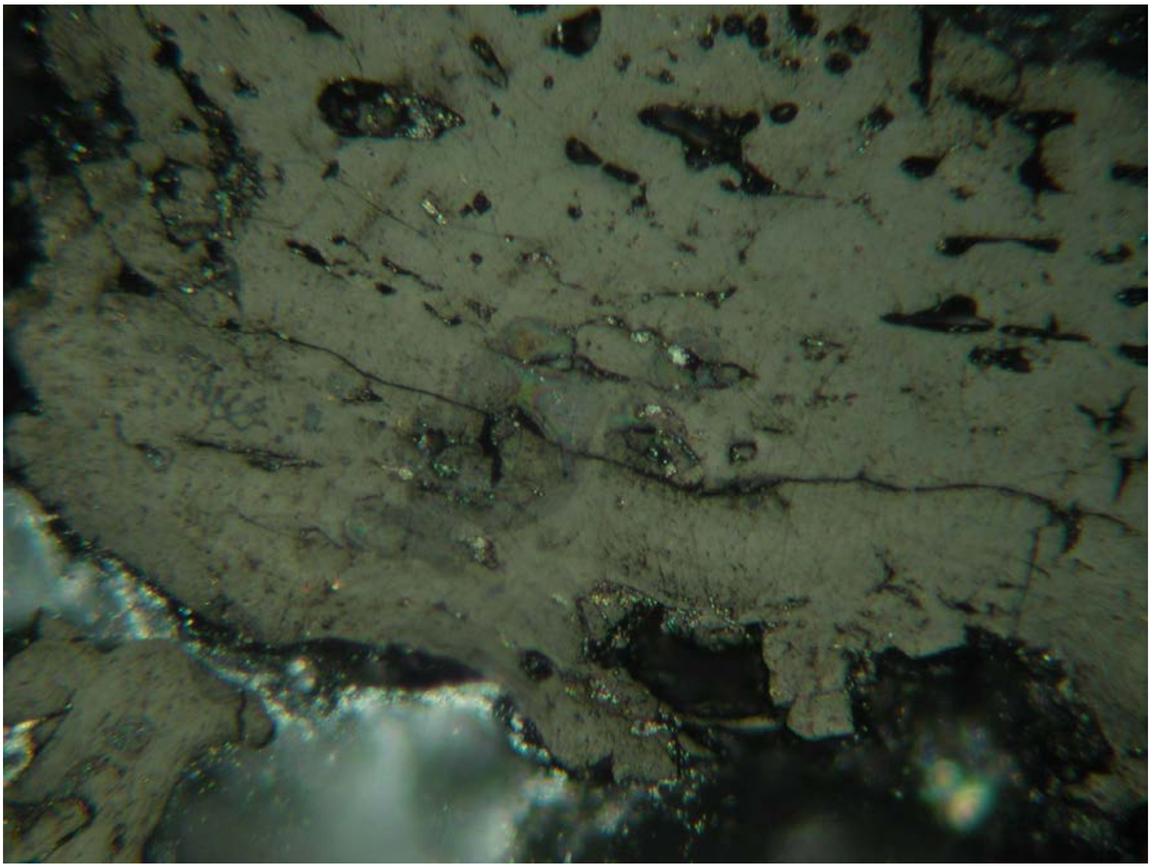

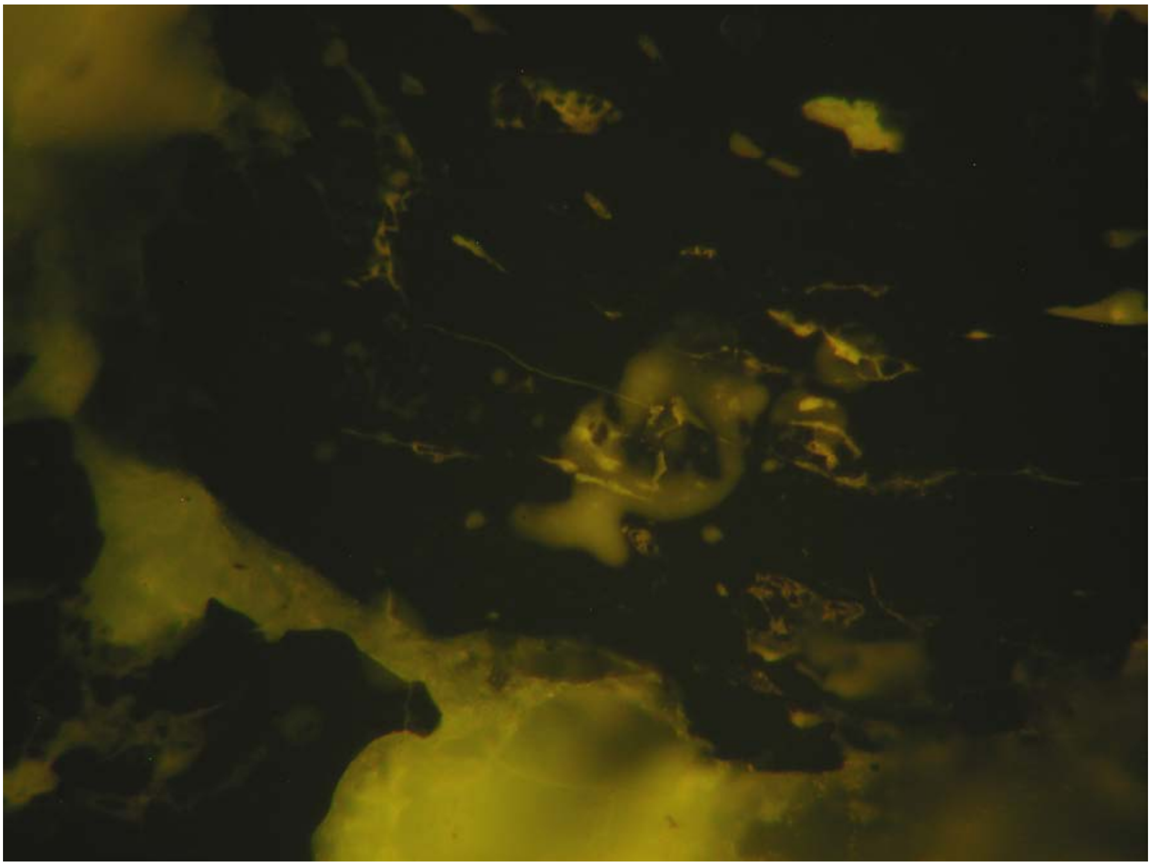

Figure 8.1.9 (previous page). Photomicrograph, sample 475135, collected approximately 1 kilometre from the Nanok-1 drillsite. Upper photo, central part: oil bleeding from cracks and cavities in a huminite particle. Note “Newton-ring” effects causing rainbow-like colouration. Lower part: same field as above, using fluorescence-inducing blue light. Note fluorescing “cloud”, following the outline of the “Newton-rings”, around oil-bleeding factures/cavities.

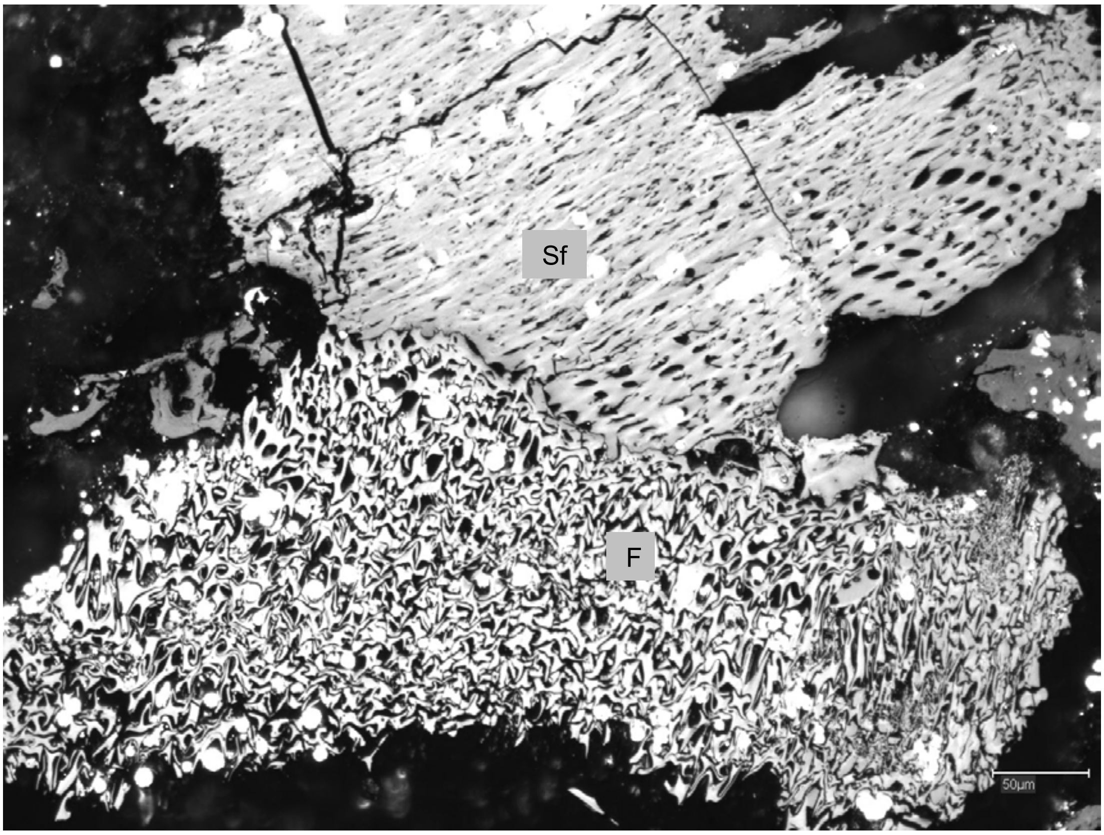

A

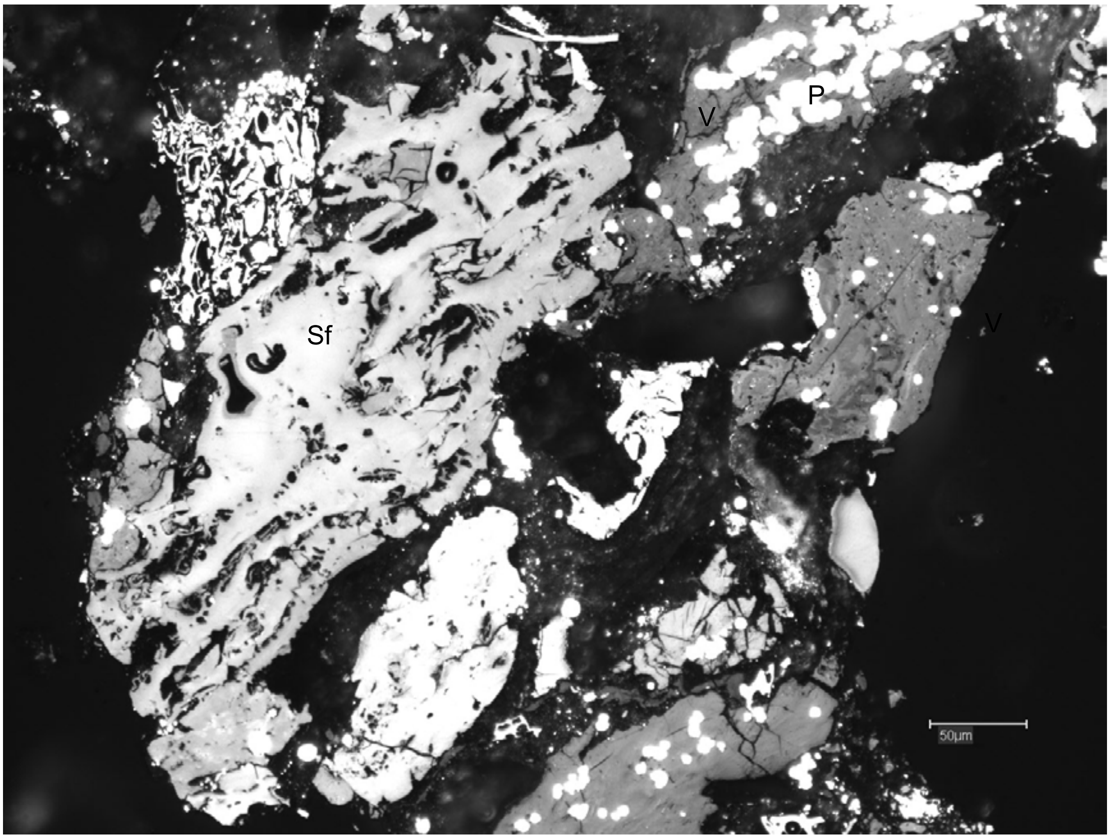

B

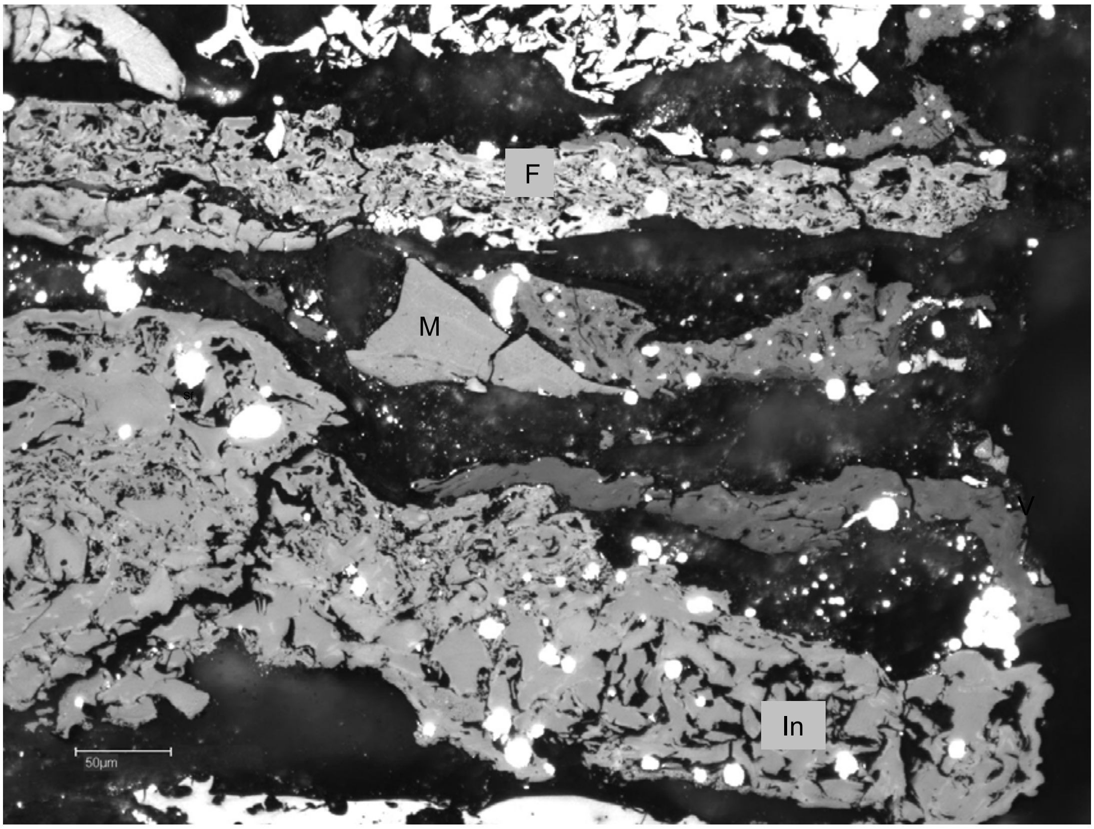

C1

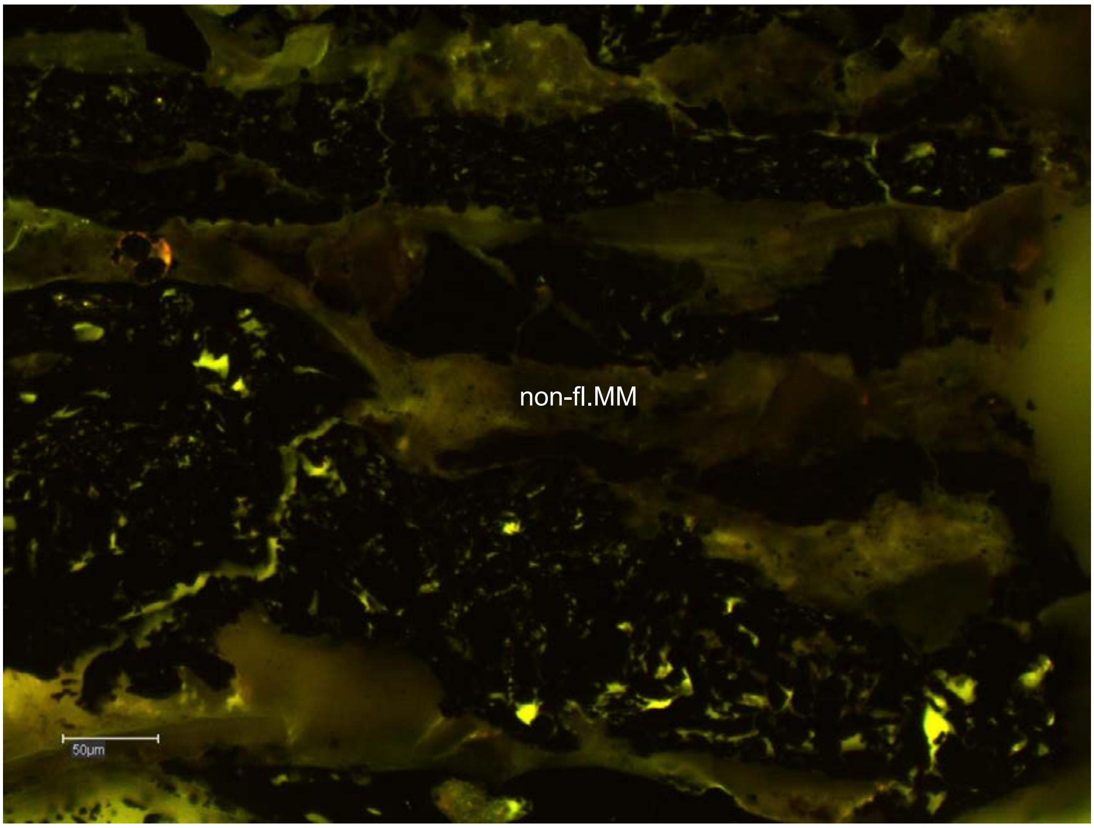

C2

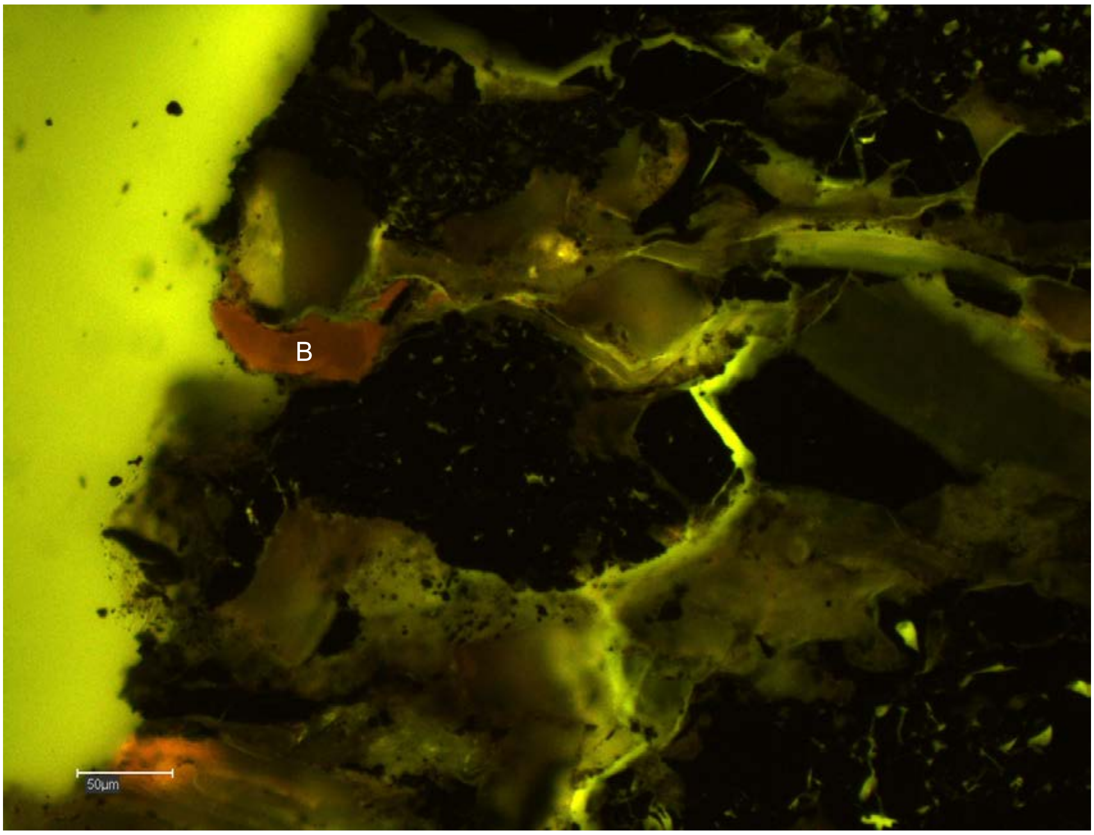

D1

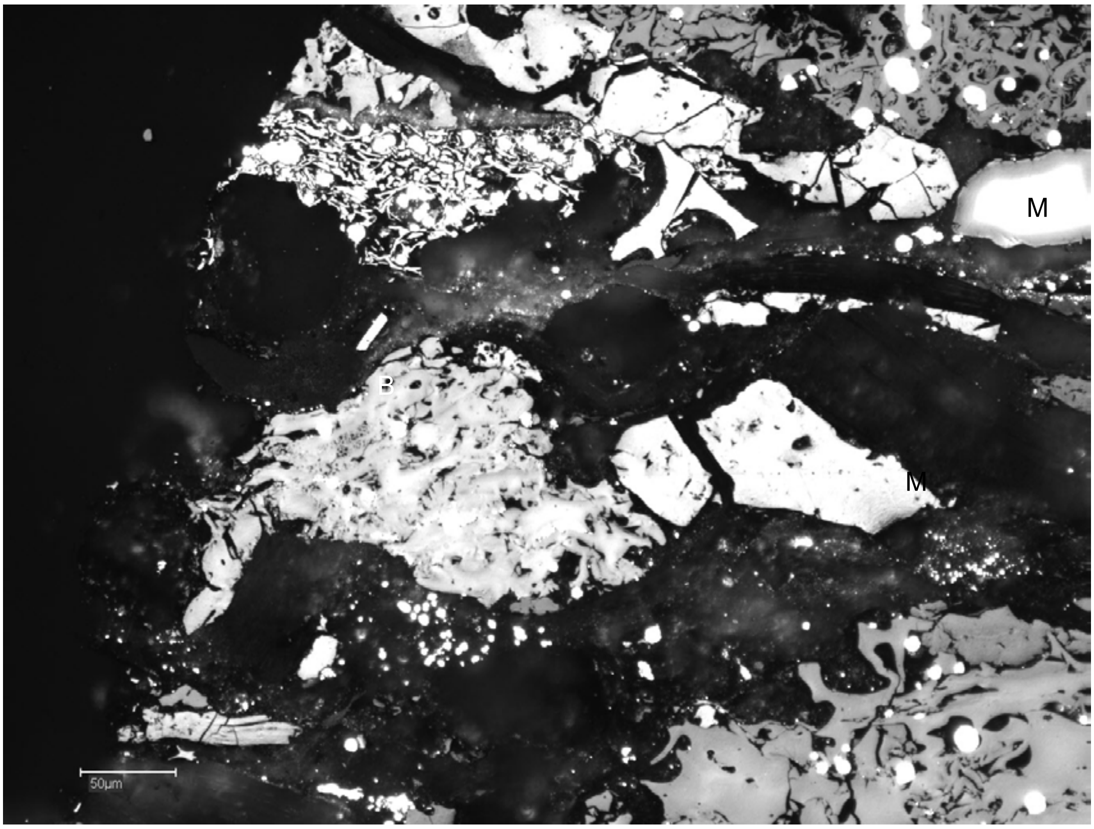

D2

Figure 8.1.10 (previous pages). Photomicrographs (incident light, oil immersion) of the kerogen in the organic-rich mudstone at 82.07 m (sample 517004-089/lab. no 20823). A, B, C1 and D2 in white reflected light, C2 and D1 in fluorescing-inducing blue light. **A**. Fusinite (F) and semifusinite (Sf). **B**. Framboidal pyrite (P) in vitrinite (V). **C1 and C2**. Abundant inertinite including fusinite (F), macrinite (M) and inertodetrinite (In) in a non-fluorescing mineral matter groundmass (non-fl. MM). **D1 and D2**. Bitumen (B) particle and abundant inertinite , including large macrinite (M) particles.

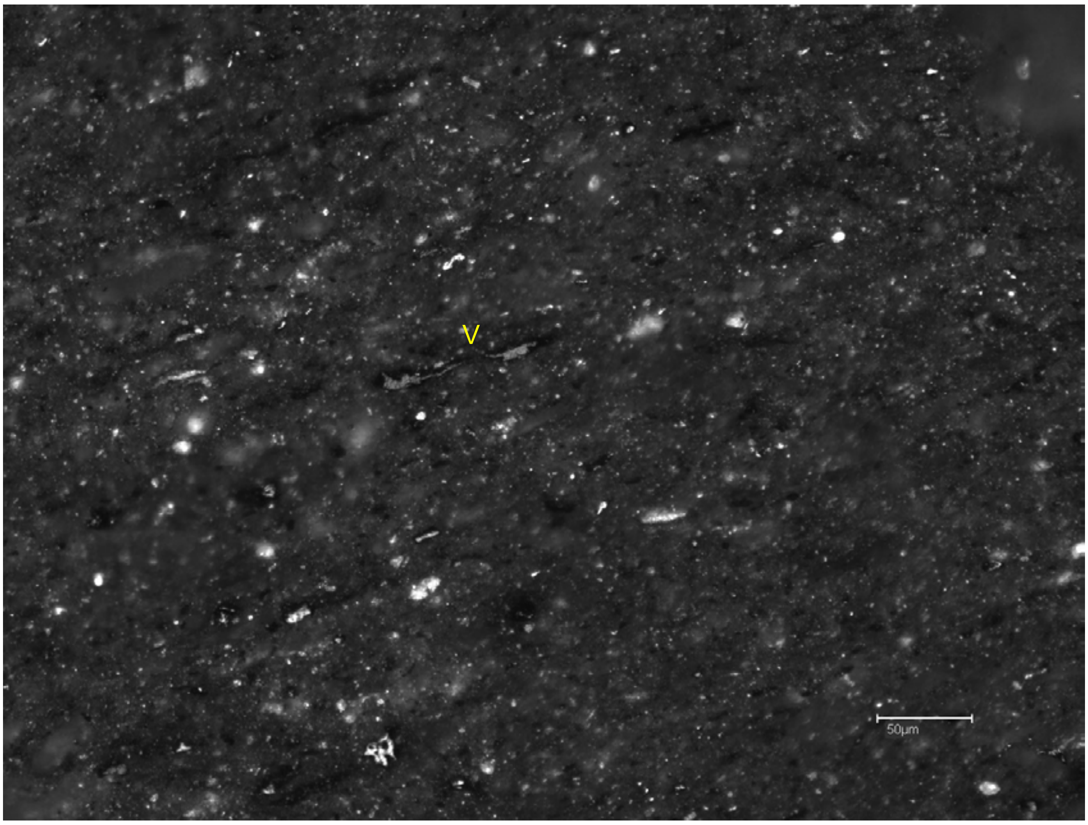

A1

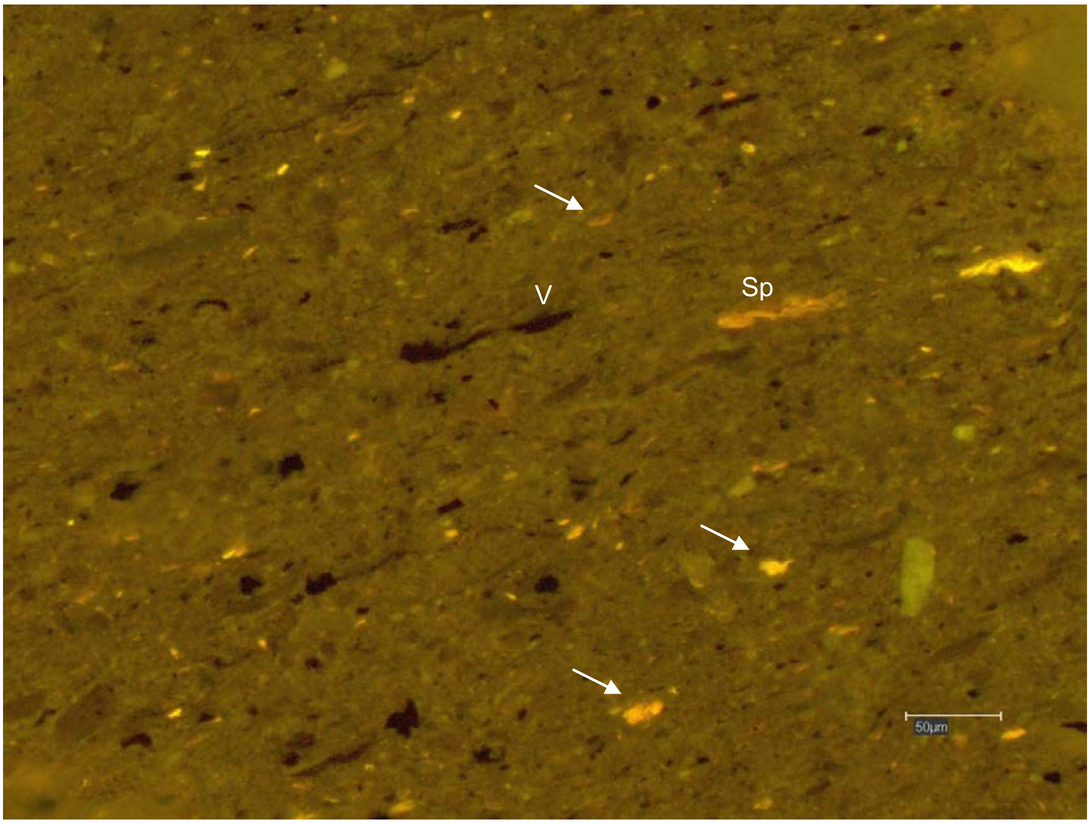

A2

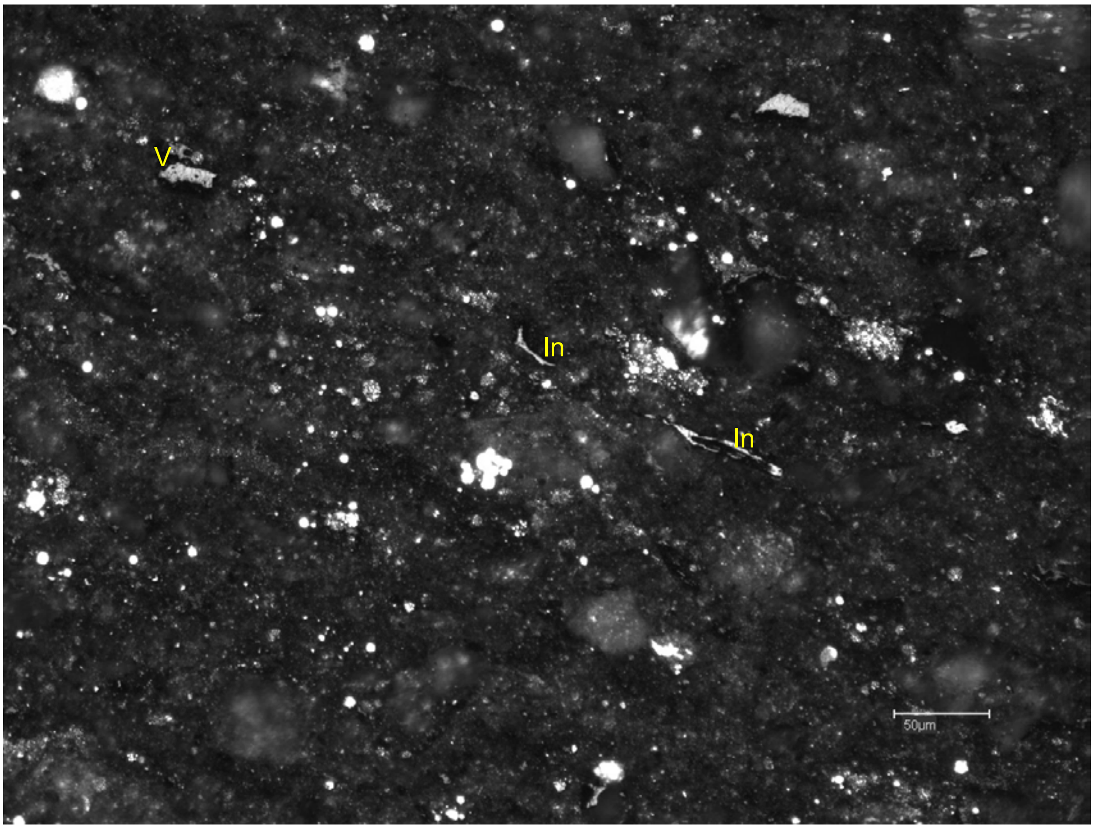

B1

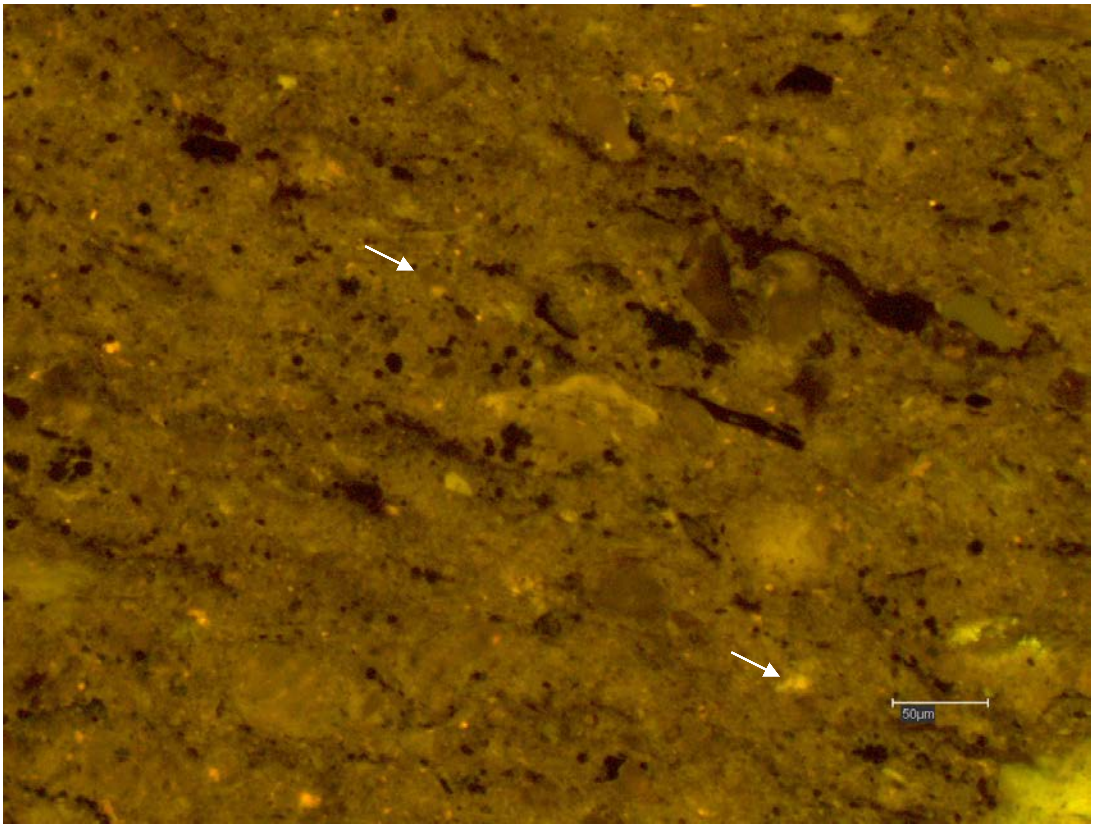

B2

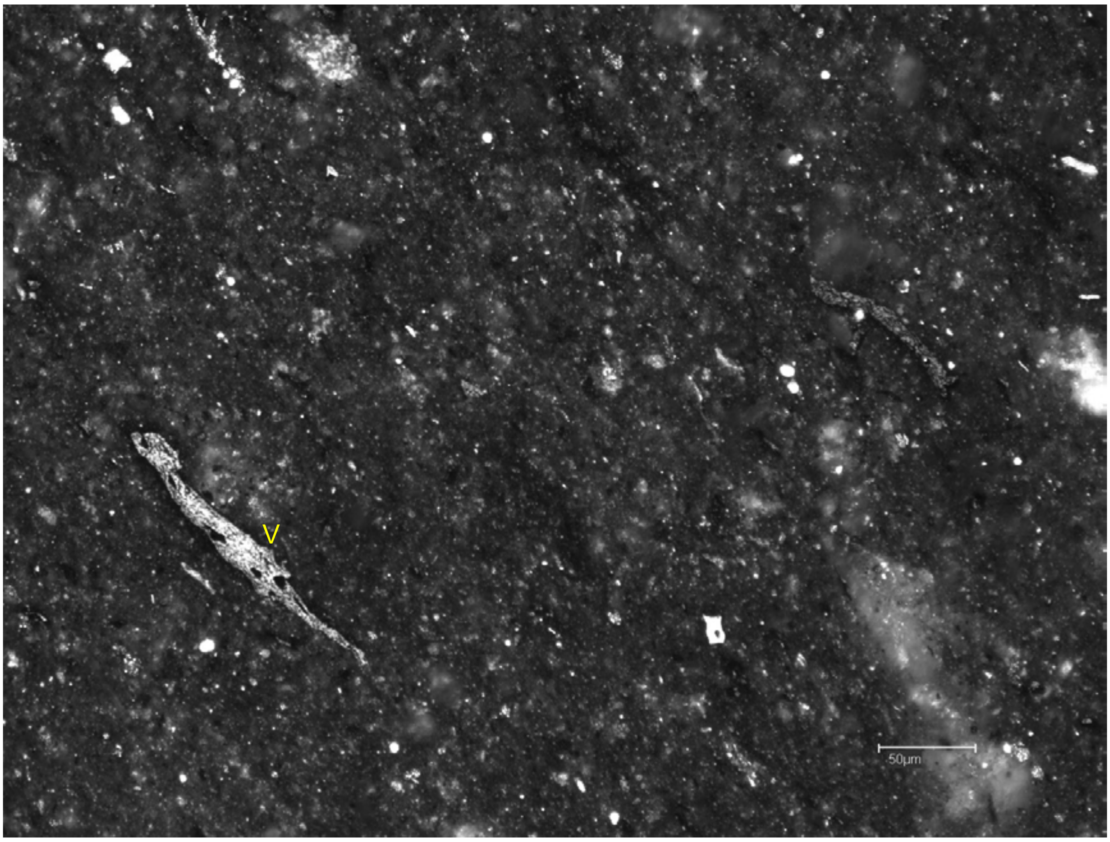

C

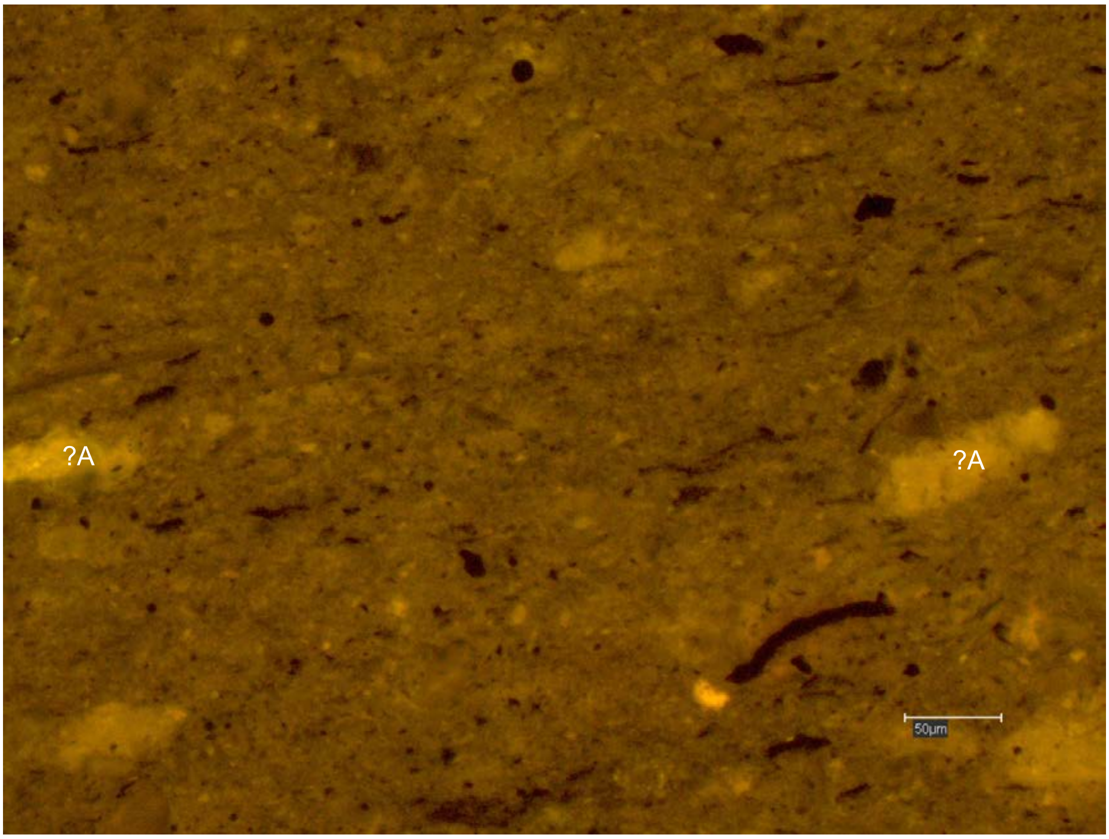

D

Figure 8.1.11 (previous pages). Photomicrographs (incident light, oil immersion) of the kerogen in the mudstones. A1, B1 and B2 in white reflected light, A2, B2 and C2 in fluorescing-inducing blue light. **A1 and A2**. Scattered vitrinite (V) particles and liptodetrinite (arrows) in a non-fluorescing to weakly fluorescing mineral matter groundmass (sample 517004-133/lab. no 20867). **B1 and B2**. Scattered vitrinite (V) and inertodetrinite (In) particles and liptodetrinite (arrows) in a non-fluorescing to weakly fluorescing mineral matter groundmass (sample 517004-146/lab. no 20880). **C1 and C2**. High-reflecting vitrinite (V) and probably alginite (?A) in a non-fluorescing to weakly fluorescing mineral matter groundmass (sample 517004-156/lab. no 20890).

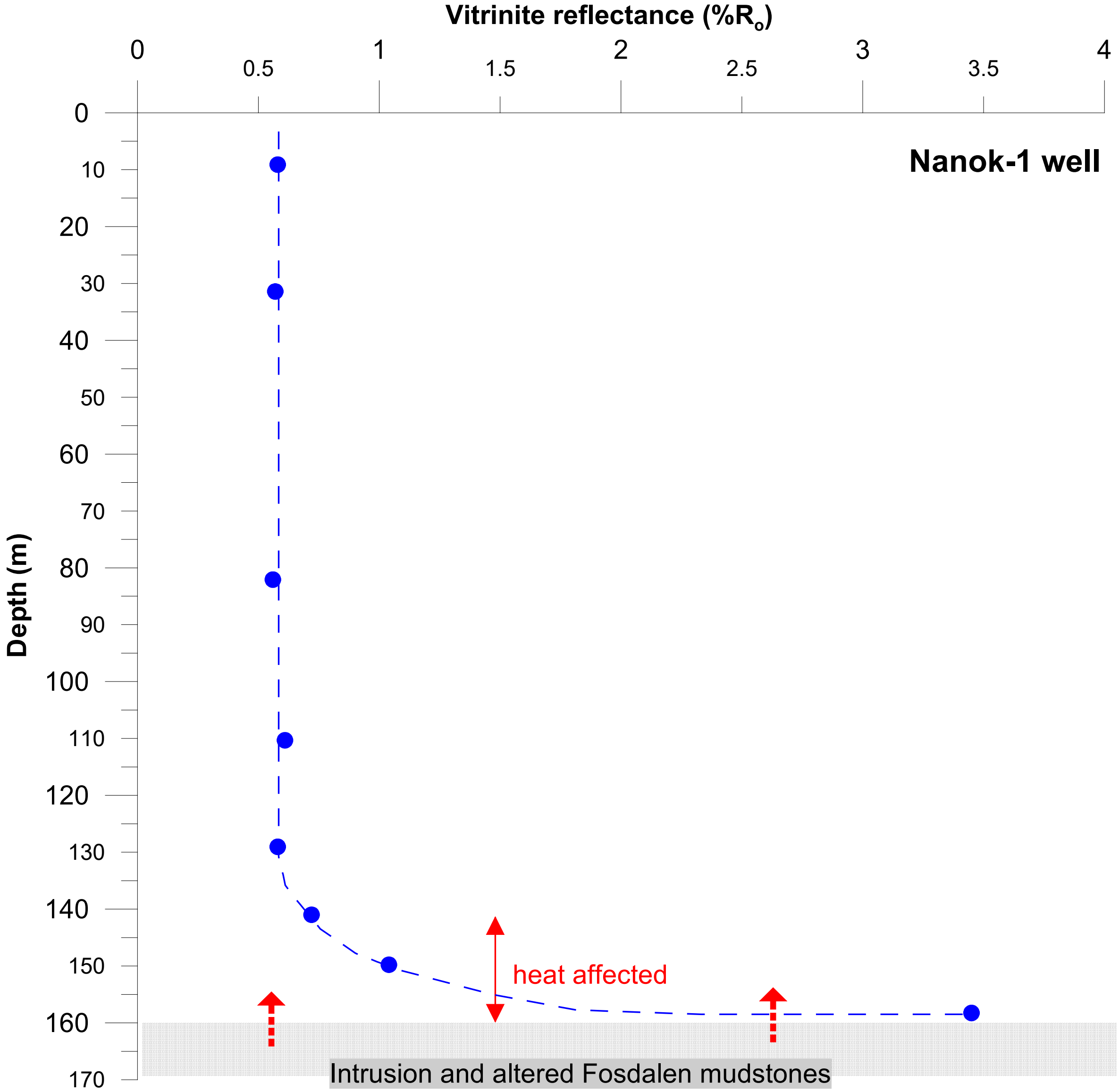

Figure 8.1.12. VR gradient of the Nanok-1 corewell.

Reconstruction of petroleum generative potential

(Procedure from Peters et al. 2005)

Input parameters	
TOC*	1,96
S1*	0,17
S2*	3,01
HI*	154
PI*	0,05

Assumed		**Calculated results**				
HIº	PIº	Fractional conversion	TOCº (wt-%)	S1º+S2º (mg/g)	$S1_{expelled}$ (mg/g)	Expulsion Efficiency
900	0,02	0,95	6,46	58	55	1,00
800	0,02	0,93	4,94	40	37	1,00
700	0,02	0,89	4,00	28	25	0,99
600	0,02	0,85	3,36	20	17	0,99
500	0,02	0,80	2,94	15	12	0,99
400	0,02	0,71	2,54	10	7	0,98
300	0,02	0,56	2,27	7	4	0,96
200	0,02	0,26	2,05	4	1	0,86

Fractional conversion = $(G_0\text{-}G_x)/G_0$, G= generation capacity, initial (G_0) and at time = x (G_x)

$S1_{expelled}$ = expelled HC calculated on the basis of loss in TOC

Expulsion efficiency = $Petroleum_{expelled}$ / $Petroleum_{generated}$

Figure 8.1.13. Example of recalculation of original petroleum potential using the method of Peters *et al.* (2005). Blue field: measured data. Green field: Original HI and PI scenarios. Yellow field. Calculated parameters based on measured data and the various original HI and Pi scenarios. In the present case, the sample is of low thermal maturity, and not very rich, and the HI^{o}=200 scenario seems reasonable. Note that Fractional Conversion is always greater than PI, since PI, being an actual measurement, does not include losses.

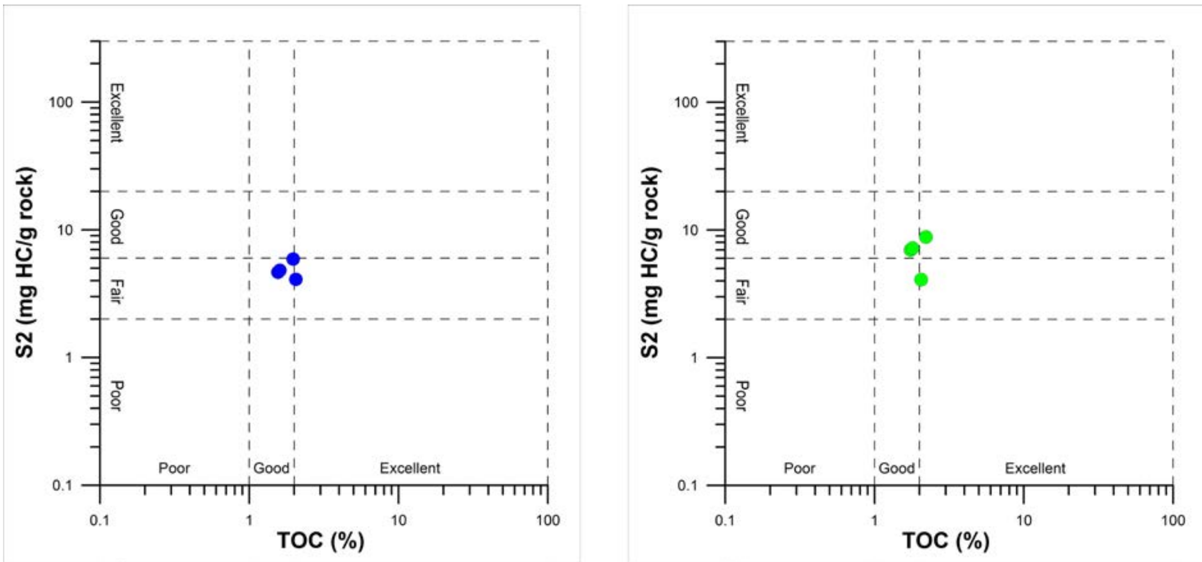

Figure 8.1.14. TOC versus S2 (= total potential, S1+S2, for immature samples) for the four samples recalculated to original potential. Left: blue symbols “conservative scenario”; right: green symbols “optimistic scenario”. See text for discussion.

Sample #	Mean Depth m	TOC (%)	TC (%)	TS (%)	Tmax (°C)	S1 (mg/g)	S2 (mg/g)	HI	PI	PC	Lab. #
517004-051	6,93	1,22	1,40	0,94	434	0,00	0,77	63	0,00	0,06	20785
517004-052	8,08	1,23	1,37	1,71	431	0,00	0,74	60	0,00	0,06	20786
517004-053	9,11	1,27	1,50	1,18	433	0,05	0,73	57	0,06	0,06	20787
517004-054	9,96	1,28	1,67	0,87	433	0,06	0,95	74	0,06	0,08	20788
517004-055	11,00	0,99	1,20	2,06	427	0,00	0,49	49	0,00	0,04	20789
517004-056	11,73	0,87	2,38	1,87	429	0,00	0,31	36	0,00	0,03	20790
517004-057	12,93	1,00	1,16	1,97	429	0,00	0,40	40	0,00	0,03	20791
517004-058	14,27	0,88	1,40	1,12	430	0,00	0,30	34	0,00	0,02	20792
517004-059	14,91	0,94	1,09	1,10	427	0,00	0,12	13	0,00	0,01	20793
517004-060	16,23	1,00	1,16	1,71	431	0,00	0,39	39	0,00	0,03	20794
517004-061	17,16	1,07	1,41	1,51	430	0,06	0,49	46	0,11	0,05	20795
517004-062	18,01	1,21	1,80	1,21	430	0,00	0,36	30	0,00	0,03	20796
517004-063	19,02	0,97	3,43	0,85	430	0,00	0,31	32	0,00	0,03	20797
517004-064	20,06	1,13	1,24	1,42	430	0,00	0,54	48	0,00	0,04	20798
517004-065	21,21	1,15	1,20	3,17	427	0,00	0,43	38	0,00	0,04	20799
517004-066	22,23	1,10	1,22	2,86	429	0,00	0,58	53	0,00	0,05	20800
517004-067	23,14	1,05	1,16	1,54	430	0,00	0,49	46	0,00	0,04	20801
517004-068	24,08	1,07	1,28	1,62	430	0,00	0,55	51	0,00	0,05	20802
517004-069	25,16	1,10	1,17	0,43	433	0,00	0,63	57	0,00	0,05	20803
517004-070	26,53	1,04	1,31	0,40	434	0,00	0,50	48	0,00	0,04	20804
517004-071	26,98	1,21	1,43	1,31	432	0,00	0,67	55	0,00	0,06	20805
517004-072	28,08	1,11	1,24	0,96	433	0,00	0,52	47	0,00	0,04	20806
517004-073	29,11	1,07	1,26	1,49	431	0,00	0,45	42	0,00	0,04	20807
517004-074	29,98	1,00	1,27	1,36	447	0,00	0,78	78	0,00	0,06	20808
517004-075	31,42	1,43	1,78	0,59	431	0,00	0,82	57	0,00	0,07	20809
517004-076	32,27	1,27	1,58	0,51	432	0,00	0,72	57	0,00	0,06	20810
517004-077	33,20	1,06	1,22	1,00	430	0,00	0,51	48	0,00	0,04	20811
517004-078	34,22	1,12	1,16	1,36	432	0,00	0,73	65	0,00	0,06	20812
517004-079	34,86	1,04	1,13	1,69	430	0,00	0,68	66	0,00	0,06	20813
517004-080	35,89	1,12	0,26	0,41	432	0,00	0,65	58	0,00	0,05	20814
517004-081	36,87	1,04	1,25	0,97	433	0,00	0,63	61	0,00	0,05	20815
517004-082	37,53	1,40	1,53	1,69	431	0,00	1,07	76	0,00	0,09	20816
517004-083	38,59	1,21	1,56	0,96	431	0,00	0,74	61	0,00	0,06	20817
517004-084	39,28	1,58	1,75	1,59	431	0,00	1,02	64	0,00	0,08	20818
517004-085	40,24	1,04	1,20	1,10	430	0,00	0,61	58	0,00	0,05	20819
517004-086	40,98	0,93	2,45	1,32	428	0,00	0,51	55	0,00	0,04	20820
517004-087	42,08	0,55	6,82	0,46	424	0,00	0,23	42	0,00	0,02	20821
517004-088	42,51	0,74	0,99	0,12	434	0,00	0,15	20	0,00	0,01	20822
517004-089	82,07	20,14	19,95	3,83	430	4,57	23,48	117	0,16	2,33	20823

Table 8.1.1.

Sample #	Mean Depth m	TOC (%)	TC (%)	TS (%)	Tmax (°C)	S1 (mg/g)	S2 (mg/g)	HI	PI	PC	Lab. #
517004-090	84,54	0,88	0,97	0,72	427	0,00	0,02	2	0,00	0,00	20824
517004-091	85,62	0,96	1,04	0,98	429	0,00	0,02	2	0,00	0,00	20825
517004-092	86,43	0,89	1,01	8,05	427	0,00	0,03	3	0,00	0,00	20826
517004-093	87,28	0,88	2,36	1,07	427	0,00	0,04	5	0,00	0,00	20827
517004-094	88,25	1,24	1,39	1,78	429	0,00	0,18	14	0,00	0,01	20828
517004-095	89,13	1,19	1,28	1,04	429	0,00	0,18	15	0,00	0,01	20829
517004-096	90,10	1,17	1,28	2,47	429	0,00	0,16	14	0,00	0,01	20830
517004-097	90,87	1,16	1,21	1,18	431	0,00	0,26	22	0,00	0,02	20831
517004-098	91,85	1,23	1,30	2,52	429	0,00	0,30	24	0,00	0,02	20832
517004-099	93,18	1,10	1,17	1,34	431	0,00	0,27	25	0,00	0,02	20833
517004-100	95,65	1,21	1,26	1,00	430	0,03	0,70	58	0,04	0,06	20834
517004-101	98,50	0,62	0,66	1,51	424	0,01	0,09	14	0,10	0,01	20835
517004-102	99,50	0,82	0,86	1,59	429	0,01	0,29	35	0,03	0,02	20836
517004-103	100,50	1,01	1,13	1,19	429	0,00	0,32	32	0,00	0,03	20837
517004-104	101,24	0,78	0,83	0,96	426	0,00	0,03	4	0,00	0,00	20838
517004-105	102,15	1,12	1,17	1,57	429	0,00	0,19	17	0,00	0,02	20839
517004-106	102,97	1,13	1,18	0,99	429	0,00	0,22	19	0,00	0,02	20840
517004-107	103,97	1,11	1,29	0,74	431	0,00	0,30	27	0,00	0,02	20841
517004-108	104,97	1,19	1,26	0,64	432	0,01	0,62	52	0,02	0,05	20842
517004-109	105,73	0,95	1,12	0,70	430	0,02	0,32	34	0,06	0,03	20843
517004-110	106,73	1,11	1,14	0,78	430	0,01	0,34	31	0,03	0,03	20844
517004-111	107,76	1,17	1,30	1,10	433	0,01	0,45	38	0,02	0,04	20845
517004-112	108,73	1,17	1,50	1,48	432	0,01	0,40	34	0,02	0,03	20846
517004-113	109,70	1,17	1,54	1,14	433	0,00	0,46	39	0,00	0,04	20847
517004-114	110,32	1,43	1,76	0,85	431	0,00	0,75	53	0,00	0,06	20848
517004-115	111,48	1,26	1,34	1,37	433	0,00	0,44	35	0,00	0,04	20849
517004-116	112,31	1,28	1,54	0,38	432	0,00	0,55	43	0,00	0,05	20850
517004-117	112,93	1,27	1,31	1,13	433	0,00	0,48	38	0,00	0,04	20851
517004-118	113,89	1,49	1,54	0,98	431	0,00	0,90	61	0,00	0,07	20852
517004-119	114,64	1,20	1,25	1,64	432	0,00	0,54	45	0,00	0,04	20853
517004-120	115,57	1,25	3,01	1,07	434	0,01	0,73	58	0,01	0,06	20854
517004-121	116,60	0,62	7,21	0,53	426	0,00	0,23	37	0,00	0,02	20855
517004-122	117,39	1,44	1,56	1,13	433	0,00	1,20	83	0,00	0,10	20856
517004-123	118,41	1,35	2,27	0,46	428	0,00	0,84	62	0,00	0,07	20857
517004-124	119,36	1,72	1,82	0,59	433	0,00	1,40	82	0,00	0,12	20858
517004-125	120,35	0,62	8,68	0,13	424	0,00	0,23	37	0,00	0,02	20859
517004-126	121,33	0,84	0,91	1,72	431	0,00	0,44	53	0,00	0,04	20860
517004-127	122,13	1,27	1,23	1,47	432	0,00	0,63	50	0,00	0,05	20861
517004-128	123,17	1,08	1,21	0,43	434	0,00	0,51	47	0,00	0,04	20862

Table 8.1.1., continued

Sample #	Mean Depth m	TOC (%)	TC (%)	TS (%)	Tmax (°C)	S1 (mg/g)	S2 (mg/g)	HI	PI	PC	Lab. #
517004-129	124,16	1,04	1,27	2,01	433	0,00	0,71	68	0,00	0,06	20863
517004-130	125,16	0,49	0,56	0,31	430	0,00	0,14	28	0,00	0,01	20864
517004-131	127,55	1,23	1,27	0,23	433	0,00	1,22	99	0,00	0,10	20865
517004-132	128,27	0,52	8,30	0,25	425	0,00	0,23	44	0,00	0,02	20866
517004-133	129,05	1,60	1,67	0,44	434	0,01	1,77	111	0,01	0,15	20867
517004-134	130,04	1,41	1,48	0,33	434	0,00	1,36	97	0,00	0,11	20868
517004-135	130,85	1,66	2,03	0,47	431	0,01	1,63	98	0,01	0,14	20869
517004-136	131,85	1,50	2,05	0,73	430	0,01	1,73	115	0,01	0,14	20870
517004-137	132,82	1,24	1,87	0,30	433	0,00	0,92	74	0,00	0,08	20871
517004-138	133,83	0,55	1,14	0,04	438	0,00	0,25	46	0,00	0,02	20872
517004-139	134,83	1,31	1,69	0,36	435	0,01	1,26	96	0,01	0,11	20873
517004-140	135,26	1,31	1,84	2,73	431	0,03	1,24	95	0,02	0,11	20874
517004-141	136,09	1,23	1,31	2,41	602	0,00	0,00	0	0,00	0,00	20875
517004-142	137,11	1,47	1,65	0,24	438	0,02	1,91	130	0,01	0,16	20876
517004-143	138,11	1,63	2,96	0,07	436	0,03	2,14	131	0,01	0,18	20877
517004-144	138,80	1,68	4,65	0,20	437	0,07	2,13	127	0,03	0,18	20878
517004-145	139,99	1,61	2,24	0,20	446	0,10	1,84	114	0,05	0,16	20879
517004-146	140,99	1,96	2,82	0,47	442	0,17	3,01	154	0,05	0,26	20880
517004-147	141,99	2,15	2,15	2,77	445	0,20	3,15	147	0,06	0,28	20881
517004-148	142,63	1,16	4,63	0,43	446	0,05	0,75	65	0,06	0,07	20882
517004-149	143,59	1,26	1,62	1,19	448	0,05	0,44	35	0,10	0,04	20883
517004-150	144,25	1,20	1,92	1,79	450	0,02	0,36	30	0,05	0,03	20884
517004-151	145,27	0,67	6,25	0,63	451	0,01	0,19	28	0,05	0,02	20885
517004-152	146,27	1,08	3,43	0,09	458	0,03	0,34	32	0,08	0,03	20886
517004-153	146,88	1,14	2,08	0,19	458	0,05	0,37	32	0,12	0,03	20887
517004-154	147,76	1,09	1,20	1,54	450	0,08	0,20	18	0,29	0,02	20888
517004-155	148,90	1,19	1,37	2,09	450	0,09	0,24	20	0,27	0,03	20889
517004-156	149,78	1,07	1,37	0,47	453	0,18	0,23	22	0,44	0,03	20890
517004-157	150,74	0,30	9,50	0,20	507	0,01	0,05	16	0,17	0,00	20891
517004-158	151,70	1,50	1,54	1,87	447	0,14	0,19	13	0,42	0,03	20892
517004-159	152,68	1,21	1,52	1,05	560	0,10	0,09	7	0,53	0,02	20893
517004-160	153,33	1,28	1,44	0,90	573	0,07	0,06	5	0,54	0,01	20894
517004-161	154,33	1,21	1,26	2,15	596	0,09	0,01	1	0,90	0,01	20895
517004-162	155,33	1,42	1,47	0,18	599	0,11	0,03	2	0,79	0,01	20896
517004-163	156,35	0,78	0,88	0,02	492	0,02	0,00	0	0,00	0,00	20897
517004-164	157,33	0,81	2,65	0,66	300	0,04	0,00	0	0,00	0,00	20898
517004-165	158,26	0,84	1,06	0,31	338	0,04	0,00	0	0,00	0,00	20899
517004-166	159,16	0,39	0,53	0,41	447	0,00	0,00	0	0,00	0,00	20900
517004-167	160,18	0,46	0,48	0,02	437	0,01	0,01	2	0,50	0,00	20901

Table 8.1.1. Organic geochemical screening data

Lab. no.	Sample	Depth (m) (m)	Material	VR %Ro	Std.	N
20787	517004-053	9,11	core	0,58	0,088	79
20809	517004-075	31,42	core	0,57	0,073	70
20823	517004-089	82,07	core	0,56	0,054	92
20848	517004-114	110,32	core	0,61	0,065	85
20867	517004-133	129,05	core	0,58	0,065	76
20880	517004-146	140,99	core	0,72	0,090	94
20890	517004-156	149,78	core	1,04	0,081	39
20899	517004-165	158,26	core	3,45	0,187	95

Table 8.1.2. Average VR (random) values derived from selected VR populations

Sample	TOC (%)	TC (%)	TS (%)	Tmax (°C)	S1 (mg/g)	S2 (mg/g)	HI	PI	North	West	Dist. from Nanok-1 (m)
475091	12,83	12,24	0,81	428	2,94	7,25	57	0,29	73,6995	20,5326	880
475096	10,54	10,50	0,62	433	2,42	4,25	40	0,36	73,6995	20,5326	880
475097	27,23	26,32	1,06	429	7,77	20,87	77	0,27	73,6995	20,5326	880
475114	2,14	2,64	0,40	435	0,98	0,83	39	0,54	73,7071	20,5415	130
475135	5,07	5,15	0,50	378	2,35	1,8	36	0,57	73,6974	20,5315	1120

Table 8.1.3. Outcrop samples of the Østersletten Mb. (Fosdalen Fm.) showing increased PI indicating oil staining, collected in the vicinity of the Nanok-1 wellsite.

Sample	Depth (m)	TOC*	S1*	S2*	HI*	PI*	HI°	PI°	Fractional conversion	TOC° (wt-%)	S1°+S2° (mg/g)	$S1_{expelled}$ (mg/g)	Expulsion Efficiency
517004-146	140,99	1,96	0,17	3,01	154	0,05	200	0,02	0,26	2,05	4,10	1,08	0,86
517004-155	148,9	1,19	0,09	0,24	20	0,27	300	0,02	0,95	1,55	4,66	4,43	0,98
517004-158	151,7	1,5	0,14	0,19	13	0,42	300	0,02	0,97	1,97	5,90	5,72	0,98
517004-161	154,33	1,21	0,09	0,01	1	0,9	300	0,02	1,00	1,61	4,82	4,81	0,98

Table 8.1.4 Recalculation of original petroleum potential for four samples collected successively closer to the intrusion. Conservative scenario. See text for discussion.

Sample	Depth (m)	TOC*	S1*	S2*	HI*	PI*	HI°	PI°	Fractional conversion	TOC° (wt-%)	S1°+S2° (mg/g)	$S1_{expelled}$ (mg/g)	Expulsion Efficiency
517004-146	140,99	1,96	0,17	3,01	154	0,05	200	0,02	0,26	2,05	4,10	1,08	0,86
517004-155	148,9	1,19	0,09	0,24	20	0,27	400	0,02	0,97	1,74	6,98	6,74	0,99
517004-158	151,7	1,5	0,14	0,19	13	0,42	400	0,02	0,98	2,21	8,83	8,64	0,98
517004-161	154,33	1,21	0,09	0,01	1	0,9	400	0,02	1,00	1,80	7,21	7,21	0,99

Table 8.1.5. Recalculation of original petroleum potential for four samples collected successively closer to the intrusion. Optimistic scenario. See text for discussion.

8.2 Biomarker analysis

– Extraction, MPLC-separation, GC, GC-MS and GC-MS-MS

This section reports the results of biomarker analysis of 13 source rock extracts/oil stains from the Nanok-1 well and three oil seeps found nearby (Fig. 8.1.7). The samples were subjected to solvent extraction, MPLC-separation, gas chromatography (GC) and gas chromatography-mass spectrometry (GC-MS and GC-MS-MS) of the saturated fraction. A few aromatic fractions were analysed in full scan mode.

- Shale extract, **9.11** m, immature, undegraded
- Oil shows, **45.77**m, **46.51** m, severely biodegraded oil
- ”Tarmat” **82.07** m, high TOC, moderately degraded oil + ?
- Oil shows, **94.04**m, **96.55**m, **97.53**m, **97.99**m, **98.44**m, **99.27**m, moderately degraded oil
- Shale extract, **129.05** m, immature, undegraded
- Shale extract, **140.99** m, ”early oil window”
- Shale extract, **149.78** m, ”oil window”
- Bitumen near Nanok-1, **475091**, **475114**, **475135**, moderately degraded oil

8.2.1 Methods

Extraction and separation

Crushed shale samples were extracted with methanol/dichloromethane 7:93 vol/vol using a Soxtec equipment (extraction yield: Table 8.2.1). The asphaltenes were removed from the extracts by precipitation in *n*-pentane. Medium pressure liquid chromatography (MPLC) fractionation of the maltenes yielded a saturated hydrocarbon, an aromatic hydrocarbon and a polar fraction (composition: Table 8.2.1). The saturated fraction was analysed by GC, GC-MS and GC-MS-MS. Selected aromatic fractions were analysed using GC-MS.

Gas chromatography (GC) of saturated hydrocarbons

Gas chromatography was performed using a Shimadzu GC-2010 instrument equipped with a splitless injector and a ZB-1 capillary column (25 m x 0.25 mm i.d., film thickness 0.10

μm). The temperature program was 5°C/min from 80 to 300°C, followed by 15 min at 300°C. The concentration for GC analyses was 5 mg / ml isooctane. Pristane/phytane ratios and relative concentrations of *n*-alkanes and isoprenoids (if any, Table 8.2.1) were obtained from peak areas in the gas chromatograms.

Gas chromatography-mass spectrometry (GC-MS and GC-MS-MS) of saturated hydrocarbons

Gas chromatography-mass spectrometry was carried out using an Agilent 6890N gas chromatograph connected to a Waters (Micromass) Quattro Micro GC tandem quadrupole mass spectrometer. A Phenomenex ZB-5 column (30 m x 0.25 mm i.d., film thickness 0.10 μm) was used. The injection temperature was 70°C (2 min hold). The temperature program was 30°C/min from 70 to 100°C and 4°C/min from 100 to 308°C followed by 8 min at 308°C. Argon was used as collision gas for MS-MS experiments. The saturated hydrocarbons were analysed by GC-MS in SIM-mode and by GC-MS-MS using relevant transitions for C_{26}-C_{30} steranes and C_{27}-C_{35} hopanes. The concentration for GC-MS and GC-MS-MS was around 5 mg / ml isooctane. The samples were analysed over a period of 8 months, so the retention times of some compounds may vary slightly from one chromatogram to another.
All sat. samples were analysed using three "standard" methods.

GC-MS, SIM

71.10	*n*-alkanes
177.16	25-norhopanes
191.18	hopanes
205.20	methylhopanes
217.20	steranes
218.20	steranes
231.21	methylsteranes
253.20	monoaromatic steranes (should be absent in sat. fraction)
355.35	25- and 28-norhopanes
369.35	hopanes

GC-MS-MS, Steranes, all samples.

358.36 → 217.20 C_{26} steranes

372.38 → 217.20 C_{27} steranes

386.39 → 217.20 C_{28} steranes

400.41 → 217.20 C_{29} steranes

414.42 → 217.20 C_{30} steranes

Additional transitions in method for samples 2011024-20902 to 2011024-20909

386.39 → 231.21 C_{28} methylsteranes

400.41 → 231.21 C_{29} methylsteranes

414.42 → 231.21 C_{30} methylsteranes

412.41 → 191.18 C_{30} hopanes

414.42 → 259.24 TPP

GC-MS-MS, Hopanes

370.36 → 191.18 C_{27} hopanes

384.38 → 191.18 C_{28} hopanes

398.39 → 191.18 C_{29} hopanes

412.41 → 191.18 C_{30} hopanes

412.41 → 369.35 C_{30} hopanes, bicadinanes

426.42 → 191.18 C_{31} hopanes

440.44 → 191.18 C_{32} hopanes

454.45 → 191.18 C_{33} hopanes

468.47 → 191.18 C_{34} hopanes

482.49 → 191.18 C_{35} hopanes

Hopanes and steranes (Tables 8.2.2–8.2.4) were quantified using peak areas from the relevant MS-MS transitions. GC-MS-MS allows quantification of C_{27}-C_{30} steranes (Table 8.2.2) with little interference from co-eluting gas chromatographic peaks which is not possible using only GC-MS. Biomarker ratios obtained using GC-MS-MS will, in some cases, be slightly different to those obtained from the usual *m/z* 191, 217 and 218 fragmentograms because of different response factors. Additional methods were used for identification and quantification of unusual and/or minor compounds.

GC-MS and GC-MS-MS chromatograms showing the most important biomarkers have been included as pdf-files in the Appendix 12.8.

Biomarker ratios and other data can be found in five tables.

Table 8.2.1:	Extraction, MPLC-separation and GC
Table 8.2.2:	Sterane data
Table 8.2.3 + 4:	Hopane data
Table 8.2.5:	Norcholestanes, bicadinanes

Gas chromatography-mass spectrometry (GC-MS) of aromatic hydrocarbons

The same instrument, GC-column and temperature program was used for GC-MS analysis of aromatic hydrocarbons. The aromatic fraction from the four shale samples and two of the oil stains were analysed in full scan mode and using GC-MS-MS (362 > 156; 404 > 198, diaromatic seco-bicadinanes only).

8.2.2 Organic matter and maturity

Shale extracts

Two shale samples (9.11 m and 129.05 m) having no source rock potential were extracted. Gas chromatography (GC) of saturated hydrocarbons shows a terrigenous distribution of *n*-alkanes maximising at *n*-C_{29} with a high Carbon Preference Index (CPI, Table 8.2.1). Isoprenoids and *n*-alkanes can also be seen in the *m/z* 71 mass chromatograms (Fig. 8.2.1). Extracts from two shales near the intrusion at 165 m (140.99 m and 149.78 m) show a more oil-like distribution of *n*-alkanes with CPI close to one (Table 8.2.1; Fig. 8.2.2).

Both shales have an immature distribution of hopanes. C_{32} hopanes are far from equilibrium (22S/(22S+22R)) = 0.13 and 0.17 respectively, Table 8.2.3) and both samples contain 17β(H),21β(H) hopanes (Fig. 8.2.4), neohop-13(18)-ene and C_{30} – C_{35} hop-17(21)-enes. Both samples also have an immature sterane composition with C_{29} 20S/(20S+20R) ratios below 0.1 (Table 8.2.2). The immature shales have a marine distribution of C_{27}, C_{28} and C_{29} steranes. C_{30} steranes are present but below 5% of C_{27}–C_{30}.

The shales near the intrusion have a more mature distribution of hopanes and steranes. The concentration of hopanes and steranes is very low in the sample closest to the intrusion (149.78 m) probably because of destruction by heating. Despite the apparent high maturity, the composition of steranes and hopanes in these two samples is not entirely oil-like but instead it resembles typical hydrous pyrolysates (oil produced in the laboratory by heating of immature source rocks with water at high temperatures and pressures).

1. The relative concentration of $\beta\alpha$-hopanes (moretanes) is high.
2. Rearranged hopanes are absent or found in very low concentrations.
3. Extended hopanes are not at equilibrium.

Moderate concentrations of bicadinanes and the corresponding diaromatic seco-bicadinanes were found in the degraded oil shows – see below. None of these compounds were detected in the immature shales or the shales affected by the intrusion.

Aromatic fractions from the immature shales were analysed by GC-MS in full scan (Fig. 8.2.13). The composition showed a mixed input of organic matter. Cadalene and retene which are typical higher-plant markers were abundant. Sulphur-containing compounds such as dibenzothiophenes and methyldibenzothiophenes (Hughes *et al.*, 1995) were nearly absent.

Biodegraded oil shows

Oil shows were found around 46 m and between 94 and 100 m. Three bitumen samples were found near the Nanok-1 well. All samples were moderately-severely biodegraded. Similar biodegraded bitumen was also extracted from an organic rich interval (20 % TOC) around 82.07 m. Asphaltenes were low in oil shows between 94 and 100 m (Table 8.2.1).

Gas chromatography (GC) of saturated hydrocarbons showed mainly an unresolved complex mixture (UCM). Late eluting resolved compounds were mainly hopanes. GC-MS in SIM-mode (*m/z* 71) showed that all samples (except 517004-089, 82.07 m) were completely devoid of *n*-alkanes and isoprenoids (Fig. 8.2.3).

GC-MS (*m/z* 191) showed a complex distribution of hopanes with abundant 25-norhopanes formed by degradation of regular hopanes (Figs. 8.2.5 – 8.2.7). Hopanes were quantified using GC-MS-MS data.

Regular $17\alpha(H),21\beta(H)$-hopanes below C_{31} in the oil shows at 45.77 m and 46.51 m are almost completely degraded whereas hopanes in all other samples are only partly degraded (Figs. 8.2.6 and 8.2.7). 17α(H),21β(H)-hopane (30$\alpha\beta$ or H30) is generally the most abundant hopane in shale-sourced oils. The least degraded oil shows have H29/H30 ratios around 0.6 and further biodegradation only leads to a slight increase (Table 8.2.3). Norhopanes which are abundant in carbonate-sourced oils (Subroto *et al.*, 1991) were not detected. H30 is almost absent in the 45.77 m and 46.51 m oil shows and its degradation product, 25-norhopane, is the most abundant hopane (Fig. 8.2.7; Fig. 8.2.10). Table 8.2.3 shows the abundance of the major hopanes normalized to H30. From Table 8.2.3 it can be deduced that H30 is less resistant than other regular hopanes and that the degradation order of regular hopanes (at least in this case) is H30 > H29 + H31 > Tm > H32 > H33 > H34 > H35. Neohopanes (Ts and 29Ts) are also degraded, although at a slower rate than the corresponding regular hopanes (Table 8.2.3; Fig. 8.2.12). Other rearranged hopanes such as diahopanes, 9.15-dimethyl-25,27-bisnorhopane and *C*(14a)-homo-26-nor-17α(H)-hopanes (Fig. 8.2.8) are usually very resistant and ratios involving these compounds and other stable compounds such as H34, H35, norgammacerane (Nytoft *et al.*, 2006) and bicadinanes are very similar (Table 8.2.4, Table 8.2.5) indicating a very similar source for all biodegraded oil shows. This assumption is corroborated by the almost identical composition of undegraded steranes in all samples – see below.

Extended hopanes (C_{31}-C_{35}) show little odd-over-even-predominance (HOEP, Bishop and Farrimond 1995, Table 8.2.3). More of the higher homohopanes are preserved under anoxic depositional conditions and the C_{35} homohopane index (HHI = $H_{35} / (H_{31} + H_{32} + H_{33} + H_{34} + H_{35})$) can thus be used as an indicator of redox potential in marine sediments during diagenesis (Peters *et al.*, 2005). HHI is usually high in oils from source rocks deposited under anoxic conditions and low in oil from terrigenous sources such as coals (see e.g. Table 8.2.2 in Nytoft 2011). Typical values for oils from the Danish North Sea are around 0.08. The most degraded Nanok-1 oil shows at 45.77 m and 46.51 m have values around 0.10 (Table 8.2.3). In this case the high values are caused by biodegradation. The least degraded oil shows in Nanok-1 (94.04 and 99.27 m) have a very low C_{35} homohopane index (Table 8.2.3, HHI = 0.024) and HHI of the undegraded oil was probably even lower (0.01 – 0.02 ?). Such low values indicate deposition of the source under fairly oxic conditions.

Isohopanes can be used in a similar way. Isohopanes are “novel" extended hopanes having a side chain with an additional methyl branch (C_{33} and higher). All C_{33} and C_{34} isohopanes have recently been identified by comparison with synthetic standards (Nytoft 2011). The relative abundance of isohopanes is low in oils sourced from marine organic matter deposited under anoxic conditions and very high in oils having a coaly source. The isohopane ratio (IHR = C_{33}-$_{34}$ isohopanes/C_{33}-$_{34}$ regular hopanes, Nytoft 2011) is around 0.16 in the least degraded Nanok oil show samples which is higher than usual for marine sourced oils (Table 2 in Nytoft 2011). Isohopanes are not readily degraded and IHR rises to 0.3 in the severely degraded oil shows at 45.77 m and 46.51 m.

Two series of rearranged hopanes are abundant in the Nanok oil shows (Fig. 8.2.8). They are the well known 17α-diahopanes (Moldowan *et al.*, 1991; Farrimond *et al.*, 1996) and the related 9.15-dimethyl-25, 27-bisnorhopanes or "early eluting rearranged hopanes". The relative abundance of the C_{30} members of the two series (30D and 30E) can be found in Table 8.2.3. 30D is more abundant than 30E in all samples.

28,30-Bisnorhopane (BNH, C_{28}, Seifert *et al.*, 1978; Moldowan and Seifert 1984; Schoell *et al.*, 1992) was identified in all oil shows together with 25,28,30-Trisnorhopane (Table 8.2.3; Figs. 8.2.6 and 8.2.7). 28,30-Bisnorhopane is often the only 28-norhopane (e.g. in the Monterey Formation, California). However, a complete series complete series of 28-norhopanes (C_{28}-C_{34}) has been identified in West Greenland and the North Sea (Bojesen-Koefoed *et al.*, 1999; Nytoft *et al.*, 2000), in Jurassic shales from North East Greenland and several other places (GEUS unpublished). No 28-norhopanes above C_{28} were detected in the Nanok-1 oil shows.

Gammacerane is very low in all samples. Gammacerane is highly specific for water-column stratification (commonly due to hypersalinity) during source rock deposition (Sinninghe Damsté *et al.*, 1995). A C_{29} ring A demythylated gammacerane (Nytoft *et al.*, 2006) was found in all samples. It is probably not derived from gammacerane or its precursors but may be formed by enlargement of ring E in hopanoids during diageneseis Nytoft *et al.*, 2006). It coelutes with the C_{30} neohopane (30Ts). The two compounds can only be quantified using GC-MS-MS (398 → 191 and 412 → 191 respectively). Norgammacerane is not biodegraded (Fig. 8.2.11).

Tetracyclic polyprenoids (TPP, Holba *et al.*, 2000, 2003) are abundant in all oil shows (Fig. 8.2.9, not tabulated). They are markers for freshwater organic matter input.

Bicadinanes were identified in all oil shows but not in immature shales from Nanok-1 (Table 8.2.5, Fig. 8.2.8). Bicadinanes are often very abundant in oils from South East Asia (Cox *et al.*, 1986; Alam and Pearson, 1990; Van Aarssen *et al.*, 1992), where they are formed by polycadinene resins produced from angiosperm trees of the tropical *Dipterocarpacea* family. Bicadinanes are also found in oils from West Greenland (Bojesen-Koefoed *et al.*, 1999; Nytoft *et al.*, 2005). The origin of bicadinanes in oils from West Greenland is not known. Bicadinanes have never been detected in Jurassic/Lower Cretaceous shales from North East Greenland. Low concentrations of bicadinanes can only be detected using GC-MS-MS (412 → 369, Fig. 8.2.8) together with *C*(14a)-Homo-26-nor-17α-hopane (Trendel *et al.*, 1997) which is an unrelated rearranged hopane. Their *m/z* 412 → 191 response is very low (Table 3 in Nytoft *et al.*, 2010; Fig. 8.2.8 top). Only two oil shows (517004-201 and 517004-203) were analysed for aromatic bicadinanes. C_{27} and C_{30} diaromatic seco-bicadinanes (Alam and Pearson, 1990; Sosrowidjojo *et al.*, 1996) were detected in both cases (Fig. 8.2.15).

Oleanane (Ekweozor and Udo, 1988; Murray *et al.*, 1997), Lupane (Nytoft *et al.*, 2002), demethylated lupanes and various demethylated and/or rearranged oleananes are also markers for angiosperms. Bicadinanes and oleananes/lupanes are often found together in Late Cretaceous/Tertiary oils but since the two groups of compounds have different precursors some oils may be rich in oleananes and low in bicadinanes (Nigeria) or vice versa (South East Asia). Identification of oleanane/lupane in the oil shows from Nanok-1 is difficult because of coelution with 22S-25-norhomohopane and several unidentified rearranged hopanes. Oils with oleanane often contain even higher concentrations of early eluting rearranged oleananes (Nytoft *et al.*, 2010 and references therein) which are usually easier to identify with certainty. None of them were detected in the oil shows (Fig. 8.2.8).

Steranes in the oil shows appear undegraded. They all have a “marine” distribution of steranes with a slight predominance of the C_{27} compounds. All samples have a very similar distribution of steranes suggesting the same source for all of them. C_{30} steranes are present but only around 5 % of C_{27}-C_{30} (Table 8.2.2). C_{30} steranes (24-*n*-propylcholestanes) is the most powerful means in order to identify input of marine organic matter to the source rock (Peters *et al.*, 2005). Diasterane/regular sterane ratios are high (Table 8.2.2). This is normal for oils from a shaly source. Isomerization of regular steranes at C-20 has not reached equilibrium and the 20S/(20S+20R) ratios for C_{29} steranes are all around 0.40 (Table 8.2.2) indicating generation from a source rock in the middle of the oil-window.

24-Nordiacholestanes and 27-Norcholestanes (Holba *et al.*, 1998a,b) are equally abundant in all samples giving C_{26} 24/(24 + 27) nordiacholestane ratios around 0.5 (Table 8.2.5, Fig.

8.2.9). Previous analyses of Jurassic - Lower Cretaceous - Shales from North East Greenland gave values around 0.2 and the source of the Nanok-1 oils is clearly much younger.

The aromatic hydrocarbons from two samples (45.77 and 94.04 m) were analysed in full scan mode (Fig. 8.2.14) and showed only an unresolved complex mixture (UCM). All naphthalenes, phenanthrenes and dibenzothiophenes were absent because of biodegradation/water washing. Mono- and triaromatic steranes, monoaromatic 8,14-secohopanes and benzohopanes were identified but not quantified. Diaromatic seco-bicadinanes were detected in low concentrations in both samples by GC-MS-MS (Fig. 8.2.15). No other aromatic fractions from oil shows were analysed.

8.2.3 Conclusions

Shale extracts 9.11 m and 129.05 m: key characteristics.

- High Carbon Preference Index (CPI)
- "Immature" distribution of hopanes. $\beta\beta$-hopanes, Neohop-13(18)-enes and hop-17(21)-enes present.
- Marine distribution of C_{27}, C_{28} and C_{29} steranes. Steranes immature.
- C_{30} steranes present but only around 4-5 %. Marine input.
- Nordiacholestane ratios (NDR) around 0.5. Not older than Cretaceous.
- Bicadinanes and other saturated markers for angiosperms absent.
- Dibenzothiophenes very low
- Cadalene and retene present in aromatic fraction (higher plant markers).
- Two samples near the intrusion at 165 m (140.99 m and 149.78 m) are in the oil-window and extracts have a "hydrous pyrolysate-like" composition of biomarkers.

Oil stains: key characteristics

- Low C_{35} homohopane index in the least degraded oils.
- High isohopane ratios.
- 28,30 bisnorhopane and 25,28,30-trisnorhopane present.
- Hopanes moderately – severely biodegraded. 25-norhopanes present. High concentration of lower 25-norhopanes.

- Diahopanes and ”early eluting hopanes” = 9,15-dimethyl-25,27-bisnorhopanes abundant.
- Low H29/H30.
- 30-Norhopanes low/absent.
- Ts/Tm and 29Ts/H29 moderate-high.
- Gammacerane low/absent.
- Moderate concentration of bicadinanes ! = angiosperm input. Similar relative concentrations in all samples. Not previously found in North East Greenland.
- Oleanane: absent. Identification difficult because of coelution with 22S-25-norhomohopane. Rearranged oleananes absent.
- Marine distribution of C_{27}, C_{28} and C_{29} steranes. $C_{27} > C_{29} > C_{28}$.
- Methylsteranes very low.
- C_{30} steranes present but only around 4-5 %. Marine input.
- Tetracyclic polyprenoids (TPP) abundant. Some freshwater organic matter input.
- Nordiacholestane ratios (NDR) around 0.5. Age of source not older than Cretaceous.
- Aromatic hydrocarbons degraded. Naphthalenes, phenanthrenes and dibenzothiophenes absent.

8.2.4 References

Alam, M. & Pearson, M.J. 1990: Bicadinanes in oils from the Surma Basin, Bangladesh. Organic Geochemistry, **15**, 461–464.

Bishop, A.N. & Farrimond, P. 1995: A new method of comparing extended hopane distributions. Organic Geochemistry, **23**, 987–990.

Bojesen-Koefoed, J.A., Christiansen, F.G., Nytoft, H.P. & Pedersen, A.K. 1999: Oil seepage onshore West Greenland: evidence of multiple source rocks and oil mixing. In: Fleet, A.S. & Boldy, S. (eds.), Petroleum Geology of NW-Europe, proceedings of the 5th Conference, 305–314.

Cox, H.C., de Leeuw, J.W., Schenck, P.A., van Koningsveld, H., Jansen, J.C., van de Graaf, B., van Geerestein, V.J., Kanters, J.A., Kruk, C. & Jans, A.W.H. 1986: Bicadinane, a C_{30} pentacyclic isoprenoid hydrocarbon found in crude oil. Nature, **319**, 316–318.

Ekweozor, C.M. & Udo, O.T. 1988: The oleananes: origin, maturation and limits of occurrence in Southern Nigeria sedimentary basins. In: Mattavelli, L. and Novelli, L. (eds.), Advances in Organic Geochemistry 1987. Pergamon Press, Oxford, pp. 131–140.

Farrimond, P. & Telnaes, N. 1996: Three series of rearranged hopanes in Toarcian sediments (northern Italy). Organic Geochemistry, **25**, 165–177.

Holba, A.G., Tegelaar, E.W., Huizinga, B.J., Moldowan, J.M., Singletary, M.S., McCaffrey, M.A. & Dzou, L.I.P. 1998a: 24-norcholestanes as age-sensitive molecular fossils. Geology, **26**, 783–786.

Holba, A.G., Dzou, L.I.P., Masterson, W.D., Hughes, W.B., Huizinga, B.J., Singletary, M.S., Moldowan, J.M., Mello, M.R. & Tegelaar, E. 1998b: Application of 24 norchole-stanes for constraining source age of petroleum. Organic Geochemistry, **29**, 1269–1283.

Holba, A.G., Tegelaar, E., Ellis, L., Singletary, M.S. & Albrecht, P. 2000: Tetracyclic polyprenoids: indicators of freshwater (lacustrine) algal input. Geology, **28**, 251–254.

Holba, A.G., Dzou, L.I., Wood, G.D., Ellis, L., Adam, P., Schaeffer, P., Albrecht, P., Greene, T. & Hughes, W.B. 2003: Application of tetracyclic polyprenoids as indicators of input from fresh-brackish water environments. Organic Geochemistry, **34**, 441–469.

Hughes, W.B., Holba, A.G & Dzou, L.I.P. 1995: The ratios of dibenzothiophene to phenanthrene and pristane to phytane as indicators of depositional environment and lithology of petroleum source rocks. Geochimica et Cosmochimica Acta, **59**, 3581–3598.

Moldowan, J.M. & Seifert, W.K. 1984: Structure proof and significance of stereoisomeric 28,30-bisnorhopanes in petroleum and petroleum source rocks. Geochimica et Cosmochimica Acta, **48**, 1651–1661.

Moldowan, J.M., Fago, F.J., Carlson, R.M.K., Young, D.V., Van Duyne, G., Clardy, J., Schoell, M., Pillinger, C.T. & Watt, D.S. 1991: Rearranged hopanes in sediments and petroleum. Geochimica et Cosmochimica Acta, **55**, 3333–3353.

Murray, A.P., Sosrowidjojo, I.B., Alexander, R., Kagi, R.I., Norgate, C.M. & Summons, R.E. 1997: Oleananes in oils and sediments: Evidence of marine influence during early diagenesis? Geochimica et Cosmochimica Acta, **61**, 1261–1276.

Nytoft, H.P., Bojesen-Koefoed, J.A., Christiansen, F.G., & Fowler, M.G. 2002. Oleanane or lupane? - reappraisal of the presence of oleanane in Cretaceous - Tertiary oils and sediments. Organic Geochemistry, **33**, 1225–1240.

Nytoft, H.P., Bojesen-Koefoed, J.A., & Christiansen, F.G. 2005: Bicadinanes in high latitude oils. 22nd International Meeting on Organic Geochemistry, Seville – Spain, September 12 - 16, 2005, Abstracts vol. 1, 245–246.

Nytoft, H.P., Lutnæs, B.F., & Johansen, J.E., 2006: 28-*Nor*-spergulanes, a novel series of rearranged hopanes. Organic Geochemistry, **37**, 772–786.

Nytoft, H.P., Kildahl-Andersen, G. & Samuel O.J. 2010: Rearranged oleananes: structural identification and distribution in a worldwide set of Late Cretaceous/Tertiary oils. Organic Geochemistry, **41**, 1104–1118.

Nytoft, H.P. 2011: Novel side-chain methylated and hexacyclic hopanes: Identification by synthesis, distribution in a world-wide set of coals and crude oils and use as markers for oxic depositional environments. Organic Geochemistry, **42**, 520–539.

Nytoft, H.P., Bojesen-Koefoed, J.A. & Christiansen, F.G. 2000: C_{26} and C_{28}-C_{34} 28-norhopanes in sediments and petroleum. Organic Geochemistry, **31**, 25–39.

Peters, K.E., Walters, C.C. & Moldowan, J.M. 2005: The Biomarker Guide Second Edition Volume 2: Biomarkers and Isotopes in Petroleum Exploration and Earth History. Cambridge University Press.

Schoell, M., McCaffrey, M.A., Fago, F.J. & Moldowan, J.M. 1992: Carbon isotopic compositions of 28,30-bisnorhopanes and other biological markers in a Monterey crude oil. Geochimica et Cosmochimica Acta, **56**, 1391–1399.

Seifert, W.K., Moldowan, J.M., Smith, G.W. & Whitehead, E.W., 1978: First proof of structure of a C_{28}-pentacyclic triterpane in petroleum. Nature, **271**, 436–437.

Sinninghe Damsté, J.S., Kenig, F., Koopmans, M.P., Köster, J., Schouten, S., Hayes, J.M. & de Leeuw, J.W. 1995: Evidence for gammacerane as an indicator of water column stratification. Geochimica et Cosmochimica Acta, **59**, 1895–1900.

Sosrowidjojo, I.B., Murray, A.P., Alexander, R., Kagi, R.I. & Summons, R.E. 1996: Bicadinanes and related compounds as maturity indicators for oils and sediments. Organic Geochemistry, **24**, 43–55.

Subroto, E.A., Alexander, R., & Kagi, R.I. 1991: 30-Norhopanes: their occurrence in sediments and crude oils. Chemical Geology, **93**, 179–192.

Trendel, J-M., Graff, R., Wehrung, P., Albrecht, P., Dessort, D. & Connan, J. 1993: *C*(14a)-Homo-26-nor-17α-hopanes, a novel and unexpected series of molecular fossils in biodegraded petroleum. Journal of the Chemical Society, Chemical Communications, **5**, 461–463.

van Aarssen, B.G.K., Hessels, J.K.C., Abbink, O.A. & de Leeuw, J.W. 1992: The occurrence of polycyclic sesqui-, tri-, and oligoterpenoids derived from a resinous polymeric cadinene in crude oils from southeast Asia. Geochimica et Cosmochimica Acta, **56**, 1231–1246.

Table 8.2.1 Extraction, MPLC-separation and GC

Lab no.	Sample no.	Depth Bottom	Yield mg/g TOC	% Asph.	% Sat.	% Aro.	% Polars	CPI	Pristane/ phytane	Pristane/ *n*C17	Phytane *n*C18
2011024-20902	517004-201	45.77	n.a.	8,20	50,00	32,20	17,80	n.a.	n.a.	n.a.	n.a.
2011024-20903	517004-202	46.51	n.a.	4,22	65,31	20,82	13,88	n.a.	n.a.	n.a.	n.a.
2011024-20904	517004-203	94.04	n.a.	0,92	51,47	26,47	22,06	n.a.	n.a.	n.a.	n.a.
2011024-20905	517004-204	96.55	n.a.	0,90	59,76	27,64	12,60	n.a.	n.a.	n.a.	n.a.
2011024-20906	517004-205	97.53	n.a.	0,76	57,14	28,57	14,29	n.a.	n.a.	n.a.	n.a.
2011024-20907	517004-206	97.99	n.a.	1,46	58,65	28,85	12,50	n.a.	n.a.	n.a.	n.a.
2011024-20908	517004-207	98.44	n.a.	1,26	58,08	29,80	12,12	n.a.	n.a.	n.a.	n.a.
2011024-20909	517004-208	99.27	n.a.	1,33	61,41	27,80	10,79	n.a.	n.a.	n.a.	n.a.
2011024-20787	517004-053	9.11	13,42	58,33	13,64	18,18	68,18	1,91	2,82	1,48	0,55
2011024-20823	517004-089	82.07	49,51	5,97	72,31	16,92	10,77	n.a.	n.a.	n.a.	n.a.
2011024-20867	517004-133	129.05	17,34	60,00	7,14	21,43	71,43	1,63	3,33	2,46	0,82
2011024-20880	517004-146	140.99	118,01	29,88	22,33	19,74	57,93	1,11	3,08	1,64	0,62
2011024-20890	517004-156	149.78	28,45	36,07	35,85	16,98	47,17	1,04	2,86	0,28	0,10
2012008-22418	475091	-	n.a.	5.82	54.50	21.69	23.81	n.a.	n.a.	n.a.	n.a.
2012008-22419	475114	-	n.a.	3.80	65.89	11.37	22.74	n.a.	n.a.	n.a.	n.a.
2012008-22420	475135	-	n.a.	20.57	39.58	7.92	52.50	n.a.	n.a.	n.a.	n.a.

Table 8.2.2

			Diasteranes/ (diasteranes + reg. steranes)				ββ steranes/ (ββ steranes + αα steranes)				Steranes 20S/(20S + 20R)				% C27, 28 & 29 Sum = 100 % Regular steranes only			% C27, 28 & 29 Sum = 100 % Diasteranes only			% C27, 28 & 29 Sum = 100 % Diasteranes + reg. steranes			% C30
Lab no.	Sample no.	Depth Bottom	C27 D/(R+D)	C28 D/(R+D)	C29 D/(R+D)	C30 D/(R+D)	C27 B/(B+A)	C28 B/(B+A)	C29 B/(B+A)	C30 B/(B+A)	C27 S/(S+R)	C28 S/(S+R)	C29 S/(S+R)	C30 S/(S+R)	C27 R-st	C28 R-st	C29 R-st	C27 Dia	C28 Dia	C29 Dia	C27 D+R	C28 D+R	C29 D+R	C30 D+R
2011024-20902	517004-201	45.77	0,739	0,706	0,681	0,618	0,306	0,471	0,499	0,459	0,508	0,375	0,396	0,331	36,76	28,70	34,55	42,11	27,96	29,93	40,57	28,17	31,26	4,11
2011024-20903	517004-202	46.51	0,768	0,730	0,703	0,643	0,317	0,517	0,530	0,516	0,526	0,402	0,422	0,382	33,14	29,69	37,18	39,45	28,87	31,68	37,78	29,09	33,14	4,73
2011024-20904	517004-203	94.04	0,704	0,684	0,660	0,634	0,314	0,461	0,481	0,471	0,493	0,387	0,401	0,369	34,29	29,15	36,56	37,76	29,32	32,92	36,66	29,27	34,07	4,86
2011024-20905	517004-204	96.55	0,702	0,688	0,659	0,631	0,305	0,455	0,484	0,485	0,495	0,387	0,409	0,370	33,35	28,90	37,75	36,55	29,57	33,88	35,53	29,35	35,11	5,28
2011024-20906	517004-205	97.53	0,706	0,692	0,663	0,638	0,316	0,458	0,482	0,489	0,497	0,388	0,405	0,366	33,74	28,90	37,36	36,92	29,57	33,51	35,92	29,36	34,72	4,94
2011024-20907	517004-206	97.99	0,707	0,697	0,669	0,646	0,316	0,462	0,486	0,494	0,489	0,368	0,416	0,370	34,83	28,35	36,81	37,53	29,20	33,28	36,69	28,94	34,37	5,01
2011024-20908	517004-207	98.44	0,701	0,684	0,662	0,636	0,320	0,453	0,470	0,486	0,488	0,393	0,397	0,369	34,09	29,20	36,72	37,08	29,43	33,49	36,13	29,36	34,52	5,05
2011024-20909	517004-208	99.27	0,706	0,685	0,659	0,639	0,310	0,466	0,474	0,510	0,489	0,387	0,417	0,361	34,25	28,88	36,87	38,06	29,04	32,89	36,86	28,99	34,15	4,73
2011024-20787	517004-053	9.11	0,350	0,615	0,300	0,436	0,115	0,435	0,377	0,340	0,329	0,170	0,067	0,116	29,24	26,28	44,48	20,54	54,62	24,83	25,46	38,59	35,95	3,56
2011024-20823	517004-089	82.07	0,802	0,777	0,753	0,699	0,387	0,581	0,578	0,590	0,564	0,386	0,431	0,329	29,04	28,72	42,24	33,87	28,90	37,22	32,79	28,86	38,35	5,27
2011024-20867	517004-133	129.05	0,361	0,479	0,319	0,355	0,068	0,322	0,318	0,317	0,318	0,140	0,060	0,101	27,11	31,07	41,82	24,14	44,99	30,86	25,96	36,48	37,56	4,89
2011024-20880	517004-146	140.99	0,450	0,458	0,357	0,310	0,082	0,278	0,272	0,276	0,410	0,311	0,291	0,289	26,43	39,78	33,79	29,19	45,46	25,35	27,60	42,19	30,20	5,48
2011024-20890	517004-156	149.78	0,604	0,592	0,561	n.a.	0,280	0,348	0,387	n.a.	0,354	0,394	0,309	n.a.	30,11	32,89	37,00	32,65	33,83	33,52	31,60	33,44	34,96	n.a.
2012008-22418	475091	-	0,721	0,722	0,699	0,653	0,324	0,496	0,502	0,469	0,528	0,385	0,391	0,334	35,12	27,69	37,19	36,46	28,90	34,65	36,07	28,55	35,38	4,62
2012008-22419	475114	-	0,752	0,721	0,672	0,634	0,324	0,482	0,505	0,484	0,539	0,415	0,417	0,327	32,11	28,99	38,90	38,62	29,77	31,61	36,77	29,55	33,68	4,80
2012008-22420	475135	-	0,750	0,734	0,705	0,673	0,306	0,480	0,491	0,451	0,537	0,402	0,417	0,358	30,99	28,66	40,35	34,66	29,50	35,84	33,67	29,27	37,06	5,09

Table 8.2.3

			Hopanes, relative abundance, 17α,21β(H)-HOPANE = 1																				Hopane ratios				
Lab no.	Sample no.	Depth Bottom	C27 27Ts	C27 27Tm	C28 BNH	C29 29αβ	C29 29Ts	C30 30E	C30 30D	C30 30αβ	C30 30Ts	C30 30βα	C31 αβ-22S	C31 αβ-22R	C32 αβ-22S	C32 αβ-22R	C33 αβ-22S	C33 αβ-22R	C34 αβ-22S	C34 αβ-22R	C35 αβ-22S	C35 αβ-22R	Ts/ (Ts + Tm)	29Ts/ (H29 + 29Ts)	C32 (S/S+R)	C31-35 HOEP	C35 HHI
2011024-20902	517004-201	45.77	2,175	1,279	0,880	0,715	1,527	0,913	1,821	1,000	0,768	0,215	0,230	0,197	0,251	0,353	0,288	0,155	0,263	0,129	0,113	0,077	0,63	0,68	0,42	0,82	0,092
2011024-20903	517004-202	46.51	1,448	0,803	0,673	0,641	1,487	1,038	1,896	1,000	0,696	0,251	0,255	0,212	0,232	0,422	0,357	0,164	0,320	0,161	0,159	0,092	0,64	0,70	0,35	0,85	0,106
2011024-20904	517004-203	94.04	0,666	0,433	0,195	0,592	0,420	0,100	0,225	1,000	0,080	0,092	0,250	0,182	0,148	0,110	0,067	0,044	0,032	0,021	0,013	0,008	0,61	0,42	0,57	0,90	0,024
2011024-20905	517004-204	96.55	0,754	0,414	0,193	0,607	0,483	0,123	0,276	1,000	0,096	0,088	0,254	0,173	0,163	0,121	0,078	0,049	0,038	0,024	0,016	0,010	0,65	0,44	0,57	0,87	0,028
2011024-20906	517004-205	97.53	1,288	0,613	0,283	0,680	0,752	0,188	0,431	1,000	0,168	0,101	0,291	0,182	0,253	0,186	0,126	0,072	0,060	0,039	0,026	0,017	0,68	0,53	0,58	0,79	0,034
2011024-20907	517004-206	97.99	1,134	0,592	0,260	0,678	0,647	0,166	0,366	1,000	0,138	0,097	0,282	0,184	0,217	0,168	0,100	0,063	0,051	0,031	0,021	0,013	0,66	0,49	0,56	0,79	0,031
2011024-20908	517004-207	98.44	0,872	0,491	0,214	0,612	0,516	0,136	0,286	1,000	0,107	0,095	0,258	0,173	0,190	0,140	0,087	0,054	0,044	0,028	0,018	0,011	0,64	0,46	0,58	0,81	0,029
2011024-20909	517004-208	99.27	0,640	0,419	0,171	0,596	0,365	0,100	0,209	1,000	0,077	0,089	0,239	0,166	0,143	0,105	0,061	0,042	0,031	0,018	0,012	0,008	0,60	0,38	0,58	0,88	0,024
2011024-20787	517004-053	9.11	0,024	0,577	0,045	0,504	0,021	0,004	0,018	1,000	0,012	0,312	0,316	1,531	0,035	0,231	0,016	0,052	0,007	0,018	0,003	0,006	0,04	0,04	0,13	1,95	0,004
2011024-20823	517004-089	82.07	1,160	0,923	0,330	0,679	0,532	0,276	0,505	1,000	0,179	0,171	0,309	0,243	0,274	0,340	0,264	0,136	0,149	0,102	0,055	0,047	0,56	0,44	0,45	0,88	0,054
2011024-20867	517004-133	129.05	0,021	0,462	0,015	0,608	0,027	0,006	0,021	1,000	0,014	0,307	0,280	0,899	0,041	0,209	0,019	0,061	0,007	0,026	0,004	0,009	0,04	0,04	0,17	1,47	0,008
2011024-20880	517004-146	140.99	0,038	0,252	0,004	0,644	0,052	0,000	0,009	1,000	0,017	0,205	0,253	0,229	0,088	0,089	0,042	0,039	0,025	0,025	0,011	0,011	0,13	0,08	0,50	1,08	0,027
2011024-20890	517004-156	149.78	0,229	0,622	0,000	1,140	0,153	0,000	0,071	1,000	0,042	0,266	0,330	0,325	0,172	0,157	0,000	0,000	0,000	0,000	0,000	0,000	0,27	0,12	0,52	0,50	0,000
2012008-22418	475091	-	2,130	1,159	0,398	0,793	0,804	0,312	0,681	1,000	0,275	0,132	0,245	0,165	0,217	0,212	0,153	0,085	0,086	0,049	0,022	0,021	0,65	0,50	0,51	0,83	0,034
2012008-22419	475114	-	2,388	1,592	0,537	0,676	0,763	0,472	1,050	1,000	0,372	0,173	0,283	0,213	0,305	0,383	0,271	0,155	0,162	0,091	0,063	0,035	0,60	0,53	0,44	0,84	0,050
2012008-22420	475135	-	1,451	0,737	0,322	0,706	0,643	0,250	0,539	1,000	0,206	0,120	0,230	0,197	0,216	0,219	0,157	0,091	0,082	0,053	0,029	0,019	0,66	0,48	0,50	0,86	0,038

Table 8.2.4 Some biodegradation insensitive biomarker ratios (GC-MS-MS)

Lab no.	Sample no.	Depth, bottom	29G/(H34+H35)	30E/(H34+H35)	30D/(H34+H35)	30D/29G	30E/29G	30E/D30
2011024-20902	517004-201	45.77	0,64	1,57	3,13	4,89	2,45	0,50
2011024-20903	517004-202	46.51	0,47	1,42	2,59	5,53	3,03	0,55
2011024-20904	517004-203	94.04	0,68	1,35	3,03	4,44	1,98	0,45
2011024-20905	517004-204	96.55	0,68	1,40	3,13	4,62	2,07	0,45
2011024-20906	517004-205	97.53	0,65	1,32	3,04	4,68	2,04	0,44
2011024-20907	517004-206	97.99	0,67	1,43	3,14	4,66	2,12	0,45
2011024-20908	517004-207	98.44	0,63	1,34	2,84	4,48	2,12	0,47
2011024-20909	517004-208	99.27	0,72	1,44	3,02	4,21	2,01	0,48
2011024-20787	517004-053	9.11	0,94	0,13	0,54	0,57	0,14	0,24
2011024-20823	517004-089	82.07	0,36	0,78	1,43	3,97	2,17	0,55
2011024-20867	517004-133	129.05	0,60	0,13	0,45	0,75	0,22	0,29
2011024-20880	517004-146	140.99	0,13	0,00	0,13	0,99	n.a	n.a
2011024-20890	517004-156	149.78	n.a	n.a	n.a	n.a	n.a	n.a
2012008-22418	475091	-	0,69	1,75	3,83	5,52	2,52	0,46
2012008-22419	475114	-	0,61	1,34	2,99	4,93	2,22	0,45
2012008-22420	475135	-	0,64	1,36	2,93	4,60	2,13	0,46

Table 8.2.5 Nordiacholestanes and bicadinanes (GC-MS-MS)

Lab no.	Sample no.	Depth, bottom	NDR 358 > 217	Bicad T 412 > 369	HH 30 412 > 369	H 30 412 > 369	Bicad T/H 30 412 > 369	Bicad T/HH 30 412 > 369
2011024-20902	517004-201	45.77	0,54	39,13	56,08	4,79	8,17	0,70
2011024-20903	517004-202	46.51	0,54	31,86	61,12	7,03	4,53	0,52
2011024-20904	517004-203	94.04	0,48	29,78	37,22	33,00	0,90	0,80
2011024-20905	517004-204	96.55	0,49	31,67	40,51	27,82	1,14	0,78
2011024-20906	517004-205	97.53	0,48	35,23	44,76	20,01	1,76	0,79
2011024-20907	517004-206	97.99	0,49	33,99	42,48	23,53	1,44	0,80
2011024-20908	517004-207	98.44	0,49	31,83	40,58	27,59	1,15	0,78
2011024-20909	517004-208	99.27	0,48	29,70	35,23	35,07	0,85	0,84
2011024-20787	517004-053	9.11	0,45	n.a.	n.a.	n.a.	n.a.	n.a.
2011024-20823	517004-089	82.07	0,50	22,16	61,23	16,61	1,33	0,36
2011024-20867	517004-133	129.05	0,50	n.a.	n.a.	n.a.	n.a.	n.a.
2011024-20880	517004-146	140.99	0,48	n.a.	n.a.	n.a.	n.a.	n.a.
2011024-20890	517004-156	149.78	n.a.	n.a.	n.a.	n.a.	n.a.	n.a.
2012008-22418	475091	-	0,51	31,34	57,30	11,36	2,76	0,55
2012008-22419	475114	-	0,53	35,95	56,28	7,78	4,62	0,64
2012008-22420	475135	-	0,51	31,42	53,45	15,13	2,08	0,59

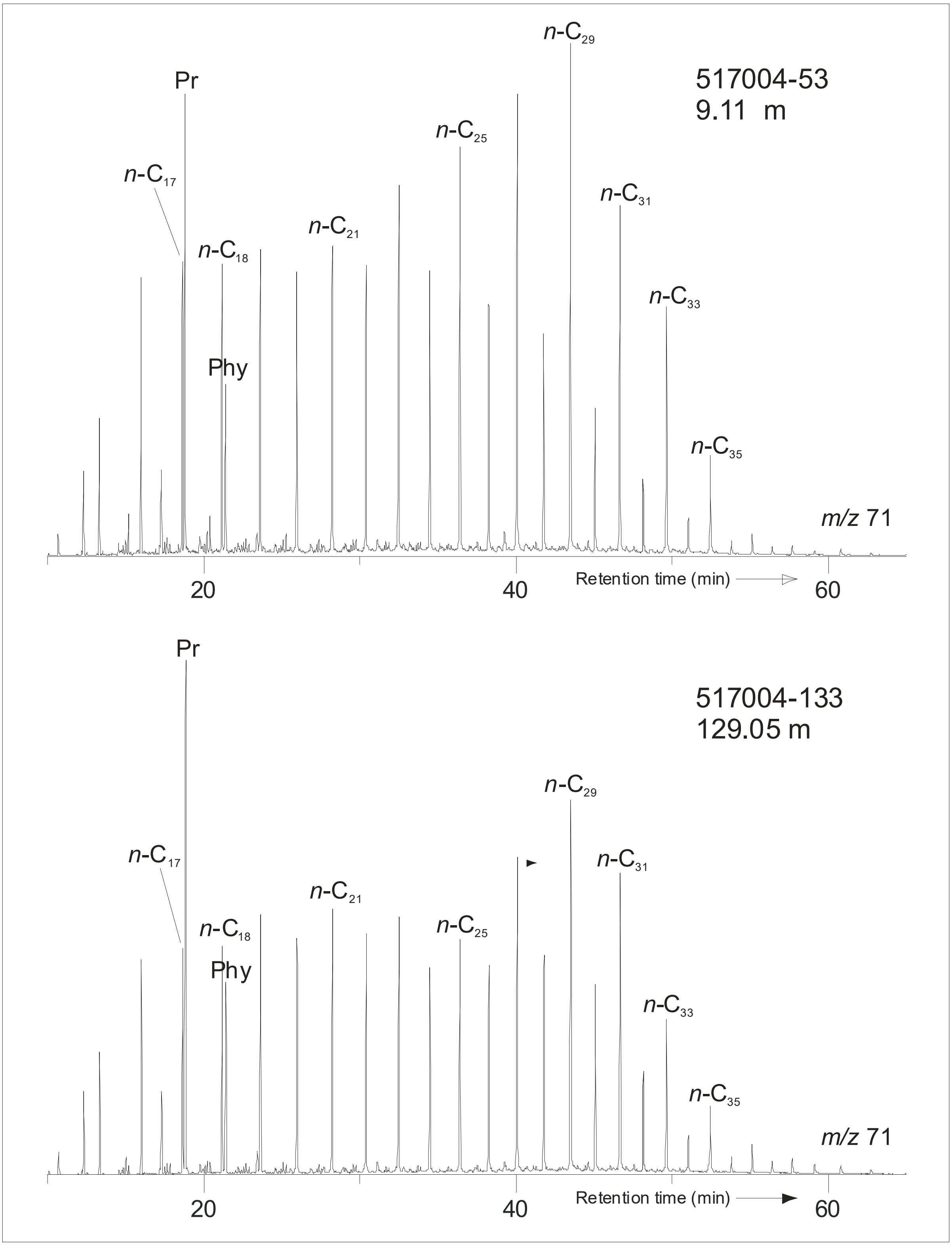

Figure 8.2.1. Isoprenoids and *n*-alkanes in two immature shales.

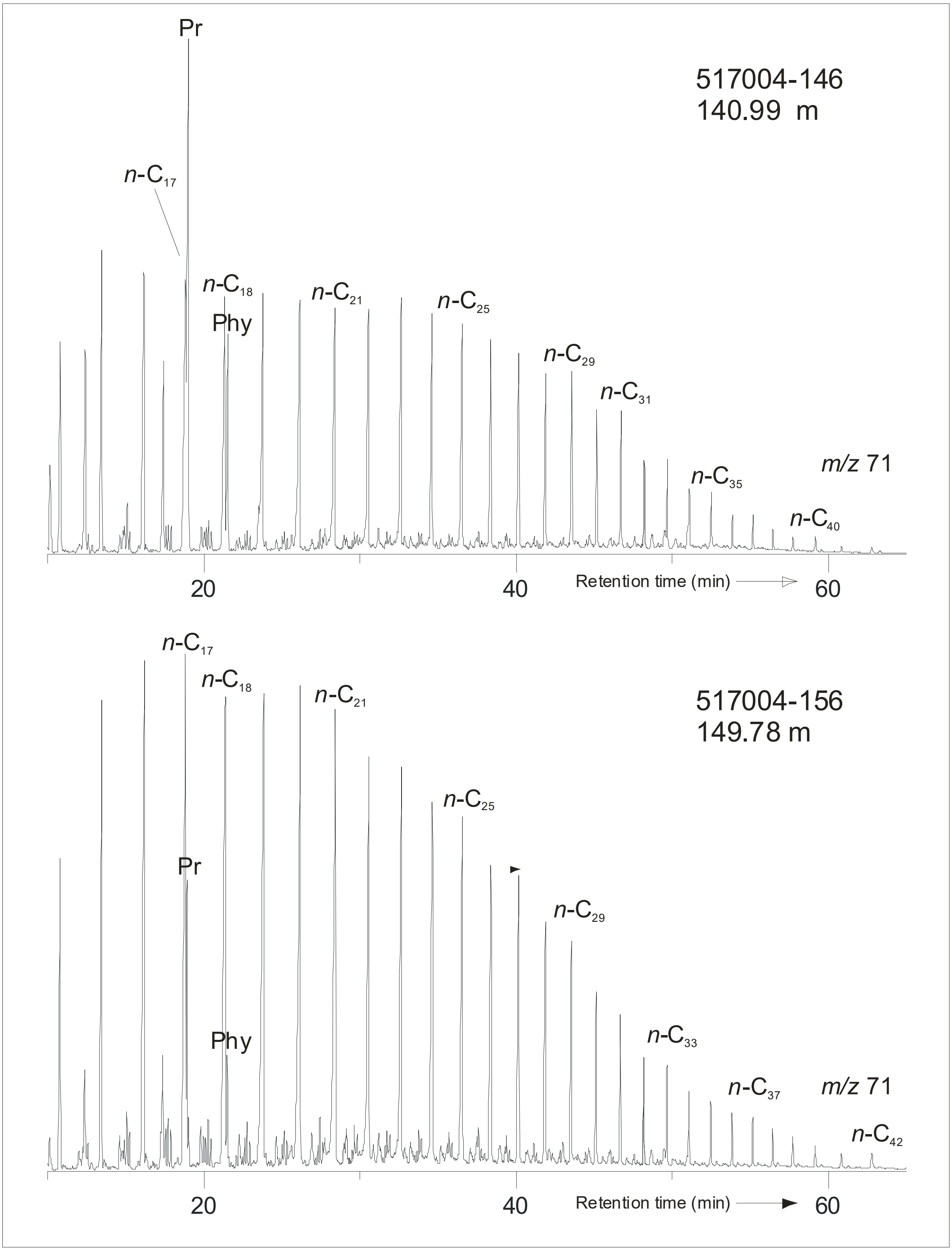

Figure. 8.2.2. Isoprenoids and *n*-alkanes in two shales matured by intrusion.

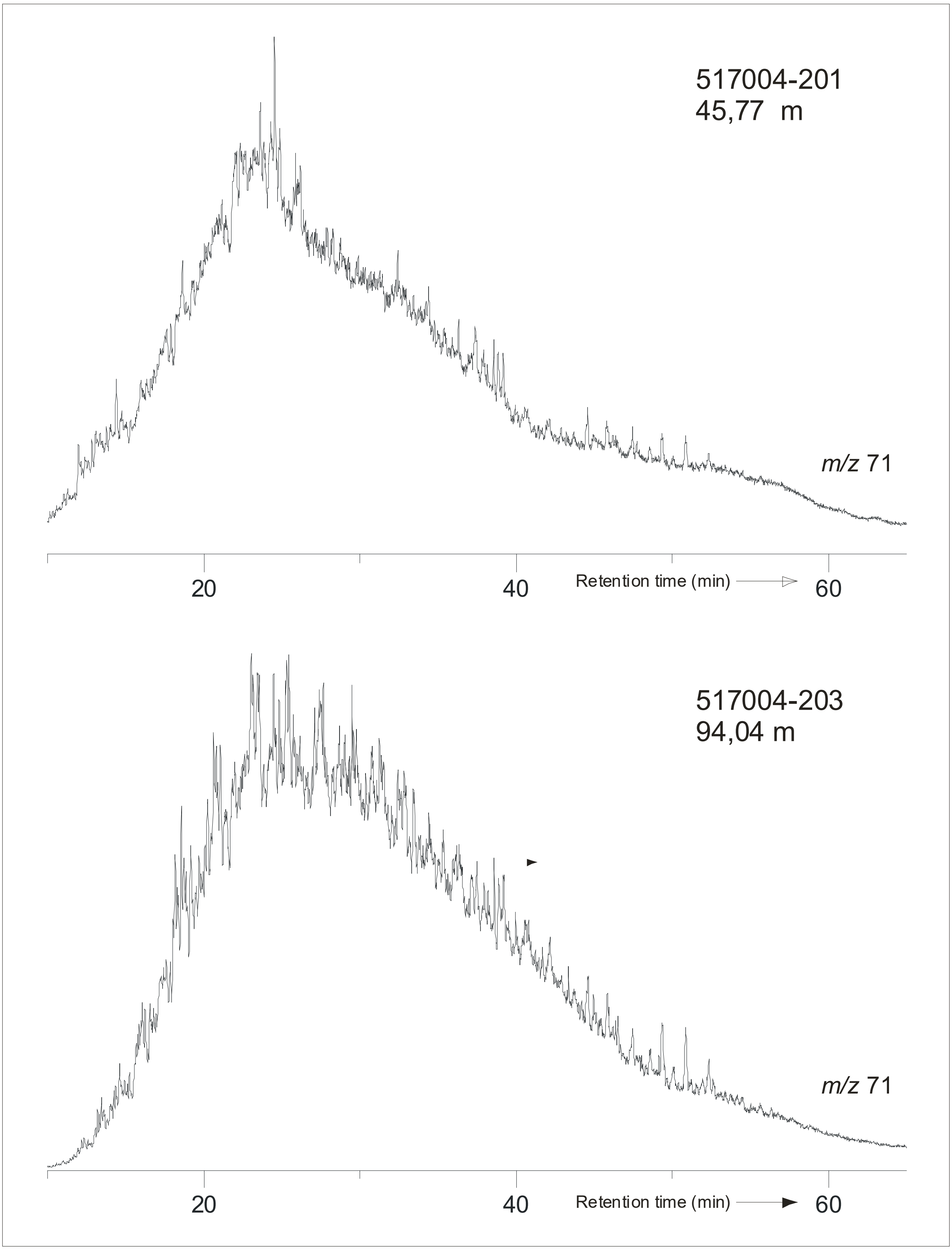

Figure 8.2.3. Degraded Nanok oils, *m/z* 71, no isoprenoids, no *n*-alkanes, just UCM !

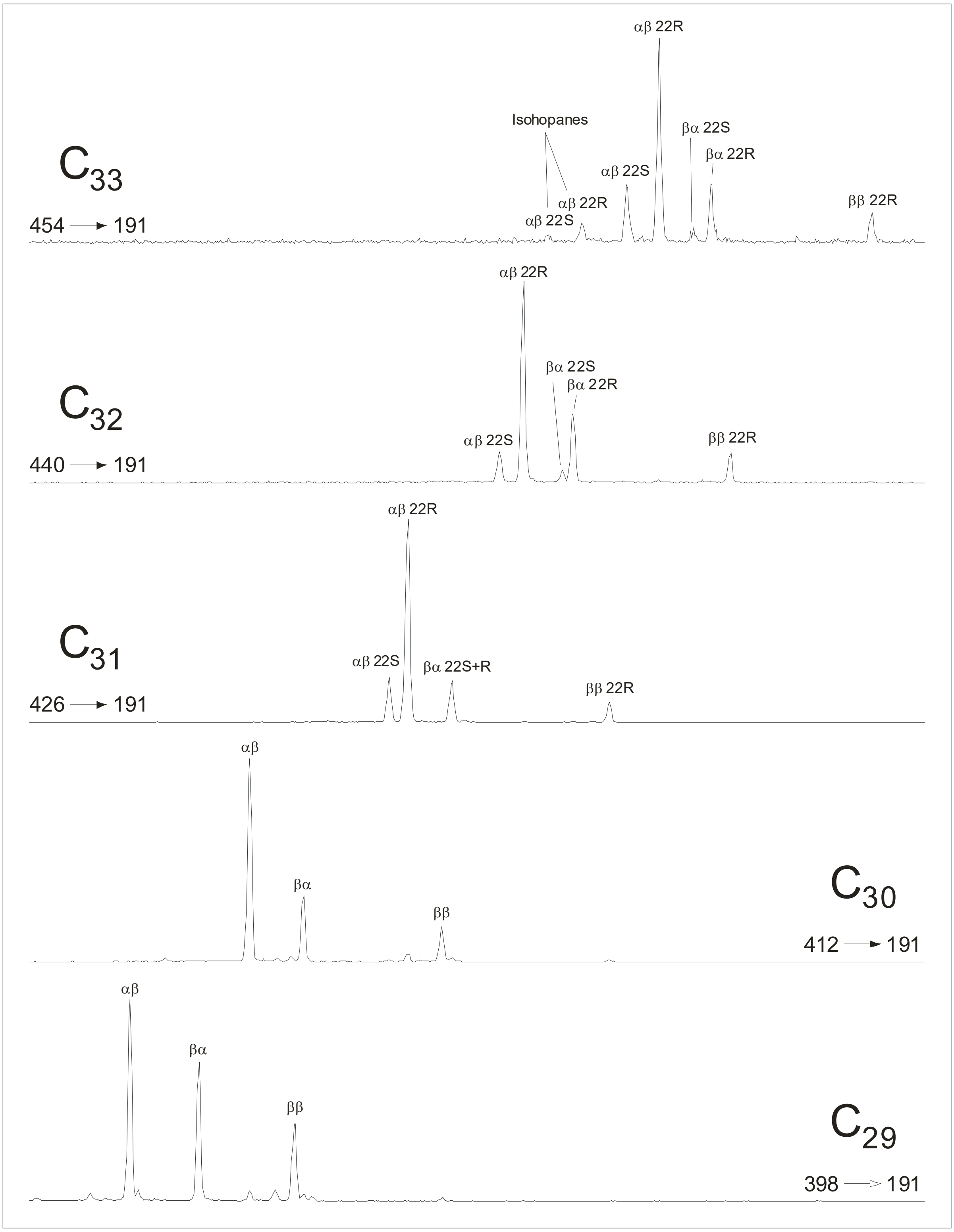

Figure 8.2.4. C_{29}-C_{33} hopanes with an “immature” distribution in a Nanok-1 shale (9.11 m).

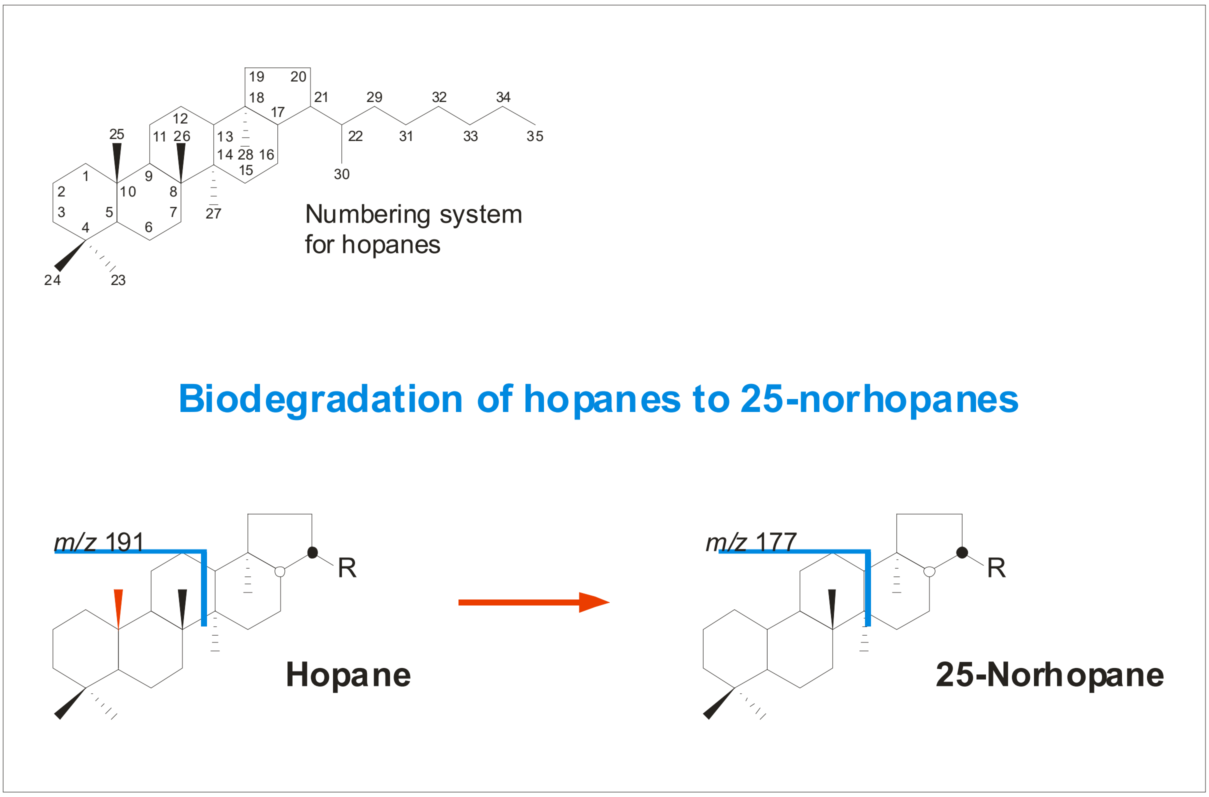

Figure 8.2.5. Degradation of hopanes to 25-norhopanes.

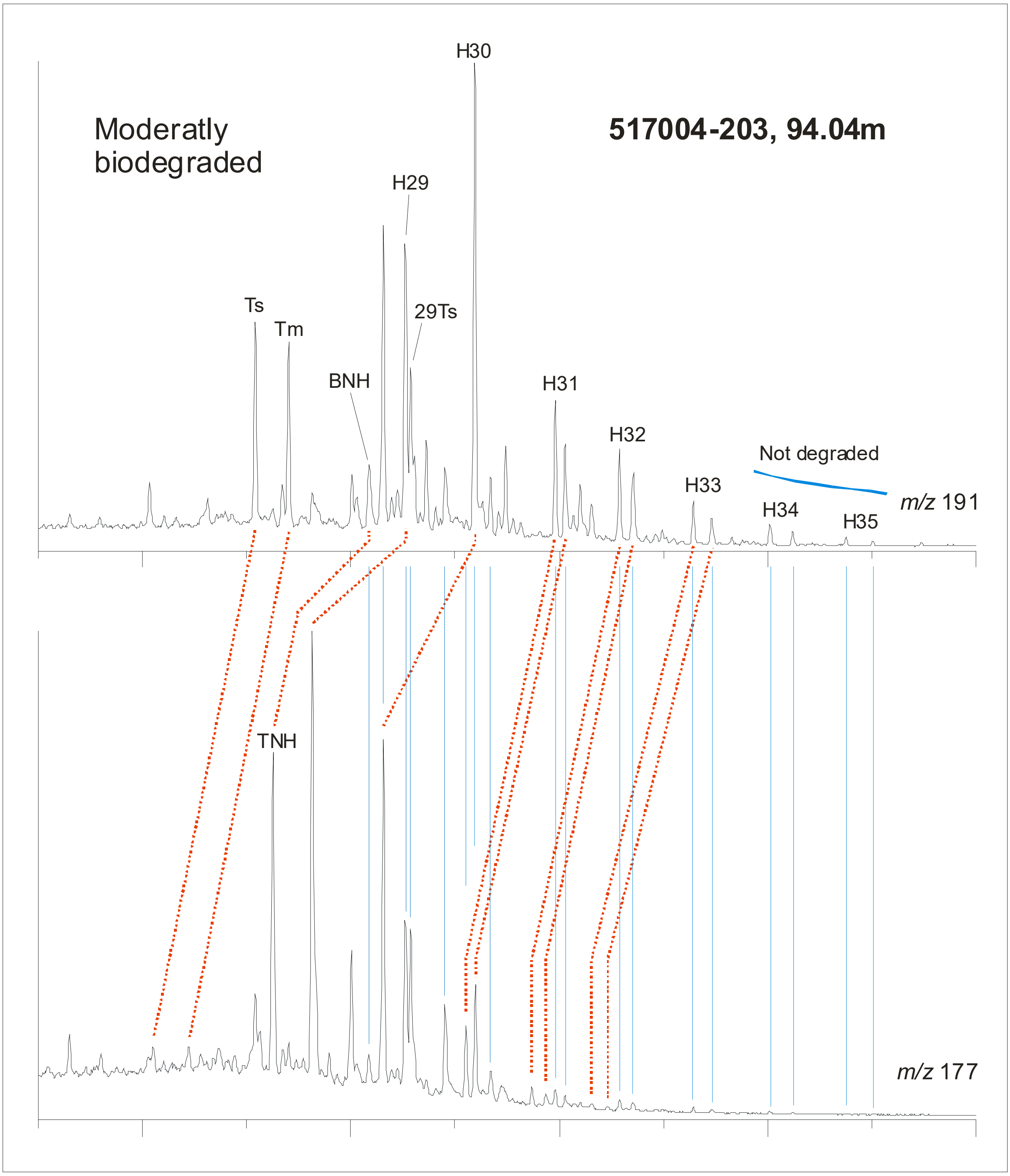

Figure 8.2.6. Hopanes in a moderately biodegraded Nanok oil. Red lines: Degradation of hopanes to 25-norhopanes. Blue lines indicate peaks that yield both m/z 191 and m/z 177 ions.

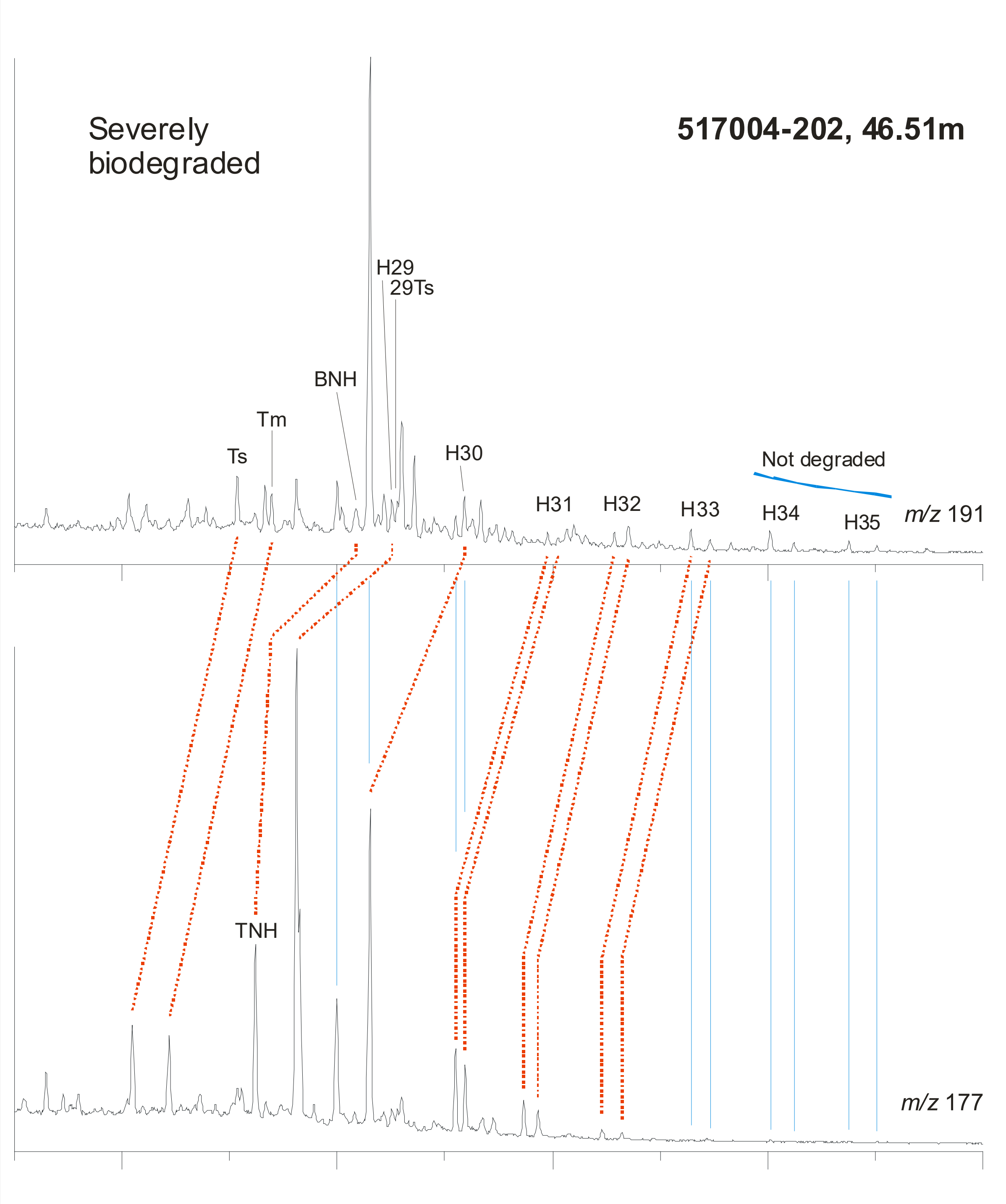

Figure. 8.2.7. Hopanes in a severely biodegraded Nanok oil. Red lines: Degradation of hopanes to 25-norhopanes. Blue lines indicate peaks that yield both *m/z* 191 and *m/z* 177 ions.

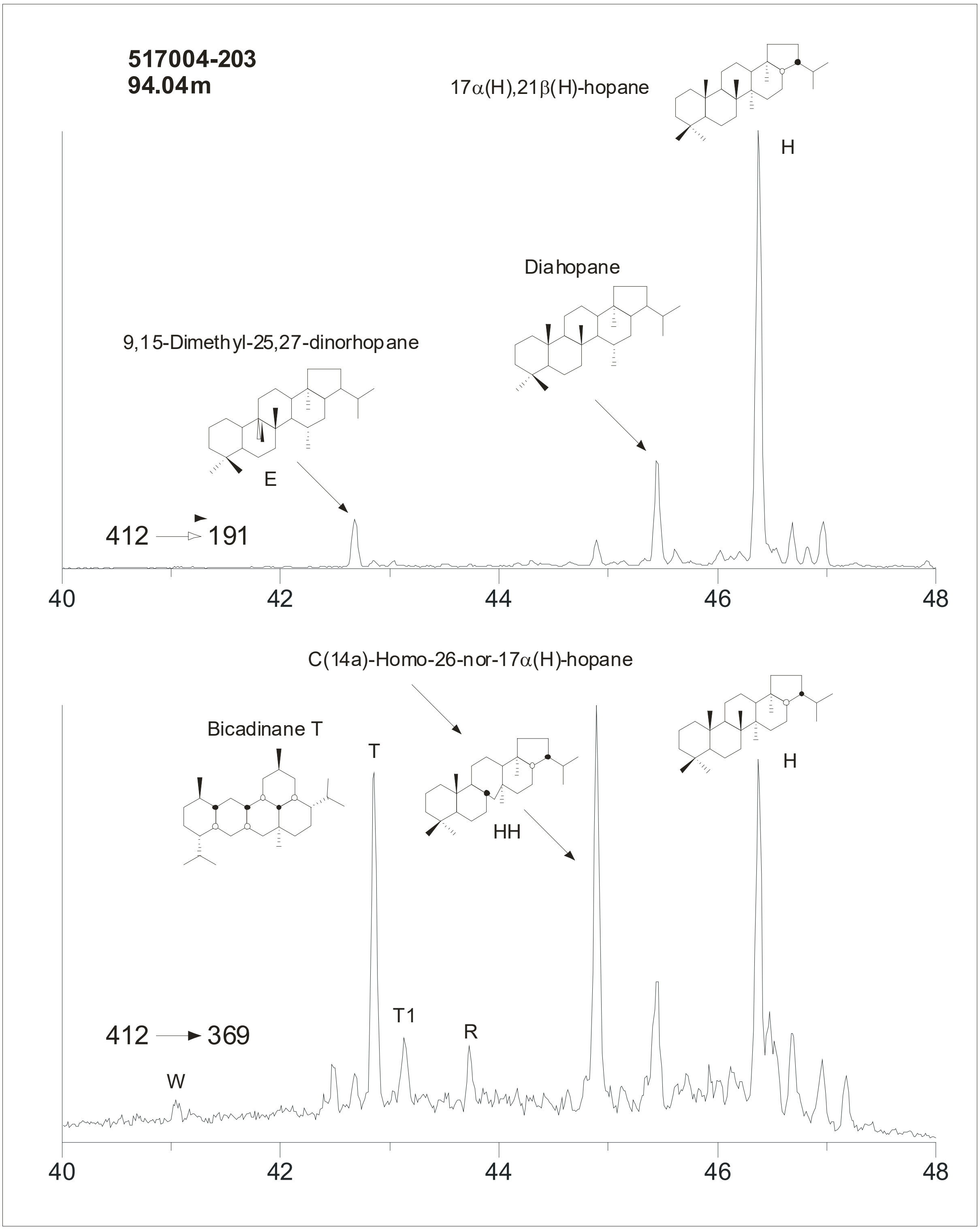

Figure 8.2.8. Bicadinanes and C_{30} hopanes in a moderately biodegraded Nanok oil.

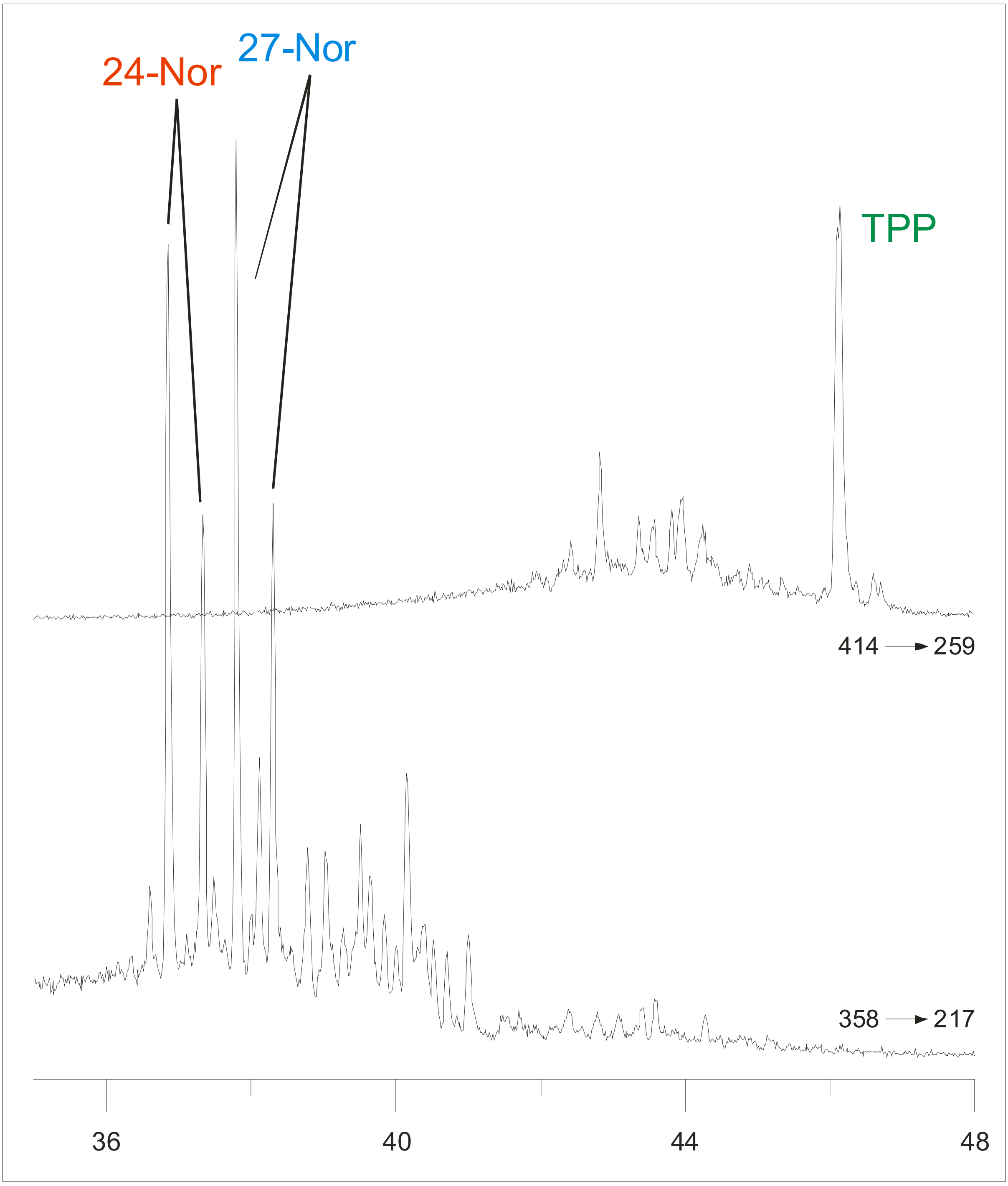

Figure 8.2.9. Nordiacholestanes and TPP in bitumen (same scale) near the Nanok-1 well (475135).

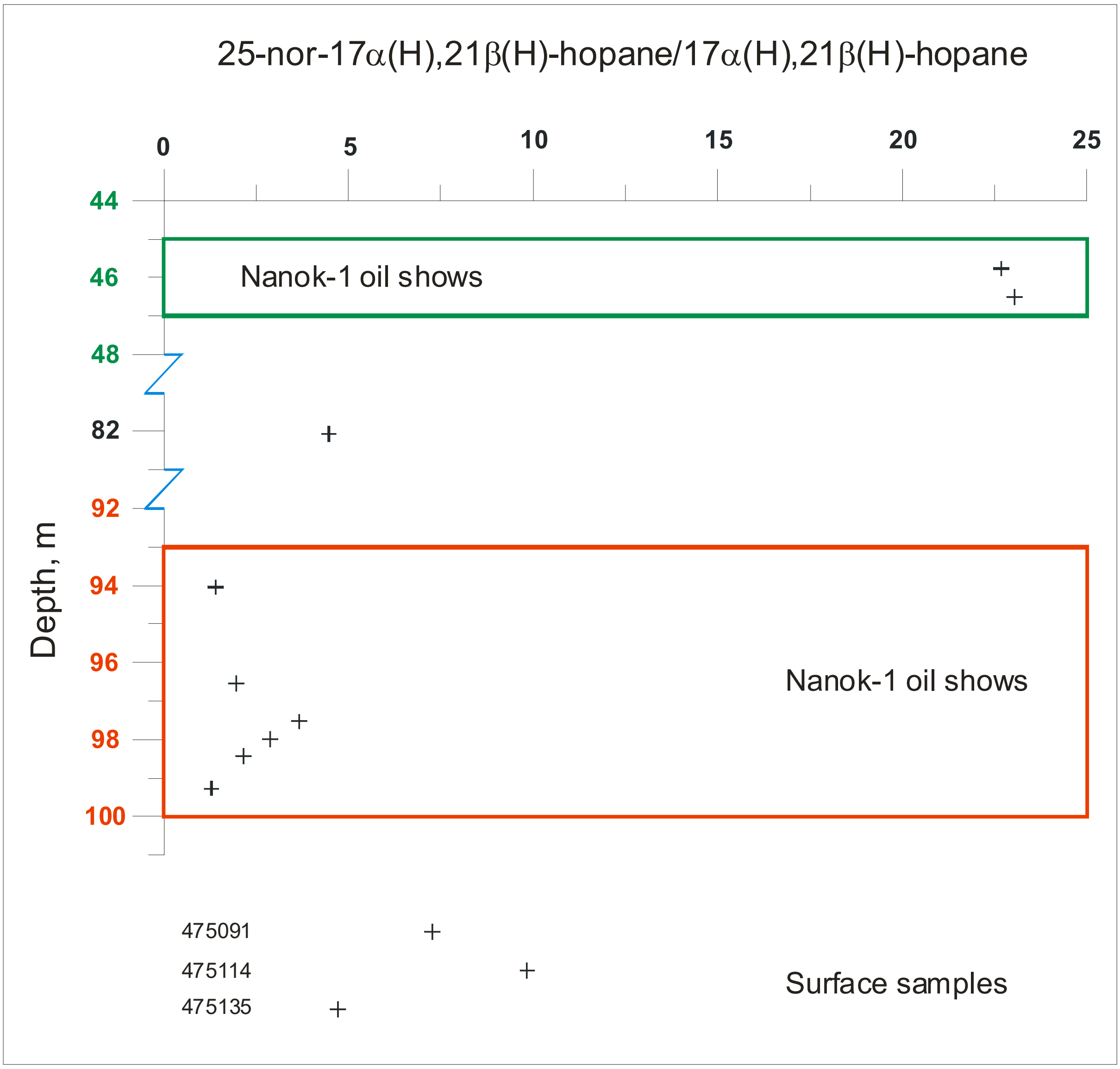

Figure 8.2.10. Biodegradation of 17α(H),21β(H)-hopane to the corresponding 25-norhopane in Nanok oils.

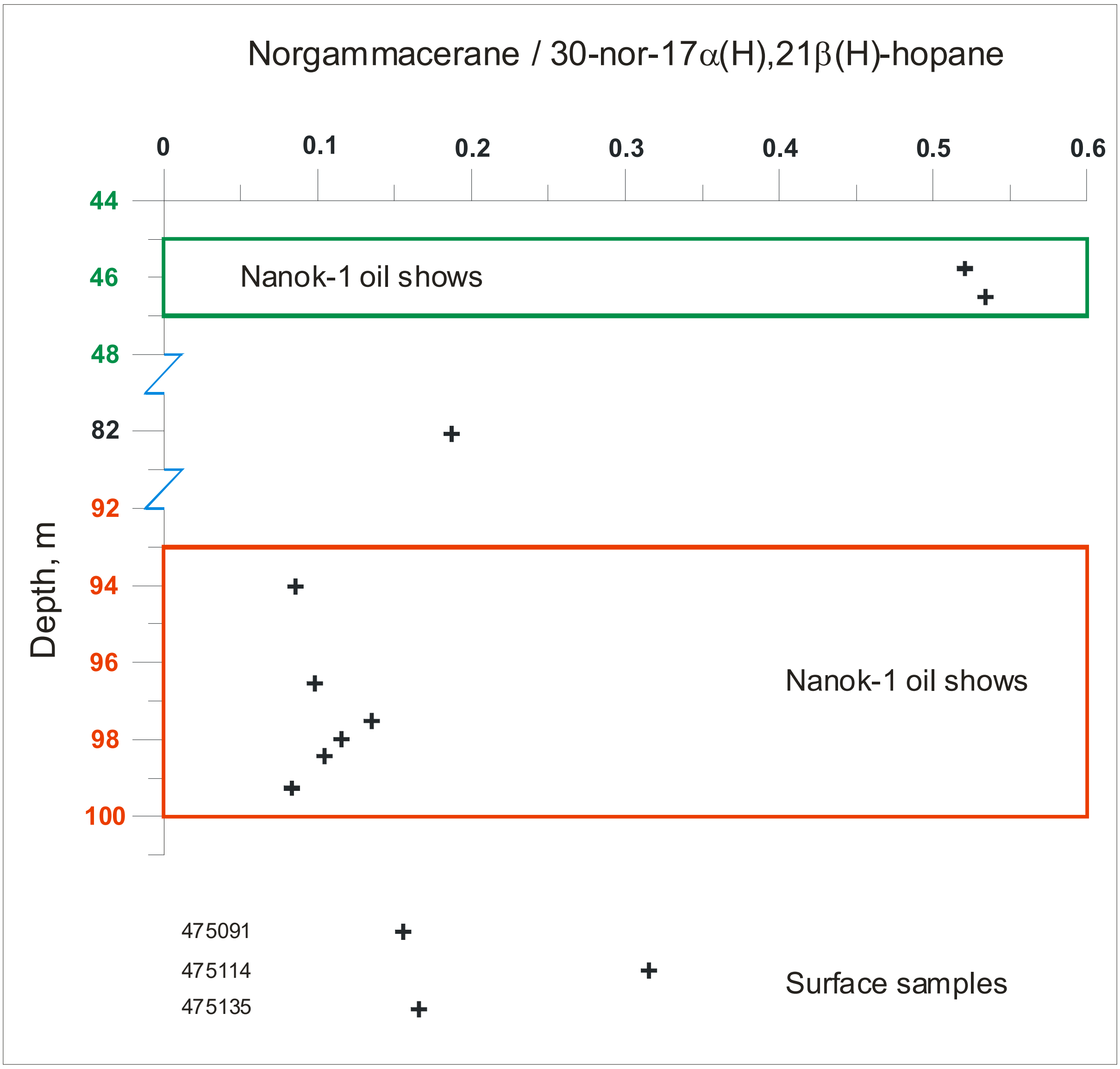

Figure 8.2.11. 30-nor-17α(H),21β(H)-hopane (degraded) vs. norgammacerane (not degraded) in Nanok-1 oils.

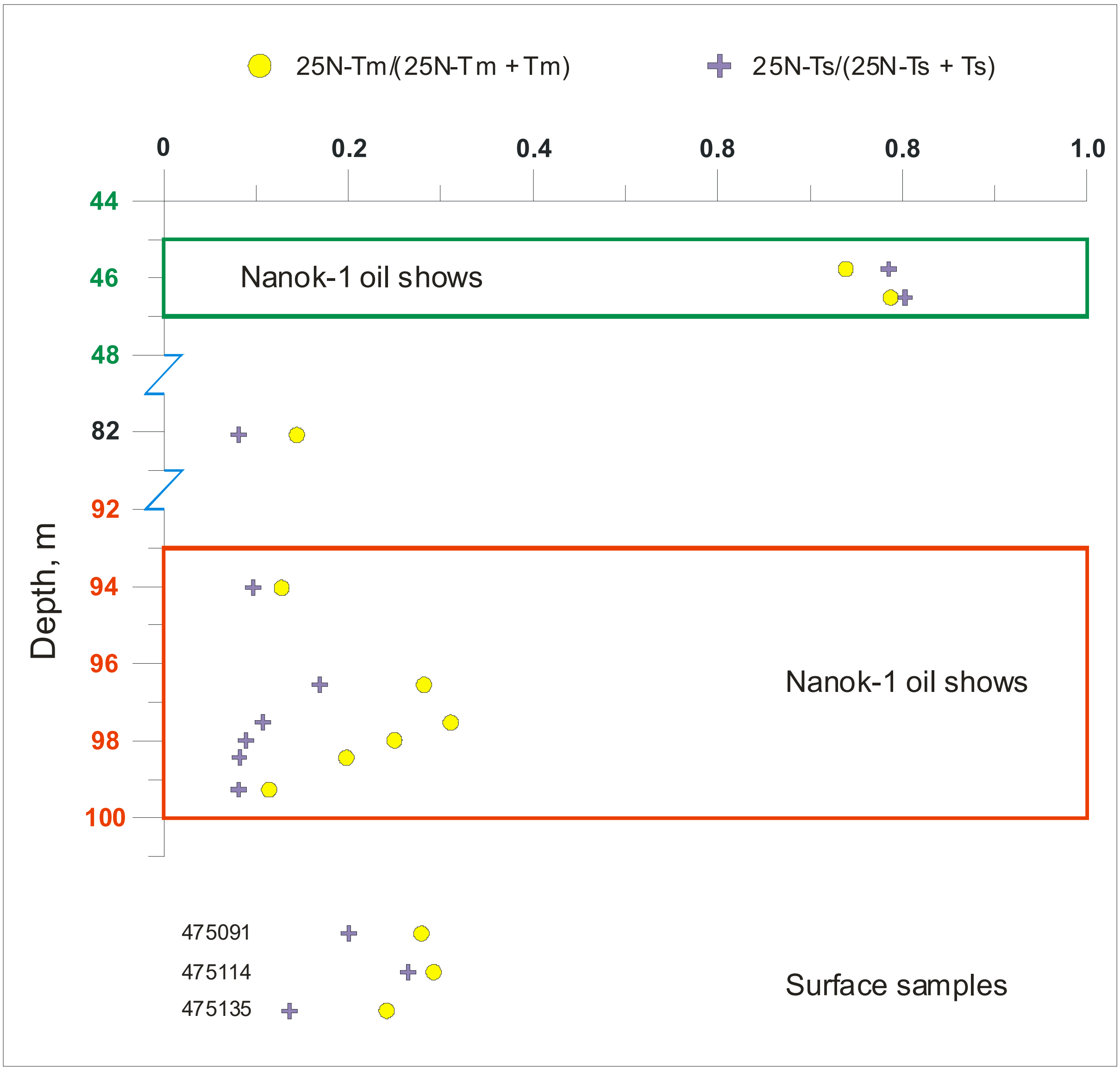

Figure 8.2.12. Degradation of 22,29,30-Trisnorhopane (Tm) and 22,29,30 Trisnorneohopane (Ts) to the corresponding C_{26} 25-norhopanes.

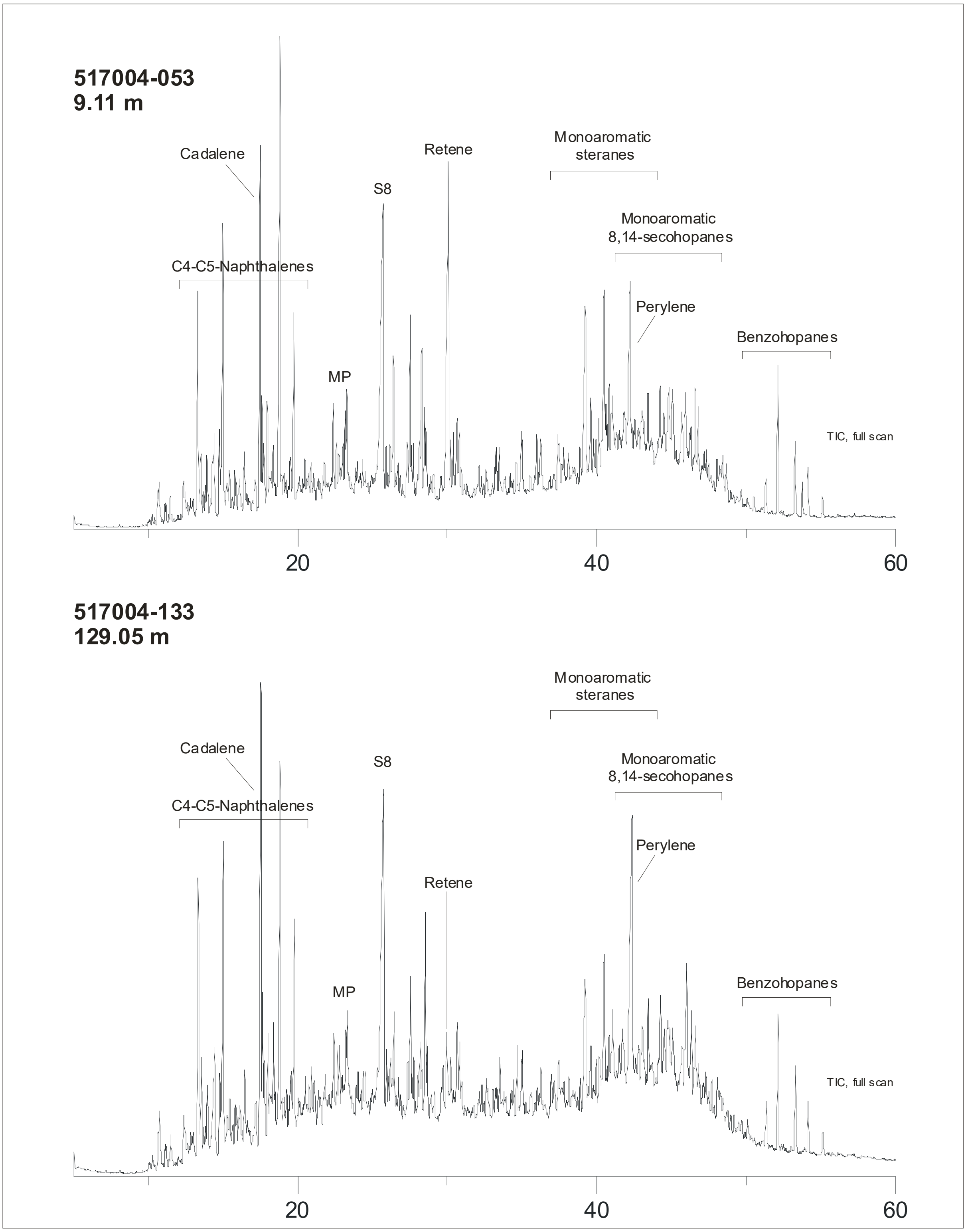

Figure 8.2.13. Aromatic hydrocarbons in two immature shales (TIC, full scan).

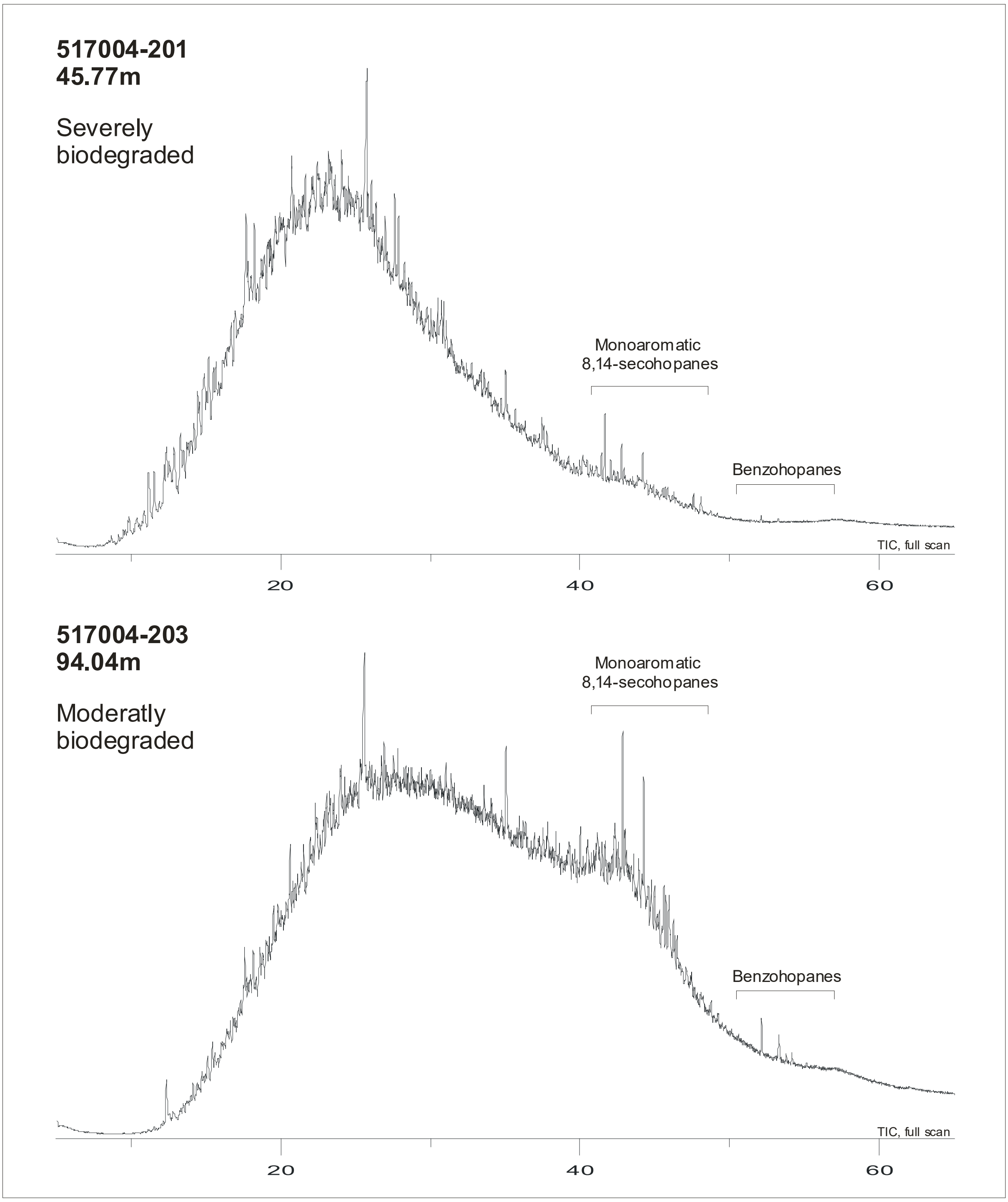

Figure 8.2.14. Aromatic hydrocarbons in two biodegraded Nanok oils (TIC, full scan).

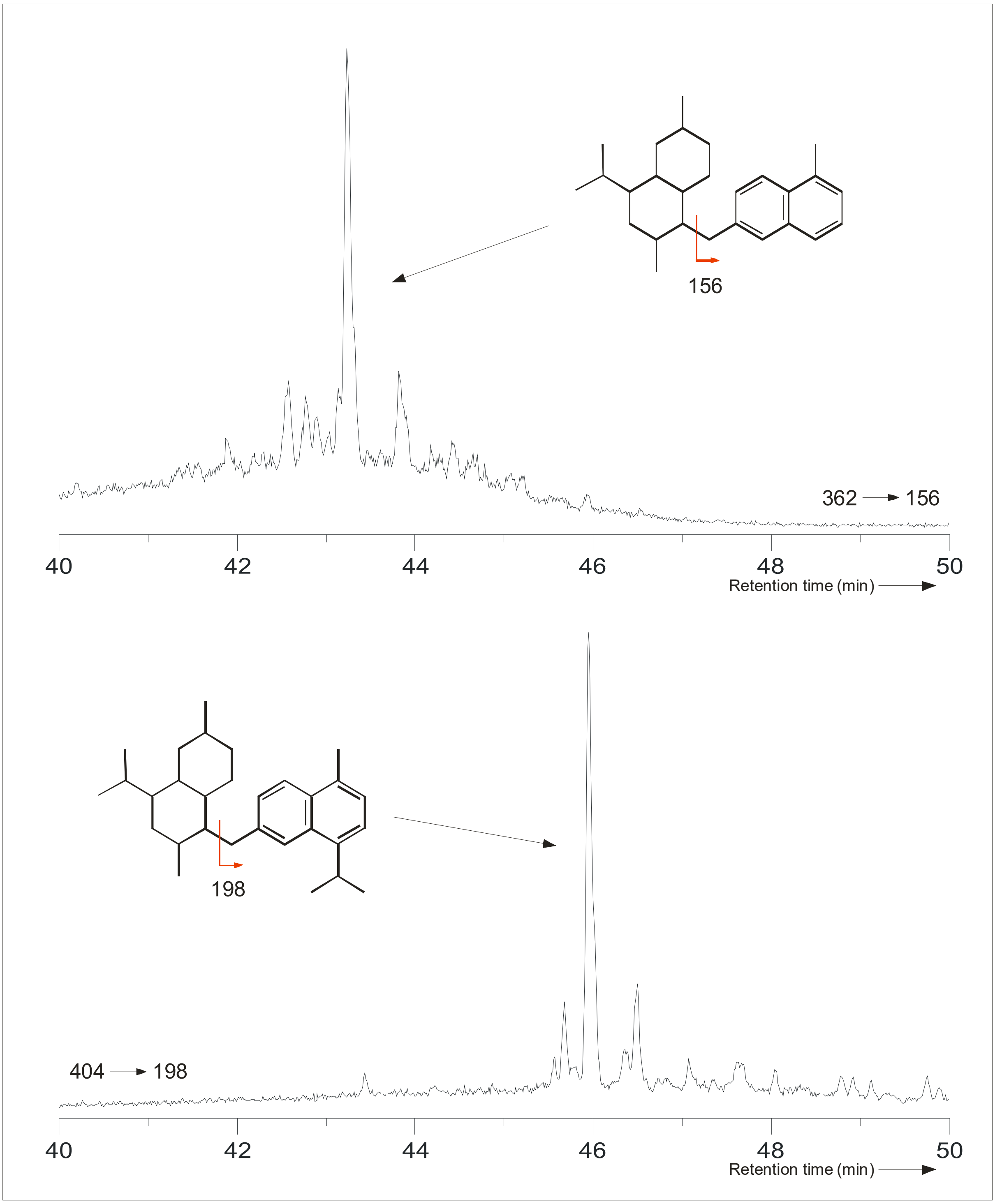

Figure 8.2.15. Diaromatic seco-bicadinanes in a Nanok-1 oil (517004-203, 94.04m).

8.3 Stable Carbon isotope analyses

Stable carbon isotope analyses of saturated, aromatic, polar and asphaltene fractions of 6 solvent extracts from the Brorson Halvø corewell were carried out by APT, Kjeller, Norway. Samples are listed in Table 8.3.1 results are reported in Table 8.3.2.

Galimov-type plots of data from all samples are shown in Figures 8.3.1 and 8.3.2. All oil-stain samples show very similar trends with respect to the relative δ^{13}C-values of saturated, aromatic, polar, and asphaltene fractions:

$$\delta^{13}\mathbf{C}_{\mathbf{(polars)}} \leq \delta^{13}\mathbf{C}_{\mathbf{(saturates)}} \leq \delta^{13}\mathbf{C}_{\mathbf{(aromatics)}} \leq \delta^{13}\mathbf{C}_{\mathbf{(asphalthenes)}}$$

In general, all oil-stain samples are very similar with differences between individual samples exceeding 1 permil δ^{13}C only seen among the asphaltene fractions.

The two shale samples analysed show mutually very similar trends, slightly different from that of the oil stain samples:

$$\delta^{13}\mathbf{C}_{\mathbf{(saturates)}} \leq \delta^{13}\mathbf{C}_{\mathbf{(aromatics)}} \leq \delta^{13}\mathbf{C}_{\mathbf{(polars)}} \leq \delta^{13}\mathbf{C}_{\mathbf{(asphalthenes)}}$$

However, the samples are separated by an difference amounting to approximately 2 permil δ^{13}C in all fractions. Moreover they are less depleted in ^{13}C (i.e. less negative δ^{13}C values), than the oil stain samples, and thus apparently show a somewhat more "terrigenous" isotope composition. This is particularly so with respect to the deeper sample, but due to the very high level of thermal maturity of this sample, data are probably not fully reliable.

A crossplot of $\delta^{13}C_{(saturates)}$ versus $\delta^{13}C_{(aromatics)}$ is shown in Figure 8.3.3. All samples plot close to the broken line that indicates the empirically defined (by Sofer 1984) best separation between "waxy" (*i.e.* terrestrially dominated, above line) and "non-waxy" (*i.e.* marine, below line) oils or extracts.

A crossplot of the "canonical variable", as defined by Sofer (1984) versus pristane/phytane ratio for the Nanok corehole samples is shown in Figure 8.3.4. The broken line indicates the empirically defined (by Sofer 1984) best separation between "waxy" (*i.e.* "terrestrial", above line) and non-waxy (*i.e.* marine, below line) oils/extracts. All samples plot in the non-waxy field, but high pristine/phytane ratios indicate terrestrial influence

However, plotting the isotopic composition of the total extracts (calculated from the isotopic compositions of the individual extract fractions and the proportions of the same fractions in the total extract, since the total extract composition was not measured) versus the pristane/phytane ratio provides a clear indication of the overall source depositional environment, with the stain samples showing a somewhat lesser terrestrial signal than the shales, although the general depositional environment is classified as terrestrially influenced marine or "deltaic" (Fig. 8.3.5, after Chung *et al.*, 1992).

In summary, stable Carbon isotopic data indicate an overall terrestrially influenced marine or "deltaic" depositional environment for all samples. All stain samples show very similar composition. The shale samples yield slightly more terrestrial signals compared to the stain samples, which is in keeping with the assumption that the oil was primarily generated by more marine shales closer to the intrusion encountered at the base of the corehole. Due to high levels of maturity these deposits do not lend themselves to analysis. See section 8 on "Petroleum Geochemistry" for discussion.

8.3.1 References

Chung, H. M., Rooney, M. A., Toon, M. B. & Claypool, G. E. 1992: Carbon isotope composition of marine crude oils. AAPG Bulletin, **76**, 1000-1007

Galimov, E. M. & Ivlev, A. A.1973: Thermodynamic isotope effects in organic compounds. I. Carbon isotope effects in straight-chain alkanes. Russian Journal of Physics, **47**, 1564-1566

Sofer, Z. 1984: Stable carbon isotope compositions of crude oils; application to source depositional environments and petroleum alteration. AAPG Bulletin, **68**, 31-49

Sample	Depth	Lab.#	Sample type
517004-202	46,51	20903	Oil stain, uppermost part of Østersletten Mb. sandstone
517004-089	82,07	20823	Oil stain, inertinite-rich interval, lower part of Østersletten Mb.
517004-204	96,55	20905	Oil stain, sandstone intercalation in Fosdalen Fm.
517004-208	99,27	20909	Oil stain, sandstone intercalation in Fosdalen Fm.
517004-146	140,99	20880	Shale extract
517004-156	149,78	20890	Shale extract

Table 8.3.1. Samples analysed.

Sample	Depth	Lab.#	δ^{13}C-Sat	δ^{13}C-Aro	δ^{13}C-Pol	δ^{13}C-Asp	δ^{13}-total	CV
517004-202	46,51	20903	-27,1	-26,6	-27,3	-26,1	-26,99	-2,14
517004-089	82,07	20823	-27,2	-26,5	-27,3	-26,7	-27,07	-1,66
517004-204	96,55	20905	-27,7	-26,9	-27,7	-27,4	-27,48	-1,29
517004-208	99,27	20909	-27,6	-27,0	-28,0	-27,6	-27,48	-1,76
517004-146	140,99	20880	-27,9	-26,6	-26,3	-25,7	-26,41	-0,12
517004-156	149,78	20890	-25,9	-25,4	-24,9	-24,2	-24,93	-2,51

Table 8.3.2. Stable Carbon isotope data for oil stains and shale extracts from the Nanok-1 corewell. Canonical variable (CV) according to Sofer (1984). Total extract isotopic composition was calculated from the isotopic signatures of the individual extract fractions (asphaltenes, saturates, aromatics, NSO's) and the proportions of the same fractions in the total extract.

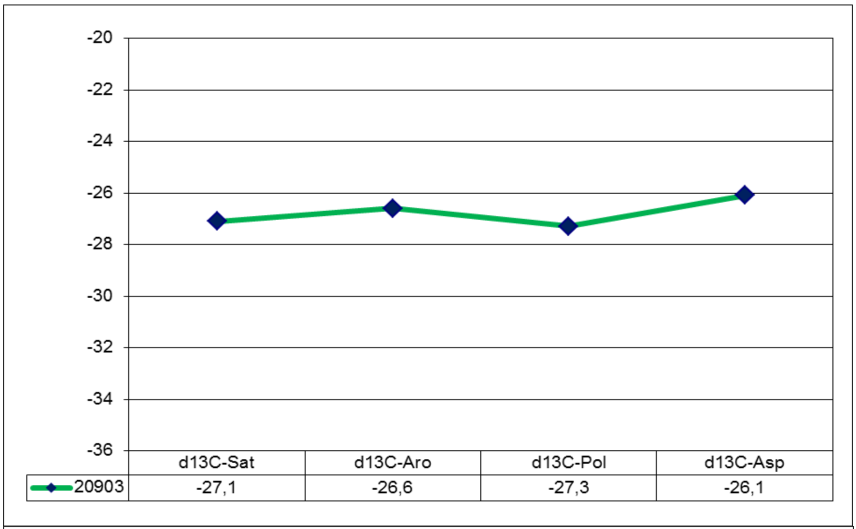

	d13C-Sat	d13C-Aro	d13C-Pol	d13C-Asp
20903	-27,1	-26,6	-27,3	-26,1

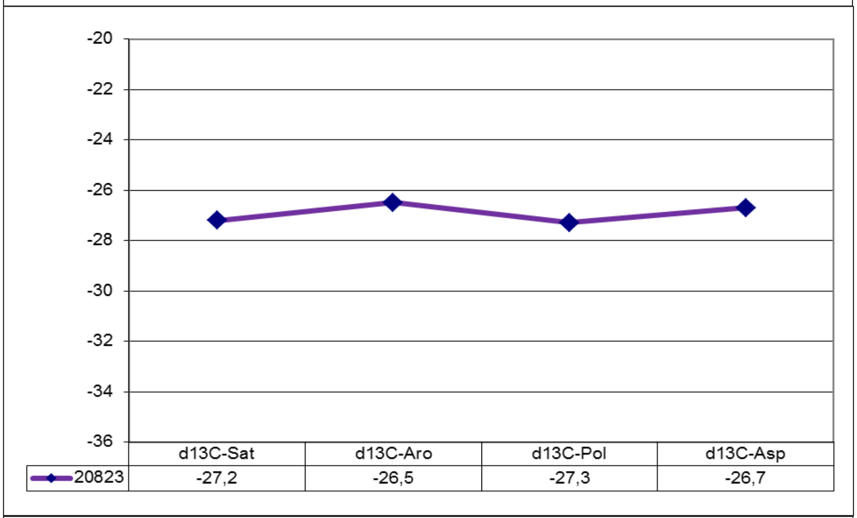

	d13C-Sat	d13C-Aro	d13C-Pol	d13C-Asp
20823	-27,2	-26,5	-27,3	-26,7

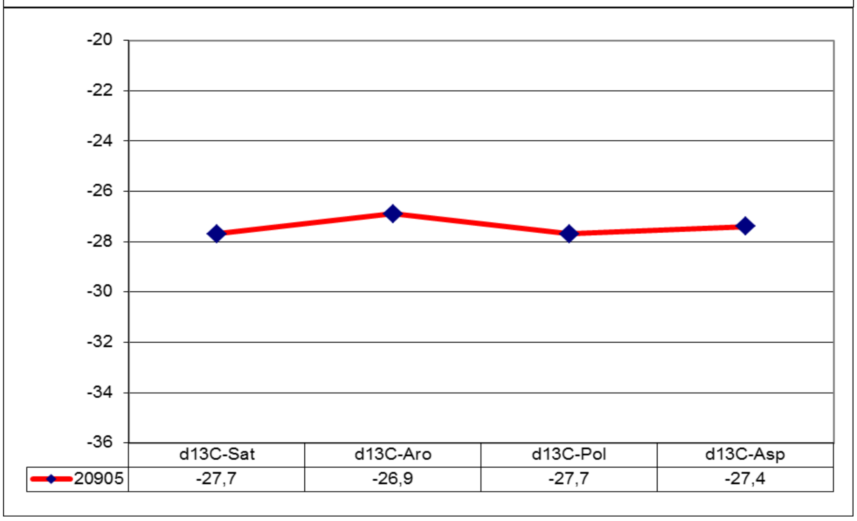

	d13C-Sat	d13C-Aro	d13C-Pol	d13C-Asp
20905	-27,7	-26,9	-27,7	-27,4

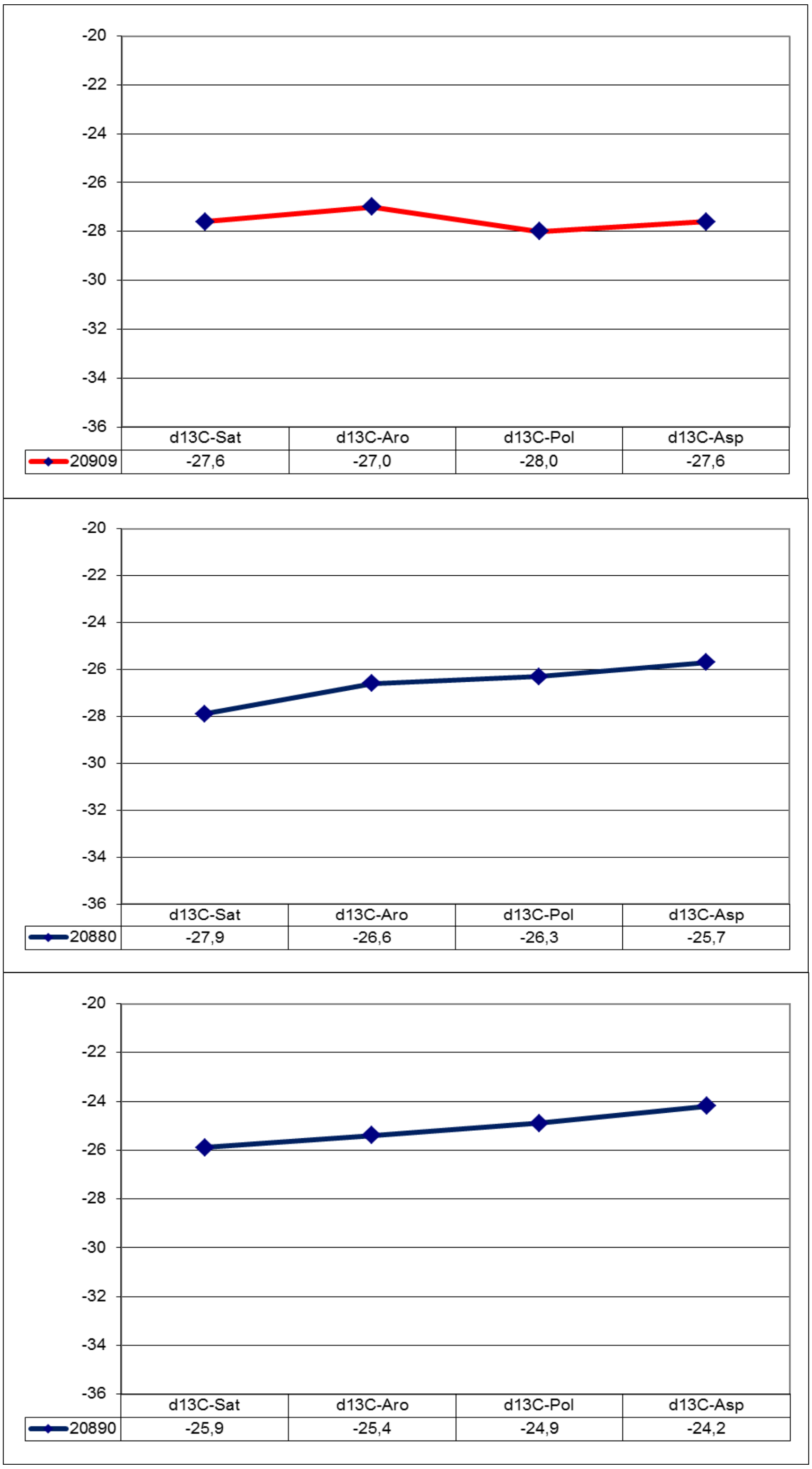

Figure 8.3.1. Galimov-type plots of stable carbon isotope data for oil stains and shale extracts from the Nanok-1 corewell. Horizontal axis: extract fraction, vertical axis δ^{13}C. Note shale sample lab.# 20890 and to a lesser extent shale sample lab.# 20880 show slightly more "terrigenous signal" than the oil stains. For sample identification, see Table 8.3.1. Plot modified from Galimov & Ivlev (1973).

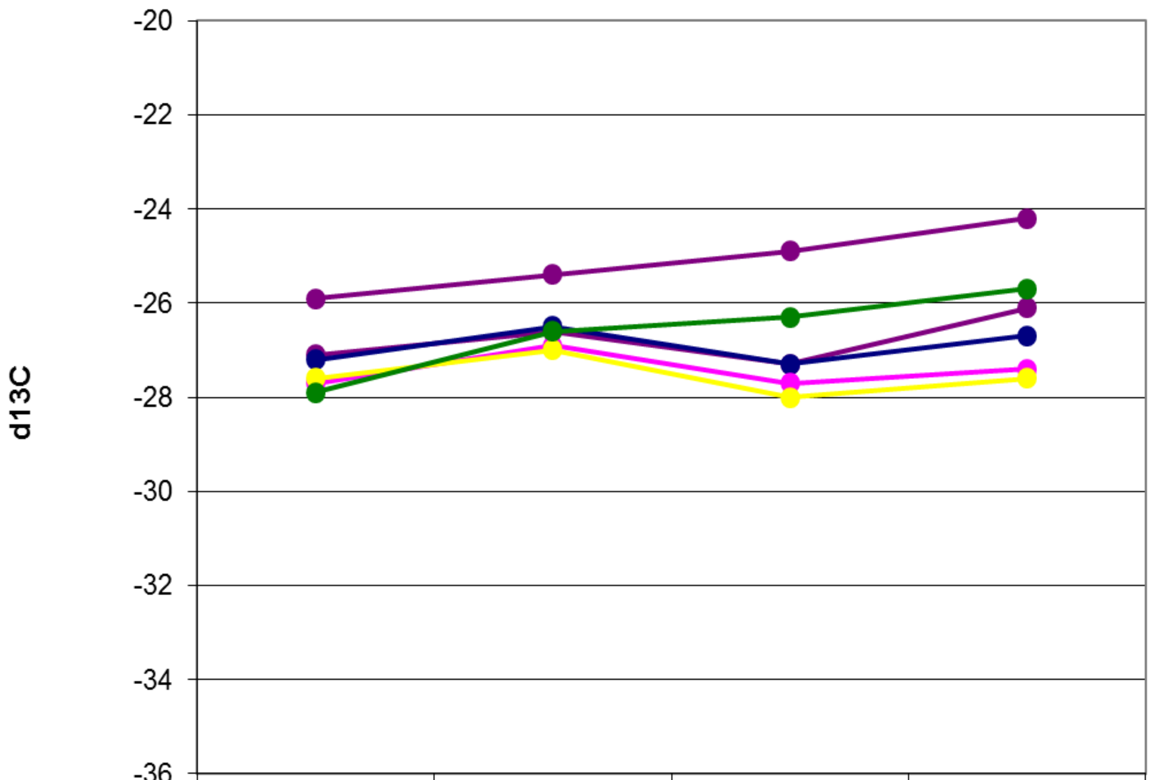

	d13C-Sat	d13C-Aro	d13C-Pol	d13C-Asp
20903	-27,1	-26,6	-27,3	-26,1
20823	-27,2	-26,5	-27,3	-26,7
20905	-27,7	-26,9	-27,7	-27,4
20909	-27,6	-27,0	-28,0	-27,6
20880	-27,9	-26,6	-26,3	-25,7
20890	-25,9	-25,4	-24,9	-24,2

Figure 8.3.2 Galimov-type plots of stable carbon isotope data for oil stains and shale extracts from the Nanok-1 corewell. Horizontal axis: extract fraction, vertical axis $\delta^{13}C$. Note shale sample lab.# 20890 and to a lesser extent shale sample lab.# 20880 show slightly more “terrigenous signal” than the oil stains. For sample identification, see Table 8.3.1. Plot modified from Galimov & Ivlev (1973).

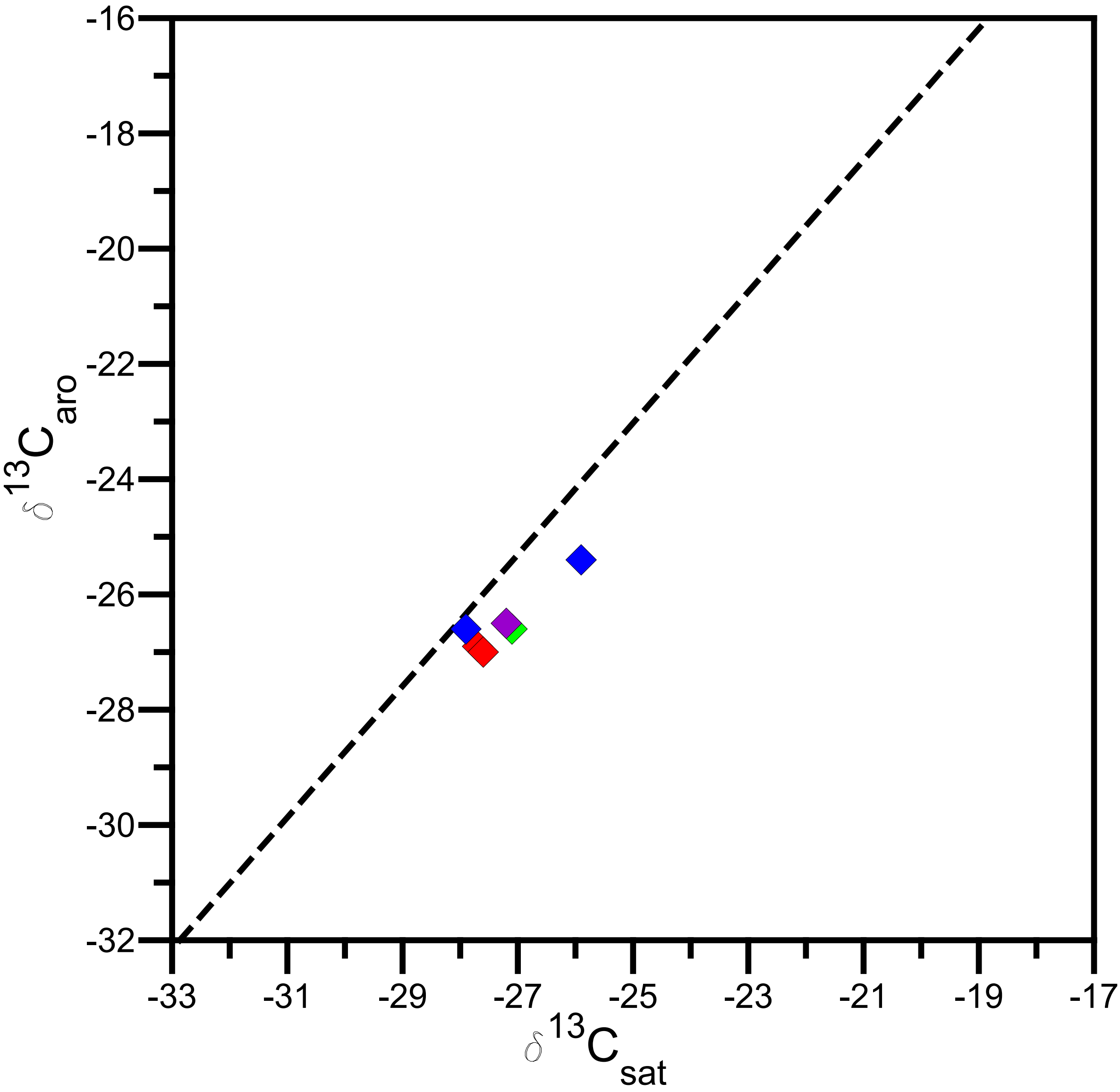

Figure 8.3.3. $\delta^{13}C_{(saturates)}$ *versus* $\delta^{13}C_{(aromatics)}$ for oil stains and shale extracts from the Nanok-1 corewell. Broken line indicates the empirically defined best separation between "waxy" (above line) and non-waxy (below line). Green symbol: upper oil stained sandstone (46.51m), purple symbol: Stained inertinite-rich layer (82.07m), Red symbol: lower oil stained sandstone (96.55m and 99.27m), blue symbol Shale extracts (140.99m and 149.78m). Adapted from Sofer (1984)

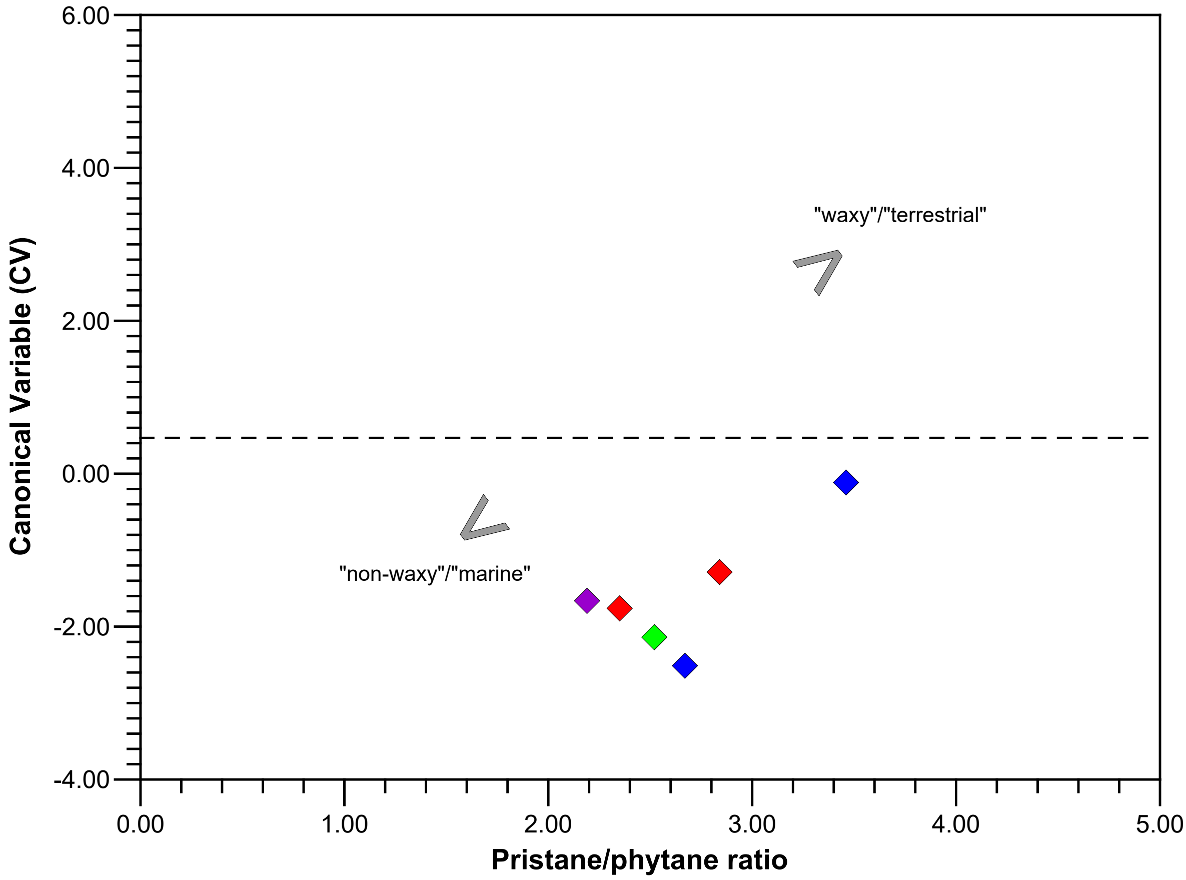

Figure 8.3.4. Canonical variable, as defined by Sofer (1984) *versus* pristane/phytane ratio for oil stains and shale extracts from the Nanok-1 corewell. Green symbol: upper oil stained sandstone (46.51 m), purple symbol: Stained inertinite-rich layer (82.07 m), Red symbol: lower oil stained sandstone (96.55 m and 99.27 m), blue symbol Shale extracts (140.99 m and 149.78 m). Broken line indicates the empirically defined best separation between “waxy” (above line) and non-waxy (below line) oils/extracts. Adapted from Sofer (1984)

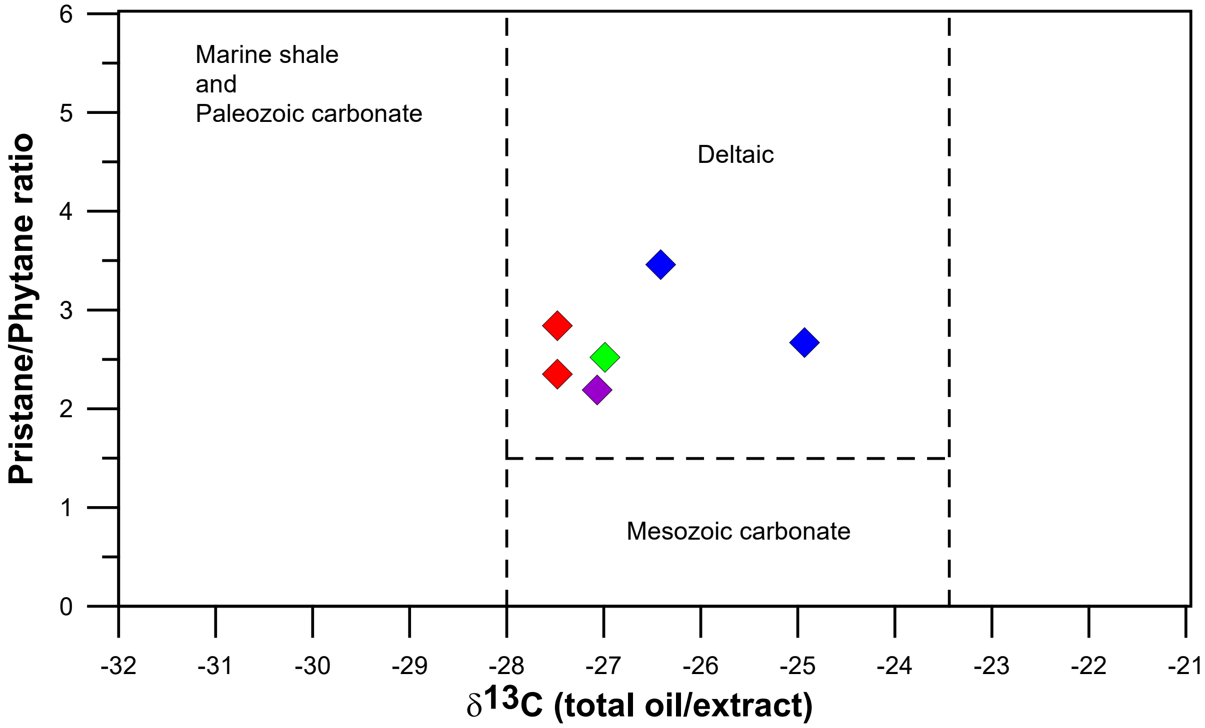

Figure 8.3.5. Carbon isotopic composition versus pristane/phytane ratio for oil stains and shale extracts from the Nanok-1 corewell. Note that the δ^{13}C values are calculated based on the isotopic signatures of individual solvent fractions (asphaltenes, saturates, aromatics and NSO's) and the proportions of the same fractions in the total extracts. Green symbol: upper oil stained sandstone (46.51 m), purple symbol: Stained inertinite-rich layer (82.07 m), Red symbol: lower oil stained sandstone (96.55 m and 99.27 m), blue symbol Shale extracts (140.99 m and 149.78 m). Plot modified from Chung *et al.* (1992).

8.4 Headspace gas analysis

Samples for headspace gas analysis include 8 core-pieces evenly spaced throughout the drilled succession. Core pieces were placed in airtight containers at the wellsite immediately after retrieval of each core-section. Compositional and isotopic data on headspace gas from the containers were produced by APT, Kjeller, Norway (Appendix 12.7).

Data are listed in Tables 8.4.1 and 8.4.2.

The gas composition is dominated by Nitrogen that constitutes from app. 78 vol-% to 96 vol-% of the total headspace gas. Hydrocarbon gas (C_1-C_5) concentrations are variable, ranging from zero to 4.1 vol-% (Fig. 8.4.1).

In terms of wetness, the gas composition is very dry.

Due to gas dryness and low concentration of HC gases in some samples the analytical dataset is not complete. This is particularly with respect to isotopic data. Based on combined compositional and isotopic data (Fig. 8.4.2) all gas seems to be microbial in origin. The Carbon versus Hydrogen isotopic crossplot (Fig. 8.4.3) corroborates this result.

The stable isotopic composition of carbon dioxide ranges from -14 to +0.4 (Fig. 8.4.4). The isotopic signature in the upper part of the well may perhaps represent a mixture of CO_2 from microbial oxydation of methane and atmospheric CO_2 (Whiticar 1999).

8.4.1 References

Bernard, B. B., Brooks, J. M. & Sackett, W. M. 1978: Light hydrocarbons in recent Texas continental slope sediments. Journal of Geophysical Research, **83**, 4053–4061.

Schoell, M. 1983: Genetic classification of natural gases. AAPG bulletin, **67**, 2225–2238.

Peters, K. E., Walters, C. C. & Moldowan, J. M. 2005: The Biomarker Guide, volumes 1+2, 1155pp. Cambridge University Press.

Whiticar, M. J. 1999: Carbon and hydrogen isotope systematics of bacterial formation and oxidation of methane. Chemical Geology, **161**, 291–314.

Sample	Depth (m)	C1 (%)	C2 (%)	C3 (%)	iC4 (%)	nC4 (%)	iC5 (%)	nC5 (%)	C6+ (%)
517004-1	38,51	1,2	0	0	0	0	0	0	0
517004-3	50,65	0,0	0	0	0	0	0	0	0
517004-4	84,73	55,0	0,091	0	0	0	0	0	0
517004-6	95,45	18,6	0,034	0	0	0	0	0	0
517004-9	108,60	57,0	0,049	0	0	0	0	0	0
517004-11	118,96	81,6	0,055	0	0	0	0	0	0
517004-13	135,33	90,7	0,069	0	0	0	0,024	0,011	0
517004-15	143,67	2,1	0	0	0	0	0	0	0

Sample	Depth (m)	HC (%)	CO2 (%)	H2 (%)	N2 (%)	O2+Ar (%)	ppm Total	Wetness
517004-1	38,51	0,0	2,6	3,5	91,0	2,9	975056	
517004-3	50,65	0,0	0,4	0,2	79,7	19,7	981171	
517004-4	84,73	0,6	0,5	1,4	95,7	1,8	971153	0,17
517004-6	95,45	0,7	3,1	0,4	94,1	1,7	972281	0,19
517004-9	108,60	2,7	2,0	0,3	93,4	1,6	973369	0,086
517004-11	118,96	3,0	0,7	1,8	92,8	1,8	972832	0,068
517004-13	135,33	4,1	0,4	2,9	90,5	2,1	973259	0,076
517004-15	143,67	0,0	0,1	0,1	78,3	21,5	981818	

Table 8.4.1. Compositional data on headspace gases from 8 corepieces. Gas composition in vol-% of total.

Sample	Depth (m)	C_1 $\delta^{13}C$	C_2 $\delta^{13}C$	C_2 $\delta^{13}C$	i-C_4 $\delta^{13}C$	n-C_4 $\delta^{13}C$	i-C_5 $\delta^{13}C$	n-C_5 $\delta^{13}C$	CO_2 $\delta^{13}C$	C_1 δD
517004-1	38,51	-66,6							-5,4	-276
517004-3	50,65								-6	
517004-4	84,73	-70,4							-9,7	-288
517004-6	95,45	-72,9							-13,8	-265
517004-9	108,60	-68							-4,7	-266
517004-11	118,96	-69,3							-8,2	-282
517004-13	135,33	-67,9							0,4	-288
517004-15	143,67								-12,4	

Table 8.4.2. Head space gas isotopic data.

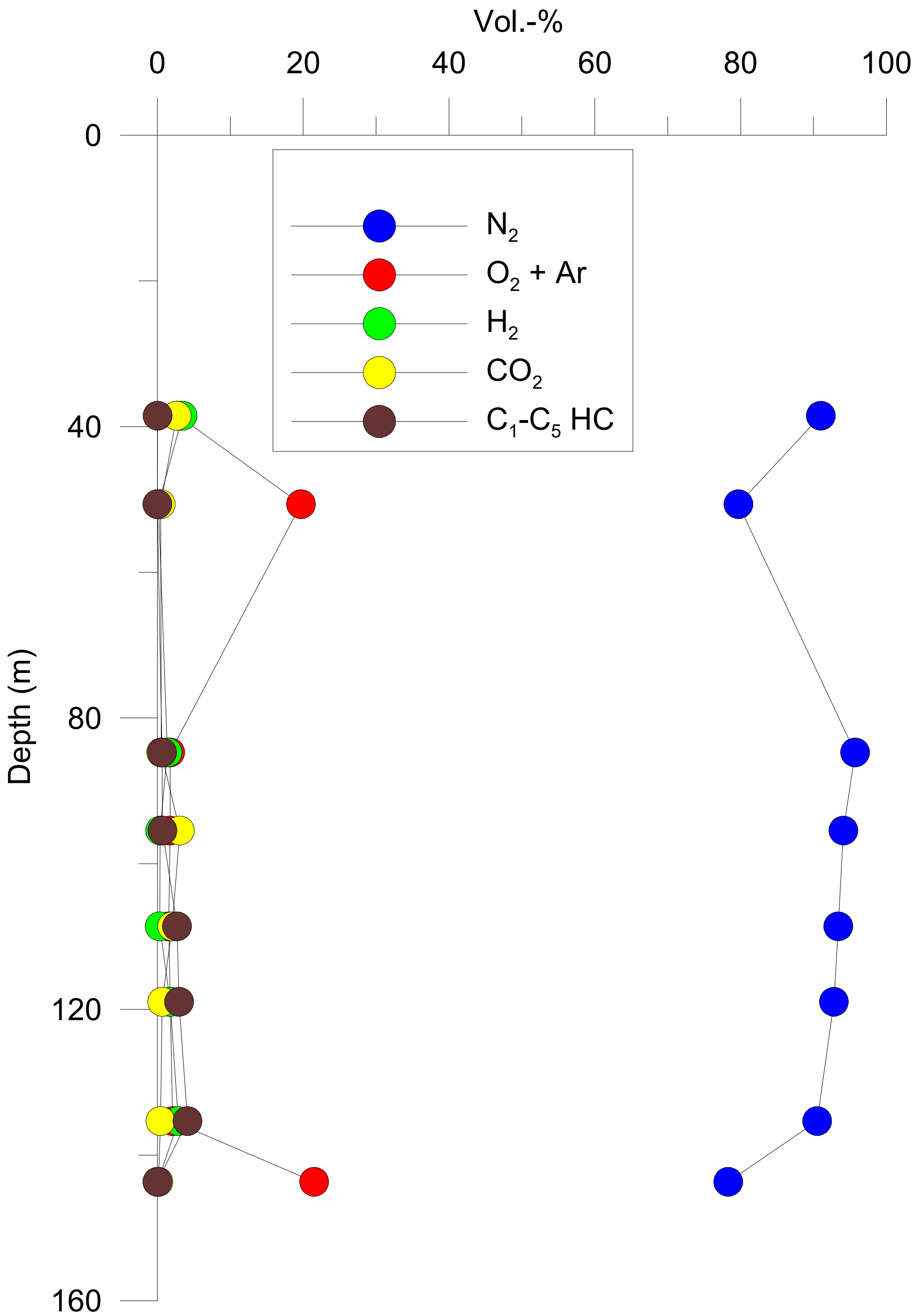

Figure 8.4.1. Total headspace gas composition.

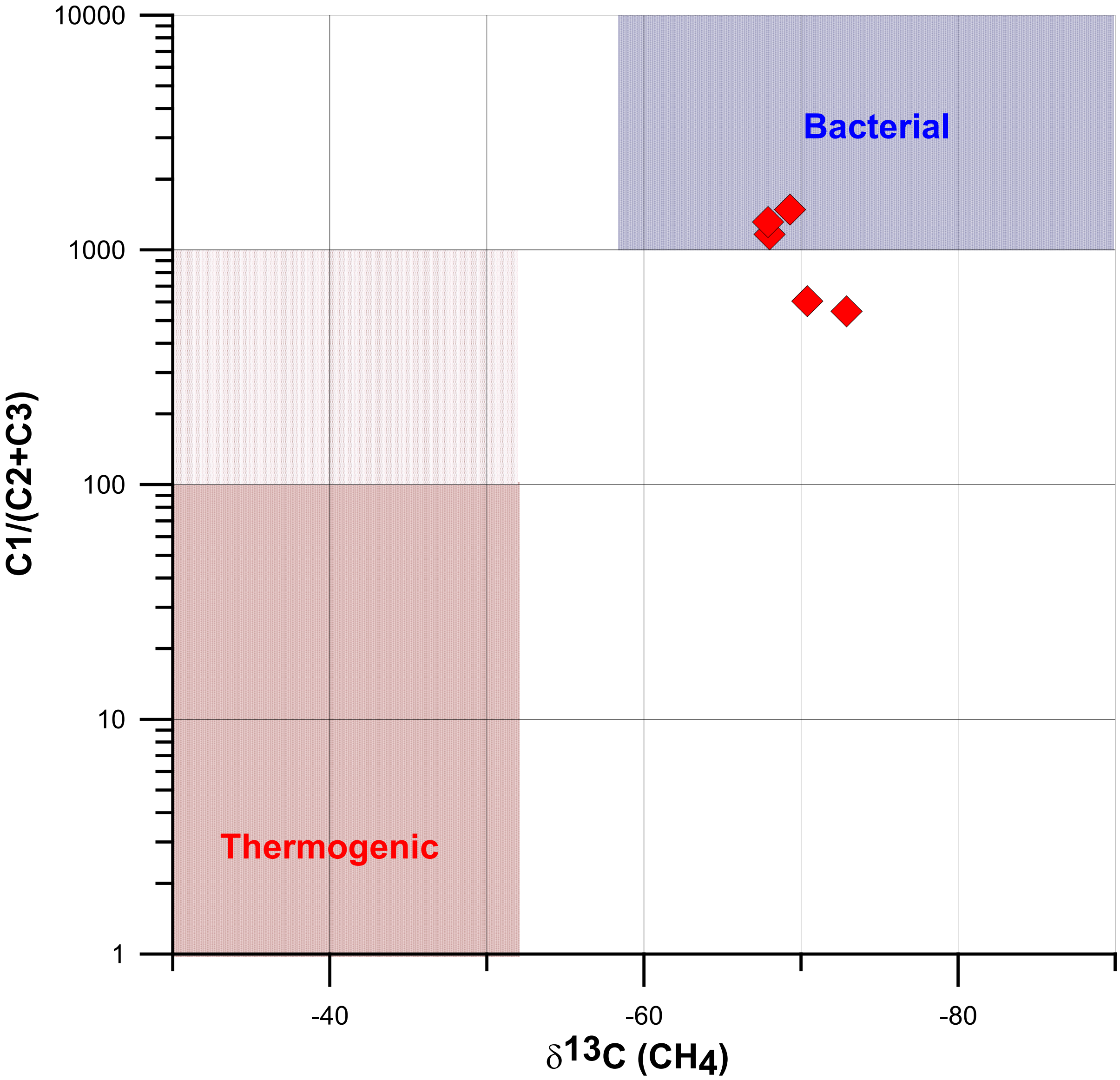

Figure 8.4.2. Bernard-plot. Based on combined isotopic and compositional data, the origin of gases is biogenic. Plot adapted from Bernard *et al.* (1978)

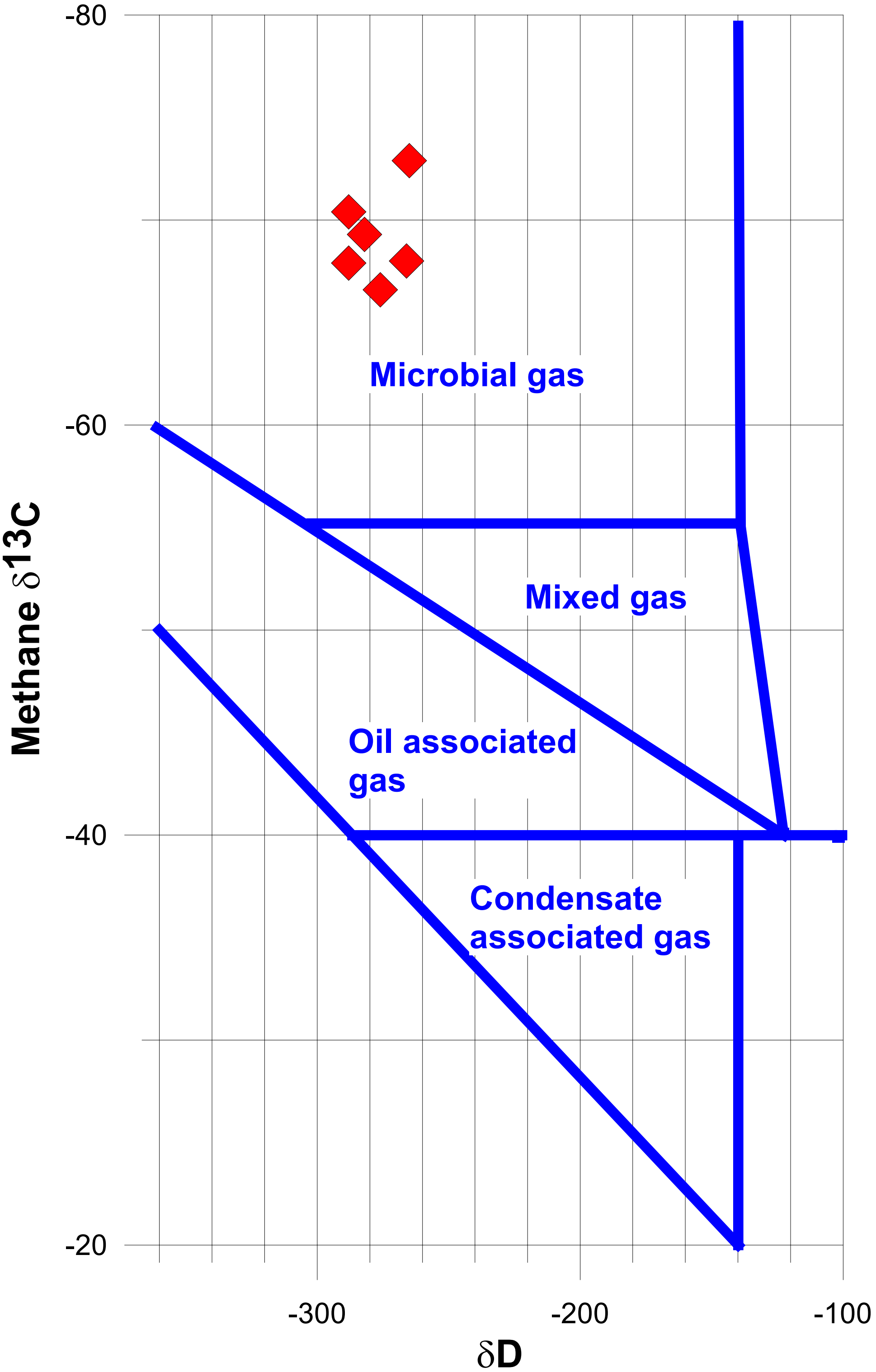

Figure 8.4.3. Methane Hydrogen versus Carbon isotopic composition. Microbial gases are present throughout the drilled succession. Plot adapted from Schoell (1983) and Peters *et al.* (2005)

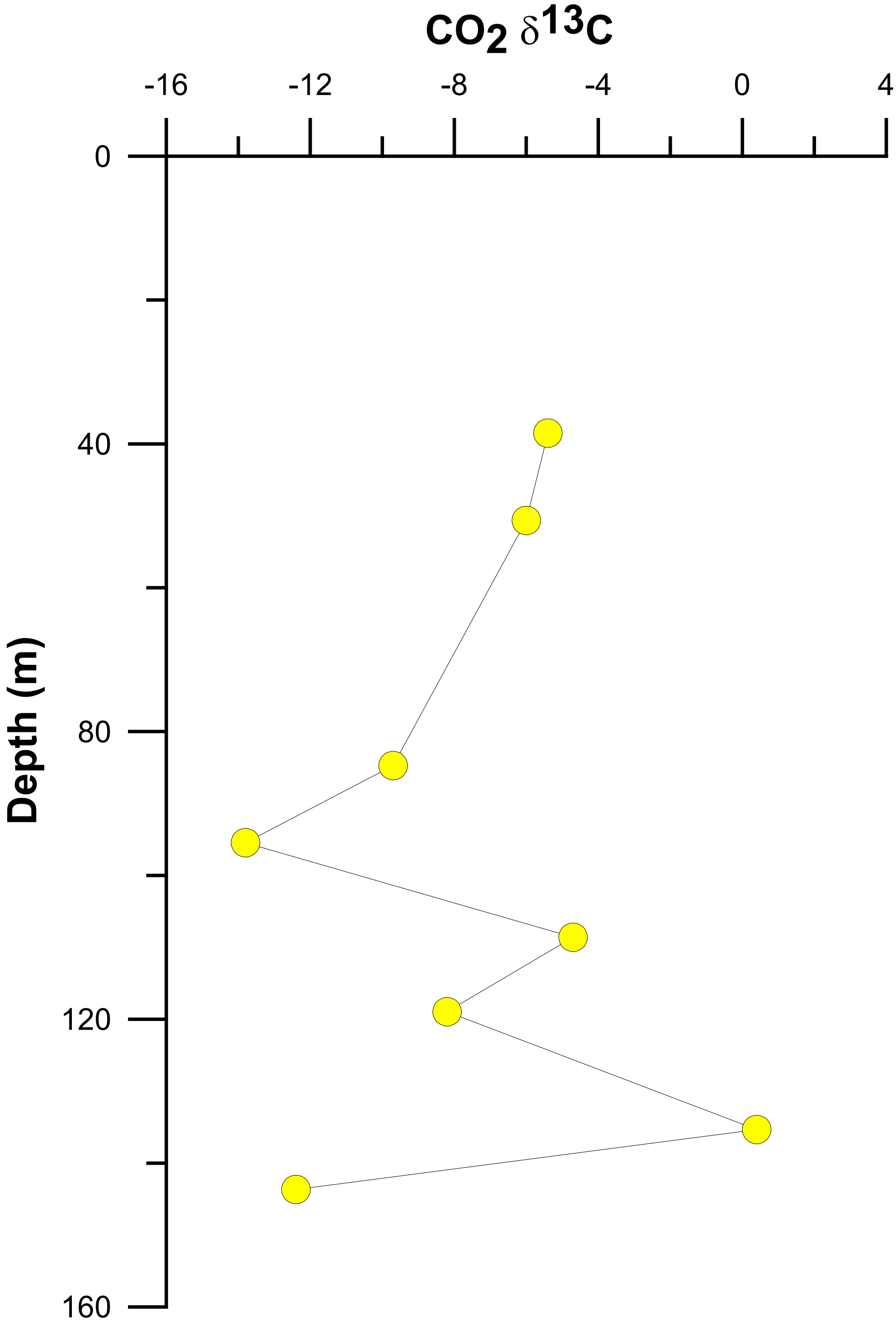

Figure 8.4.4. Stable carbon isotope composition of CO2.

9. Interpreted thermal history based on AFTA and VR data

9.1 Introduction

A single sample of core from the Nanok-1 borehole was collected for apatite fission-track analysis (AFTA). The borehole intersected ~167 metres of Upper Cretaceous (Cenomanian–Campanian) section, containing a 40 m thick sandstone unit (Østerssletten Member) from which sample GC1104-24 was collected for AFTA. The analytical details are given in Geotrack Report GC1104. A nearby outcrop sample, GC1016-41, of the same sandstone unit was also analysed for AFTA. The analytical details and the interpretation of that sample are given in Geotrack Report GC1016.

In addition a suite of vitrinite reflectance (VR) values from the borehole (Table 9.1) have been integrated with the thermal history interpretation of AFTA data from sample GC1104-24. The combined dataset are interpreted in terms of the nature of the underlying thermal and tectonic history, within the context of regional results presented in Geotrack Reports GC1077 and GC1104.

9.2 AFTA data and thermal history interpretation

The measured fission track age and mean track length data in sample GC1104-24 are summarised in Table 9.1 where these parameters are contrasted with the values predicted from the Default Thermal History (i.e. assuming that each sample is now at its maximum temperature since deposition). The Default Thermal History was based on the burial history defined from the section intersected in the well, using an assumed present day thermal gradient of 30°C/km, and the predicted AFTA parameters correspond to the range of apatite chlorine contents measured in sample GC1104-24.

An excellent apatite yield was obtained from the core sample, and the normal "target" numbers of 20 single grain fission track ages and 100 track lengths were obtained, resulting in AFTA data of the highest quality. The thermal history constraints obtained from the AFTA data are therefore regarded as highly reliable.

Assessment of the AFTA data in the sample, in terms of evidence that the sample may have been hotter in the past, is summarised in Table 9.2. Track length data in sample GC1104-24 can only be explained in terms of higher temperatures at some time after deposition, while the lack of significant fission track age reduction in this sample suggests that post-depositional heating has been only of moderate magnitude, sufficient to produce significant length reduction but not age reduction.

Quantitative thermal history constraints have been extracted from the AFTA data by modelling the parameters expected through various thermal history scenarios and iterating towards the best-fit solution by isolating the range of conditions (maximum palaeotemperature and time at which cooling from that palaeotemperature began in one or two episodes) for which predicted parameters are consistent with measured data (within 95% confidence limits). The resulting thermal history constraints for sample GC1104-24 are summarised in Table 9.3.

The AFTA data clearly require cooling from a palaeotemperature between 60 and 80°C, which began sometime between 30 and 0 Ma, to explain the shortening of the longest tracks in the sample. The AFTA data also provide tentative evidence for an earlier cooling episode from a higher palaeotemperature between 90 and 100°C some time earlier than 40 Ma, although this could alternatively represent pre-depositional cooling in sediment provenance terrains. As discussed below, integration with VR data from the well confirm that this episode post-dates deposition of the Santonian/Campanian sandstone sample.

9.3 Thermal history interpretation of VR data

Results of vitrinite reflectance analyses are summarised in Table 9.4. Mean VR values increase from 0.58% at a depth of 9 m to 3.45% near the base of the well at a depth of 158 m. This is clearly a rapid increase over a relatively narrow depth range.

Using the kinetic description underlying the thermal evolution of vitrinite reflectance from Burnham and Sweeney (1989) these data have been converted to maximum post-depositional palaeotemperatures for the sampled sedimentary units, using an assumed heating and cooling rates of 1°C/Ma and 10°C/Ma, respectively. These rates are assumed in order to be consistent with the interpretation of the AFTA data in sample GC1104-24. The resulting palaeotemperatures, also listed for each sample in Table 9.4, increase from

~90°C at shallow depths to 239°C over a depth interval of only ~150 m. Integration of the information derived from VR data with AFTA data from the well and over the wider region, discussed in Section 9.4, shed light on the processes responsible for the observed VR values.

9.4 Integration of AFTA and VR data

Palaeotemperature constraints derived from AFTA and VR data in the Nanok-1 borehole are plotted as a function of depth sub-surface in Figure 9.1. VR values from depths above and below sample GC1104-24 define maximum palaeotemperatures between 93 and 100°C which are highly consistent with the range of 90 to 100°C in the earlier episode tentatively defined from the AFTA data in sample GC1104-24. The VR data therefore confirm that this episode represents post-depositional heating and that these VR values represent a palaeo-thermal maximum from which cooling began sometime after deposition of the sedimentary sequence (Campanian) and 40 Ma.

Deeper VR data show the effects of contact heating due to a buried intrusion intersected at depth in the borehole. The likely age of the intrusion is thought to be 53-54 Ma (information provided by GEUS), and the timing of the earlier event identified from AFTA is consistent with this timing. It therefore seems likely that the whole section above the intrusion cooled from maximum post-depositional palaeotemperatures following emplacement of the intrusion in the Early Eocene. While contact heating effects are likely to be restricted to the vicinity of the intrusion, more widespread effects may be caused by hydrothermal effects as a result of the intrusive activity, and such effects were identified in Geotrack Report GC1077 in a number of samples from locations close to the Nanok-1 borehole, e.g. the north coast of Hold with Hope.

In this respect, it should be noted that in Geotrack Report GC1077, AFTA data in sample GC1016-41, which is located close to the Nanok-1 borehole, were interpreted as defining two palaeo-thermal episodes, with a tentatively identified earlier episode involving cooling from between 60 and 100°C some time prior to 30 Ma. In Geotrack Report GC1077 this earlier episode was attributed to the Late Eocene regional episode, in which cooling began between 37 and 35 Ma. But on the basis of results from sample GC1104-24 it seems clear that the early episode in sample GC1016-41, together with that in sample GC1104-24, should be attributed to the Early Eocene (56-48 Ma) episode.

AFTA data in both samples GC1104-24 and GC1016-41 define a later cooling episode from between 60 and 80°C which began sometime between 30 and 0 Ma for sample GC1104-24 and between 37 and 2 Ma for sample GC1016-41. This episode in both samples is attributed to the Late Miocene regional palaeo-thermal episode, in which cooling began around 10 Ma, representing the uplift of the modern-day continental margin and development of the present-day landscape.

Figure 9.2 provides a schematic illustration of the likely thermal history of the section intersected in the Nanok-1 borehole. This reconstruction embodies one additional feature derived from the wider study described in Geotrack Report GC1077. AFTA and VR data in numerous samples from the region around Hold with Hope and to the north and south define a major period of cooling at ~35 Ma, which is interpreted as representing the initial post-rift uplift of the continental margin. AFTA data in sample GC1104-24 show no direct evidence of such an event, but given the consistent regional evidence for cooling at this time, it seems highly likely that this event affected the region in the vicinity of the Nanok-1 borehole. Therefore the earlier event identified from AFTA in sample GC1104-24 probably represents the unresolved effects of the two Palaeogene palaeo-thermal episodes identified in this region.

9.5 References

Burnham, A.K. & Sweeney, J.J. 1989: A chemical kinetic model of vitrinite reflectance maturation. Geochimica et Cosmochimica Acta., **53**, 2649–2657.

Table 9.1. Summary of apatite fission track data in a sample from the Nanok-1 borehole (Geotrack Report GC1104)

Sample Number\ Source Number	Average depth\ Elevation asl (m)	Present temp-erature (°C)	Strati-graphic age (Ma)	Mean track length (μm)	Predicted mean track length* (μm)	Fission track age (Ma)	Predicted fission track age* (Ma)
GC1104-24 517004-26	67.7 4.7	2	86-84	10.93±0.21	15.0	190.0±17.2	86

* Values predicted from the Default Thermal History; i.e. assuming that each sample is now at its maximum temperature since deposition. The values refer only to tracks formed after deposition. Samples may contain tracks inherited from sediment provenance areas. Calculations refer to apatites within the measured compositional range for each sample.

Table 9.2. Summary of thermal history interpretation of AFTA data in a sample from the Nanok-1 borehole (Geotrack Report GC1104)

Sample No. **Source No.** Depth Present temp Strat. Age	Evidence of higher temperatures in the past from length data?	Evidence of higher temperatures in the past from fission track age data?	Conclusion
GC1104-24 **517004-26** 67.7 m asl 1°C 86-84 Ma	Yes [Mean track length is ~4.1 μm less than predicted by the Default Thermal History. Modelling AFTA parameters through likely thermal history scenarios shows that the observed track length reduction cannot be explained by inheritance from sediment source terrains, and must be due to higher palaeotemperatures at some time after deposition.]	No [Central fission track age and almost all single grain ages are significantly older than predicted from Default Thermal History. No single grain ages are significantly younger than predicted on this basis.]	Track length data show that the sample has been hotter than the present-day temperature at some time after deposition. Lack of significant age reduction suggests that heating was only moderate.

Note: Interpretation of AFTA data is based on comparison of measured AFTA parameters with values predicted from “Default Thermal History”; i.e., assuming that each sample is now at its maximum temperature since deposition. The predicted values for each sample are summarised in Table 1, and refer only to tracks formed after deposition. Samples may also contain tracks inherited from sediment provenance areas, which must be allowed for in interpreting the data. Calculations refer to apatites with the compositional range appropriate to each sample.

Table 9.3. Estimates of timing and magnitude of elevated palaeotemperatures from AFTA data in a sample from the Nanok-1 borehole (Geotrack Report GC1104)

Sample Details	**Palaeo-thermal constraints**			**Comments**
Sample No. Depth Present temp Strat. age	Event	Maximum palaeo-temperature (°C)	Onset of cooling (Ma)	
GC1104-24 **517004-26** 67.7 m asl 1°C 86-84 Ma	1: 2:	*90-100* 60-80	*>40* 30-0	The AFTA data in this sample are best explained in terms of two post-depositional episodes of heating and cooling, as shown (left). From the AFTA data alone, the earlier episode could possibly represent the effects of pre-depositional heating, but VR data confirm that this heating must be post-deposition. Cooling from between 60 and 80°C beginning sometime in the interval 30 to 0 Ma is defined from the observed shortening of longer tracks within the track length distribution, while the earlier episode, involving cooling from between 90 and 100°C some time prior to 40 Ma is defined by the shorter track lengths in the distribution. High quality data in this sample (20 single grain ages, 104 lengths) provide a reliable interpretation within the stated uncertainty limits, although some aspects remain equivocal. **Equivalent $R_o$max: 0.540.61% (assuming the earlier event allowed by the AFTA data represents post-depositional heating)**. Measured VR values of 0.57% and 0.56% from adjacent depths (Table 2), equivalent to maximum palaeotemperatures of 94 and 93°C, respectively (Table 1), are highly consistent with the range of palaeotemperatures allowed by AFTA data in this earlier event, confirming that this palaeo-thermal event does indeed represent post-depositional heating.

All thermal history constraints are based on assumed heating rates of 1°C/Myr and cooling rates of 10°C/Myr.

Table 9.4. Maximum palaeotemperatures from VR data in samples from the Nanok-1 borehole (Geotrack Report GC1104)

Sample number	Average depth (m)	Stratigraphic age (Ma)	Supplied mean VR (%)	Number of readings (%)	Maximum palaeotemperature[*1] (°C)
20787	9	83.5-80	0.58	79	96
20809	31	83.5-80	0.57	70	94
20829	82	87-85.8	0.56	92	93
20848	110	94-93	0.61	85	100
20867	129	94-93	0.58	76	96
20880	141	94-93	0.72	94	118
20890	150	96-94	1.04	39	145
20899	158	96-94	3.45	98	239

[*1] All estimates of maximum palaeotemperature were determined using assumed heating rates of 1°C/Myr and cooling rates of 10°C/Myr. See Geotrack Report GC1104 for further details.

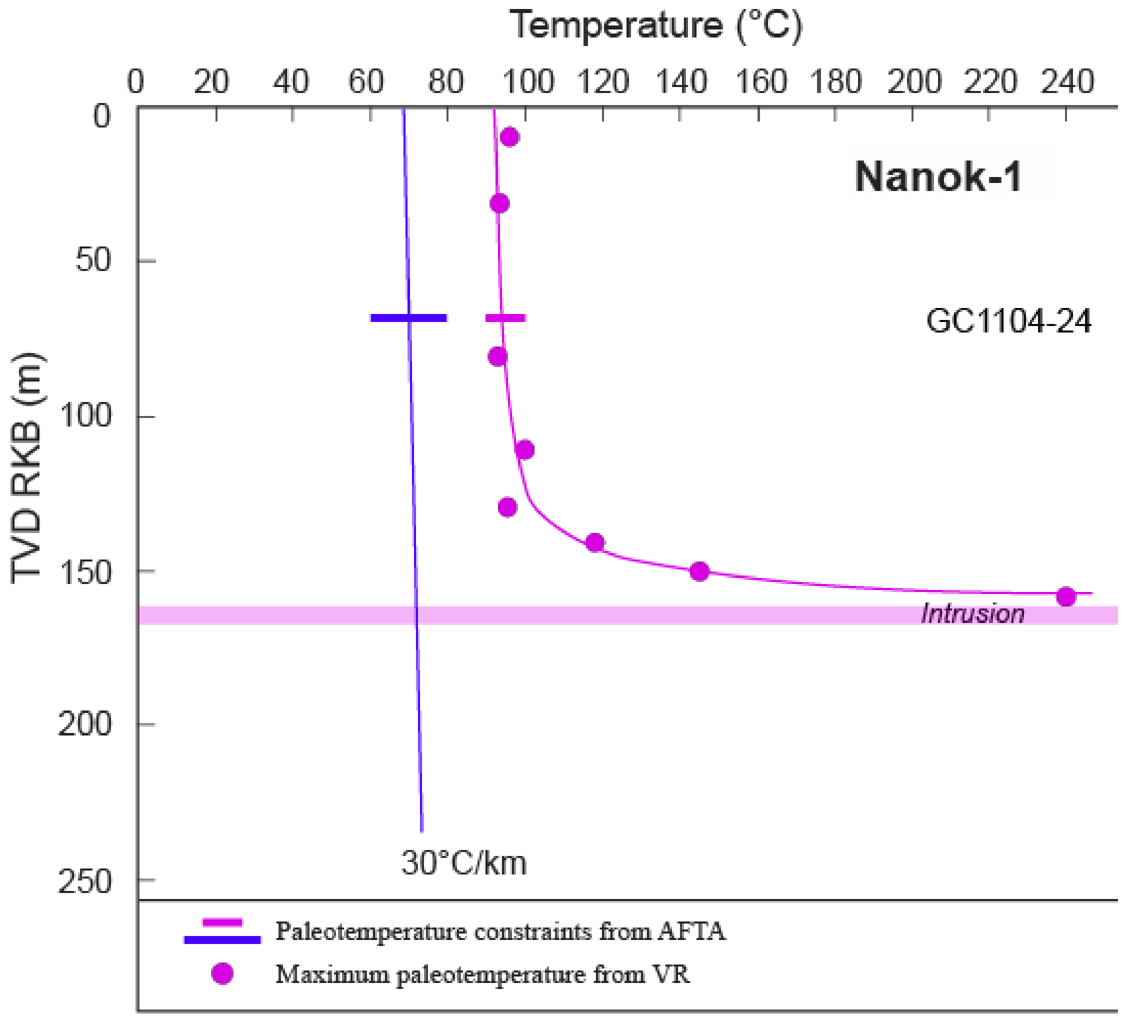

Figure 9.1. Palaeotemperature constraints derived from AFTA and VR data in the Nanok-1 borehole, plotted against depth below the local ground surface (which is 63 m above mean sea level). AFTA data in a single sample, GC1104-24, from this borehole define two discrete episodes of cooling from elevated palaeotemperatures, an earlier episode from 90 to 100°C which began prior to 40 Ma (Magenta line) and a later episode from between 60 and 80°C which began in the interval 30 to 0 Ma. VR data from depths adjacent to the AFTA sample define maximum palaeotemperatures which are highly consistent with those from AFTA in sample GC1104-24 while deeper VR data show the effects of contact heating due to a buried intrusion intersected at depth in the borehole. The likely age of the intrusion is thought to be 53-54 Ma, and the timing of the earlier event identified from AFTA is consistent with this timing. It therefore seems likely that the whole section above the intrusion cooled from maximum post-depositional palaeotemperatures following emplacement of the intrusion in the Early Eocene.

AFTA data in outcrop sample GC1016-41, which is located close to the Nanok-1 borehole, are consistent with this interpretation.

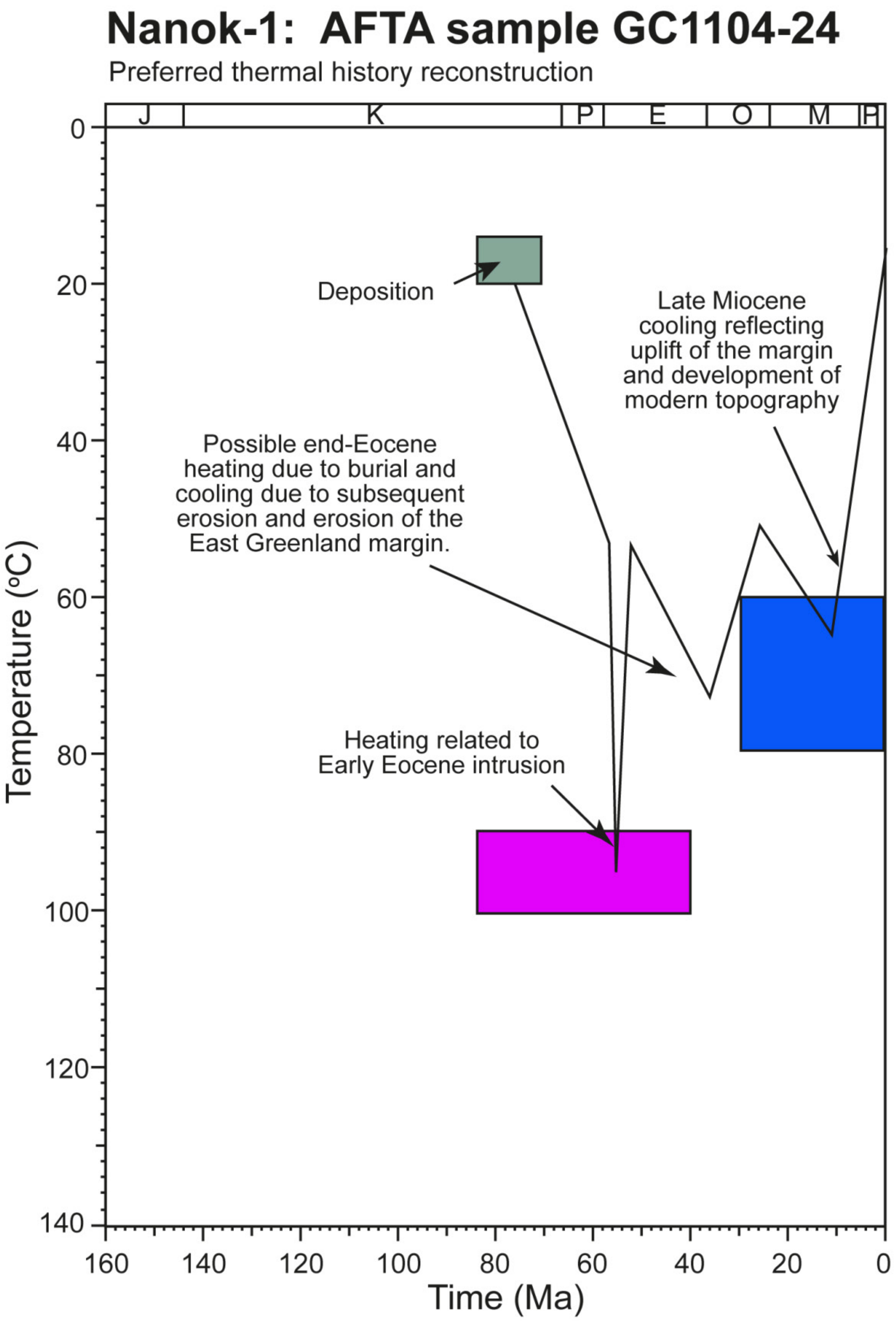

Figure 9.2. Schematic illustration of our preferred thermal history reconstruction for AFTA sample GC1104-24 from the Nanok-1 borehole.

10. Sonic Velocity

Sonic velocity, porosity and grain density were measured on 14 core pieces. Sonic velocity measurements were done at GEO, Denmark, whereas porosity and grain density were measured at GEUS. The samples analysed were full diameter core pieces ranging from ~47 mm to ~63 mm in length.

10.1 Methods

CCAL

The conventional core analysis (CCAL) of the Nanok-1 core was carried out at GEUS Core Laboratory. The methodology is described in Chapter 7. The only methodological difference is that the samples were not cleaned, but were directly dried at 60°C for 24 hours upon reception from GEO.

For a more detailed description of methods, instrumentation and principles of calculation, the reader is referred to American Petroleum Institute (API) recommended practice for core-analysis procedure (API 1998).

The porosity and grain density results are shown in the Table 10.1.

Sonic Velocity

The methodology and equipment used for sound velocity measurements are briefly presented in the Appendix 12.6. Prior to measurements, the samples were kept in an oven at 60^{0}C for 24 h. Moreover, some of the samples were trimmed in order to ensure plane-parallel surfaces. The sound velocity measurements comprised determination of compressional wave (P-wave) velocity and shear wave velocity in two orthogonal directions (S1 and S2; Table 10.2).

10.2 Results and Conclusions

Results are presented in Tables 10.1 and 10.2. Figure 10.1 shows cross-plots of the different parameters (porosity, grain densities and sonic velocity).

Sonic velocity measurements suggest that the Fosdalen Formation mudstones (the Knudshoved Mb and undifferentiated Fosdalen Fm) commonly show similar velocities (Vp) 2750–3100m/s (*n*=6). Figure 10.1 cross-plots illustrate the narrow range of porosity, grain densities and sonic velocity values of the mudstone samples.

The Østersletten Mb sandstones show a wide range of sonic velocity values ranging from 1750 m/s to 3250 m/s (*n*=6). Similarly, the analysed samples show scattered porosity values (6–22%). The results reflect the variable lithology of the analysed samples: the sample recording the highest velocity value (3250 m/s) and anomalously low porosity (6%) represents a mudstone-rich interbed (Facies 4B/C; Chapter 4). In additon, the sample recording lowest velocity (1750m/s) shows also anomalously low grain density, which probably reflects elevated coal content in the sample. The structureless sandstones (Facies 4A) that form the bulk of unit record less variable values 2250–2750 m/s.

Finally, two samples from the igneous intrusion from the base of the core show extreme velocity values 4350 and 5250 m/s. Likewise, these samples record also the lowest porosity and highest grain density values.

10.3 References

American Petroleum Institute (API) 1998: Recommended Practices For Core Analysis. Exploration and Production Department, American Petroleum Institute, Second edition.

Plug	Depth (m)	Porosity$_{(He)}$ [%]	Grain density [g/cc]	Unit
434	29,8	7,50	2,642	Knudshoved Mb
435	35,035	7,87	2,650	
436	35,285	7,65	2,642	
437	42,945	14,32	2,739	Østersletten Mb
438	45,115	17,10	2,685	
439	49,675	6,23	2,652	
440	50,025	16,02	2,337	
441	51,015	21,60	2,691	
442	82,855	12,58	2,625	
443	128,625	7,70	2,742	Undifferentiated Fosdalen Fm
444	132,595	6,66	2,624	
445	153,945	6,25	2,623	
446	162,505	1,71	2,971	Igneous intrusion
447	166,375	3,13	2,950	

Table 10.1. Porosity and grain density of the measured samples.

Table 10.2. Summary of sonic velocity data.

Sound measurements at unconfined conditions

		Dry specimens (as delivered)					Saturated specimens				
Specimen sub no.	**Height** [mm]	t_p [micro. Sec]	t_{s1} [micro. Sec]	t_{s2} [micro. Sec]	v_p [m/s]	v_s [m/s]	t_p [micro. Sec]	t_{s1} [micro. Sec]	t_{s2} [micro. Sec]	v_p [m/s]	v_s [m/s]
434	52.87	17.7	40.4	39.6	3000	1300					
435	54.53	17.6	-	32.8	3100	1650					
436	55.01	17.9	43.4	44.6	3050	1250					
437	55.95	18.2	35.5	33.3	3100	1650					
438	54.74	19.8	41.4	43.4	2750	1300					
439	58.69	18.1	41.4	39.9	3250	1450					
440	62.90	35.8	86.7	95.2	1750	700					
441	54.13	24.3	54.1	65.6	2250	900					
442	56.36	21.5	50.8	48.8	2600	1150					
443	46.89	15.9	31.3	33.2	2950	1450					
444	57.15	20.2	53.0	51.3	2850	1100					
445	49.33	18.1	35.4	36.0	2750	1400					
446	57.54	13.2	40.9	41.3	4350	1400					
447	57.56	10.9	26.0	26.1	5250	2200					

A

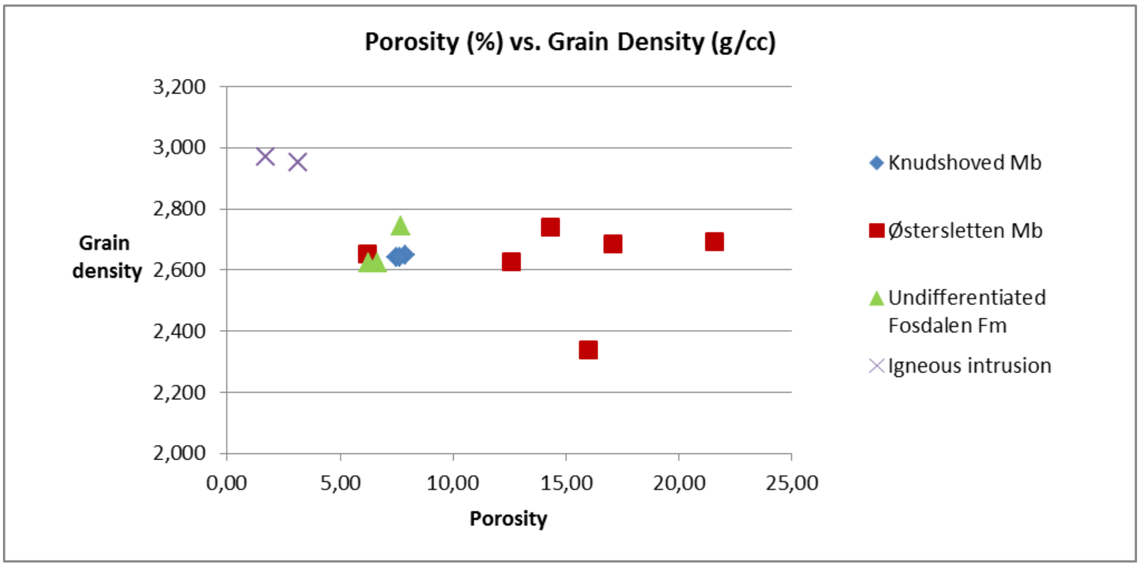
Porosity (%) vs. Grain Density (g/cc)
3,200
3,000
2,800
2,600
2,400
2,200
2,000
Grain density
0,00
5,00
10,00
15,00
20,00
25,00
Porosity
Knudshoved Mb
Østersletten Mb
Undifferentiated Fosdalen Fm
Igneous intrusion

B

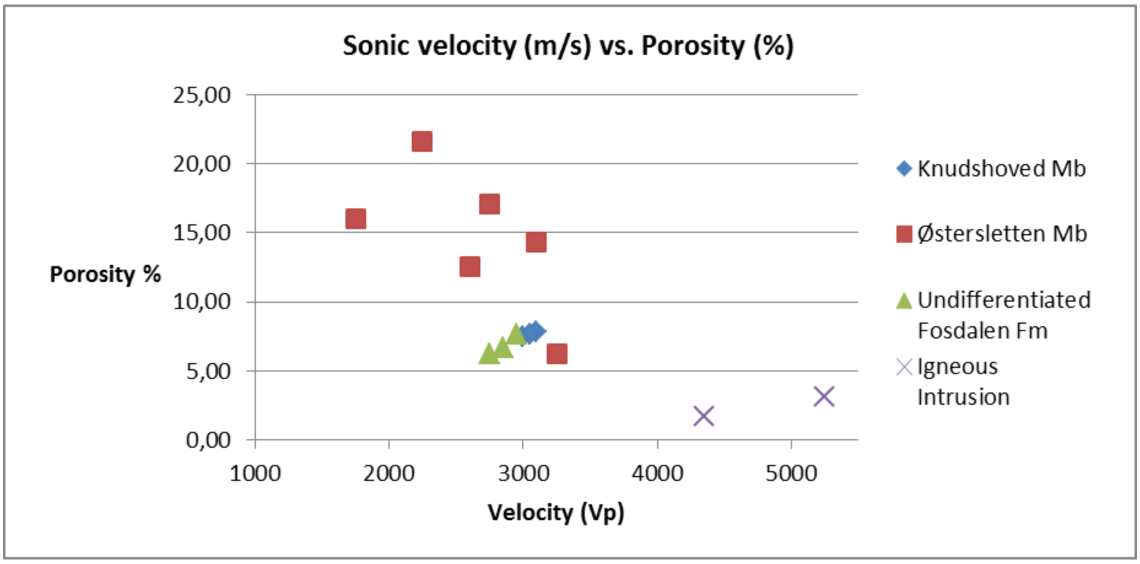
Sonic velocity (m/s) vs. Porosity (%)
25,00
20,00
15,00
10,00
5,00
0,00
Porosity %
1000
2000
3000
4000
5000
Velocity (Vp)
Knudshoved Mb
Østersletten Mb
Undifferentiated Fosdalen Fm
Igneous Intrusion

C

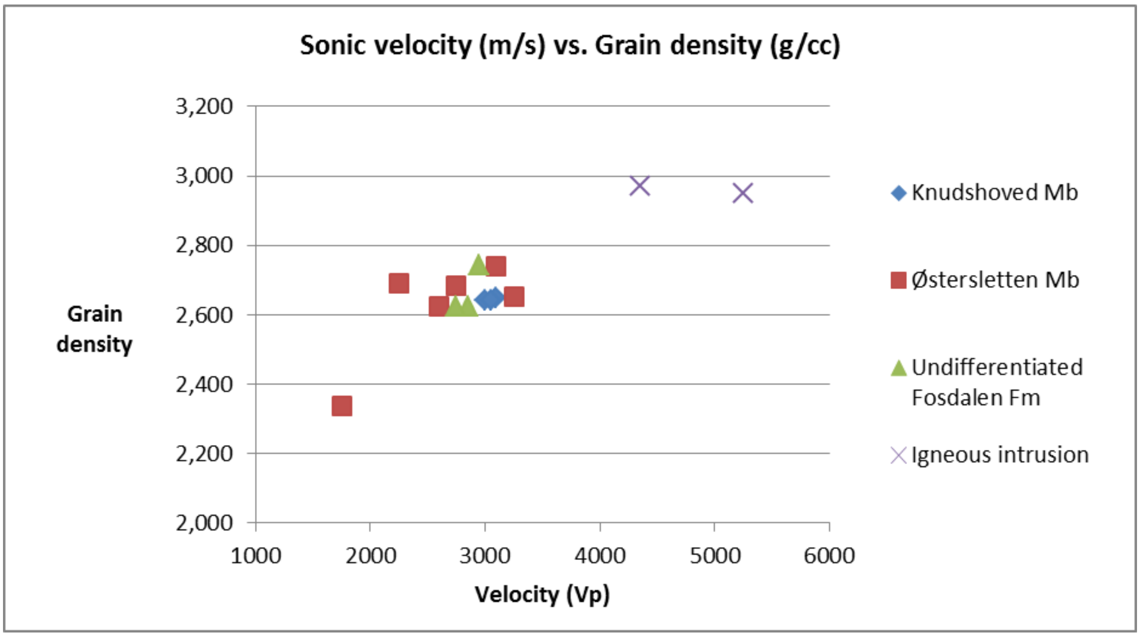

Figure 10.1. Relationships between porosity, grain density and sonic velocity.

11. Igneous intrusion

The succession in the Nanok drill core is cut by an intrusive igneous rock from 160.36 m depth to the end of the core at 168.35 m, i.e., the lowermost 8.0 m of the core. The upper contact is irregular but appears to be steep, and the igneous body may be an inclined sheet. The mudstone above the contact is slightly more massive (better core) up to 80 cm from the contact, which may be a baking phenomenon. The magma was pillowed at the contact, and there are centimetre-sized chilled pillows in the mudstone up to c. 10 cm from the main contact; likewise there are millimetre- to 1-cm sized rounded mudstone clasts a few centimetres down into the chill zone.

11.1 Lithology

The intrusion is aphanitic to very fine-grained up to 15 cm down from the contact. Thereafter, the grain size gradually increases to fine-grained. In the lowermost *c*. 30 cm of the core the grain size decreases again to very fine-grained, and comparison with the upper chill zone suggests that the lower contact is situated only 0.1–0.2 m below the end of the core.

The rock is aphyric to weakly plagioclase-microphyric, and in the lower part a few dark prismatic augite (?) crystals are seen. The lower part also contains scattered 1–2 mm sized rounded bodies, presumably vesicles, filled with dark clay.

The upper chill zone is cut by up to 4 mm wide irregular calcite veins. At 162.10–162.40 m a 1 mm wide calcite vein cuts steeply through the rock. At *c*. 165.0–165.2 m, the rock is cut by a steep, 1 cm wide vein of calcite and dark clay. The whole zone at 165–168 m is strongly fractured and around one metre of the core between 165 m and 167 m seems to be lost. Some of the steeply inclined fractures show fine slickensides.

11.2 Petrography

Thin section 517004-292: 163.50 m. Fine-grained rock with a few plagioclase microphenocrysts ≤1 mm and one 1 mm olivine microphenocryst completely altered to brown clay. Groundmass intergranular with plagioclase, clinopyroxene, Fe-Ti oxide, and abundant mesostasis heavily altered to brown clay.

Thin section 517004-293: 166.11 m. Fine-grained rock with a few small (around 1 mm) glomerocrysts of plagioclase laths not much bigger than those in the groundmass (around 0.5 mm), a few 1–2 mm olivine phenocrysts completely altered to brown clay, and one clinopyroxene microphenocryst around 1 mm, intergrown with plagioclase. Groundmass intergranular with plagioclase, clinopyroxene, Fe-Ti oxide, and abundant mesostasis heavily altered to clay. There are also a few perfectly circular areas that appear to be vesicles, filled with brown clay. Vesiculation in intrusions normally takes place only at shallow levels less than *c*. 50 m below the surface, but if the magma has picked up some extra volatiles from the surrounding sediments, this level could be considerably deeper. There are no vesicles in sample 517004-292.

11.3 Chemical composition

Sample 517004-291 taken at 163.46 m was sent for chemical analysis. Major elements were analysed by J.G. Fitton at University of Edinburgh by X-ray fluorescence spectrometry (XRF) and procedures as described by Fitton *et al.* (1998). Trace elements were analysed in GEUS's Rock Geochemical Laboratory using a PerkinElmer Elan 6100 DRC Quadrupole Inductively coupled Plasma Mass Spectrometer (ICP-MS). Sample dissolution followed a modified version of the procedure used by Turner *et al.* (1999) and Ottley *et al.* (2003). Calibration was done using two certified REE solutions and three international reference standards. Results for reference samples processed and run simultaneously with the unknowns are normally within 5% of the reference value for most elements with concentrations > 0.1 ppm. The results are shown in Table 11.1, with comparisons.

The intrusion consists of slightly enriched tholeiitic basalt. It is similar to other intrusions (dykes) in NE Greenland, and in particular to dykes from Hold With Hope and Wollaston Forland (Table 11.1). In terms of trace elements it clearly groups with the other dykes in the region, as shown for the REE ratios in Figure 11.1. These dykes are dissimilar to the sills and dykes in the Jameson Land region (Fig. 11.1).

Upton *et al.* (1980) described a NE-oriented dyke swarm in the southern part of Hold With Hope, which they related to the Myggbugta central complex. The analyses of dykes from this swarm are very variable but a few do show similarities to the Nanok intrusion. However, Upton's samples are not analysed for the full REE spectrum and therefore cannot be shown in Figure 11.1. A NE-oriented dyke from Tværelv in north-eastern Hold With Hope may belong to this group (Table 11.1, no 517301).

11.4 Age of the intrusion

The two thin sections from the Nanok intrusion show that the rock is unsuited for dating by the $^{39}Ar/^{40}Ar$ method. The plagioclase phenocrysts are too few and too small to make a good separate, and moreover they contain clay inclusions. The groundmass plagioclases are intergrown with clay and will not separate well either, and they are so small that they may cause argon recoil problems during analysis.

The dykes that compare most closely with the Nanok intrusion (Table 11.1, 517301 and 475287) have not been dated (for similar reasons as for the Nanok intrusion). A dyke from the NE-trending dyke swarm on Hold With Hope has been K-Ar dated at 48 Ma (Upton *et al.* 1984), but the chemical composition of this dyke is not known and the K-Ar age of an altered basalt may be questioned. However, two dated dykes from Wollaston Forland and Bontekoe Ø, which are not too different from the Nanok intrusion (Table 11.1), have $^{39}Ar/^{40}Ar$ ages of 51–53 Ma, and this is the most likely age of the Nanok intrusion.

11.5 References

Fitton, J.G., Saunders, A.D., Larsen, L.M., Hardarson, B.S. & Norry, M.J. 1998: Volcanic rocks from theSoutheast Greenland margin at 63°N: composition, petrogenesis and mantle sources. *In* Saunders, A. D., Larsen, H. C. and Wise, S. H. (Eds.), *Proceedings of the Ocean Drilling Program, Scientific Results* **152**: College Station, TX (Ocean Drilling Program), 331–350.

Ottley, C.J., Pearson, D.G. & Irvine, G.J. 2003: A routine method for the dissolution of geological samples for the analysis of REE and trace elements via ICP-MS. In: Holland, J.G. & Tanner, S.D. (eds), *Plasma Source Mass Spectrometry: Applications and Emerging Technologies*, 221–230. Cambridge: Royal Society of Chemistry.

Upton, B. G. J., Emeleus, C. H. & Hald, N. 1980: Tertiary volcanism in northern E Greenland: Gauss Halvø and Hold With Hope. Journal of the Geological Society, London **137**, 491–508.

Upton, B. G. J., Emeleus, C. H., Beckinsale, R. D. & Macintyre, R. M. 1984: Myggbukta and Kap Broer Ruys: the most northerly of the East Greenland Tertiary igneous centres(?). Mineralogical Magazine, **48**, 323–343.

Turner, S.P., Platt, J.P., George, R.M.M., Kelly, S.P., Pearson, D.G. & Nowell, G.M. 1999: Magmatism associated with orogenic collapse of the Beltic–Alboran domain, SE Spain. Journal of Petrology, **40**, 1011–1036.

Table 11.1. Chemical analysis of intrusion in the Nanok drill core, with comparisons

	Nanok core	NE-dyke, 4 m NE HW Hope	NW-dyke, 10 m N. Woll. Forland	NNW-dyke, 5 m C.Woll. Forland	NNE-dyke, 5 m Bontekoe Ø
Age				**53.68 ±1.58 Ma**	**51.28 ±1.20 Ma**
Sample no	**517004.291**	**517301**	**475287**	**475289**	**517310**
Major elements, wt%					
SiO2	48.58	46.84	48.79	48.50	49.15
TiO2	2.33	2.29	2.39	2.54	2.13
Al2O3	13.88	13.24	13.89	13.65	16.07
Fe2O3	12.77	13.36	13.31	15.22	11.46
MnO	0.18	0.189	0.19	0.226	0.159
MgO	6.43	6.06	6.45	5.35	5.65
CaO	10.99	10.57	10.81	10.72	11.32
Na2O	2.51	2.23	2.37	2.44	2.37
K2O	0.570	0.574	0.522	0.306	0.716
P2O5	0.243	0.223	0.257	0.249	0.240
LOI	1.42	4.40	0.19	0.44	0.39
Sum	99.89	99.96	99.17	99.64	99.65
Trace elements, ppm					
Sc	36.43	37.36	34.20	38.98	30.45
V	337.26	371.61	289.82	353.97	293.61
Cr	246.36	60.09	136.25	47.68	67.44
Co	47.46	52.21	50.22	49.01	43.31
Ni	101.20	53.24	81.28	58.92	50.76
Cu	127.08	80.08	153.27	236.20	62.82
Zn	97.77	111.90	103.14	122.16	92.72
Ga	20.11	21.93	20.12	22.07	21.51
Rb	11.79	13.09	10.89	4.45	18.65
Sr	298.86	317.86	315.99	224.82	366.09
Y	31.48	31.96	30.40	41.96	28.97
Zr	159.99	166.97	167.79	171.18	170.34
Nb	21.92	21.11	19.48	13.78	22.67
Cs	0.237	0.163	0.332	0.220	0.331
Ba	195.71	222.99	*451.84*	89.65	210.38
La	16.35	16.73	16.10	12.58	18.78
Ce	37.82	38.45	38.90	32.68	42.10
Pr	5.24	5.41	5.45	4.77	5.74
Nd	23.24	23.93	24.69	22.71	25.15
Sm	5.61	5.98	6.06	6.22	5.86
Eu	1.847	1.918	1.972	2.004	1.805
Gd	6.189	6.324	6.360	7.221	6.027
Tb	0.970	0.984	0.994	1.234	0.889
Dy	5.816	5.845	5.818	7.198	5.255
Ho	1.143	1.180	1.123	1.520	1.073
Er	3.113	3.098	2.785	3.988	2.698
Tm	0.442	0.428	0.404	0.596	0.382
Yb	2.621	2.746	2.384	3.487	2.330
Lu	0.396	0.396	0.344	0.538	0.346
Hf	3.943	4.323	4.130	4.309	4.107
Ta	1.666	1.693	1.363	0.924	1.490

Pb	1.341	1.439	1.190	0.887	3.359
Th	1.565	1.862	1.474	1.091	2.389
U	0.407	0.486	0.425	0.329	0.607
La/Sm(N)	1.82	1.75	1.66	1.26	2.00
Dy/Yb(N)	1.45	1.39	1.60	1.35	1.48

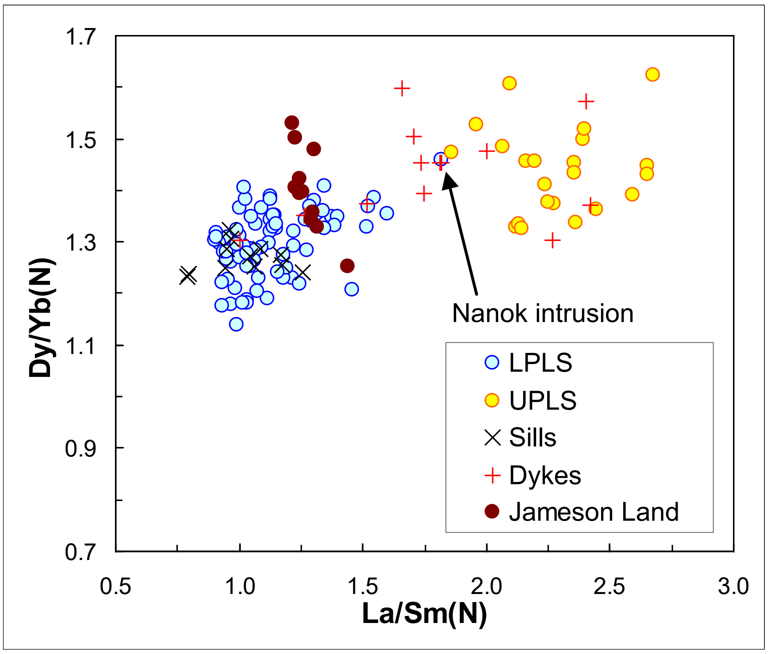

Figure 11.1. The intrusion in the Nanok drill core groups with other dykes in the region. LPLS: Lower Plateau Lava Series; UPLS: Upper Plateau Lava Series.

12. Appendix

12.1 Core photographs

Contents Dry, UV-light and wet photos of the core boxes. Base of the core boxes in the lower left, top in the upper right corner. Depths of the boxes are shown in the table below.

CoreBox	Depth Interval
Box 01	0 - 13,3 m
Box 02	13,7 - 19,24 m
Box 03	19,06 - 25,55 m
Box 04	25,4 - 31,75 m
Box 05	31,76 - 37,46 m
Box 06	37,36 - 43,39 m
Box 07	43,44 - 50,06 m
Box 08	50,15 - 51,9 m
Box 09	32,52 - 38,53 m
Box 10	38,52 - 45,23 m
Box 11	45,27 - 52,22 m
Box 12	52,08 - 58,64 m
Box 13	59,31 - 65,58 m
Box 14	65,36 - 72,15 m
Box 15	72,28 - 78,92 m
Box 16	79,91 - 87,26 m
Box 17	87,2 - 93,98 m
Box 18	93,8 - 100,05 m
Box 19	100,23 - 106,7 m
Box 20	106,8 - 112,9 m
Box 21	112,69 - 119,29 m
Box 22	119,17 - 125,68 m
Box 23	125,59 - 131,82 m
Box 24	131,91 - 138,08 m
Box 25	137,86 - 144,22 m
Box 26	143,77 - 150,71 m
Box 27	150,73 - 157,3 m
Box 28	157,25 - 163,45 m
Box 29	163,22 - 168,35 m

TOP
6,90
7,95
9,00
9,90
10,72
11,40
12,20
12,90
cm 10 20 30 40 50 60 70 80 100
GEUS NANOK-1 0,00 - 13,30 m
BOX
1

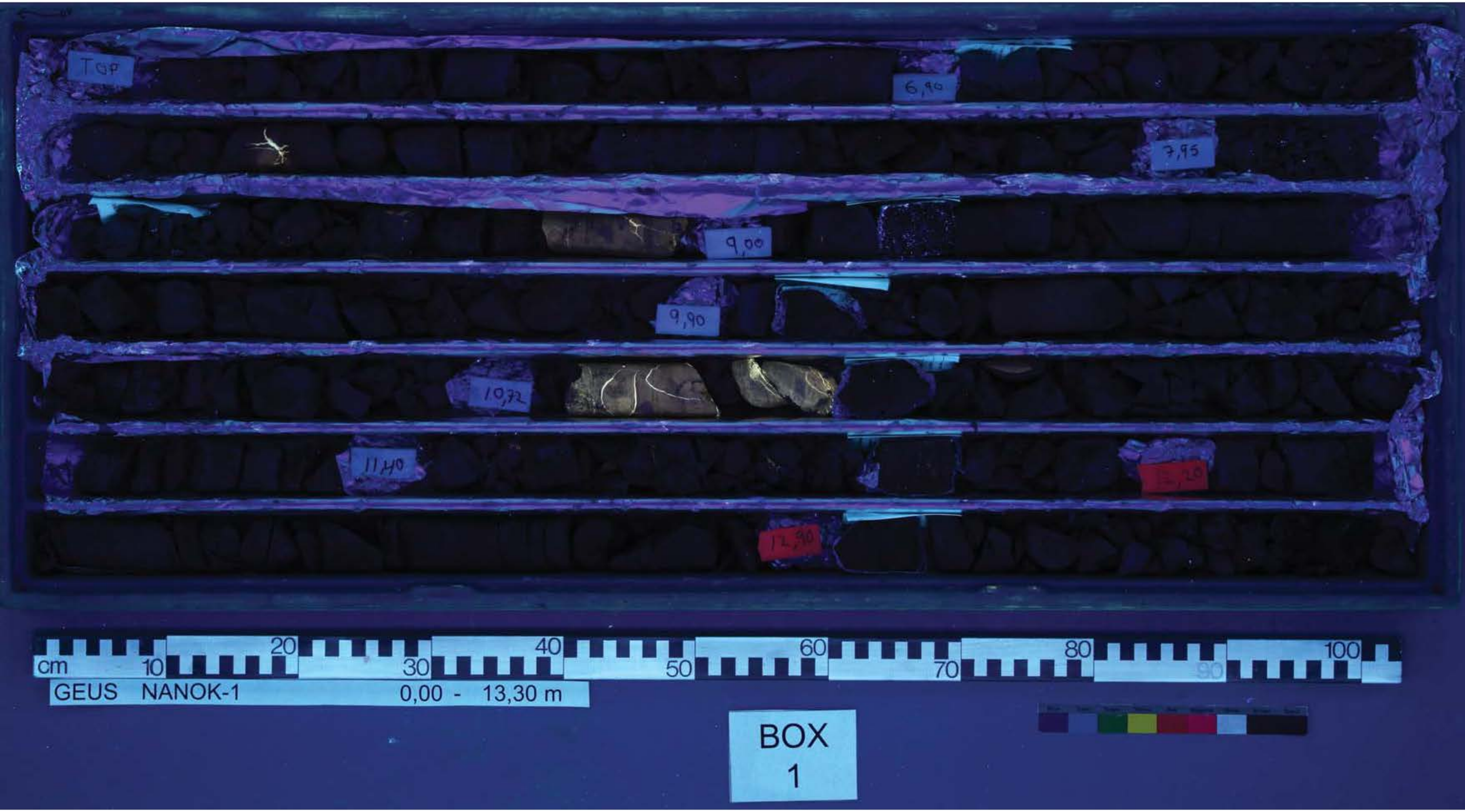
Top
6,90
7,95
9,00
9,90
10,72
11,40
12,90
cm
GEUS NANOK-1 0,00 - 13,30 m
BOX
1


TOP
6,90
7,95
9,00
9,90
10,72
11,40
12,20
12,90
cm
10
20
30
40
50
60
70
80
100
GEUS NANOK-1 0,00 - 13,30 m
BOX
1

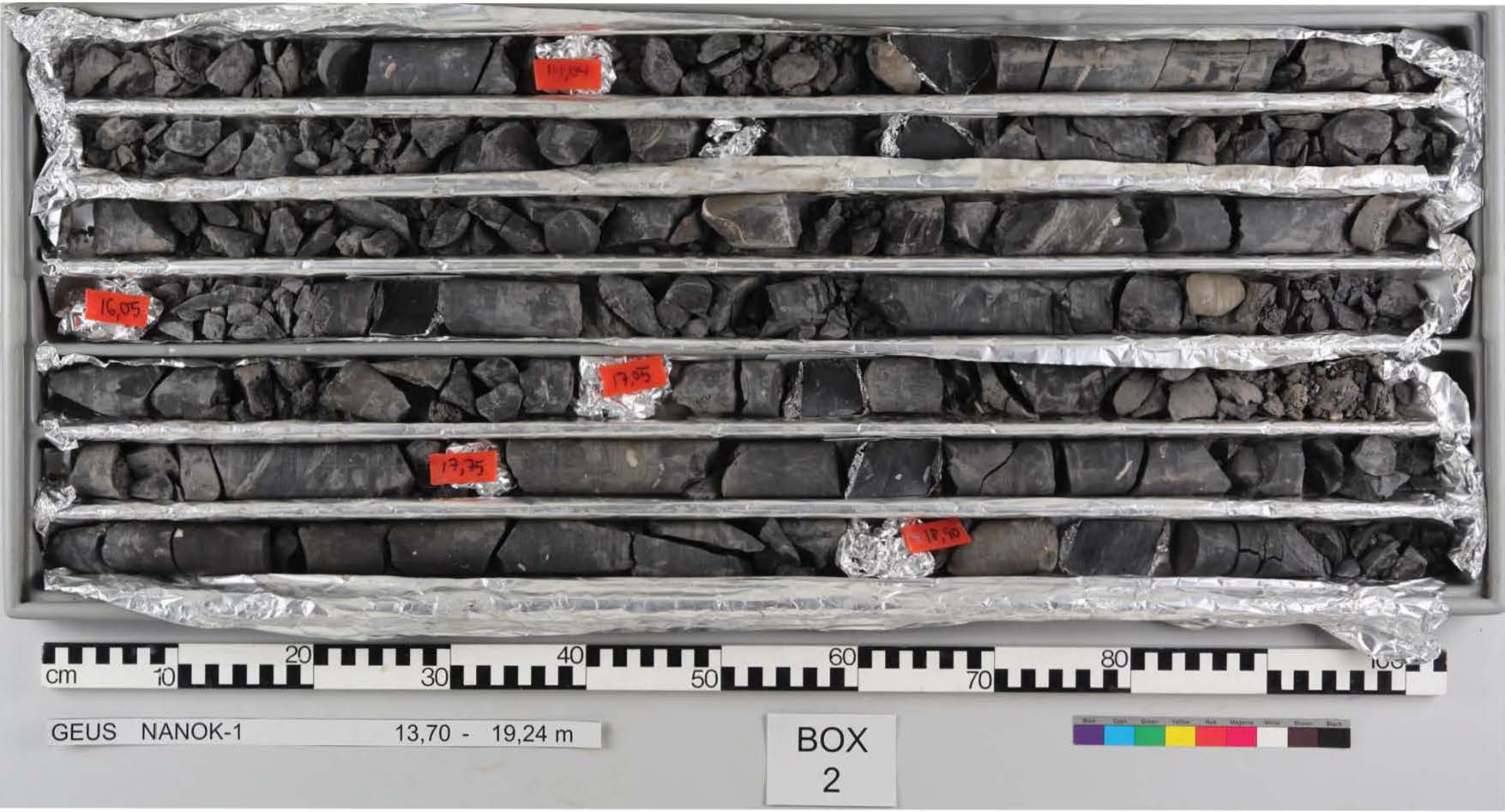
14,04
16,05
17,05
17,75
18,50
cm
10
20
30
40
50
60
70
80
GEUS NANOK-1 13,70 - 19,24 m
BOX
2

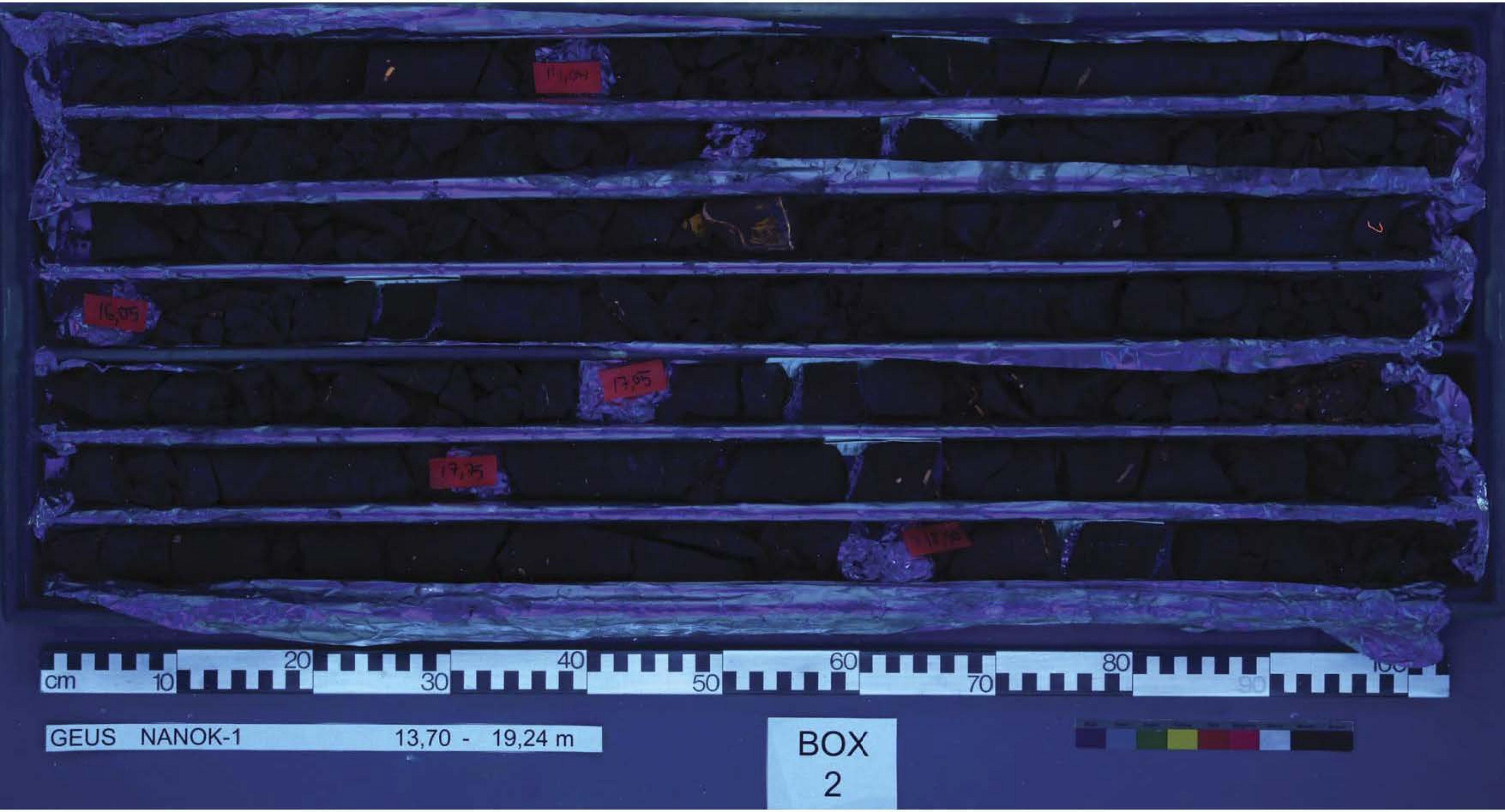
cm
10
20
30
40
50
60
70
80
90
100
GEUS NANOK-1 13,70 - 19,24 m
BOX
2
16,05
17,05
17,35


17,04
16,05
17,05
17,75
18,50
cm 10 20 30 40 50 60 70 80 100
GEUS NANOK-1 13,70 - 19,24 m
BOX
2
Blue Cyan Green Yellow Red Magenta White Brown Black


19,79
21,13
21,90
22,83
24,58
cm 10 20 30 40 50 60 70 80 90 100
GEUS NANOK-1 19,06 - 25,55 m
BOX
3

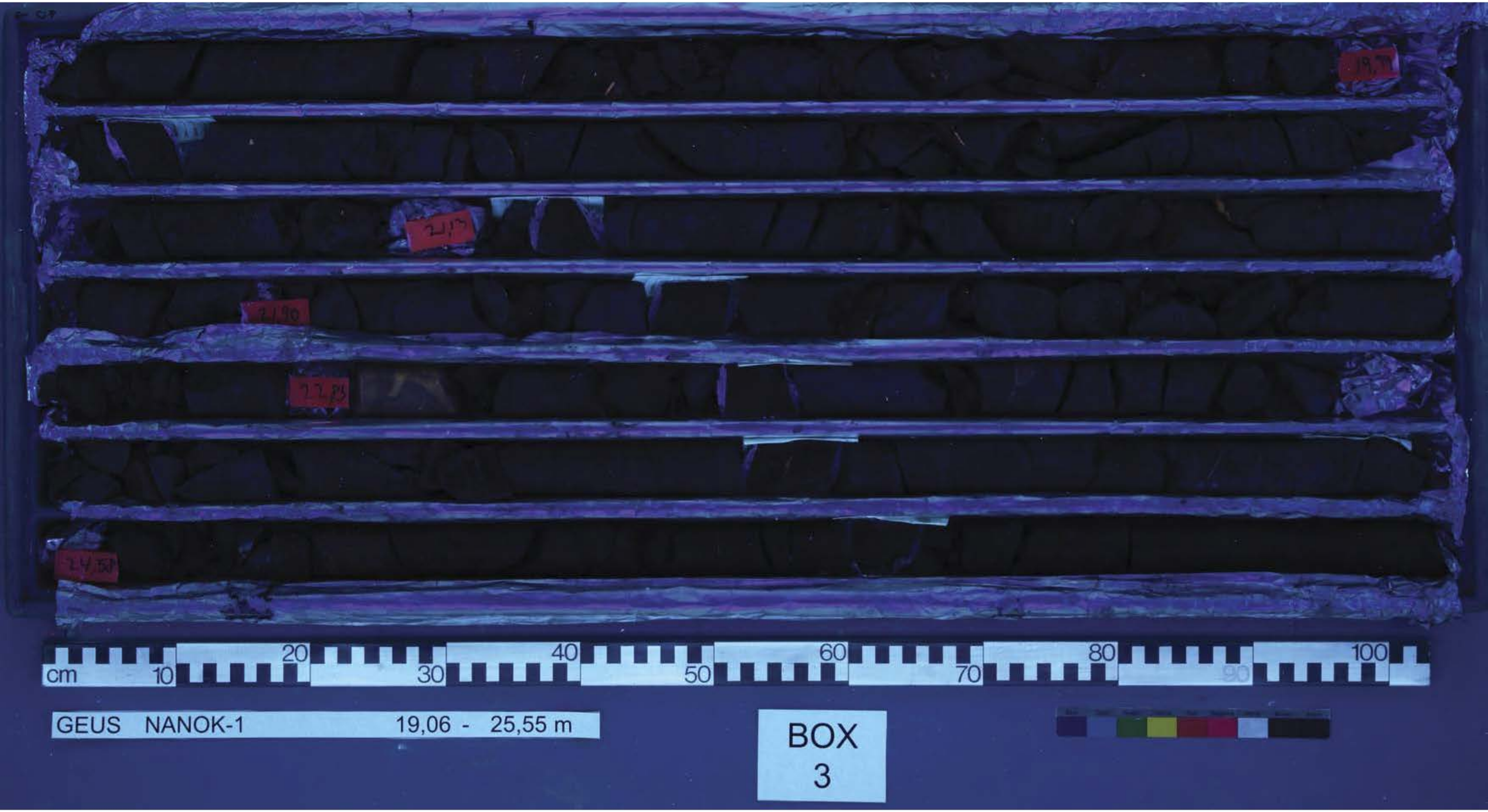
cm
10
20
30
40
50
60
70
80
90
100
GEUS NANOK-1 19,06 - 25,55 m
BOX
3


19,99
21,90
24,58
cm 10 20 30 40 50 60 70 80 90 100
GEUS NANOK-1 19,06 - 25,55 m
BOX
3

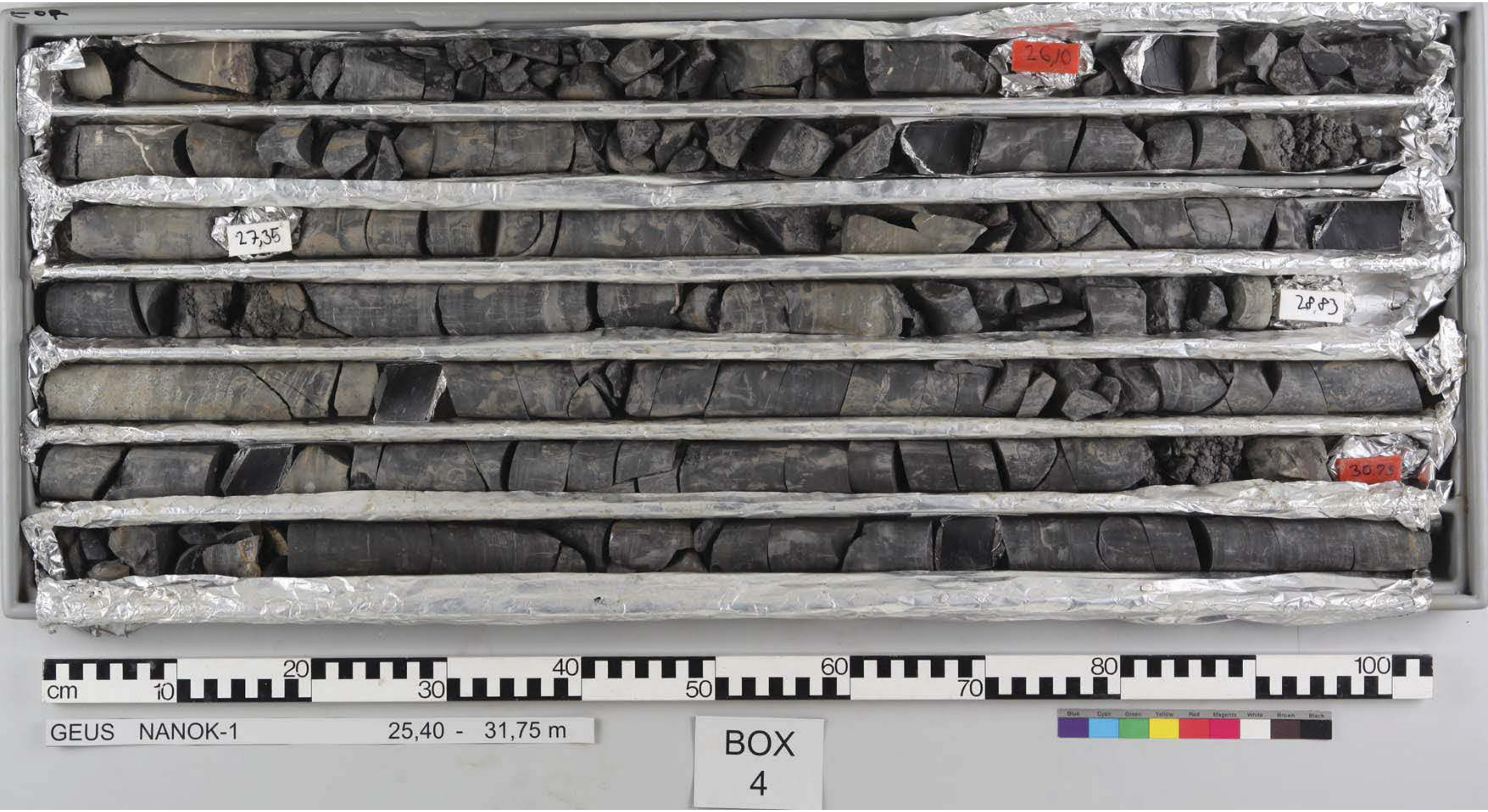

26,10
27,35
28,83
30,75
cm
10
20
30
40
50
60
70
80
100
GEUS NANOK-1 25,40 - 31,75 m
BOX
4

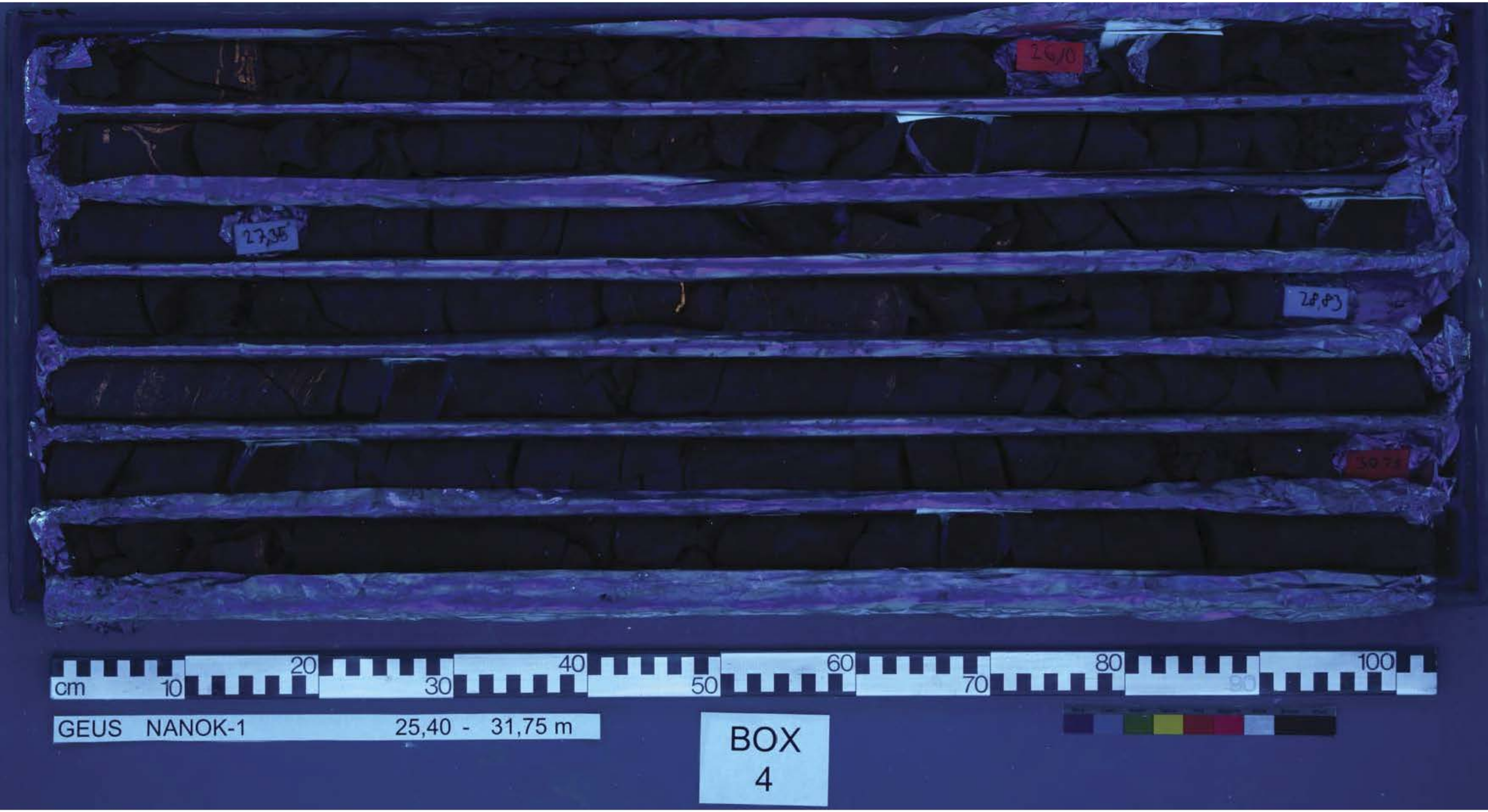
26,10
27,35
28,83
cm 10 20 30 40 50 60 70 80 90 100
GEUS NANOK-1 25,40 - 31,75 m
BOX
4

26,10
27,35
28,83
30,75
cm
10
20
30
40
50
60
70
80
100
GEUS NANOK-1 25,40 - 31,75 m
BOX
4


32,10
33,13
34,68
35,87
37,46
cm 10 20 30 40 50 60 70 80 100
GEUS NANOK-1 31,76 - 37,46 m
BOX
5

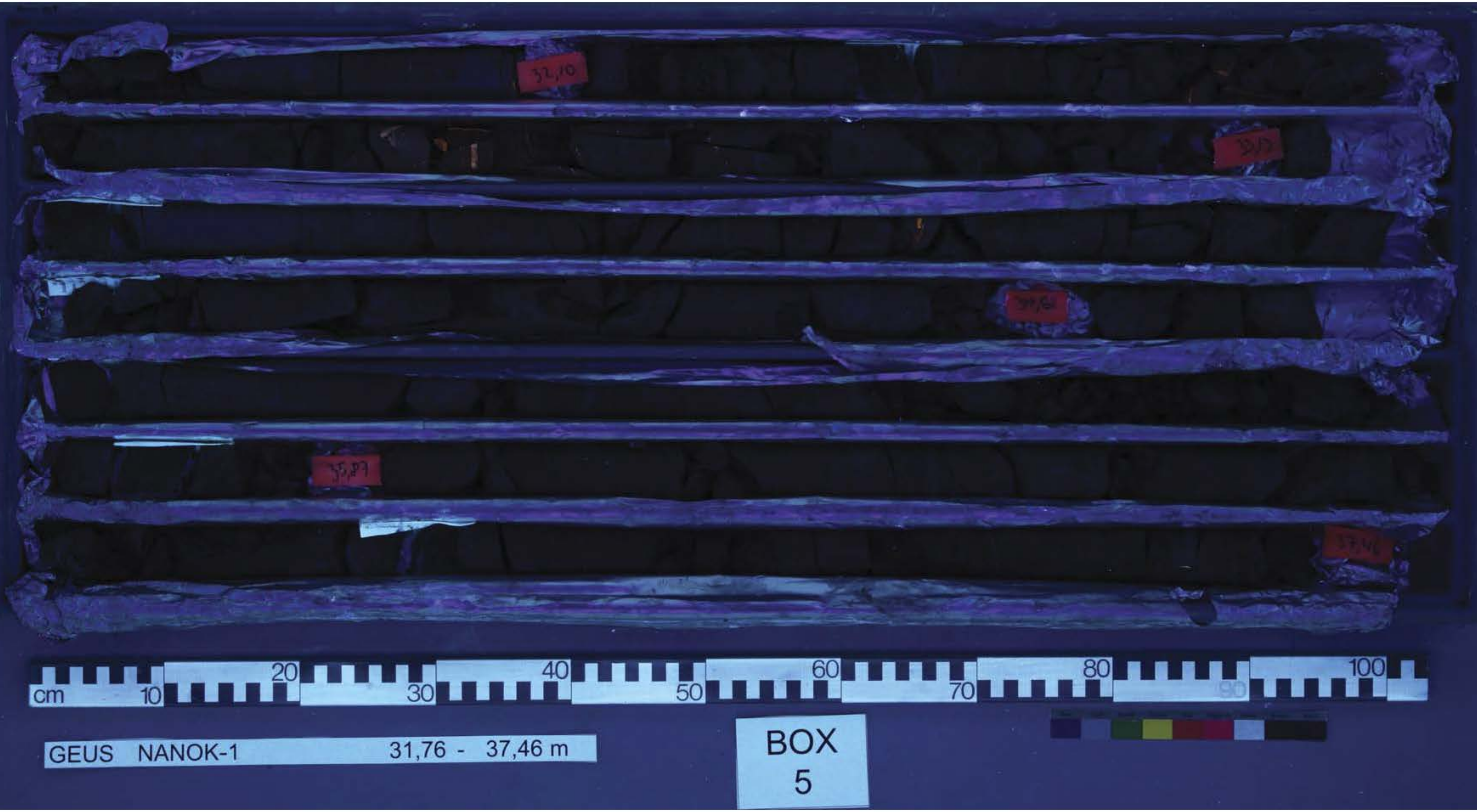

32,10
35,87
cm 10 20 30 40 50 60 70 80 90 100
GEUS NANOK-1 31,76 - 37,46 m
BOX
5

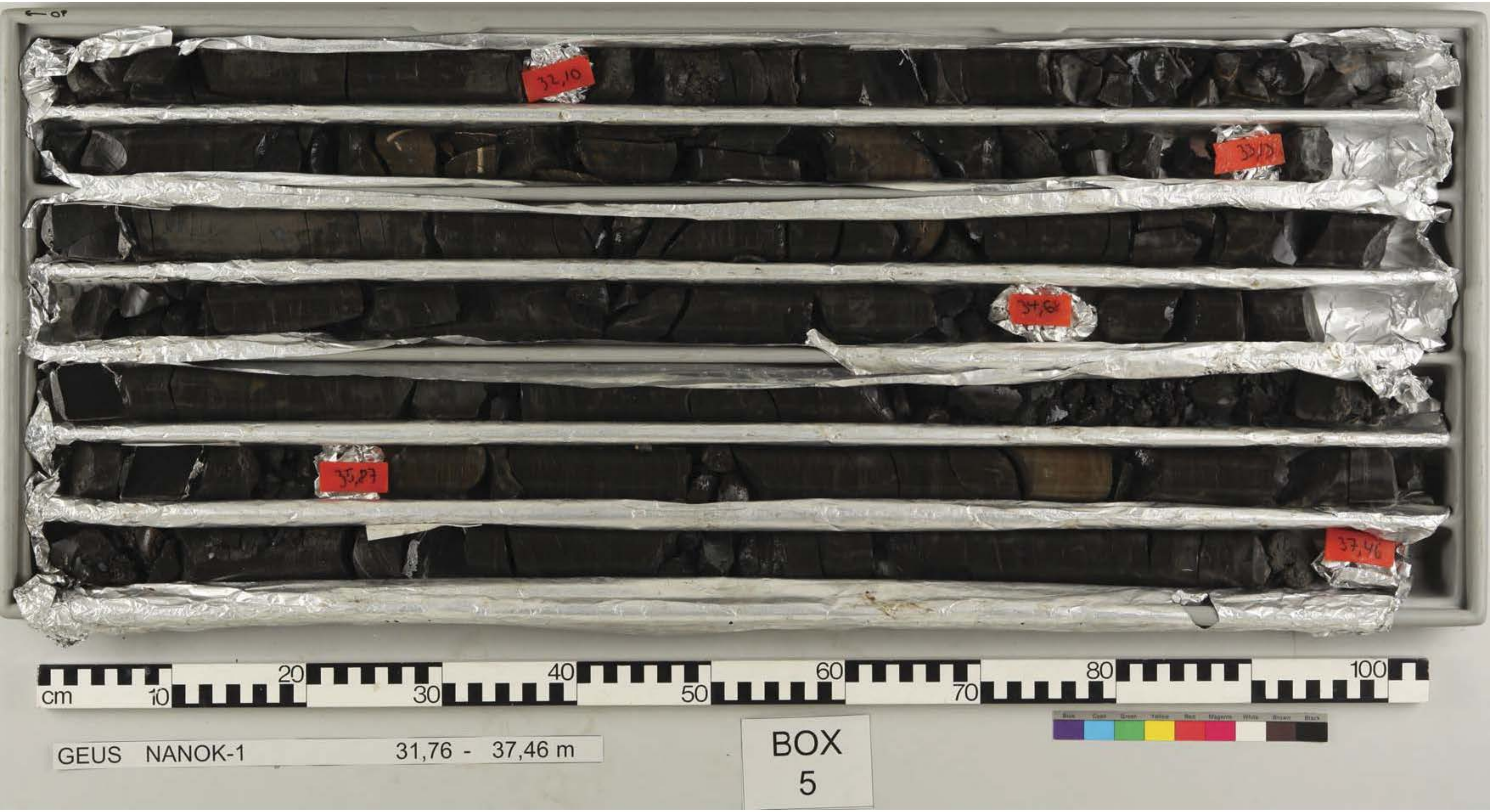

32,10
33,10
34,6?
35,87
37,46
cm 10 20 30 40 50 60 70 80 100
GEUS NANOK-1 31,76 - 37,46 m
BOX
5

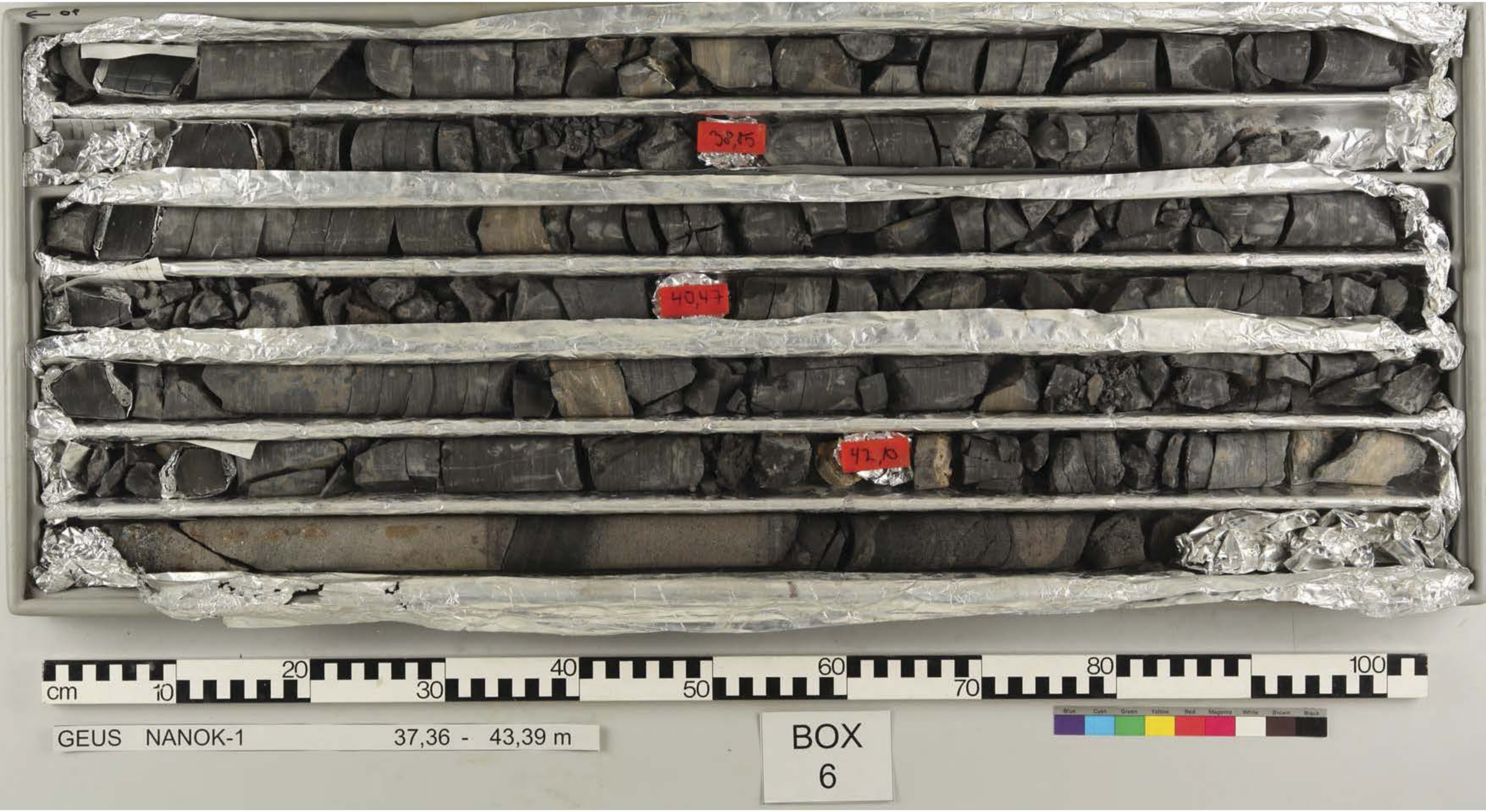
38,85
40,47
42,10
cm 10 20 30 40 50 60 70 80 100
GEUS NANOK-1 37,36 - 43,39 m
BOX
6

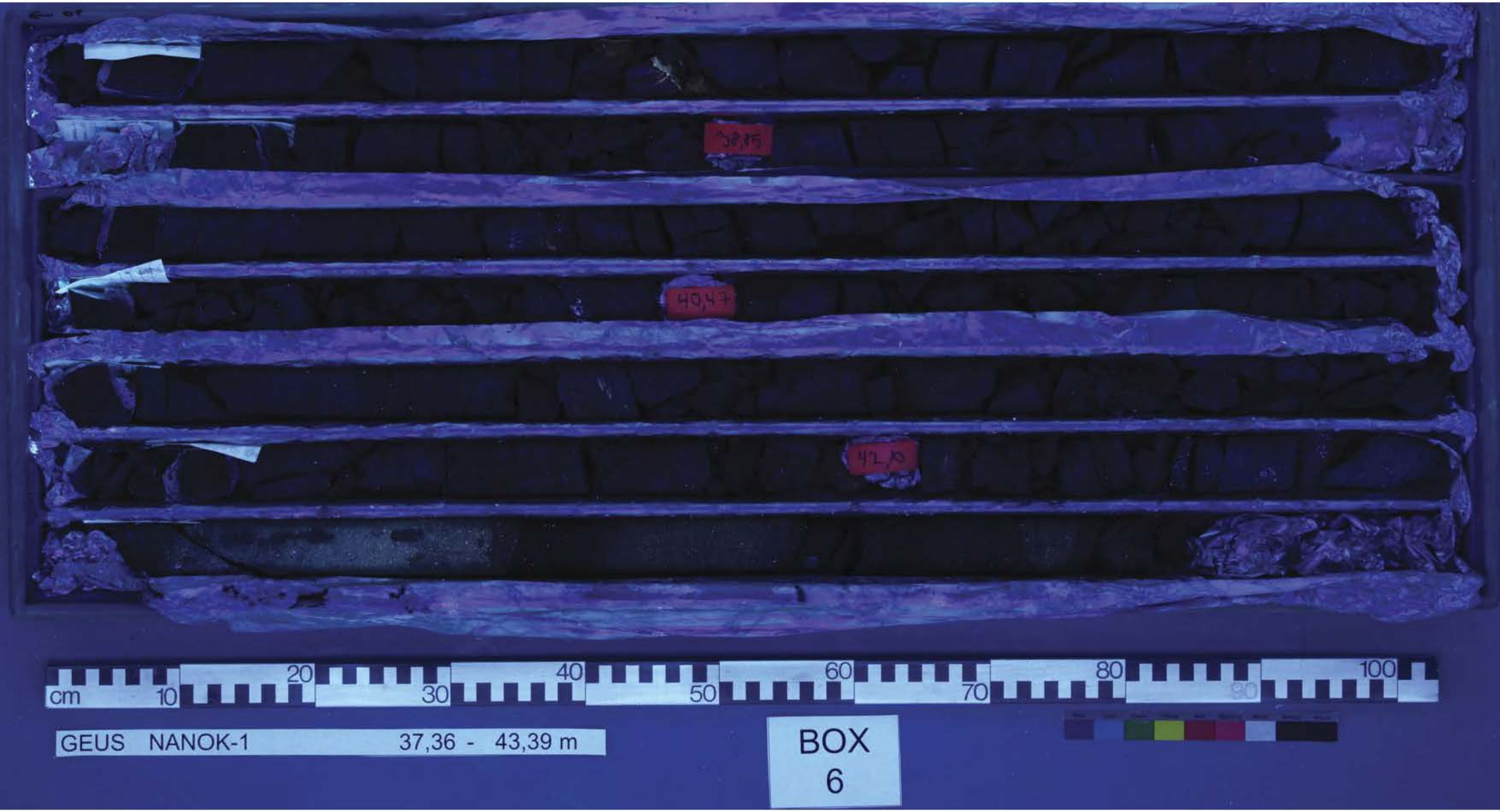

38,85
40,47
42,10
cm 10 20 30 40 50 60 70 80 90 100
GEUS NANOK-1 37,36 - 43,39 m
BOX
6

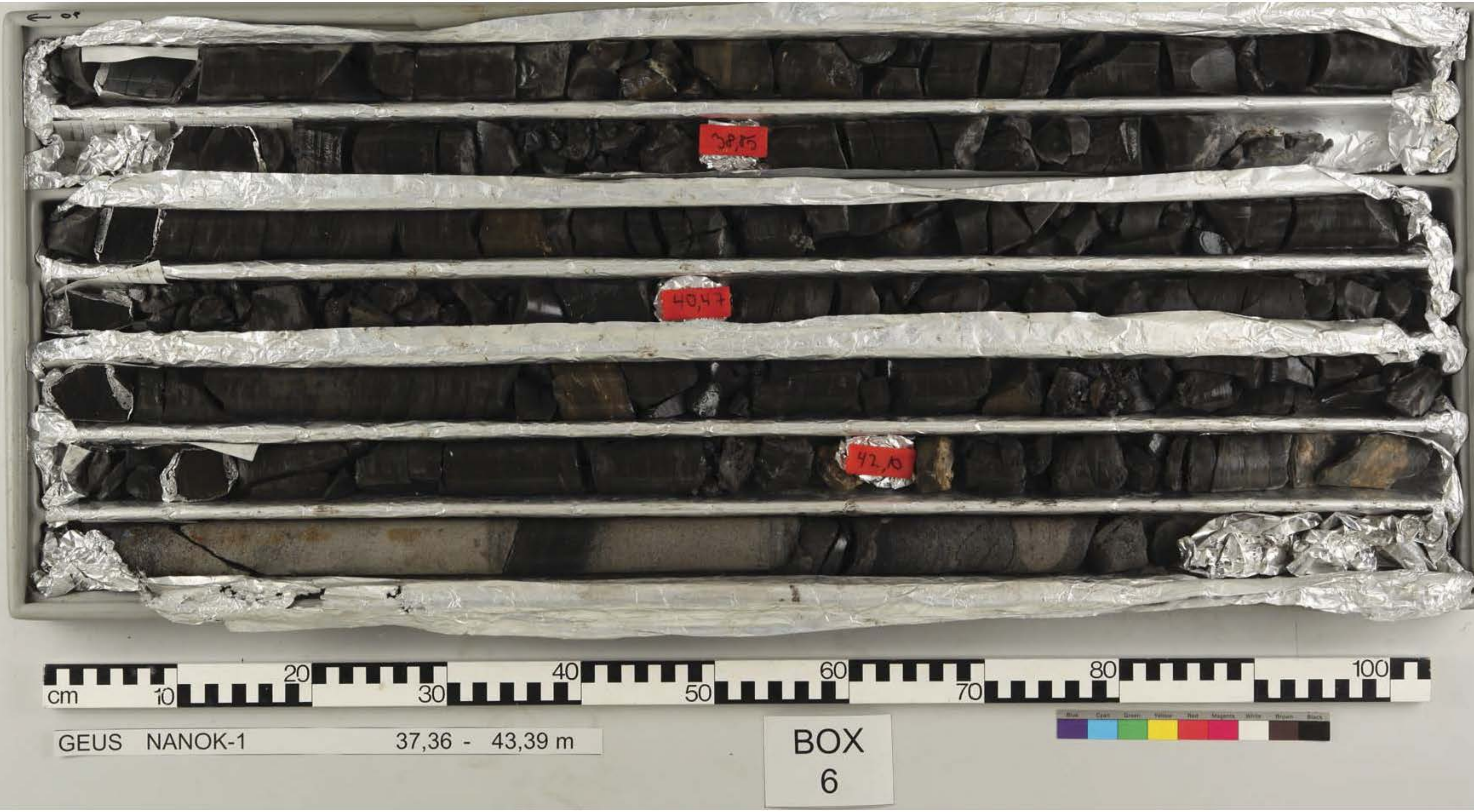
38,85
40,47
42,10
cm 10 20 30 40 50 60 70 80 100
GEUS NANOK-1 37,36 - 43,39 m
BOX
6

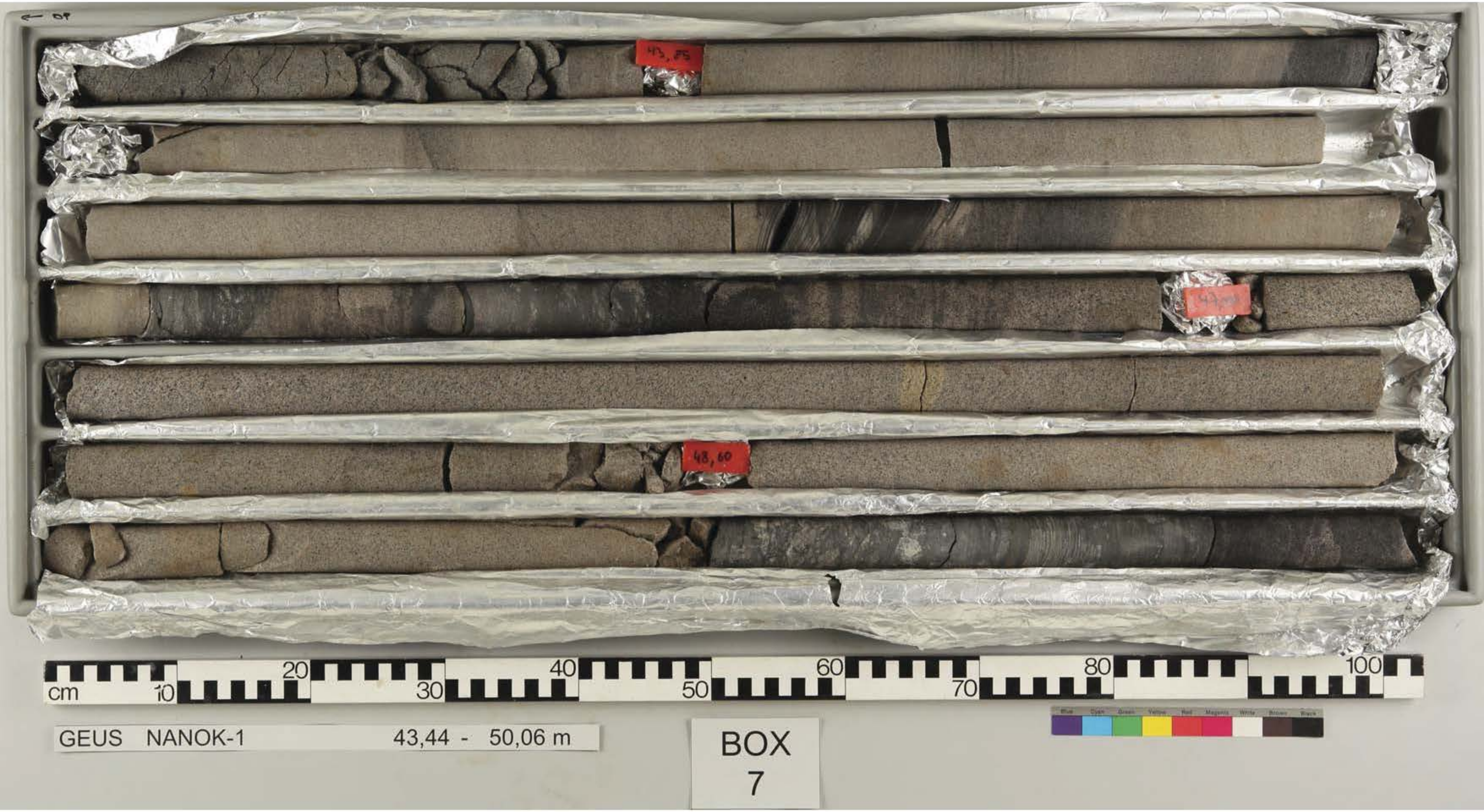
43,85
48,60
cm
10
20
30
40
50
60
70
80
100
GEUS NANOK-1 43,44 - 50,06 m
BOX
7

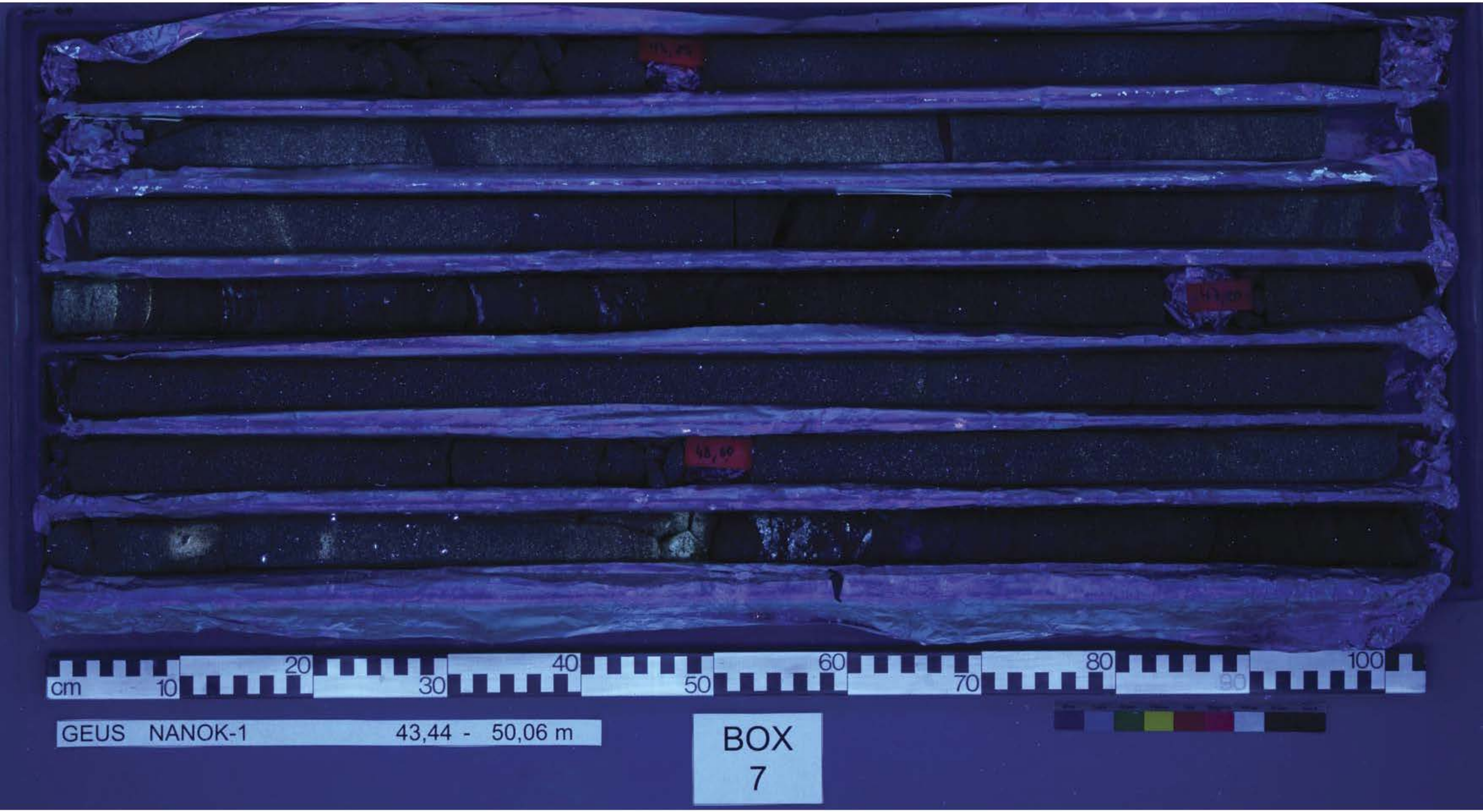

cm 10 20 30 40 50 60 70 80 90 100
GEUS NANOK-1 43,44 - 50,06 m
BOX
7

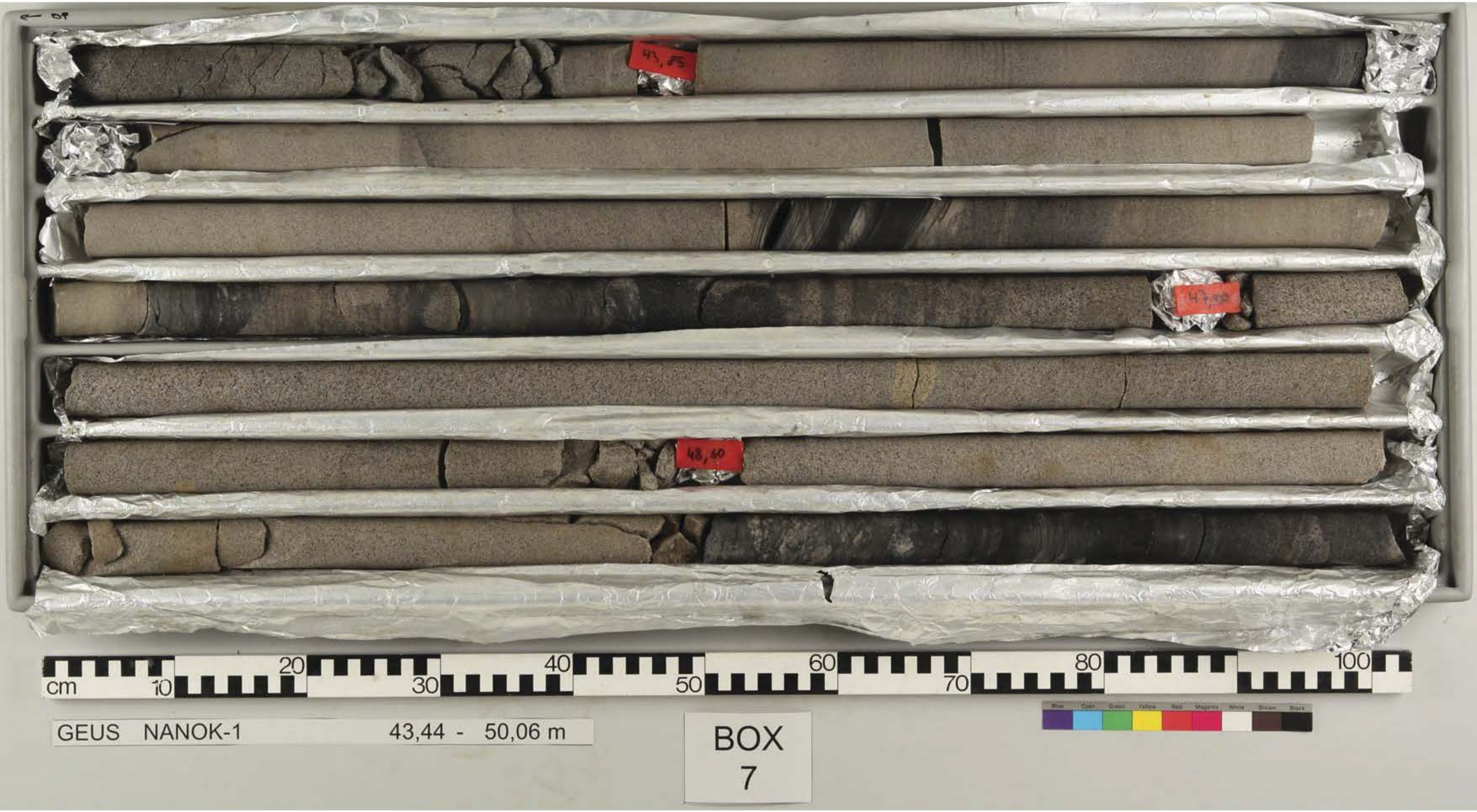
cm 10 20 30 40 50 60 70 80 100
GEUS NANOK-1 43,44 - 50,06 m
BOX
7

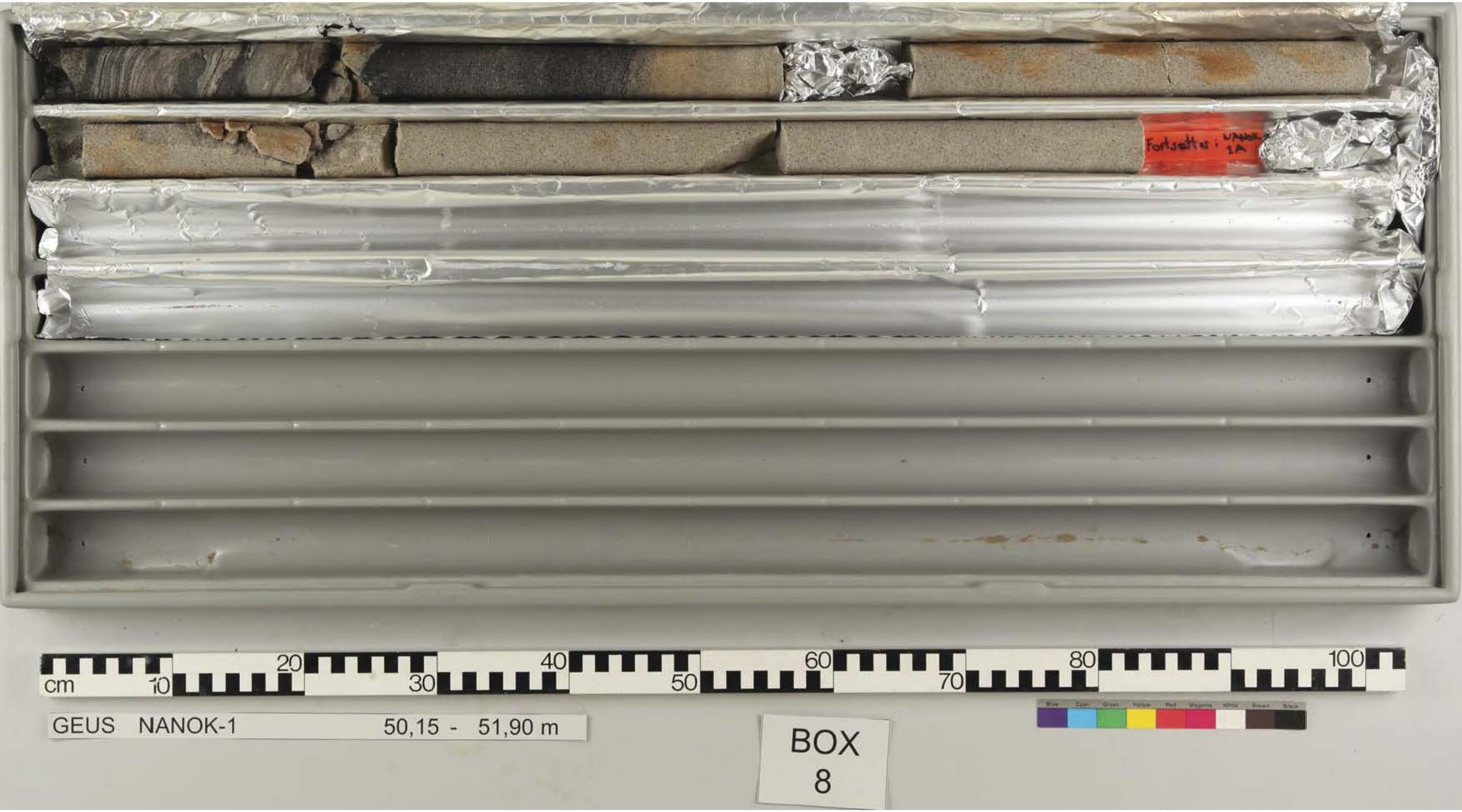

Fortsættes: NANOK-1A
cm 10 20 30 40 50 60 70 80 100
GEUS NANOK-1 50,15 - 51,90 m
BOX 8

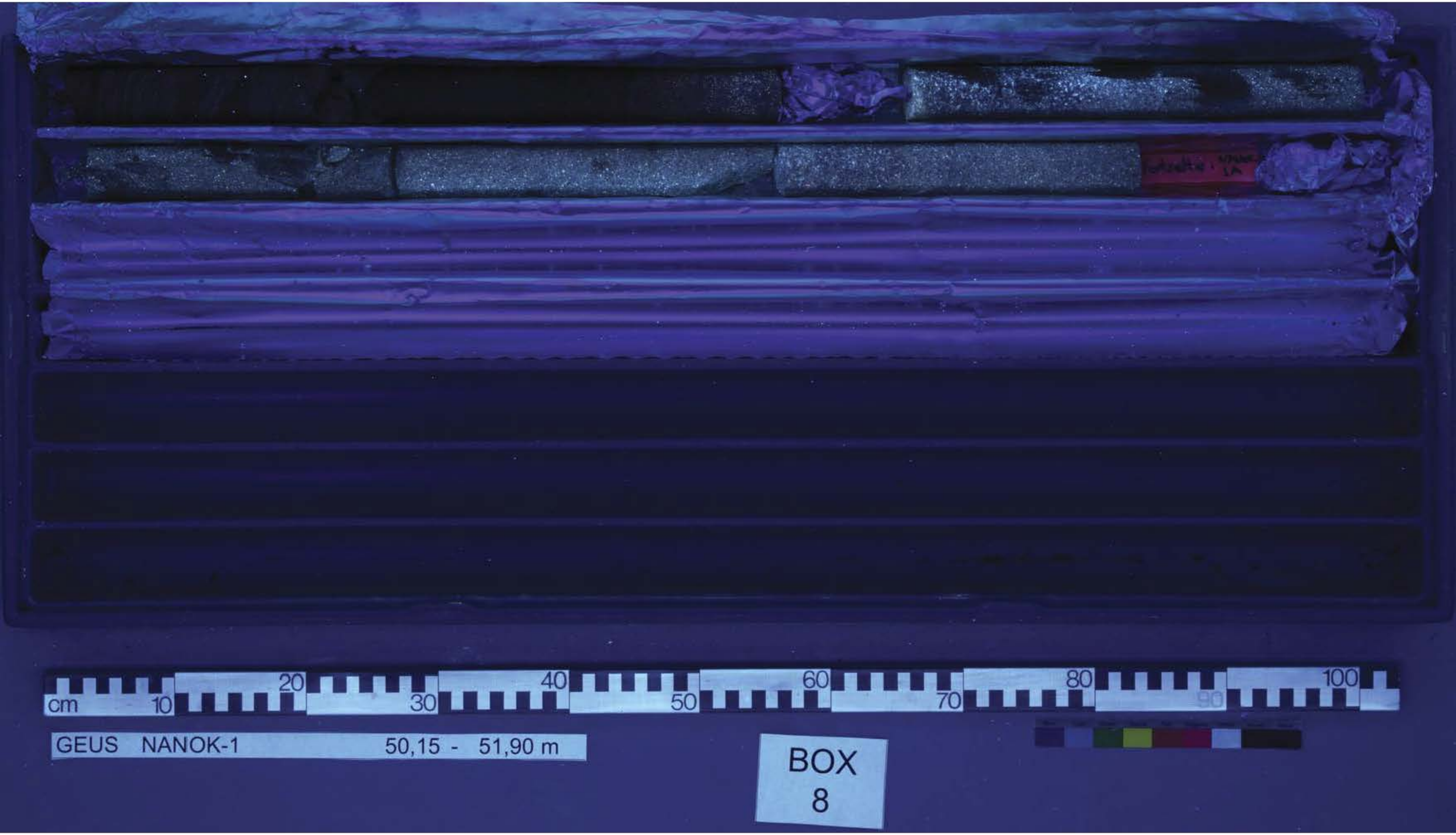
cm
10
20
30
40
50
60
70
80
90
100
GEUS NANOK-1 50,15 - 51,90 m
BOX
8

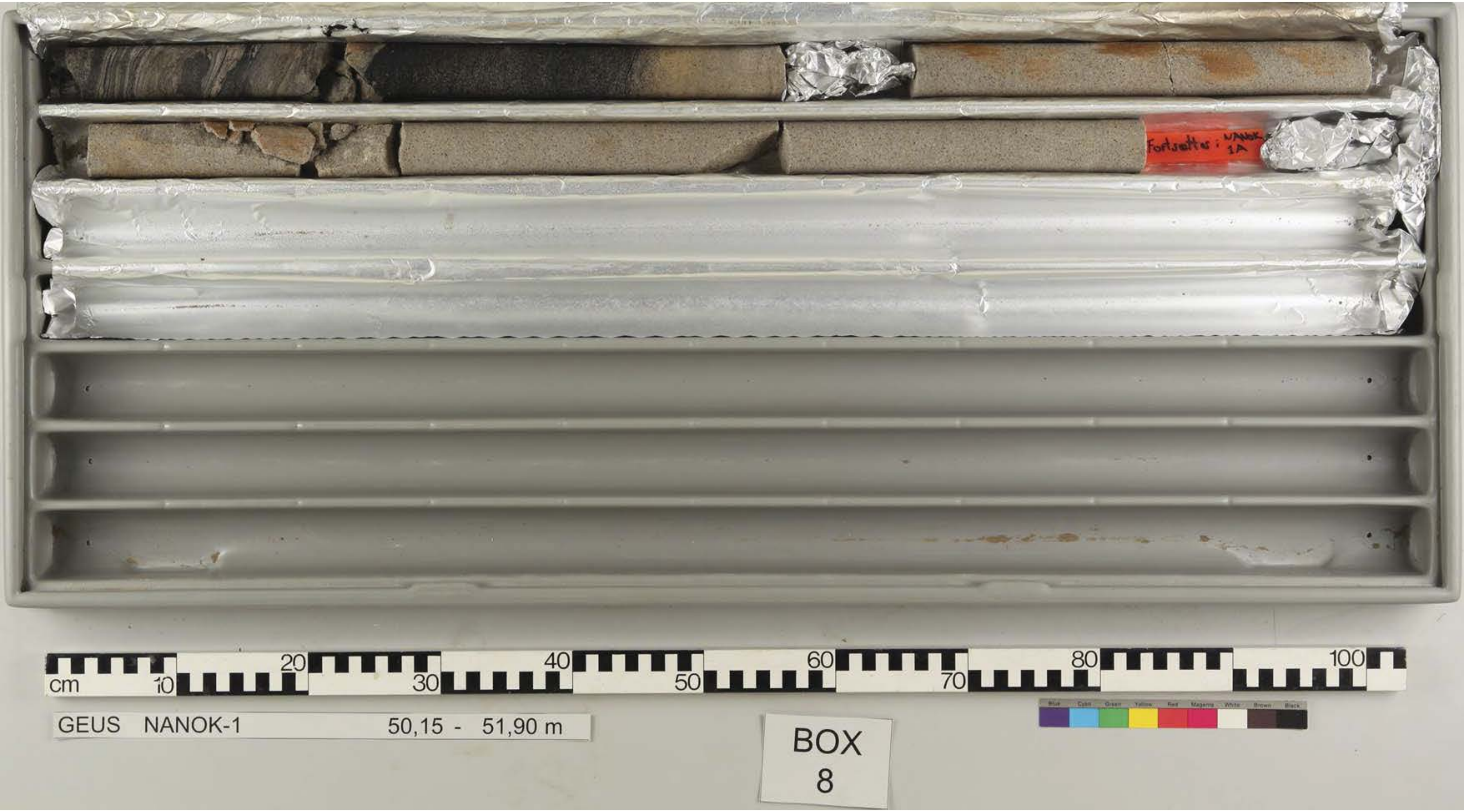
Fortsættes i NANOK 1A
cm
10
20
30
40
50
60
70
80
100
GEUS NANOK-1 50,15 - 51,90 m
BOX
8
Blue
Cyan
Green
Yellow
Red
Magenta
White
Brown
Black


34,86
36,57
37,90
cm
10
20
30
40
50
60
70
80
100
GEUS NANOK-1A 32,52 - 38,53 m
BOX
9

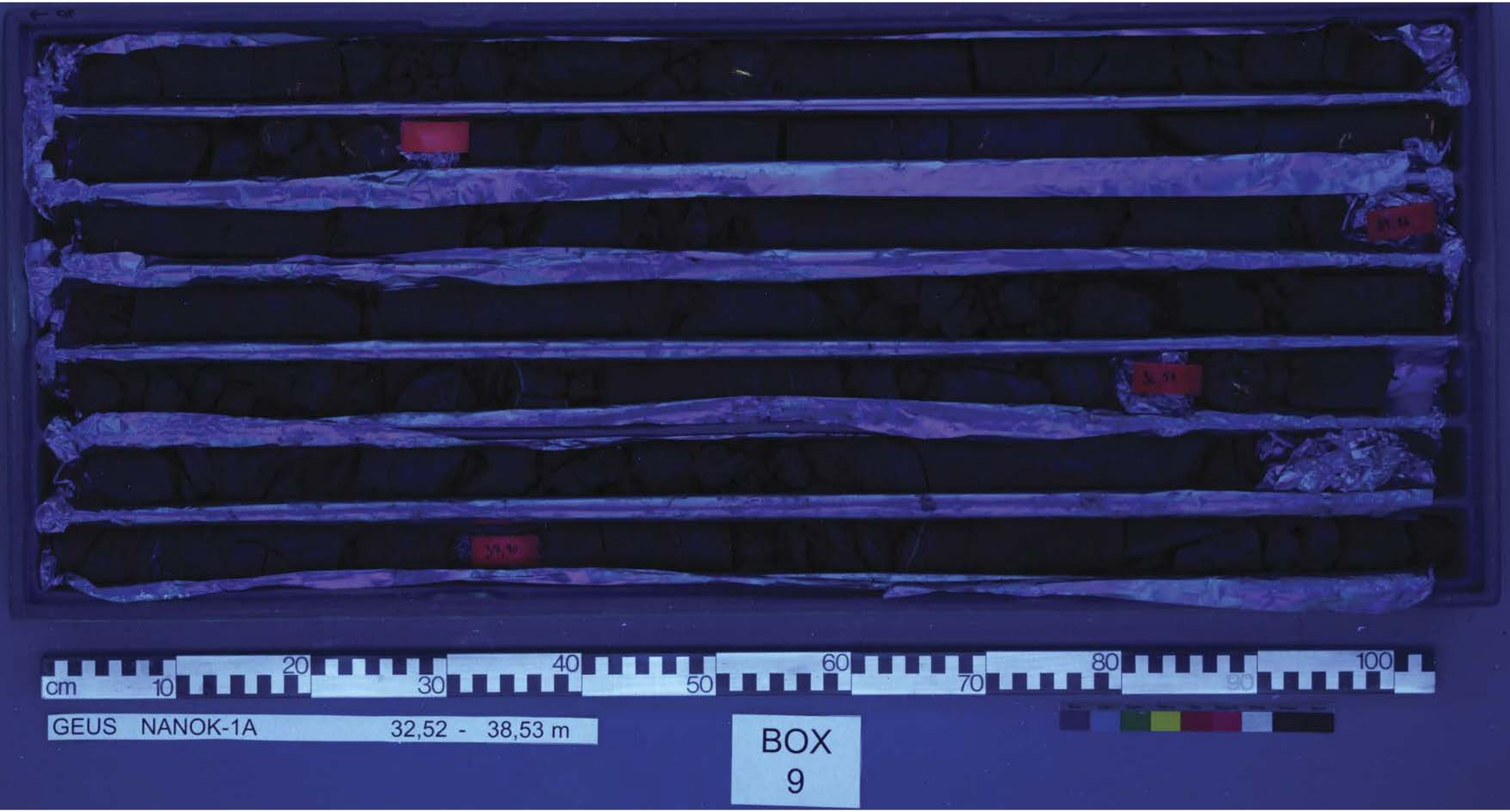

cm 10 20 30 40 50 60 70 80 90 100
GEUS NANOK-1A 32,52 - 38,53 m
BOX
9


cm 10 20 30 40 50 60 70 80 100
GEUS NANOK-1A 32,52 - 38,53 m
BOX
9

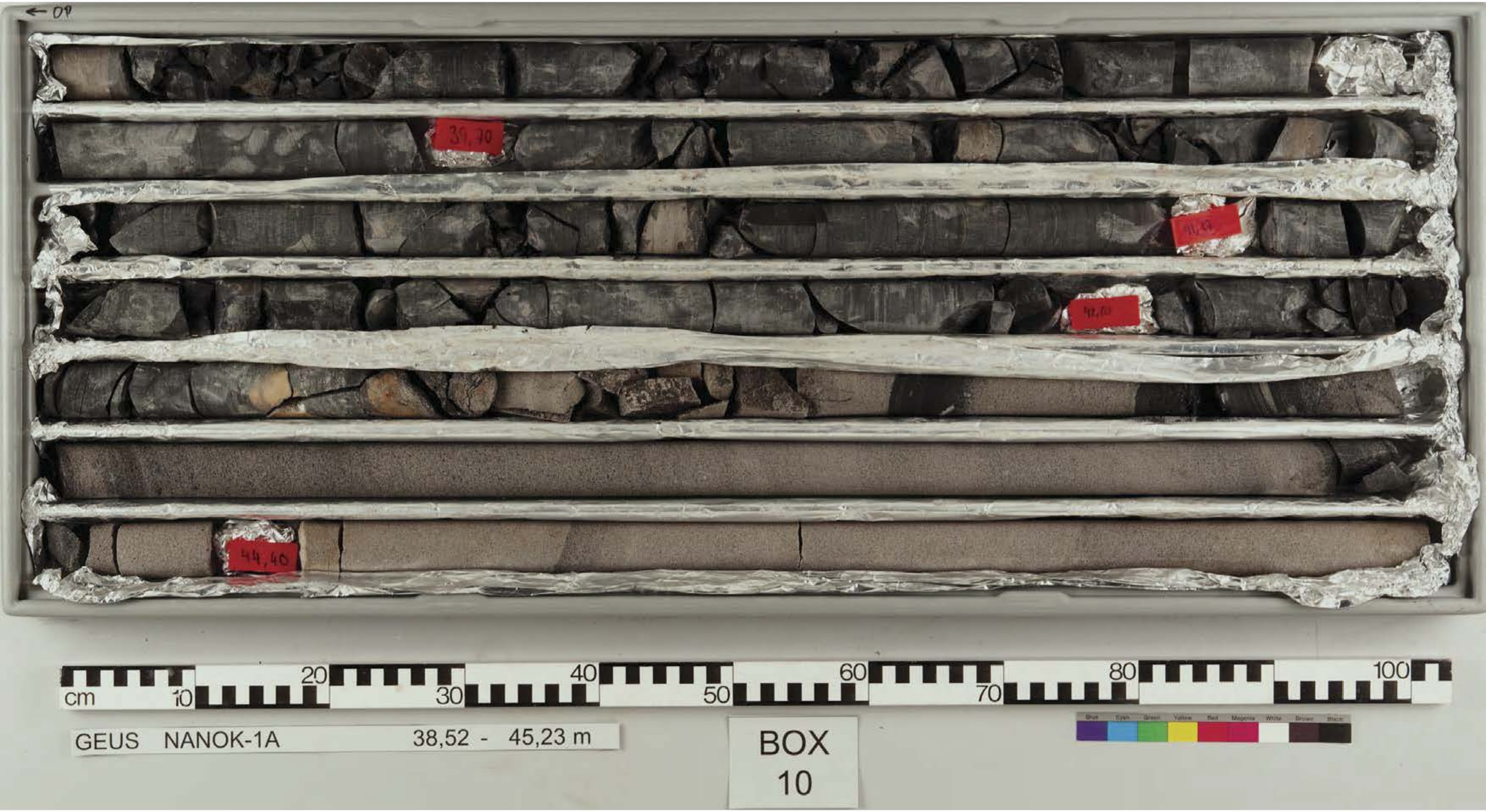

←OP
39,70
41,14
42,60
44,40
cm
10
20
30
40
50
60
70
80
100
GEUS NANOK-1A 38,52 - 45,23 m
BOX
10

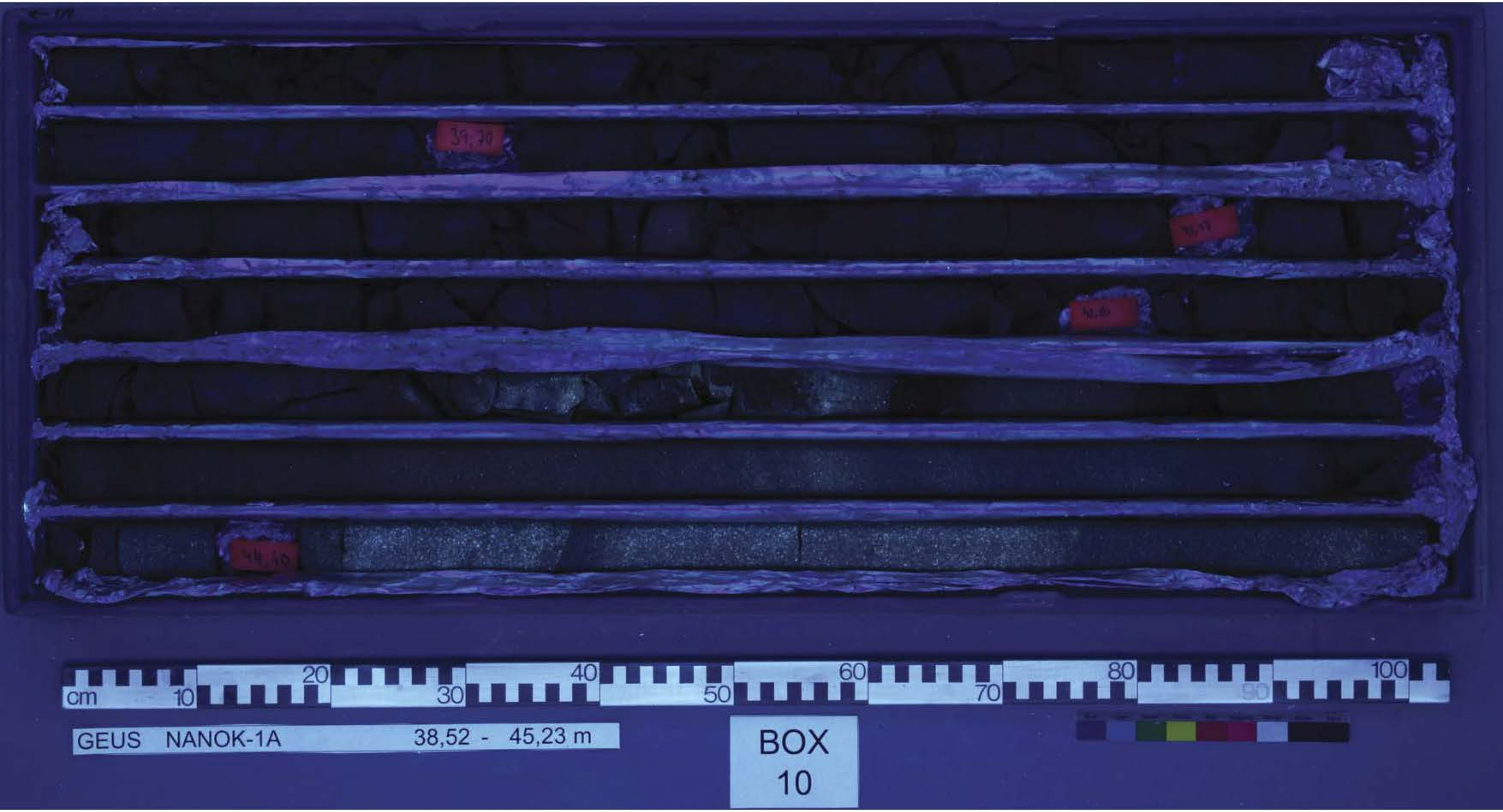
cm 10 20 30 40 50 60 70 80 90 100
GEUS NANOK-1A 38,52 - 45,23 m
BOX
10
39,70

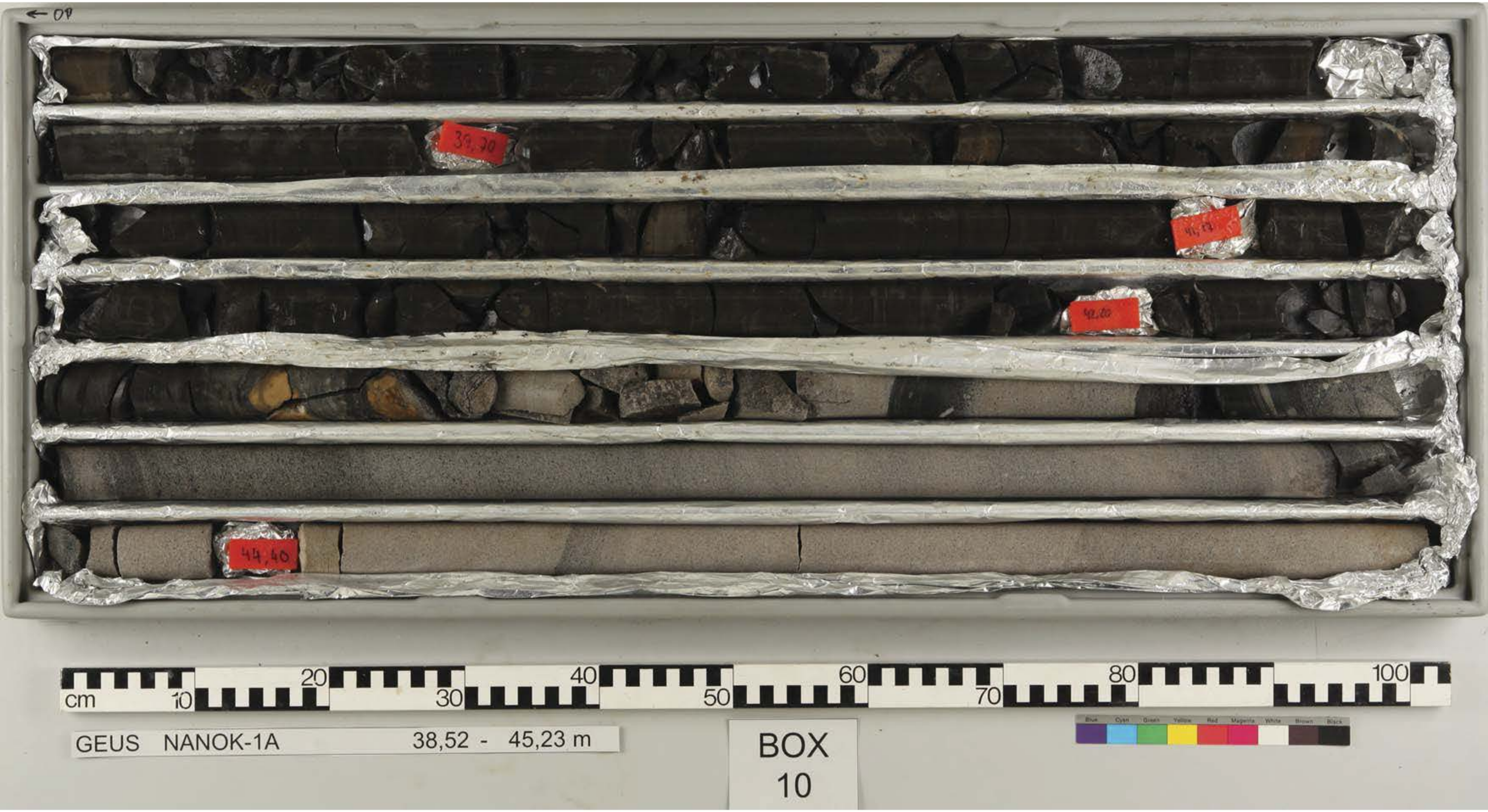

← OP
39,70
40,87
42,00
44,40
cm 10 20 30 40 50 60 70 80 100
Blue Cyan Green Yellow Red Magenta White Brown Black
GEUS NANOK-1A 38,52 - 45,23 m
BOX
10

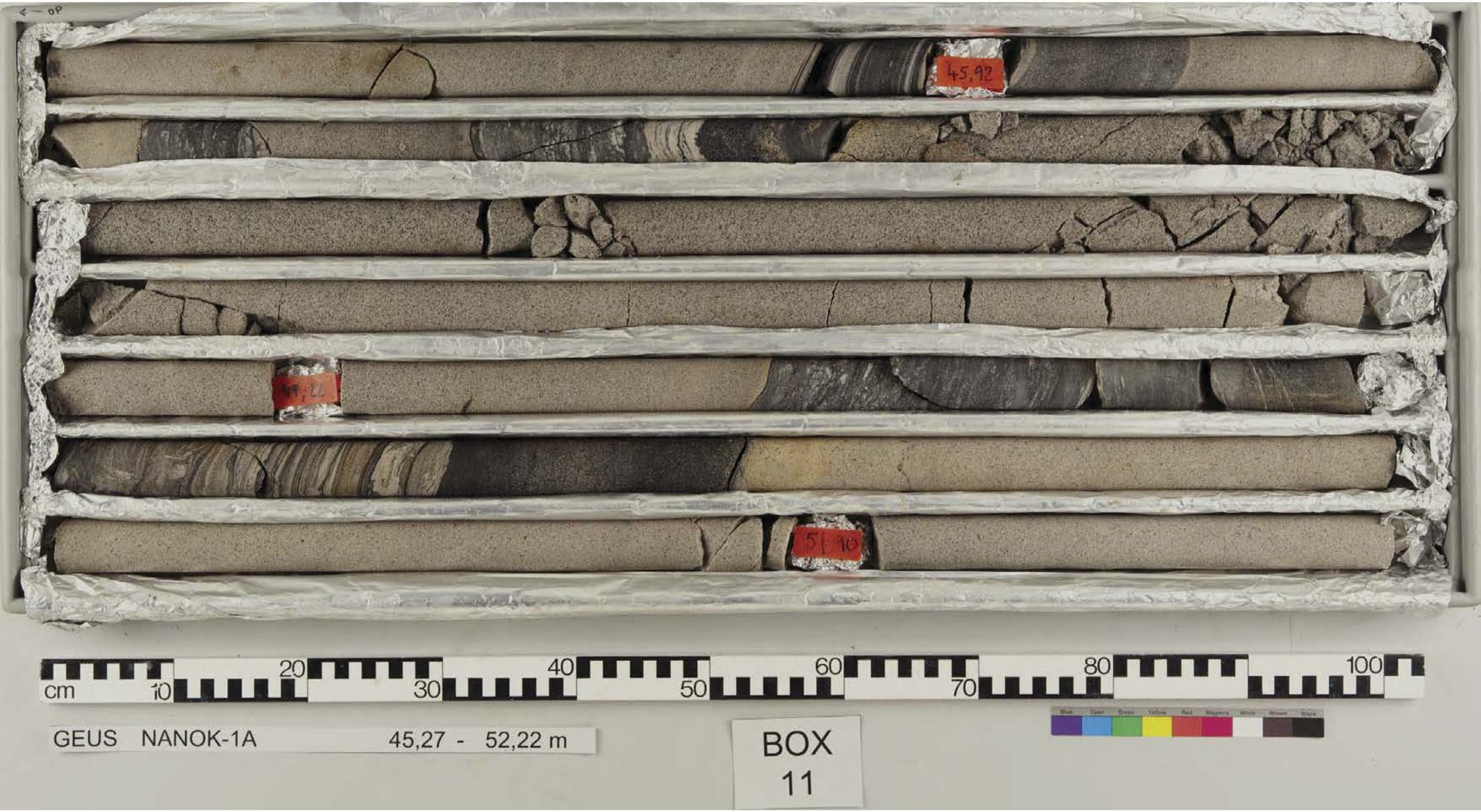
45,92
51,90
cm
10
20
30
40
50
60
70
80
100
Blue
Cyan
Green
Yellow
Red
Magenta
White
Brown
Black
GEUS NANOK-1A 45,27 - 52,22 m
BOX
11

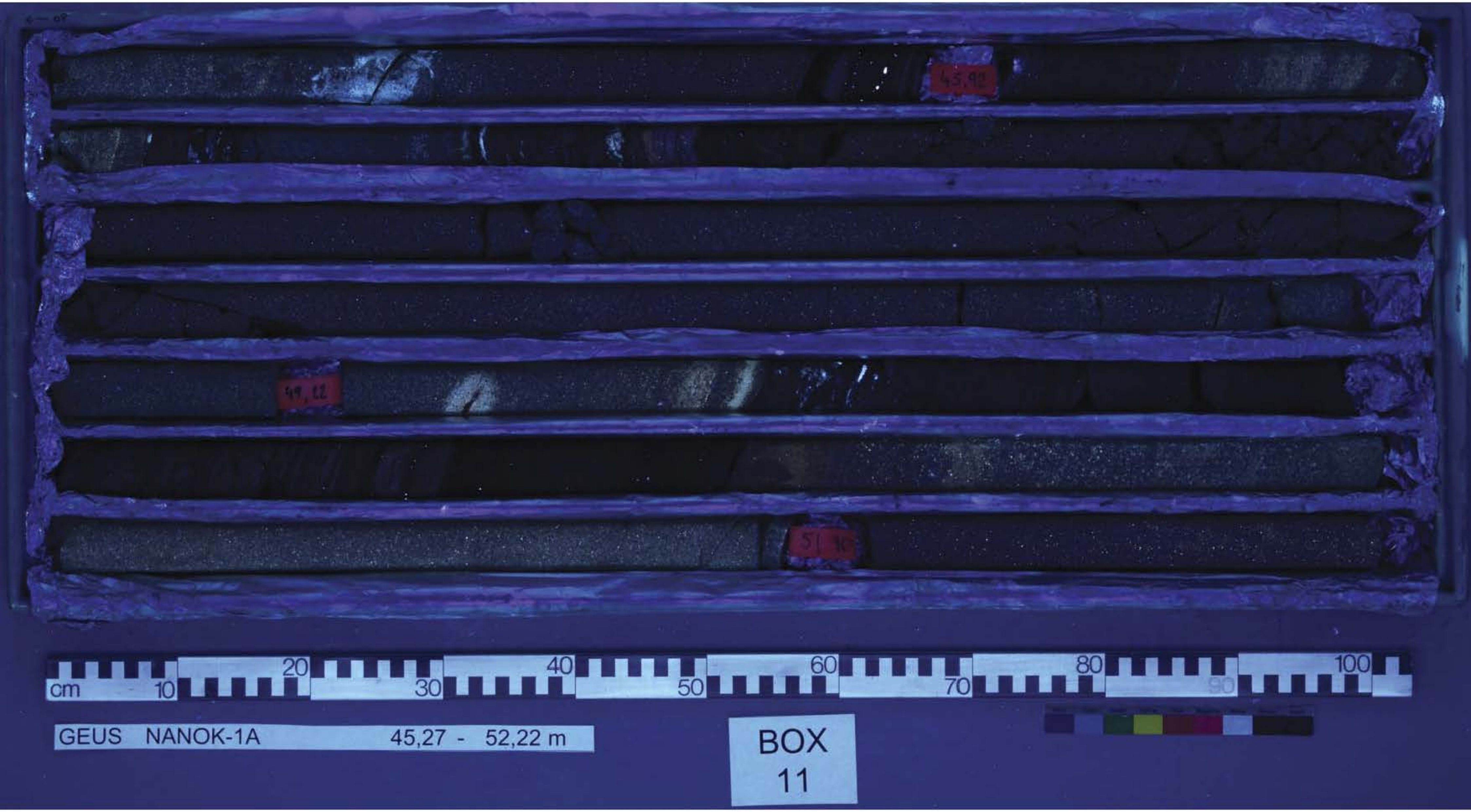
cm 10 20 30 40 50 60 70 80 90 100
GEUS NANOK-1A 45,27 - 52,22 m
BOX
11

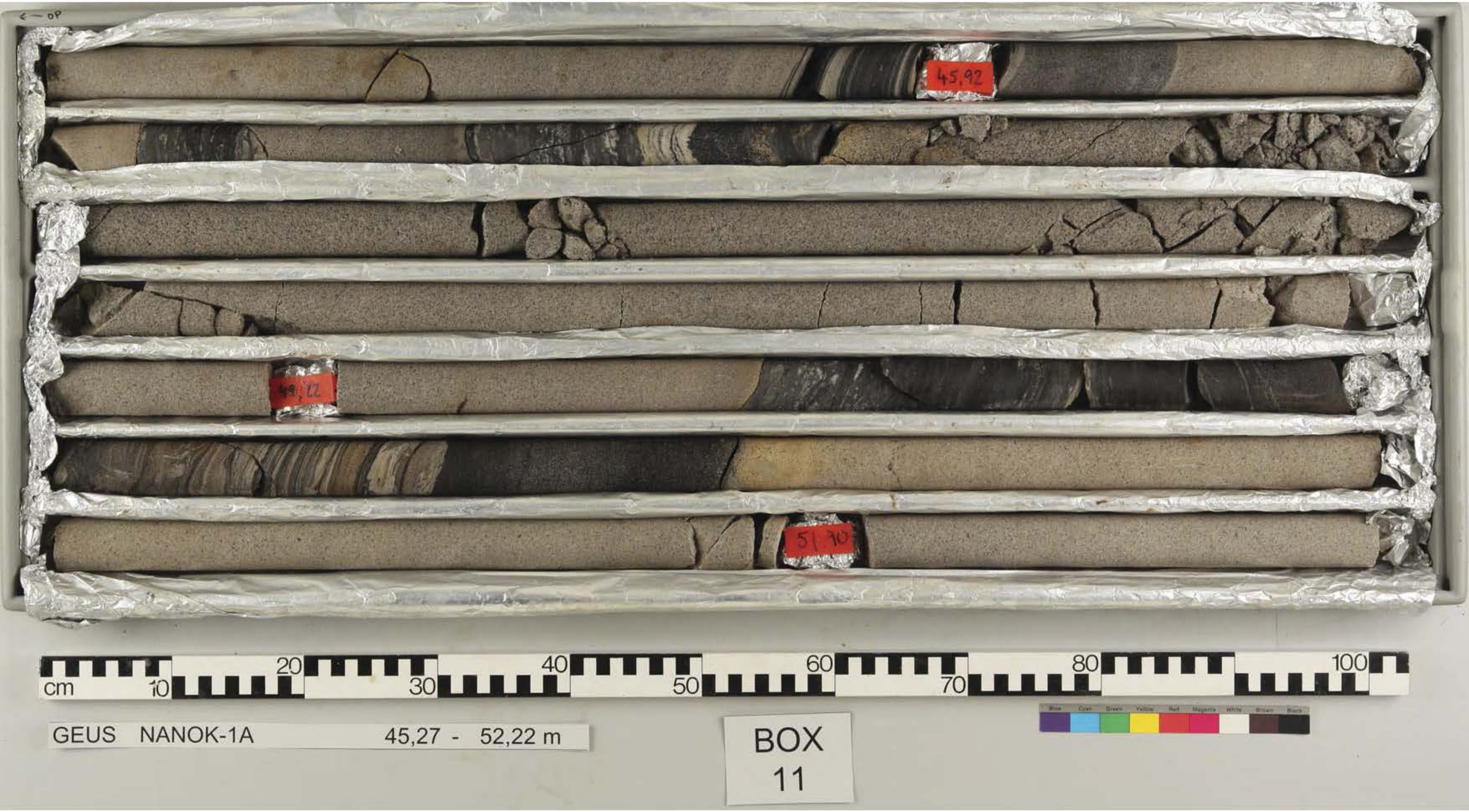
45,92
cm 10 20 30 40 50 60 70 80 100
GEUS NANOK-1A 45,27 - 52,22 m
BOX
11


54,90
57,90
cm 10 20 30 40 50 60 70 80 100
GEUS NANOK-1A 52,08 - 58,64 m
BOX
12

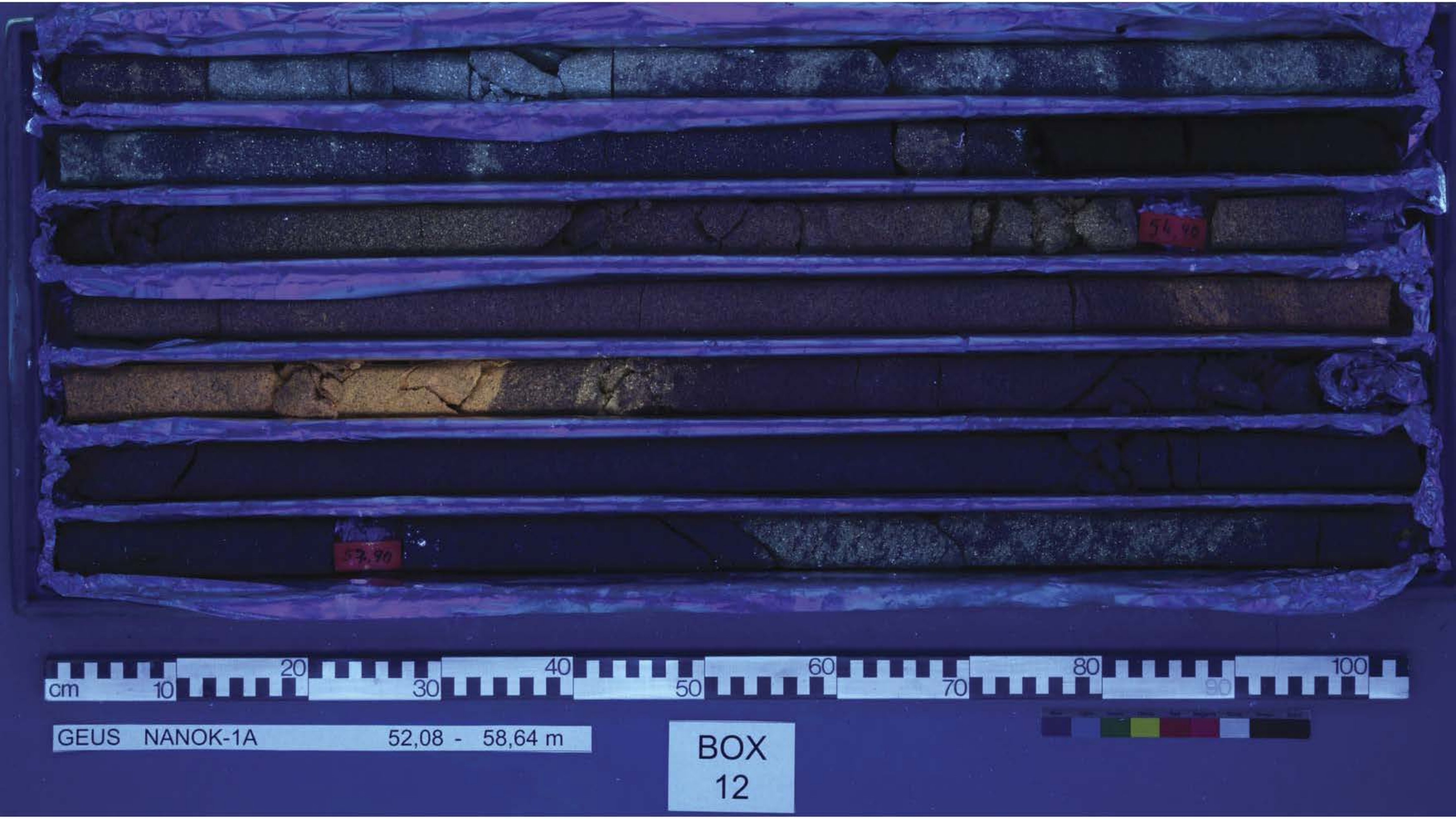

54,40
57,90
cm 10 20 30 40 50 60 70 80 90 100
GEUS NANOK-1A 52,08 - 58,64 m
BOX
12


54,90
57,90
cm 10 20 30 40 50 60 70 80 100
GEUS NANOK-1A 52,08 - 58,64 m
BOX
12

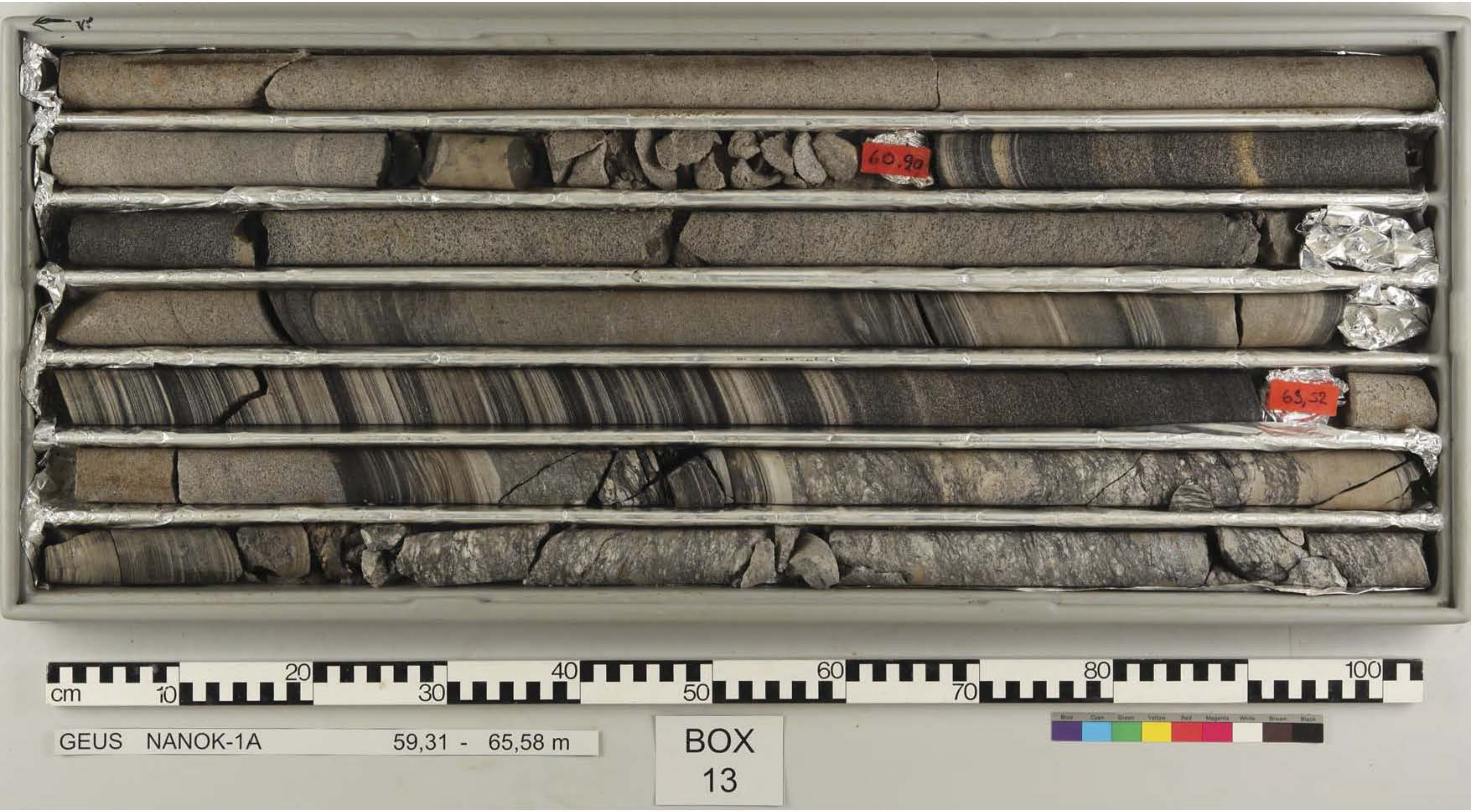

60,90
63,52
cm
10
20
30
40
50
60
70
80
100
GEUS NANOK-1A 59,31 - 65,58 m
BOX
13

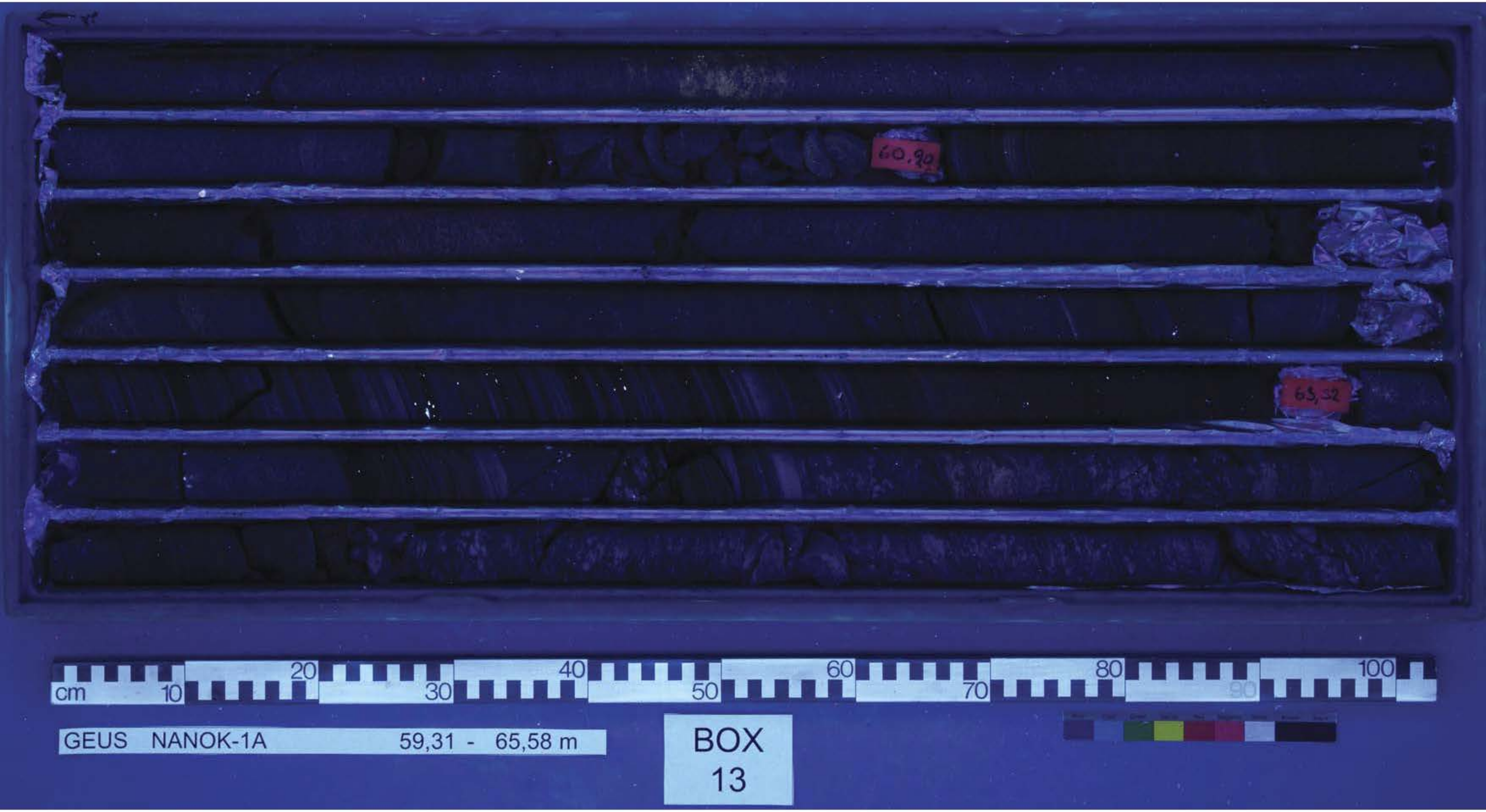

60,90
63,32
cm
10
20
30
40
50
60
70
80
90
100
GEUS NANOK-1A 59,31 - 65,58 m
BOX
13

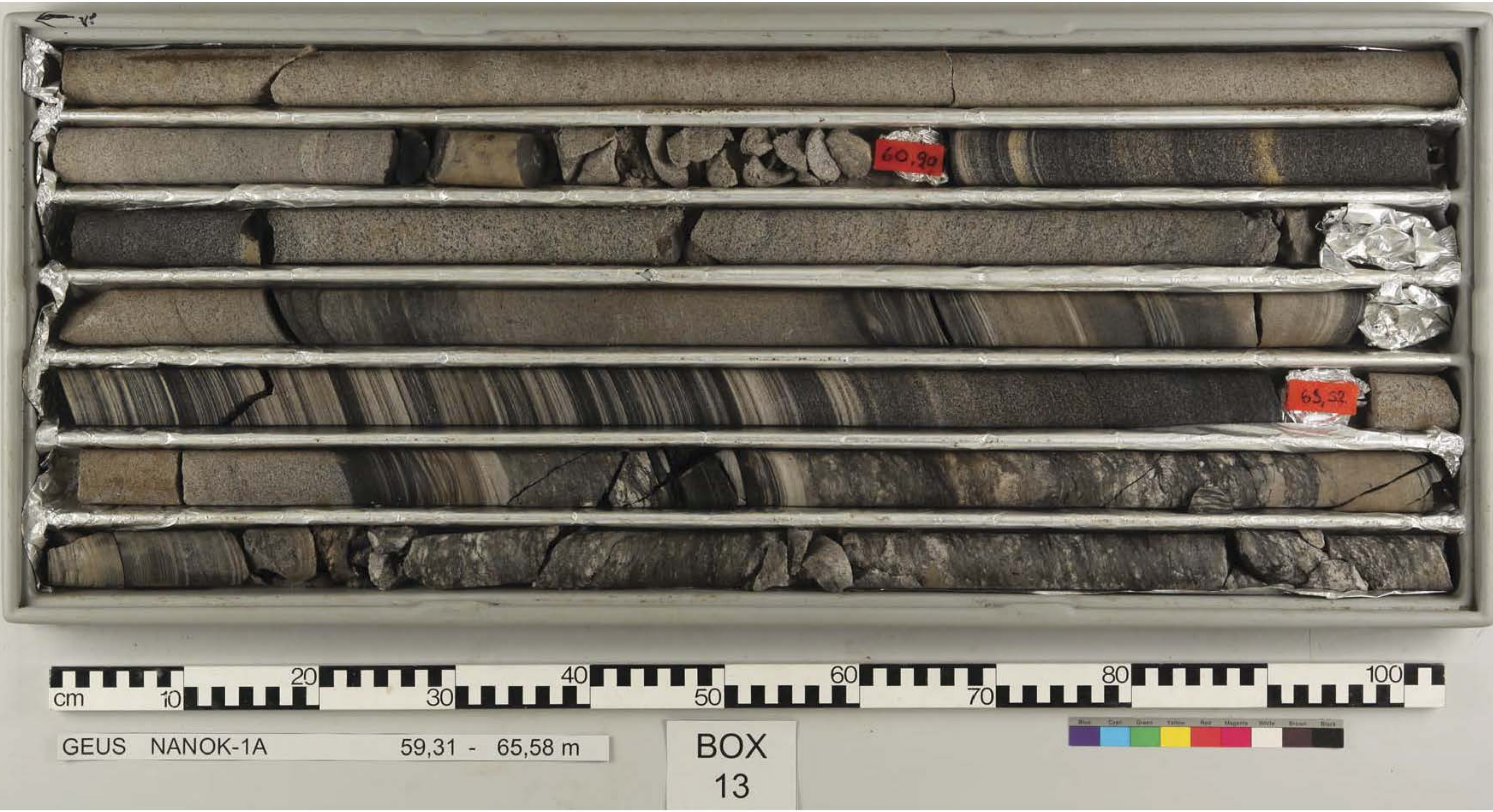
60,90
65,52
cm
10
20
30
40
50
60
70
80
100
GEUS NANOK-1A 59,31 - 65,58 m
BOX
13

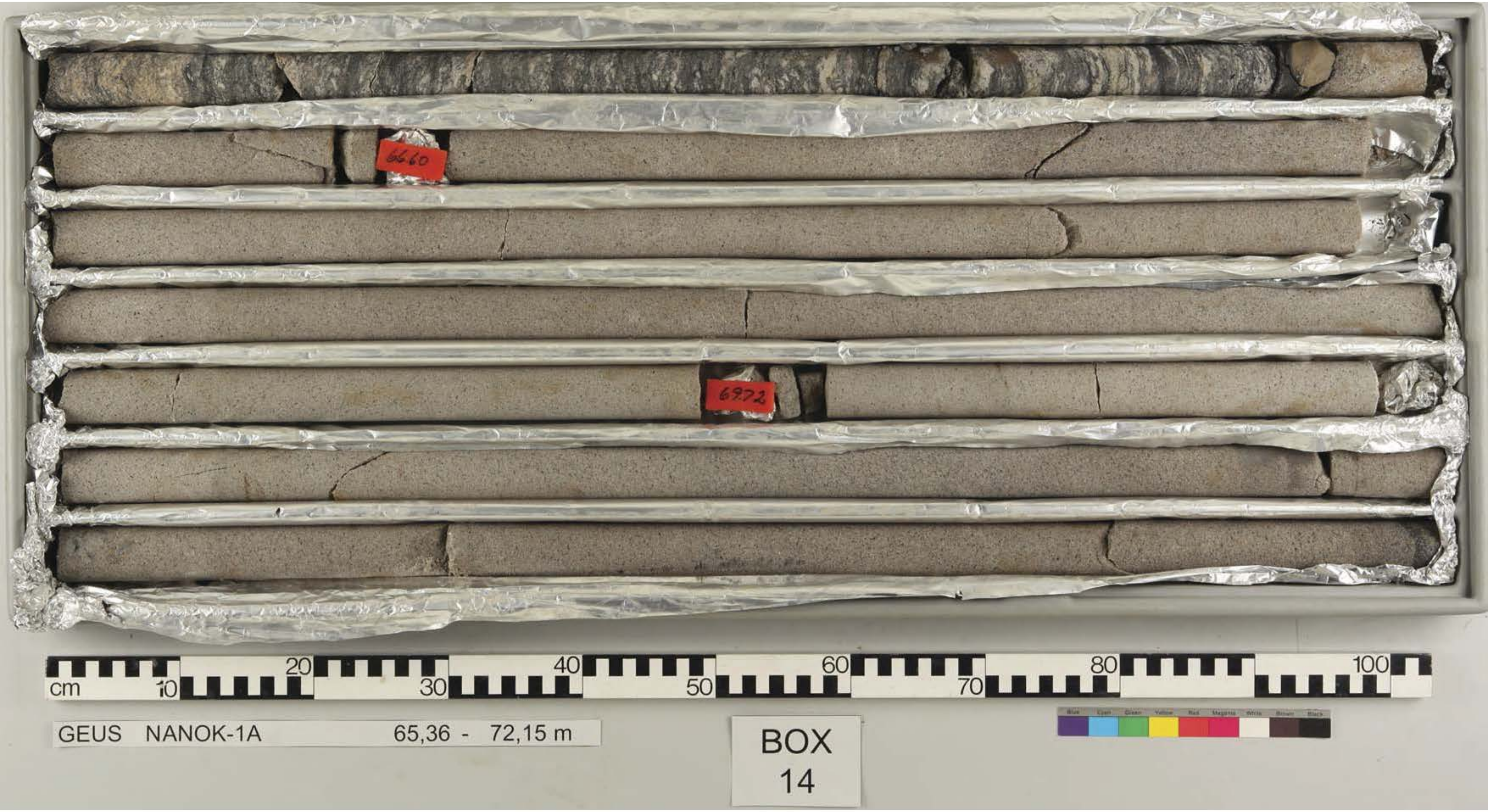
66.60
69.72
cm
10
20
30
40
50
60
70
80
100
GEUS NANOK-1A 65,36 - 72,15 m
BOX
14

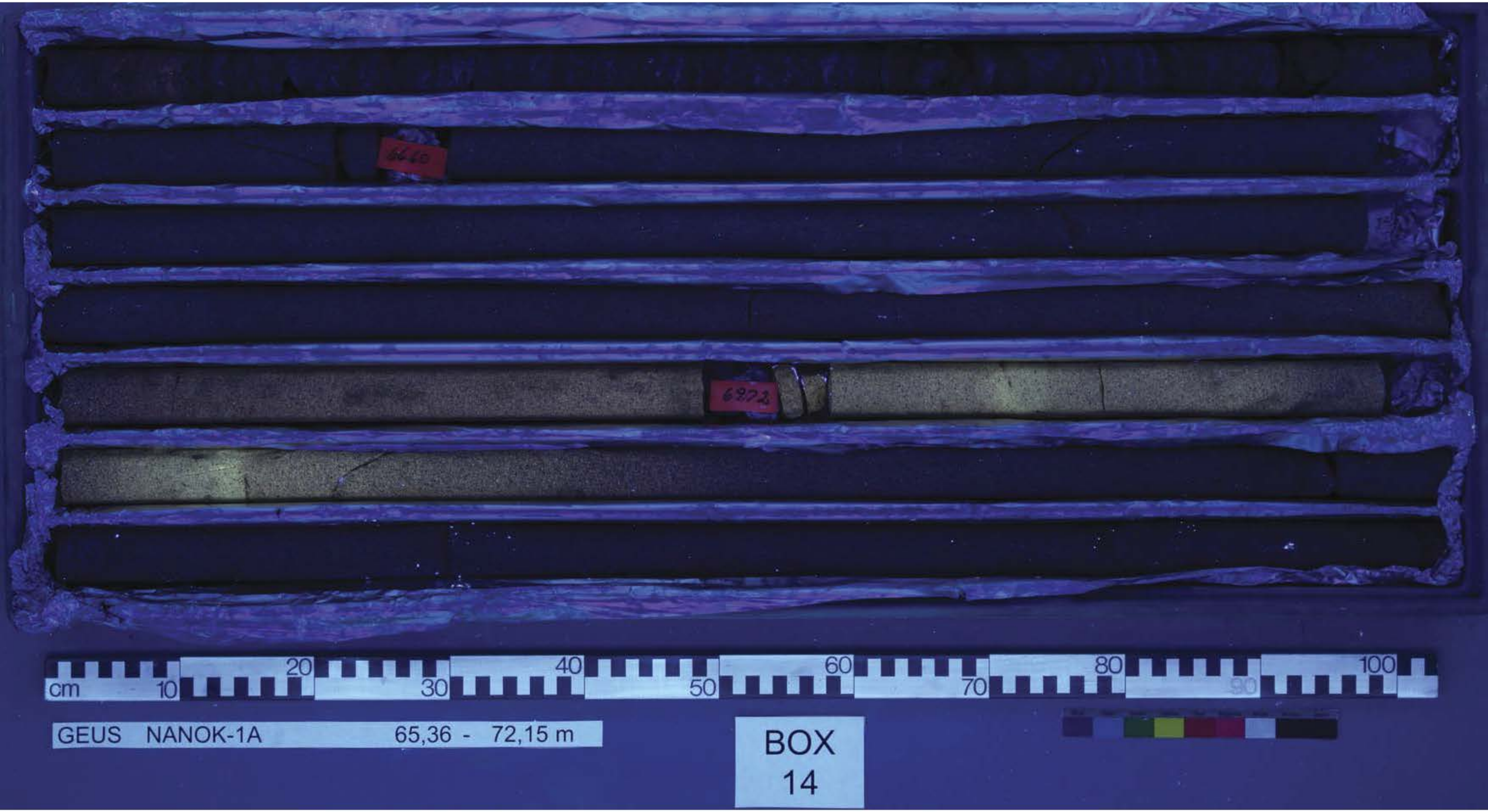
cm 10 20 30 40 50 60 70 80 90 100
GEUS NANOK-1A 65,36 - 72,15 m
BOX
14

66.60
69.72
cm
10
20
30
40
50
60
70
80
100
GEUS NANOK-1A 65,36 - 72,15 m
BOX
14

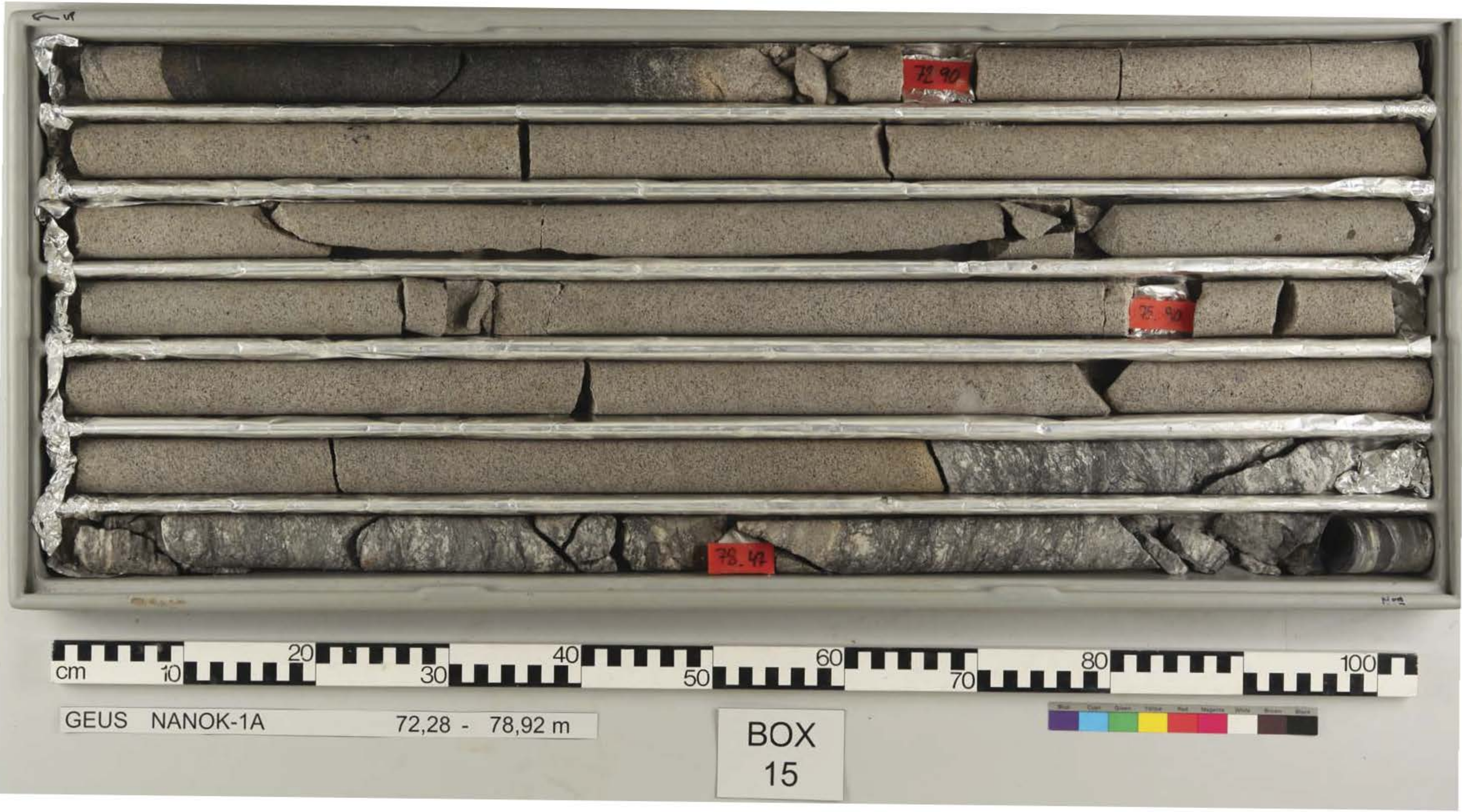
GEUS NANOK-1A 72,28 - 78,92 m
BOX
15
72.90
75.90
78.47
cm

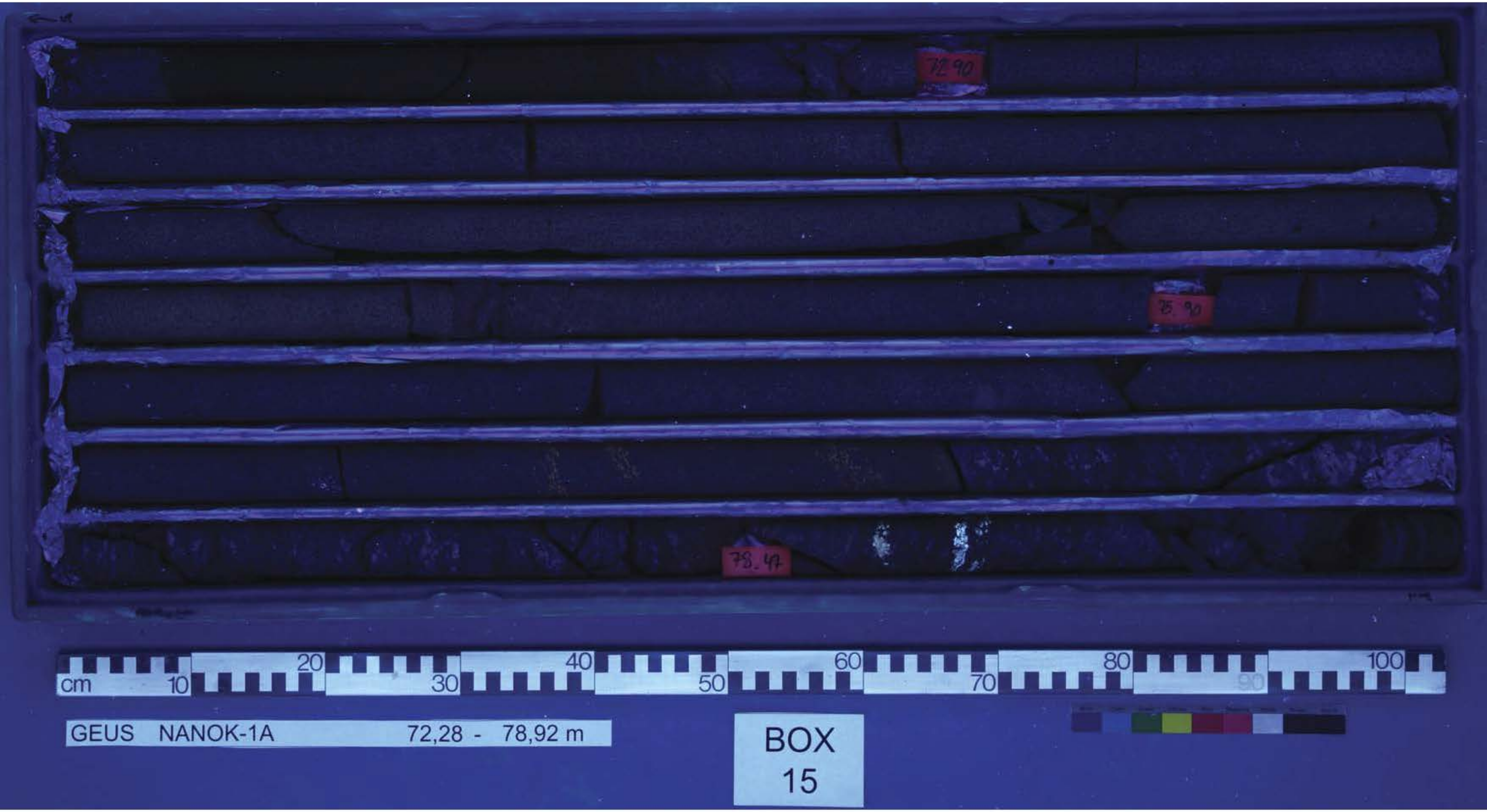
72.90
75.90
78.47
cm 10 20 30 40 50 60 70 80 90 100
GEUS NANOK-1A 72,28 - 78,92 m
BOX
15

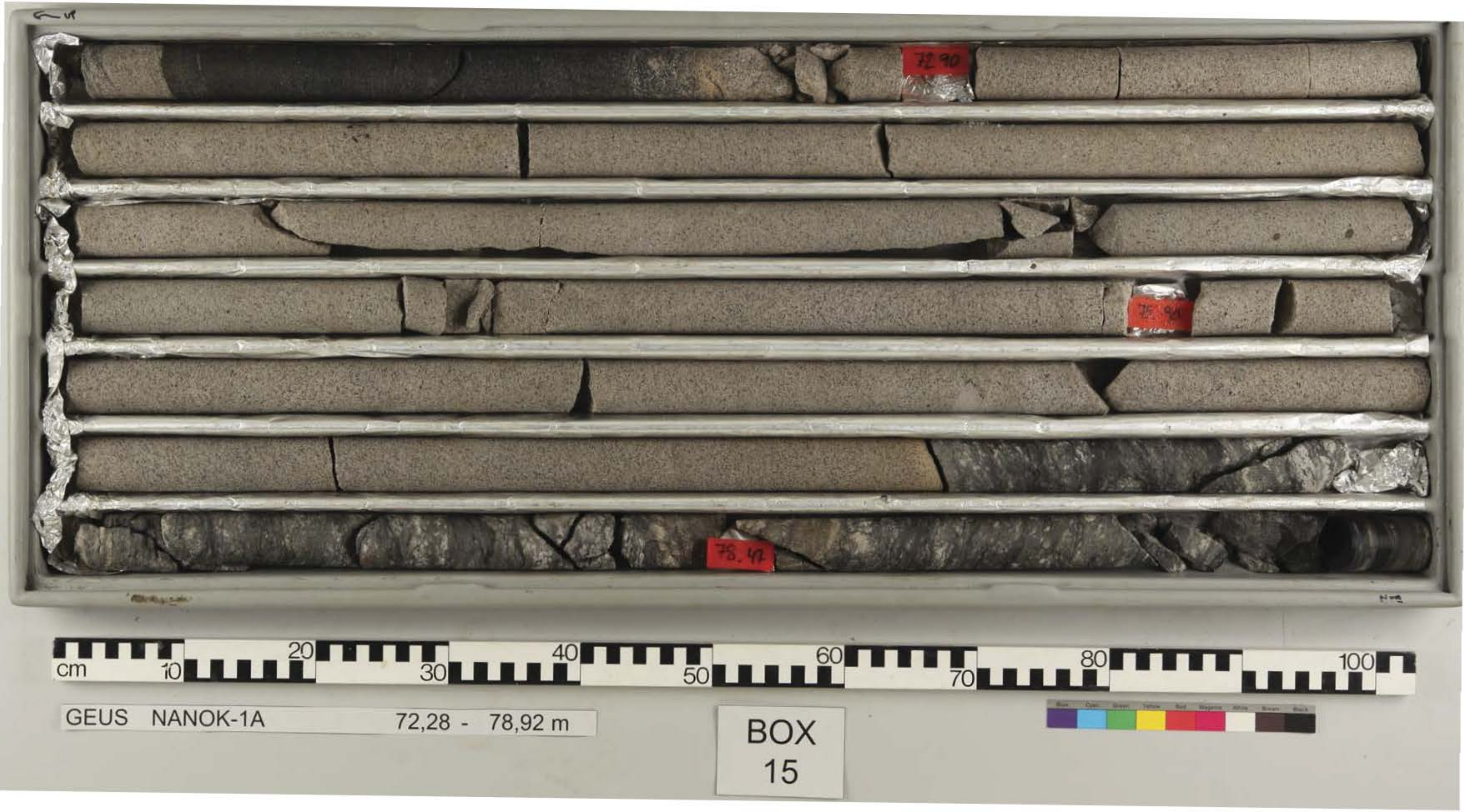
72.90
75.96
78.47
cm
10
20
30
40
50
60
70
80
100
GEUS NANOK-1A 72,28 - 78,92 m
BOX
15

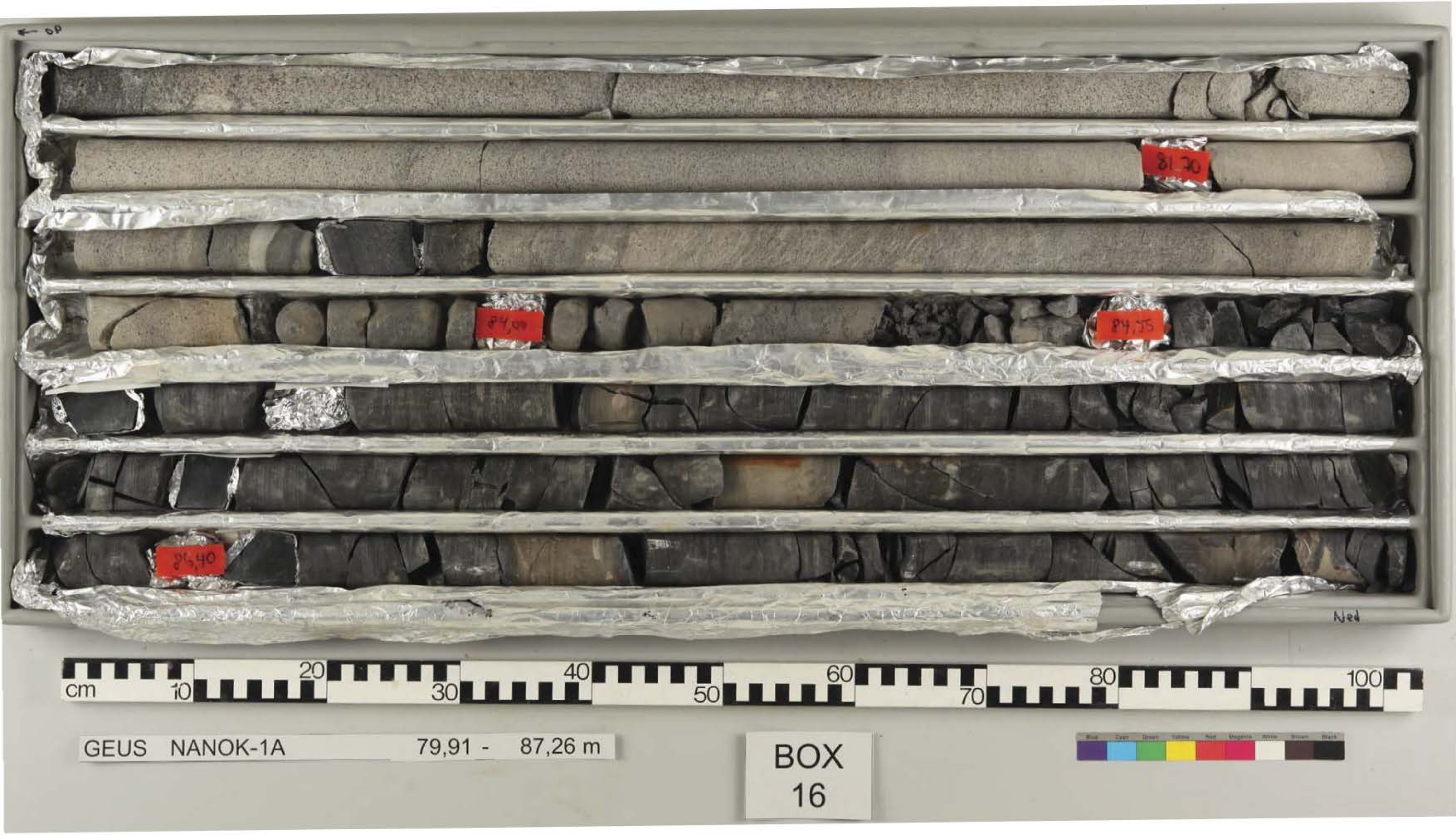
81,70
84,00
84,35
86,40
cm 10 20 30 40 50 60 70 80 100
GEUS NANOK-1A 79,91 - 87,26 m
BOX
16

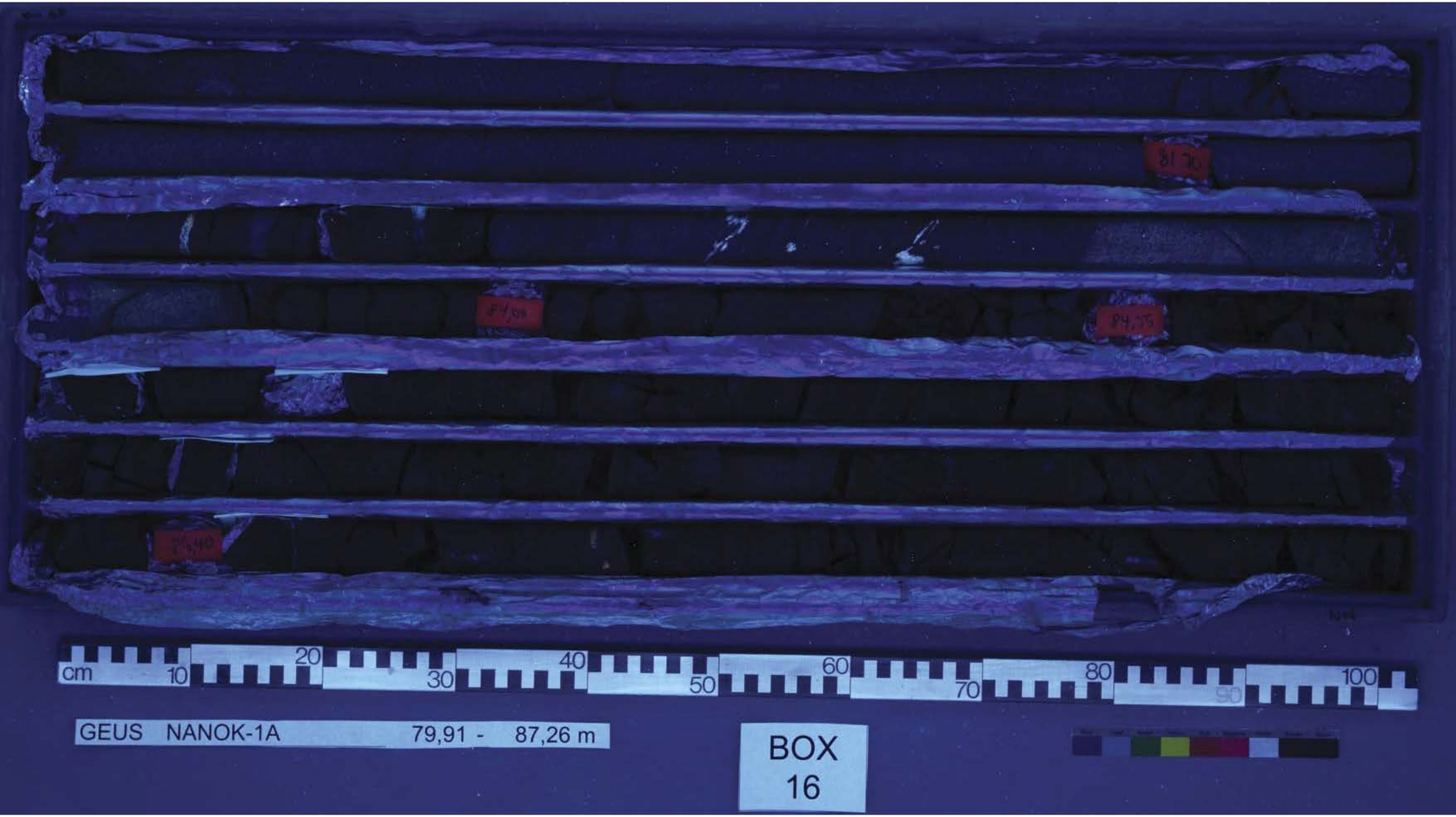
81,70
84,00
84,55
cm 10 20 30 40 50 60 70 80 90 100
GEUS NANOK-1A 79,91 - 87,26 m
BOX
16


81,70
84,00
84,55
85,40
Ned
cm 10 20 30 40 50 60 70 80 100
GEUS NANOK-1A 79,91 - 87,26 m
BOX
16

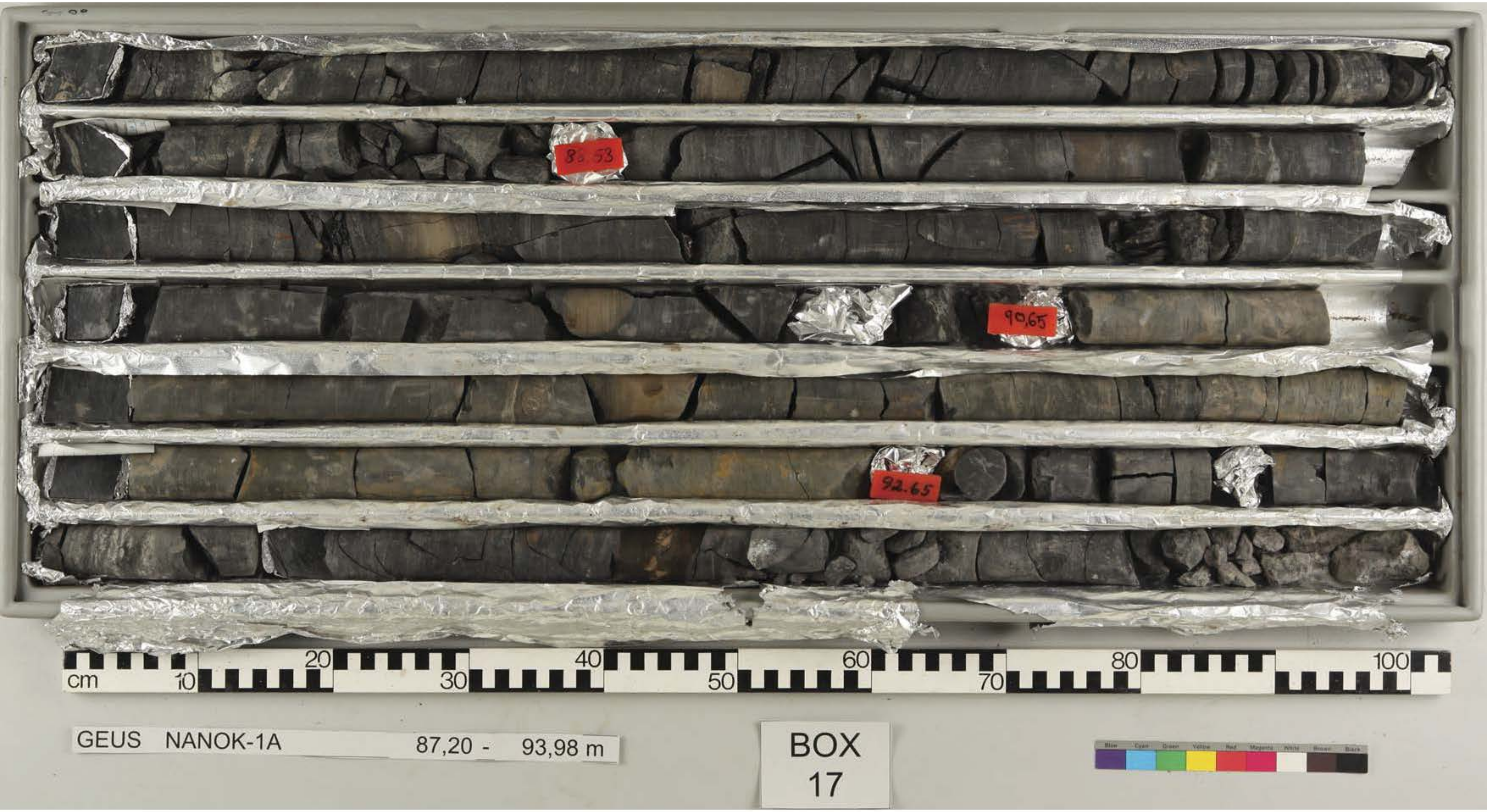
88.53
90,65
92.65
cm 10 20 30 40 50 60 70 80 100
GEUS NANOK-1A 87,20 - 93,98 m
BOX
17
Blue Cyan Green Yellow Red Magenta White Brown Black

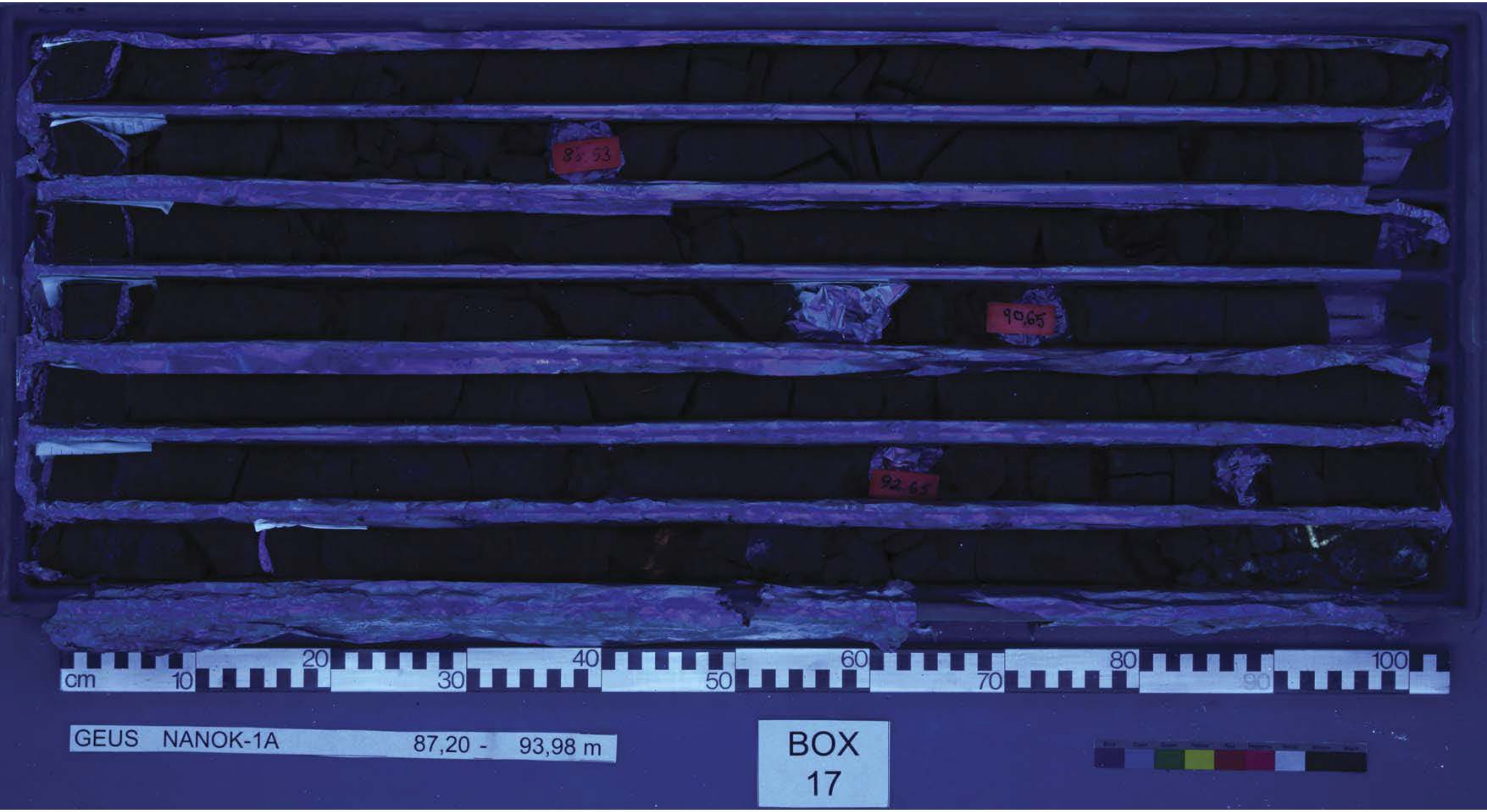
88,53
90,65
92,65
cm 10 20 30 40 50 60 70 80 90 100
GEUS NANOK-1A 87,20 - 93,98 m
BOX
17

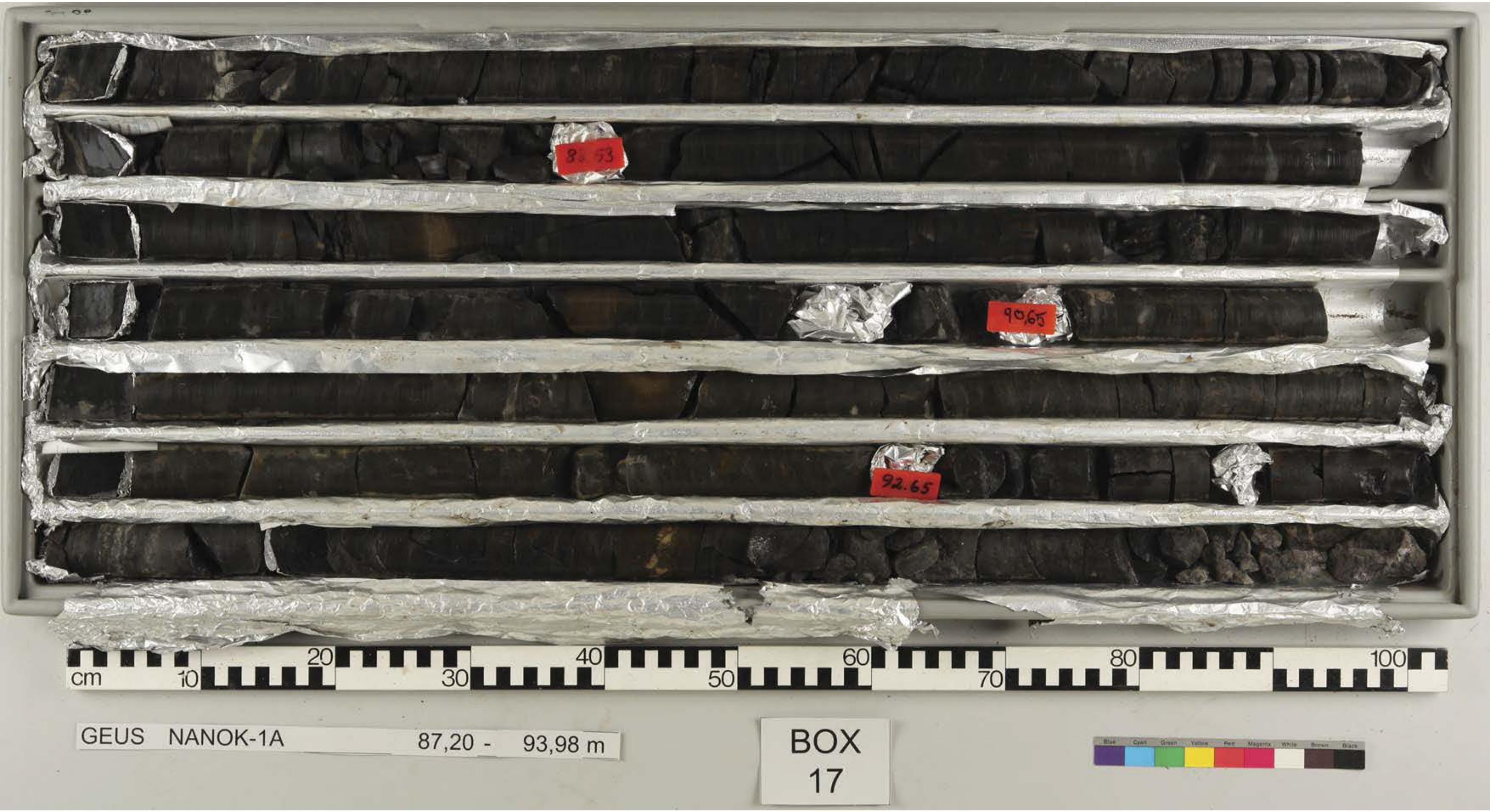
90,65
92.65
cm
10
20
30
40
50
60
70
80
100
GEUS NANOK-1A 87,20 - 93,98 m
BOX
17
Blue
Cyan
Green
Yellow
Red
Magenta
White
Brown
Black

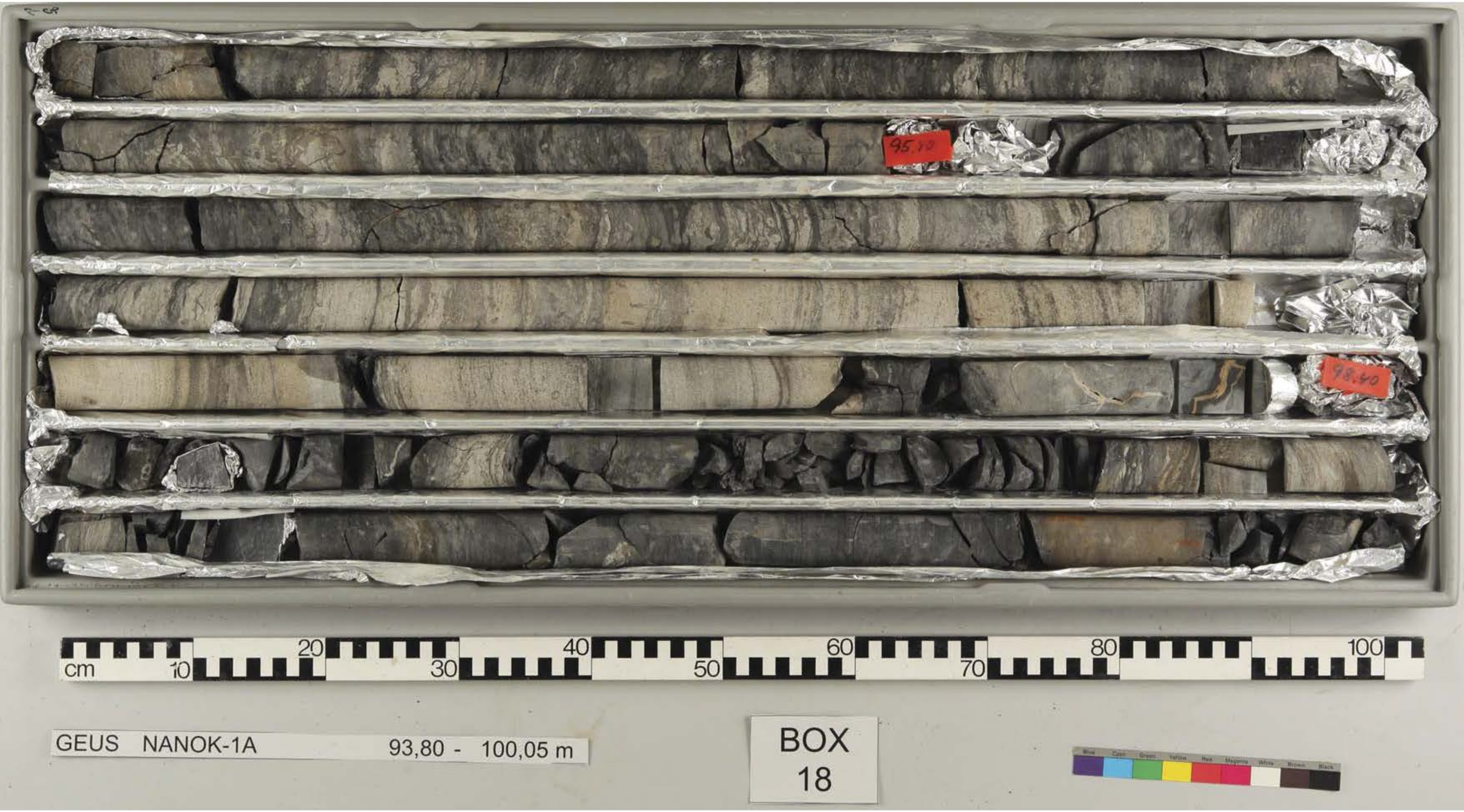
95.40
98.40
cm
GEUS NANOK-1A 93,80 - 100,05 m
BOX
18

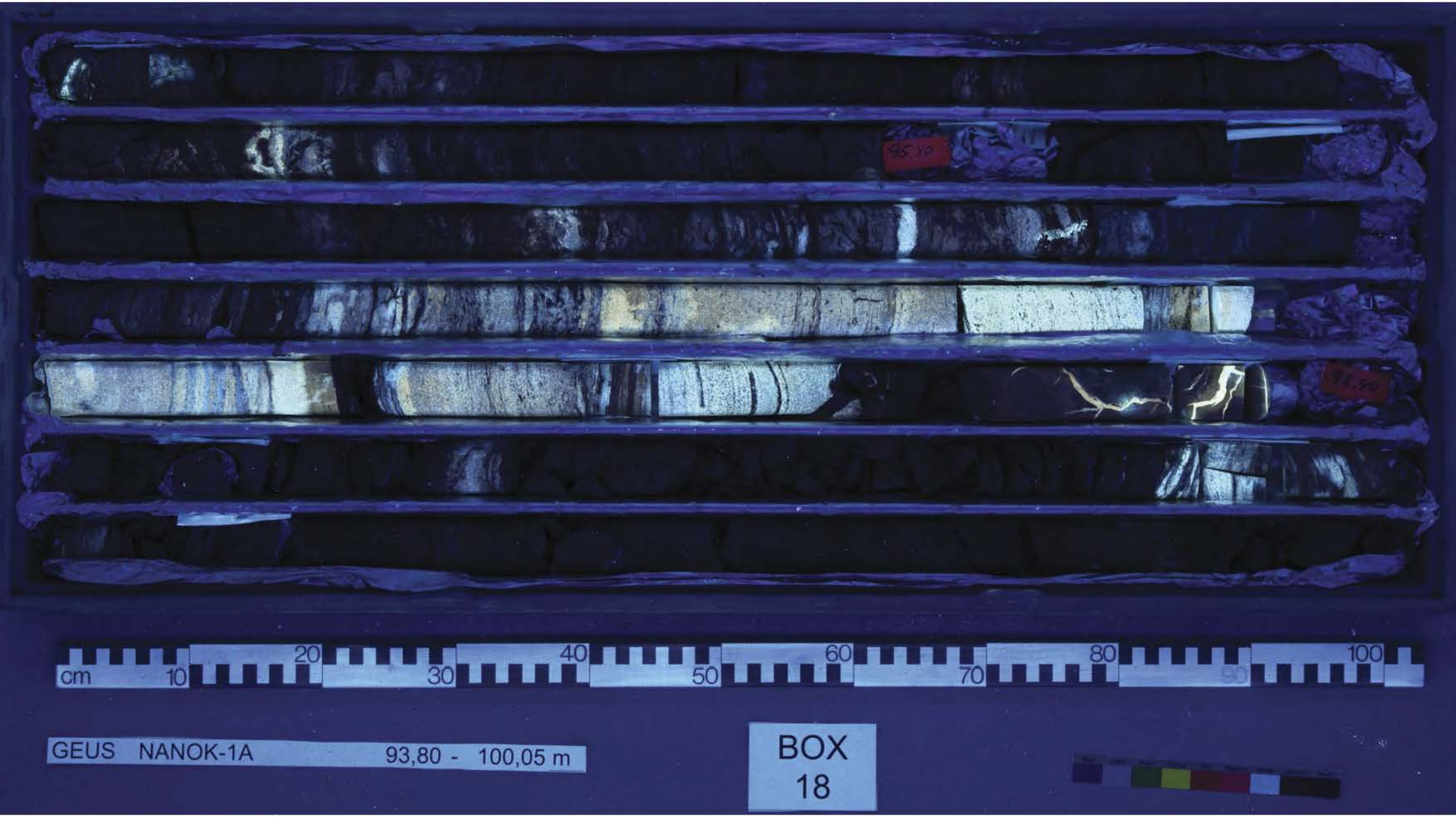

95,50
98,50
cm 10 20 30 40 50 60 70 80 90 100
GEUS NANOK-1A 93,80 - 100,05 m
BOX
18

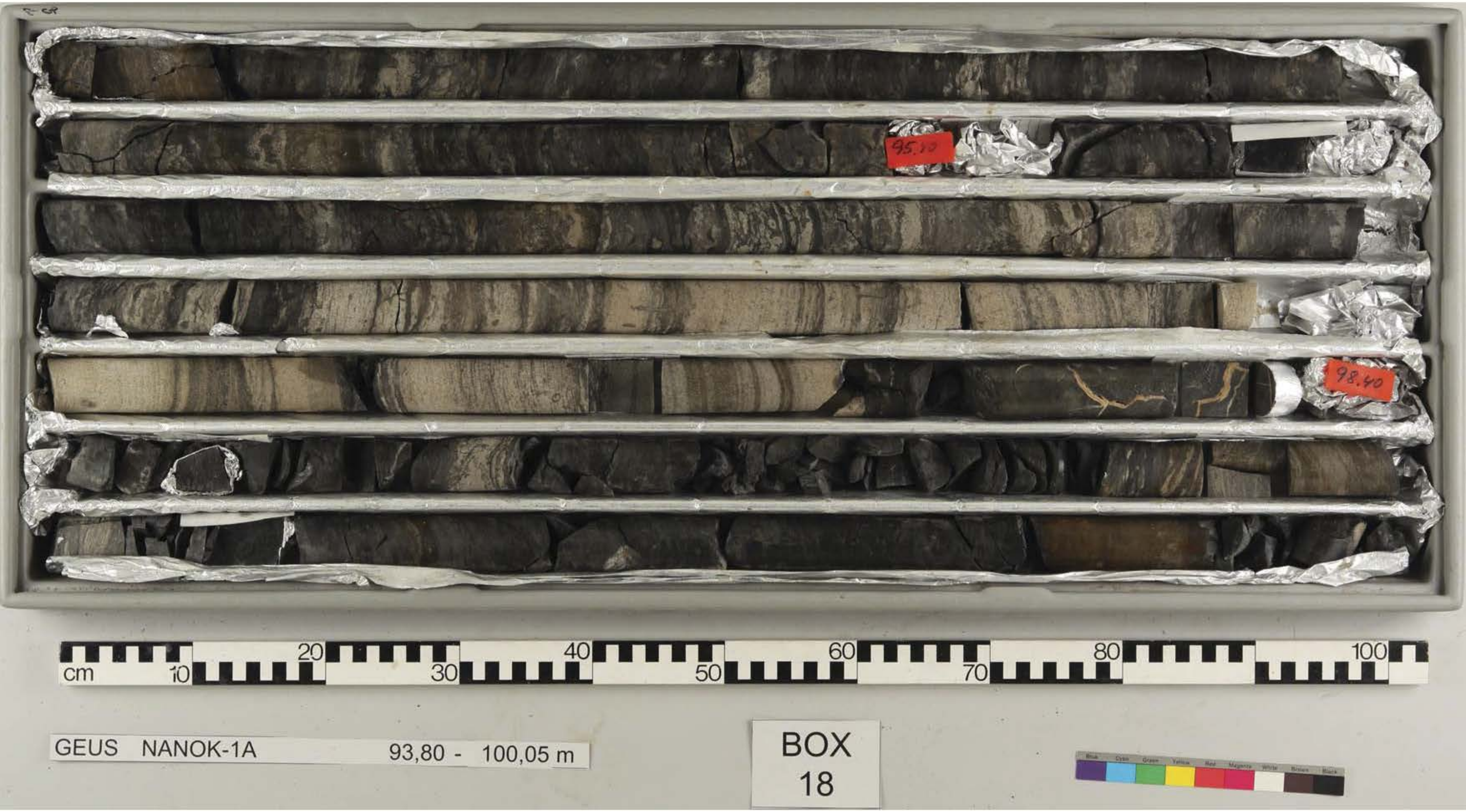

95.40
98.40
cm
10
20
30
40
50
60
70
80
100
GEUS NANOK-1A 93,80 - 100,05 m
BOX
18

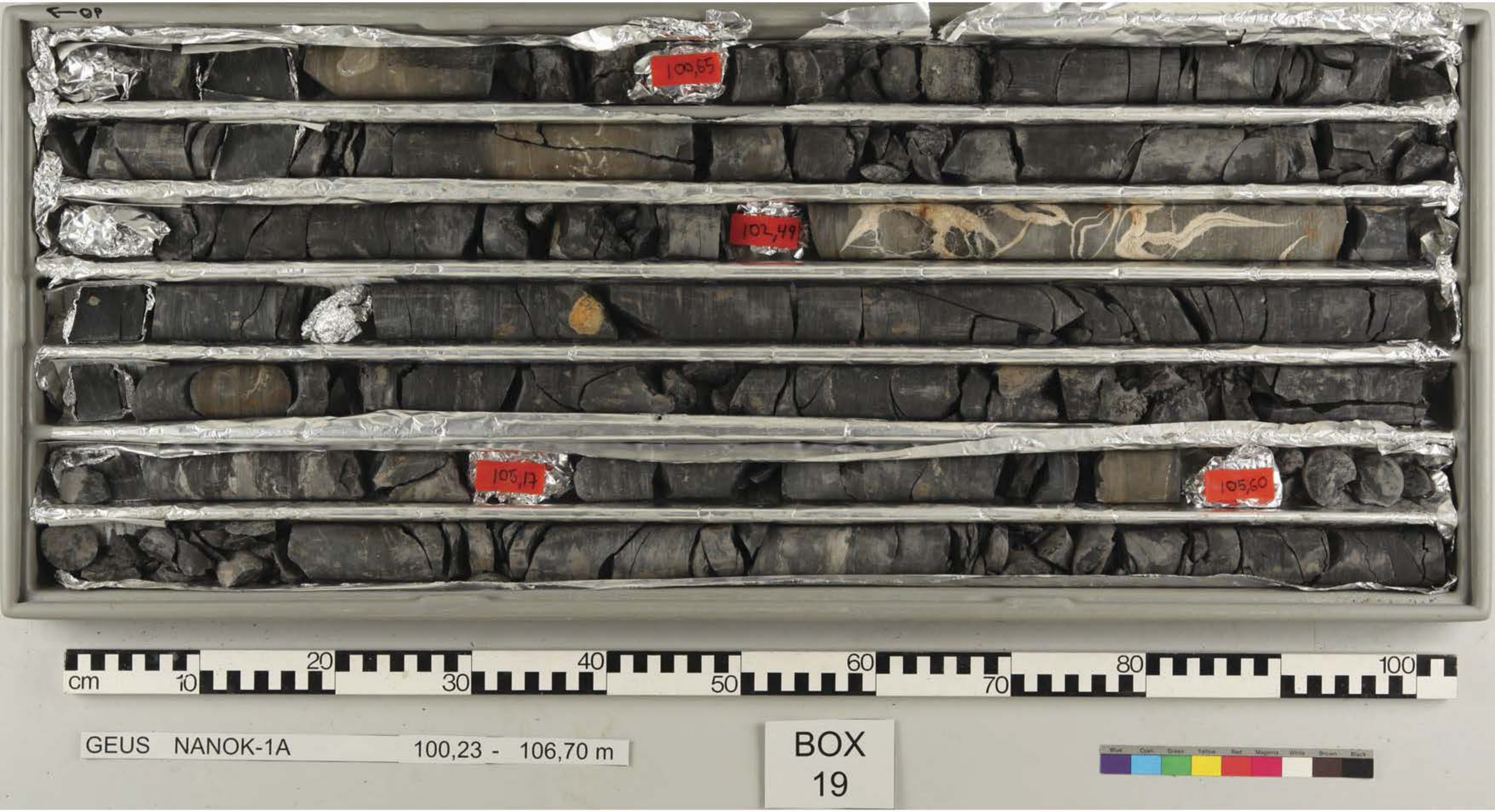
TOP
100,65
102,49
103,17
105,60
cm 10 20 30 40 50 60 70 80 100
GEUS NANOK-1A 100,23 - 106,70 m
BOX 19
Blue Cyan Green Yellow Red Magenta White Brown Black

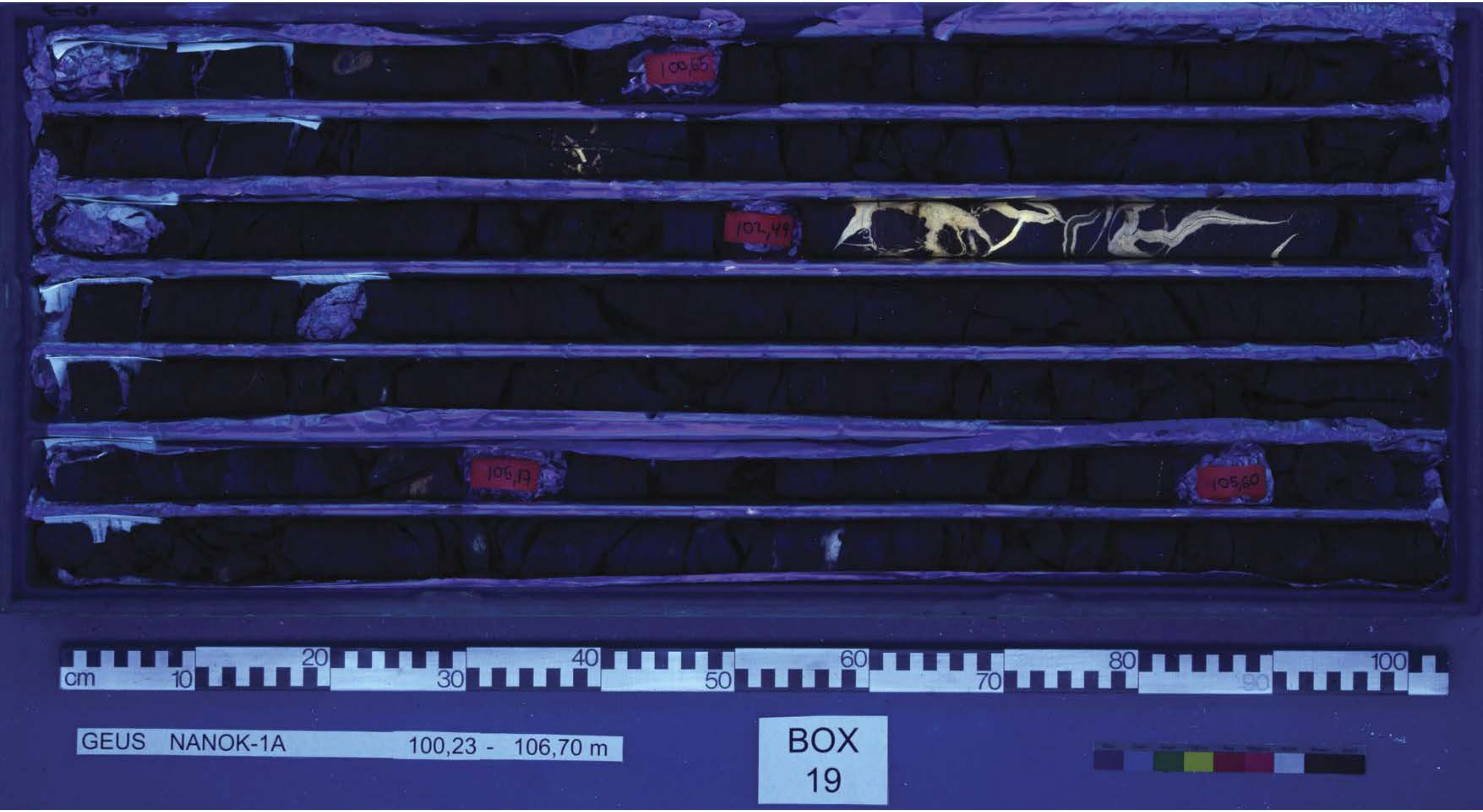
100,65
102,49
106,17
105,60
cm 10 20 30 40 50 60 70 80 90 100
GEUS NANOK-1A 100,23 - 106,70 m
BOX
19

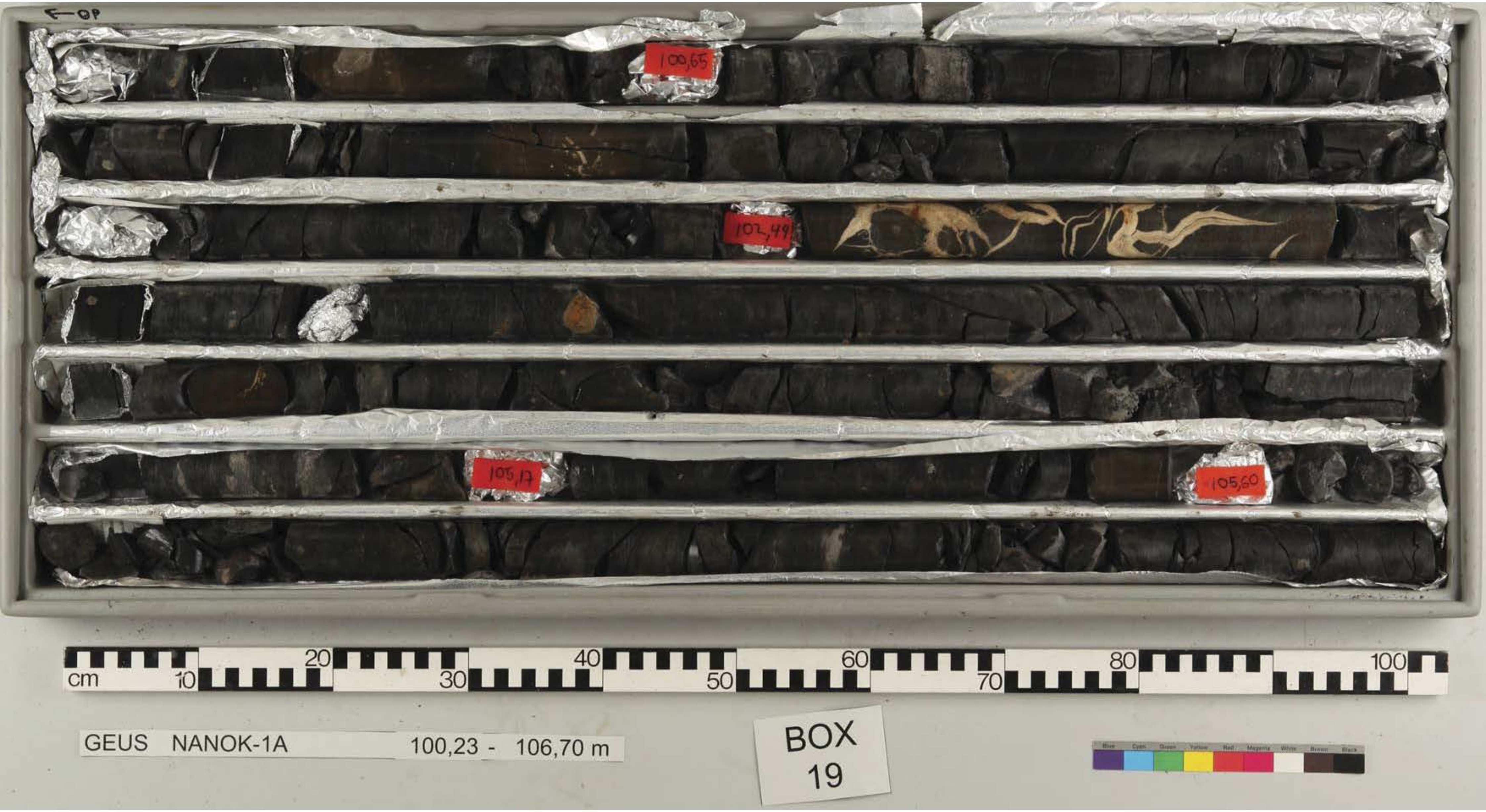

Top
100,65
102,49
105,17
105,60
cm 10 20 30 40 50 60 70 80 100
GEUS NANOK-1A 100,23 - 106,70 m
BOX
19
Blue Cyan Green Yellow Red Magenta White Brown Black

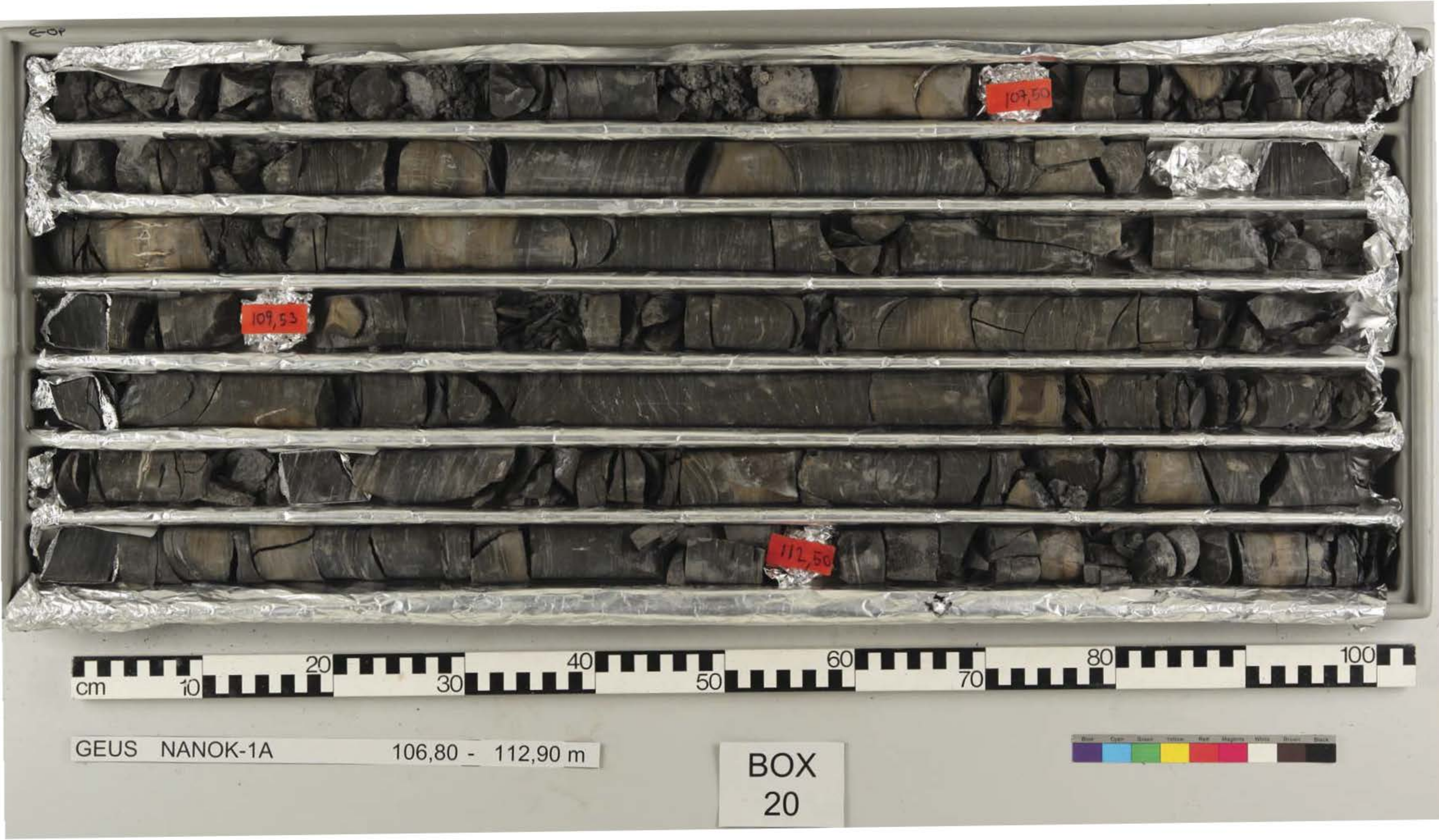

107,50
109,53
112,50
cm
10
20
30
40
50
60
70
80
100
GEUS NANOK-1A 106,80 - 112,90 m
BOX
20

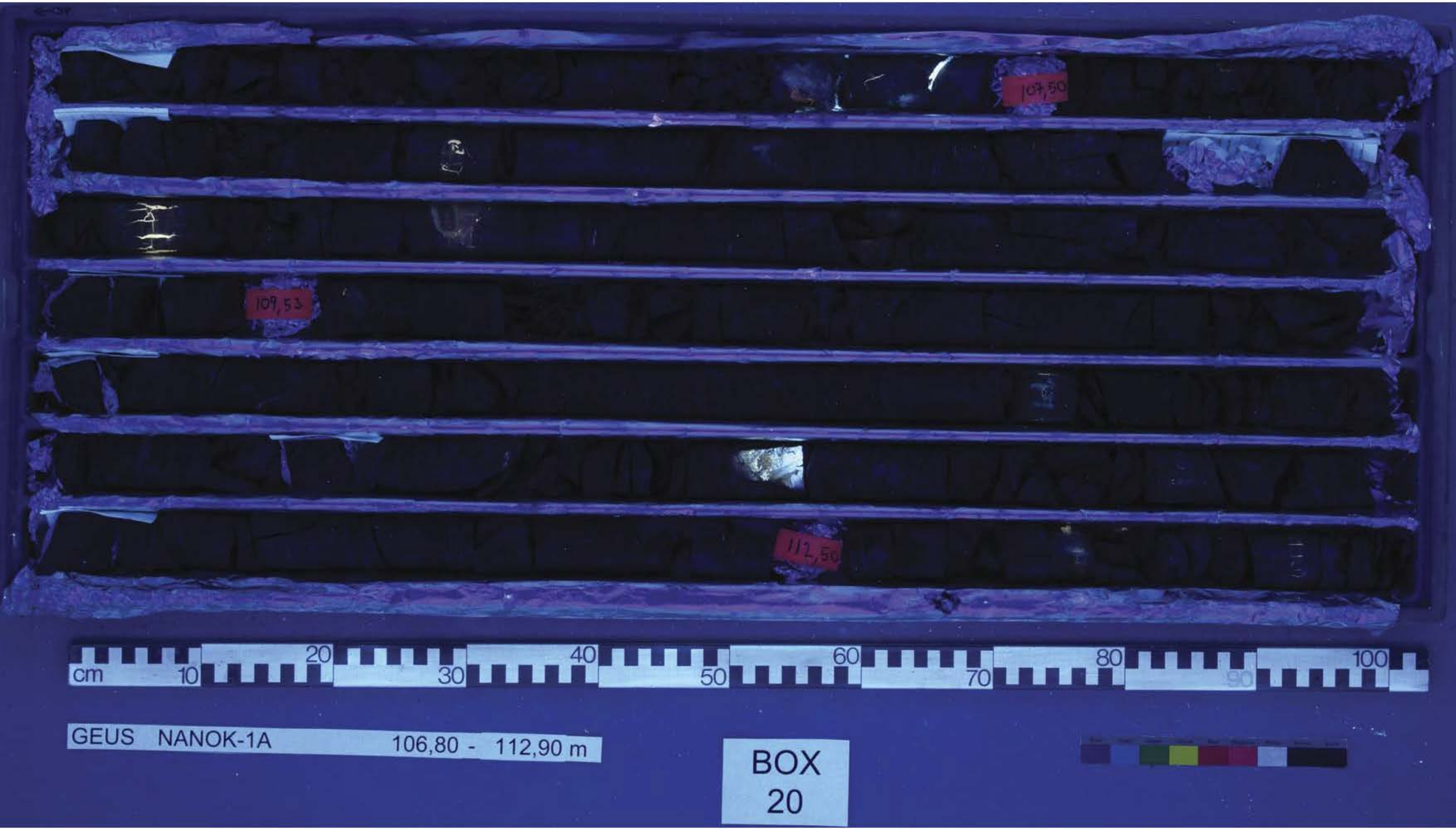
107,50
109,53
112,50
cm 10 20 30 40 50 60 70 80 90 100
GEUS NANOK-1A 106,80 - 112,90 m
BOX
20


107,50
109,53
112,50
cm 10 20 30 40 50 60 70 80 100
GEUS NANOK-1A 106,80 - 112,90 m
BOX
20


113,97
117,07
118,85
cm 10 20 30 40 50 60 70 80 100
GEUS NANOK-1A 112,69 - 119,29 m
BOX
21

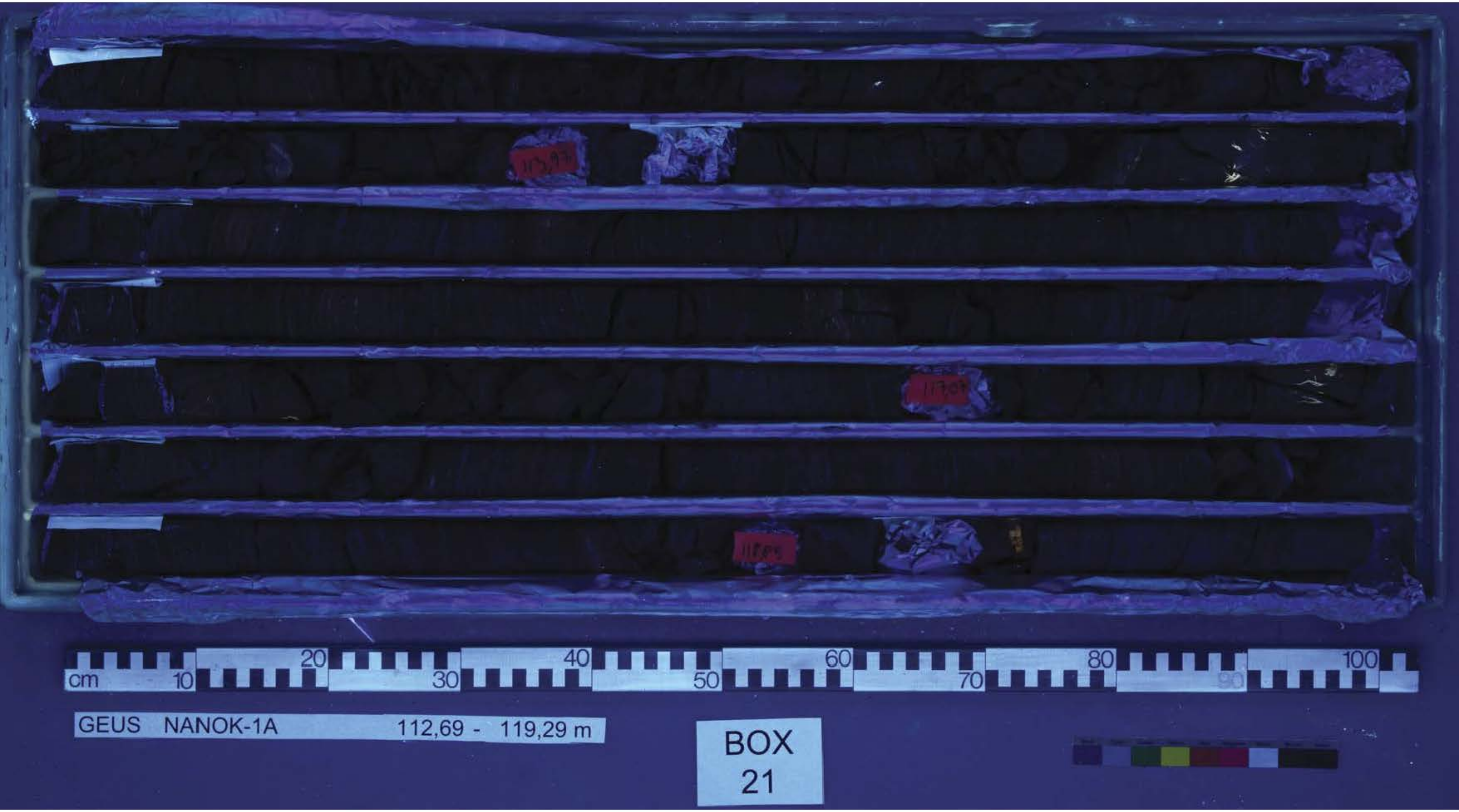
cm 10 20 30 40 50 60 70 80 90 100
GEUS NANOK-1A 112,69 - 119,29 m
BOX
21


113,97
117,07
118,85
cm 10 20 30 40 50 60 70 80 100
GEUS NANOK-1A 112,69 - 119,29 m
BOX
21
Blue Cyan Green Yellow Red Magenta White Brown Black


121,50
125,00
cm
10
20
30
40
50
60
70
80
100
GEUS NANOK-1A 119,17 - 125,68 m
BOX
22
Blue
Cyan
Green
Yellow
Red
Magenta
White
Brown
Black


cm 10 20 30 40 50 60 70 80 90 100
GEUS NANOK-1A 119,17 - 125,68 m
BOX
22


121,00
125,00
cm 10 20 30 40 50 60 70 80 100
GEUS NANOK-1A 119,17 - 125,68 m
BOX 22

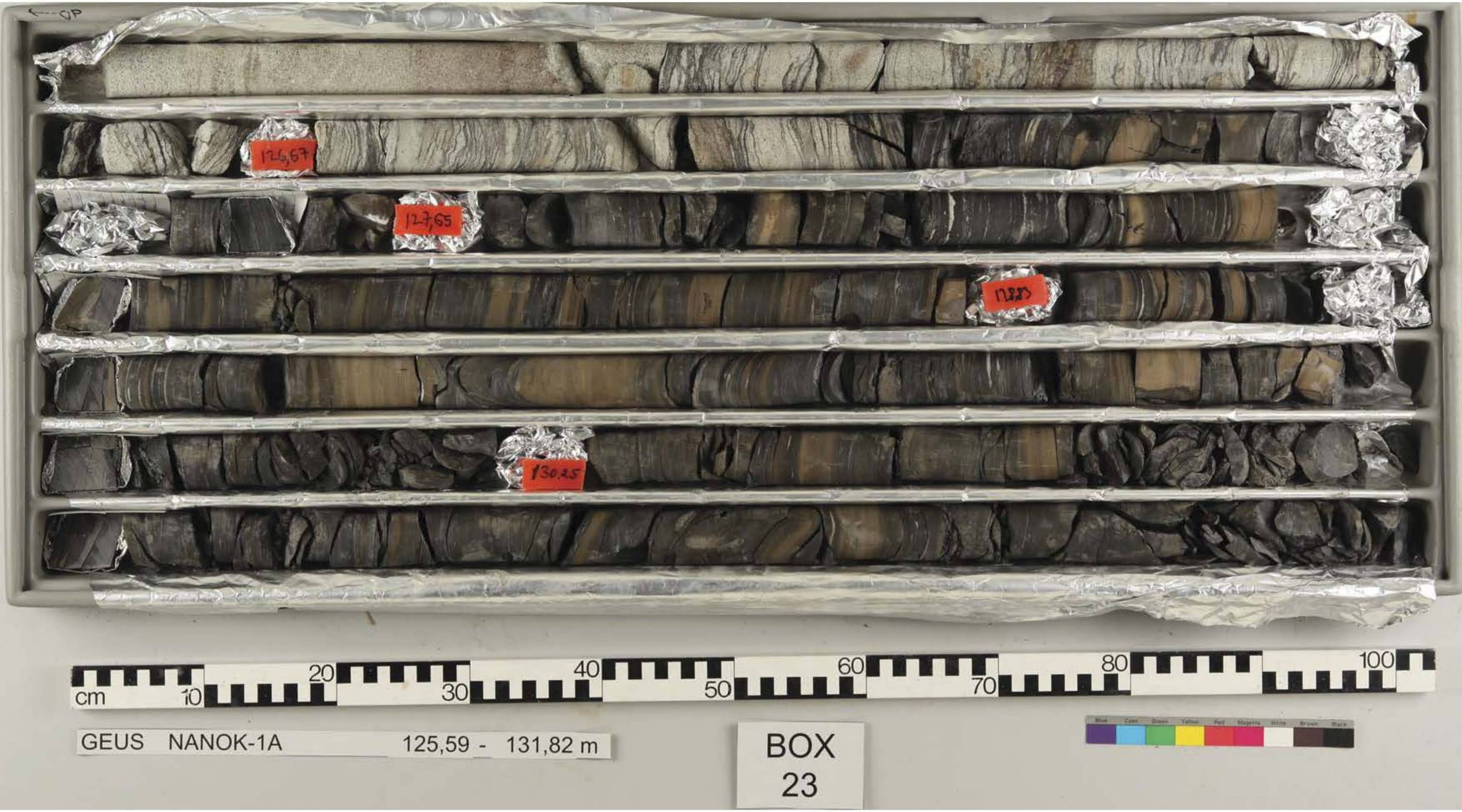
126,67
127,65
128,83
130,25
cm 10 20 30 40 50 60 70 80 100
Blue Cyan Green Yellow Red Magenta White Brown Black
GEUS NANOK-1A 125,59 - 131,82 m
BOX
23

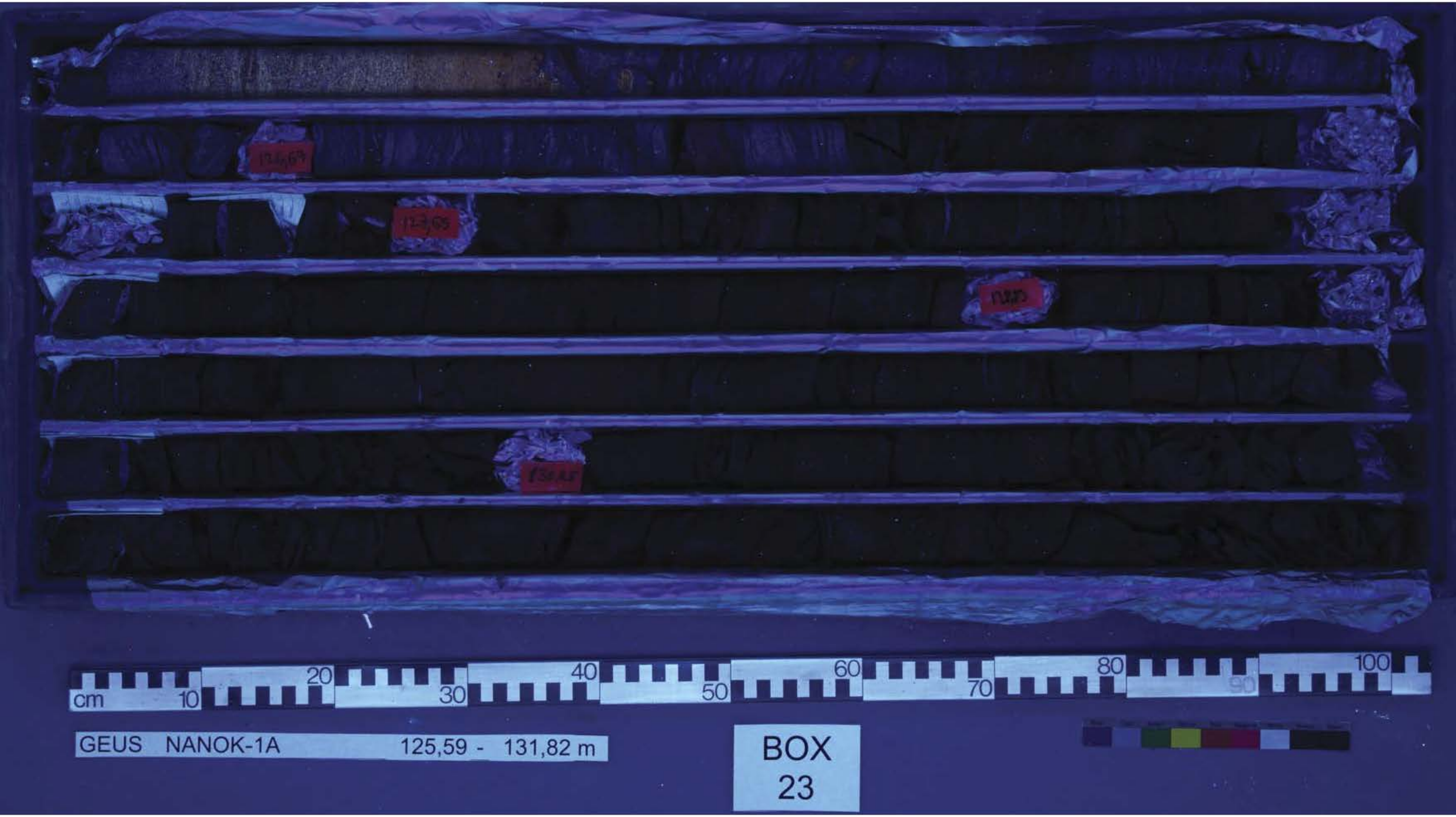
cm 10 20 30 40 50 60 70 80 90 100
GEUS NANOK-1A 125,59 - 131,82 m
BOX
23

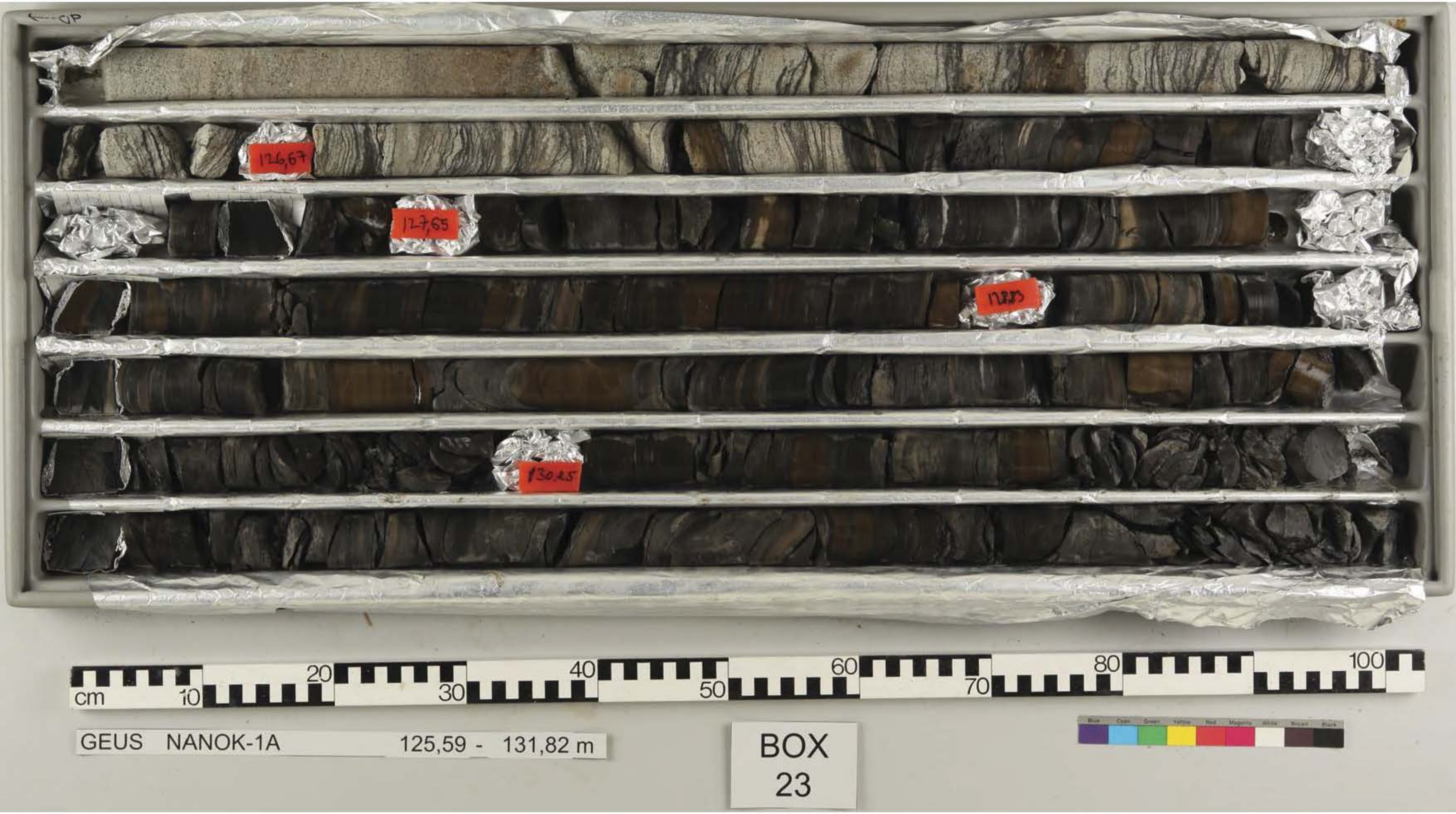

126,67
127,65
128,83
130,25
cm 10 20 30 40 50 60 70 80 100
GEUS NANOK-1A 125,59 - 131,82 m
BOX
23

132,48
133,63
134,58
135,83
cm 10 20 30 40 50 60 70 80 100
GEUS NANOK-1A 131,91 - 138,08 m
BOX
24

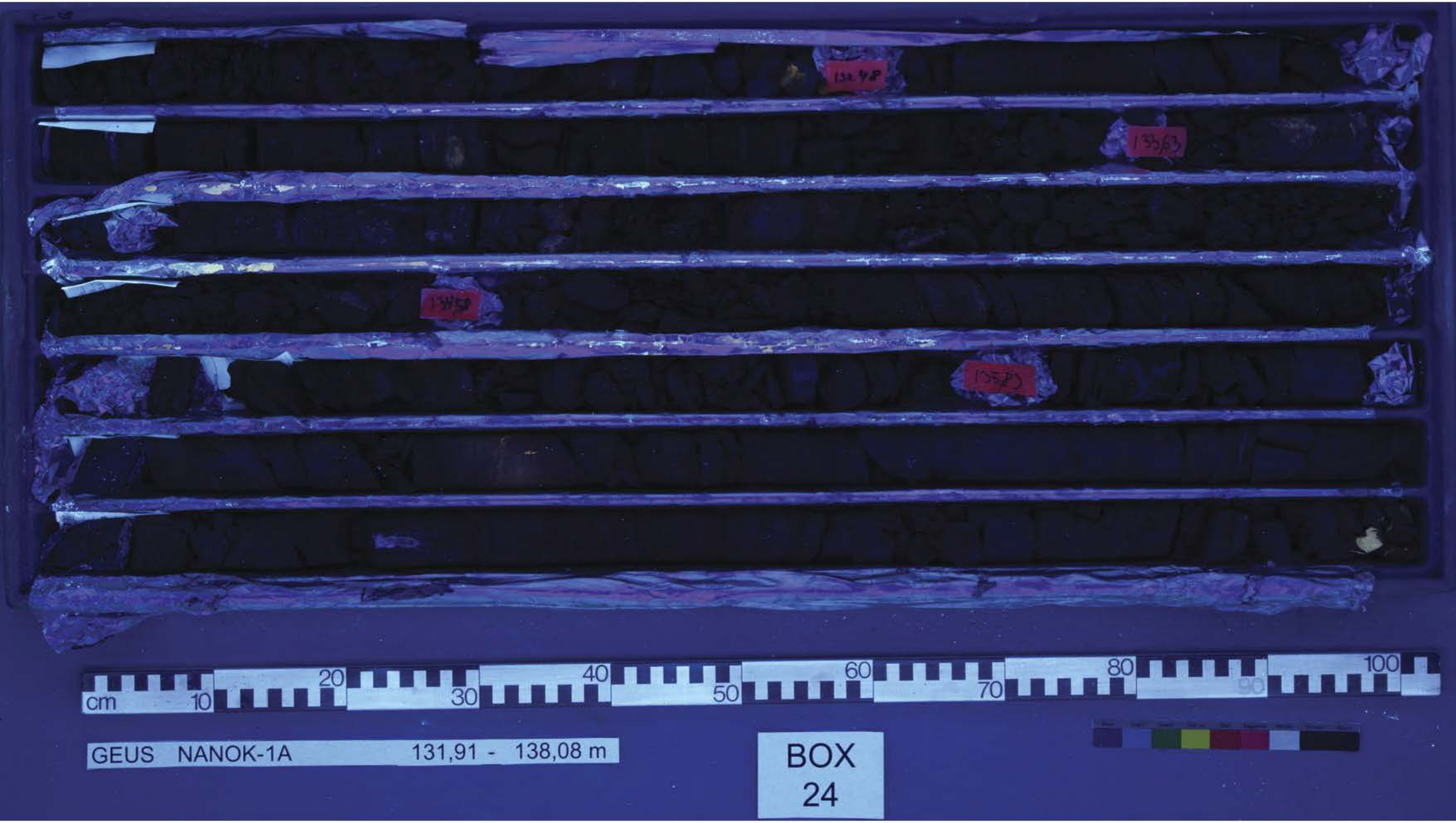
cm 10 20 30 40 50 60 70 80 90 100
GEUS NANOK-1A 131,91 - 138,08 m
BOX
24


132.48
133,63
134,58
135,83
cm 10 20 30 40 50 60 70 80 100
GEUS NANOK-1A 131,91 - 138,08 m
BOX
24


138,15
139,60
141,92
145,60
cm
10
20
30
40
50
60
70
80
100
GEUS NANOK-1A 137,86 - 144,22 m
BOX
25

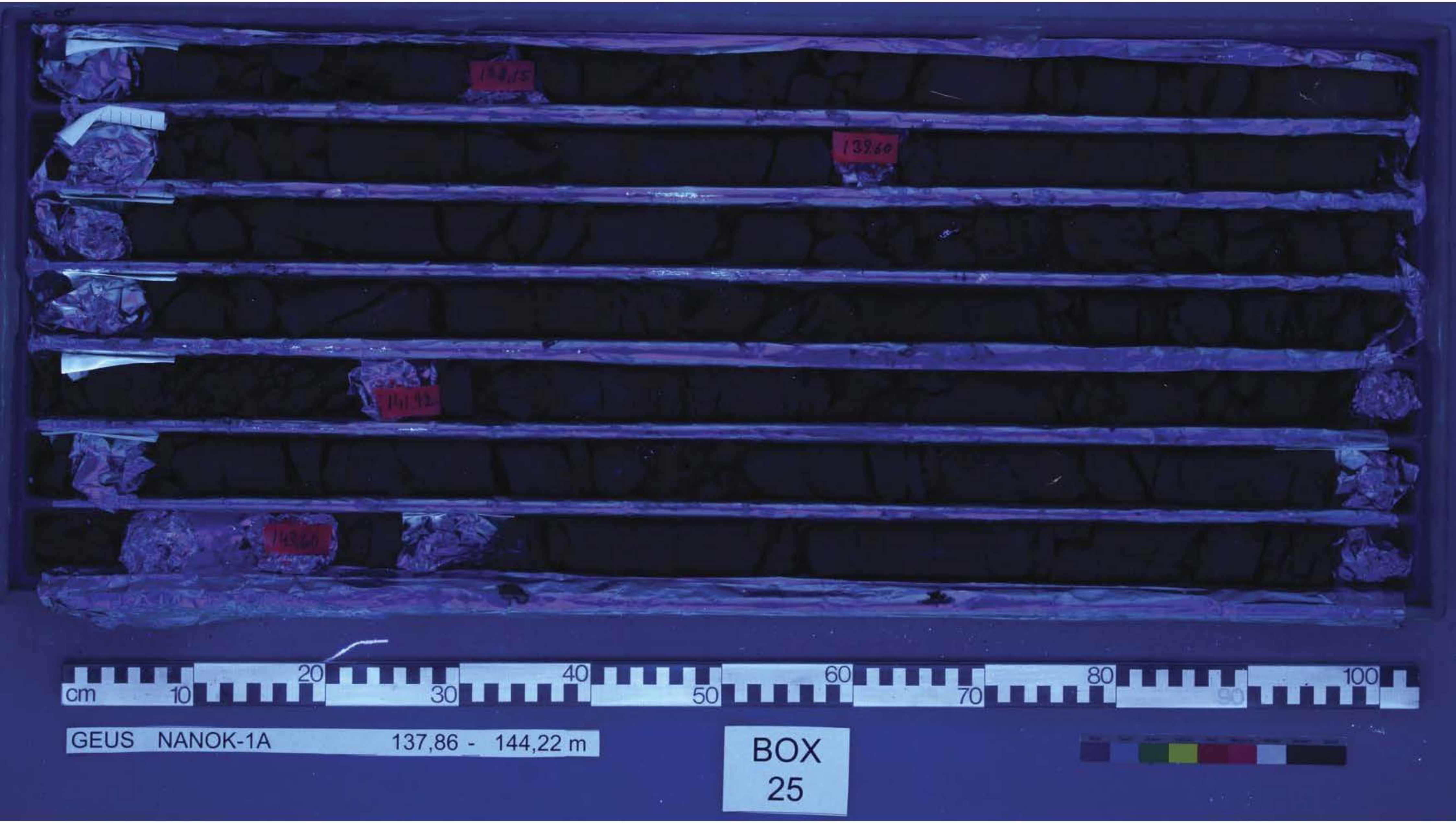

138,15
139,60
141,42
143,60
cm 10 20 30 40 50 60 70 80 90 100
GEUS NANOK-1A 137,86 - 144,22 m
BOX
25


138,15
139.60
141.92
143.60
cm 10 20 30 40 50 60 70 80 100
GEUS NANOK-1A 137,86 - 144,22 m
BOX
25


146,25
cm 10 20 30 40 50 60 70 80 100
GEUS NANOK-1A 150,73 - 157,30 m
BOX 26

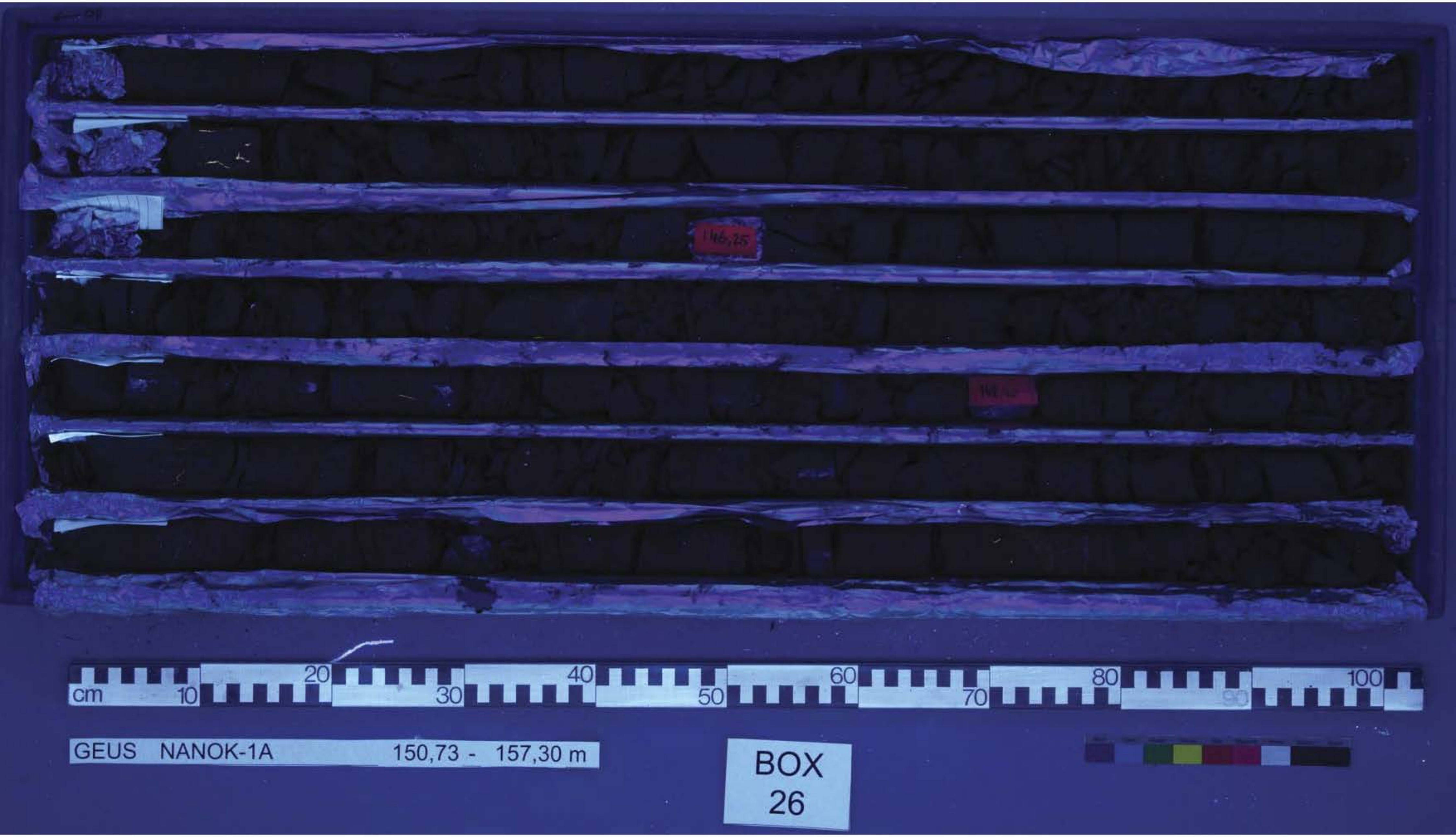

146,25
cm
10
20
30
40
50
60
70
80
90
100
GEUS NANOK-1A 150,73 - 157,30 m
BOX
26

← op
146,25
148,40
cm
10
20
30
40
50
60
70
80
100
GEUS NANOK-1A 150,73 - 157,30 m
BOX
26

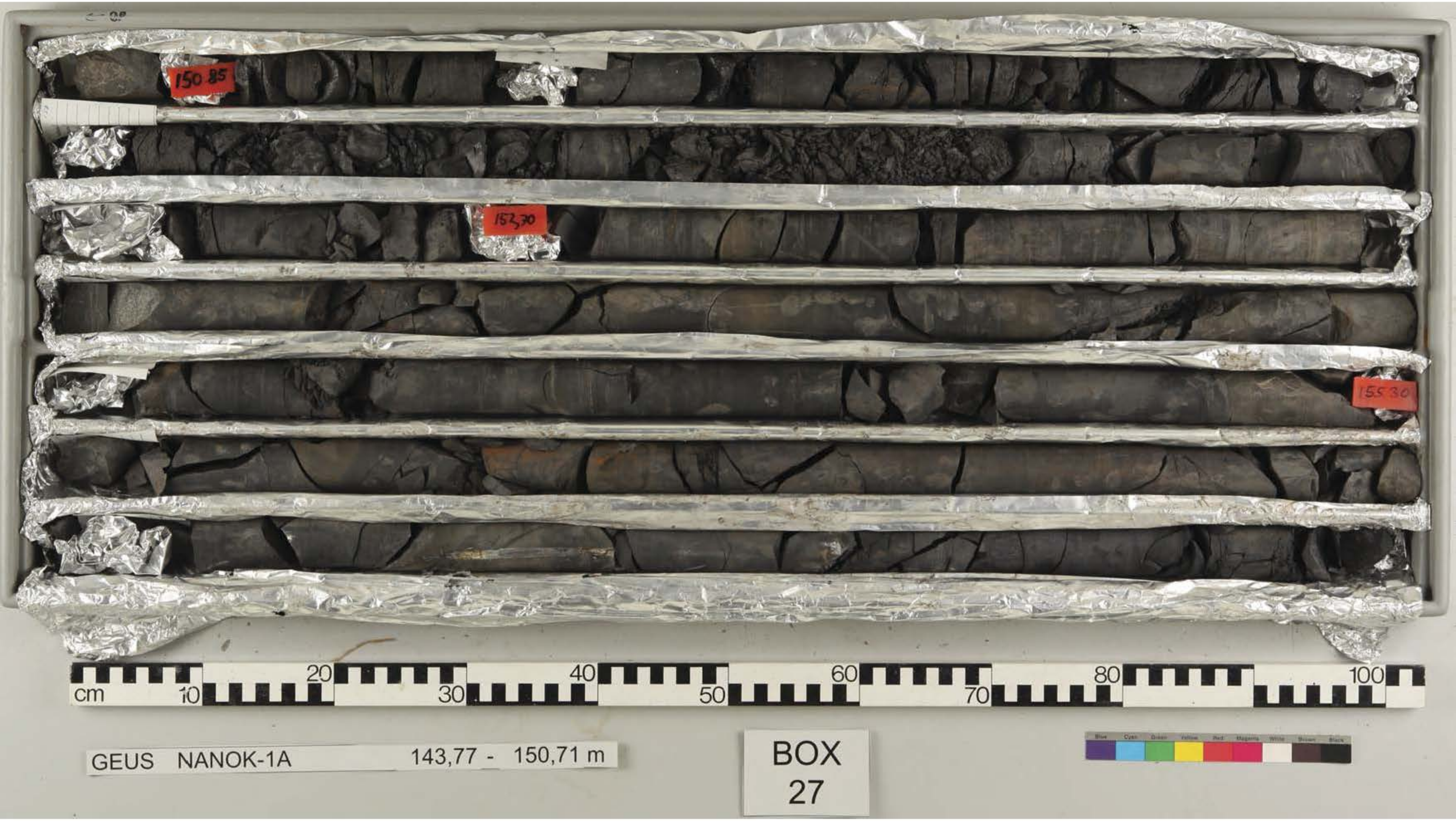
150 85
152,70
155 30
cm 10 20 30 40 50 60 70 80 100
GEUS NANOK-1A 143,77 - 150,71 m
BOX
27

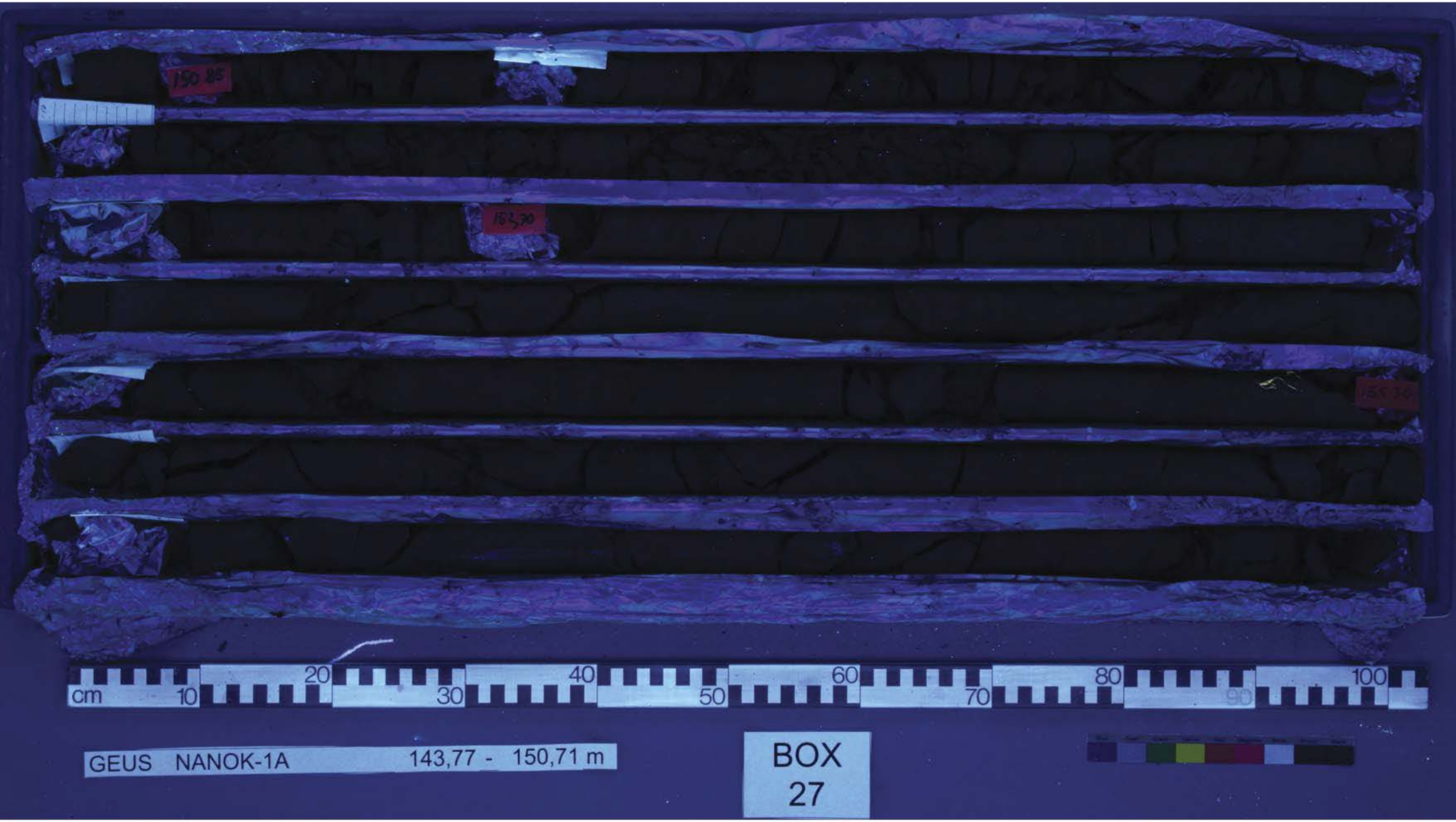

cm 10 20 30 40 50 60 70 80 90 100
GEUS NANOK-1A 143,77 - 150,71 m
BOX
27


150 85
152,70
155 30
cm
GEUS NANOK-1A 143,77 - 150,71 m
BOX
27


cm 10 20 30 40 50 60 70 80 100
GEUS NANOK-1A 157,25 - 163,45 m
BOX 28

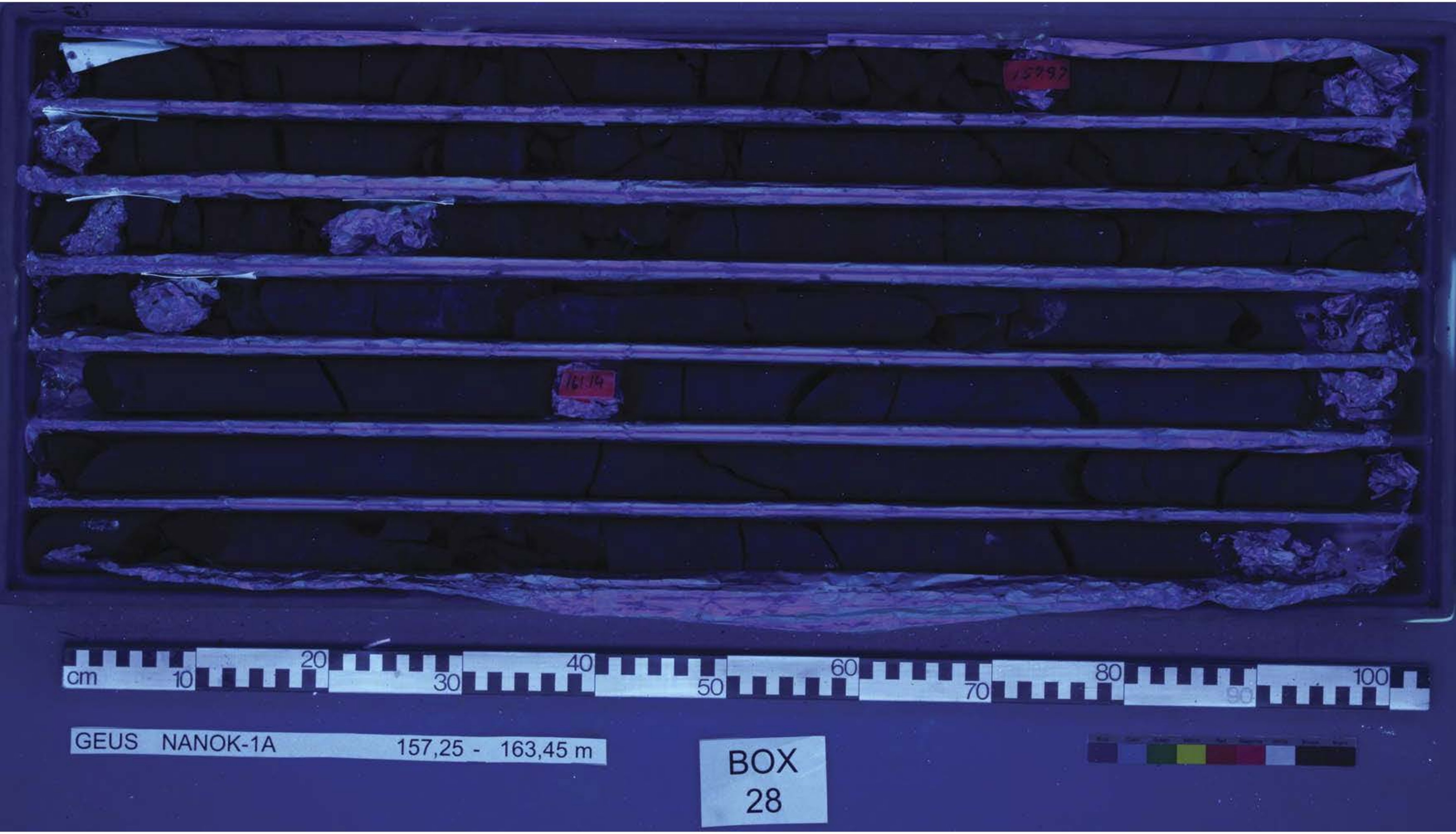
161.14
cm 10 20 30 40 50 60 70 80 90 100
GEUS NANOK-1A 157,25 - 163,45 m
BOX 28

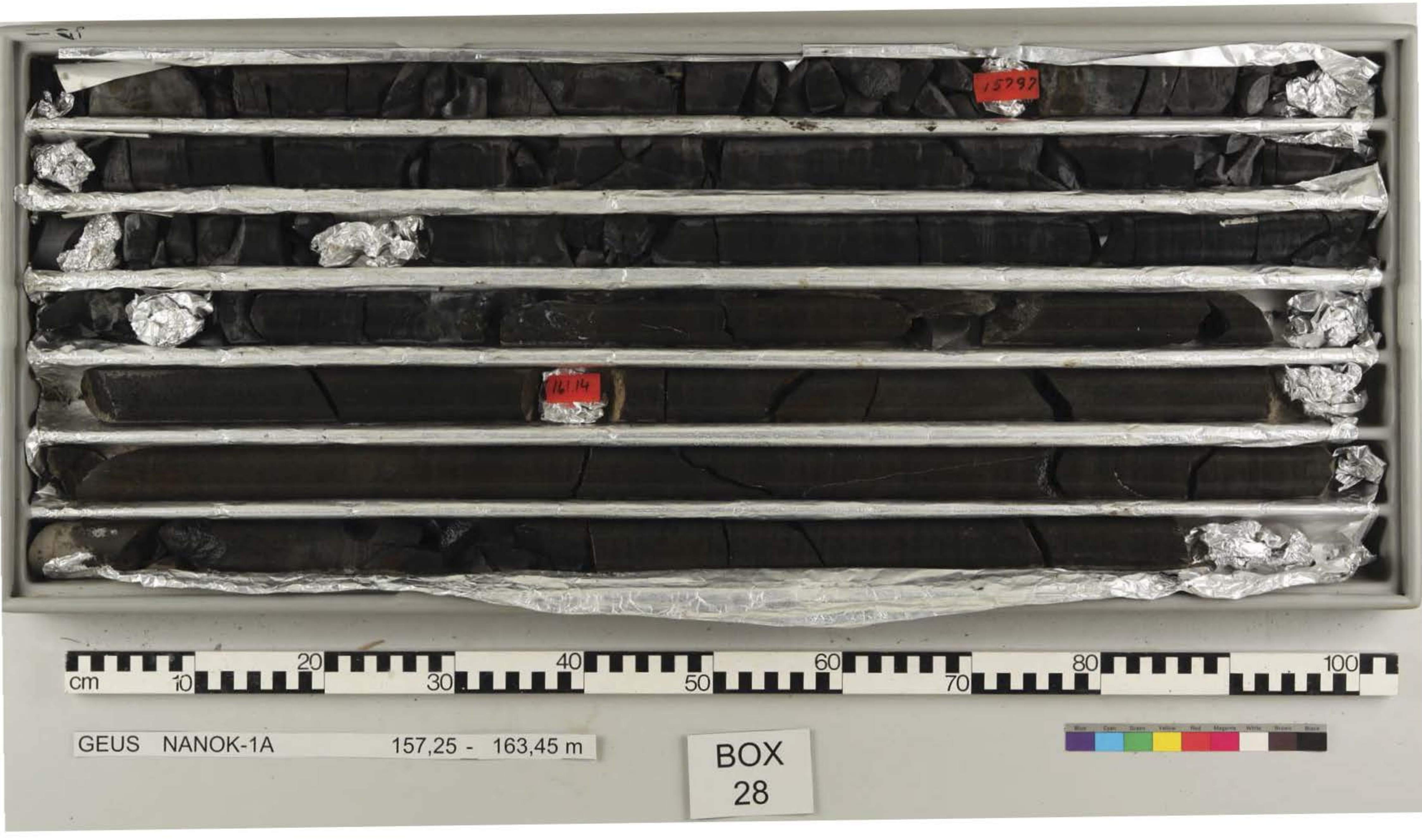
GEUS NANOK-1A 157,25 - 163,45 m
BOX
28

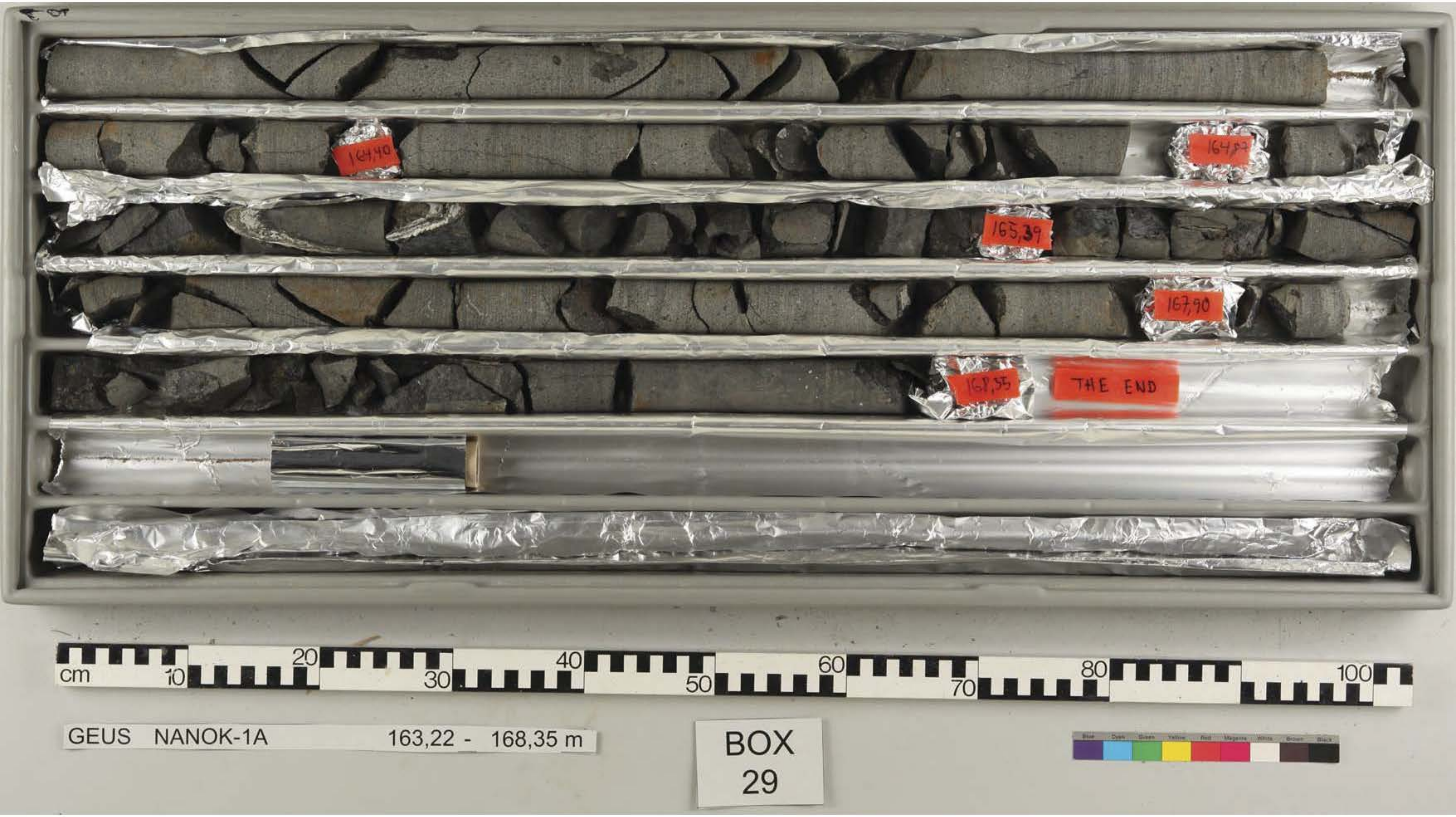

164,40
165,39
167,90
168,35
THE END
cm
10
20
30
40
50
60
70
80
100
GEUS NANOK-1A 163,22 - 168,35 m
BOX
29

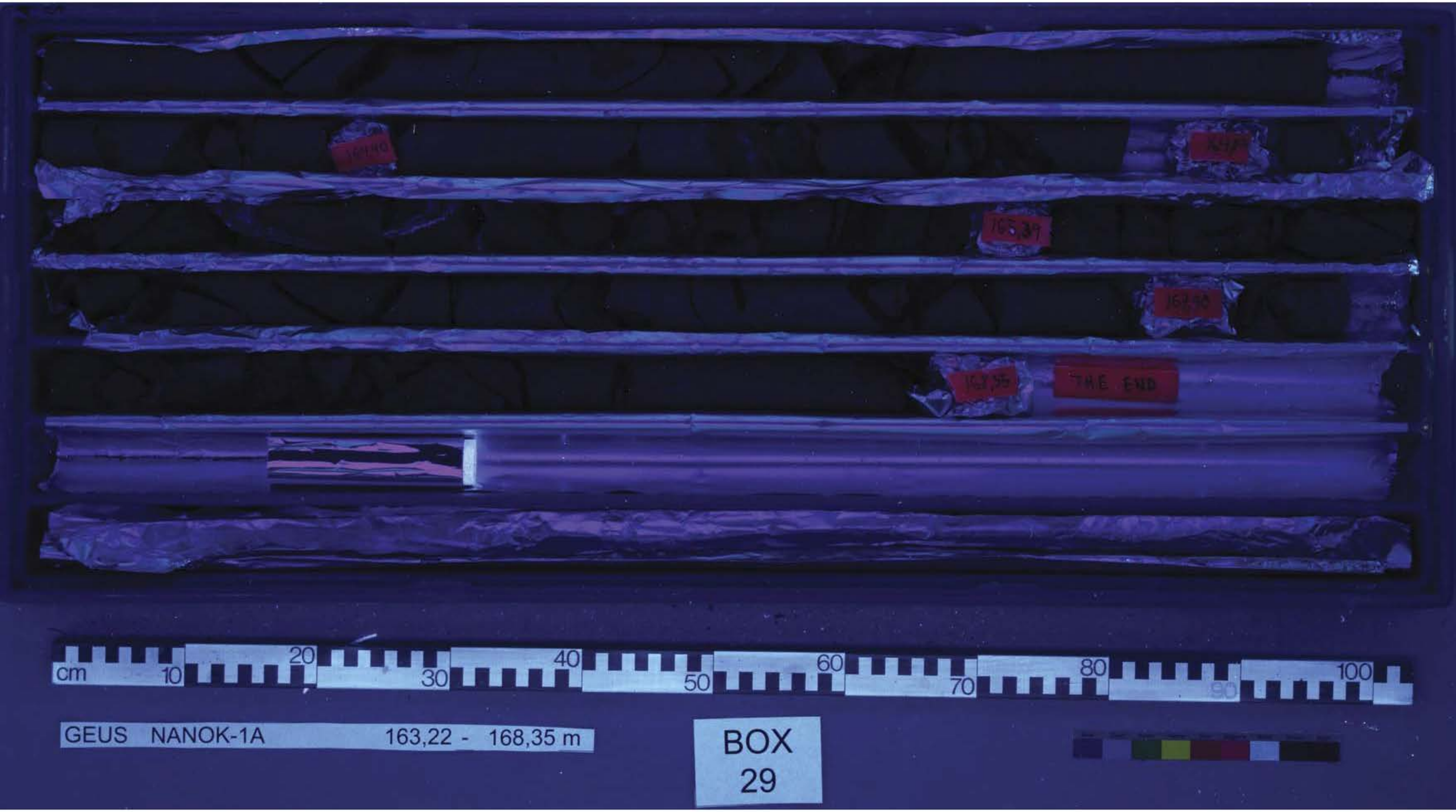
THE END
cm 10 20 30 40 50 60 70 80 90 100
GEUS NANOK-1A 163,22 - 168,35 m
BOX
29

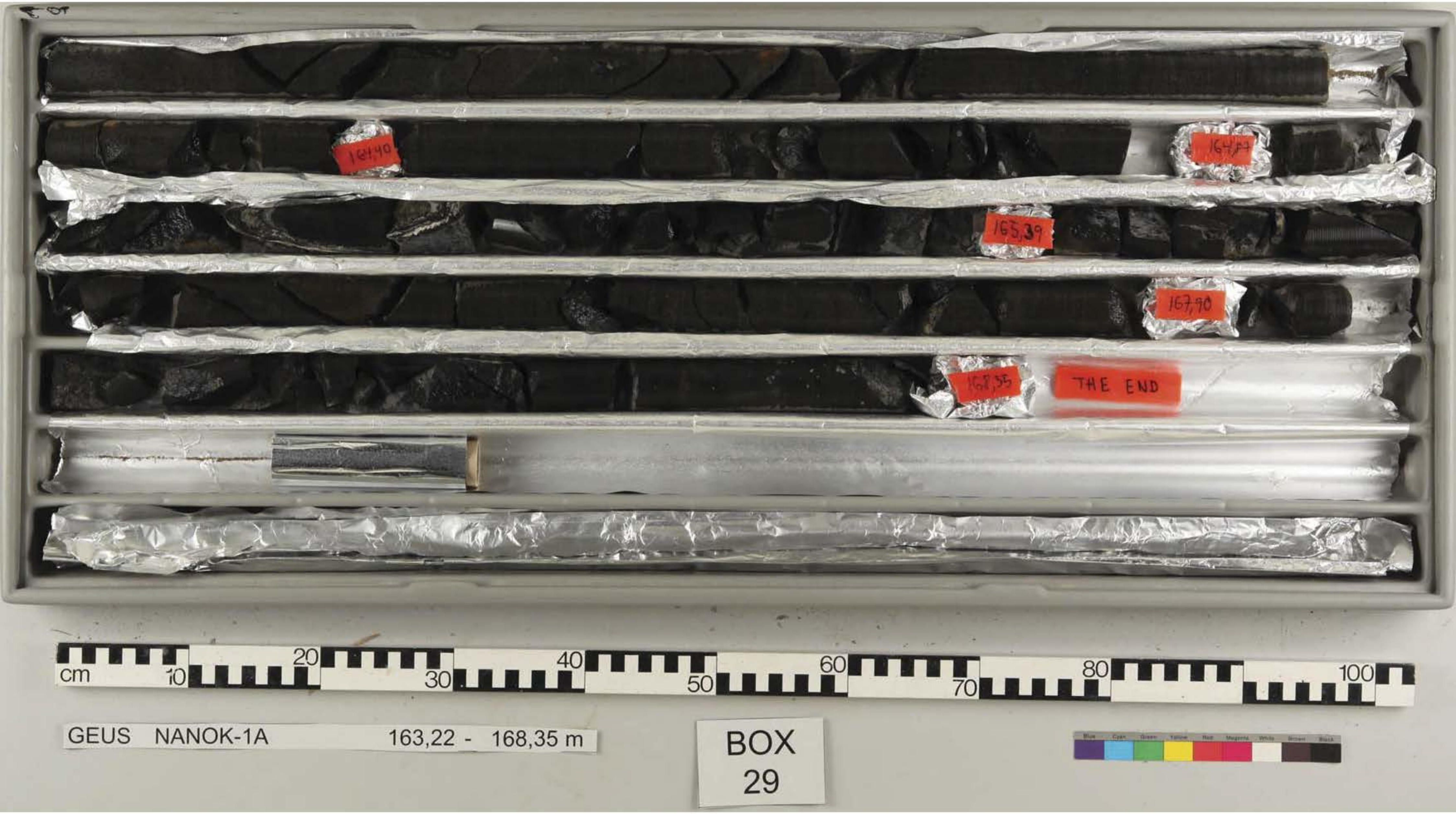
164,40
164,87
165,39
167,90
168,35
THE END
cm 10 20 30 40 50 60 70 80 100
GEUS NANOK-1A 163,22 - 168,35 m
BOX 29

12.2 Thin sections

Contents: Thin section photographs without and with crossed nicoles. Geus sample number, orientation and core depth are indicated in the thin sections.

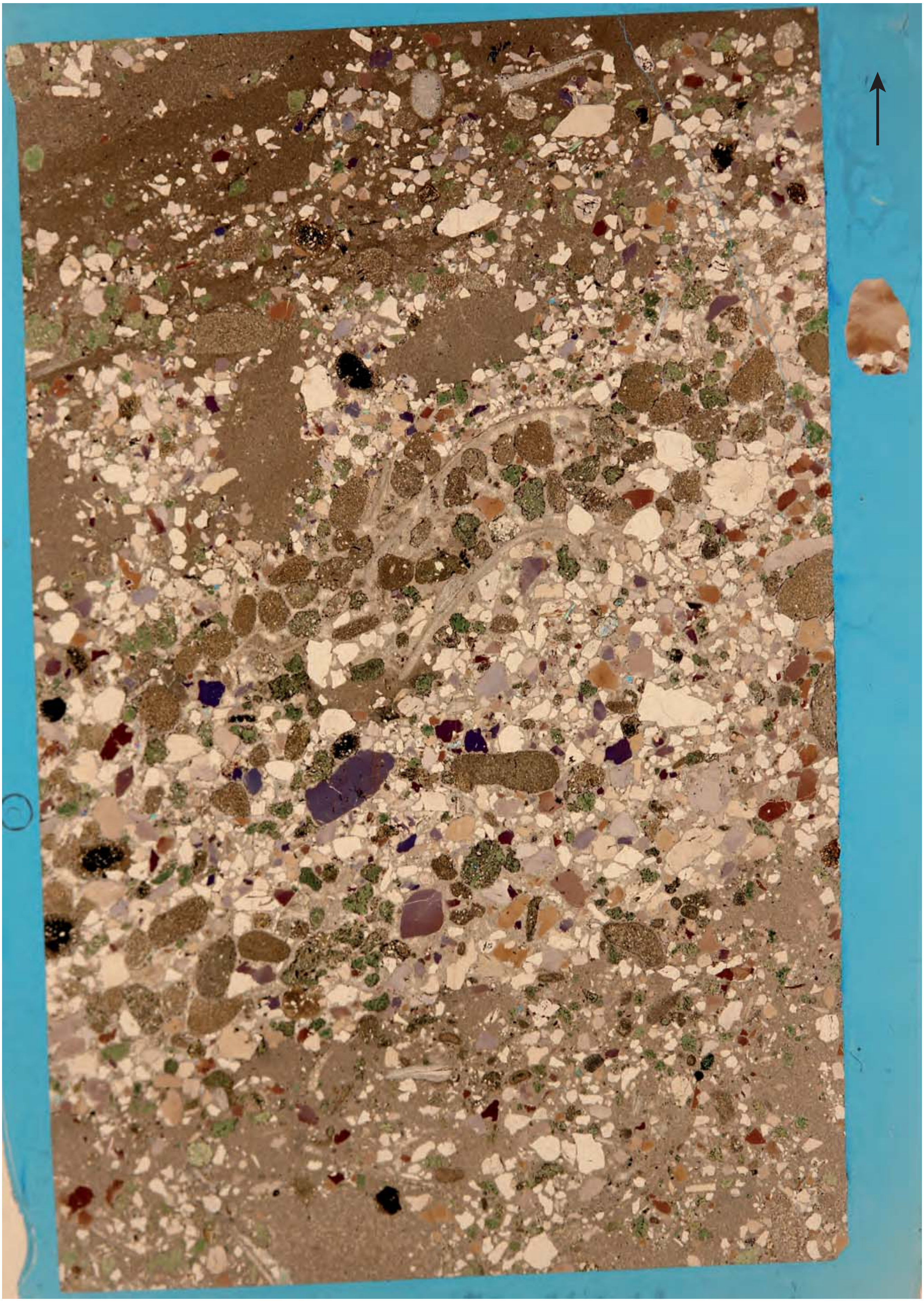

10 mm

517004–408

28.96 m

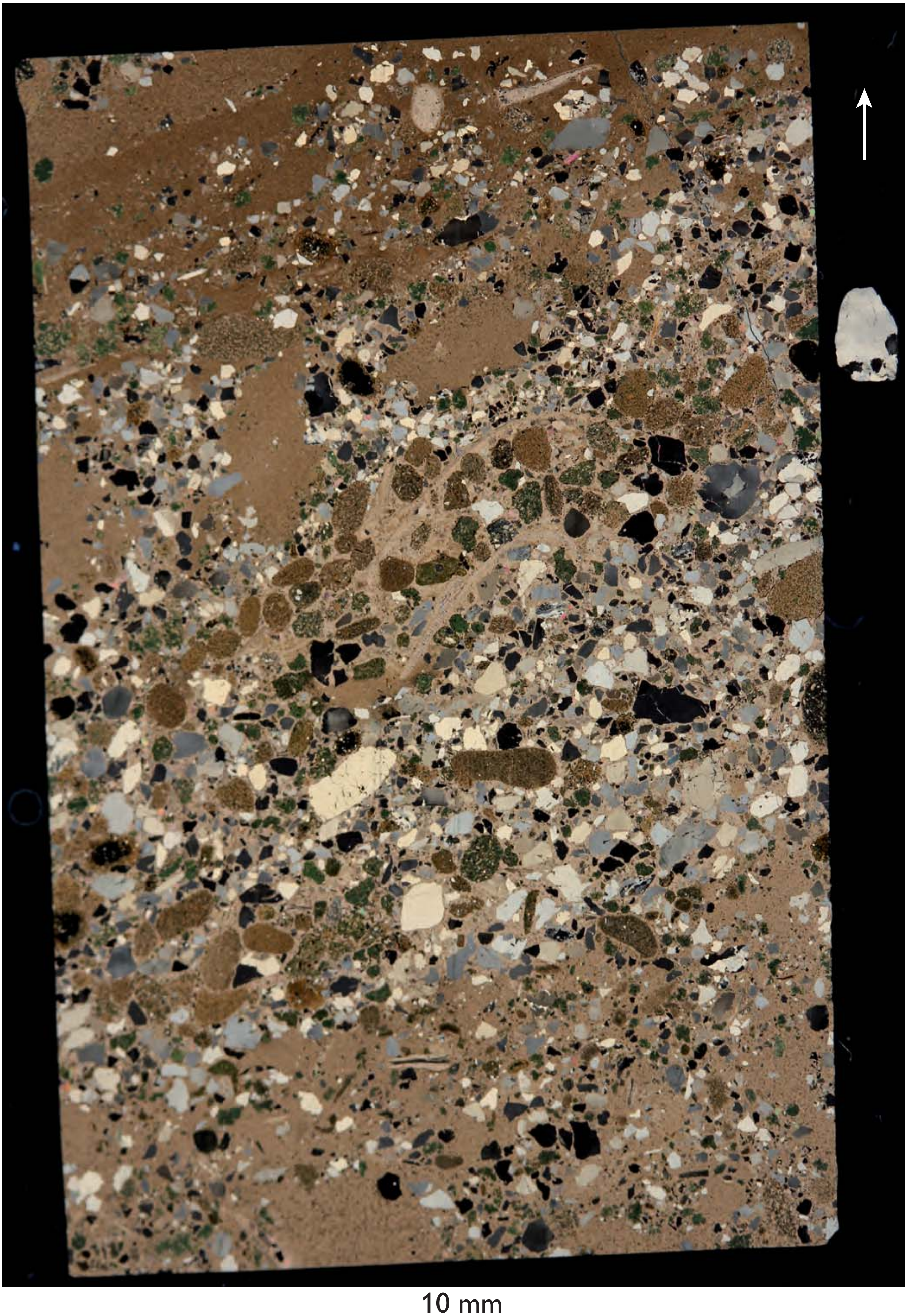

517004–408

28.96 m

517004–406 10 mm 32.65 m

517004–406

32.65 m

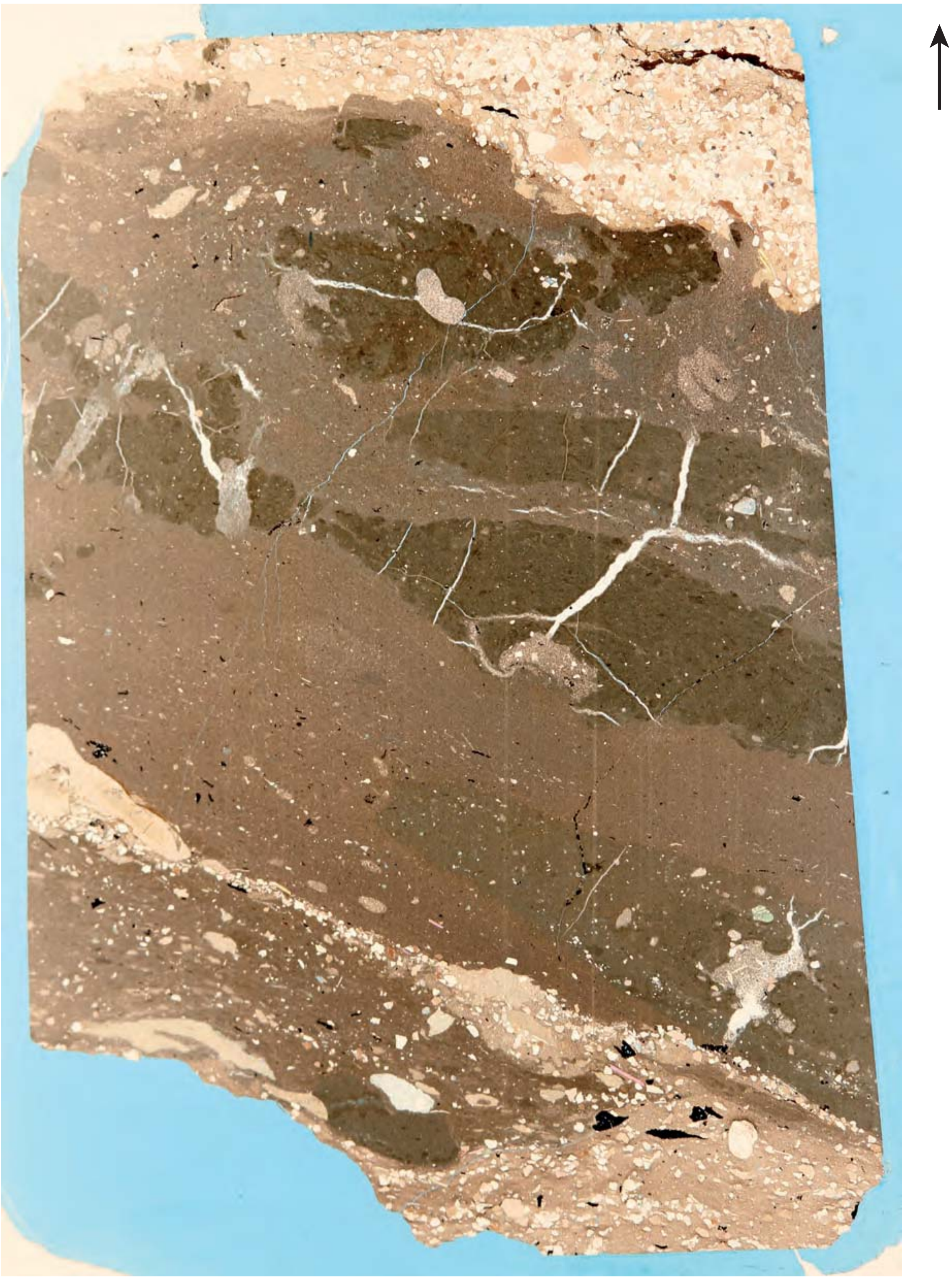

517004–404 10 mm 42.47 m

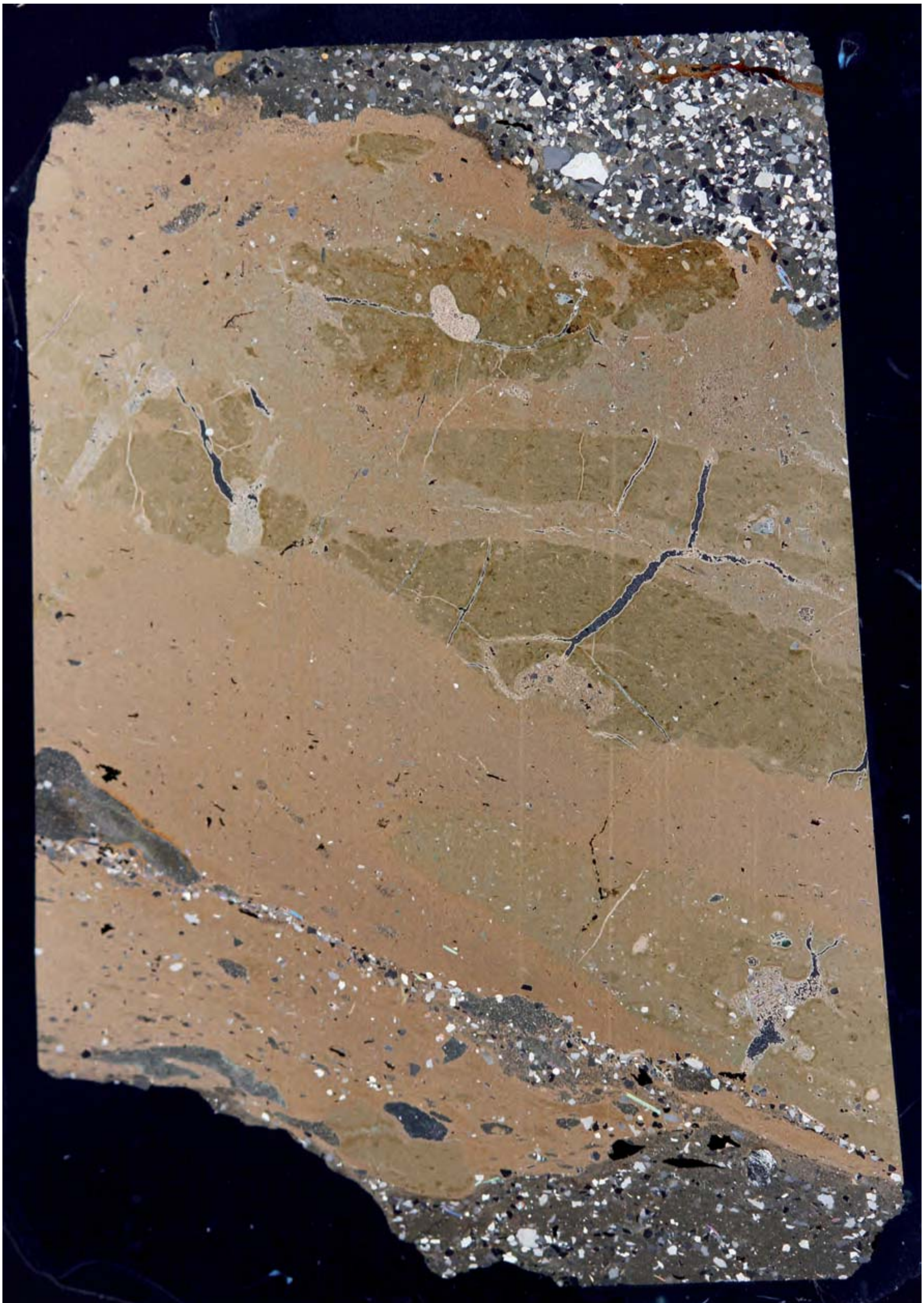

10 mm

517004–404

42.47 m

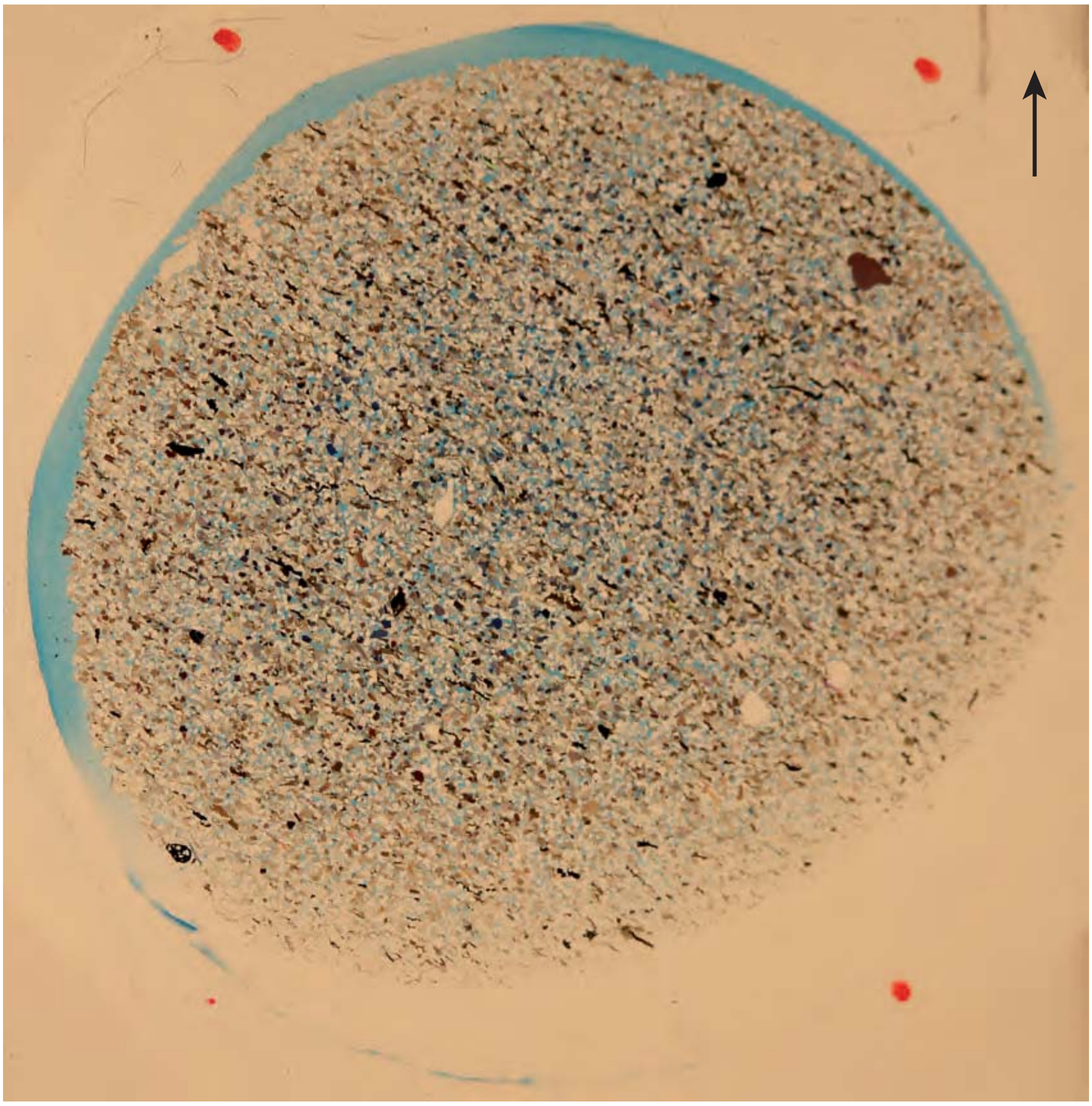

10 mm

517004–211

45.40 m

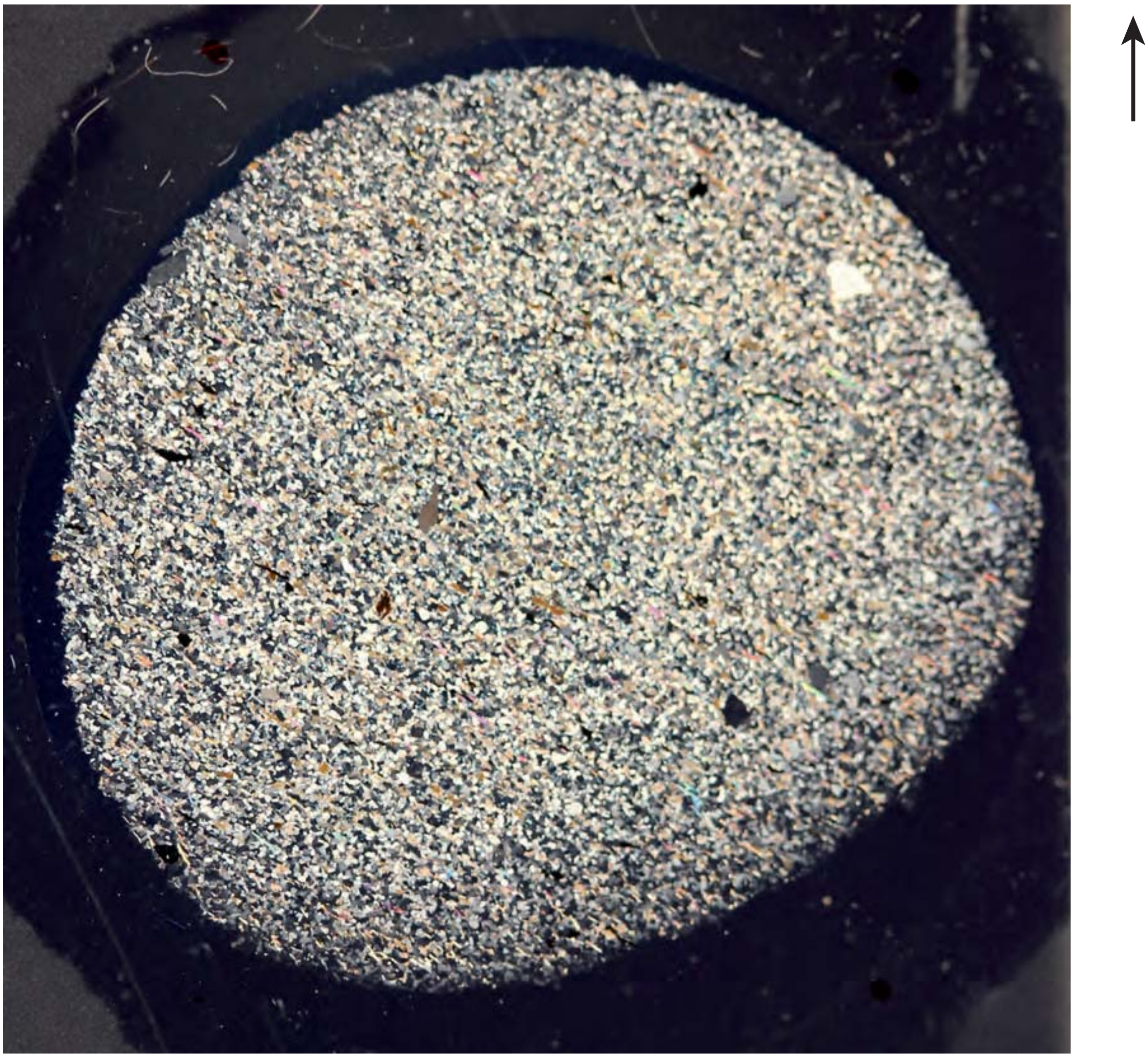

10 mm

517004–211

45.40 m

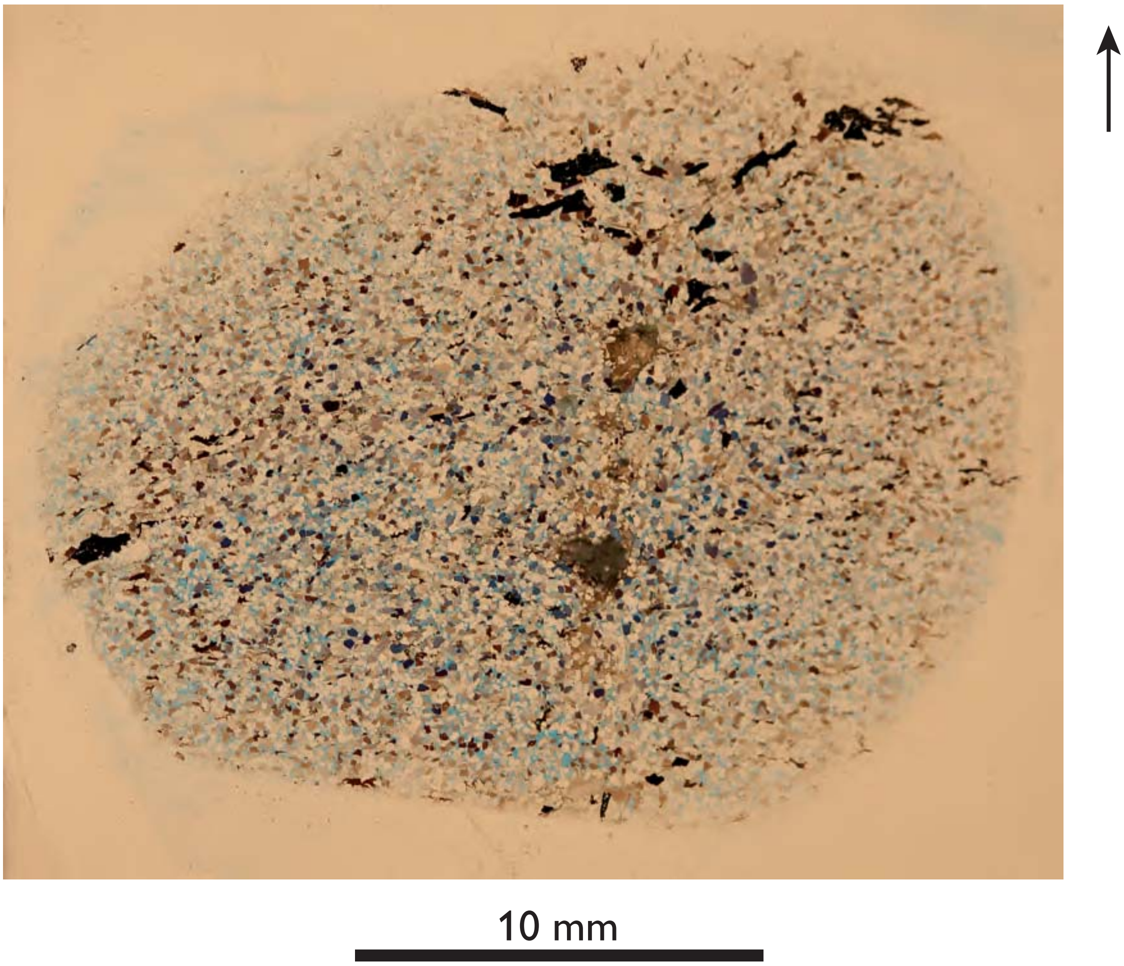

517004–212

46.82 m

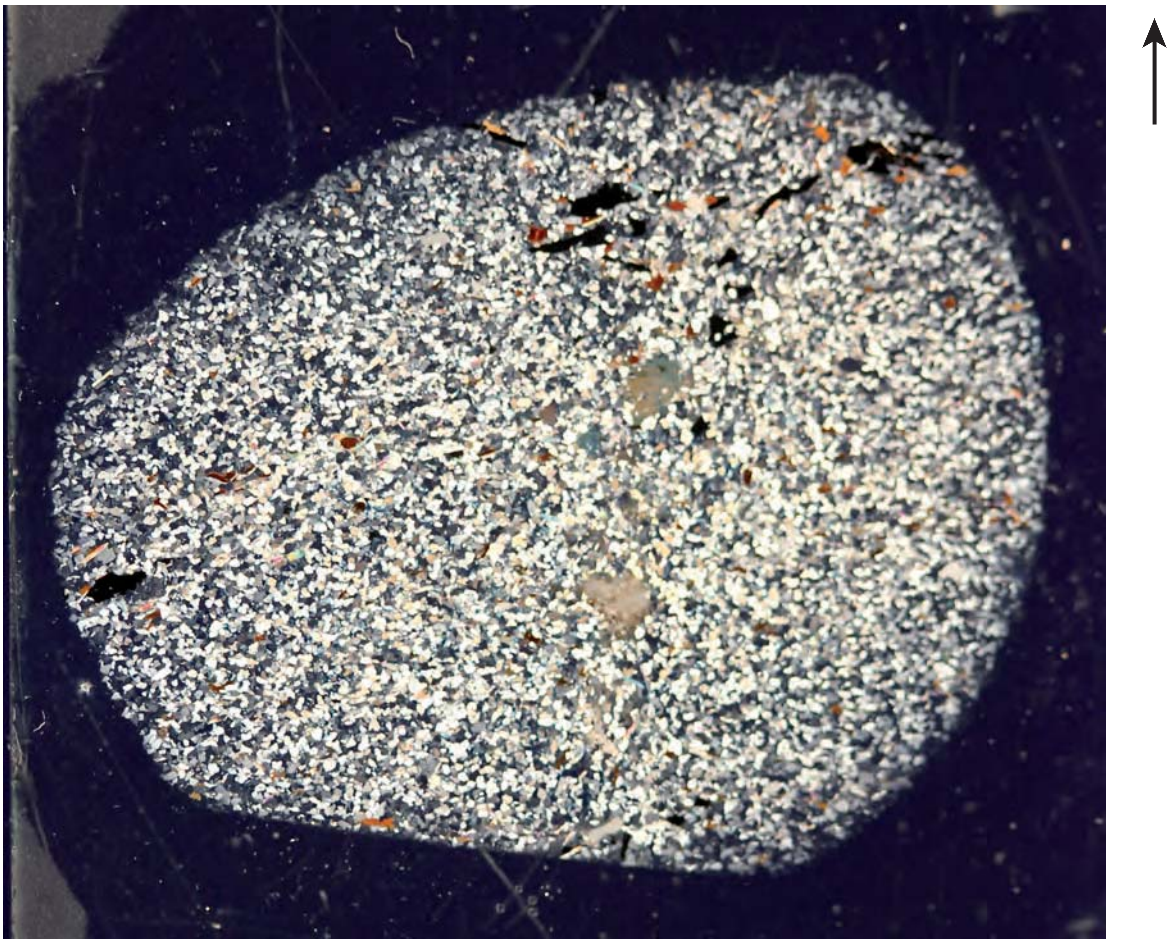

10 mm

517004–212

46.82 m

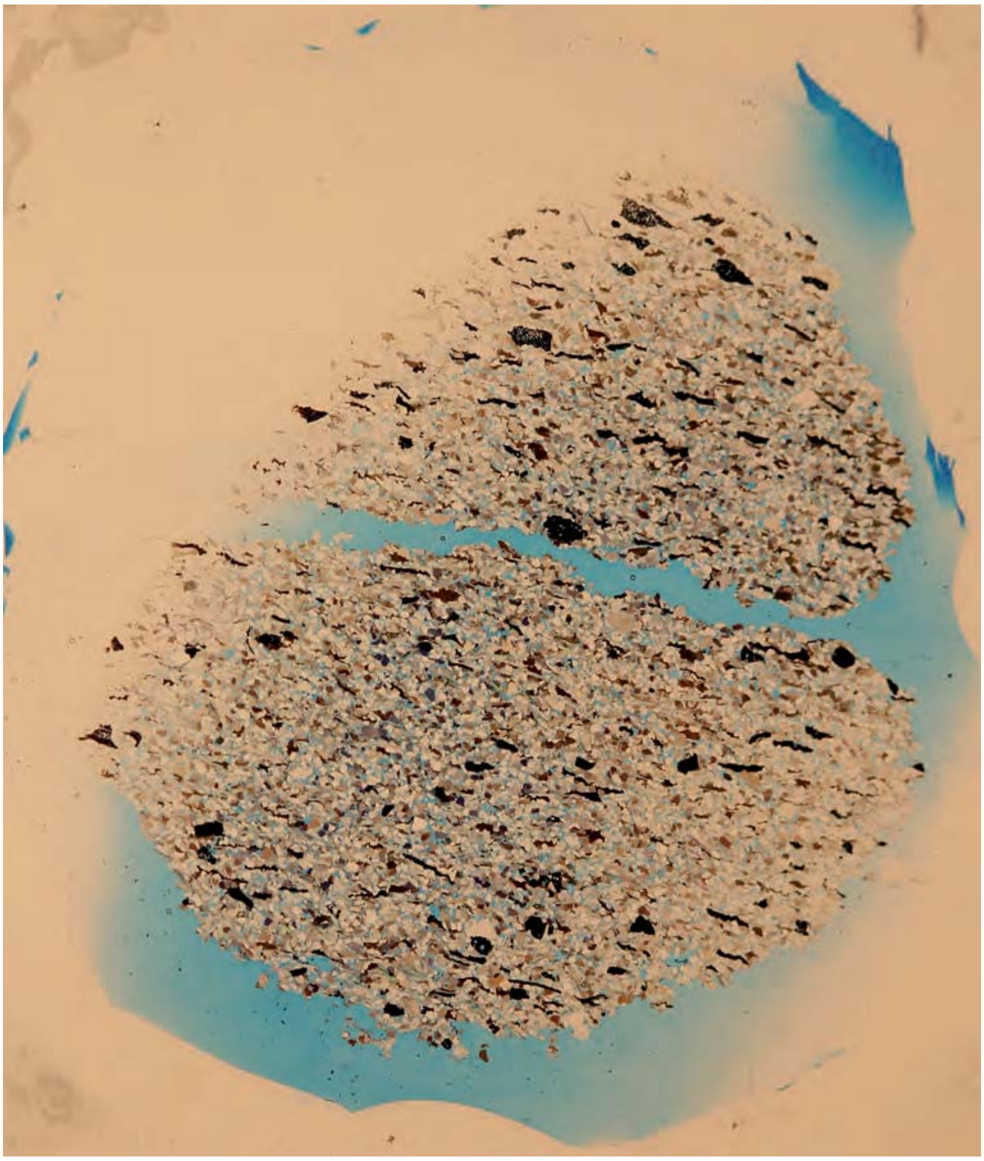

10 mm

517004–213

48.47 m

517004–213

48.47 m

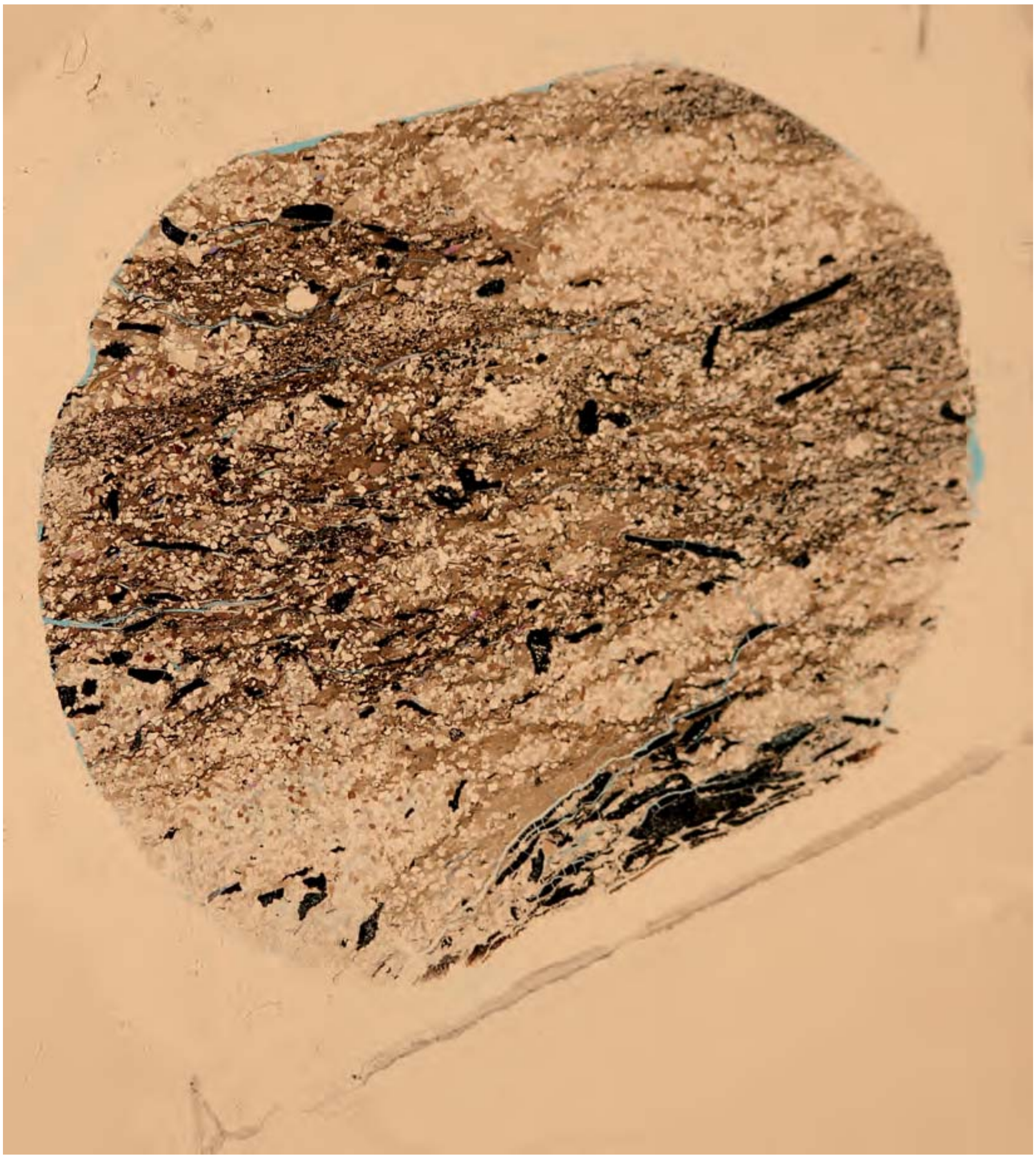

10 mm

517004–214

49.72 m

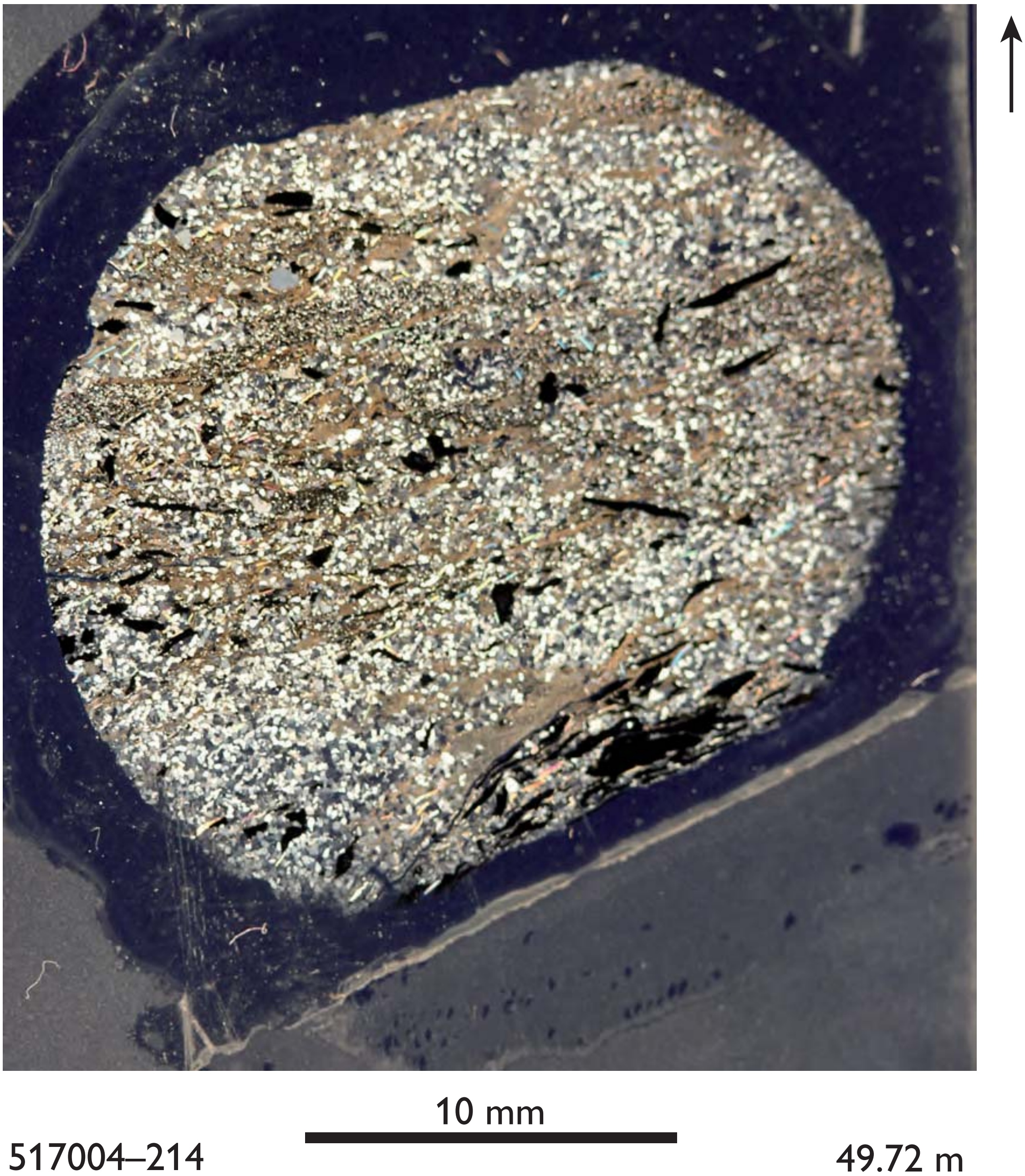

517004–214

49.72 m

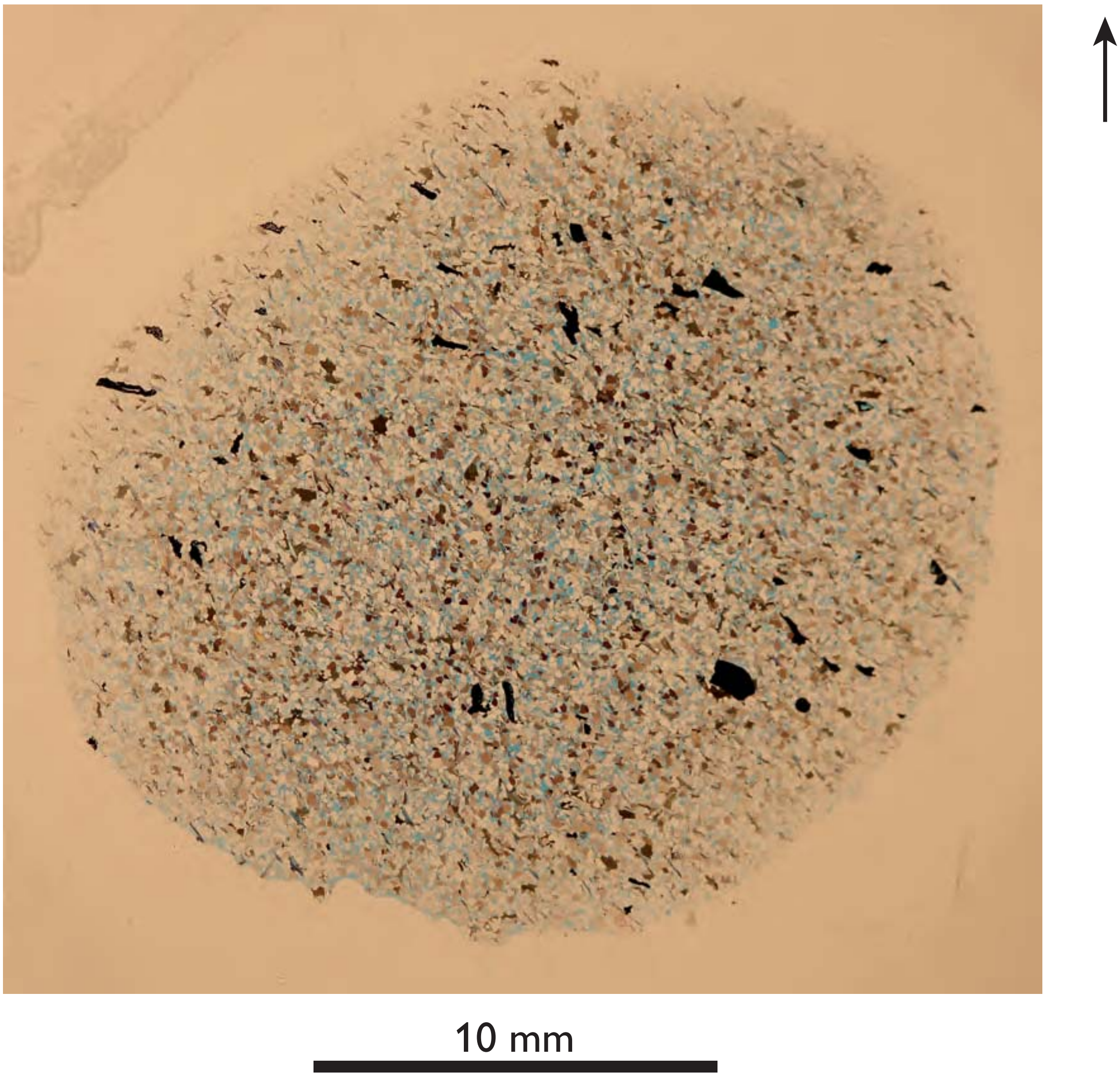

517004–215

51.22 m

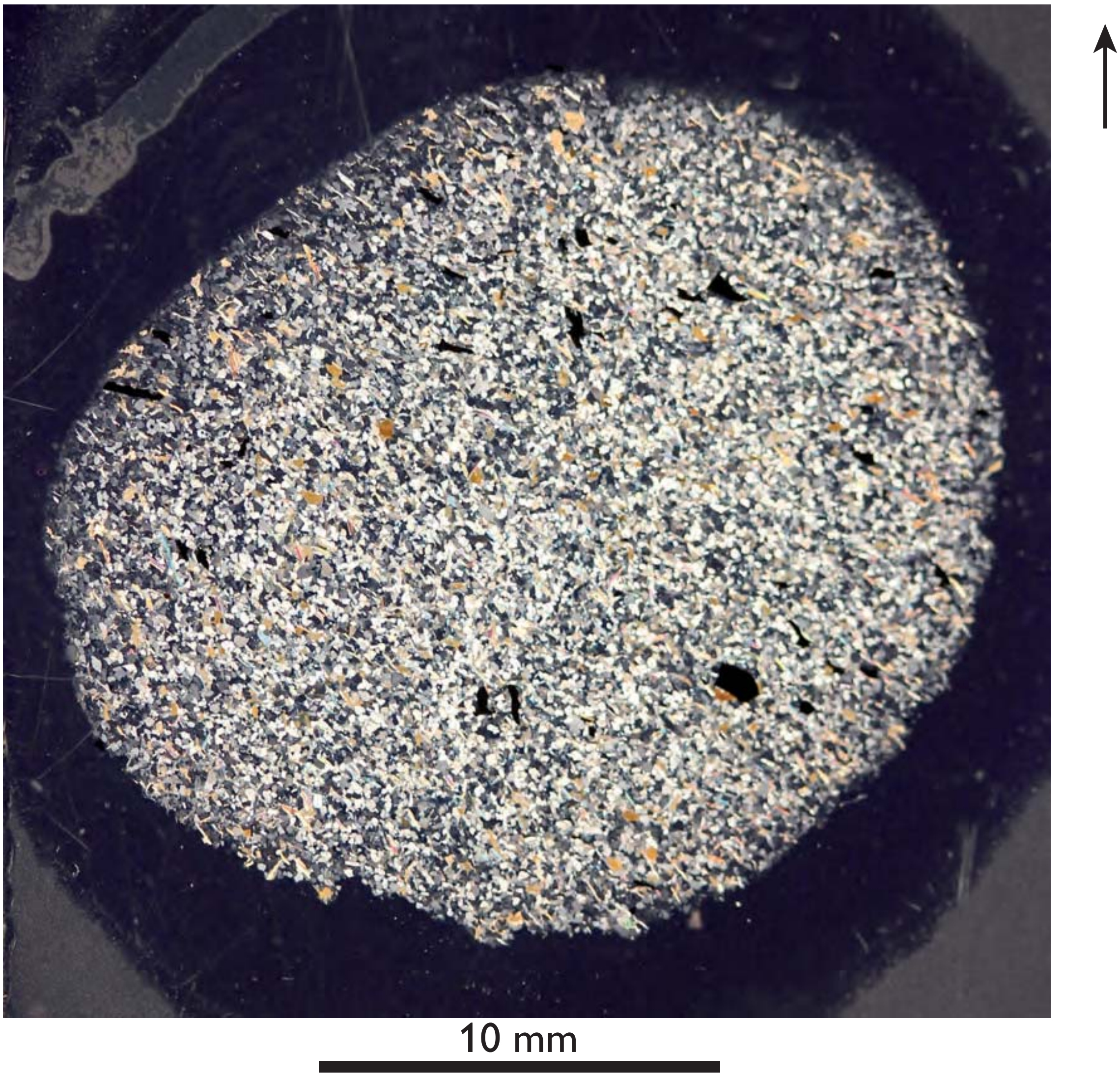

517004–215

51.22 m

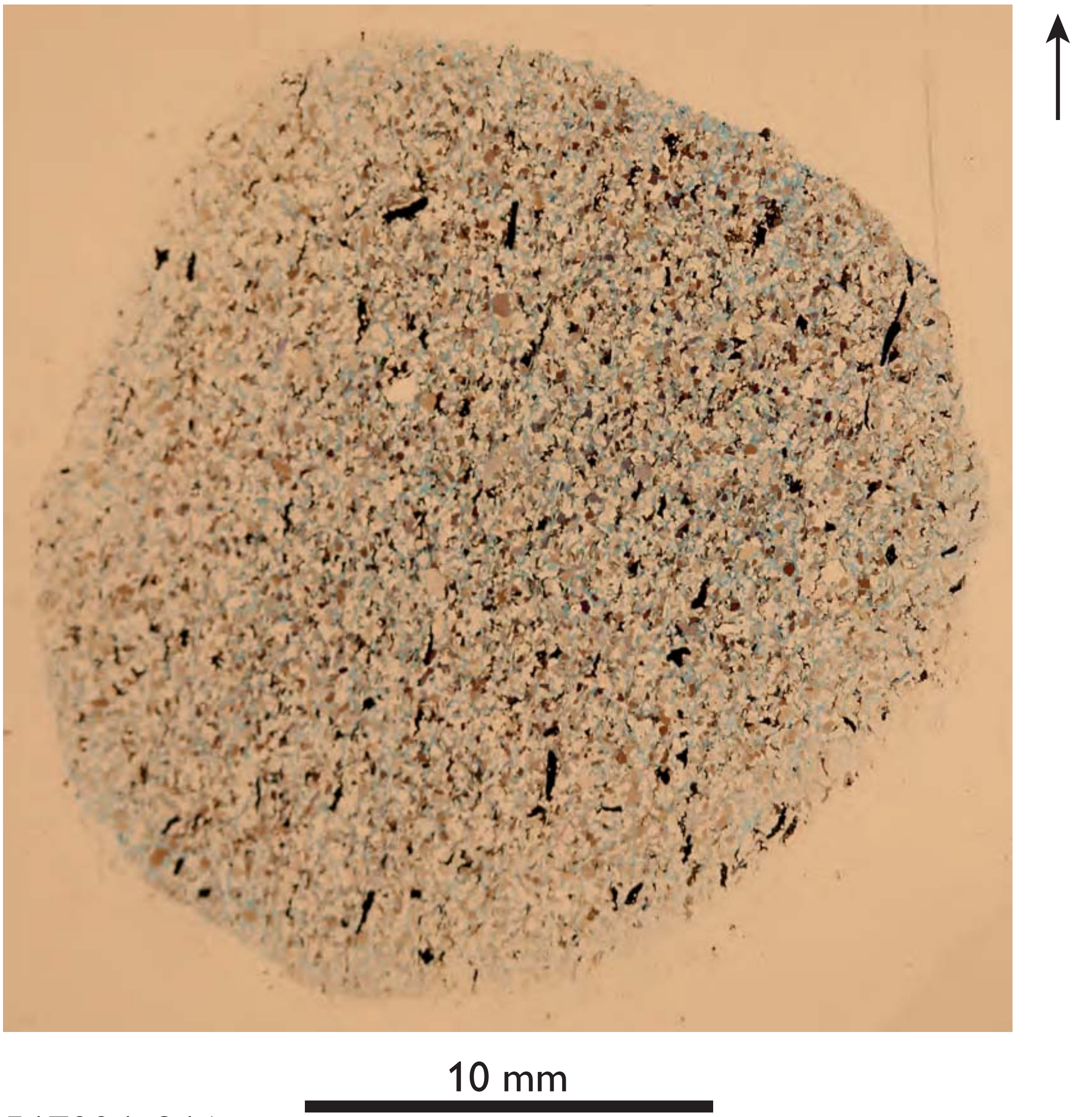

517004–216

54.00 m

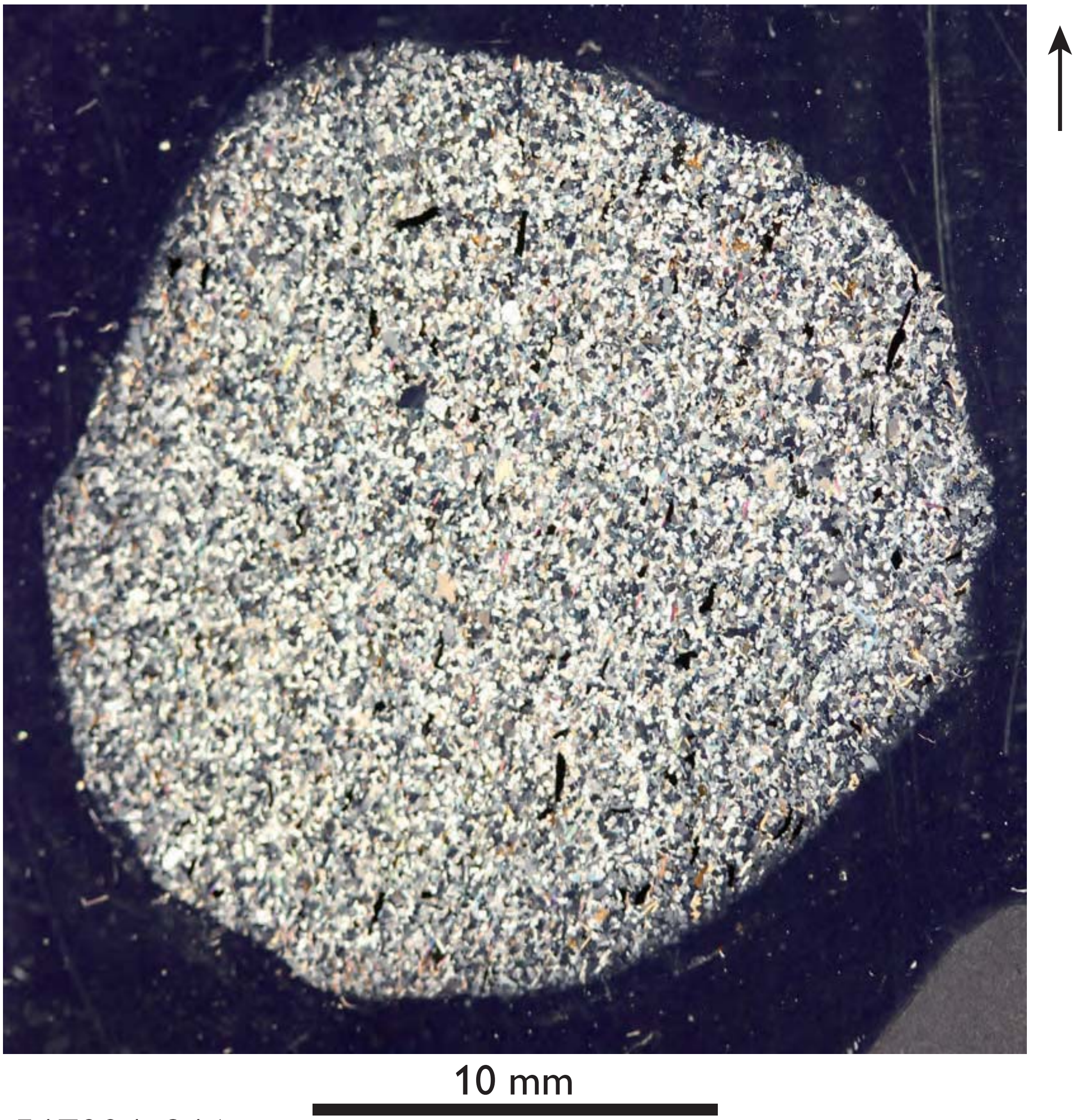

517004–216

54.00 m

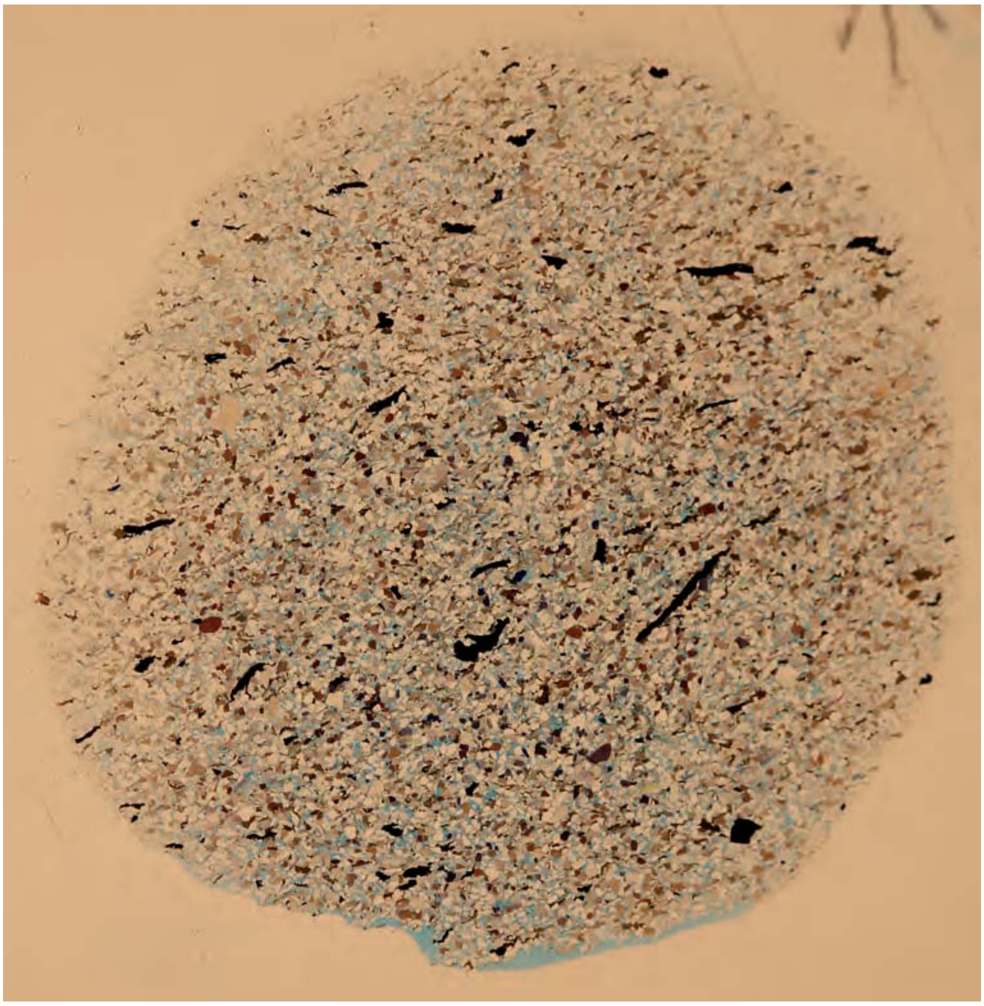

10 mm

517004–218

57.10 m

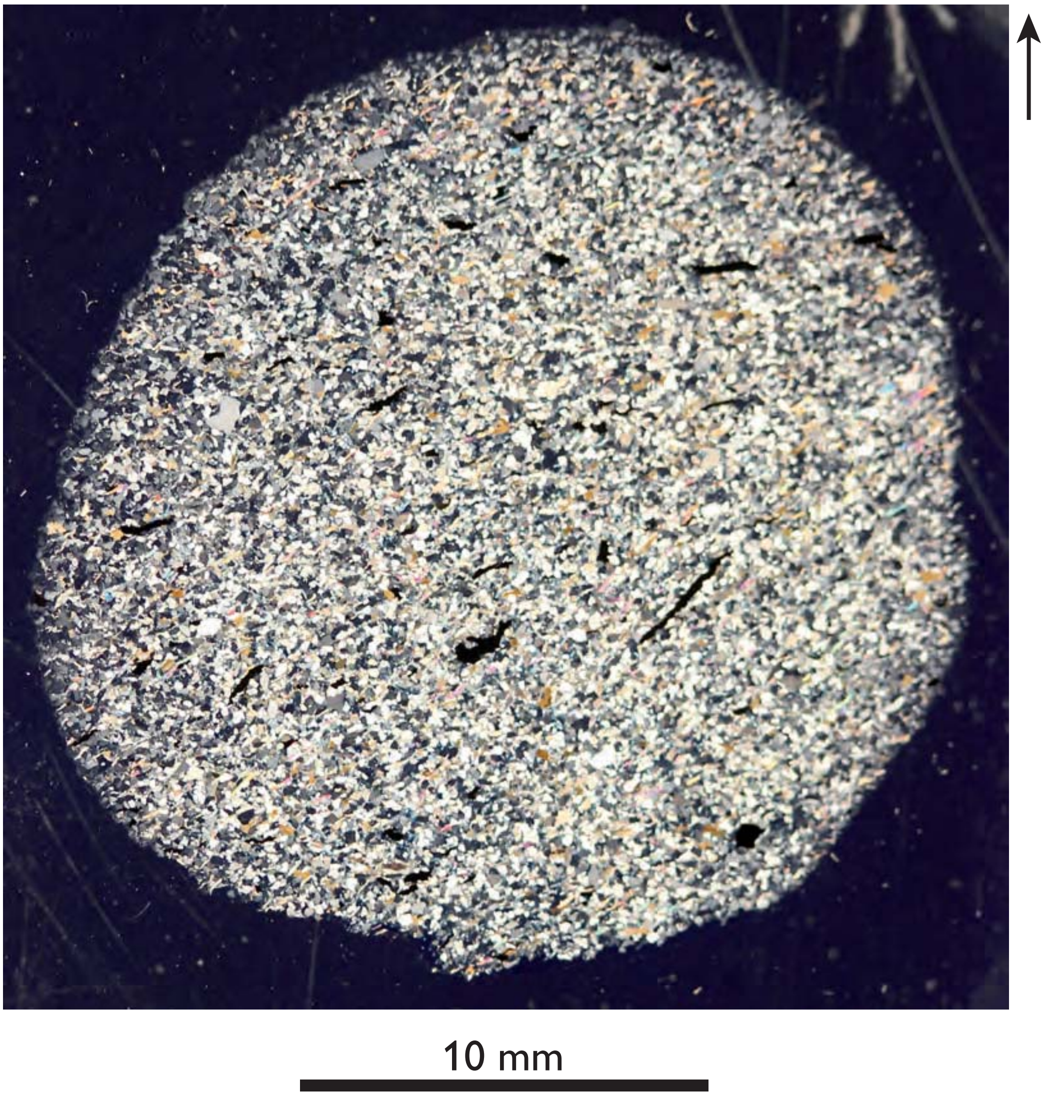

517004–218

57.10 m

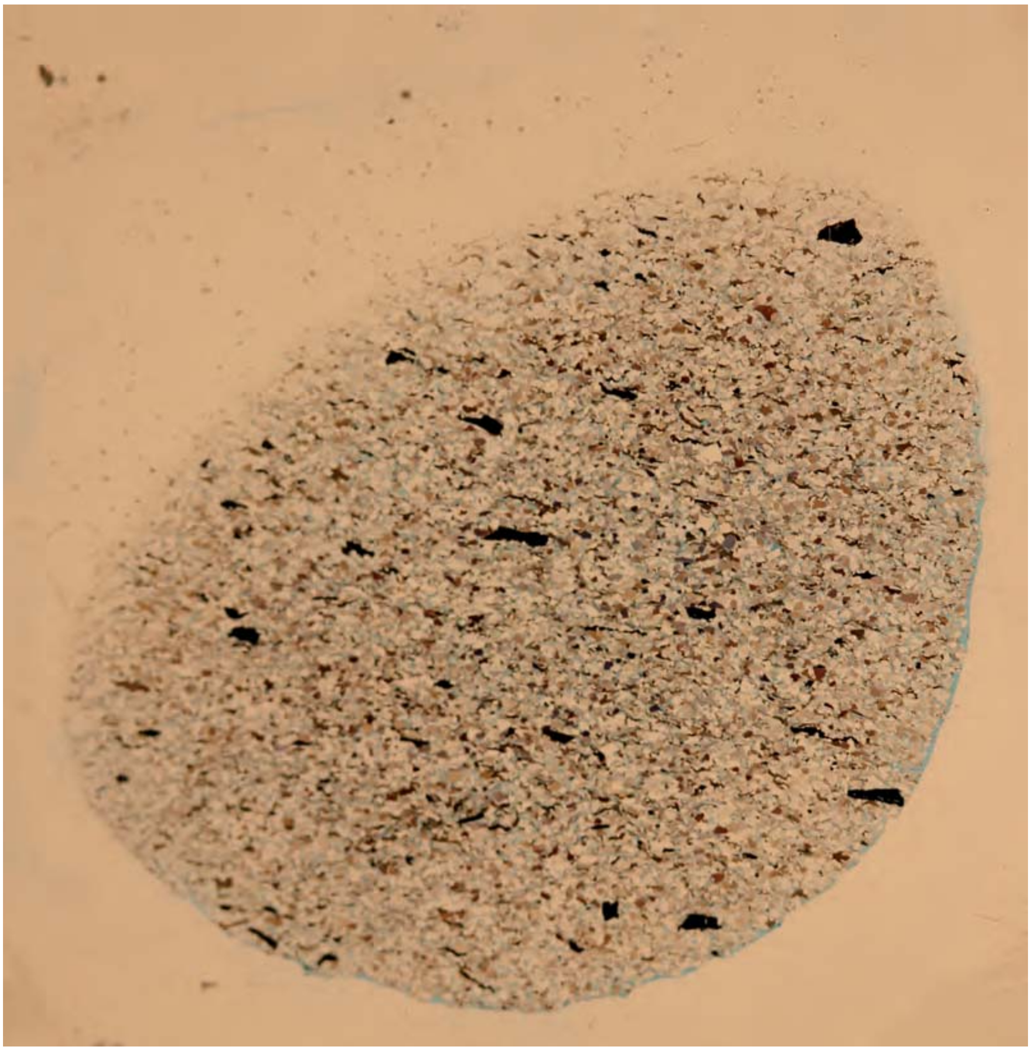

10 mm

517004–219

59.75 m

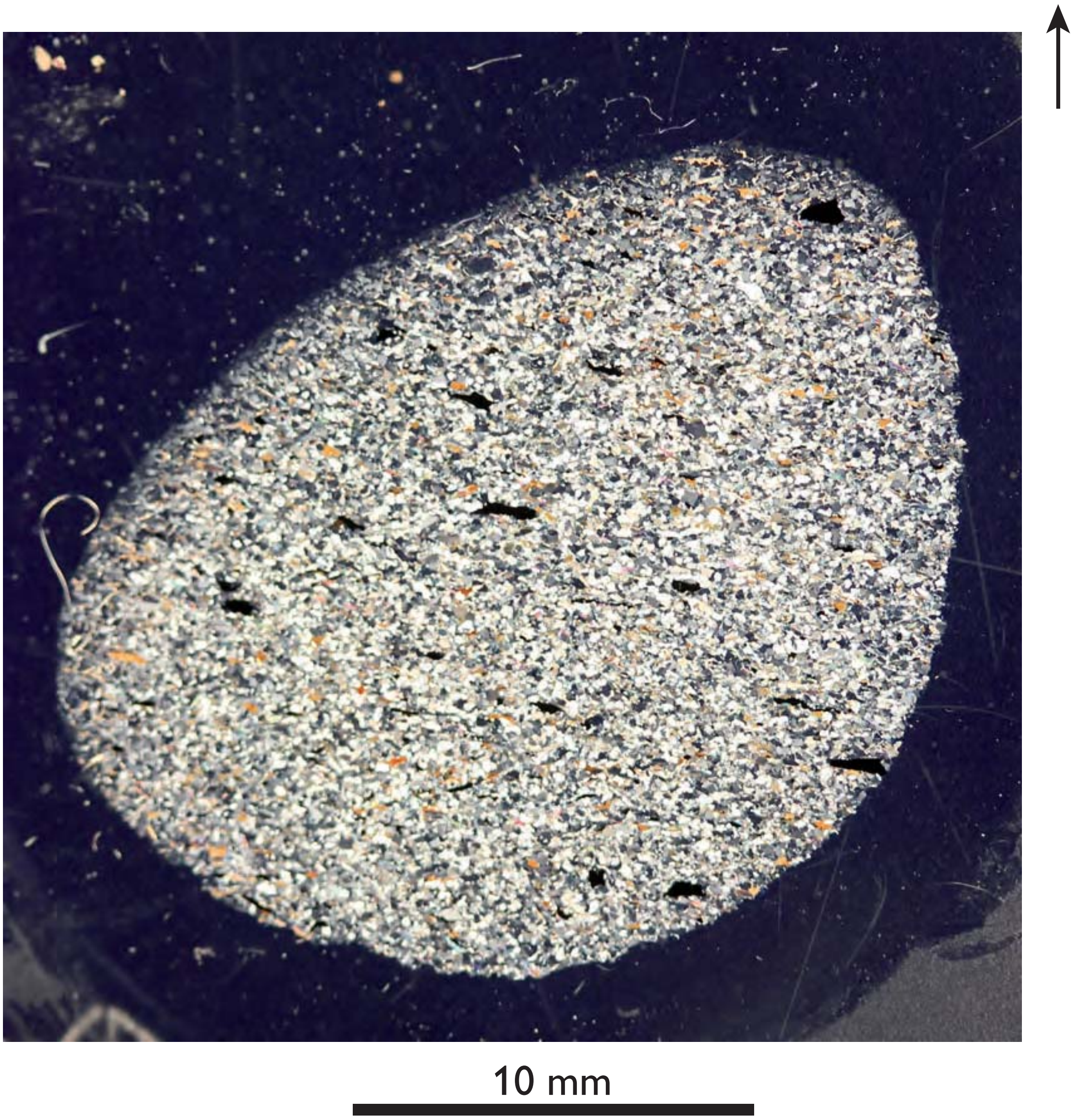

517004–219

59.75 m

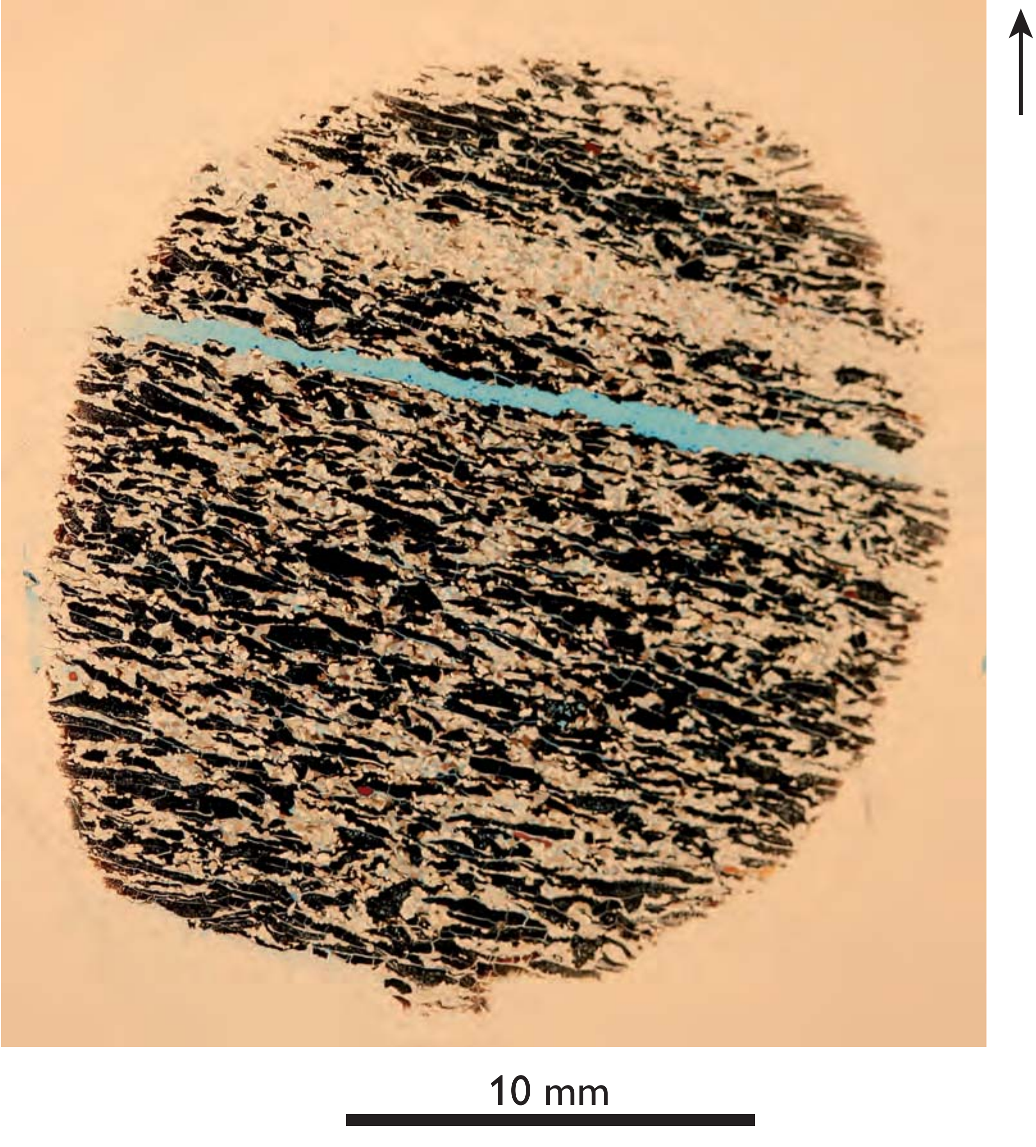

517004–220

60.90 m

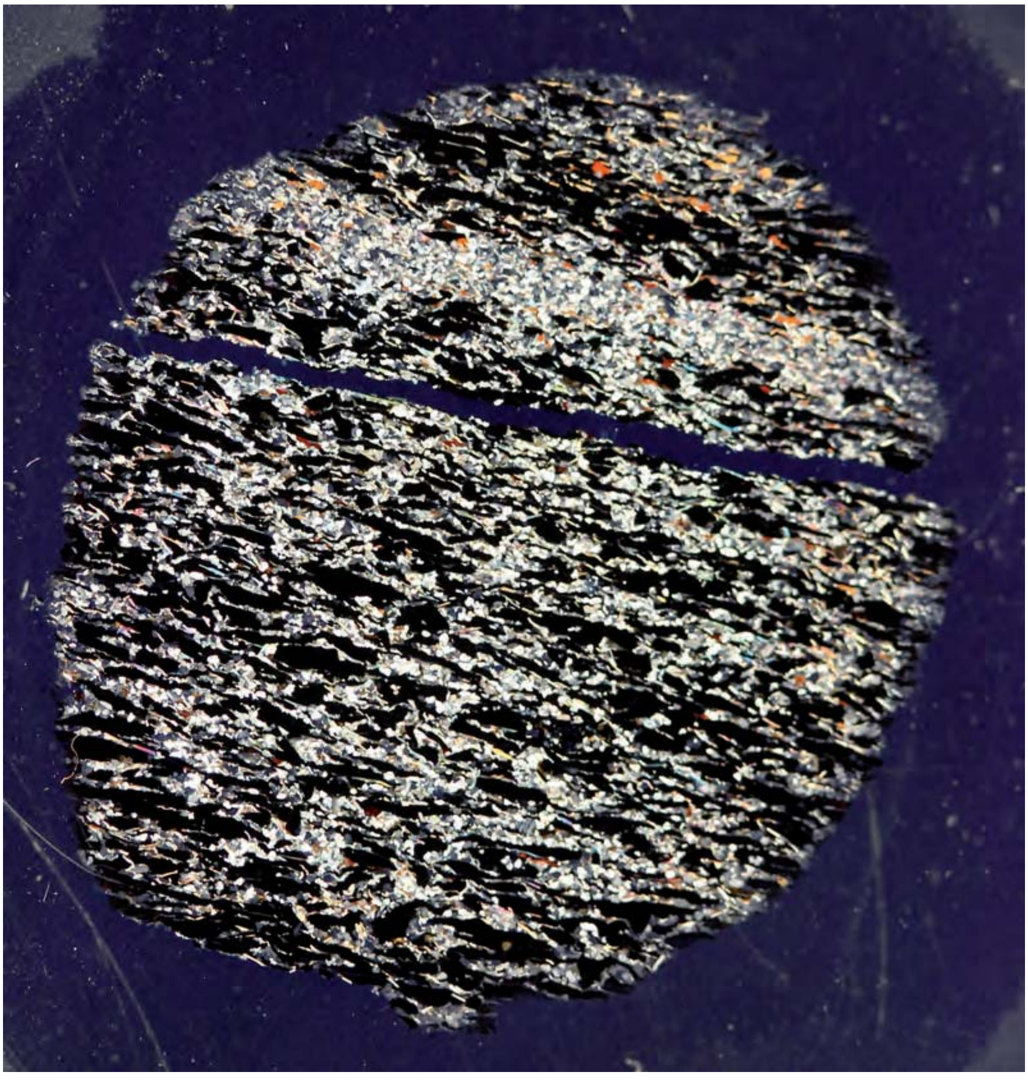

10 mm

517004–220

60.90 m

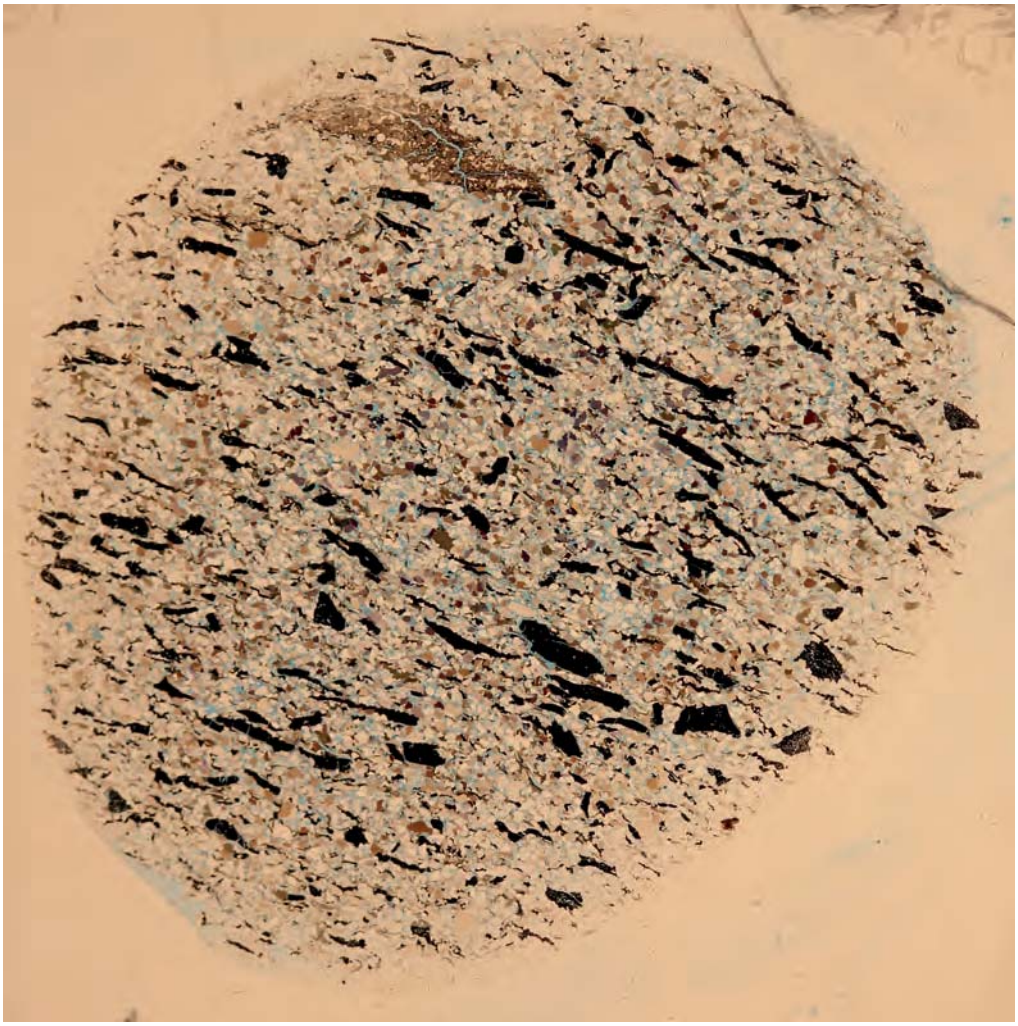

517004–221 10 mm 62.25 m

517004–221 10 mm 62.25 m

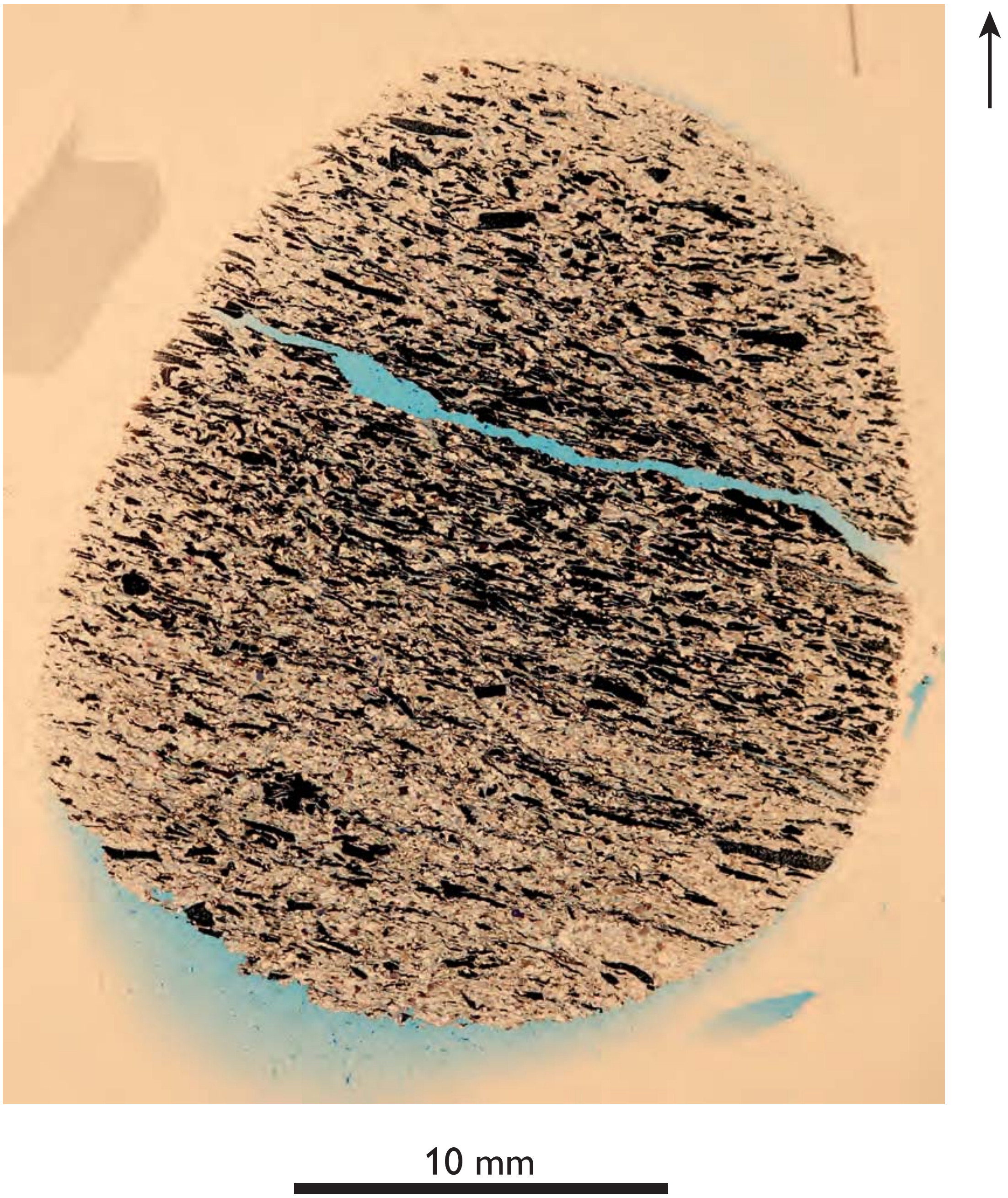

517004–222 62.45 m

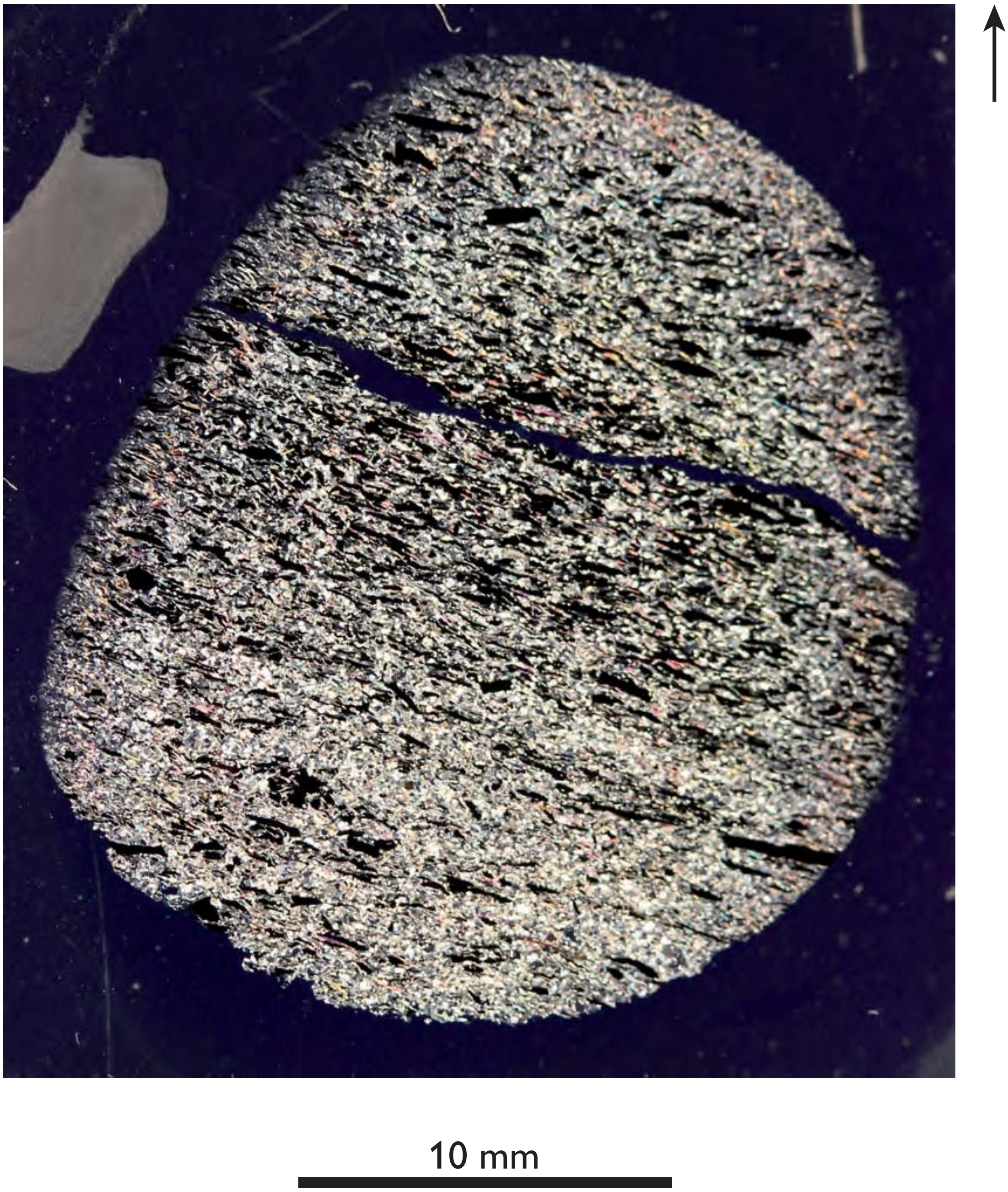

517004–222

62.45 m

10 mm

517004–223 63.45 m

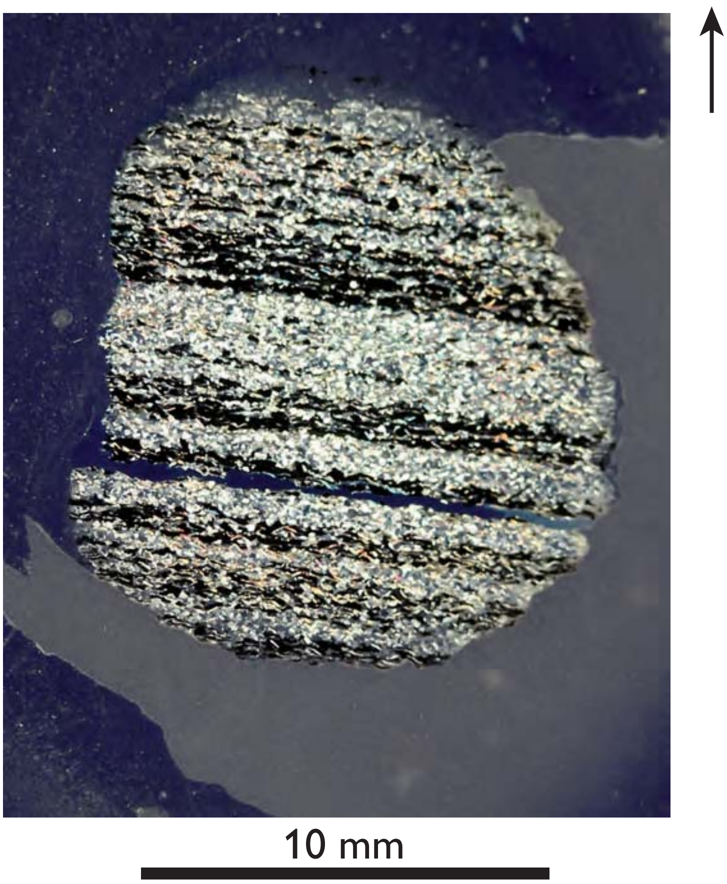

517004–223 63.45 m

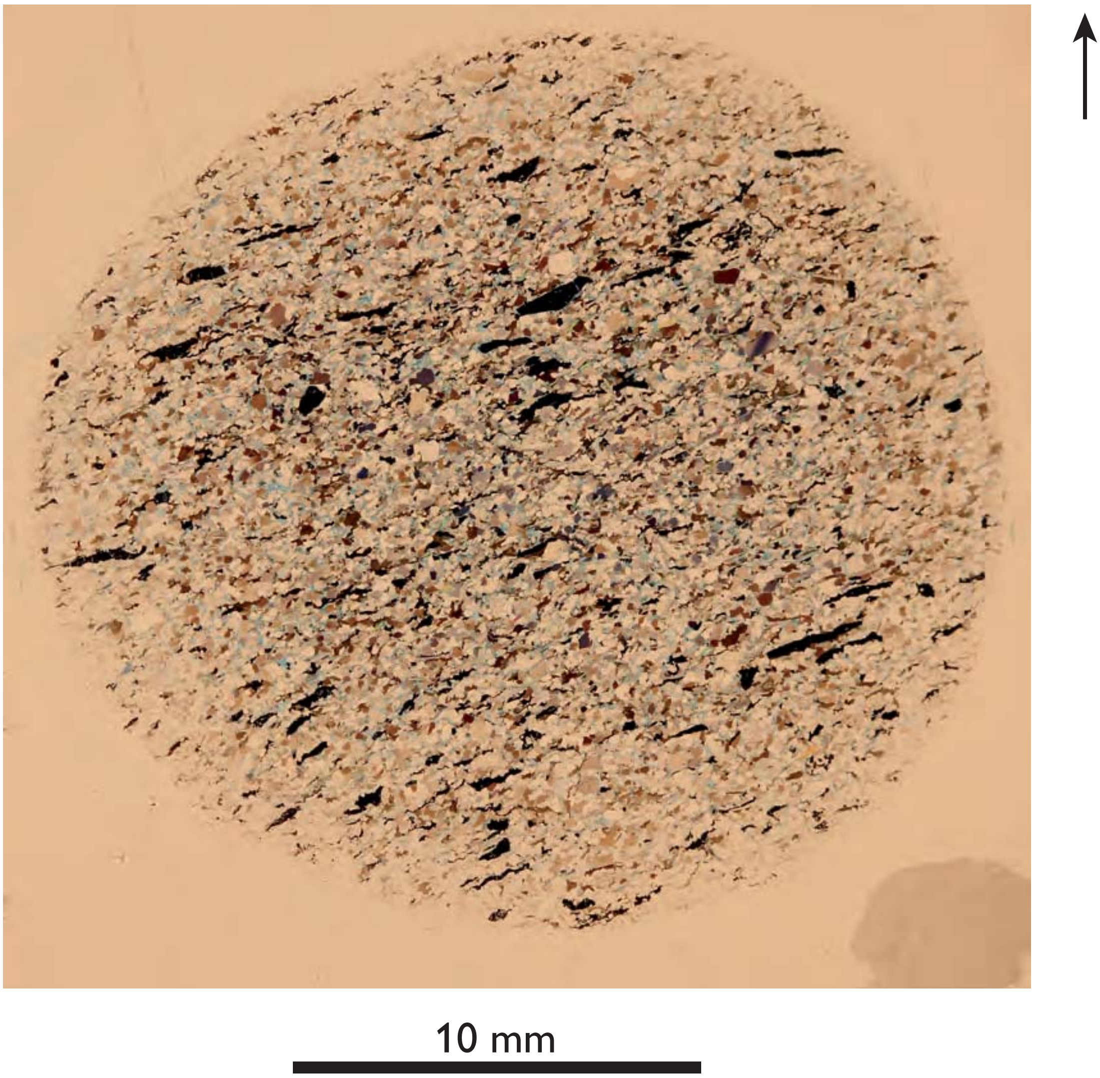

517004–225

63.72 m

10 mm

517004–225

63.72 m

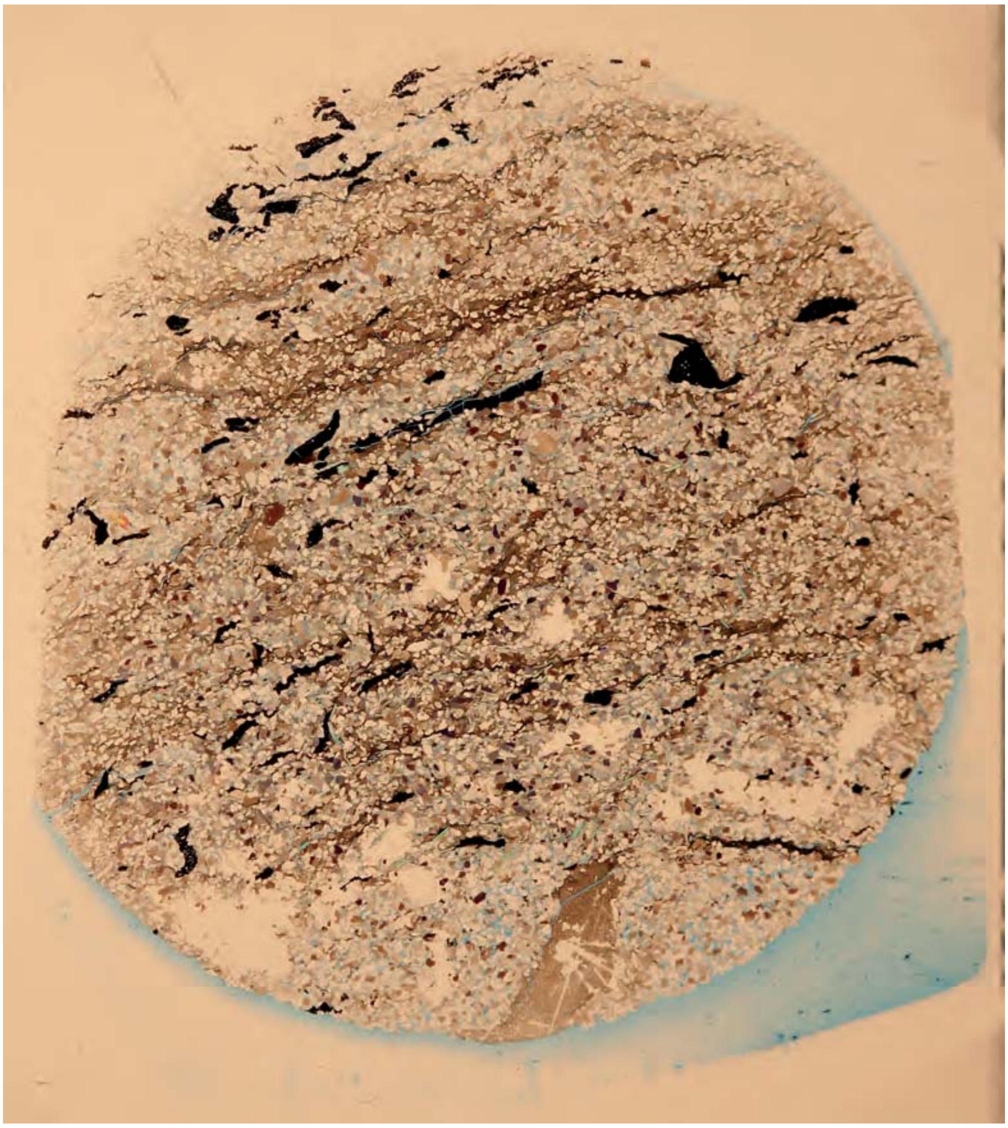

10 mm

517004–226

66.22 m

10 mm

517004–226

66.22 m

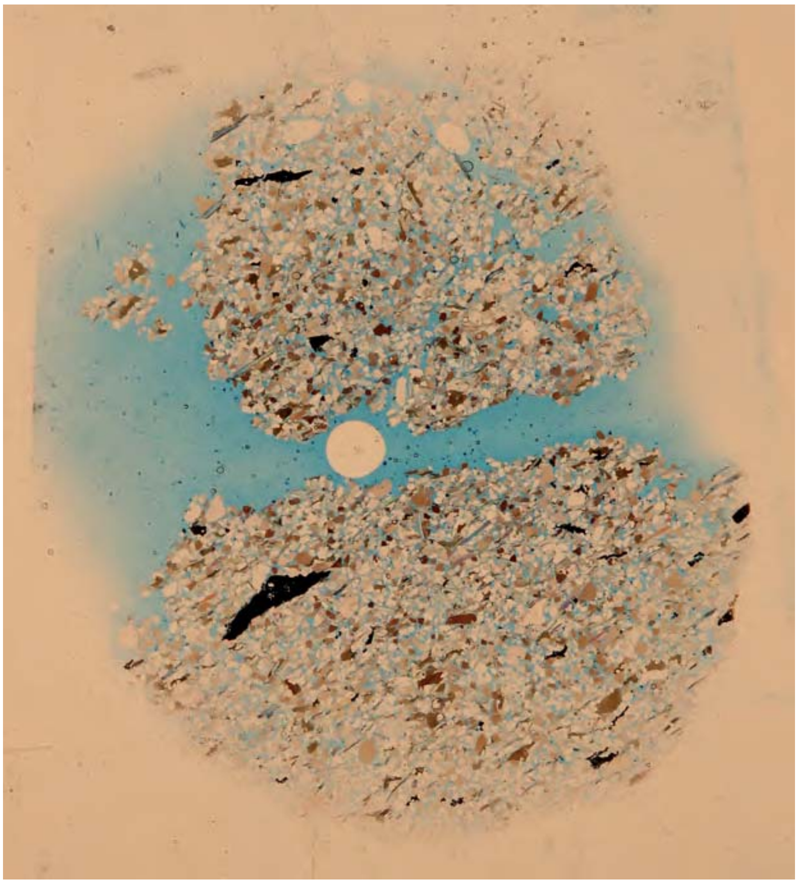

10 mm

517004–228

66.72 m

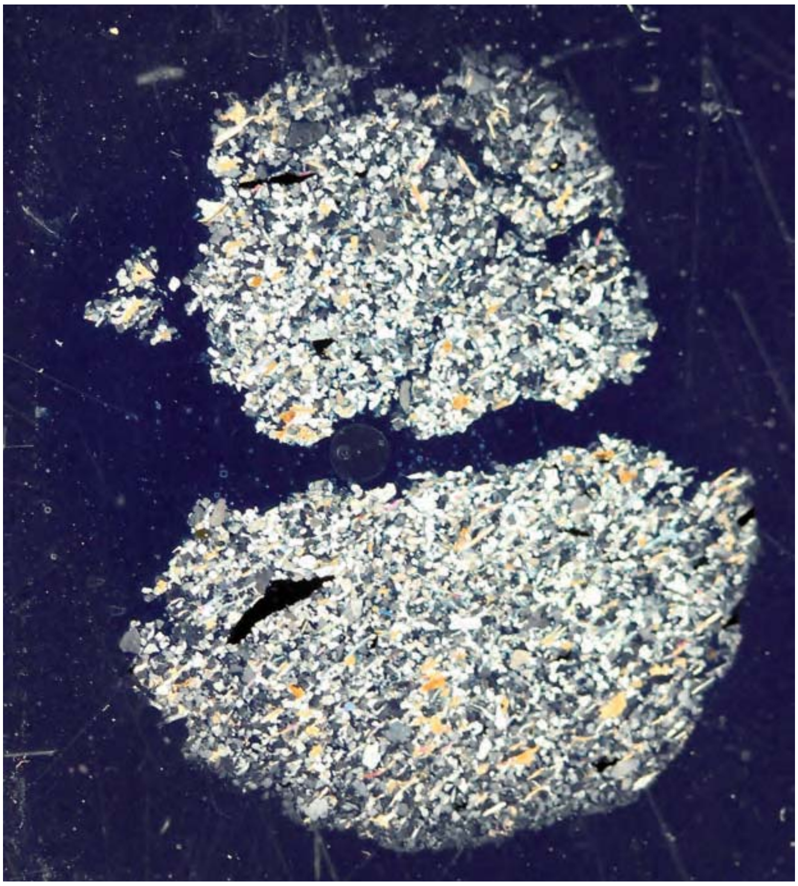

10 mm

517004–228

66.72 m

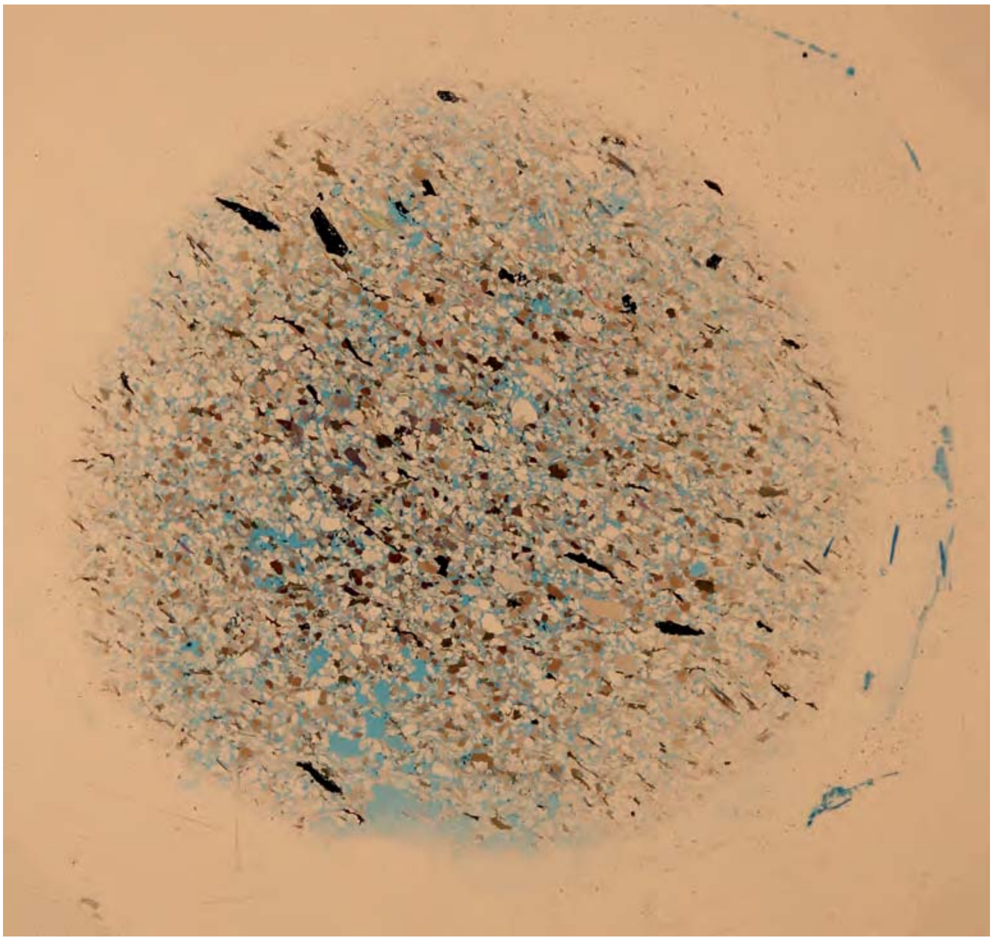

10 mm

517004–229

68.85 m


10 mm

517004–229

68.85 m

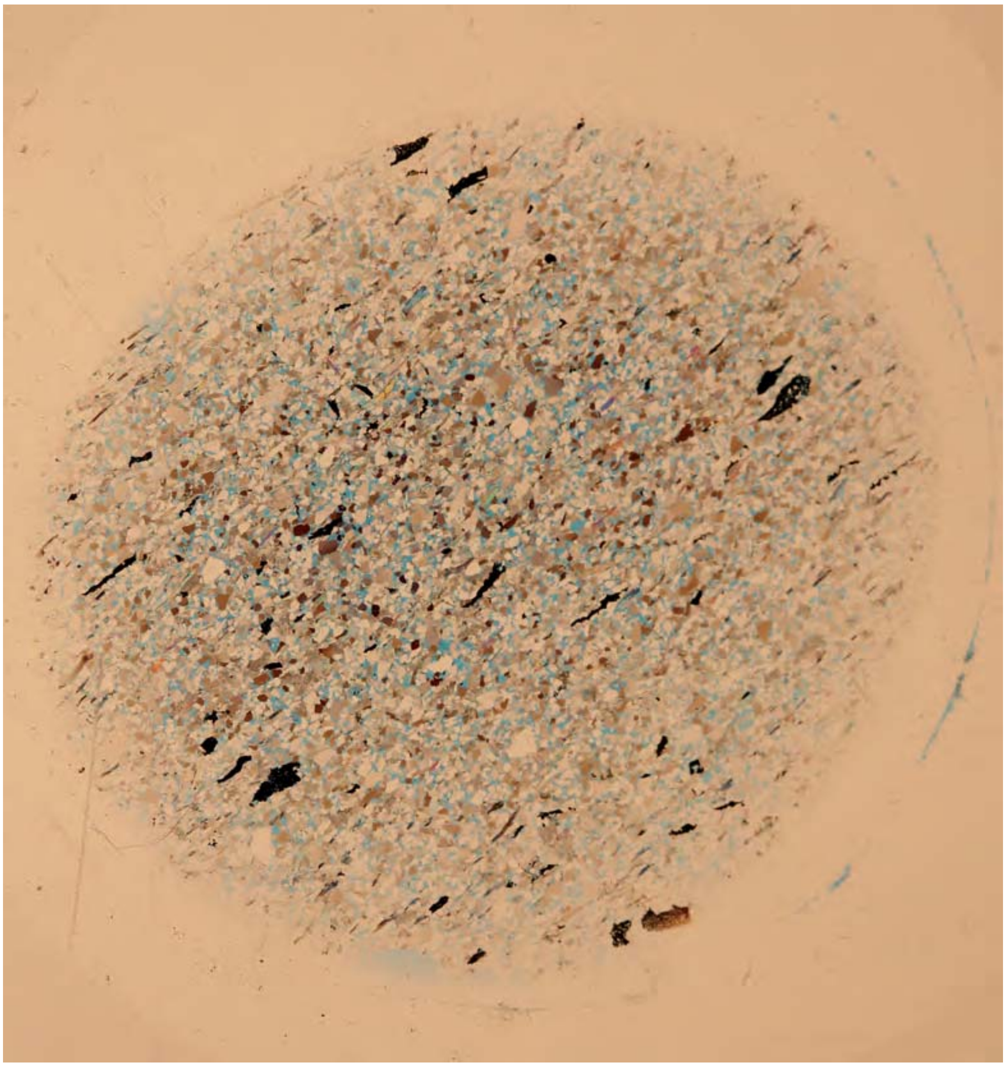

517004–231 | 10 mm | 69.50 m

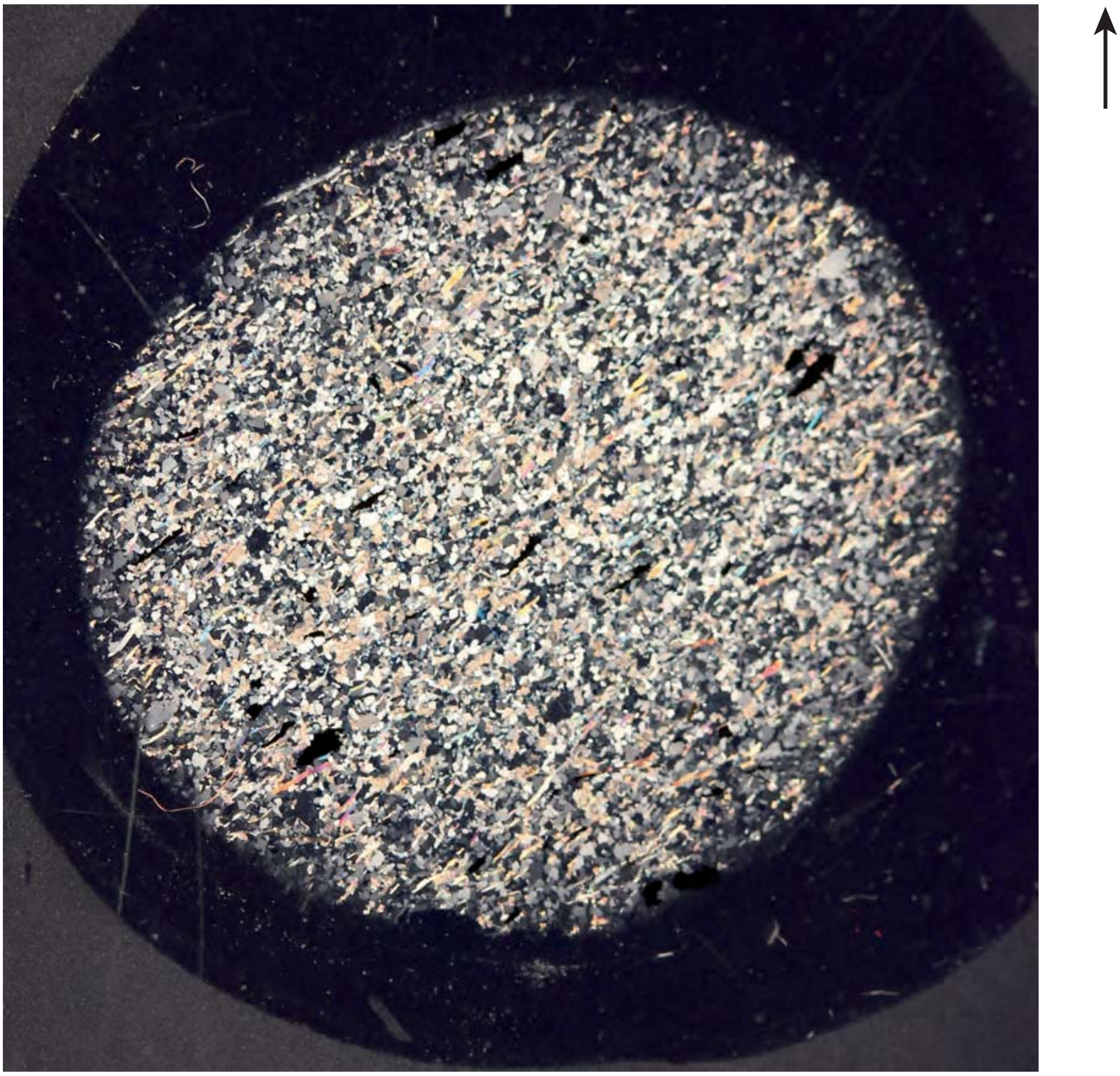

517004–231 10 mm 69.50 m

10 mm

517004–232 72.38 m

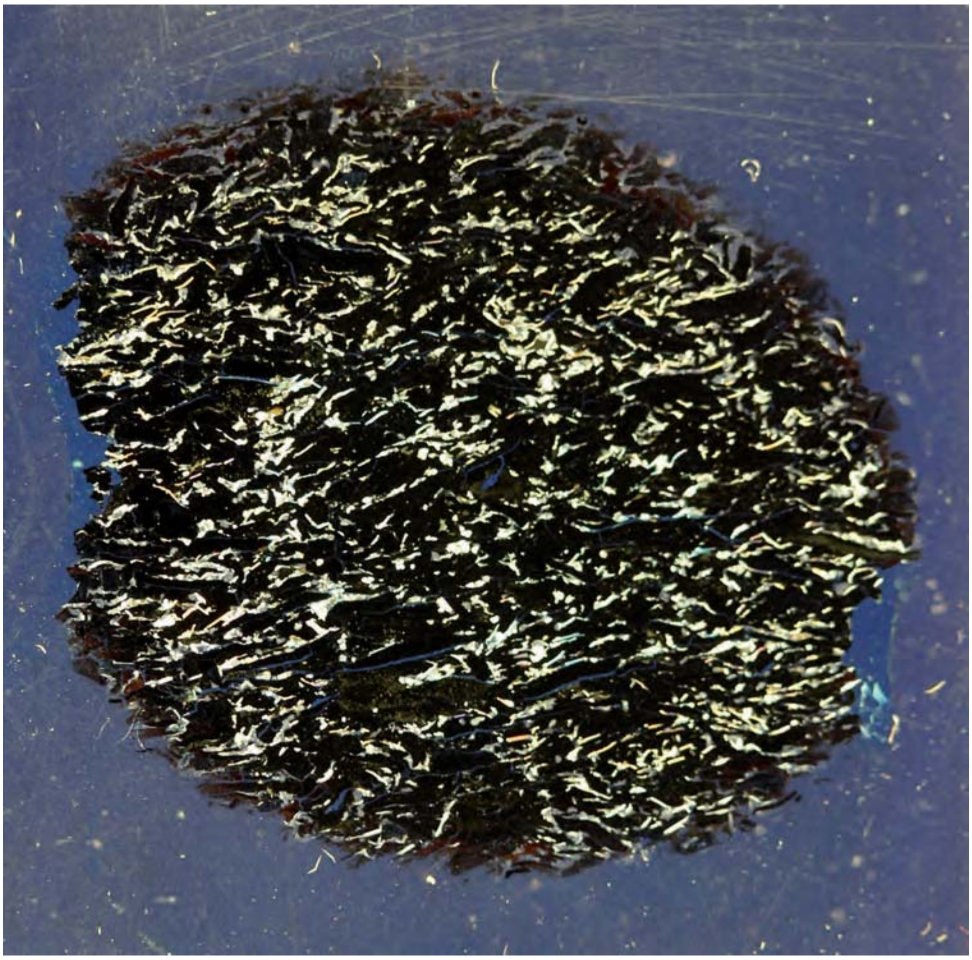

10 mm

517004–232

72.38 m

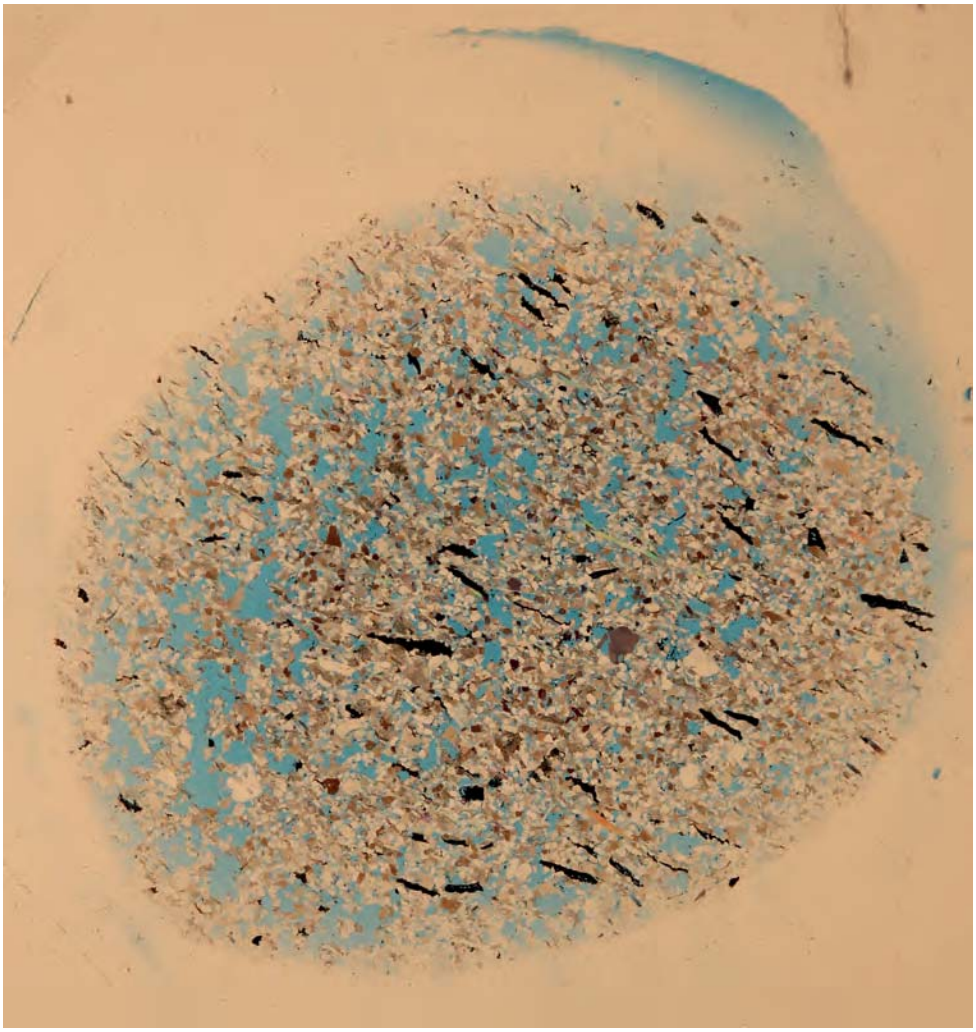

10 mm

517004–234

75.40 m

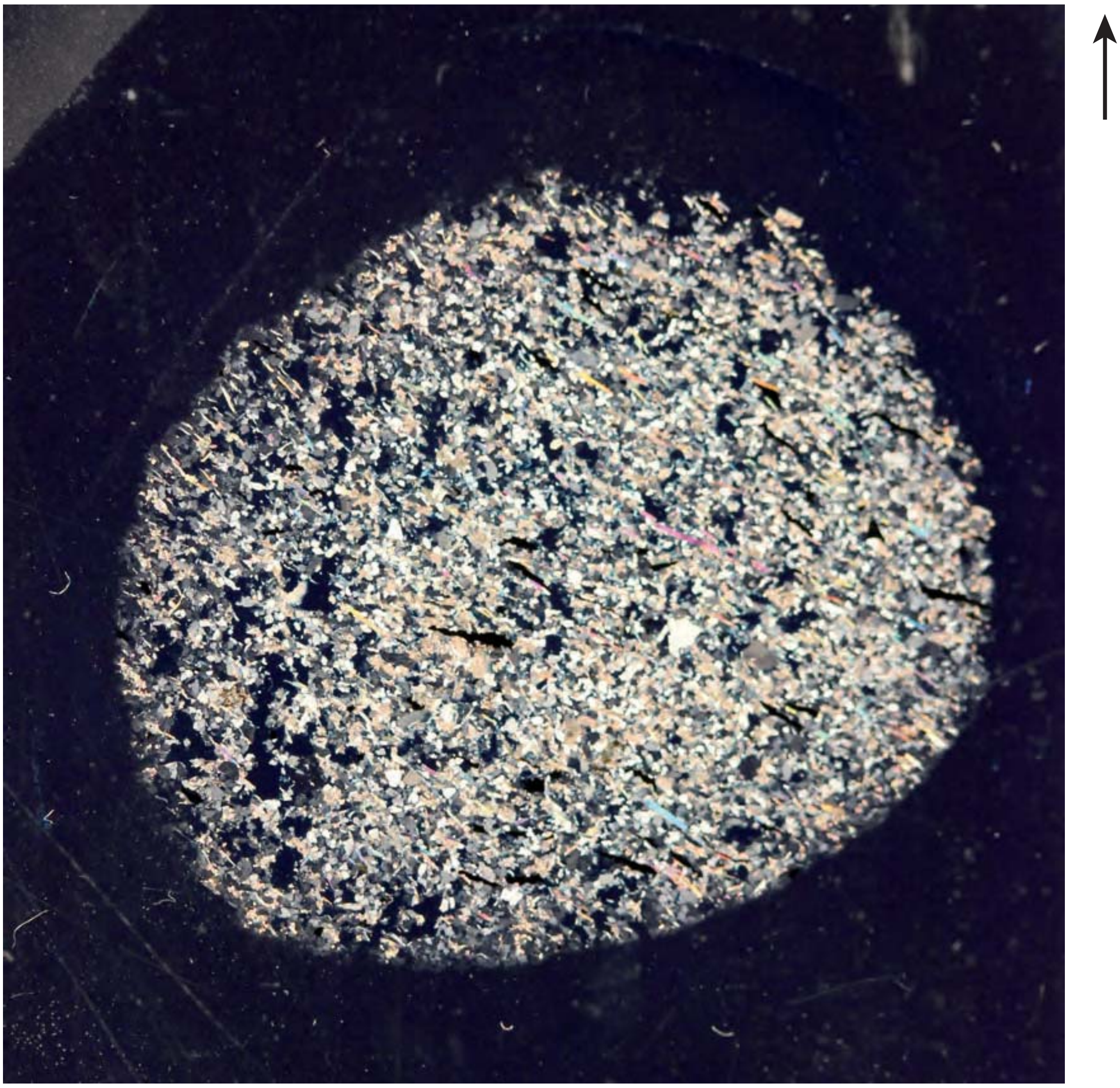

10 mm

517004–234

75.40 m

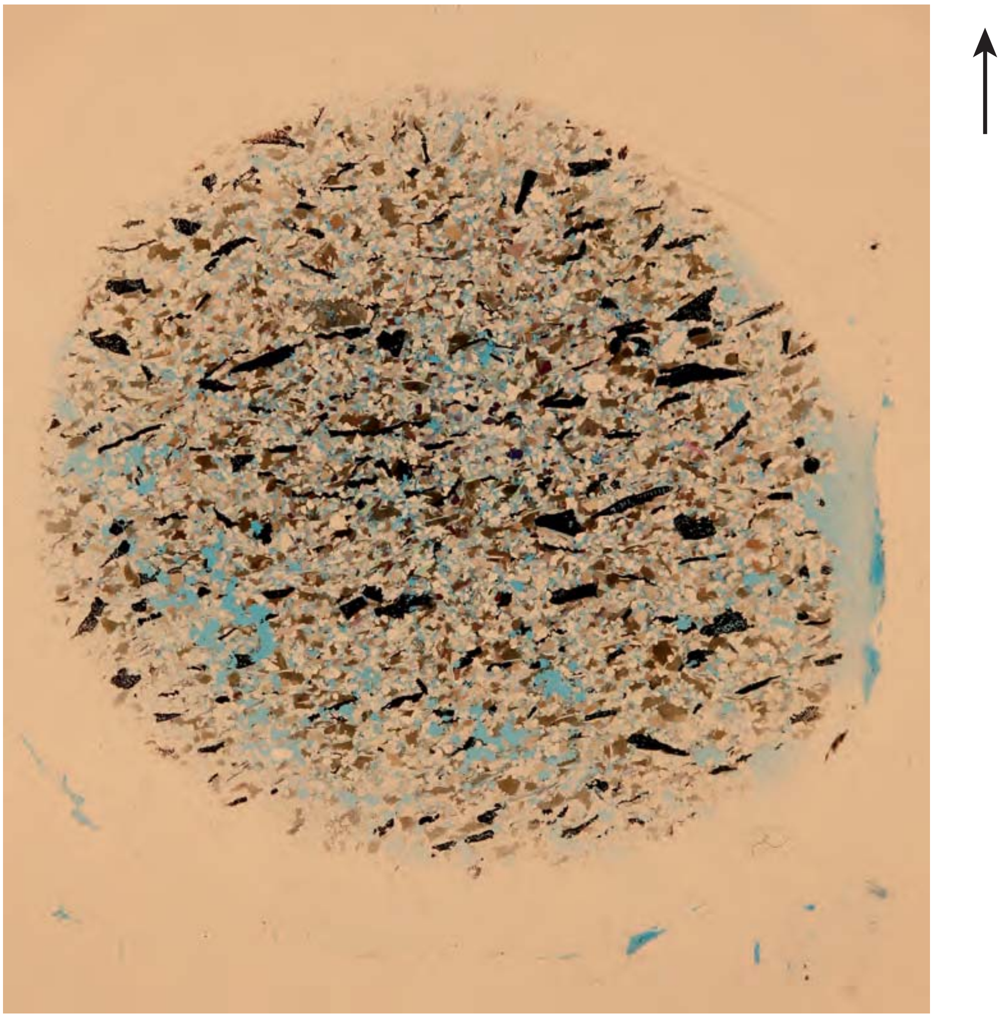

10 mm

517004–235 77.65 m

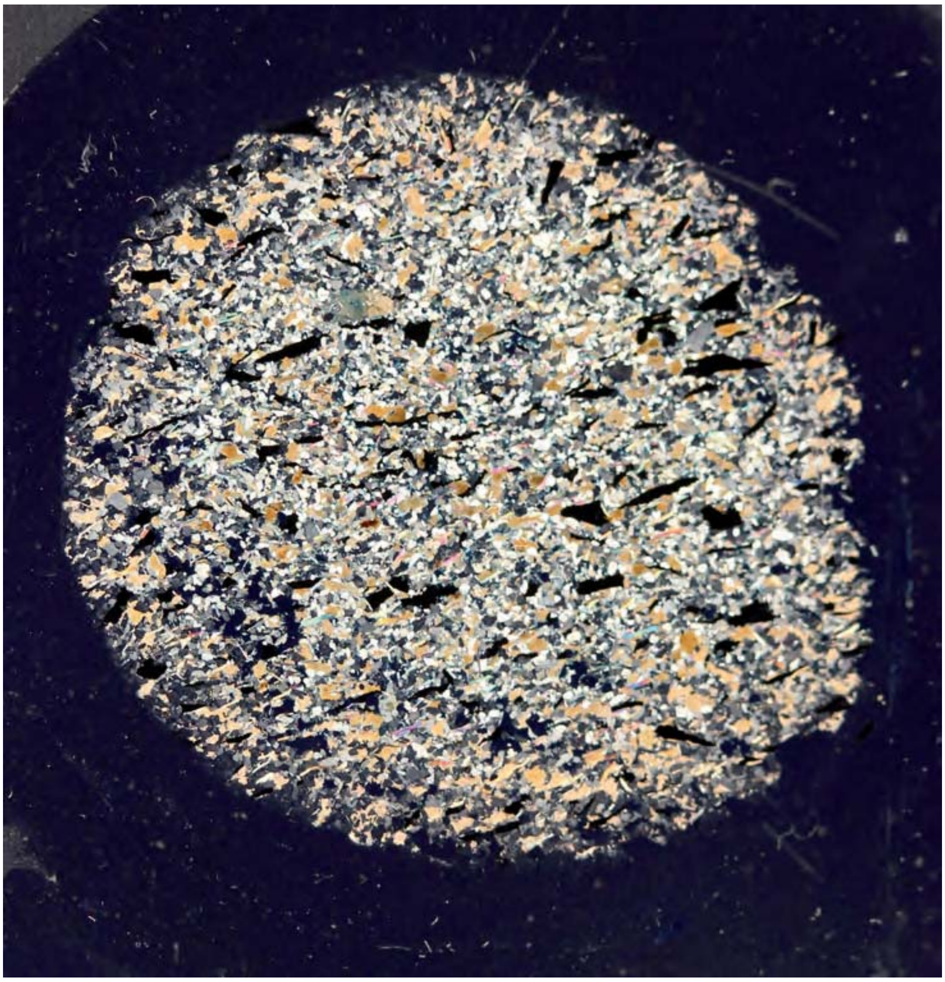

10 mm

517004–235 77.65 m

10 mm

517004–266

114.30 m

10 mm

517004–266

114.30 m

517004–265 10 mm 120.95 m

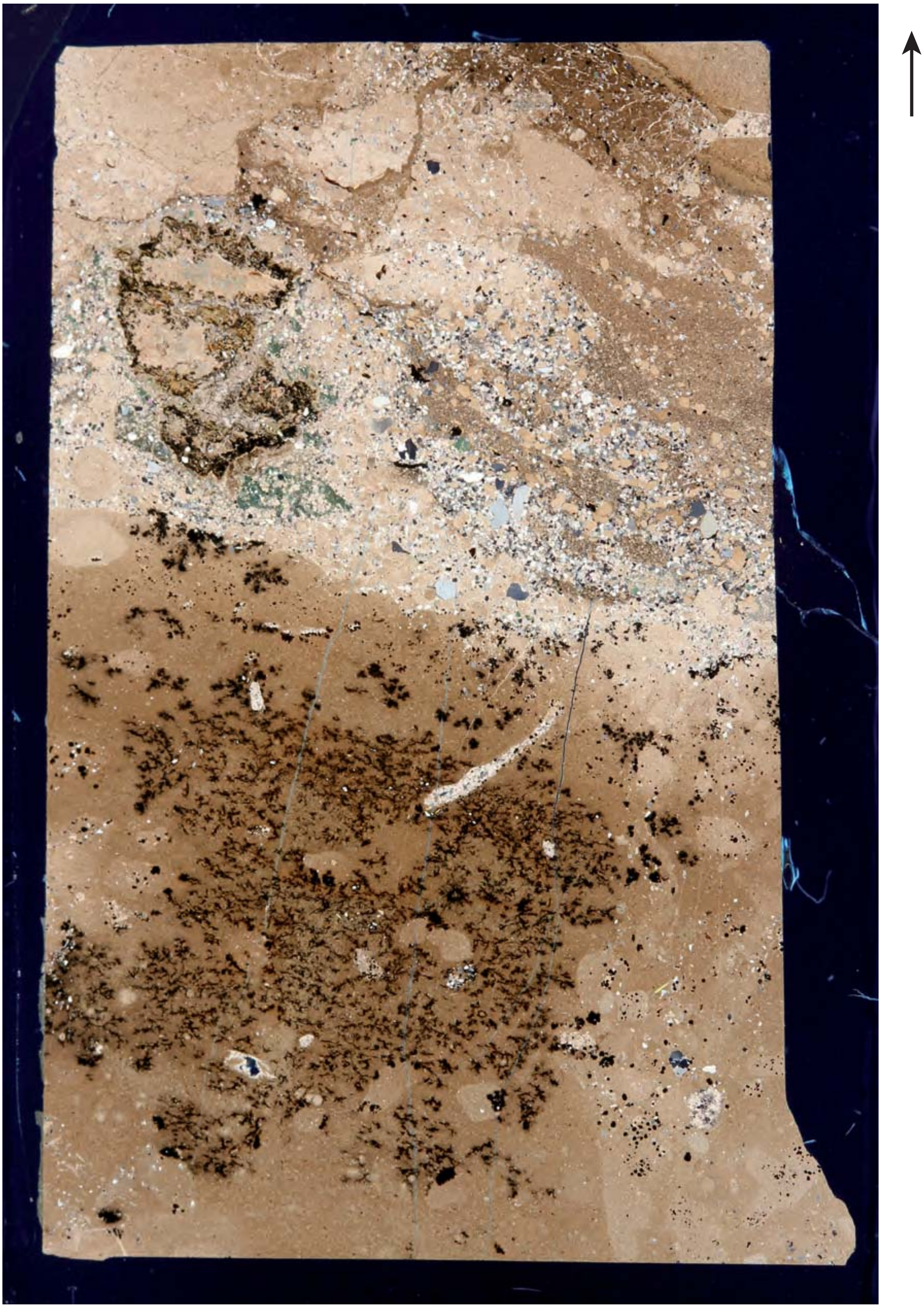

517004–265

10 mm

120.95 m

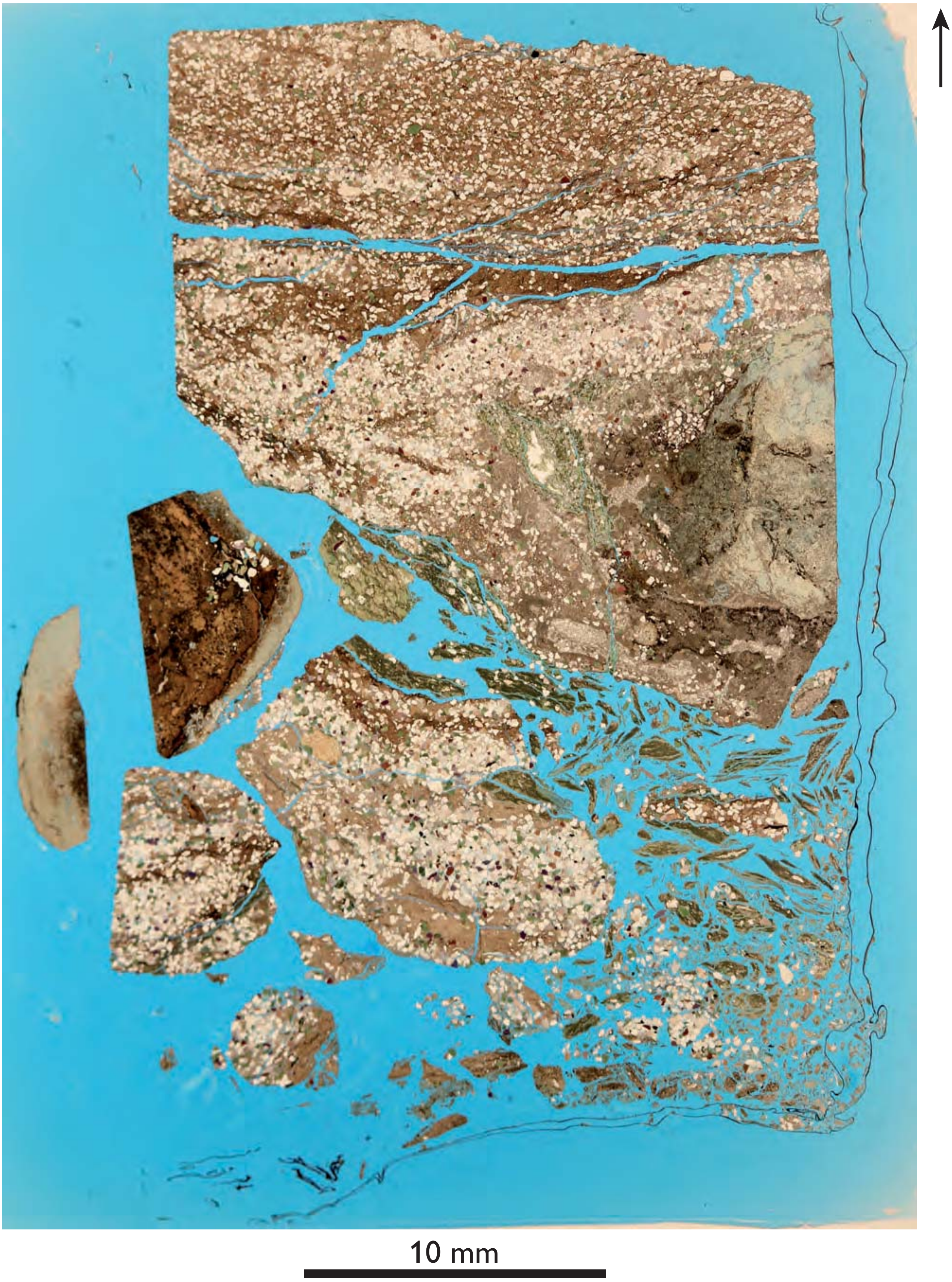

517004–261

133.10 m

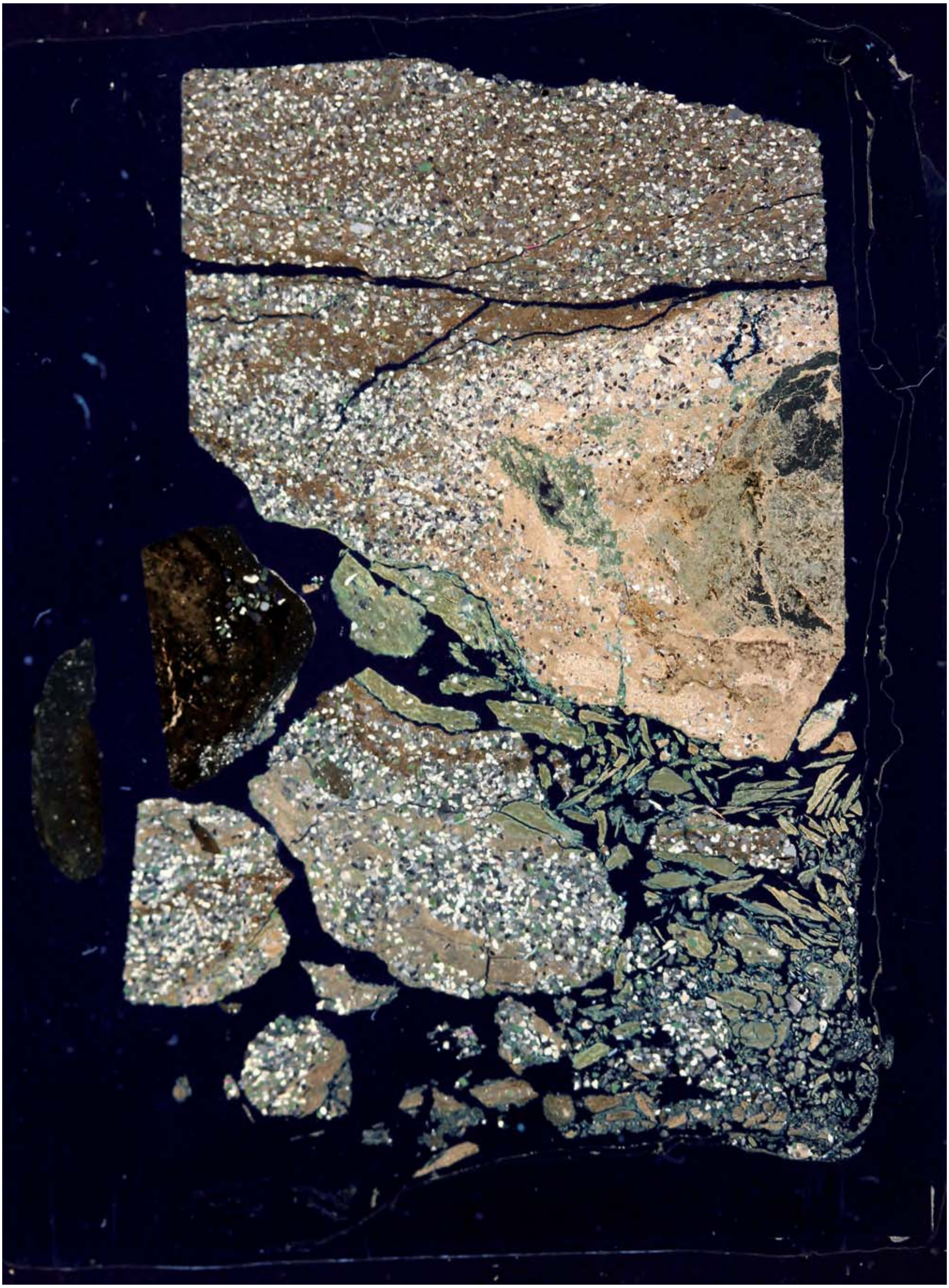

10 mm

517004–261

133.10 m

Nanok Mb; Outcrop sample

10 mm

Nanok Mb; Outcrop sample

12.3 Petrography of the Østersletten Mb

Thin section/sample: NA-1 45.40

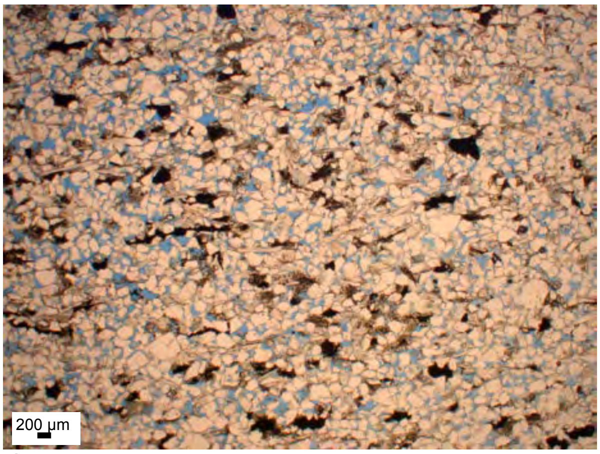

Overview

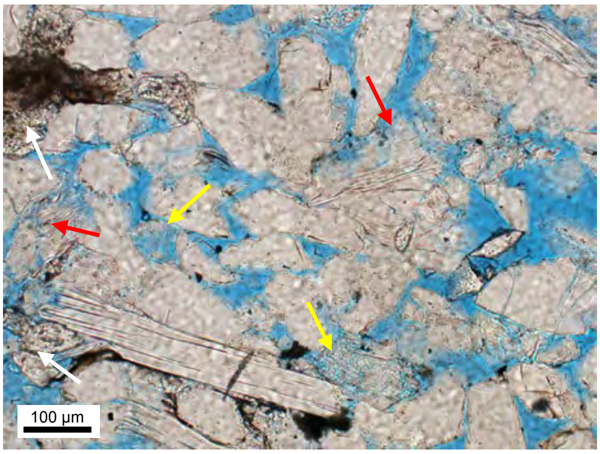

Close up of common authigenic phases: ankerite cement (white arrows), altered mica/kaolinite (red arrows). Notice partially dissolved feldspars (yellow arrows).

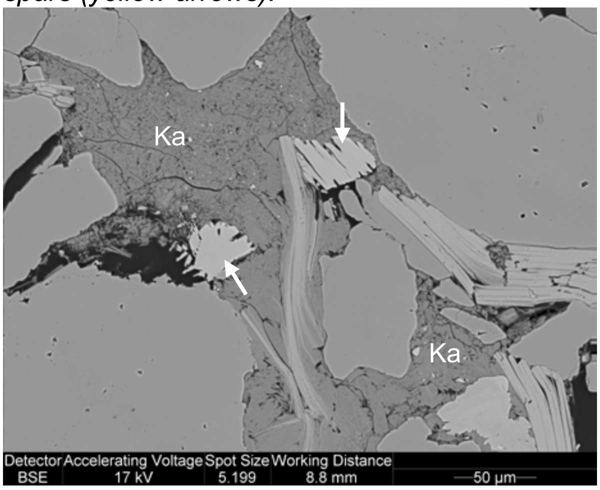

Pore-occluding dense kaolinite (Ka), together with mica and partially dissolved K-feldspars (arrows) (BSE image).

Well / locality: NANOK-1

Depth: 45.40 m

Fm / Mb: Østersletten Mb

Facies: Gravity flow

Sample preparation: None

Grain size range: Very fine − medium sand

Mean grain size: fine

Sorting: well

Porosity and permeability:
21 % and 184 mD

Framework grains:

Quartz dominates, K-feldspar is common (often partially or completely dissolved), mica flakes are common. Coal fragments are common. Heavy minerals occur sporadic.

Diagenetic changes:

Pyrite often associated with coal fragments. Early siderite cement, locally clustered or as single rhomboids. Kaolinite often replaces mica and may occur pore-occluding. Ankerite cement, which occur as single crystals or patchy pore-occluding cement. Feldspars are often wholly or partially dissolved. Sparse and incipient quartz cement.

Conclusion:

Fine-grained sandstone with relatively sparse quartz, siderite, ankerite and kaolinite cement and consequently of relatively good porosity and permeability.

Thin section/sample: NA-1 46.82

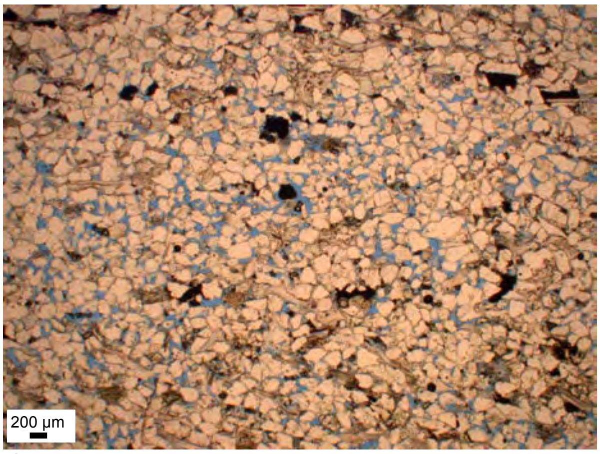

Overview

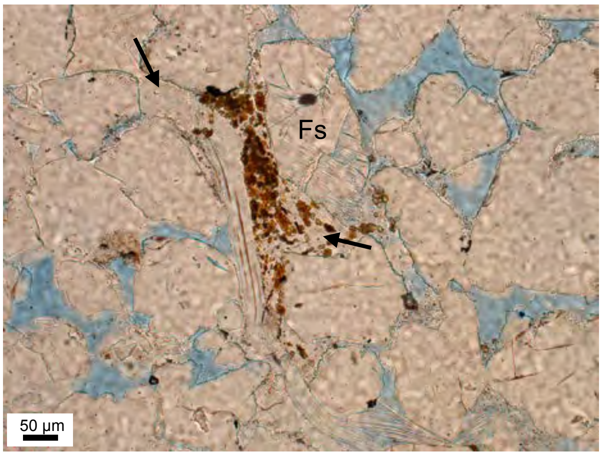

Kaolinite (arrows) from altered mica filling pores. Within kaolinite occurs siderite as brownish minute rhombs. Notice partially dissolved feldspars (Fs).

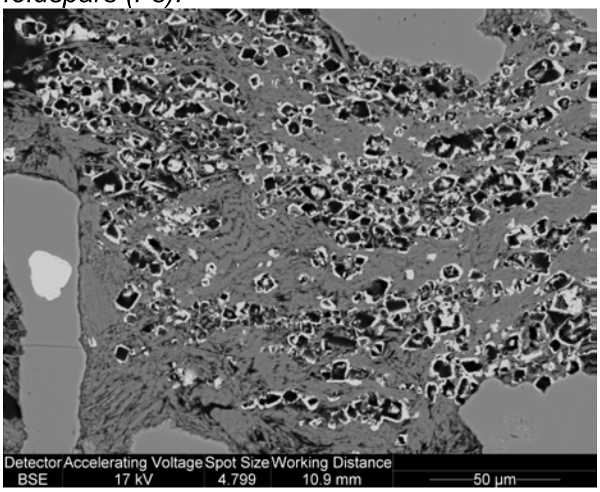

Pore-occluding kaolinite (grey matrix) containing siderite rhombs (white) (BSE image).

Well / locality: NANOK-1

Depth: 46.82 m

Fm / Mb: Østersletten Mb

Facies: Gravity flow

Sample preparation: None

Grain size range: Very fine – coarse sand

Mean grain size: Fine

Sorting: Well

Porosity and permeability:
24 % and 535 mD

Framework grains:

Quartz dominates, feldspar (dominantly K-feldspar) is common (often partially or completely dissolved), mica flakes are common. Coal fragments occur scattered and heavy minerals occur sporadic.

Diagenetic changes:

Sparse pyrite, which is often associated with coal fragments. Minor early siderite cement, which occur as single or clustered rhombs. Sporadic ankerite cement. Feldspars are often wholly or partially dissolved. Minor kaolinite as scattered pore-filling cement. Minor incipient quartz overgrowths.

Conclusion:

Fine grained sandstone with sparse quartz, carbonate and kaolinite cement and consequently of good porosity and permeability.

Thin section/sample: NA-1 48.47

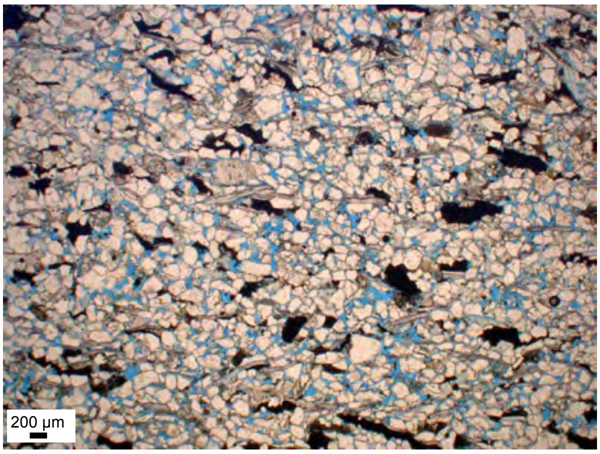

Overview

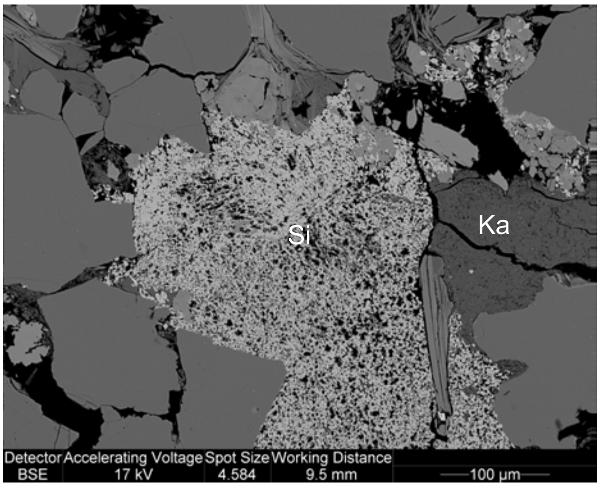

BSE image of pore-occluding siderite (Si) consisting of amalgamated rhombs forming vuggy texture. Kaolinite (Ka) is postdating the previously mentioned cement. Note secondary porosity from partially dissolved K-feldspar in upper right corner.

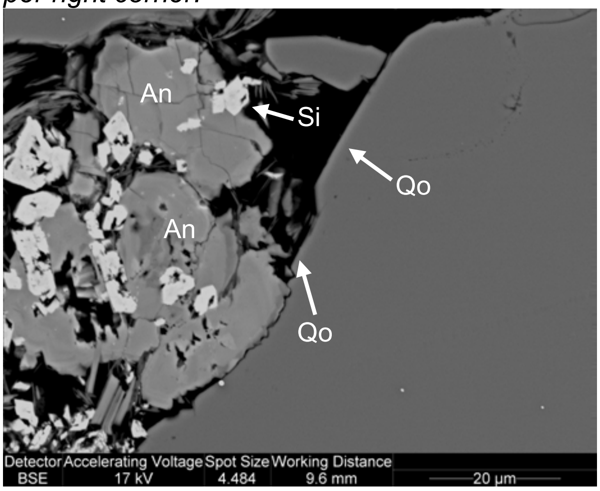

BSE image showing ankerite (An) enclosing rhombs of siderite (Si) and kaolinite booklets. Note incipient quartz overgrowth (Qo), which seems to postdate the dolomite.

Well / locality: NANOK-1

Depth: 48.47 m

Fm / Mb: Østersletten Mb

Facies: Gravity flow

Sample preparation: None

Grain size range: Very fine − coarse sand

Mean grain size: Fine

Sorting: Well

Porosity and permeability:
21 % and 87 mD

Framework grains:

Quartz dominates, feldspar (dominantly K-feldspar) is common and occur often partially or completely dissolved, mica flakes are common and may occur partially transformed into kaolinite. Coal fragments are common. Heavy minerals occur sporadic.

Diagenetic changes:

Minor pyrite which is often associated with coal fragments. Early siderite, which occur amalgamated or as single rhombs. Kaolinite often replaces mica and may occur dense and pore-occluding. Feldspar dissolution often contributing to secondary porosity. Ankerite cement, which may occur as single rhombohedral crystals or patchy pore-occluding cement. The dolomite is commonly zoned. The ankerite is often enclosing siderite and kaolinite. Only minor and incipient quartz cement occurs.

Conclusion:

Fine grained sandstone with relatively sparse quartz, carbonate and kaolinite cement and consequently of relatively good porosity and permeability.

Thin section/sample: NA-1 49.72

Overview

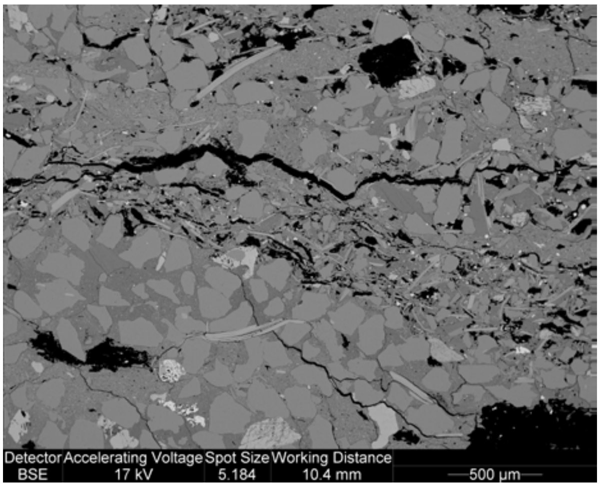

Overview (BSE image). Note that detrital clasts are floating in clayey matrix.

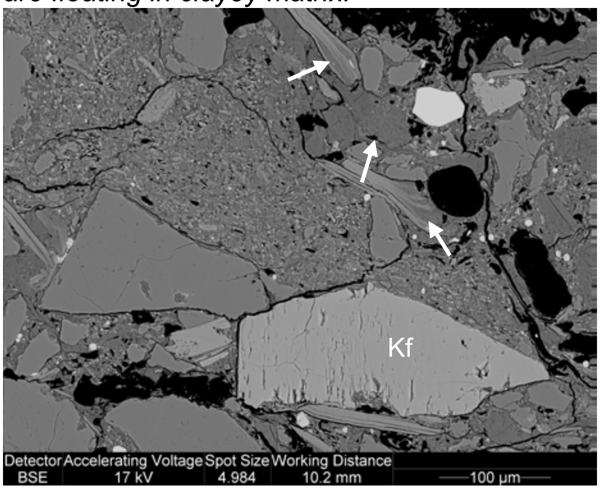

Close up on chaotic detrital clayey matrix consisting of kaolinitic/illitic clay. Authigenic kaolinite replacement of mica (arrows).Note weak K-feldspar (Kf) dissolution (BSE image).

Well / locality: NANOK-1

Depth: 49.72 m

Fm / Mb: Østersletten Mb

Facies: Gravity flow

Sample preparation: None

Grain size range: clayey – medium sand

Mean grain size: -

Sorting: very poor

Porosity and permeability:

No analysis

Framework grains:

Quartz dominate, feldspar (dominantly K-feldspar), mica flakes and coal fragments are common. Heavy minerals occur sporadic. Clayey matrix is kaolinitic/illitic.

Diagenetic changes:

Pyrite which is often associated with coal fragments.

Kaolinite which is often replacing mica.

Feldspars occur weakly partially dissolved.

Conclusion:

Bioturbated muddy fine-grained sandstone with abundant detrital clay in-filling pore spaces. In more sandy areas, without detrital clayey matrix the pore spaces are commonly occluded by authigenic kaolinite. In all this contributes to a very poor porosity and permeability in the sandstone.

Thin section/sample: NA-1 51.22

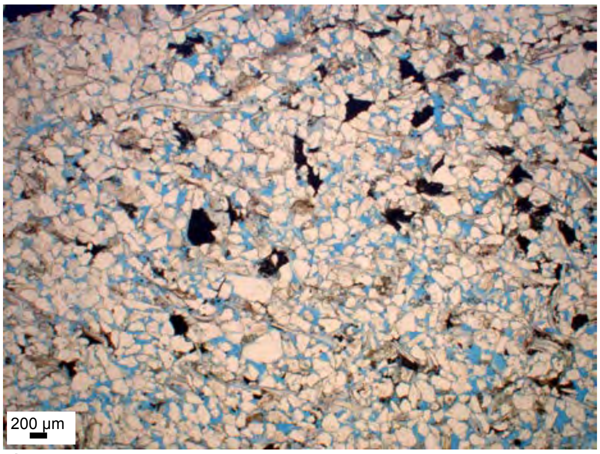

Overview

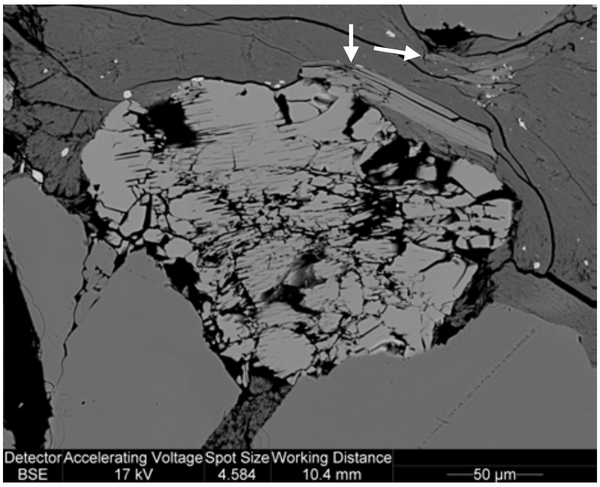

Close up of partially dissolved K-feldspar, surrounded by dense kaolinite. Note that the kaolinite is closely associated with mica (arrows).

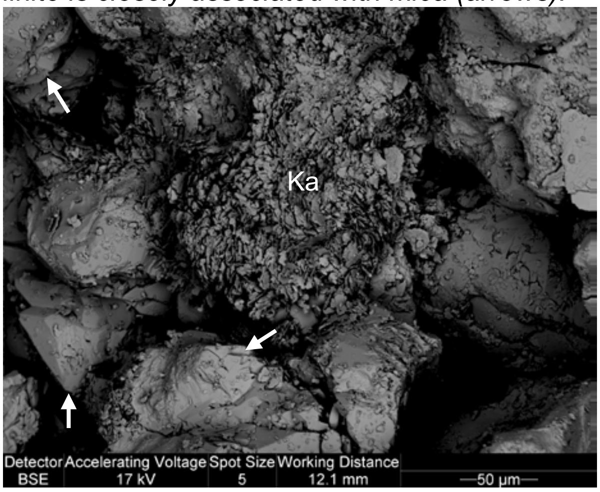

Pore-occluding kaolinite (Ka) and incipient euhedral quartz overgrowths (arrows). The quartz overgrowths are overgrowing kaolinite (SEM image).

Well / locality: NANOK-1

Depth: 51.22 m

Fm / Mb: Østersletten Mb

Facies: Gravity flow

Sample preparation: None

Grain size range: Very fine – coarse sand

Mean grain size: Fine (– medium)

Sorting: Moderate – well

Porosity and permeability:
22 % and 133 mD

Framework grains:

Quartz dominates, feldspar (dominantly K-feldspar) is common and often partially or completely dissolved, mica flakes are common and may occur partially transformed into kaolinite. Coal fragments are common. Heavy minerals occur sporadic.

Diagenetic changes:

Pyrite often associated with coal fragments. Early siderite cement, locally clustered or as single rhomboids. Kaolinite often replaces mica and may occur pore-occluding. Ankerite cement, which occur as single crystals or patchy pore-occluding cement. Feldspars are often wholly or partially dissolved. Sparse incipient quartz cement.

Conclusion:

Fine-grained sandstone with relatively sparse quartz, carbonate and kaolinite cement and consequently of relatively good porosity and permeability.

Thin section/sample: NA-1 54.00

Overview

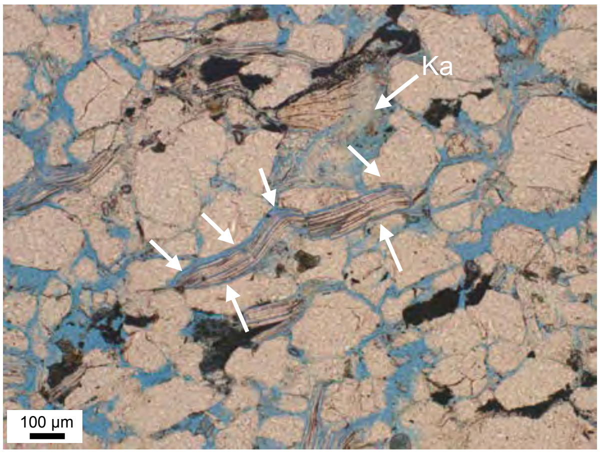

Quartz dissolution when in contact with mica flake. Above that notice kaolinite (Ka) in-filling oversized pore and partially transformation of mica into kaolinite.

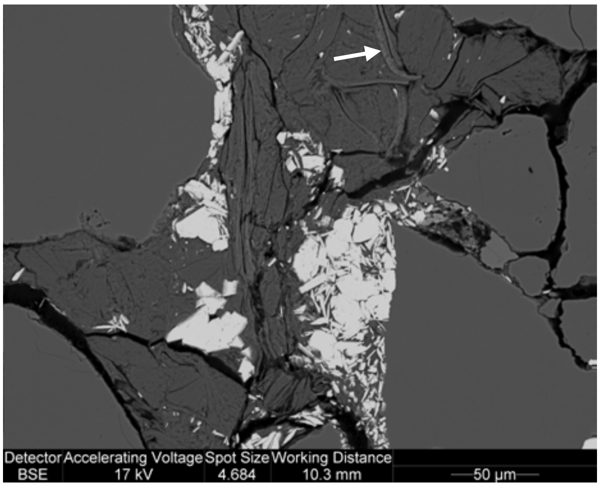

Pore-occluding vermiform and dense kaolinite, replacing mica (arrow). White mineral is pyrite (BSE image).

Well / locality: NANOK-1

Depth: 54.00 m

Fm / Mb: Østersletten Mb

Facies: Gravity flow

Sample preparation: None

Grain size range: Very fine – coarse sand

Mean grain size: Fine

Sorting: Well

Porosity and permeability:

23 % and 86 mD

Framework grains:

Quartz dominates, feldspar (dominantly K-feldspar) is common (often partially or completely dissolved), mica flakes are very common and may occur partially transformed into kaolinite. Coal fragments are common. Heavy minerals occur sporadic.

Diagenetic changes:

Early pyrite which is often associated with coal fragments, but also may occur as large crystals in pore spaces. Minor Early siderite and ankerite cement. Common pore-filling kaolinite. Feldspars are often wholly or partially dissolved. Quartz cement is minor and incipient.

Conclusion:

Fine grained sandstone with relatively sparse quartz, carbonate, but common kaolinite cement and c onsequently of relatively good porosity but lower permeability.

Thin section/sample: NA-1 57.10

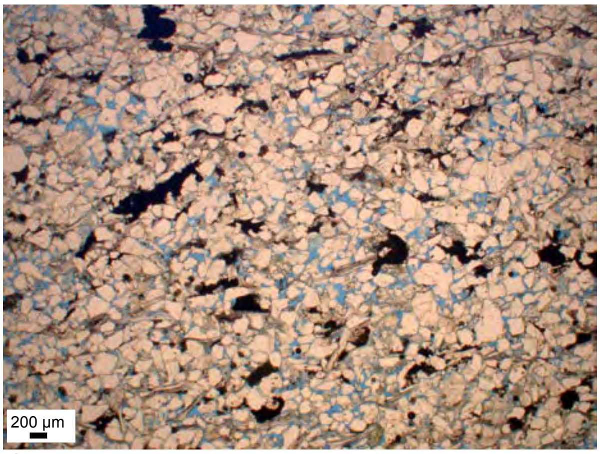

Overview

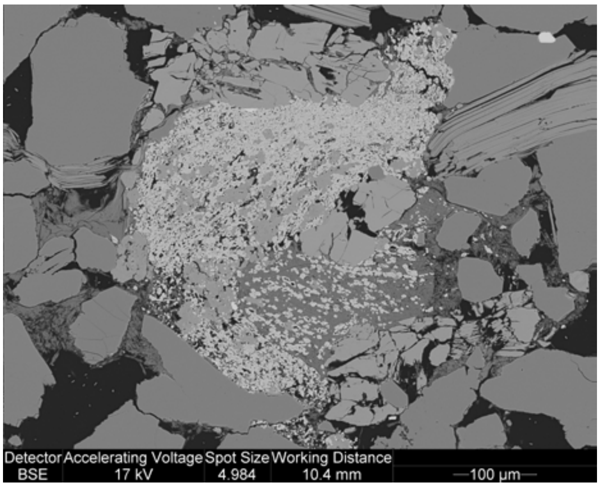

Pore-occluding kaolinite and siderite. Siderite could be replacement of former biotite clast. Notice partially dissolved feldspars at upper part of photo (BSE image).

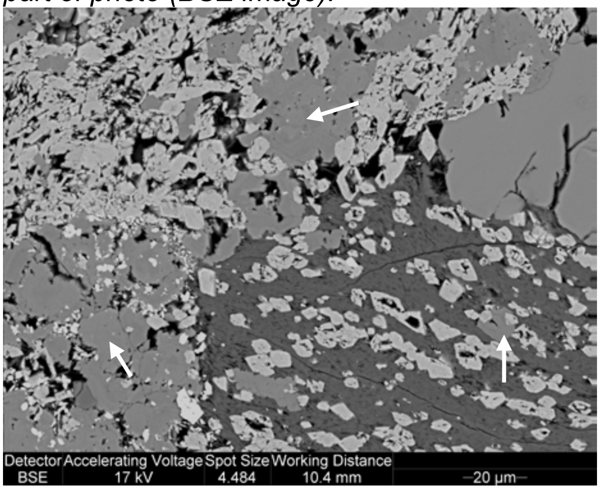

Close up on pore-occluding kaolinite and siderite from photo above. Within kaolinite occurs siderite as greyish-white minute rhombs. Grey cement (arrow) between rhombs and in kaolinite is ankerite (BSE image).

Well / locality: NANOK-1

Depth: 57.10 m

Fm / Mb: Østersletten Mb

Facies: Gravity flow

Sample preparation: None

Grain size range: Very fine – coarse sand

Mean grain size: Fine

Sorting: Well

Porosity and permeability:
19 % and 43 mD

Framework grains:

Quartz dominates, feldspar (dominantly K-feldspar) is common (often partially or completely dissolved), mica flakes are common and may occur partially transformed into kaolinite. Coal fragments are common. Heavy minerals occur sporadic.

Diagenetic changes:

Minor early pyrite which is often associated with coal fragments. Common early siderite and ankerite cement, which may be pore-occluding. Common kaolinite, which often is pore occluding. Feldspars are often wholly or partially dissolved, contributing to secondary porosity. Minor and incipient quartz cement.

Conclusion:

Fine grained sandstone with relatively sparse quartz, but common carbonate and kaolinite cement resulting in relatively good porosity but lower permeability.

Thin section/sample: NA-1 59.75

Overview

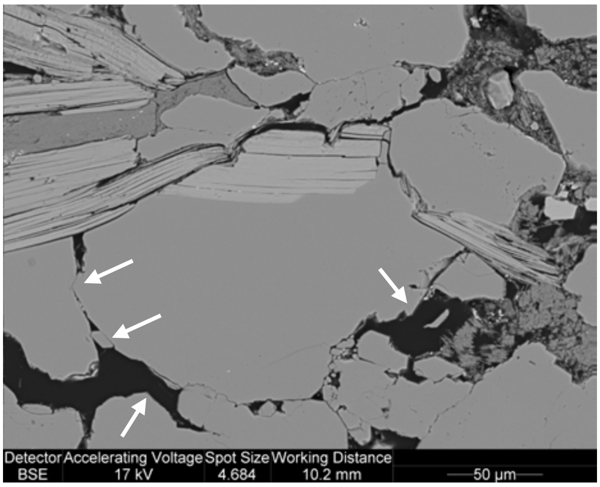

BSE image showing incipient quartz overgrowths on detrital quartz (arrows). Authigenic dense kaolinite between mica (upper left) and booklets in pore space on the right of photo. Note conformable/straight contacts between quartz and mica (on the left of the photo).

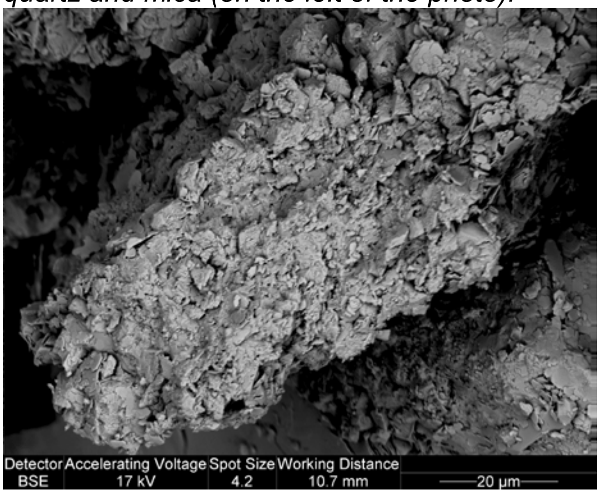

Pore-occluding siderite in association with kaolinite booklets (SEM image).

Well / locality: NANOK-1

Depth: 59.75 m

Fm / Mb: Østersletten Mb

Facies: Gravity flow

Sample preparation: None

Grain size range: Very fine – coarse sand

Mean grain size: Fine

Sorting: Well

Porosity and permeability:
16 % and 7 mD

Framework grains:

Quartz dominates, feldspar (dominantly K-feldspar) is common (often partially or completely dissolved), mica flakes are common and may occur partially transformed into kaolinite. Heavy minerals occur sporadic. Coal fragments are common.

Diagenetic changes:

Minor early pyrite which is commonly associated with coal fragments. Common early carbonate cement and abundant pore-filling kaolinite. Feldspars are often wholly or partially dissolved. Minor and incipient quartz cement.

Conclusion:

Fine grained sandstone with relatively minor quartz cement, common carbonate cement but abundant mica and authigenic pore-filling kaolinite causing low porosity and permeability.

Thin section/sample: NA-1 60.90

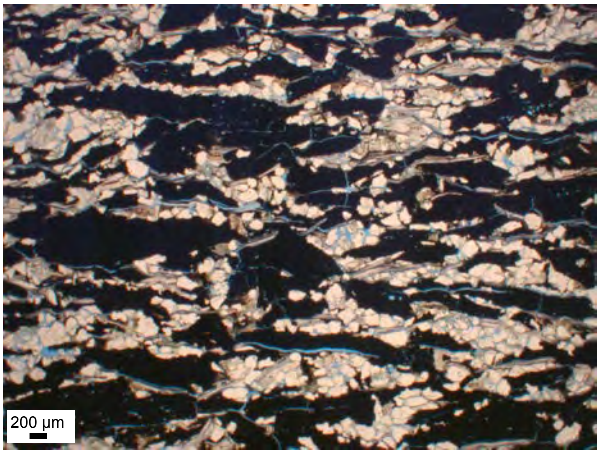

Overview

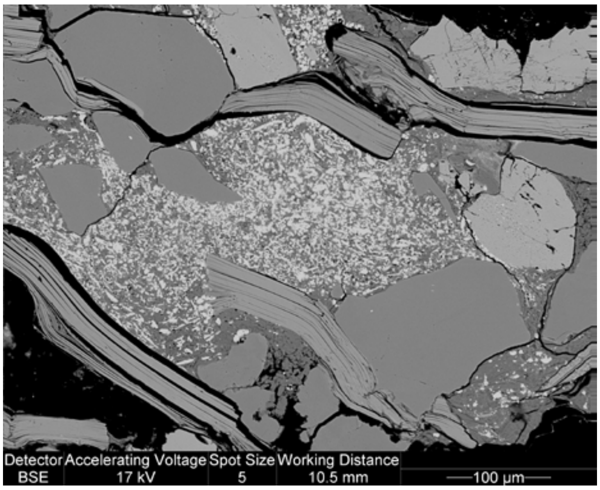

Pore-occluding kaolinite containing white minute rhombs of siderite (BSE image).

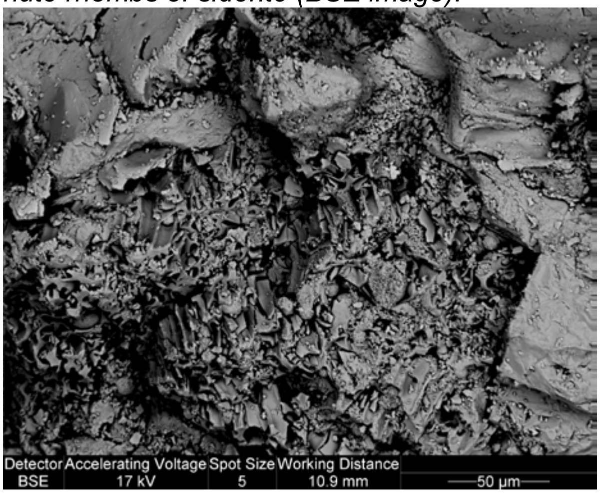

SEM image showing woody tissue texture of coal fragment, where tissue cells contains pyrite.

Well / locality: NANOK-1

Depth: 60.90 m

Fm / Mb: Østersletten Mb

Facies: Gravity flow

Sample preparation: None

Grain size range: Very fine – medium sand

Mean grain size: Fine

Sorting: Well

Porosity and permeability:

No analysis

Framework grains:

Quartz dominates, feldspar (dominantly K-feldspar) is common (often partially or completely dissolved), mica flakes are common and may occur partially transformed into kaolinite. Heavy minerals occur sporadic. Coal fragments are abundant and constitute 40-50 % of the sample.

Diagenetic changes:

Early pyrite which is often associated with coal fragments. Common early siderite cement and abundant pore-filling kaolinite. Feldspars are often wholly or partially dissolved. Very little and incipient quartz.

Conclusion:

Fine grained sandstone with a large content of coal fragments. Areas in sample consisting of sand contain a large amount of pore-occluding kaolinite. The sample therefore is assessed to have very low porosity and permeability.

Thin section/sample: NA-1 62.25

Overview

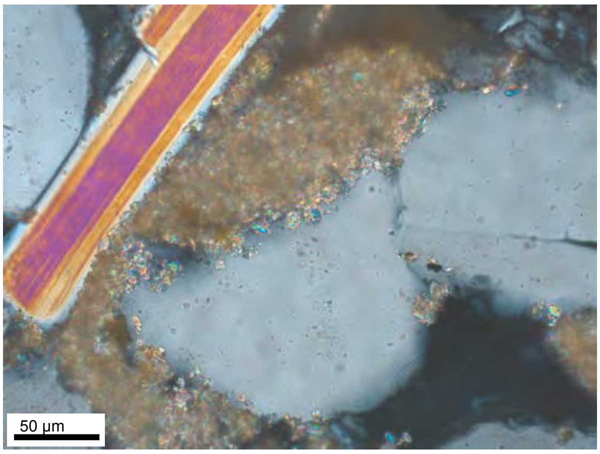

Minute brownish siderite rhombs in association with mica and overgrown by incipient quartz cement (XN: Crossed Nicols).

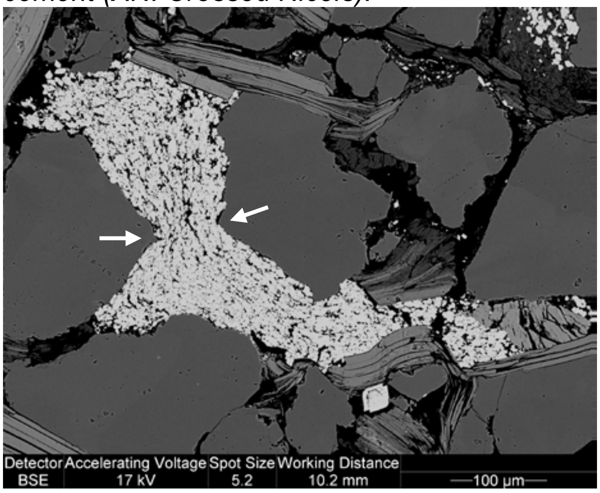

Pore-occluding and expanded (arrows) cement consisting of amalgamated siderite rhombs. Probably replacement of former biotite flake (BSE image).

Well / locality: NANOK-1

Depth: 62.25 m

Fm / Mb: Østersletten Mb

Facies: Gravity flow

Sample preparation: None

Grain size range: Very fine – coarse sand

Mean grain size: Fine (– medium)

Sorting: Well

Porosity and permeability:
19 % and 15 mD

Framework grains:

Quartz dominates, feldspar (dominantly K-feldspar) is common (often partially or completely dissolved), mica flakes are common and may occur partially transformed into kaolinite. Coal fragments are very common. Heavy minerals occur sporadic.

Diagenetic changes:

Minor early pyrite which is often associated with coal fragments. Common early siderite cement and abundant pore filling kaolinite. Feldspars are often wholly or partially dissolved, contributing to secondary porosity. Minor incipient quartz cement.

Conclusion:

Fine grained sandstone with relatively minor quartz cement but common siderite and abundant pore-filling kaolinite and consequently of relatively low porosity and permeability.

Thin section/sample: NA-1 62.45

Overview

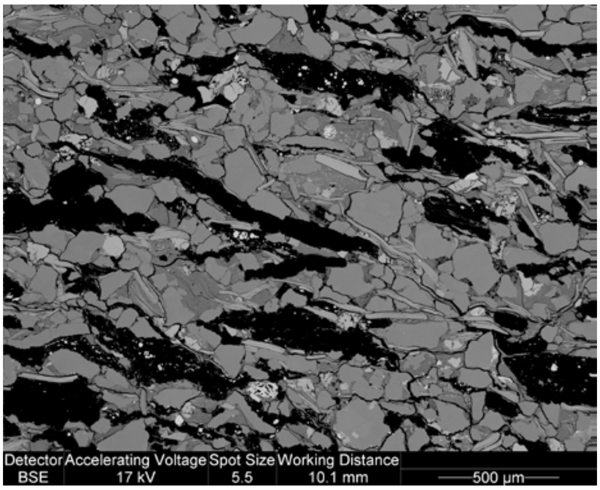

BSE image showing an overview, revealing abundant pore-occluding kaolinite as the predominant authigenic phase.

Close up of pore-occluding kaolinite. Note bended and partially transformed muscovite on the left of photo (arrow). Whitish mineral in centre of photo is rare Ti-oxide (BSE image).

Well / locality: NANOK-1

Depth: 62.45 m

Fm / Mb: Østersletten Mb

Facies: Gravity flow

Sample preparation: None

Grain size range: Very fine – medium

Mean grain size: Fine

Sorting: Well

Porosity and permeability:

No analysis

Framework grains:

Quartz dominates, feldspar (dominantly K-feldspar) is common (often partially or completely dissolved), mica flakes are very common and may occur partially transformed into kaolinite. Coal fragments are very common. Heavy minerals occur sporadic.

Diagenetic changes:

Common early pyrite which is often associated with coal fragments. Minor early siderite cement and abundant pore-occluding kaolinite. Feldspars are often wholly or partially dissolved, contributing to secondary porosity. Quartz cement is sparse and only incipient.

Conclusion:

Fine grained sandstone with abundant coal fragments, mica and pore occluding kaolinite, resulting in low porosity and permeability.

Thin section/sample: NA-1 63.45

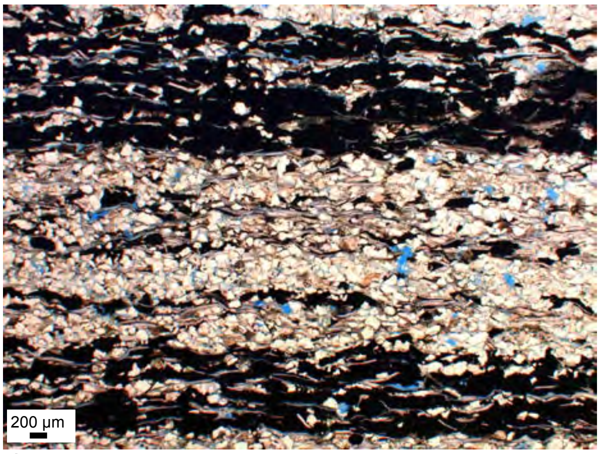

Overview

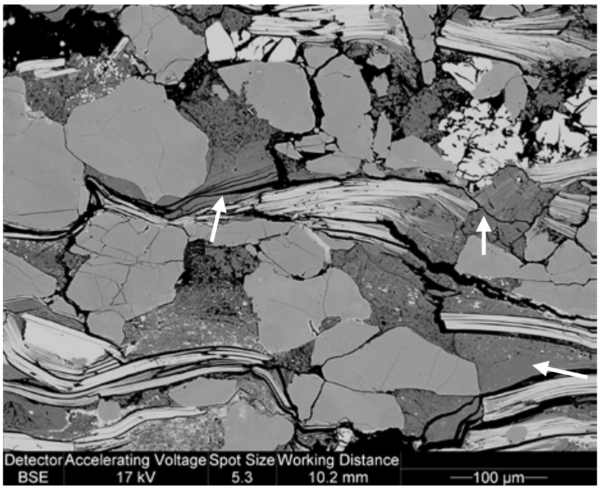

Close up of common authigenic phases: kaolinite from altered mica (arrows) and scattered siderite as whitish minute rhombs (BSE-image).

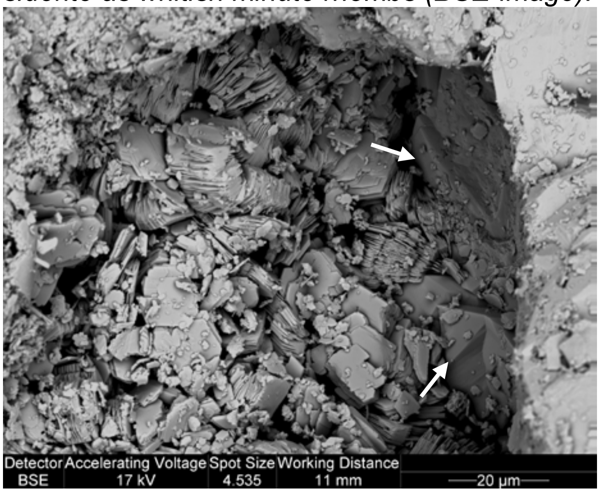

Pore-occluding kaolinite booklets. Minor incipient quartz overgrowths (arrows)(SEM image).

Well / locality: NANOK-1

Depth: 63.45 m

Fm / Mb: Østersletten Mb

Facies: Gravity flow

Sample preparation: None

Grain size range: Very fine – medium sand

Mean grain size: Fine

Sorting: Well

Porosity and permeability:

No analysis

Framework grains:

Quartz dominates, feldspar (dominantly K-feldspar) is common (often partially or completely dissolved), mica flakes are very common and may occur partially transformed into kaolinite. Heavy minerals occur sporadic.

Coal fragments are abundant and occur in laminae.

Diagenetic changes:

Common early pyrite which is often associated with coal fragments. Scattered early siderite rhombs, which mostly occurs in abundant pore-occluding kaolinite. Feldspars are often wholly or partially dissolved, contributing to secondary porosity. Sparse incipient quartz cement.

Conclusion:

Laminated fine-grained sandstone and allochthonous coal. The sandstone laminae contain abundant mica and pore-occluding kaolinite resulting in low porosity and permeability.

Thin section/sample: NA-1 63.72

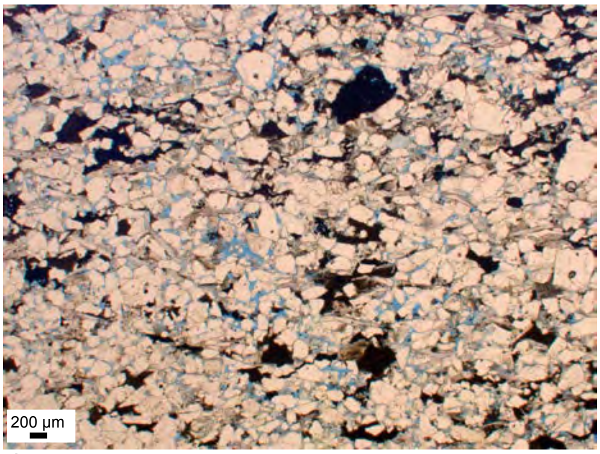

Overview

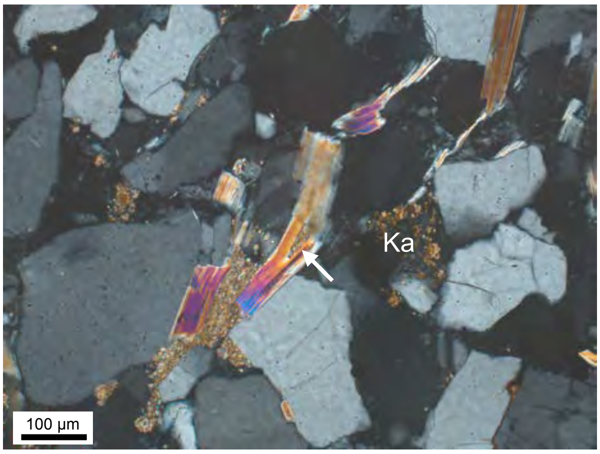

Displacive siderite within muscovite flake (ar-row) and associated with mica. Siderite as brownish minute rhombs also occurs within kaolinite (Ka)(XN).

SEM image of rhombohedrale siderite (Si), to-gether with kaolinite in-filling pore spaces. Note incipient quartz overgrowths (arrows).

Well / locality: NANOK-1

Depth: 63.72 m

Fm / Mb: Østersletten Mb

Facies: Gravity flow

Sample preparation: None

Grain size range: Very fine – coarse sand

Mean grain size: Fine – medium

Sorting: Moderate

Porosity and permeability:
19 % and 26 mD

Framework grains:

Quartz dominates, feldspar (dominantly K-feldspar) is common (often partially or com-pletely dissolved), mica flakes are common and may occur partially transformed into kaolinite. Coal fragments are common. Heavy minerals occur sporadic.

Diagenetic changes:

Minor early pyrite which is often associated with coal fragments. Common early siderite and common pore-filling kaolinite. Feldspars are often wholly or partially dissolved. Minor and incipient quartz cement.

Conclusion:

Fine grained sandstone with relatively minor quartz cement, but common carbonate cement and pore-filling kaolinite, which results in lower porosity and permeability.

Thin section/sample: NA-1 66.22

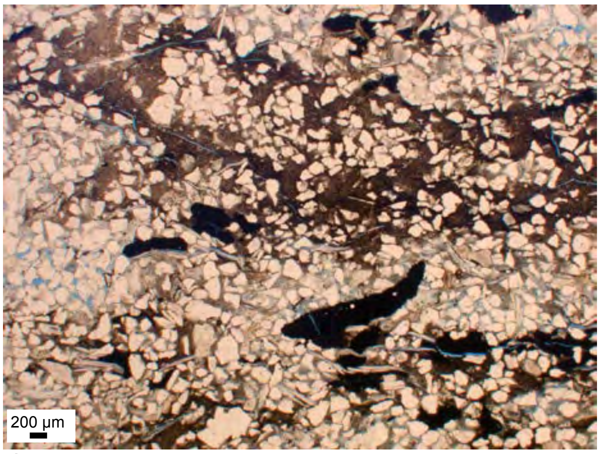

Overview

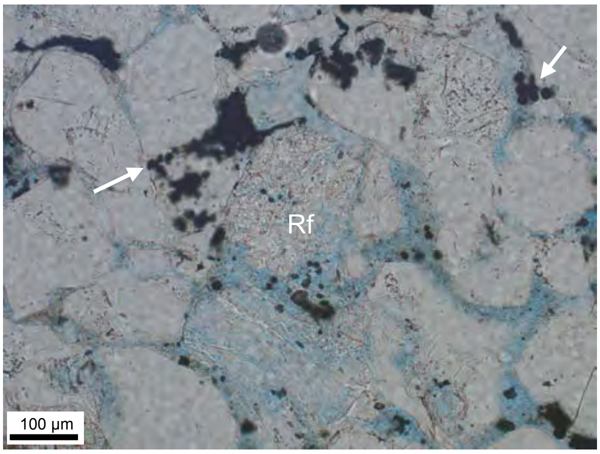

Close up of partially dissolved rock fragment (Rf). Black dots and black areas are pyrite framboids (arrows)and organic matter.

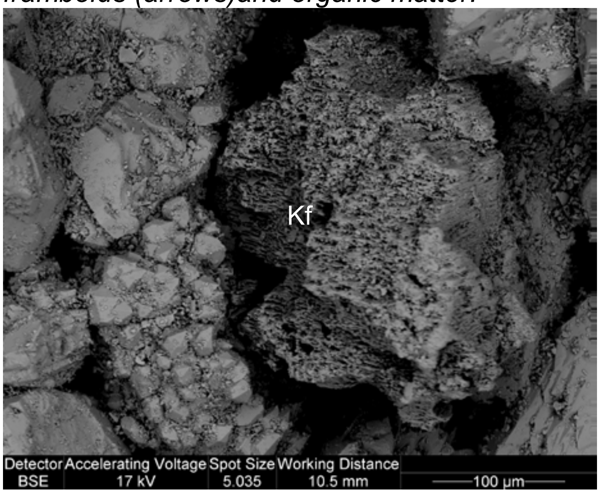

SEM image showing partially dissolved K-feldspar (Kf). Note incipient syntaxial quartz overgrowths on the grain to the left.

Well / locality: NANOK-1

Depth: 66.22 m

Fm / Mb: Østersletten Mb

Facies: Gravity flow

Sample preparation: None

Grain size range: Clayey – coarse sand

Mean grain size: -

Sorting: Very poor

Porosity and permeability:
13 % and 4 mD

Framework grains:

Quartz dominates, feldspar (dominantly K-feldspar) is common (often partially or completely dissolved), mica flakes are common and may occur partially transformed into kaolinite. Heavy minerals occur sporadic. Coal fragments are common. Detrital clay and silt is very common in pore spaces.

Diagenetic changes:

Minor early pyrite which is often associated with coal fragments. Minor early siderite and common kaolinite. Feldspars are often wholly or partially dissolved. Sparse incipient quartz cement.

Conclusion:

Muddy fine-grained sandstone with abundant detrital pore-filling clay and common Mg-siderite and authigenic kaolinite in pore spaces, results in very low porosity and permeability.

Thin section/sample: NA-1 66.72

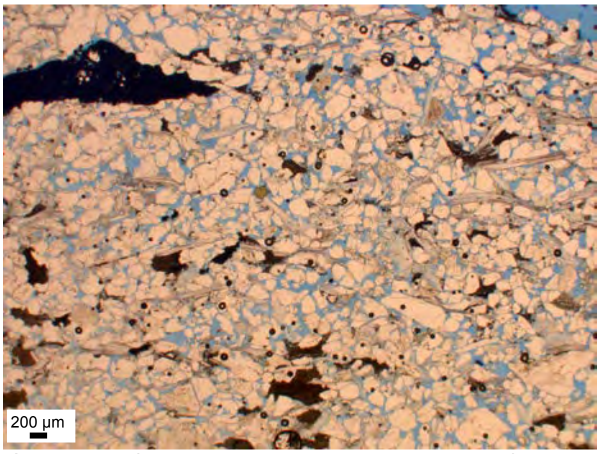

Overview (Black dots are contamination from thin section preparation).

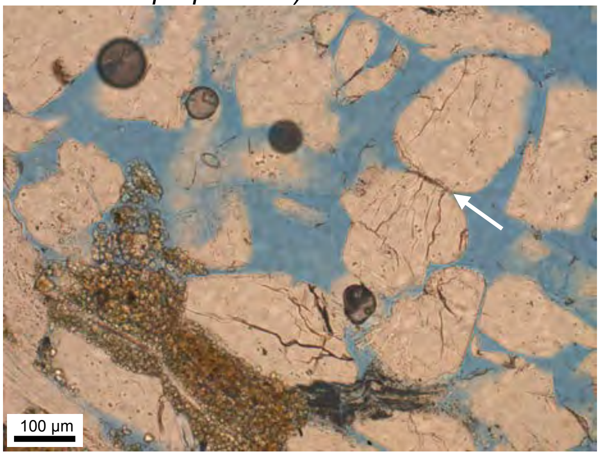

Rare example of grain fracturing due to compaction (arrow). Associated with mica occurs siderite as brownish minute rhombs. Notice partially dissolved feldspars.

Whitish rhombs of siderite scattered and some engulfed by patchy ankerite (arrows). Note incipient quartz overgrowths, kaolinite booklets and partially dissolved K-feldspar (BSE image).

Well / locality: NANOK-1

Depth: 66.72 m

Fm / Mb: Østersletten Mb

Facies: Gravity flow

Sample preparation: None

Grain size range: Very fine – very coarse sand

Mean grain size: Fine (– medium)

Sorting: Moderate

Porosity and permeability:
23 % and 265 mD

Framework grains:

Quartz dominates, feldspar (dominantly K-feldspar) is common (often partially or completely dissolved), mica flakes are common and may occur partially transformed into kaolinite. Coal fragments occurs scattered. Heavy minerals occur sporadic.

Diagenetic changes:

Minor early pyrite which is often associated with coal fragments. Minor early siderite cement and ankerite with zonation. Minor pore-filling kaolinite. Feldspars are often wholly or partially dissolved, contributing to secondary porosity. Quartz cement is minor and only incipient.

Conclusion:

Fine grained sandstone with relatively sparse quartz and carbonate cement and only minor kaolinite, resulting in good porosity and permeability.

Thin section/sample: NA-1 68.85

Well / locality: NANOK-1

Depth: 68.85 m

Fm / Mb: Østersletten Mb

Facies: Gravity flow

Sample preparation: None

Grain size range: Very fine – very coarse sand

Mean grain size: Fine – medium

Sorting: Moderate

Porosity and permeability:
21 % and 148 mD

Framework grains:

Quartz dominates, feldspar (dominantly K-feldspar) is common (often partially or completely dissolved), mica flakes are common and may occur partially transformed into kaolinite. Coal fragments are common. Heavy minerals occur sporadic.

Diagenetic changes:

Early but minor pyrite which is often associated with coal fragments. Minor early siderite. Minor pore-occluding kaolinite and ankerite. Feldspars are often wholly or partially dissolved, contributing to secondary porosity. Minor and incipient quartz cement.

Conclusion:

Fine grained sandstone with relatively minor quartz cement, carbonate and kaolinite cement and consequently of relatively good porosity and permeability.

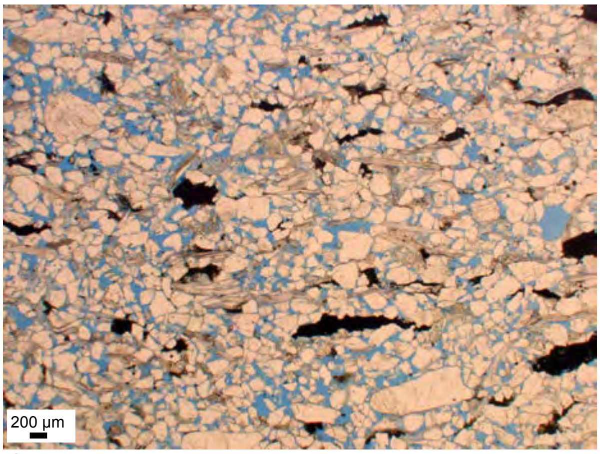

Overview

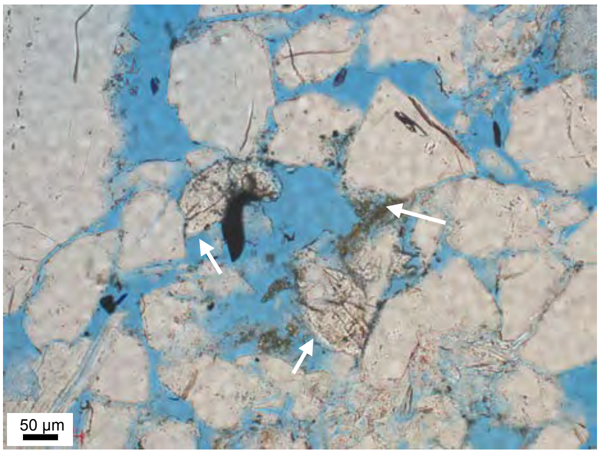

Minute brownish siderite rhombs and patchy ankerite in secondary pore (arrows).Kaolinite and partially transformed mica in lower right corner.

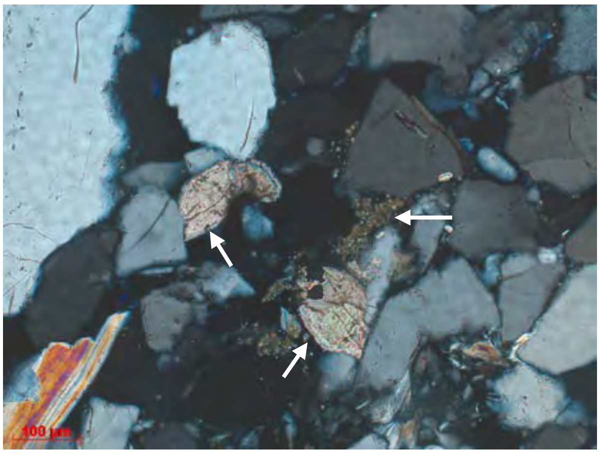

Same image as above (XN).

Thin section/sample: NA-1 69.50

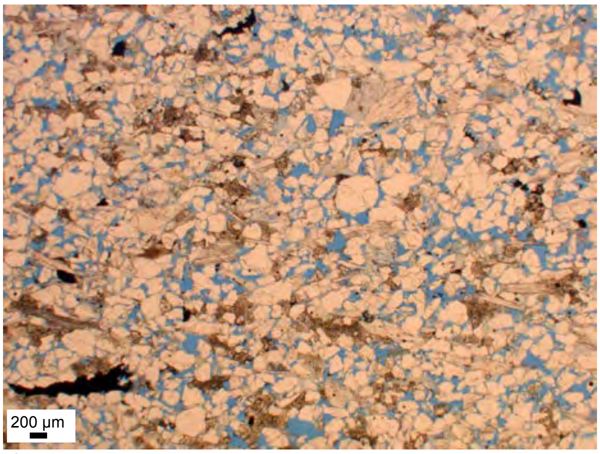

Overview.

BSE image showing zoned patchy ankerite. Partially dissolved K-feldspars in lower left and right corner.

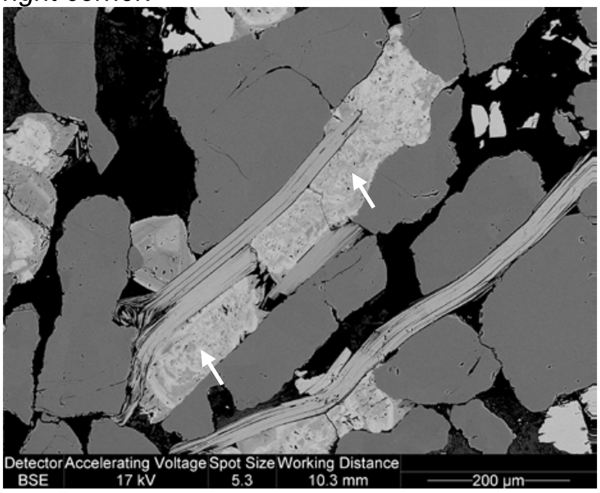

Displacive? ankerite (arrows) (BSE image).

Well / locality: NANOK-1

Depth: 69.50 m

Fm / Mb: Østersletten Mb

Facies: Gravity flow

Sample preparation: None

Grain size range: Very fine - coarse sand

Mean grain size: Fine (– medium)

Sorting: Well

Porosity and permeability:
19 % and 155 mD

Framework grains:

Quartz dominates, feldspar (dominantly K-feldspar) is common (often partially or completely dissolved), mica flakes are common and may occur partially transformed into kaolinite. Coal fragments occur scattered. Heavy minerals occur sporadic.

Diagenetic changes:

Pyrite which is often associated with coal fragments. Early siderite cement. Mica is often replaced by kaolinite. The kaolinite may be pore occluding. Ankerite is patchy and may occlude pore spaces. Feldspars are often wholly or partially dissolved, contributing to secondary porosity. Quartz cement is sparse and incipient.

Conclusion:

Fine grained sandstone with relatively minor quartz cement, ankerite and kaolinite cement and consequently of relatively good porosity and permeability.

Thin section/sample: NA-1 72.38

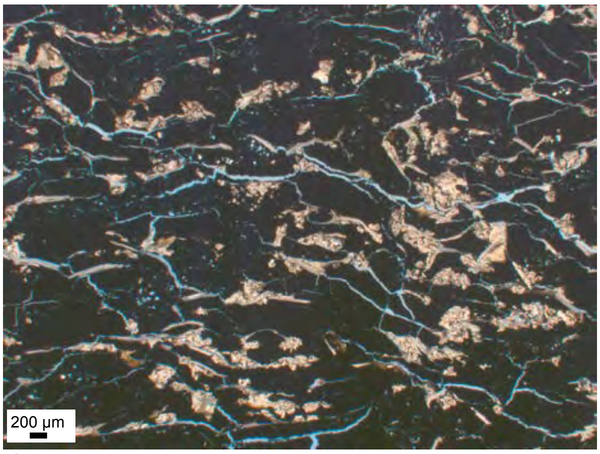

Overview

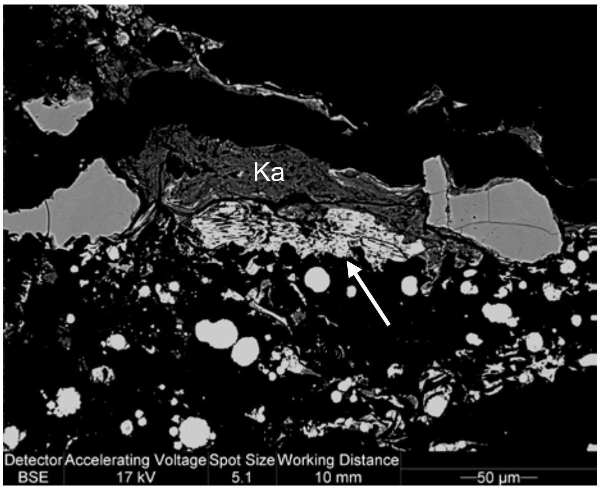

Close up of pyrite framboids in coal fragments (black). Further is seen kaolinite (Ka) and partially dissolved K-feldspar (greyish-white; arrow) (BSE-image).

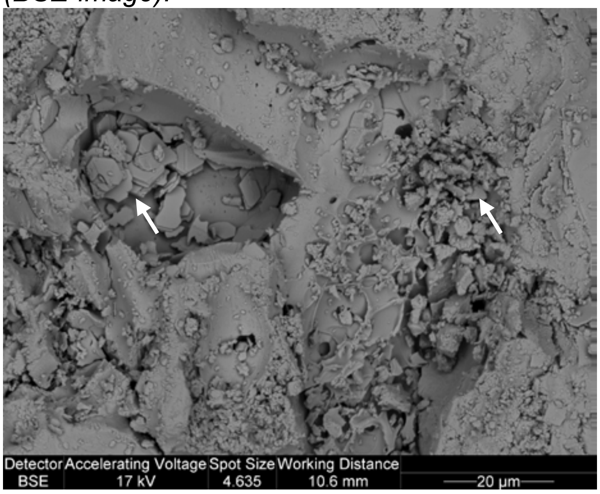

Kaolinite booklets (arrows) in woody tissue cells of coal fragment (SEM image).

Well / locality: NANOK-1

Depth: 72.38 m

Fm / Mb: Østersletten Mb

Facies: Gravity flow

Sample preparation: None

Grain size range: -

Mean grain size: -

Sorting: -

Porosity and permeability:

No analysis

Framework grains:

The samples may be characterized as sandy allochthonous coal. The inorganic clasts which occur are quartz, feldspar (dominantly K-feldspar) and mica flakes.

Diagenetic changes:

Abundant pyrite which is normally associated with coal fragments.

Kaolinite occur densely pack and as booklets in tissue cells in the coal fragments.

Feldspars are often wholly or partially dissolved.

Conclusion:

Accumulation of coal fragments with no reservoir properties.

Thin section/sample: NA-1 75.40

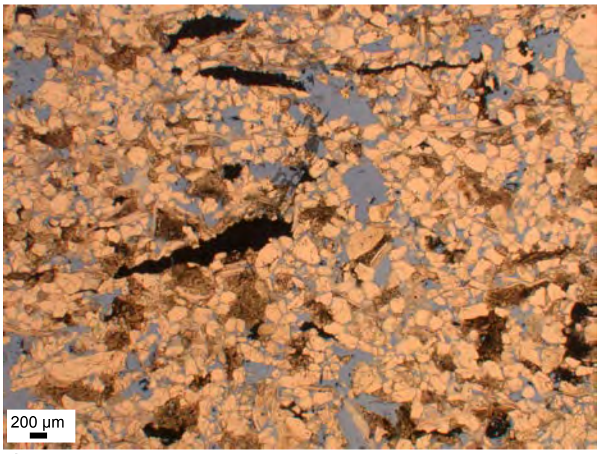

Overview. Brownish areas are mainly dolomite cement.

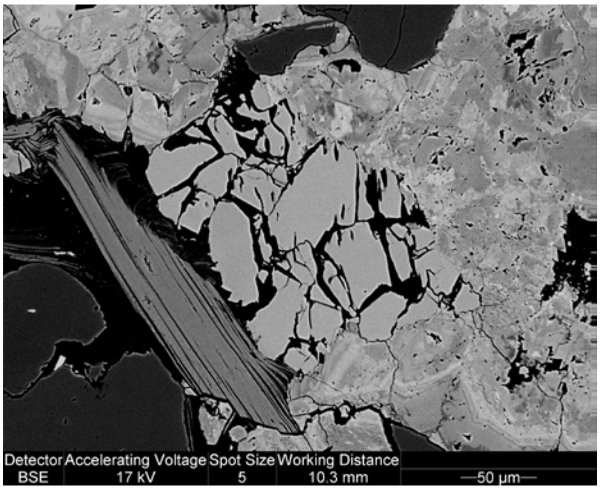

Pore occluding ankerite surrounding or only weakly growing into partially dissolved feldspar. K-feldspar dissolution therefore postdates ankerite precipitation (BSE image).

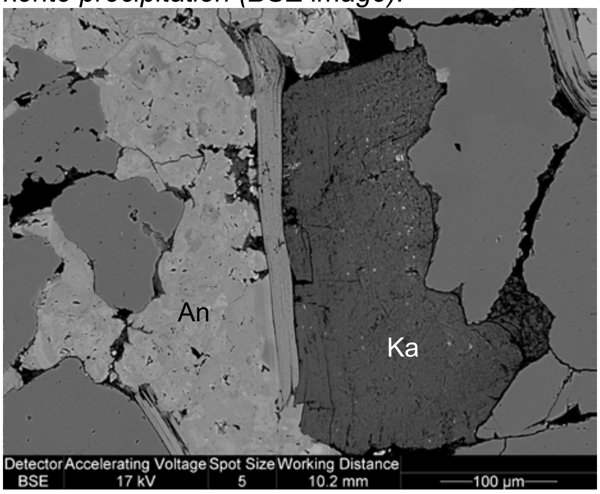

Pore-filling ankerite (An) and kaolinite (Ka). Note dense striated appearance of kaolinite, which probably is a reminiscences from mica transformation (BSE image).

Well / locality: NANOK-1

Depth: 75.40 m

Fm / Mb: Østersletten Mb

Facies: Gravity flow

Sample preparation: None

Grain size range: Very fine–coarse sand

Mean grain size: Fine (– medium)

Sorting: Moderate

Porosity and permeability:

20% and 197 mD

Framework grains:

Quartz dominates, feldspar (dominantly K-feldspar) is common (often partially or completely dissolved), mica flakes are common and may occur partially transformed into kaolinite. Coal fragments are common. Heavy minerals occur sporadic.

Diagenetic changes:

Minor pyrite which is often associated with coal fragments. Minor early siderite cement. Kaolinite replacement of mica. Patchy ankerite cement. Sparse and incipient quartz cement. Feldspars are often wholly or partially dissolved, contributing to secondary porosity.

Conclusion:

Fine-grained sandstone with relatively minor quartz cement, only patchy kaolinite and ankerite cement and consequently of relatively good porosity and p ermeability. Enhancing secondary porosity contributes to total porosity.

Thin section/sample: NA-1 77.65

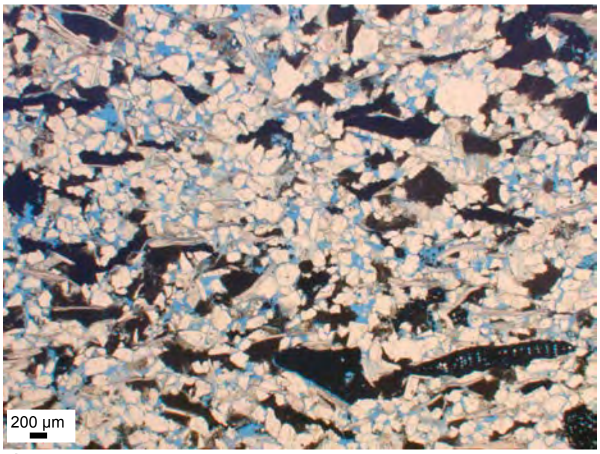

Overview

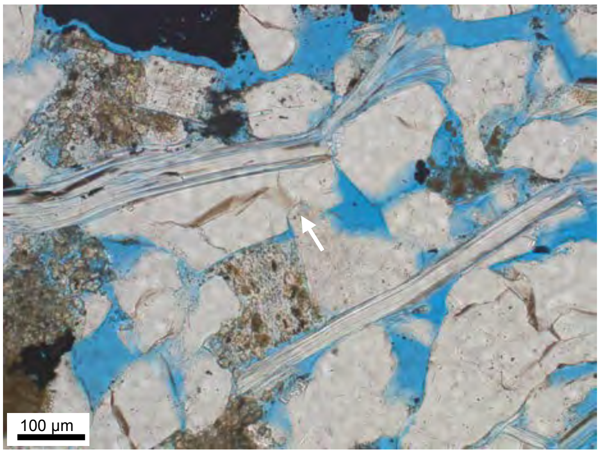

Kaolinite wherein siderite occurs as brownish minute rhombs. Notice straight/conformable contacts between mica and quartz as well as contact dissolution between detrital quartz grains (arrow).

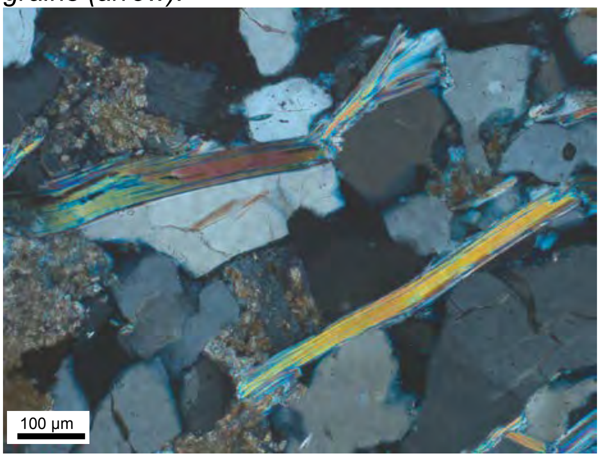

Same photograph as previously (XN).

Well / locality: NANOK-1

Depth: 77.65 m

Fm / Mb: Østersletten Mb

Facies: Gravity flow

Sample preparation: None

Grain size range: Very fine – coarse sand

Mean grain size: Fine (– medium)

Sorting: Moderate

Porosity and permeability:

20 % and 48 mD

Framework grains:

Quartz dominates, feldspar (dominantly K-feldspar) is common (often partially or completely dissolved), mica flakes are common and may occur partially transformed into kaolinite. Heavy minerals occur sporadic. Coal fragments are very common.

Diagenetic changes:

Pyrite which is often associated with coal fragments. Early siderite cement is very common (replacement of detrital biotite flakes?). Kaolinite often occurs as pore-filling cement. Feldspars are often wholly or partially dissolved. Sparse and incipient quarts cement.

Conclusion:

Fine grained sandstone with relatively minor quartz cement but with some carbonate cement and kaolinite in pore spaces. Porosity is relatively good but limited permeability.